Physics of the Solid State, Vol. 44, No. 2, 2002, pp. 199–203. Translated from Fizika Tverdogo Tela, Vol. 44, No. 2, 2002, pp. 193–197.

METALS AND SUPERCONDUCTORS

Electrical Resistivity of Microinhomogeneous $PdMn_xFe_{1-x}$ Alloys

N. I. Kourov, M. A. Korotin, and N. V. Volkova

Institute of Metal Physics, Ural Division, Russian Academy of Sciences, ul. S. Kovalevskoĭ 18, Yekaterinburg, 620219 Russia
e-mail: kourov@imp.uran.ru

Received May 15, 2001

Abstract—The electronic band-structure calculations of the PdFe ferromagnet and the PdMn antiferromagnet performed in this work permit one to conclude that the specific features of the electrical resistivity observed in the ternary $PdMn_xFe_{1-x}$ alloy system [the deviation from the Nordheim–Kurnakov rule $\rho_0(x) \sim x(1-x)$, which is accompanied by a high maximum of residual resistivity (not typical of metals) $\rho_0^m \sim 220$ μΩ cm at $x_C \sim 0.8$ and a negative temperature resistivity coefficient in the interval $0.5 \le x \le 1$] are due to the microinhomogeneous (multiphase) state of the alloys and a variation in the band-gap parameter *d* spectrum caused by antiferromagnetic ordering of a PdMn-type phase. © *2002 MAIK "Nauka/Interperiodica".*

1. The concentration dependence of the residual resistivity $\rho_0(x)$ of the $PdMn_xFe_{1-x}$ ternary alloy system determined experimentally in [1] has a fairly unusual form (Fig. 1). It does not follow the Nordheim–Kurnakov relation, which is usually satisfied in quasi-binary solid solutions [2]:

$$\rho_0 \sim x(1-x). \quad (1)$$

First, the maximum of $\rho_0(x)$ is observed at a critical concentration $x_C \sim 0.8$, which does not coincide with its value 0.5 following from Eq. (1). In contrast to Eq. (1), the $\rho_0(x)$ relation for $PdMn_xFe_{1-x}$ alloys has an asymmetric shape. Second, near x_C, the residual resistivity increases up to maximum values $\rho_0^m \sim 220$ μΩ cm, which are unusually high for metal alloys. Accepting the weak potential scattering approximation in which Eq. (1) was derived, this growth should be ~10 μΩ cm.

It appears natural to relate the behavior of $\rho_0(x)$ observed in $PdMn_xFe_{1-x}$ ternary alloys to specific features in their structural and magnetic states [3–5]. These alloys may only be considered single phase and ordered in the $L1_0$ structure close to extreme compositions. For $x < x_1 \sim 0.2$, they are ferromagnets with the limiting value of the Curie temperature $T_{C1} = 730$ K for PdFe and antiferromagnets for $x > x_2 \sim 0.8$ with $T_N = 815$ K for PdMn. In the intermediate concentration region $0.2 < x < 0.8$, the alloys represent a microinhomogeneous multiphase medium, both structurally and magnetically, which simultaneously contains two phases (of the PdMn and PdFe type) shaped as extended platelets typically measuring 1–100 μm or greater. For $T < 1000$ K, both the phases have the $L1_0$ structure but with different weakly concentration-dependent lattice parameters and degrees of tetragonality. The magnetic moments in the PdFe-type phase are ordered ferromagnetically (F_1) [3–6]; in the PdMn-type phase, antiferromagnetically (*A*) [7]. Moreover, an additional F_2 phase with noncollinearly ordered moments forms in the intermediate alloy concentration region, most likely, along the precipitation boundaries of the main F_1 and *A* phases. In view of such a multiphase state, there are indeed no grounds to expect the $PdMn_xFe_{1-x}$ system to follow the Nordheim–Kurnakov rule of Eq. (1).

2. A comparison of the concentration dependences of the electrical resistivity measured at $T = 4.2$ K $\ll (T_{C1}, T_N)$ and for $T \sim 850$ K $\ge T_{C1}$ shows that the behavior of $\rho_0(x)$ in the $PdMn_xFe_{1-x}$ ternary system is related primarily to specific features of the magnetic state of the alloys. As seen from Fig. 1a, for $T > T_{C1}, T_N$, the resistivity varies weakly with concentration and can be described, within experimental accuracy, by the expression

$$\rho(x) = 138 - 34x + 130x(1-x). \quad (2)$$

This appears only natural, because for $T > (T_{C1}, T_N, \Theta_D)$, where $\Theta_D = 374$–340 K is the Debye temperature [5], the spin-disordered and phonon components of the resistivity are dominant and their variation with concentration can be roughly fitted by a linear function. The electronic component can be neglected because of its being comparatively small.

In addition to these contributions, an analysis of the $\rho(x)$ relation for the $PdMn_xFe_{1-x}$ alloys using Eq. (2) should take into account, for any temperature, contributions of the type of Eq. (1), which originate from conduction electron scattering on nonuniformities of the Coulomb potential. This resistivity component (without the inclusion of the potential nonuniformities associated with exchange interaction) should remain constant in the transition from the paramagnetic to a magnetically ordered state, because the crystalline structure of all samples of the system under study does not change in the magnetic phase transition [4, 5].

1063-7834/02/4402-0199$22.00

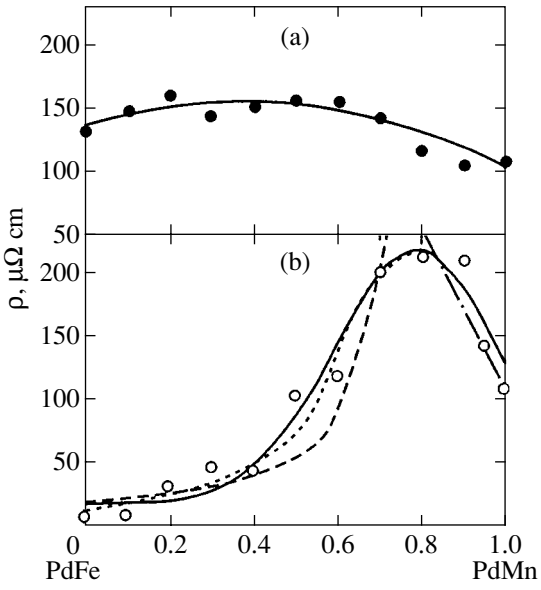

Fig. 1. Electrical resistivity of $PdMn_xFe_{1-x}$ alloys presented for T equal to (a) 850 and (b) 4.2 K. (a) The solid line is a plot of Eq. (2); (b) $\rho_0(x)$ calculation: the dashed line was calculated following the percolation theory, Eq. (5); the solid line, following the effective-medium model, Eq. (7); dotted line, using Eq. (4) for $x < x_C = 0.8$. The dot-and-dash line shows the $\rho_0(x) \sim (1 - x)$ relation for $x > x_C$.

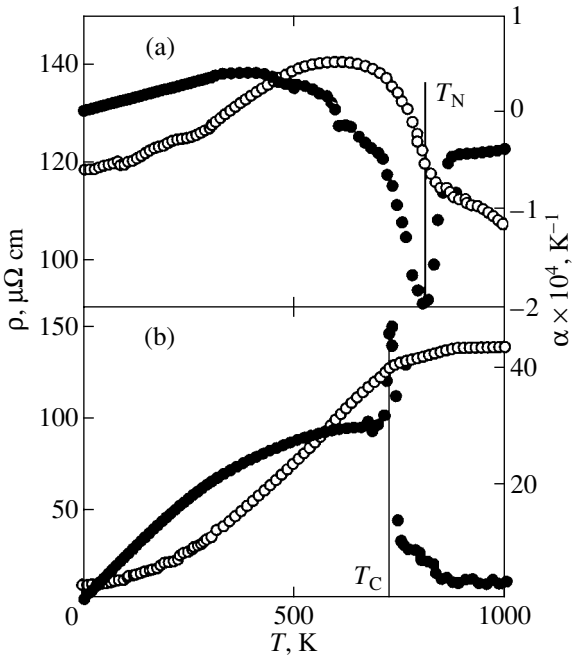

Fig. 2. Temperature dependences of the electrical resistivity (open circles) and of the temperature coefficient of resistivity (filled circles) drawn for samples of extreme composition: (a) PdMn and (b) PdFe.

Hence, the fact that Eq. (2) is satisfied in the paramagnetic temperature region indicates that the specific features in the behavior of $\rho_0(x)$ are practically not connected with conduction electron scattering from structural inhomogeneities of the $PdMn_xFe_{1-x}$ alloys. The dominant role of the magnetic component in $\rho_0(x)$ is also suggested by its unusually high maximum value $\rho_0^m \sim 200$ μΩ cm, which exceeds even the spin-disordered resistivity $\rho_m(T > T_C, T_N)$. Note that the $\rho_0(x)$ has a maximum at the critical concentration $x_C = x_2 \sim 0.8$, at which the F_1 phase of the PdFe type and the noncollinear F_2 phase are formed with decreasing x. It should be pointed out that the critical concentration $x_1 \sim 0.2$ for the nucleation of the PdMn-type A phase does not manifest itself in any way in the $\rho_0(x)$ curve.

3. The above features in the structural and magnetic states of $PdMn_xFe_{1-x}$ alloys are accompanied by a qualitative change in the pattern of the temperature dependences of the electrical resistivity. As seen from Fig. 2, a PdFe alloy exhibits a $\rho(T)$ behavior typical of ferromagnets, with a positive temperature coefficient of resistivity α that has a spin-fluctuation anomaly at the Curie point. In contrast, the coefficient $\alpha(T)$ of the PdMn antiferromagnet reverses its sign to negative for $T \geq 600$ K. The behavior of $\alpha(T)$ and, hence, of $\rho(T)$ observed in PdMn for $T < T_N = 815$ K is characteristic of metallic antiferromagnets and can be related to the band-gap formation in the electronic spectrum near E_F as a result of the sample becoming magnetically ordered [8].

Our LMTO calculations of the electronic energy spectrum show (Fig. 3) that when PdMn undergoes A ordering, an unusually deep dip does indeed appear near the Fermi level E_F in the density-of-states $N(E)$ curve. If one considers only the d band, magnetic ordering brings about, in essence, the formation of an energy gap in the electron spectrum near E_F. As seen from Fig. 3, the gap width is $\Delta \sim 1$ eV and the density of states at E_F decreases as a result of the A ordering by approximately 20 times, from $N(E_F) = 6.7$ state/eV per unit cell in the paramagnetic state to $N(E_F) = 0.19$ state/eV per unit cell in the A state. Using self-consistent calculations of the Mn A state (such as the eigenvectors and eigenvalues of the Hamiltonian matrix for the 3d spin-up and spin-down Mn bands), we also computed the parameter J of exchange interaction between the 3d electron shells of the nearest neighboring Mn atoms, which is defined in the Heisenberg model as $H = 2JS_1S_2$. The J parameter was calculated following the technique proposed in [9]. The calculation yielded $J \sim 63.5$ meV, which is in agreement with the value expected from $T_N = 815$ K for the PdMn antiferromagnet.

According to [6], the Fermi level in a ferromagnetically ordered PdFe alloy lies between the density-of-states peaks formed by the d states of the spin-up and spin-down Fe atoms. Here, however, $N(E_F)$ in both paramagnetic and magnetically ordered states derives

from the *s*, *p*, and *d* states. The density of states at E_F for PdFe is $N(E_F)$ = 6.2 state/eV per unit cell in the paramagnetic state and $N(E_F)$ = 1.55 state/eV per unit cell in the magnetically ordered state.

A comparison of the electronic band-structure calculations made for the ferromagnet PdFe and the antiferromagnet PdMn in the paramagnetic and magnetically ordered states shows that the resistivity in a PdMn-type phase can indeed be described using the model from [8], provided the *d* electrons are considered to be the majority carriers in the magnets under study.

At the Néel point, an $\alpha(T)$ anomaly takes place in PdMn, which would appear standard under magnetic ordering if it were not for the additional magnetic contribution having, in this case, a negative sign. This experimental observation, appearing fairly strange at first glance, can be assigned to the fact that the magnetic component of the resistivity of an antiferromagnet, which originates from gap formation in the electronic band spectrum caused by magnetic-cell doubling under *A* ordering, is proportional to the squared sublattice magnetization, $\rho_m \sim M_i^2$ [8]. As follows from [7], the variation of the PdMn sublattice magnetization with temperature for $T \le T_N$ can be described in terms of the fluctuation theory [10] by a power law relation,

$$M_i \sim [(T_N - T)/T_N]^\beta. \quad (3)$$

From Eq. (3), it follows that the magnetic "gap" contribution to the temperature coefficient of the resistivity $\alpha_m(T) = (1/\rho_m)(d\rho_m/dT) \sim -[(T_N - T)/T_N]^{2\beta - 1}$ is negative and has a maximum magnitude at the Néel point and its temperature dependence is similar to Eq. (3), differing only in the magnitude and sign of the critical exponent.

As seen from Fig. 2, the sign of $\alpha(T)$ in PdMn is also negative for $T > T_N$, up to the temperature $T_S \sim 1000$ K of the martensitic transition to another *B*2 phase [5]. This experimental finding suggests that the energy gap in the *d* spectrum of the given antiferromagnet also exists in the paramagnetic temperature region. Electronic-spectrum calculations carried out for the paramagnetic PdMn do not indicate the presence of a gap singularity in $N_d(E)$ near E_F. One may only conjecture that the short-range *A* order and, hence, remnants of the *d* gap in the electronic spectrum are retained in PdMn above T_N.

4. As shown by analyzing the temperature dependences of electrical resistivity in samples with extreme compositions, PdFe and PdMn, as well as in samples with intermediate concentrations (see [1]), a metal–semiconductor phase transition takes place in the *d* carrier subsystem (in addition to the *F*–*A* magnetic phase transition) in ternary $PdMn_xFe_{1-x}$ alloys with increasing *x*. This conjecture is borne out by measurements of the Seebeck coefficient *S*(*T*) of the alloys under study [1]. At room temperature ($T \ll T_{C1}, T_N$), the sign of *S* is changed from negative to positive with increasing manganese concentration near $x_2 \sim 0.8$, while at high temperatures, $T \ge (T_{C1}, T_N)$, the *S* value is positive almost everywhere over the region of existence of the PdMn-type *A* phase with $x > x_1 \sim 0.2$.

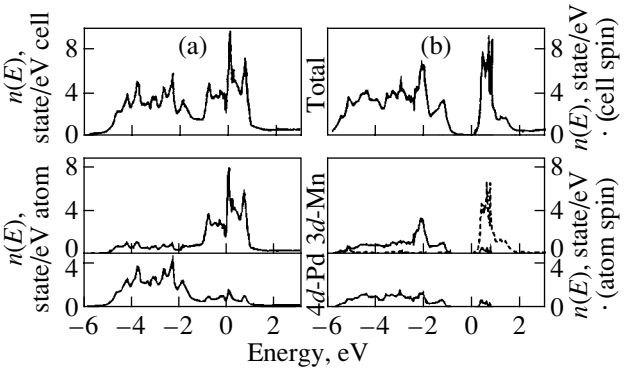

Fig. 3. Total and partial densities of states of the PdMn intermetallic compound for (a) paramagnetic and (b) antiferromagnetic solutions. The Fermi level corresponds to $E = 0$. The dashed and solid lines in the central panel of (b) show the densities of states for two projections of the Mn spin.

Hence, for $T < (T_{C1}, T_N)$, the alloys with concentrations $x < 0.8$ can be considered a mixture of two phases with residual resistivities differing by almost two orders in magnitude. Note that the high-resistivity phase consists not only of the *A* but also of the noncollinear F_2 phase. The latter, due to the magnetic moments being almost completely disordered, should have the largest possible magnetic component of the resistivity already at low temperatures. The high-resistivity F_2 phase is present only in the region of coexistence of the main collinear phases ($0.2 < x < 0.8$), and its volume is maximum at $x \sim 0.5$ [3, 4].

X-ray diffraction measurements show [4] that manganese atoms virtually do not dissolve in a PdFe-type phase. One could thus assume that $PdMn_xFe_{1-x}$ alloys exhibit a tendency to nucleation of the PdMn-type phase already at low Mn concentrations. As the concentration *x* increases, the volume of the conducting PdFe-type phase decreases and that of the "insulating" PdMn-type phase, conversely, grows. Near the threshold concentration (percolation threshold) $x_C = x_2 \sim 0.8$, the conducting PdFe-type phase almost disappears. It should be stressed that we attribute the large magnitude of ρ_0 of the PdMn-type *A* phase to the existence of an energy gap in its *d* spectrum at E_F, which persists to very low temperatures.

For this reason, we attempted to describe $\rho_0(x)$ of the microinhomogeneous alloys under consideration in terms of the percolation theory in the effective-mass approximation. We used the well-known expression for

the effective conductivity of a two-phase medium (the Kondorskiĭ–Odolevskiĭ equation) [11]

$$\sigma^* = 1/\rho^* = (1/4)[(3x_F - 1)\sigma_F + (3x_A - 1)\sigma_A] + \{[(3x_F - 1)\sigma_F + (3x_A - 1)\sigma_A]^2/16 + \sigma_F\sigma_A/2\}^{1/2} \quad (4)$$

and the expression from percolation theory [12]

$$\rho_0 \sim [(x - x_C)/x_C]^{-\varepsilon}. \quad (5)$$

Here, σ_F and σ_A are the conductivities of the low- and high-resistivity phases, respectively, and x_F and x_A are the corresponding concentrations. The ε and x_C are the critical exponent and the percolation threshold concentration for the conducting F_1 phase. The concentration dependences of the volumes of the F_1, F_2, and A phases were determined from studies on magnetic properties [3, 4]. It was assumed that the F_1 phase is a conducting insulator and that the F_2 and A phases are high-resistivity insulators. We note immediately that none of these two models is capable of fitting the experimental $\rho_0(x)$ relation throughout the concentration range studied ($0 \le x \le 1$).

In these two approximations, one succeeds at deriving a $\rho_0(x)$ relation close to that determined in experiment [1] only for the region where the two phases, conducting and insulating, coexist, i.e., for $x < x_C = x_2 \sim 0.8$. Figure 1b shows the results of a mathematical treatment of the $\rho_0(x)$ relation made using Eqs. (4) and (5). It was assumed that $\sigma_A = 1/\rho_0^m$, i.e., that this quantity differs from the conductivity of the PdMn antiferromagnet. As seen from Fig. 1b, the effective-medium model [11] provides the best fit to the experimental data on the residual resistivity of the $PdMn_xFe_{1-x}$ alloys within the above concentration range. This conclusion may be considered reasonable, because the scatter in the values of $\rho_0(x)$ for the alloy system under study is comparable to its mean value in order of magnitude [12].

Above the threshold concentration ($x > x_C \sim 0.8$), the situation with these alloys is different. According to [4], Fe impurity atoms dissolve fairly well in a PdMn-type host. This should bring about changes in the parameters of the *d* gap in the electronic energy spectrum, which originates from the *A* ordering. It may be conjectured that in the first stage of Mn replacement by Fe, the gap singularity in the spectrum of the PdMn-ordered $PdMn_xFe_{1-x}$ ternary alloys becomes more significant. For $T < T_N$, the change in the electronic spectrum will give rise to an increase in the electrical resistivity; in first approximation, this change will be proportional to the iron concentration in the sample. Obviously enough, for $T > T_N$, the magnitude of ρ should vary with concentration x substantially more weakly as a result of the strong decrease in the gap singularity in the *d* spectrum of *A* alloys in the paramagnetic temperature region.

This conjecture on the electron energy spectrum of the PdMn antiferromagnet changing as a result of the substitution of Fe atoms for Mn is in complete agreement with experimental data. As seen from Figs. 1 and 2 (see also [1]), a decrease in the manganese concentration in $PdMn_xFe_{1-x}$ *A* alloys within the range $1 \ge x \ge x_C \sim 0.8$ is accompanied by not only an increase in ρ_0 but also a considerable growth of the negative coefficient α in magnitude for $T < T_N$. In our case, both these characteristics are governed by the magnitude of the energy gap in the *d* spectrum, which appears as a result of the *A* ordering, and the change in these characteristics observed experimentally to occur with decreasing x indicates enhancement of the gap singularity in the $N_d(E)$ curve. However, LMTO band-structure calculations indicate, conversely, that the gap singularity in the electron spectrum of the PdMn antiferromagnet disappears when the Mn atoms are replaced by Fe.

5. While not excluding the above explanation of the behavior of the $\rho_0(x)$ relation of the $PdMn_xFe_{1-x}$ ternary alloys, we suggest another alternative. As already mentioned, the microstructure of these alloys can be represented in the form of low-resistivity F_1 regions surrounded by high-resistivity *A* regions, which are separated by F_2 layers. In this case, the electrical resistivity of the low-Ohmic F_1 regions remains virtually constant with x. At the same time, ρ of the higher resistivity *A* and F_2 regions varies fairly strongly throughout the volume of the alloy and as a function of concentration x, because it is in this part of the alloy volume that the Fe atoms are replaced by Mn.

The electrical structure of such an inhomogeneous state of the alloys can be approximated in the effective-medium model by a random network of resistances (or conductances) [13]; the random-valued resistances should be interpreted as those of microcontacts, and the equivalent circuit of a microcontact can be represented in the form of resistances connected in series (as was done, for instance, in [14, 15]), more specifically, of ρ_F of the metallic F_1 regions and ρ_A of the intermediate volume including the F_2 and *A* phases:

$$\rho_0(x) = \rho_F + \rho_A. \quad (6)$$

Actually, the random-valued resistance network is replaced in this case by a regular network of equal, averaged microcontact resistances.

Taking into account the variation in phase volume with concentration and the random nature of substitution of the manganese and iron atoms in the F_2 and *A* phases, the resistivity of these phases can be described, as in [15], by a normal distribution [16]. Therefore, we can write

$$\rho_0(x) = \rho_F + A/[\omega(\pi/2)^{0.5}] \times \exp\{-2[(x - x_C)/\omega]^2\}. \quad (7)$$

As seen from Fig. 1b, the $\rho_0(x)$ relation for $PdMn_xFe_{1-x}$ microinhomogeneous alloys is approximated well by Eq. (7) within the whole concentration region studied here ($0 \le x \le 1$). This supports the validity of the proposed effective-medium model for the ternary alloys under consideration, which assumes that ρ_F is constant and that the values of ρ_A are given by a normal distribution [16]. We find that the center of the distribution is at $x_C = 0.785$ and the variance is $\omega^2 = 0.14$.

The concentration dependence of the residual resistivity of $PdMn_xFe_{1-x}$ microinhomogeneous alloys can also be described in terms of other possible equivalent electric circuits of microcontacts. In particular, satisfactory results are obtained by treating $\rho_0(x)$ experimental data with the use of a random-valued conductance network, whose analysis yields the expression

$$1/\rho_0(x) = 1/\rho_F + 1/\rho_A. \quad (8)$$

Other, more complex variants of electric circuits of microcontacts can be conceived based on their connection in series or parallel. In any case, in order for a concrete scheme chosen for description of an experiment to be adequate, the $\rho_A(x)$ dependence must follow a normal distribution [16].

6. It should be noted in conclusion that $\rho_0(x)$ dependences similar to the one displayed in Fig. 1 were also observed earlier for solid solutions of noble and transition metals (see, e.g., [2]). The deviation of the $\rho_0(x)$ curves from the form of Eq. (1) was likewise related in that case, as a rule, to features in the electron band structure of the alloys, but with a pattern differing from that suggested in this work. It is known that the resistivity in the two-band Mott model is proportional to the density of *d* states at E_F; i.e., $\rho_0(x) \sim N_d(x)$. Hence, the anomalous increase in $\rho_0(x)$ at some x_C can be accounted for by a considerable increase in N_d associated with rearrangement of the narrow *d* band, for instance, with a formation of virtually coupled *d* states near E_F. Such an approach does not, however, agree with the band-structure calculations of the PdMn antiferromagnet and is at odds with the multiphase nature of the magnetic and structural states of $PdMn_xFe_{1-x}$ alloys.

Thus, the behavior of the electrical resistivity of $PdMn_xFe_{1-x}$ ternary alloys with concentration and temperature can be properly understood only by taking into account specific features in their structural and magnetic states. Two approaches are employed in this work to describe the residual resistivity of the microinhomogeneous alloys under study in terms of the effective-medium approximation. In one of them, the whole concentration range is divided into two regions separated by a critical concentration $x_C = x_2 \sim 0.8$. For $x < x_C$, the microinhomogeneous (heterogeneous) state of the alloys consisting of magnetic phases with the values of ρ_0 differing by almost two orders of magnitude is simulated by an effective medium within the Kondorskiĭ–Odolevskiĭ model [11]. In the range $1 \ge x > x_C$, the alloys under study are considered to be single-phase with a PdMn-type *A* ordering. The parameters of the *d* band of the *A* phase are assumed to vary in proportion to the concentration of the Fe impurity atoms. Therefore, in this range, the $\rho_0(x - 1) \sim (1 - x)$ relation is approximately satisfied, as is evident from Fig. 1b. In the other approach, the microinhomogeneous state of the alloys is described, throughout the region in which the alloys are ranged from the PdFe ferromagnet to the PdMn antiferromagnet, in terms of the effective-medium model, which represents a microcontact network whose equivalent electric circuit consists of resistances of the metallic F_1 regions with constant ρ_F connected in series and resistances of the F_2 and *A* phases which separate the F_1 regions and are characterized by the resistivity ρ_A whose concentration dependence is described by a normal distribution [16].

ACKNOWLEDGMENTS

The authors are indebted to Yu.P. Irkhin and E.A. Mityushov for useful discussions and valuable criticism.

REFERENCES

1. N. I. Kourov, Yu. G. Karpov, N. V. Volkov, and L. N. Tyulenev, Fiz. Met. Metalloved. **84** (6), 86 (1997).
2. J. M. Ziman, *Electrons and Phonons* (Clarendon, Oxford, 1960; Inostrannaya Literatura, Moscow, 1962).
3. L. N. Tyulenev, N. V. Volkova, I. I. Piratinskaya, *et al.*, Fiz. Met. Metalloved. **83** (1), 75 (1997).
4. N. V. Volkova, N. M. Kleĭnerman, N. I. Kourov, *et al.*, Fiz. Met. Metalloved. **89** (1), 39 (2000).
5. N. I. Kourov, V. A. Kazantsev, L. N. Tyulenev, and N. V. Volkova, Fiz. Met. Metalloved. **89** (5), 24 (2000).
6. V. I. Anisimov and M. A. Korotin, Fiz. Met. Metalloved. **68** (3), 474 (1989).
7. E. Kre'n and J. So'lyom, Phys. Lett. **22** (3), 273 (1966).
8. Yu. P. Irkhin, Fiz. Met. Metalloved. **6** (4), 586 (1957).
9. A. I. Lichtenstein, M. I. Katsnelson, V. P. Antropov, and V. A. Gubanov, J. Magn. Magn. Mater. **67**, 65 (1987).
10. A. Z. Patashinskiĭ and V. L. Pokrovskiĭ, *Fluctuation Theory of Phase Transitions* (Nauka, Moscow, 1975; Pergamon, Oxford, 1979).
11. V. I. Odolevskiĭ, Zh. Tekh. Fiz. **21** (6), 667 (1951).
12. B. I. Shklovskiĭ and A. L. Éfros, Usp. Fiz. Nauk **117** (3), 401 (1975) [Sov. Phys. Usp. **18**, 845 (1975)].
13. S. Kirkpatrick, Rev. Mod. Phys. **45**, 574 (1973); in *Theory and Properties of Disordered Materials* (Mir, Moscow, 1977).
14. G. E. Pike and C. H. Seager, J. Appl. Phys. **48** (12), 5152 (1977).
15. Ping Sheng, Phys. Rev. B **21** (6), 2180 (1980).
16. D. Hudson, *Statistics. Lectures on Elementary Statistics and Probability* (Geneva, 1964; Mir, Moscow, 1970).

Translated by G. Skrebtsov

Physics of the Solid State, Vol. 44, No. 2, 2002, pp. 204–209. Translated from Fizika Tverdogo Tela, Vol. 44, No. 2, 2002, pp. 198–202.

METALS AND SUPERCONDUCTORS

Formation of the Metastable Phase upon Crystallization of Light Amorphous Mg–Ni–Y Alloys

G. E. Abrosimova

Institute of Solid-State Physics, Russian Academy of Sciences, Chernogolovka, Moscow oblast, 142432 Russia
e-mail: gabros@issp.ac.ru

Received January 26, 2001; in final form, June 28, 2001

Abstract—The decomposition of the amorphous phase upon heating of the $Mg_{87}Ni_{13}$ and $Mg_{83}Ni_{13}Y_4$ amorphous alloys prepared by rapid quenching of the melt is investigated. The nanocrystalline structure is formed at the first crystallization stage and contains crystals of magnesium and the metastable phase. The structure of the metastable phase (the lattice parameters and space group) is determined. The possible chemical compositions of the metastable phase are considered. No differences are revealed in the structures of the metastable phases in the yttrium-containing and yttrium-free alloys. Heating of the alloys results in decomposition of the metastable phase. After completion of the transformations, the alloy structure consists of Mg and Mg_2Ni in accordance with the equilibrium phase diagram. © *2002 MAIK "Nauka/Interperiodica"*.

1. INTRODUCTION

Metallic glasses based on magnesium belong to the group of light alloys and exhibit a rather high tendency to vitrification. Among light materials, these glasses possess record-high strength characteristics. For example, the tensile strength of the $Mg_{65}Cu_{25}Y_{10}$ alloy reaches 800 MPa, which is nearly twice as large as that for a crystalline alloy of the same composition [1]. The physical properties of materials depend on their structure. It is known that the strength of light alloys based on aluminum substantially increases at the initial stages of devitrification. As was shown earlier in [2], the microhardness of the $Al_{86}Ni_{11}Yb_3$ alloy increases from 1.6 GPa in the amorphous state to 4.2 GPa after annealing with the formation of a nanocrystalline structure. It is reasonable to expect the properties of metallic glasses based on magnesium also to change at different stages of crystallization. In particular, Kobelev *et al.* [3] studied the $Mg_{84}Ni_{12.5}Y_{3.5}$ amorphous alloy and observed considerable changes in the elastic and dissipative properties. In this respect, investigations into the physical properties of alloys should involve a study of the alloy structure and its thermal stability at different stages of the structural transformation. Amorphous alloys in the Mg–Ni–Y system crystallize in several stages. At the initial stage, the decomposition of the amorphous phase brings about the formation of the metastable phase with a large Young's modulus [3]. The purpose of the present work was to investigate the structure of this metastable phase.

2. EXPERIMENTAL TECHNIQUE

The Mg–Ni–Y amorphous alloys (containing 13 at. % Ni and 0 or 4 at. % Y) were prepared in the form of 25-μm-thick ribbons by rapid quenching of the melt. The alloy samples were placed in evacuated sealed tubes and were then annealed at different temperatures. The structure was investigated by x-ray diffraction on a Siemens D-500 diffractometer (CuK_α radiation, reflection geometry). The samples were mounted on plates cut out from silicon single crystals that were oriented in such a way as to exclude their own reflections. The x-ray powder diffraction analysis was performed using a software package. This made it possible to carry out automatic correction for the background, to determine the positions and intensities of diffraction maxima, to resolve the overlapping maxima, and to perform a qualitative phase analysis of the multiphase systems in an automatic mode.

3. RESULTS AND DISCUSSION

The as-prepared samples have an amorphous structure. No indications of crystalline phases are revealed in the x-ray diffraction patterns. The amorphous phase crystallizes in the course of heating.

The x-ray diffraction pattern of the $Mg_{87}Ni_{13}$ alloy after the initial crystallization stage (heating to 210°C and cooling to room temperature) is displayed in Fig. 1 (curve *1*). As can be seen, the diffraction pattern exhibits a series of sufficiently broad diffraction maxima. This indicates that the sample has a fine-crystalline structure after the initial crystallization stage. According to the Mg–Ni phase diagram [4], the crystallized alloy should contain two phases, namely, Mg and Mg_2Ni. A number of reflections in the x-ray diffraction pattern actually correspond to the hexagonal close-packed lattice of magnesium (these reflections in the x-ray diffraction pattern are designated by I). However,

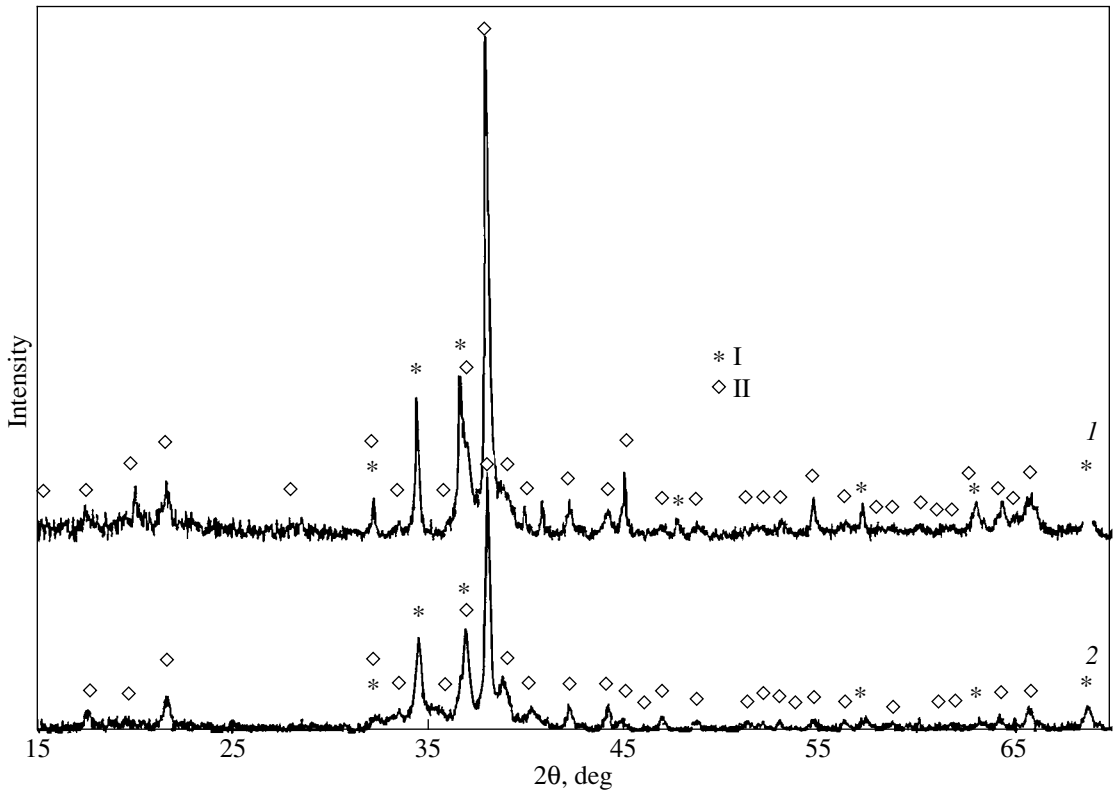

Fig. 1. X-ray diffraction patterns of the (*1*) $Mg_{87}Ni_{13}$ and (*2*) $Mg_{83}Ni_{13}Y_4$ alloys after the first crystallization stage.

the majority of the diffraction maxima (denoted as II in the diffraction patterns shown in Fig. 1) can be assigned to none of the crystalline phases known for the system under investigation.

Analysis of the positions of the most intense diffraction maxima allows us to assume that reflections II are attributed to the same crystalline phase. This phase has a cubic structure with the parameter $a = 10.04$ Å. Table 1 presents the positions of all the reflections observed in the x-ray diffraction pattern (Fig. 1, curve *1*).

The presence of the *hkl* reflections ($h, k, l \neq 0$) with even and odd indices h, k, and l ($h + k + l = 2n$ and $h + k + l = 2n + 1$) in the x-ray diffraction pattern suggests that the observed phase has a primitive lattice. As was noted above, this phase has a cubic structure; hence, the crystal lattice can belong to either of two Laue classes, $m3$ or $m3m$. Analysis of the series of *hk*0, *hhl*, and *h*00 reflections demonstrates that no constraints are imposed on the *hk*0 and *hhl* reflections, whereas the *h*00 reflections are observed only in the case when the index h is equal to $2n$ (even). This indicates that the unit cell can be described by either the $P2_13$ space group (the Laue class $m3$) or the $P4_232$ space group (the Laue class $m3m$).

The available experimental data are obviously insufficient to decide between these two space groups. However, according to the universally accepted principle of preferring a more symmetric structure (all other factors being the same), preference should be given to the space group $P4_232$.

Another essential problem concerns the chemical composition of the metastable phase. In this respect, it is necessary to dwell on two important aspects of the problem.

(1) The precipitates of the metastable phase are very small in size, as judged from the broad lines in the x-ray diffraction pattern. The size of nanocrystals can be estimated from the linewidths of the diffraction patterns. The grain size is conveniently determined using the Selyakov–Scherrer formula [5], according to which the grain size L is represented as

$$L = \lambda(1/\cos\theta)/\Delta(2\theta),$$

where λ is the emission wavelength, θ is the reflection angle, and $\Delta(2\theta)$ is the half-width of the relevant diffraction line. Since the half-width of the diffraction reflections is rather large, the instrumental broadening can be ignored. The mean nanocrystal size thus determined does not exceed 10 nm. At the early crystallization stages, the mean grain size is no more than 5 nm.

It is known that a decrease in the precipitate size is accompanied by an increase in the equilibrium concentration of the solute. As follows from the Gibbs–Thomson equation, the concentration $C_\beta(r)$ of a component B

Table 1. Experimental (d_{exp}) and calculated (d_{calcd}) interplanar distances for the x-ray diffraction pattern shown in Fig. 1 (curve *1*)

N	d_{exp}, Å	d_{calcd}, Å		*hkl* (Mg)	*hkl* (new phase)
1	5.787	5.796			111
2	5.015	5.019			200
3	4.510	4.489			210
4	4.089	4.098			211
5	2.679	2.683			321
6	2.602		2.605	002	
7	2.432	2.435,	2.452	101	322, 410
8	2.366	2.366			330, 411
9	2.310	2.303			331
10	2.237	2.245			420
11	2.139	2.140			332
12	2.047	2.049			422
13	1.932	1.932			511, 333
14	1.867	1.864			432, 520
15	1.775	1.775			440
16	1.720	1.722			433, 530
17	1.673	1.673			442, 600
18	1.629	1.6285			532, 611
19	1.566	1.568			540, 621, 443
20	1.535	1.531			533
21	1.514	1.5134			622
22	1.470		1.473	103	
23	1.449	1.449			444
24	1.421	1.420			543, 550, 710
25	1.366	1.366,	1.366	112	522, 721, 633
26	1.331	1.330			722, 544
27	1.288	1.285			643, 650
28	1.235	1.2357			554, 811, 741
29	1.217	1.2174			820, 644
30	1.145	1.144			832, 654
31	1.0949	1.095			842

dissolved in a small-sized crystal of a component *A* depends on the crystal size *r* according to the law

$$C_\beta(r) = C_\beta(\infty)(1 + 2\sigma V_m/RTr),$$

where $C_\beta(\infty)$ is the equilibrium concentration of the *B* component in the crystal lattice of the *A* component at a given temperature, σ is the interfacial energy (assumed to be isotropic), V_m is the molar volume, *R* is the universal gas constant, and *T* is the temperature [6]. The specific free energy of the metallic precipitate–metallic matrix interface is generally equal to 0.02–0.6 J m^{-2}. Setting the interfacial energy σ = 0.2 J m^{-2} and the temperature *T* = 500 K, we found that the solute concentration increases by approximately 25% for nanocrystals 5 nm in size and by approximately 13% for nanocrystals 10 nm in size. This implies that, even if the equilibrium crystalline phases (Mg and Mg_2Ni in accordance with the phase diagram) are formed at the first stage of the crystallization of the amorphous phase, the magnesium concentration in the intermetallic compound will increase appreciably at the early crystalliza-

tion stages, because the nucleation and growth of this phase occur in the magnesium-rich matrix.

(2) In the case under consideration, the metastable phase is formed during crystallization of the amorphous phase produced by rapid quenching of the melt. The initial amorphous alloy has a relatively homogeneous chemical composition and inherits the structure of the melt before its quenching. In alloys of the eutectic and hypoeutectic compositions, the crystallization is attended by redistribution of the chemical components. As a rule, the alloy components have no time to be completely redistributed at the early crystallization stages. The amount of dissolved components in the phase formed upon crystallization is larger than that predicted from the phase diagram. In the course of subsequent annealing or heating, the concentration of the dissolved component decreases and reaches an equilibrium value. A typical example of this behavior is provided by the Fe–B system. In the Fe–B system, the crystallization brings about the formation of the metastable tetragonal phase Fe_3B (or $Fe_{3.5}B$). This phase undergoes a series of phase transitions with a gradual decrease in the iron concentration to the point of decomposition into Fe or Fe_2B [7]. This situation is not uncommon with the metal–metalloid and metal–metal systems.

In our case, the sequence of transformations occurring during the crystallization is as follows:

$$\text{Amorphous phase} \longrightarrow \text{Mg} + \text{metastable phase}$$
$$\longrightarrow \text{Mg} + \text{Mg}_2\text{Ni}.$$

As in the case discussed above, it can be assumed that the magnesium concentration in the metastable phase is higher than that in the Mg_2Ni phase. In our experiment, the formation of magnesium crystals occurs simultaneously with the formation of the metastable phase. Analysis of the x-ray diffraction patterns recorded after the heat treatments performed at different temperatures revealed that the volume fractions of these phases are comparable to each other. For this reason, it is difficult, if not impossible, to determine which of these phase is formed first. Now, we attempt to evaluate the chemical composition of the phase formed upon crystallization. It is known that several equilibrium crystalline phases can be formed in the Mg–Ni system. As the nickel concentration increases, the specific volume (the unit cell volume per atom of any sort) varies from 23.24 Å^3/atom for pure Mg to 10.94 Å^3/atom for pure Ni (Fig. 2). For phases of intermediate composition, the specific volume monotonically decreases with an increase in the nickel concentration. For example, the specific volume of the Mg_2Ni phase is 17.28 Å^3/atom. Knowing the lattice parameter of the metastable phase (10.04 Å), it is an easy matter to determine the unit cell volume. For this phase, the unit cell volume is approximately equal to 1012 Å^3. By using the unit cell volume and the data displayed in Fig. 2, we can estimate the possible number of atoms in the unit cell.

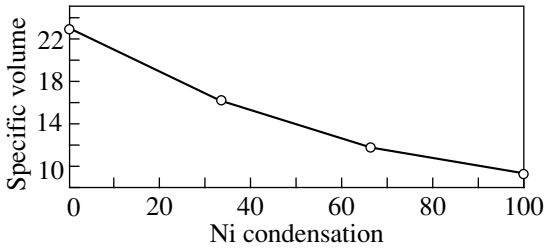

Fig. 2. Concentration dependence of the unit cell volume per atom for crystalline phases in the Mg–Ni system.

The specific volumes and the numbers of atoms per unit cell in the phases of different possible compositions from Mg_6Ni to Mg_5Ni_2 are given in Table 2. Since the alloy crystallizes with the formation of the metastable phase and magnesium, the ratio Mg : Ni in this phase cannot exceed 6 : 1. Spassov and Koster [8] examined the crystallization of the $Mg_{87}Ni_{12}Y_1$ amorphous alloy and observed the precipitation of magnesium crystals at the first crystallization stage and the formation of the cubic metastable phase Mg_6Ni upon subsequent decomposition of the residual amorphous matrix. The phase studied in [8] has a face-centered cubic lattice and is isomorphic with respect to the Mg_6Pd phase (F-43m, a_0 = 20.09 Å). The lattice parameter of the former phase is nearly twice as large as that for the crystalline phase observed in our case. However, we did not observe reflections that would allow us to judge the presence of the aforementioned phase in the structure. In particular, our x-ray diffraction patterns contain no relatively intense (for the Mg_6Pd-type lattice) (620) reflection corresponding to an interplanar distance of 3.18 Å and a weaker (331) reflection corresponding to an interplanar distance of 4.61 Å. Moreover, there are certain differences in the relevant ranges of reflections with higher indices. It follows from Table 2 that the observed phase has either the chemical composition Mg_6Ni, but with a different crystal lattice (cubic primitive with a lattice parameter of 10.04 Å), or

Table 2. Specific volumes and numbers of molecular units and atoms per unit cell for crystalline phases of different compositions

Phase composition	Specific volume, Å^3/ atom	Number of molecular units per unit cell	Number of atoms per unit cell
Mg_6Ni	20.4	7	42Mg + 7Ni
Mg_5Ni	20	8.4	42.5Mg + 8.5Ni
Mg_4Ni	19.4	10.4	42Mg + 10.5Ni
Mg_7Ni_2	18.9	6	42Mg + 12Ni
Mg_3Ni	18.2	14	42Mg + 14Ni
Mg_5Ni_2	17.8	16.25	40.6Mg + 16.25Ni

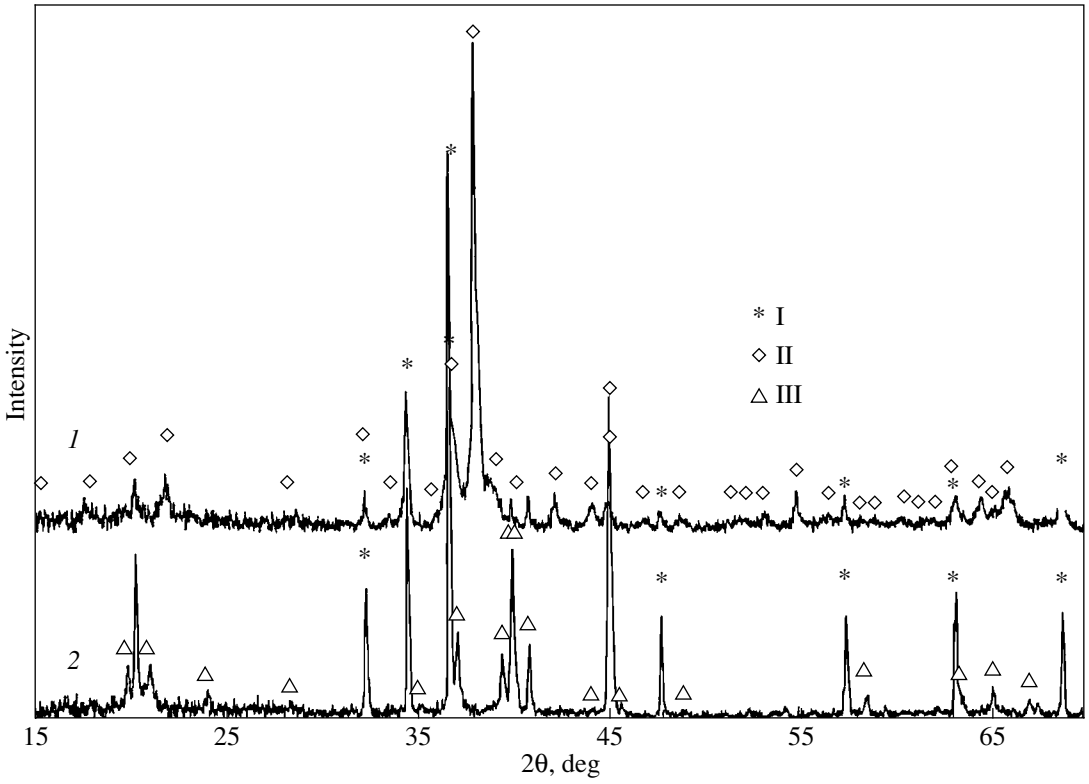

Fig. 3. X-ray diffraction patterns of the $Mg_{87}Ni_{13}$ alloy after heating to (*1*) 210 and (*2*) 350°C.

one of the two chemical compositions of the formulas Mg_7Ni_2 or Mg_3Ni, i.e., the chemical composition with the Mg : Ni ratio equal to 3.5 : 1 or 3 : 1. In this case, the unit cell should involve 12 or 14 formula units, respectively. From analyzing the possible positions of atoms in the unit cells described by the space groups $P2_13$ and $P4_232$ [9], it is easy to see that both cells actually contain positions for 42 Mg atoms and 14 (or 12) Ni atoms.

The metastable phase described above is observed in the yttrium-free (Fig. 1, curve *1*) and yttrium-containing (Fig. 1, curve *2*) samples. No appreciable differences in the lattice parameters for alloys of different compositions are revealed. In the case of the yttrium-containing alloy, the question arises as to whether the yttrium atoms occupy the magnesium lattice or if they are located in the crystal lattice of the metastable phase. The solubility of yttrium in pure magnesium at a temperature of 230°C is approximately equal to 2 at. %. Undeniably, the presence of nickel affects the solubility of yttrium in magnesium; however, the true solubilities in the ternary system are as yet unknown. Making allowance for the size of precipitated crystals and the observed increase in equilibrium solubility in small-sized crystals, we can assume that yttrium is dissolved in both magnesium and metastable phase crystals. At this stage of investigation, the question remains open.

As the heat treatment temperature increases, the x-ray diffraction pattern changes substantially. After heating to 210°C, the samples contain the magnesium and metastable phases. The reflections of these phases in Fig. 3 (curve *1*) are designated by I and II, respectively. Upon heating to 330°C (Fig. 3, curve *2*), the cubic metastable phase, which is formed at the first stage of the crystallization of the amorphous alloy, undergoes decomposition. The observed reflections correspond to two equilibrium phases, namely, Mg (reflections I similar to those in curve *1*) and Mg_2Ni (reflections III).

4. CONCLUSIONS

Thus, the first stage of the crystallization of the $Mg_{87}Ni_{13}$ and $Mg_{83}Ni_{13}Y_4$ amorphous alloys leads to the formation of magnesium crystals and the cubic metastable phase with the space group $P4_232$ and a lattice parameter of 10.04 Å. According to the estimates, this phase has either the chemical composition Mg_6Ni or one of two similar compositions, Mg_7Ni_2 or Mg_3Ni.

ACKNOWLEDGMENTS

I would like to thank Ya.M. Soĭfer and N.P. Kobelev for supplying the samples used in this work.

This work was supported by the Russian Foundation for Basic Research, project no. 99-02-17477.

REFERENCES

1. R. Busch, W. Liu, and W. L. Johnson, J. Appl. Phys. **83**, 4134 (1998).
2. G. E. Abrosimova, A. S. Aronin, Yu. V. Kir'janov, *et al.*, Nanostruct. Mater. **12**, 617 (1999).
3. N. P. Kobelev, Ya. M. Soĭfer, I. G. Brodova, and A. N. Manukhin, Fiz. Tverd. Tela (St. Petersburg) **41**, 561 (1999) [Phys. Solid State **41**, 501 (1999)].
4. M. Hansen and K. Anderko, *Constitution of Binary Alloys* (McGraw-Hill, New York, 1958; Metallurgizdat, Moscow, 1962), Vol. 2, p. 965.
5. A. A. Rusakov, *X-ray Diffraction of Metals* (Atomizdat, Moscow, 1977).
6. J. W. Martin and R. D. Doherty, *Stability of Microstructure in Metallic Systems* (Cambridge Univ. Press, Cambridge, 1976; Atomizdat, Moscow, 1978).
7. G. Abrosimova and A. Serebryakov, in *Physics of Amorphous Alloys* (Udmurd. Gos. Univ., Izhevsk, 1984), p. 116.
8. T. Spassov and U. Koster, J. Alloys Compd. **287**, 243 (1999).
9. *International Tables for Crystallography*, Ed. by T. Hahn (Kluwer, Dordrecht, 1989, 3rd ed.), Vol. A.

Translated by O. Borovik-Romanova

Physics of the Solid State, Vol. 44, No. 2, 2002, pp. 210–215. Translated from Fizika Tverdogo Tela, Vol. 44, No. 2, 2002, pp. 203–208.

METALS AND SUPERCONDUCTORS

Cyclotron Resonance and the de Haas–van Alfven Effect in the $(BEDT\text{-}TTF)_8Hg_4Cl_{12}(C_6H_5Cl)_2$ Organic Conductor

I. B. Voskoboĭnikov*, S. V. Demishev*, R. N. Lyubovskaya, V. V. Moshchalkov***, N. A. Samarin*, and N. E. Sluchanko***

** Institute of General Physics, Russian Academy of Sciences, ul. Vavilova 38, Moscow, 117942 Russia*

*** Institute of Problems in Chemical Physics, Russian Academy of Sciences, Chernogolovka, Moscow oblast, 142432 Russia*

**** Laboratorium voor Vaste-Stoffysica en Magnetisme, Katholieke Universiteit Leuven, B-3001 Leuven, Belgium*

Received May 15, 2001; in final form, June 28, 2001

Abstract—This paper reports on measurements of the de Haas–van Alfven effect in the quasi-two-dimensional organic conductor $(BEDT\text{-}TTF)_8Hg_4Cl_{12}(C_6H_5Cl)_2$ performed within the temperature range 0.33–1.44 K in magnetic fields of $B \le 50$ T. An analysis of quantum oscillations together with cyclotron resonance data obtained in the 40–120-GHz frequency range revealed that the complex quantum-oscillation spectrum is formed by the fundamental frequencies $\alpha \sim 256$ T and $\beta \sim 670$–610 T, as well as by combination and multiple frequencies. It is shown that the character of the temperature-induced oscillation-spectrum rearrangement can be interpreted within a model taking into account the existence of a magnetic phase transition at $T_c \sim 0.9$ K and the closeness of the fundamental frequency α with effective mass $m^* = 1.48m_0$ to the spin damping condition.

1. INTRODUCTION

This paper reports on an investigation into the ground state of an organic conductor of the $(BEDT\text{-}TTF)_8Hg_4X_{12}(C_6H_5Y)_2$ family, where BEDT-TTF stands for bis(ethylenedithio)tetrathiofulvalene and X, Y = Cl, Br. We shall denote subsequently, for the sake of simplicity, various compounds in the (X–Y) form; for instance, (Cl–Cl) corresponds to $(BEDT\text{-}TTF)_8Hg_4Cl_{12}(C_6H_5Cl)_2$ and so on.

The $(BEDT\text{-}TTF)_8Hg_4X_{12}(C_6H_5Y)_2$ compounds have a layered structure and exhibit two-dimensional conduction involving the BEDT-TTF molecular layers [1–6]. The low-temperature behavior of these organic conductors depends essentially on the chemical composition: while the (Br–Br) and (Br–Cl) compounds undergo a metal–insulator transition with decreasing temperature, the ground state of (Cl–Cl) and (Cl–Br) remains metallic down to liquid-helium temperatures [1–6]. In (Cl–Cl) and (Cl–Br), Shubnikov–de Haas (SH) and de Haas–van Alfven (HA) quantum oscillations were observed to exist [6–9], which makes these materials promising in Fermi-surface studies.

The pioneering paper [7] reported a complex structure for the SH oscillations observed in (Cl–Cl) samples in magnetic fields of $B \le 16$ T. At $T \sim 1.4$ K, the spectrum consisted of six frequencies: $F_1 = 150$ T, $F_2 = 250$ T (dominant), $F_3 = 400$ T, $F_4 = 500$ T, $F_5 = 650$ T, and $F_6 = 910$ T, whose conditions of observation depended on the direction of the measuring current relative to the crystallographic axes. At the same time, measurements of the HA effect showed the HA spectrum to be not so rich and, for $B < 14$ T, to consist of three frequencies, namely, F_2, F_4, and F_5. Extending the field range covered to $B \sim 35$ T also revealed a number of features in the SH oscillation spectrum with frequencies in excess of 1000 T [9].

The complex oscillation spectrum observed is difficult to reconcile with the theoretical model proposed in [10], according to which the Fermi surface is made up of two cylinders with approximately equal cross-sectional areas. The explanation proposed in [9] suggests that some of the frequencies in the spectra are of combination nature and result, for instance, from magnetic breakdown or magnetic interaction [11].

Another unclear point is the effective mass of carriers in (Cl–Cl). The temperature dependence of the SH oscillation amplitude yields $m^* = 1.35m_0$ [7], which differs noticeably from the value $m^* = 1.9m_0$ derived from optical experiments [12].

To establish the nature of these contradictions, we carried out measurements of the HA effect in magnetic fields of up to 50 T at temperatures from 0.33 to 1.44 K, as well as cyclotron resonance (CR) measurements in the millimeter-wavelength range. The data obtained allowed one to interpret the complex oscillation spectrum of the (Cl–Cl) samples and the specific features of its temperature-induced rearrangement.

2. EXPERIMENTAL TECHNIQUE

The samples used in the HA measurements were single crystals typically measuring $1 \times 1 \times 0.5$ mm; in

the CR studies, they measured $3 \times 3 \times 0.5$ mm. Each technique was tested on several samples, and each of them exhibited identical behavior.

The preparation technique employed and the structure of the samples are described in [1]. The magnetic field used in the CR and HA studies was directed perpendicular to the planes in which the two-dimensional carriers moved.

The studies of the HA effect were performed on a pulsed magnetic field setup at the Katholieke Universiteit Leuven (Belgium) [13]. The magnetic properties in pulsed magnetic fields of up to 50 T were investigated using the induction method [11] with pulses 20-ns long. The temperature measurements in the 0.33–1.44 K range were performed in a He^3 cryostat.

The magnetic properties in a strong pulsed field were studied on three (Cl–Cl) crystals; all of them exhibited the same quantum-oscillation pattern. To reduce random error and check the reproducibility of experimental data, the pulsed measurements were repeated several times for each fixed temperature and with varied pulsed-field amplitude (10, 20, 30, 40, and 50 T). The accuracy of reproducibility of receiving the coil signals was no worse than 0.3%, with the error being primarily due to the baseline displacement, and the oscillating part did not depend, within experimental error, on the pulse amplitude and did not vary under repeated pulses of the same amplitude.

The CR measurements were performed at the Institute of General Physics, RAS, using a custom-built millimeter-range magnetooptical spectrometer. 40–120 GHz radiation was generated with backward-wave tube generators, a carbon bolometer in thermal contact with the sample serving as the sensor. As shown earlier [14, 15], this measurement circuit permits one to measure the power absorbed in a sample as a function of the magnetic field, $P(B)$. To enhance the sensitivity in studies of (Cl–Cl) crystals, two identical bridge-connected bolometers, one of them attached to the sample and the other left free, were placed into the radiation channel. This sensor connection circuit substantially suppressed the instabilities associated with uncontrollable temperature fluctuations and made it possible to increase the sensitivity to the sample response by a factor of approximately 10–15 compared to the sensitivity level reported earlier in [14, 15]. In addition, the bridge arrangement turned out to be very convenient in performing temperature measurements in the 1.7–4.2 K range.

3. CYCLOTRON RESONANCE IN $(BEDT\text{-}TTF)_8Hg_4Cl_{12}(C_6H_5Cl)_2$ CRYSTALS

Because the CR detection technique employed assumes that not only the sample but also the components of the measuring cell are acted upon by microwave radiation, check $P_0(B)$ measurements on the cell without a sample were carried out in order to separate

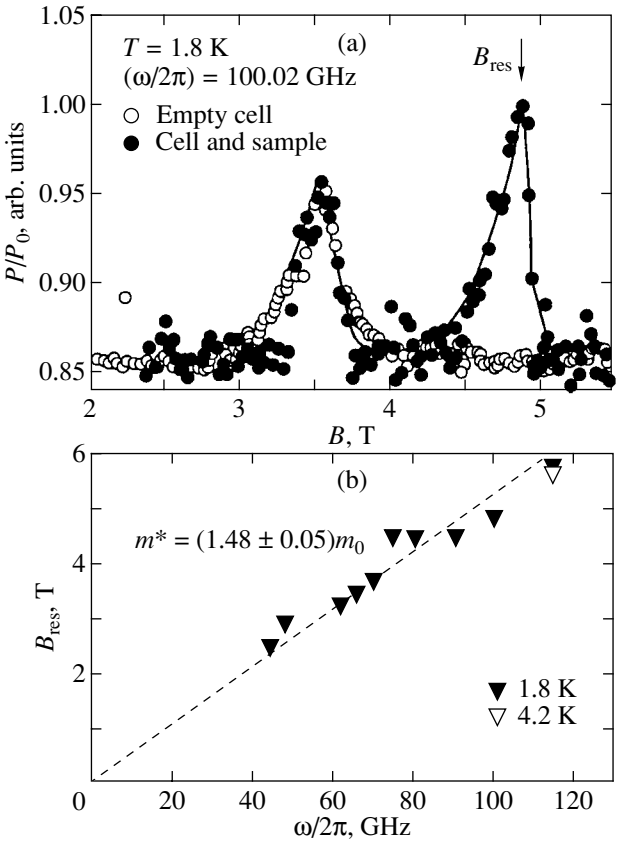

Fig. 1. (a) Resonance magnetoabsorption of microwave radiation in a (Cl–Cl) sample and (b) resonance field vs. radiation frequency plot.

the resonant magnetoabsorption associated with the sample, $P(B)$. Such a comparison is illustrated in Fig. 1a. We readily see that placing a sample into the cell at a frequency $\omega/2\pi = 100$ GHz gives rise to a resonance at $B_{res} \sim 4.9$ T, whereas the resonance at $B \sim 3.5$ T has the same amplitude as in the case of the empty cell and originates from EPR in the bolometer material.

The slope of the linear $B_{res}(\omega)$ plot (Fig. 1b) yielded an effective mass $m^* = (1.48 \pm 0.05)m_0$. This is close to the value derived earlier from the SH effect, $m^* = 1.35m_0$ [3]. Figure 2 presents the temperature dependences of the CR parameters (the amplitude $\Delta P/P = P(B_{res})/P_0(B_{res}) - 1$ and the relaxation time τ, calculated from the absorption line width). Note that the CR amplitude first grows with decreasing temperature, to fall off subsequently for $T \leq 2.6$K. At the same time, for $T \leq 3$ K, one observes a strong (practically threefold) decrease in the relaxation time τ.

Thus, the conditions of CR observation in (Cl–Cl) samples become less favorable with decreasing temperature (i.e., the parameter $\omega\tau$ decreases). This behavior appears anomalous, because in the organic metals investigated earlier [14, 15], as well as in conventional metals and semiconductors, a decrease in temperature

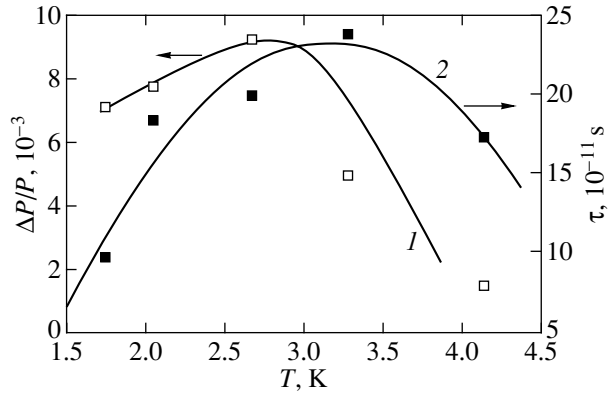

Fig. 2. Temperature dependences of (*1*) the cyclotron resonance amplitude and (*2*) relaxation time.

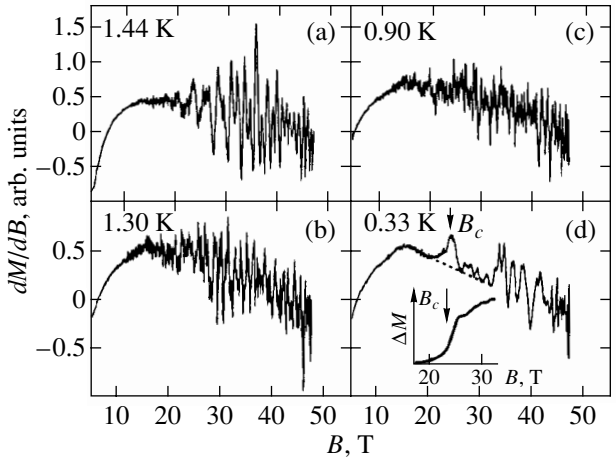

Fig. 3. Quantum oscillations of the magnetization of a (Cl–Cl) sample measured at different temperatures.

brings about an increase in CR absorption rather than a decrease.

4. DE HAAS–VAN ALFVEN EFFECT IN $(BEDT\text{-}TTF)_8Hg_4Cl_{12}(C_6H_5Cl)_2$

The induction technique used in the pulsed magnetic-field experiments permits one to measure the derivative of the magnetic moment $(dM/dB) = f(B)$ [11]. The experimental data on dM/dB obtained on a (Cl–Cl) sample at different temperatures are displayed in Fig. 3. At $T = 1.44$ K, one observes distinct quantum oscillations of the magnetization consisting of several frequencies for $B \geq 15$ T (Fig. 3a). Lowering the temperature to $T = 0.9$ K results in a strong suppression of the oscillations (Fig. 3c). A further decrease in temperature restores the oscillatory pattern for $T \leq 0.7$ K (Fig. 3d).

Interestingly, HA quantum oscillations are observed for $T \leq 0.7$ K only in the region $B \geq B_c = 25$ T and are not seen for $B \leq B_c$. At $B = B_c$, the $dM(B)/dB$ curve exhibits a maximum characteristic of a magnetic phase transition, which is accompanied by an abrupt increase in the sample magnetization (inset to Fig. 3d). Because the amplitude of quantum oscillations usually grows with decreasing temperature as a result of Landau level narrowing [11], it is probably the magnetic phase transition in (Cl–Cl) induced by the temperature decrease that is the origin of the anomalous suppression of the oscillation amplitude at $T \sim T_c \sim 0.9$ K.

Indeed, the decrease in the oscillation amplitude at temperatures close to the phase-transition point can be accounted for, for instance, by an increase in scattering from magnetic fluctuations and additional Landau level broadening caused by them. Note that the trend towards poorer CR observation conditions with decreasing temperature (Section 3) is in qualitative agreement with this hypothesis.

The data of Fig. 3 suggest that the formation of a phase with a new type of magnetic ordering for $T < T_c$ results in a strong increase in carrier scattering and that the application of a strong field $B > B_c$ suppresses this effect, making observation of the HA oscillations again possible. Apparently, for $B > B_c$, magnetic order recovers to a level close to that of the original high-temperature ($T > T_c$) phase.

Note that a strong effect of the magnetic phase transition on the amplitude and harmonic composition of the quantum oscillations was observed earlier in the strongly correlated metal $PrCu_2$ [16].

To test the above conjectures, we consider the variation of the HA oscillation frequency spectra in more detail. To compute the spectra, we subtracted the monotonic component from the dM/dB curves and represented the data as a function of the inverse magnetic field. Prior to describing the results thus obtained, we note that the position of each feature in a complex oscillation spectrum with closely lying lines can be determined only to within a certain error. In this case, some lines which can be observed in computed Fourier spectra are not stable and depend substantially on the actual choice of the window function. For instance, for $T = 1.44$ K, such unstable features lie in the 750–950 and 100–200 T ranges (Fig. 4). These frequencies will not be considered in what follows, and we shall limit ourselves to a discussion of the spectral features whose positions are reproduced at different temperatures and do not depend on the method used in data processing. The data on the frequencies characterizing the HA spectra at different temperatures are displayed in Fig. 5 and listed in the table.

We consider first the result obtained for $T > T_c \sim 0.9$ K (Fig. 4). For $T = 1.44$ K, there is a good correlation between the data presented in this work and those derived earlier from an analysis of the SH oscillations (in Fig. 4a, the frequencies F_1–F_6 taken from [5] are denoted by triangles). As in [5], in the HA spectrum

obtained at 1.44 K and dominated by the frequency $\alpha \approx F_2$, one also observes the frequencies $y \approx F_3$, $x \approx F_4$, and $\beta \approx F_5$. At the same time, the HA oscillation spectrum does not contain the frequencies $F_1 \sim 150$ T and $F_6 \sim 900$ T, while one observes a new frequency $\gamma \sim 1000$ T. The decrease in temperature in the range $1.11 \leq T \leq 1.44$ K results in suppression of the α and x frequencies relative to the y and β frequencies (Fig. 4).

In the phase-transition region, $T \sim T_c \sim 0.9$ K, all oscillation frequencies in the spectra disappear, except γ, a frequency which is observed both for $T < T_c$ and for $T > T_c$ (Fig. 4).

Below the phase-transition temperature, $T < T_c$, the spectra do not contain the α frequency (Fig. 4) and the harmonic frequencies β and y decrease slightly, while x and γ remain unchanged within experimental error (Figs. 4, 5 and table). Thus, the analysis of the HA oscillation spectra suggests that the magnetic phase transition can apparently induce a change in the elements of the Fermi surface of the (Cl–Cl) sample.

5. DISCUSSION OF RESULTS

As follows from our preceding consideration, the HA oscillation spectrum obtained in this work at $T = 1.44$ K resembles an SH spectrum rather than the HA spectra measured in [9] for $B \leq 14$ T. A possible reason for these contradictions consists in that additional frequencies in our spectra appear for $B \geq 15$ T and the SH and HA oscillation spectra are in actual fact identical. There is, however, another possibility associated with induction currents that are generated in a sample in pulsed experiments and modulated by SH magnetoresistance oscillations. The modulated induction current should produce, in turn, an additional component of the signal in an induction coil not connected with dM/dB. As a result, the quantum oscillations detected in an induction experiment may turn out to be intermediate between the cases of pure SH and HA effects and this should affect the character of the observed spectra. In view of the strong temperature dependence of the features in Figs. 4 and 5, a final conclusion as to the pure or combined nature of the HA spectrum obtained in this work requires data on the SH oscillations at temperatures $T < 1$ K.

However, irrespective of the nature of the discrepancies between the variants of measurement of the HA effect, the main problem in interpretation of the oscillation data is how to reconcile a complex oscillation spectrum consisting of five or six frequencies with the relatively simple form of the Fermi surface, which is made up, according to calculations [10], of two closed parts. CR data confirm this result, because our experiments revealed one absorption line for $m^* = 1.48m_0$, whereas in the case of a Fermi surface consisting of many parts, there would have been several resonant magnetoabsorption features.

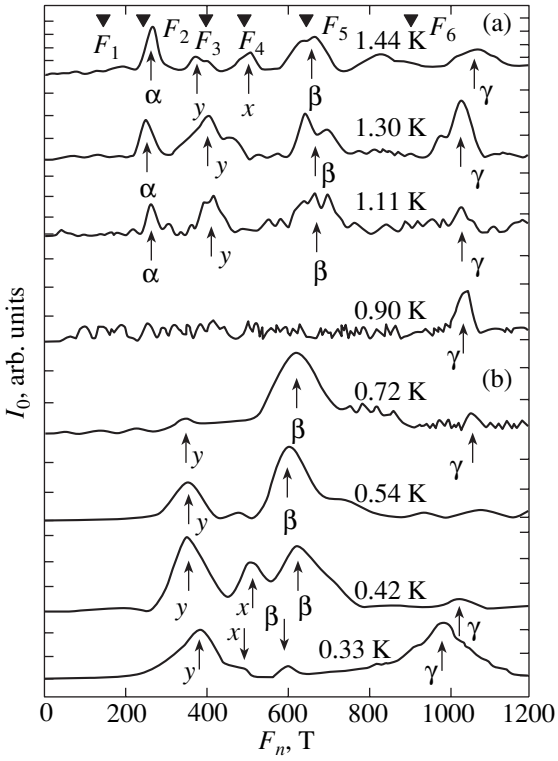

Fig. 4. Quantum-oscillation spectra of (Cl–Cl) samples for (a) $T > T_c$ and (b) $T < T_c$; I_0 is the amplitude and F_n is the frequency of oscillations.

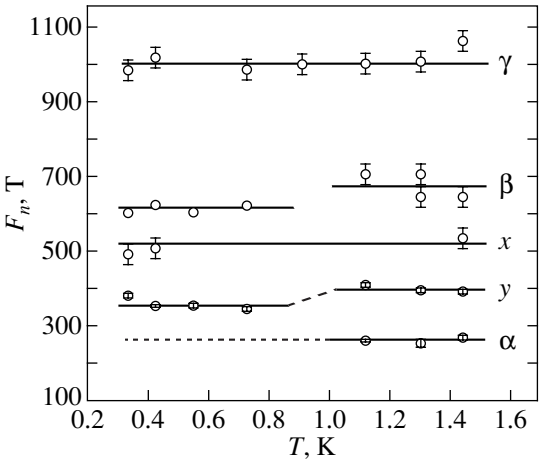

Fig. 5. Temperature-induced rearrangement of the fundamental frequencies in a quantum-oscillation spectrum.

We consider the possibility of interpreting our experimental data under the assumption [9] that some frequencies in the spectra are multiple- and combination-type. Following [9], we assume that the fundamental frequencies are α and β and that α corresponds to the effective mass $m_\alpha^* = 1.48m_0$, while the effective mass m_β^* for the frequency β is very high and lies out-

Oscillation frequencies for a (Cl–Cl) sample derived from the de Haas–van Alfven effect

Temperature range	Frequency, T				
	α	*y*	*x*	β	γ
$T > T_c$	256 ± 7	396 ± 8	515 ± 18	670 ± 33	
$T \sim T_c$	–	–	–	–	1008 ± 30
$T < T_c$	–	347 ± 4	515 ± 18	610 ± 12	

side the magnetooptic-spectrometer range (for $\omega/2\pi \geq 40$ GHz and $B \leq 7$ T, estimates yield $m^*_\beta = 4.9m_0$). First, we consider the region $T > T_c$. As seen from the data in Fig. 5 and the table, the frequencies *x* and *y* satisfy, within experimental accuracy, the relations

$$x = 2\alpha, \quad (1)$$

$$y = \beta - \alpha; \quad (2)$$

i.e., *x* is the second harmonic of the frequency α and *y* is a combination frequency. As for the nature of the frequency γ, it remains unclear, because one cannot choose a proper combination of the type $m\beta \pm n\alpha$ for it (*n* and *m* are integers).

Within the $T < T_c$ range, one has first to explain the disappearance of the frequency α. One possible interpretation is that the Fermi surface of (Cl–Cl) undergoes a strong rearrangement at temperatures below the phase transition. However, this hypothesis is at odds with the frequencies γ and *x* remaining unchanged. Therefore, within this approach, one has to assume that only certain parts of the (Cl–Cl) Fermi surface are sensitive to changes in the magnetic order type.

Another possible explanation can be obtained using the approach proposed in [17] and applied successfully to description of the anomalous decrease in the oscillation amplitude of $(BEDT\text{-}TTF)_2KHg(SCN)_4$ samples at low temperatures. The model of [17] consists essentially in that the *g* factor becomes renormalized by carrier interaction with the magnetic subsystem and, in general, is a function of the magnetic field and temperature, $g(B, T)$. As a result, when describing the temperature dependence of the quantum-oscillation amplitude, one has to take into account the spin factor for the *p* harmonic $\cos[(1/2)p\pi g(B, T)(m^*/m_0)]$ [11]. One clearly sees that if a mode is close to the condition of spin damping of the first harmonic

$$g\frac{m^*}{m_0} = 2n + 1, \quad n = 0, 1, 2, \ldots, \quad (3)$$

small changes in the *g* factor are capable of giving rise to strong features in the oscillation amplitude.

It is such a case that is realized for the frequency α in the (Cl–Cl) samples, because $m^* \sim 1.5m_0$ and $g \approx 2$. Indeed, CR measurements yield $1.48m_0$ for the effective mass (Section 3), which is close to the critical value $1.5m_0$, and a relatively small renormalization of the *g* factor is enough for the condition of Eq. (3) to become satisfied and, hence, for the amplitude of the first harmonic of frequency α to vanish. The amplitude of the second harmonic will remain finite in this case; this feature [for the frequency *x* in the case of (Cl–Cl)] is observed in quantum-oscillation spectra (Figs. 4, 5). Note that, because the amplitude of all oscillation features is strongly suppressed for $T \sim T_c$, observation of the 2α frequency requires the temperature to be lowered to $T \sim 0.4$ K (Fig. 4).

Considered within this interpretation, the constancy of the frequency *x* implies constancy of the frequency α for $T > T_c$ and $T < T_c$. According to the data in Fig. 5 and the table, the frequency β decreases approximately by 60 T for $T < T_c$; however, Eq. (2) is still met within experimental accuracy, which, on the one hand, buttresses the combination nature of the frequency *y*, while on the other, is in accord with the assumption of an invisible presence of frequency α, in full accordance with the model from [17].

Combination frequencies in quantum-oscillation spectra can arise as a result of magnetic breakdown or magnetic interaction [8]. However, estimation of the Shoenberg parameter for the (Cl–Cl) sample yields $\alpha = 4\pi(dM/dB) \sim 10^{-2}$, which practically excludes the latter effect from consideration [8]. Thus, the frequency *y* and the orbit associated with it originate most probably from magnetic breakdown. It may be conjectured that the frequency γ can also be accounted for by the magnetic breakdown effect; however, additional studies are required to provide a final answer to the nature of this feature in the quantum-oscillation spectrum.

In accordance with the proposed interpretation, the combination frequency *y* is a difference rather than a sum frequency and should be due to the subtraction of some electronic orbits. This is possibly connected with the fact that the fundamental frequency β, in turn, is a combination of frequencies and results from magnetic breakdown. Analysis of the possible Fermi surface structure and making the corresponding theoretical calculations is, however, beyond the scope of the present work.

Thus, a combined study of cyclotron resonance and the HA effect has established that the complex quantum-oscillation spectrum and the character of its rearrangement in the 0.33–1.44 K temperature range in (Cl–Cl) samples can be interpreted in terms of a model that assumes the existence of a magnetic phase transition at $T_c \sim 0.9$ K and the closeness of one of the fundamental harmonics to the spin damping condition.

The magnetic transition manifests itself experimentally as a feature in the monotonic part of the field dependence of magnetization, which is observed for $T < 0.9$ K, and as suppression of the amplitude of the oscillating part in *dM*/*dB* in the vicinity of $T \sim 0.9$ K (Figs. 3, 4).

The complex temperature-induced rearrangement of quantum-oscillation spectra can be qualitatively accounted for within the hypothesis by assuming *g*-factor renormalization to occur as a result of interaction with the magnetic subsystem, as well as the existence of parts of the Fermi surface and/or orbits sensitive to the postulated magnetic phase transition.

At the same time, the origin of magnetism in (Cl–Cl) samples remains unclear and the hypothesis formulated in this work requires further experimental testing. This would require further investigation of the magnetic properties and magnetic structure of (Cl–Cl) samples at low temperatures.

ACKNOWLEDGMENTS

The authors are indebted to R.B. Lyubovskiĭ and L. Brossard for useful discussions.

This study was supported by the Ministry of Industry, Science, and Technologies ("Physics of microwaves" and "Fundamental spectroscopy" programs). The experiments performed at the Katholieke Universiteit Leuven (Belgium) were supported by the GOA and FWO-Vlaandren programs.

REFERENCES

1. R. N. Lyubovskaya, T. V. Afanas'eva, O. A. D'yachenko, *et al.*, Izv. Akad. Nauk SSSR, Ser. Khim., No. 11, 2872 (1990).
2. R. N. Lyubovskaya, O. A. Dyachenko, V. V. Gritsenko, *et al.*, Synth. Met. **41–43**, 1907 (1991).
3. O. A. D'yachenko, V. V. Gritsenko, Sh. G. Mkoyan, *et al.*, Izv. Akad. Nauk SSSR, Ser. Khim., No. 9, 2062 (1991).
4. V. V. Gritsenko, O. A. D'yachenko, G. B. Shilov, *et al.*, Izv. Akad. Nauk SSSR, Ser. Khim., No. 4, 894 (1991).
5. R. N. Lyubovskaya, O. A. Dyachenko, and R. B. Lyubovskii, Synth. Met. **55–57**, 2899 (1993).
6. R. B. Lyubovskiĭ, S. I. Pesotskiĭ, and R. N. Lyubovskaya, Pis'ma Zh. Éksp. Teor. Fiz. **62**, 35 (1995) [JETP Lett. **62**, 37 (1995)].
7. R. B. Lyubovskiĭ, S. I. Pesotskiĭ, A. Gilevskiĭ, and R. N. Lyubovskaya, Zh. Éksp. Teor. Fiz. **107**, 1698 (1995) [JETP **80**, 946 (1995)].
8. R. B. Lyubovskii, R. N. Lyubovskaya, and O. A. Dyachenko, J. Phys. I **6**, 1609 (1996).
9. R. B. Lyubovskii, S. I. Pesotskii, C. Proust, *et al.*, Synth. Met. **113**, 227 (2000).
10. L. F. Verious and E. Canadell, J. Phys. I **4**, 939 (1994).
11. D. Shoenberg, *Magnetic Oscillations in Metals* (Cambridge Univ. Press, Cambridge, 1984; Mir, Moscow, 1986).
12. M. G. Kaplunov and R. N. Lyubovskaya, J. Phys. I **2**, 1811 (1992).
13. F. Herlach, C. C. Agosta, R. Bogaerts, *et al.*, Physica B (Amsterdam) **216**, 161 (1996).
14. S. V. Demishev, A. V. Semeno, N. E. Sluchanko, *et al.*, Phys. Rev. B **53**, 12794 (1996).
15. S. V. Demishev, A. V. Semeno, N. E. Sluchanko, *et al.*, Zh. Éksp. Teor. Fiz. **111**, 979 (1997) [JETP **84**, 540 (1997)].
16. Y. Onuki, R. Settai, and H. Aoki, Physica B (Amsterdam) **223–224**, 141 (1996).
17. S. V. Demishev, J. Vanacken, L. Weckhuysen, *et al.*, Europhys. Lett. **42**, 455 (1998).

Translated by G. Skrebtsov

Physics of the Solid State, Vol. 44, No. 2, 2002, pp. 216–220. Translated from Fizika Tverdogo Tela, Vol. 44, No. 2, 2002, pp. 209–212.

METALS AND SUPERCONDUCTORS

The Ground-State Energy of the *B*–*B*'–*U* Hubbard Model in the Static-Fluctuation Approximation

G. I. Mironov

Mari State Pedagogical Institute, Ĭoshkar Ola, 424002 Russia

e-mail: mir@mgpi.mari.ru

Received February 13, 2001; in final form, June 13, 2001

Abstract—The ground-state energy of the two-sublattice two-dimensional Hubbard model is calculated in the static-fluctuation approximation with allowance for electron transfer from sites to next-to-nearest neighbor sites. In a specific case, the energy of the one-dimensional Hubbard model is calculated and compared with an exact solution. © *2002 MAIK "Nauka/Interperiodica".*

1. Some properties of high-temperature superconductors (HTSCs) in both superconducting and normal states can be explained only if one takes into account both the copper–oxygen hopping integrals B and the hopping integrals B' between nearest neighbor oxygen atoms. Qualitative consideration reveals that the oxygen–oxygen hole transfer can affect the physical properties of HTSCs. Therefore, it is of considerable interest to calculate the characteristics of the system with allowance for electron (or hole) transfer to next-to-nearest neighbor sites of the crystal lattice.

In [1, 2], we developed a method for solving equations of the *B*–*B*'–*U* Hubbard model in the static-fluctuation approximation (SFA) and investigated (in [2]) the dependence of the energy spectrum and magnetization of the system on the magnitude of the transfer integral B' to a next-to-nearest neighbor site in the two-dimensional bipartite Hubbard model [3, 4].

The objective of this paper is to calculate the ground-state energy of the *B*–*B*'–*U* Hubbard model in the SFA.

2. By analogy with the Emery model, it is assumed that, in contrast to the standard Hubbard model, the lattice is composed of two sublattices of atoms of different species. We also assume that electrons can be transferred to next-to-nearest neighboring atoms of the crystal lattice. The Hamiltonian of this two-dimensional bipartite *B*–*B*'–*U* Hubbard model has the form

$$H = H_0 + V, \tag{1}$$

$$H_0 = \sum_{\sigma,\, f \in A} \varepsilon_1 n_{f\sigma} + \sum_{\sigma,\, l \in C} \varepsilon_2 n_{l\sigma} + \sum_{\sigma,\, f,\, l} B_{fl}(a^+_{f\sigma}a_{l\sigma} + a^+_{l\sigma}a_{f\sigma}) + \sum_{\sigma,\, l',\, l} B_{l'l}a^+_{l'\sigma}a_{l\sigma}, \tag{2}$$

$$V = \frac{U_1}{2}\sum_{\sigma,\, f \in A} n_{f\sigma}n_{f\bar{\sigma}} + \frac{U_2}{2}\sum_{\sigma,\, f \in C} n_{f\sigma}n_{f\bar{\sigma}}, \tag{3}$$

where $a^+_{j\sigma}$ and $a_{j\sigma}$ are the creation and annihilation Fermi operators, respectively, of an electron with spin σ at lattice site j ($j = f, l$); $n_{f\sigma} = a^+_{j\sigma}a_{f\sigma}$; ε_1 and ε_2 are the self-energies of an electron at a site of the A and C sublattices, respectively; $B_{fl} = B(f - l)$, $B_{l'l} = B(l' - l)$ are the transfer integrals describing electron hopping (due to the kinetic energy of the crystal field) to a nearest and a next-to-nearest neighbor site, respectively; $\bar{\sigma} = -\sigma$; and U_1 and U_2 are the Coulomb repulsion energies of two electrons at one site of the A and C lattices, respectively. In order for Hamiltonian (1) to be used to describe the case of holes moving in CuO_2 planes in HTSCs, only the electrons of one sublattice (as in the case of oxygen in CuO_2 planes) are assumed to be able to transfer along the diagonals of a square unit cell to sites of the same sublattice (for the sake of simplicity, we consider a hypothetical square lattice).

3. In [2], the electron creation operators in the Heisenberg representation, which determine the evolution of the system, were found to have the form

$$\begin{aligned} a^+_{k\sigma}(\tau) &= \{[a^+_{k\sigma}(0)[((\varepsilon'_1 - \varepsilon'_{2k})/2t_k)\sinh(t_k\tau) \\ &+ \cosh(t_k\tau)] + b^+_{k\sigma}(0)\sinh(t_k\tau)B_k/t_k]\cosh(U_1\Phi\tau) \\ &+ [\Delta n_{1\bar{\sigma}}a^+_{k\sigma}(0)[((\varepsilon'_1 - \varepsilon'_{2k})/2t_k)\sinh(t_k\tau) \\ &+ \cosh(t_k\tau)] + \Delta n_{1\bar{\sigma}}b^+_{k\sigma}(0)\sinh(t_k\tau)B_k/\tau_k] \\ &\times \sinh(U_1\Phi\tau)/\Phi\}\exp(\tau(\varepsilon'_1 + \varepsilon'_{2k})/2), \\ b^+_{k\sigma}(\tau) &= \{[b^+_{k\sigma}(0)[((\varepsilon'_{2k} - \varepsilon'_1)/2t_k)\sinh(t_k\tau) \end{aligned} \tag{4}$$

1063-7834/02/4402-0216$22.00 © 2002 MAIK "Nauka/Interperiodica"

$$+\cosh(t_k\tau)] + a^+_{k\sigma}(0)\sinh(t_k\tau)B_k/t_k]\cosh(U_2\Phi\tau)$$
$$+[\Delta n_{2\bar\sigma}b^+_{k\sigma}(0)[((\varepsilon'_{2k}-\varepsilon'_1)/2t_k)\sinh(t_k\tau) \quad (5)$$
$$+\cosh(t_k\tau)] + \Delta n_{2\bar\sigma}a^+_{k\sigma}(0)\sinh(t_k\tau)B_k/\tau_k]$$
$$\times\sinh(U_2\Phi\tau)/\Phi\}\exp(\tau(\varepsilon'_1+\varepsilon'_{2k})/2),$$

where

$$\varepsilon'_1+\varepsilon'_{2k} = \varepsilon_1+\varepsilon_2+(U_1+U_2)/2$$
$$+\sigma S(U_1-U_2)-4B'\cos(k_xa)\cos(k_ya),$$
$$\varepsilon'_1-\varepsilon'_{2k} = \varepsilon_1-\varepsilon_2+(U_1-U_2)/2$$
$$+\sigma S(U_1+U_2)+4B'\cos(k_xa)\cos(k_ya).$$

The remainder of the notation is the same as that in [2].

Using Eqs. (4) and (5), we will calculate the ground-state energy (the average energy of the Hubbard model $E_0 = \langle H\rangle$ at the temperature $T \longrightarrow 0$).

Following the method developed in [2], we calculate the anticommutator Green's functions:

$$\langle a^+_{k\sigma}|b_{k\sigma}\rangle_E = \frac{i}{2\pi}\frac{1}{4}\frac{B_k}{t_k}\left\{\frac{1}{E-U_1\Phi-t_k-(\varepsilon'_1+\varepsilon'_{2k})/2}\right.$$
$$+\frac{1}{E+U_1\Phi-t_k-(\varepsilon'_1+\varepsilon'_{2k})/2} \quad (6)$$
$$-\frac{1}{E-U_1\Phi+t_k-(\varepsilon'_1+\varepsilon'_{2k})/2}$$
$$\left.-\frac{1}{E+U_1\Phi+t_k-(\varepsilon'_1+\varepsilon'_{2k})/2}\right\}.$$

The anticommutator Green's functions $\langle b^+_{k\sigma}|a_{k\sigma}\rangle_E$ are also given by Eq. (6) with U_2 in place of U_1. In order to take into account the contribution from the Coulomb repulsion energy (3) to the ground-state energy, we should also calculate the anticommutator Green's functions $\langle a^+_{k+k_1-k_2\downarrow}|a_{k_1\downarrow}(0)a^+_{k_2\uparrow}(0)a_{k\uparrow}(0)\rangle_E$ and $\langle b^+_{k+k_1-k_2\downarrow}|b_{k_1\downarrow}(0)b^+_{k_2\uparrow}(0)b_{k\uparrow}(0)\rangle_E$ for electrons of different subsystems and sum them over all possible values of k_1, k_2, and k in the first Brillouin zone.

Using Eq. (4), it can be found that

$$\frac{2U}{N}\sum_{k_1,k_2,k}\langle a^+_{k+k_1-k_2\uparrow}|a_{k_1\uparrow}(0)a^+_{k_2\downarrow}(0)a_{k\downarrow}(0)\rangle_E$$
$$= \frac{i}{2\pi}\frac{U}{4}\sum_{k_1,k}\langle a^+_{k_1\downarrow}a_{k_1\downarrow}\rangle\left\{\frac{1+(\varepsilon'_1-\varepsilon'_{2k})/2t_k}{E-U_1\Phi-t_k-(\varepsilon'_1+\varepsilon'_{2k})/2}\right.$$
$$+\frac{1+(\varepsilon'_1-\varepsilon'_{2k})/2t_k}{E+U_1\Phi-t_k-(\varepsilon'_1+\varepsilon'_{2k})/2}$$
$$+\frac{1-(\varepsilon'_1-\varepsilon'_{2k})/2t_k}{E-U_1\Phi+t_k-(\varepsilon'_1+\varepsilon'_{2k})/2}$$
$$\left.+\frac{1-(\varepsilon'_1-\varepsilon'_{2k})/2t_k}{E+U_1\Phi+t_k-(\varepsilon'_1+\varepsilon'_{2k})/2}\right\} \quad (7)$$
$$+\frac{i}{2\pi}\frac{U}{4\Phi}\sum_{k_1,k}\langle\Delta n_{1\downarrow}a^+_{k_1\downarrow}a_{k_1\downarrow}\rangle$$
$$\times\left\{\frac{1+(\varepsilon'_1-\varepsilon'_{2k})/2t_k}{E-U_1\Phi-t_k-(\varepsilon'_1+\varepsilon'_{2k})/2}\right.$$
$$-\frac{1+(\varepsilon'_1-\varepsilon'_{2k})/2t_k}{E+U_1\Phi-t_k-(\varepsilon'_1+\varepsilon'_{2k})/2}$$
$$+\frac{1-(\varepsilon'_1-\varepsilon'_{2k})/2t_k}{E-U_1\Phi+t_k-(\varepsilon'_1+\varepsilon'_{2k})/2}$$
$$\left.-\frac{1-(\varepsilon'_1-\varepsilon'_{2k})/2t_k}{E+U_1\Phi+t_k-(\varepsilon'_1+\varepsilon'_{2k})/2}\right\}.$$

A similar expression can also be found for the Green's function $\langle b^+_{k+k_1-k_2\downarrow}|b_{k_1\downarrow}(0)b^+_{k_2\uparrow}(0)b_{k\uparrow}(0)\rangle_E$. (We do not write it out, because it is cumbersome.)

We consider the case where, on the average, there is one electron per site of the crystal lattice ($n = 1$); it is not difficult to extend the results to the case of an arbitrary electron concentration n. Using Eqs. (6) and (7) and the fluctuation–dissipation theorem, the average energy of the system is calculated to be

$$E_0 = \langle H_0\rangle + \langle V\rangle, \quad (8)$$

where

$$\langle H_0\rangle = -\sum_{k,\sigma}\frac{B_k^2}{4t_k}\left\{f^+\left(U_1\Phi-t_k-\frac{B'_k+\sigma S(U_1-U_2)}{2}\right)\right.$$
$$+f^+\left(U_1\Phi-t_k+\frac{B'_k+\sigma S(U_1-U_2)}{2}\right) \quad (9)$$
$$+f^+\left(U_2\Phi-t_k-\frac{B'_k+\sigma S(U_1-U_2)}{2}\right)$$
$$\left.+f^+\left(U_2\Phi-t_k+\frac{B'_k+\sigma S(U_1-U_2)}{2}\right)\right\},$$

$$
\begin{aligned}
\langle V\rangle = \frac{U_1}{8N}\sum_k\Bigg\{&\left(1+\frac{S(U_1+U_2)-B'_k}{2t_k}\right)\\
&\times f^+\left(t_k-U_1\Phi+\frac{S(U_1-U_2)+B'_k}{2}\right)\\
&\times\left(1-\frac{S(U_1+U_2)-B'_k}{2t_k}\right)\\
&\times\left[1+f^+\left(U_1\Phi-t_k+\frac{S(U_1-U_2)+B'_k}{2}\right)\right]\Bigg\}\\
&\times\sum_p\Bigg\{\left(1-\frac{S(U_1+U_2)+B'_p}{2t_p}\right)\\
&\times f^+\left(t_p-U_\Phi+\frac{B'_p-S(U_1-U_2)}{2}\right)\\
&+\left(1+\frac{S(U_1+U_2)+B'_p}{2t_p}\right)\\
&\times\left[1+f^+\left(U_1\Phi-t_p+\frac{B'_p-S(U_1-U_2)}{2}\right)\right]\Bigg\}\\
&+\frac{U_2}{8N}\sum_k\Bigg\{\left(1-\frac{S(U_1+U_2)-B'_k}{2t_k}\right)\\
&+f^+\left(t_k-U_2\Phi+\frac{S(U_1-U_2)+B'_k}{2}\right)\\
&+\left(1+\frac{S(U_1+U_2)-B'_k}{2t_k}\right)\\
&\times\left[1+f^+\left(U_2\Phi-t_k+\frac{S(U_1-U_2)+B'_k}{2}\right)\right]\\
&\times\sum_p\Bigg\{\left(1+\frac{S(U_1+U_2)+B'_p}{2t_p}\right)\Bigg\}\\
&\times f^+\left(t_p-U_2\Phi+\frac{B'_p-S(U_1-U_2)}{2}\right)\\
&+\left(1-\frac{S(U_1+U_2)+B'_p}{2t_p}\right)\\
&\times\left[1+f^+\left(U_2\Phi-t_p+\frac{B'_p-S(U_1-U_2)}{2}\right)\right]\Bigg\}\\
&-\frac{U_1\Phi}{4}\sum_k\Bigg[\left(1+\frac{S(U_1+U_2)-B'_k}{2t_k}\right)\\
&\times f^+\left(t_k-U_1\Phi+\frac{S(U_1-U_2)+B'_k}{2}\right)\\
&+\left(1-\frac{S(U_1+U_2)-B'_k}{2t_k}\right)\\
&\times f^+\left(t_k-U_1\Phi-\frac{S(U_1-U_2)+B'_k}{2}\right)\Bigg]\\
&-\frac{U_2\Phi}{4}\sum_k\Bigg[\left(1-\frac{S(U_1+U_2)-B'_k}{2t_k}\right)\\
&\times f^+\left(t_k-U_2\Phi+\frac{S(U_1-U_2)+B'_k}{2}\right)\\
&+\left(1+\frac{S(U_1+U_2)-B'_k}{2t_k}\right)\\
&\times f^+\left(t_k-U_2\Phi-\frac{S(U_1-U_2)+B'_k}{2}\right)\Bigg].
\end{aligned}
\tag{10}
$$

In Eqs. (9) and (10), $f^+(x) = [1 + \exp(\beta x)]^{-1}$ is the Fermi distribution function, $\Phi = \sqrt{0.25 - S^2}$, $B_k = -2B[\cos(k_x a) + \cos(k_y a)]$, $B'_k = -4B'\cos(k_x a)\cos(k_y a)$, and summation is carried out over k and p lying in the first Brillouin zone.

In Fig. 1, the ground-state energy E_0 is plotted as a function of $(U_1 + U_2)/2$ for three different values of the transfer integral to a next-to-nearest neighboring site (along a square diagonal). Analysis of these dependences reveals that in the region of strong correlations, the ground-state energy for $B' < 0$ decreases as the transfer integral to a next-to-nearest neighboring site increases in magnitude. This is due to the fact that allowance for the transfer integral B' in the case of strong correlations leads to delocalization of electrons, which causes the total energy of the system to decrease. If electron correlations are weak, then, conversely, the ground-state energy increases, because the electrons that are itinerant in the case of a small Coulomb interaction energy tend to localize when the transfer integral B' is taken into account.

4. Now, we compare our results with those available in the literature. An exact expression for the ground-state energy of the one-dimensional Hubbard model was derived in [5]. For comparison purposes, we consider the ground-state energy in this particular case.

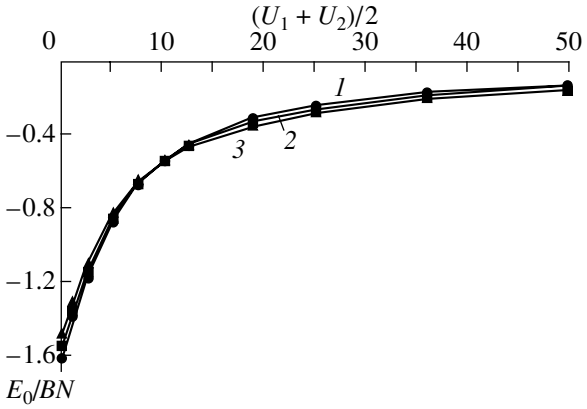

Fig. 1. Ground-state energy E_0 as a function of $(U_1 + U_2)/2$ for $n = 1$, $B = 1.5$ eV, $T = 0$, and B' equal to (*1*) 0, (*2*) –0.3*B*, and (*3*) –0.45*B*.

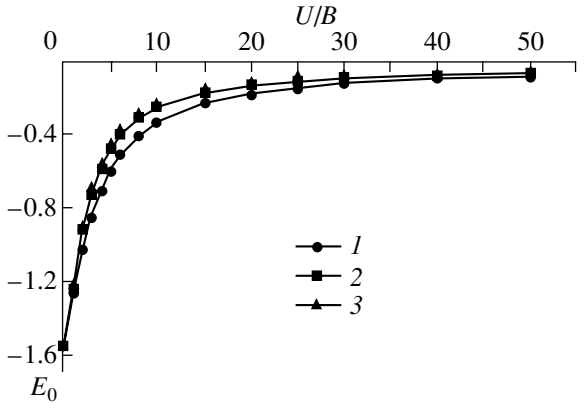

Fig. 2. Ground-state energy E_0 as a function of U/B for $n = 1$ and $T = 0$: (*1*) an exact solution [5], (*2*) a calculation from Eq. (11) with allowance for the dependence of S on the Coulomb repulsion energy U, and (*3*) a calculation from Eq. (11) for $S = 1/2$.

Putting $U_1 = U_2 = U$, $B_k = -2B\cos(k_x a)$, and $B_k' = 0$ in Eqs. (8) and (9), we obtain

$$\frac{E_0}{BN} = -\frac{2}{BN}\sum_k \frac{B_k^2}{t_k} f^+(U\Phi - t_k)$$

$$+ \frac{U}{4B}\left\{1 - \left[\frac{2}{N}\sum_k \frac{SU}{t_k} f^+(U\Phi - t_k)\right]^2\right\} \qquad (11)$$

$$-\frac{u\Phi}{BN}\sum_k f^+(-U\Phi + t_k).$$

Figure 2 shows the dependences of the ground-state energy E_0 on the ratio U/B as calculated from three different formulas: (i) the exact expression derived by Lieb and Wu [5], (ii) Eq. (11) with allowance for the dependence of the spin S on the Coulomb repulsion energy U, and (iii) Eq. (11) with $S = 1/2$. It is seen from Fig. 2 that the values of E_0 given by the exact expression in the limits of $U = 0$ and ∞ are identical to those calculated from Eq. (11) and the SFA solution is seen to be qualitatively similar to the exact solution. There is also reasonable quantitative agreement between the exact and approximate solutions; for example, the ratio $((E_0 - E_0^{\text{exact}})/E_0^{\text{exact}})$, which can be considered to be the relative error, is roughly 18% for $U/B = 4$ and 2% for $U/B = 2$. Thus, comparison of the exact and approximate solutions shows that the SFA adequately describes the Hubbard model under study in the cases of weak and strong correlations. In the intermediate case of moderate correlations, the SFA is likely to overestimate the effect of the Coulomb interaction. This overestimation becomes smaller in amount when the dependence of the spin S on the Coulomb repulsion energy is taken into account (curve *2* in Fig. 2).

It should be noted that in the case of strong correlations, the ground-state energy of the antiferromagnetic phase is found to be lower than that of the paramagnetic phase. The same result was obtained in [6] using the variational method. In the case of weak correlations at low temperatures (near $T = 0$), there is a tendency for the energy of the paramagnetic state to decrease in comparison with that of the antiferromagnetic phase (calculated in the SFA); for example, at $U/B = 1$, we have $\left|\frac{E_0^{\text{PM}} - E_0^{\text{AFM}}}{E_0^{\text{PM}}}\right| = 4\%$, where E_0^{PM} and E_0^{AFM} are the average energies of the system in the paramagnetic and antiferromagnetic states, respectively. Therefore, we may anticipate that at low temperatures, the antiferromagnetic–paramagnetic phase transition can occur as the Coulomb repulsion energy U is decreased (we recall that the case of half-filling is considered). It seems likely that a decrease in U at a fixed low temperature is similar in effect to an increase in temperature at a fixed value of U. As for the magnetic structure of the ground state in the weak-correlation regime (at $T = 0$), it should be investigated taking into account the character of elementary excitations at $T = 0$ [7–11].

Thus, the method developed in [1, 2] for calculating an anticommutator Green's function in the SFA enables one to investigate the energy spectrum of the *B*–*B*'–*U* Hubbard model and the magnetization of the system [2] and to calculate the ground-state energy. The electron transfer to next-to-nearest neighboring sites is shown to affect the ground-state energy of the Hubbard model.

ACKNOWLEDGMENTS

The author is grateful to R.R. Nigmatullin for his encouragement and interest in this work.

REFERENCES

1. G. I. Mironov, Fiz. Tverd. Tela (St. Petersburg) **39** (9), 1594 (1997) [Phys. Solid State **39**, 1420 (1997)].
2. G. I. Mironov, Fiz. Tverd. Tela (St. Petersburg) **41** (6), 951 (1999) [Phys. Solid State **41**, 864 (1999)].
3. V. I. Belinicher and A. L. Chernyshev, Phys. Rev. B **49** (14), 9746 (1994).
4. F. Onufrieva and J. Rossat-Mignod, Phys. Rev. B **52** (10), 7572 (1995).
5. H. Lieb and F. Wu, Phys. Rev. Lett. **20** (25), 1445 (1968).
6. Yu. B. Kudasov, Zh. Éksp. Teor. Fiz. **117** (3), 624 (2000) [JETP **90**, 544 (2000)].
7. J. Carnelo and A. A. Ovchinnikov, J. Phys.: Condens. Matter **3**, 757 (1991).
8. H. Frahm and V. E. Korepin, Phys. Rev. B **43**, 5653 (1991).
9. J. Solyom, Adv. Phys. **28** (2), 202 (1979).
10. A. E. Mattson, S. Eggert, and H. Jahanesson, cond-mat/9711204 (1997).
11. H. Tasaki, cond-mat/9707286 (1997).

Translated by Yu. Epifanov

Physics of the Solid State, Vol. 44, No. 2, 2002, pp. 221–222. Translated from Fizika Tverdogo Tela, Vol. 44, No. 2, 2002, pp. 213–214.

SEMICONDUCTORS AND DIELECTRICS

Thermal Conductivity of GaS and GaSe Layered Semiconductors

N. A. Abdullaev, M. A. Aldzhanov, and É. M. Kerimova

Institute of Physics, Academy of Sciences of Azerbaijan, pr. Dzhavida 33, Baku, 370143 Azerbaijan

e-mail: farhad@azintex.com

Received April 26, 2001

Abstract—This paper reports on the results of experimental investigations into the thermal conductivity of GaS and GaSe layered semiconductor crystals in directions parallel and perpendicular to the crystal layers in the temperature range 5–300 K. Specific features of the thermal conductivity of these crystals are analyzed. © *2002 MAIK "Nauka/Interperiodica".*

A substantial difference between weak interlayer interaction and strong intralayer interaction leads to a number of interesting features in the phonon spectra of layered crystals. The specific features in the phonon spectra of layered semiconductor crystals in relation to the temperature behavior of the heat capacity and thermal expansion have been investigated theoretically and experimentally. However, data on the thermal conductivity of layered semiconductor crystals at low temperatures either have not been adequately covered in the literature or are unavailable.

In this paper, the results of investigations into the thermal conductivity of a GaSe layered crystal in the temperature range 5–300 K (Fig. 1a) are presented for the first time. For comparison, we report data on the thermal conductivity of a GaS isostructural layered crystal (Fig. 1b) [1]. It should be noted that the thermal conductivity of GaS and GaSe at temperatures above 100 K has been studied by Guseinov *et al.* [2]. The results we obtained at room temperature agree satisfactorily with the data reported in [2]. Mamedov *et al.* [3] demonstrated that, at low temperatures, the temperature dependences of the heat capacity $C_p(T)$ for GaS and GaSe layered semiconductor crystals are characterized by temperature ranges in which bending waves play a dominant role. Moreover, the investigation of the thermal expansion in GaS and GaSe layered semiconductor crystals revealed temperature ranges in which the thermal expansion coefficient $\alpha_\parallel(T)$ in the plane of the crystal layers is negative due to the manifestation of the membrane effect, which is specific to layered semiconductors [4]. In this respect, the influence of the features of the phonon spectrum of layered semiconductors on the thermal conductivity is undoubtedly of scientific interest.

The thermal conductivity κ was measured by the stationary method described earlier in [5]. The maximum error in measurements did not exceed 5%. Note that the temperature behavior of the thermal conductivity coefficient $\kappa_\perp$ in the direction perpendicular to the layer plane slightly differs for different samples. This is likely caused by the difficulties associated with orientation of the samples along the [001] direction. The data on the thermal conductivity $\kappa_\perp$ were obtained by averaging measurements for two samples. It is clearly seen from Fig. 1 that the temperature dependences of the thermal conductivity have a specific bell-like shape, which is characteristic of phonon thermal conductivity

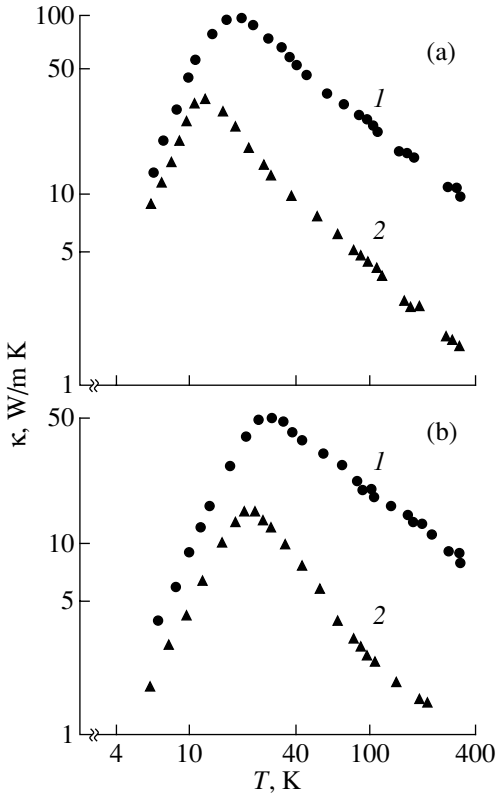

Fig. 1. Temperature dependences of the thermal conductivity coefficient for (a) GaSe and (b) GaS layered semiconductors in directions (*1*) parallel to the plane of crystal layers ($\kappa_\parallel$) and (*2*) perpendicular to the plane of crystal layers ($\kappa_\perp$).

1063-7834/02/4402-0221$22.00

in crystals. Analysis of the experimental data represented in Fig. 1 revealed the following features in the thermal conductivity of GaS and GaSe layered semiconductor crystals.

(1) The thermal conductivity is anisotropic (at room temperature, $\kappa_\parallel/\kappa_\perp \sim 10$). The anisotropy of thermal conductivity decreases with a decrease in the temperature.

(2) In the range of the temperature increase in the thermal conductivity, the temperature dependences of the thermal conductivities $\kappa_\parallel$ and $\kappa_\perp$ are approximated by the following power laws: $\kappa_\parallel \sim T^{2.4 \pm 0.1}$ and $\kappa_\perp \sim T^{2.1 \pm 0.1}$ for GaS and $\kappa_\parallel \sim T^{2.5 \pm 0.1}$ and $\kappa_\perp \sim T^{2.2 \pm 0.1}$ for GaSe.

(3) The temperature location of the maxima of the thermal conductivity in the direction of the stronger bond (in the layer plane) is displaced toward the high-temperature range. The maxima in the dependences $\kappa_\parallel(T)$ and $\kappa_\perp(T)$ are located at temperatures of 24 and 20 K for GaS and 19 and 13 K for GaSe, respectively.

(4) In the temperature range beyond the maximum, the thermal conductivity κ follows an exponential law over a wide temperature range: $\kappa = a(T/\Theta_i)^n \exp(\Theta_i/bT)$, where Θ_i is the characteristic temperature and a, b, and n are constants [6].

The thermal conductivity anisotropy in GaS and GaSe has defied interpretation on the basis of peculiarities in the acoustic spectrum and can only be explained in terms of the features of carrier scattering by defects typical of layered semiconductor crystals. A characteristic property of virtually all layered semiconductor crystals is the existence of stacking faults that give rise to strong scattering of phonons during their motion in the direction perpendicular to the plane of layers and does not affect their motion in the plane of these layers.

The temperature increase in the thermal conductivity of GaS and GaSe layered semiconductors according to the law T^{2+X} is due to the corresponding increase in the heat capacity of these crystals [3].

Different temperatures of the thermal conductivity peaks in the dependences $\kappa_\parallel(T)$ and $\kappa_\perp(T)$ can be explained by different times of switching-off the umklapp processes, which, in turn, is due to the anisotropy of bonding forces in these crystals.

In the range of exponential decay of the thermal conductivity, we performed a careful graphical analysis of the dependences $\kappa_\parallel(T)$ for GaS and GaSe. On this basis and with due regard for the results obtained in [3], we estimated the quantity Θ/b for GaS and GaSe at approximately 110 and 65, respectively. According to the experimental data [3], the Debye temperatures Θ_D for GaS and GaSe are approximately equal to 260 and 190 K, respectively. Hence, we can argue that the constant b is larger than two for GaS and GaSe. Moreover, Anders *et al.* [7] calculated the possible umklapp processes with the participation of three phonons belonging to only a bending branch of the acoustic spectrum and obtained the constant $b \sim 1$. Therefore, we can state that the efficiency of these processes in GaS and GaSe layered semiconductor crystals is rather low.

In conclusion, it should be emphasized that all the aforementioned features of the thermal conductivity in GaS and GaSe are inherent in the most typical representatives of layered crystals, namely, graphite [8] and boron nitride [9].

REFERENCES

1. M. A. Aldzhanov, M. D. Nadzhafzade, and Z. Yu. Seidov, Fiz. Tverd. Tela (St. Petersburg) **41**, 24 (1999) [Phys. Solid State **41**, 20 (1999)].
2. G. D. Guseinov, A. I. Rasulov, E. M. Kerimova, and M. Z. Ismailov, Phys. Lett. **22**, 562 (1966).
3. K. K. Mamedov, M. A. Aldzhanov, I. G. Kerimov, and M. I. Mekhtiev, Fiz. Tverd. Tela (Leningrad) **19**, 1471 (1977) [Sov. Phys. Solid State **19**, 857 (1977)]; Fiz. Tverd. Tela (Leningrad) **20**, 42 (1978) [Sov. Phys. Solid State **20**, 22 (1978)].
4. G. L. Belen'kiĭ, R. A. Suleĭmanov, N. A. Abdullaev, and V. Ya. Shteĭnshraĭber, Fiz. Tverd. Tela (Leningrad) **26**, 3560 (1984) [Sov. Phys. Solid State **26**, 2142 (1984)].
5. M. A. Aldzhanov, K. K. Mamedov, A. B. Abdullaev, and S. A. Aliev, Fiz. Tverd. Tela (Leningrad) **27**, 284 (1985) [Sov. Phys. Solid State **27**, 174 (1985)].
6. J. M. Ziman, *Electrons and Phonons* (Clarendon Press, Oxford, 1960; Inostrannaya Literatura, Moscow, 1962).
7. É. E. Anders, I. V. Volchok, and B. Ya. Sukharevskiĭ, Fiz. Nizk. Temp. **4**, 1202 (1978) [Sov. J. Low Temp. Phys. **4**, 566 (1978)].
8. B. M. Mogilevskiĭ and A. F. Chudnovskiĭ, *Thermal Conductivity of Semiconductors* (Nauka, Moscow, 1972), p. 374; C. A. Klein and M. G. Holland, Phys. Rev. **136**, A575 (1964).
9. A. Simpson and A. D. Stuckes, J. Phys. C **4**, 1710 (1971).

Translated by O. Moskalev

Physics of the Solid State, Vol. 44, No. 2, 2002, pp. 223–234. Translated from Fizika Tverdogo Tela, Vol. 44, No. 2, 2002, pp. 215–225.

SEMICONDUCTORS AND DIELECTRICS

Normal Quasiparticle Scattering and Kinetic Effects in Degenerate Semiconductors

I. G. Kuleev

Institute of Metal Physics, Ural Division, Russian Academy of Sciences, ul. S. Kovalevskoĭ 18, Yekaterinburg, 620219 Russia

e-mail: kuleev@imp.uran.ru

Received May 14, 2001

Abstract—The influence of normal processes of electron–electron and phonon–phonon scattering on quasiparticle momentum relaxation in nonequilibrium electron–phonon systems of degenerate semiconductors is investigated. A system of kinetic equations is solved for the electron and phonon distribution functions, and the kinetic coefficients of a semiconductor are calculated in the linear approximation in the degeneracy parameter. The influence of normal scattering of quasiparticles on the electrical conductivity, thermopower, and heat conductivity of a degenerate semiconductor is analyzed. Redistribution of the phonon momentum in *N* processes within each branch of the vibrational spectrum, as well as among different branches, is taken into account.

1. INTRODUCTION

In investigating the influence of electron–phonon drag on kinetic effects in conductors, it was assumed [1–12] that the quasiparticle momentum relaxation in a nonequilibrium electron–phonon system can be described through the introduction of total relaxation rates for quasiparticles. In this approximation, normal processes (*N*-processes) of electron–electron scattering were not taken into account, while phonon–phonon normal scattering was included into the total relaxation rates for phonons. This approach is not accurate for sufficiently pure conductors at low temperatures when the quasiparticle relaxation rates in *N*-processes become comparable to (or even higher than) the resistive relaxation rates for electrons and phonons. It is well known [13–18] that the *N* processes of quasiparticle scattering do not lead to electron and phonon momentum relaxation but cause the subsystems to relax to a drifting local equilibrium distribution of quasiparticles. Therefore, in order to describe the nonequilibrium distribution of each of the subsystems with allowance for *N* processes, three parameters should be introduced: two relaxation rates (the resistive rate and that characterizing quasiparticle relaxation in *N* processes) and the average drift velocity. In this case, the system of kinetic equations should be complemented with two momentum balance equations for the drift characteristics of the electron and phonon subsystems to be determined.

This new approach was developed in [19] when analyzing the kinetic effects in metals. It was shown that *N* processes in electron–electron scattering contribute only to diffusion fluxes and, therefore, to the thermopower and thermal conductivity of metals. The phonon drift caused by *N* processes in phonon–phonon scattering can lead to enhancement of mutual electron and phonon drag in electrical conduction and to a dramatic growth in the phonon component of the thermopower. The three-parameter approximation proved to be more adequate for describing the nonequilibrium electron–phonon system and kinetic effects in metals. In [20], the influence of *N* processes in phonon–phonon scattering upon the electron–phonon drag and kinetic effects in degenerate semiconductors was examined. It is noteworthy that the system of integral equations for the parameters that characterize the electron distribution function in metals [19] is simpler than that in the case of degenerate semiconductors [20], because the phonon wave vectors involved in expressions for the relaxation rates due to electron–phonon collisions in metals are limited by the Debye wave vector q_d [21].

The purpose of the present paper is to investigate the influence of drift motion of quasiparticles caused by *N* processes upon electron–phonon drag and kinetic effects in degenerate semiconductors. First, in contrast to [20], we will completely treat the problem on mutual electron–phonon drag with allowance for *N* processes in the scattering of electrons and phonons. Second, in contrast to [20], where the momentum redistribution of longitudinal and transverse phonons due to *N* processes is considered only within each branch of the vibrational spectrum (Simons's mechanism [22]), we will also analyze Herring's *N*-process mechanism of relaxation [23], which leads to redistribution of the phonon momentum among different branches. We will show that the effective electron relaxation rate, the thermopower due to electron–phonon drag, and the lattice heat conductivity of sufficiently pure semiconductors and semimetals depend heavily on the type of phonon momentum relaxation due to *N* processes [22, 23]. The influence of

1063-7834/02/4402-0223$22.00

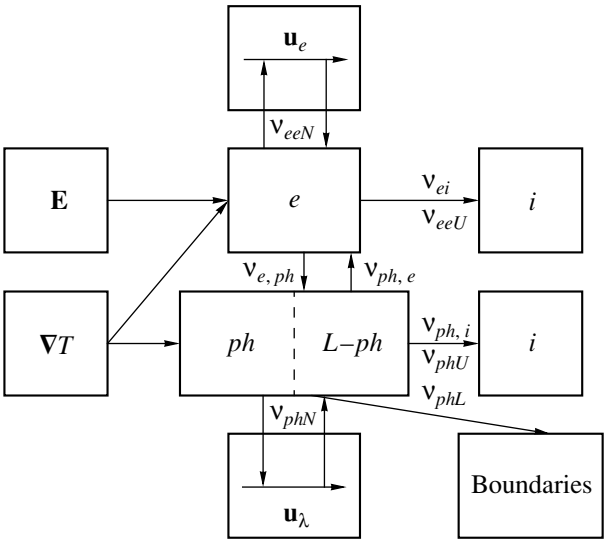

Schematic illustrating momentum relaxation in a nonequilibrium electron–phonon system with allowance for normal quasiparticle scattering.

N processes on the phonon-drag thermopower is the most important conclusion made in the present study, which has further practical applications. It is shown that the phonon-drag thermopower is completely determined by the resistive phonon relaxation rate averaged over frequency if the phonon relaxation rate due to *N* processes $\nu_{phN}(q)$ is much greater than the resistive phonon relaxation rate $\nu_{phR}(q)$. In the one-parameter model of the nonequilibrium electron–phonon system [1–12], the phonon-drag thermopower in this extreme case is determined by the phonon relaxation rate due to *N* processes.

In Section 2, the set of kinetic equations and of phonon- and electron-momentum balance equations is transformed into a set of three integral equations for the parameters that characterize the nonequilibrium electron distribution function. In Section 3, the latter set is solved in the linear approximation in the degeneracy parameter $k_BT/\zeta \ll 1$ (where ζ is the Fermi energy). In Section 4, the electrical conductivity and thermopower of a degenerate semiconductor are calculated with allowance for mutual electron–phonon drag. In Section 5, the Onsager relations and the contribution of normal scattering of quasiparticles into the electron and phonon heat conductivity are analyzed.

2. A SET OF KINETIC EQUATIONS FOR THE NONEQUILIBRIUM ELECTRON–PHONON SYSTEM INCLUDING NORMAL SCATTERING OF QUASIPARTICLES

A set of kinetic equations for the nonequilibrium electron $f(\mathbf{k}, \mathbf{r})$ and phonon $N^\lambda(\mathbf{q}, \mathbf{r})$ distribution functions can written as [2–5, 19]

$$\begin{aligned}\frac{e}{\hbar}\mathbf{E}_0\frac{\partial f_\mathbf{k}}{\partial \mathbf{k}} + (\mathbf{v}_\mathbf{k}\nabla_\mathbf{r})f_\mathbf{k} &= I_{ei}(f_\mathbf{k}) + I_{e,ph}(f_\mathbf{k}, N^\lambda_\mathbf{q}) \\ &+ I_{ee}(f_\mathbf{k}, f_\mathbf{k}), \\ \mathbf{v}^\lambda_\mathbf{q}\nabla_\mathbf{r}N^\lambda_\mathbf{q} &= -(N^\lambda_\mathbf{q} - N^0_{q\lambda})\nu^{(1)\lambda}_{ph}(q) \\ &-(N^\lambda_q - N(\mathbf{q}, \mathbf{u}_\lambda))\nu^\lambda_{phN} + I_{ph,e}(N^\lambda_\mathbf{q}, f_\mathbf{k}),\end{aligned} \tag{1}$$

where $\mathbf{v}^\lambda_q = s_\lambda\mathbf{q}/q$ is the group velocity of acoustic phonons with polarization λ, $\nu^\lambda_{phN}(q)$ is the phonon relaxation rate due to *N* scattering, and the rate $\nu^{(1)\lambda}_{ph}(q) = \nu^\lambda_{pht}(q) + \nu^\lambda_{phL}(q) + \nu^\lambda_{phU}(q)$ includes all nonelectron resistive phonon relaxation rates due to phonon scattering on phonons (Umklapp processes), on defects, and on the boundaries of the sample. The collision integrals of electrons with impurities (I_{ei}), with electrons (I_{ee}), and with phonons ($I_{e,ph}$) and of phonons with electrons ($I_{ph,e}$) are defined in [2–5, 17–19]. In Eq. (1), it is taken into account that *N* scattering of phonons brings the phonon subsystem to a local equilibrium characterized by Planck's distribution with a drift velocity $\mathbf{u}_\lambda$, which can be different for phonons with different polarization λ [13–16]:

$$\begin{aligned}N(\mathbf{q}, \mathbf{u}_\lambda) &= \left[\exp\left(\frac{\hbar\omega_{q\lambda} - \hbar\mathbf{q}\mathbf{u}_\lambda}{k_BT}\right) - 1\right]^{-1} \\ &\cong N^0_{q\lambda} + \frac{\hbar\mathbf{q}\mathbf{u}_\lambda}{k_BT}N^0_{q\lambda}(N^0_{q\lambda} + 1),\end{aligned} \tag{2}$$

where $N^0_{q\lambda}$ is Planck's function.

Figure 1 illustrates the redistribution and relaxation of the momentum gained by an electron–phonon system from the electric field and the temperature gradient. Due to the electron–phonon relaxation mechanisms characterized by relaxation rates $\nu_{e,ph}$ and $\nu_{ph,e}$, the momentum is redistributed in the electron–phonon subsystem. The scattering of electrons on impurities (characterized by a relaxation rate ν_{ei}), the electron–electron scattering and phonon–phonon scattering accompanied by Umklapp processes (relaxation rates ν_{eeU} and ν_{phU}, respectively), the phonon scattering on the boundaries (relaxation rate ν_{phL}), and the scattering of phonons on impurities (Rayleigh's mechanism, relaxation rate $\nu_{ph,i}$) result in relaxation of the total momentum of the electron–phonon system. The phonon–phonon *N* scattering causes a momentum redistribution among different phonon modes and leads to a phonon drift with velocity $\mathbf{u}_\lambda$. The electron–electron *N* scattering causes a momentum redistribution to take place in the electron subsystem, because of which a local equilibrium Fermi distribution is established that is characterized by a

mean drift velocity $\mathbf{u}$ and described [17–19] by the function

$$f(\mathbf{k}, \mathbf{u}) = \left[\exp\left(\frac{\varepsilon_k - \zeta - \hbar\mathbf{k}\mathbf{u}}{k_B T}\right) + 1\right]^{-1} = f_0(\varepsilon_k) - (\hbar\mathbf{k}\mathbf{u})\left(-\frac{\partial f_0}{\partial \varepsilon_k}\right). \quad (3)$$

The electron and phonon distribution functions can be written as

$$f_\mathbf{k} = f_0(\varepsilon_k) + \delta f_\mathbf{k}, \quad N^\lambda_\mathbf{q} = N^0_{q\lambda} + g_\lambda(\mathbf{q}), \quad (4)$$

where $f_0(\varepsilon_k)$ and $N^0_{q\lambda}$ are local equilibrium distribution functions and $\delta f_\mathbf{k}$ and $g_\lambda(\mathbf{q})$ are nonequilibrium additions that are linear in external perturbations. We linearize the collision integrals with respect to these additions. Then, in the relaxation time approximation, the collision integral I_{ee} can be represented as [18, 19]

$$I_{ee}(f_\mathbf{k}, f_\mathbf{k}) \cong -\nu_{eeU}(k)\delta f_\mathbf{k} - \nu_{eeN}(k)\left[\delta f_\mathbf{k} - (\hbar\mathbf{k}\mathbf{u})\left(-\frac{\partial f_0}{\partial \varepsilon_k}\right)\right]. \quad (5)$$

The relaxation rates $\nu_{eeN}(k)$ and $\nu_{eeU}(k)$ are determined in [18]. The collision integrals $I_{ei}(\delta f_\mathbf{k})$ and $I_{ph,e}(f_0, g_\lambda(\mathbf{q}))$, as well as $I_{e,ph}(\delta f_\mathbf{k}, N^0_{q\lambda})$, are expressed through relaxation rates in the elastic scattering approximation [12]. In calculating the collision integral $I_{e,ph}(f_0, g_\lambda(\mathbf{q}))$, we take into account the inelasticity of collisions of electrons with phonons to the first order in the inelasticity parameter $\hbar\omega_{q\lambda}/\zeta$. The electron distribution function $\delta f_\mathbf{k}$ is represented in the standard form [2–5]

$$\partial f_\mathbf{k} = \left(-\frac{\partial f_0}{\partial \varepsilon_k}\right)(\mathbf{v}_k \boldsymbol{\chi}(\varepsilon_k)). \quad (6)$$

In order to find the quasiparticle drift velocities, the set of kinetic equations (1) should be complemented with two momentum equilibrium equations for the electron and phonon subsystems [19]. Taking into account that the total momentum of the electron subsystem is conserved in normal electron–electron scattering, we express the electron drift velocity $\mathbf{u}$ through $\boldsymbol{\chi}(\varepsilon)$ as in [19] as

$$\mathbf{u} = \frac{1}{m_F \nu_{eeN}(\zeta)} \int_0^\infty d\varepsilon \left(-\frac{\partial f}{\partial \varepsilon}\right) \tilde{k}^3 \nu_{eeN}(\varepsilon)\boldsymbol{\chi}(\varepsilon). \quad (7)$$

Hence, as in [19], the nonequilibrium electron subsystem is described by three parameters: two relaxation rates $\nu_{eeN}(k)$ and $\nu_{eR}(k)$ (here, $\nu_{eR}(k) = \nu_{ei}(k) + \nu_{e,ph}(k) + \nu_{eeU}(k)$ is the resistive relaxation rate of the electron momentum) and the mean electron drift velocity $\mathbf{u}$.

Substituting Eqs. (2)–(4) into Eq. (1), we find the phonon distribution function $g_\lambda(q)$ [20] to be

$$g_\lambda(\mathbf{q}) = -\frac{N^0_{q\lambda}(N^0_{q\lambda}+1)}{\nu^\lambda_{ph}(q)}\frac{\hbar\omega_{q\lambda}}{k_B T^2}(\mathbf{v}^\lambda_q \nabla T) + \frac{\hbar\mathbf{q}\mathbf{u}_\lambda}{k_B T} \times N^0_{q\lambda}(N^0_{q\lambda}+1)\frac{\nu^\lambda_{phN}(q)}{\nu^\lambda_{ph}(q)} - \frac{\nu^\lambda_{ph,e}(q)}{\nu^\lambda_{ph}(q)}\frac{N^0_{q\lambda}(N^0_{q\lambda}+1)}{k_B T} \times \int_{\varepsilon_q/2}^\infty d\varepsilon\left(-\frac{\partial f_0(\varepsilon)}{\partial \varepsilon}\right)\tilde{m}(\varepsilon)(\hbar\mathbf{q}\boldsymbol{\chi}(\varepsilon)), \quad (8)$$

where $\nu^\lambda_{ph} = \nu^{(l)\lambda}_{ph} + \nu^\lambda_{phN} + \nu^\lambda_{ph,e}$ and $\nu^\lambda_{ph,e}(k_F, q)$ is the phonon momentum relaxation rate due to collisions with electrons. The first and second terms in Eq. (8) are due to diffusion and drift of phonons, respectively, while the last term is due to the electron system being in a nonequilibrium state. The phonon drift velocity $\mathbf{u}_\lambda$ can be found from the momentum balance equation, which can be derived from Eq. (1) and the law of phonon subsystem momentum conservation in normal phonon–phonon scattering and has the form

$$\frac{1}{V}\sum_\mathbf{q} \hbar\mathbf{q}\nu^\lambda_{phN}(q)(N^\lambda_q - N(\mathbf{q}, \mathbf{u}_\lambda)) = \frac{1}{V}\sum_\mathbf{q} \hbar\mathbf{q}\nu^\lambda_{phN}(q) \times \left[g_\lambda(\mathbf{q}) - \frac{\hbar\mathbf{q}\mathbf{u}_\lambda}{k_B T}N^0_{q\lambda}(N^0_{q\lambda}+1)\right] = 0. \quad (9)$$

Two mechanisms of normal three-phonon scattering are known, Herring's mechanism [23] and Simons's mechanism [22]. The transverse-phonon relaxation rate for Herring's mechanism ($\nu^t_{phN} \cong B_t T^4 \omega_t$) is defined by three-phonon scattering ($t + l \rightleftharpoons l$) in which one transverse and two longitudinal phonons are involved [16]. The longitudinal-phonon relaxation rate in an anisotropic continuum model ($\nu^L_{phN} \cong B_L T^3 \omega_l^2$) is defined by three-phonon processes of either the decay of a longitudinal phonon into two transverse phonons belonging to different branches or the fusion of two transverse phonons into a longitudinal phonon ($l \rightleftharpoons t_1 + t_2$). Thus, phonons of different polarizations are involved in Herring's scattering mechanism and this relaxation mechanism provides drift-momentum redistribution among longitudinal and transverse phonons. This is the reason why, in the nonequilibrium phonon system, three-phonon Herring processes tend to establish a local equilibrium distribution with the same drift velocity for phonons of both polarizations: $\mathbf{u}_l = \mathbf{u}_t = \mathbf{u}_H$.

Simons's relaxation mechanism [22] involves phonons of the same polarization. For this scattering mechanism ($\nu^\lambda_{phN} \cong B_\lambda T^4 \omega_\lambda$), the momentum conservation law is fulfilled in N processes for each branch of the phonon spectrum and the drift velocities of longitudinal and transverse phonons are different. For this rea-

son, we will consider two cases of phonon momentum relaxation due to N processes: first, when N processes redistribute momentum only within each branch of the vibrational spectrum and, second, when momentum redistribution among different branches prevails.

The phonon drift velocities $\mathbf{u}_\lambda$ for Herring's relaxation mechanism [23] ($\mathbf{u}_H$) and Simons's relaxation mechanism [22] ($\mathbf{u}_S$) can be found from the phonon momentum balance equation (9), and Eq. (8) and can be expressed through the function $\chi(\varepsilon)$:

$$\mathbf{u}^{(H)} = \frac{s_L^2}{T}\beta_\lambda^{(H)}(-\nabla T) + \frac{2s_L^2}{k_B T}\left(\frac{k_F}{q_{TL}}\right)^3\int_0^\infty d\varepsilon\left(-\frac{\partial f_0}{\partial\varepsilon}\right)\tilde{m}(\varepsilon) \times \boldsymbol{\chi}(\varepsilon)\beta_{e,phN}^{(H)}(\varepsilon) = \mathbf{u}_0^{(H)} + \Delta\mathbf{u}^{(H)}, \quad (10)$$

$$\mathbf{u}_\lambda^{(S)} = \frac{s_\lambda^2}{T}\beta_1^{(S)}(-\nabla T) + \frac{2s_\lambda^2}{k_B T}\left(\frac{k_F}{q_{T\lambda}}\right)^3\int_0^\infty d\varepsilon\left(-\frac{\partial f_0}{\partial\varepsilon}\right)\tilde{m}(\varepsilon) \times \beta_{e,phN}^{(S)}(\varepsilon)\boldsymbol{\chi}(\varepsilon) = \mathbf{u}_{0\lambda}^{(S)} + \Delta\mathbf{u}_\lambda^{(S)}, \quad (11)$$

$$\beta_1^{(S)} = \frac{\Psi_N^\lambda}{\Psi_{NR}^\lambda}, \quad \beta_{e,phN}^{(S)}(\varepsilon) = \frac{\psi_{e,phN}^\lambda(\varepsilon)}{\Psi_{NR}^\lambda},$$

$$\beta_\lambda^{(H)} = \left(\frac{s_\lambda}{s_L}\right)^2\beta_1^{(H)}, \quad \beta_1^{(H)} = \frac{\Psi_N^L + 2S_*^3\Psi_N^t}{\Psi_{NR}^L + 2S_*^5\Psi_{NR}^t},$$

$$\beta_{e,phN}^{(H)}(\varepsilon) = \frac{\psi_{e,phN}^L(\varepsilon) + 2\psi_{e,phN}^t(\varepsilon)}{\Psi_{NR}^L + 2S_*^5\Psi_{NR}^t}.$$

Here,

$$S_* = s_L/s_t, \quad z_q^\lambda = \frac{\hbar\omega_{q\lambda}}{k_B T} = \frac{q}{q_{T\lambda}}, \quad q_{T\lambda} = \frac{k_B T}{\hbar s_\lambda},$$

$$z_{2k}^\lambda = \frac{2k}{q_{T\lambda}}, \quad \tilde{m}(\varepsilon) = \frac{m(\varepsilon)}{M_F},$$

and $m_F = m(\zeta)$ and k_F are the effective mass and the electron wave vector at the Fermi level, respectively. The other functions are defined as

$$\Psi_N^\lambda = \left\langle\left\langle\frac{\nu_{phN}^\lambda(q)}{\nu_{ph}^\lambda(q)}\right\rangle\right\rangle_{z_{d\lambda}} \equiv \int_0^{z_{d\lambda}} dz_q^\lambda (z_q^\lambda)^4\frac{\nu_{phN}^\lambda(q)}{\nu_{ph}^\lambda(q)}N_{q\lambda}^0(N_{q\lambda}^0+1),$$

$$\Psi_{NR}^\lambda = \left\langle\left\langle\frac{\nu_{phR}^\lambda(q)\nu_{phN}^\lambda(q)}{\nu_{ph}^\lambda(q)}\right\rangle\right\rangle_{z_{d\lambda}}, \quad (12)$$

$$\psi_{e,phN}^\lambda(\varepsilon) = \left\langle\left\langle\frac{\nu_{e,ph}^\lambda(k_F,q)\nu_{phN}^\lambda(q)}{\nu_{ph}^\lambda(q)}\right\rangle\right\rangle_{z_{2k}^\lambda} = \int_0^{z_{2k}^\lambda} dz_q^\lambda\frac{\nu_{e,ph}^\lambda(k_F,q)\nu_{phN}^\lambda(q)}{\nu_{ph}^\lambda(q)}\frac{k_B T}{2m_F s_\lambda^2}\left(\frac{q_{T\lambda}}{k_F}\right)^3\Psi_{ph,eN}^\lambda(\varepsilon),$$

where $\nu_{ph}^\lambda(q) = \nu_{phN}(q) + \nu_{phR}^\lambda(q)$ is the total phonon momentum relaxation rate, $\nu_{phR}^\lambda(q) = \nu_{ph}^{(l)\lambda} + \nu_{ph,e}^\lambda(q)$ is the resistive phonon relaxation rate, and $\nu_{ph,e}^\lambda(q)$ is the phonon momentum relaxation rate due to scattering on electrons [10, 12], $z_{d\lambda} = \hbar\omega_{d\lambda}/k_B T$ ($\omega_{d\lambda}$ is the Debye frequency of phonons with polarization λ). We separated the phonon drift velocity $\mathbf{u}_\lambda$ into two parts, one of which ($\mathbf{u}_{0\lambda}$) is determined by the temperature gradient, while the other ($\Delta\mathbf{u}_\lambda$) is due to the electrons being in a nonequilibrium state. Therefore, when normal phonon scattering is taken into account, the nonequilibrium phonon subsystem is also described by three parameters (the relaxation rates $\nu_{phN}^\lambda(q)$ and $\nu_{phR}^\lambda(q)$ and the mean velocity of the phonon drift) rather than by one parameter (the total phonon momentum relaxation rate [1–12]).

We substitute Eq. (8) into the expression for the phonon distribution function $g_\lambda(\mathbf{q})$ and unite the drift and diffusion contributions, both of which are proportional to the temperature gradient. Then, $g_\lambda(\mathbf{q})$ can be represented as the sum of three terms [20]:

$$g_\lambda(\mathbf{q}) = g_\lambda^{(1)}(\mathbf{q}) + g_{\Delta\mathbf{u}\lambda}(\mathbf{q}) + g_\lambda^{(2)}(\mathbf{q}),$$

$$g_{\Delta\mathbf{u}\lambda} = \frac{(\hbar\mathbf{q}\Delta\mathbf{u}_\lambda)}{k_B T}N_{q\lambda}^0(N_{q\lambda}^0+1)\frac{\nu_{phN}^\lambda(q)}{\nu_{ph}^\lambda(q)},$$

$$g_\lambda^{(1)}(\mathbf{q}) = -\frac{N_{q\lambda}^0(N_{q\lambda}^0+1)}{\tilde{\nu}_{ph}^\lambda(q)}\frac{\hbar\omega_{q\lambda}}{k_B T^2}(\mathbf{v}_q^2\nabla T), \quad (13)$$

$$\tilde{\nu}_{ph}^\lambda(q) = \nu_{ph}^\lambda(q)(1+\nu_{phN}^\lambda(q)\beta_1^{(S,H)})^{-1},$$

$$g_\lambda^{(2)}(\mathbf{q}) = -\frac{\nu_{ph,e}(q)}{\nu_{ph}^\lambda(q)}\frac{N_{q\lambda}^0(N_{q\lambda}^0+1)}{k_B T} \times \int_{\varepsilon_q/2}^\infty d\varepsilon\left(-\frac{\partial f_0(\varepsilon)}{\partial\varepsilon}\right)\tilde{m}(\varepsilon)(\hbar\mathbf{q}\boldsymbol{\chi}(\varepsilon)),$$

where $\tilde{\nu}_{ph}^\lambda(q)$ is the effective phonon momentum relaxation rate renormalized by normal phonon scattering. The functions $g_\lambda^{(2)}(\mathbf{q})$ and $g_{\Delta\mathbf{u}\lambda}(\mathbf{q})$ include the influence of the nonequilibrium electron subsystem on the drift and diffusion of phonons. The nonequilibrium addition $g_\lambda^{(1)}(\mathbf{q})$ derives from the immediate action of the tem-

perature gradient on the diffusion and drift of phonons. In contrast to [20], we show here that this renormalization and, hence, the expressions for the phonon-drag thermopower and lattice heat conductivity are different for Simons's relaxation mechanism [2] (which implies the phonon momentum redistribution to be within each branch) and Herring's mechanism [23], which implies the momentum exchange to be between different branches in the *N* processes. It is evident that if the inequality $\nu^{\lambda}_{phN}(q) \ll \nu^{\lambda}_{phR}(q)$ is valid, then $\tilde{\nu}_{ph}(\lambda) \approx \nu^{\lambda}_{phR}(q)$ and the contribution of the phonon drift to the distribution function $g_{\lambda}(\mathbf{q})$ can be neglected. In this extreme case, the one-parameter approximation used in [1–12] to describe the influence of the nonequilibrium phonon subsystem on electron transport phenomena in degenerate semiconductors is adequate. In the opposite extreme case of $\nu^{\lambda}_{phN}(q) \gg \nu^{\lambda}_{phR}(q)$, one must take into account the influence of phonon drift on the momentum exchange in the nonequilibrium electron–phonon system. Thus, if normal processes play a significant role in the phonon momentum redistribution, description of the phonon system in an extended basis is required.

The present study is focused on the influence of the quasiparticle drift caused by *N* processes on the electron transport phenomena. If the *N* processes are taken into account, an equation can be derived for the function $\boldsymbol{\chi}(\varepsilon)$ in the same way as was done in [12, 20]. This equation is more conveniently represented in the form of Volterra's integral equation:

$$\boldsymbol{\chi}(\varepsilon) = \boldsymbol{\chi}_1(\varepsilon) + \boldsymbol{\chi}_u(\varepsilon) + \boldsymbol{\chi}_{\Lambda}(\varepsilon) + \frac{\tilde{m}^2(\varepsilon)\tau(\varepsilon)}{\tilde{k}^3}\mathbf{Q}(\varepsilon) \equiv \boldsymbol{\chi}^*(\varepsilon) + \frac{\tilde{m}^2(\varepsilon)\tau(\varepsilon)}{\tilde{k}^3}\mathbf{Q}(\varepsilon), \tag{14}$$

$$\mathbf{Q}(\varepsilon) = \Phi(\varepsilon)\int_{\varepsilon}^{\infty} d\varepsilon'\left(-\frac{\partial f_0}{\partial \varepsilon'}\right)\tilde{m}(\varepsilon')\boldsymbol{\chi}(\varepsilon') + \int_0^{\varepsilon} d\varepsilon'\left(-\frac{\partial f_0}{\partial \varepsilon'}\right)\tilde{m}(\varepsilon')\Phi(\varepsilon')\boldsymbol{\chi}(\varepsilon') = \Phi(\varepsilon)\mathbf{K}^{>}(\varepsilon) + \mathbf{K}^{<}(\varepsilon), \tag{15}$$

$$\Phi(\varepsilon) = \sum_{\lambda}\left\langle \frac{\nu^{\lambda}_{ph,e}(k_F, q)\nu^{\lambda}_{e,ph}(k_F, q)}{\nu^{\lambda}_{ph}(q)}\right\rangle_{z^{\lambda}_{2k}}.$$

Here, $\tilde{k} = k/k_F$, $\hbar k_F$ is the Fermi momentum, and $\tau(\varepsilon)$ is the total electron relaxation time,

$$\tau^{-1}(\varepsilon_k) = \nu_e(k) = \nu_{eR}(k) + \nu_{eeN}(k).$$

The inverse quantity $(\Phi(\varepsilon))^{-1}$ characterizes the time τ_{e-ph-e} in which the momentum given by electrons to the phonon system would return to the electrons [12]. The function $\mathbf{Q}(\varepsilon)$ takes into account the influence of the nonequilibrium electron distribution on electrons through the phonon subsystem caused by mutual drag of electrons and phonons.

The function $\boldsymbol{\chi}_1(\varepsilon)$ takes into account the direct action of the electric field and the temperature gradient upon the electron subsystem, as well as the electron drag by phonons involving normal phonon–phonon scattering, and is equal to

$$\boldsymbol{\chi}_1(\varepsilon) = -e\tau(\varepsilon) \times\left(\mathbf{E} + \frac{k_B}{e}\left(\frac{(\tilde{m}(\varepsilon))^2}{\tilde{k}^3}\tilde{A}_{ph}(\varepsilon) + \frac{\varepsilon-\zeta}{k_BT}\right)\nabla T\right), \tag{16}$$

$$\tilde{A}_{ph}(\varepsilon) = \sum_{\lambda}\frac{m_F s^2_{\lambda}}{k_BT}\left\langle \frac{\nu^{\lambda}_{e,ph}(k_F, q)}{\tilde{\nu}^{\lambda}_{ph}(q)}\right\rangle_{z^{\lambda}_{2k}},$$

where the functions $\tilde{A}_{ph}(\varepsilon)$ and $\Phi(\varepsilon)$ depend on the energy ε only through the upper limit of integration $z^{\lambda}_{2k(\varepsilon)}$ [12]. The quantities $\boldsymbol{\chi}_u(\varepsilon)$ and $\boldsymbol{\chi}_{\Lambda}(\varepsilon)$ are determined by electron–electron and phonon–phonon normal scattering, which causes quasiparticle drift. These functions have the form

$$\boldsymbol{\chi}_u(\varepsilon) = \frac{m(\varepsilon)\nu_{eeN}(\varepsilon)}{\nu_e(\varepsilon)}\mathbf{u}, \quad \boldsymbol{\chi}_{\Lambda}(\varepsilon) = \frac{\tilde{m}^2(\varepsilon)\tau(\varepsilon)}{\tilde{k}^3}\boldsymbol{\Lambda}(\varepsilon),$$

$$\boldsymbol{\Lambda}(\varepsilon) = \sum_{\lambda} m_F \Delta\mathbf{u}_{\lambda}\psi^{\lambda}_{e,phN}(\varepsilon),$$

$$\boldsymbol{\Lambda}^{(H,S)}(\varepsilon) = \sum_{\lambda}\frac{K^{\lambda}_{(H,S)}(\varepsilon)\nu_F}{\beta^{(H,S)}_{e,phN}(\zeta)} \times\int_0^{\infty} d\varepsilon'\left(-\frac{\partial f_0}{\partial \varepsilon'}\right)\tilde{m}(\varepsilon')\beta^{(H,S)}_{e,phN}(\varepsilon')\boldsymbol{\chi}(\varepsilon'), \tag{17}$$

$$K^{\lambda}_{(H,S)}(\varepsilon) = \frac{2m_F s^2_{\lambda}}{k_BT}\left(\frac{k_F}{q_{T\lambda}}\right)^3\frac{\psi^{\lambda}_{e,phN}(\varepsilon)\beta^{(H,S)}_{e,phN}(\zeta)}{\nu_F} = \frac{\psi^{\lambda}_{e,phN}(\varepsilon)\beta^{(H,S)}_{ph,eN}(\zeta)}{\nu_F\Psi^{\lambda}_{NR}},$$

$$K^{(H,S)}(\varepsilon) = \sum_{\lambda}K^{\lambda}_{(H,S)}(\varepsilon).$$

In what follows, the indices (*H*) and (*S*) for the functions $K(\varepsilon)$ and $\boldsymbol{\Lambda}(\varepsilon)$ will be omitted to simplify the notation.

Formulas (7) and (14)–(17) represent a set of three integral equations for the functions **u**, $\mathbf{Q}(\varepsilon)$, and $\boldsymbol{\Lambda}(\varepsilon)$ characterizing the nonequilibrium electron subsystem.

In [12], it was shown that the integral equation (14) allows a regular scheme of the function $\mathbf{Q}(\varepsilon)$ to be calculated without expanding in powers of a small parameter characterizing the strength of the electron–phonon interaction or without assuming that the influence of the nonequilibrium electron and phonon subsystems on each other is small. We will show further that the set of equations (14)–(17) can also be solved taking into account normal quasiparticle scattering using only the condition of strong degeneracy $k_B T/\zeta \ll 1$.

3. SOLUTION OF THE KINETIC EQUATION FOR ELECTRONS IN SEMIMETALS AND DEGENERATE SEMICONDUCTORS

In solving the set of integral equations (14)–(17), it is convenient to find the function $\mathbf{Q}(\varepsilon)$ rather than $\boldsymbol{\chi}(\varepsilon)$. Using Eqs. (14)–(17), we express the electron drift velocity $\mathbf{u}$ and the quantity $\boldsymbol{\Lambda}(\varepsilon)$ (characterizing the influence of the phonon drift on the electron distribution function) through the function $\mathbf{Q}(\varepsilon)$:

$$\mathbf{u} = \frac{1}{m_F \nu_F}\left\{\mathbf{F} - e\boldsymbol{\Delta}_N - \mathbf{Q}(\zeta) + \frac{\nu_F}{\nu_{eeN}(\zeta)} \times \int_0^\infty d\varepsilon\left(-\frac{\partial f_0}{\partial \varepsilon}\right)\frac{\nu_{eeN}(\varepsilon)}{\nu_e(\varepsilon)}\varphi(\varepsilon)\mathbf{Q}(\varepsilon)\right\},$$

$$\varphi(\varepsilon) = \left(\frac{\tilde{m}(\varepsilon)}{\tilde{k}(\varepsilon)}\right)^3 \tau(\varepsilon),$$

$$\boldsymbol{\Lambda}(\varepsilon) = \sum_\lambda K^\lambda(\varepsilon)\left\{\mathbf{F} - \mathbf{Q}(\zeta) + \frac{\nu_F}{\beta^{(H,S)}_{e,phN}(\zeta)} \times \int_0^\infty d\varepsilon'\left(-\frac{\partial f_0}{\partial \varepsilon'}\right)\varphi(\varepsilon')\beta^{(H,S)}_{e,phN}(\varepsilon')\mathbf{Q}(\varepsilon')\right\} - e\boldsymbol{\Delta}_\Lambda(\varepsilon), \quad (18)$$

$$\mathbf{E}_A = \mathbf{E} + \frac{k_B}{e}\tilde{A}_{ph}(\zeta)\nabla T, \quad \boldsymbol{\Delta}_N = \frac{k_B}{e}\frac{\pi^2}{3}D_n \nabla T,$$

$$D_N = k_B T \frac{d}{d\varepsilon}\left[\ln\left(\frac{k^3(\varepsilon)\nu_{eeN}(\varepsilon)}{\nu_e(\varepsilon)}\right)\right]_{\varepsilon=\zeta},$$

$$\boldsymbol{\Delta}_\Lambda(\varepsilon) = \frac{k_B}{e}\frac{\pi^2}{3}D_\Lambda(\varepsilon)\nabla T,$$

$$D_\Lambda(\varepsilon) = \sum_\lambda K^\lambda_{(H,S)}(\varepsilon)D^{(H,S)}_{e,phN},$$

$$D^{(H,S)}_{e,phN} = k_B T \frac{d}{d\varepsilon}[\ln(m(\varepsilon)\tau(\varepsilon)\beta^{(H,S)}_{e,phN}(\varepsilon))]_{\varepsilon=\zeta}.$$

Here, we introduced an auxiliary vector $\mathbf{F}$, which significantly simplifies solution of the problem. This vector is defined as

$$\mathbf{F} = -e\mathbf{E}_A + m_F\nu_{eeN}(\zeta)\mathbf{u} + \boldsymbol{\Lambda}(\zeta) + \mathbf{Q}(\zeta) = \boldsymbol{\chi}(\zeta)/\tau_F. \quad (19)$$

In solving the set of three integral equations (14), (15), and (18), the Gurevich–Korenblit method [10] can be used, substituting $(-\partial f_0/\partial\varepsilon) \cong \delta(\varepsilon - \zeta)$ into the integral operator in Eq. (15) under the strong-degeneracy condition. However, this method enables one to correctly analyze the transport properties with allowance for the mutual electron–phonon drag only in the zeroth order in the electron gas degeneracy parameter. For this reason, we apply the method proposed in [12], which is sufficiently universal (cf. [19–21]) and the most convenient for use in parametrical solution of the set of integral equations. This method allows one to find a solution to these equations in the linear approximation in the degeneracy parameter without specifying the dependence of the functions $\Phi(\varepsilon)$, $\tau(\varepsilon)$, and $m(\varepsilon)$ on the electron energy ε. In this method, the problem is solved in two stages. First, the $\mathbf{Q}(\varepsilon)$ energy dependence is found, and then, the integral equations are reduced to a set of three algebraic equations.

In the first stage, we expand $\mathbf{Q}(\varepsilon)$ in a power series in $(\varepsilon - \zeta)$:

$$\mathbf{Q}(\varepsilon) = \mathbf{Q}(\zeta) + \sum_{n=1}^\infty \frac{(\varepsilon-\zeta)^n}{n!}\mathbf{Q}^{(n)}(\zeta), \quad \mathbf{Q}^{(n)}(\zeta) = \left(\frac{d^n\mathbf{Q}(\varepsilon)}{d\varepsilon^n}\right)_{\varepsilon=\zeta}. \quad (20)$$

Using the integral equation (15), we calculate the derivatives $\mathbf{Q}^{(n)}(\zeta)$ and keep only linear terms in the parameter $(k_B T/\zeta)$, neglecting quadratic terms. As shown in [12], the expansion in Eq. (20) is made, in effect, in the parameter $\eta = (\varepsilon - \zeta)/k_B T$. Since the inequality $|\eta| \ll 1$ is not satisfied, one cannot keep a finite number of terms in the expansion. Summing the infinite series yields [12]

$$\mathbf{Q}(\varepsilon) = \mathbf{Q}(\zeta) + k_B T\Phi^{(1)}(\zeta)\{\eta\mathbf{K}^>(\zeta) - f_1(\eta)\boldsymbol{\chi}(\zeta) - f_2(\eta)\tau_F(-k_B\nabla T)\}, \quad (21)$$

where

$$\mathbf{K}^>(\zeta) = \int_\zeta^\infty d\varepsilon\left(-\frac{\partial f_0}{\partial\varepsilon}\right)\tilde{m}(\varepsilon)\chi(\varepsilon),$$

$$f_1(\eta) = \ln(\sinh(\eta/2)),$$

$$f_2(\eta) = \eta f_1(\eta) - 2\int_0^\eta d\eta' f_1(\eta').$$

In the linear approximation in (k_BT/ζ), we expand the function $\Phi(\varepsilon) - \Phi(\zeta) \approx (\varepsilon - \zeta)\Phi^{(1)}(\zeta)$ and represent Eq. (15) in the form

$$\mathbf{Q}(\zeta) = \int_{-\infty}^{\infty} d\eta\left(-\frac{\partial f_0}{\partial \eta}\right)\Phi(\varepsilon)\tilde{m}(\varepsilon)\boldsymbol{\chi}(\varepsilon) - \Phi(\zeta)D_\Phi\int_0^{\infty} d\eta\left(-\frac{\partial f_0}{\partial \eta}\right)\eta\tilde{m}(\varepsilon)\boldsymbol{\chi}(\varepsilon), \tag{22}$$

where

$$\varepsilon = \zeta + \eta k_BT, \quad D_\Phi = k_BT\frac{d}{d\varepsilon}[\ln(\Phi(\varepsilon))]_{\varepsilon=\zeta}.$$

In order to determine $\mathbf{Q}(\zeta)$, $\mathbf{u}$, and $\boldsymbol{\Lambda}(\zeta)$ to the first order in the degeneracy parameter, we substitute Eq. (21) into Eqs. (14), (18), and (22) and integrate them over η. As a result, we obtain a set of three algebraic equations for the functions in question, which is much easier to solve using the auxiliary vector $\mathbf{F}$. In the zeroth order in the degeneracy parameter, we have

$$\mathbf{u} = \frac{1}{m_F\nu_F}\mathbf{F}_0, \quad \mathbf{Q}_0(\zeta) = \Gamma_R\mathbf{F}_0, \quad \boldsymbol{\Lambda}_0(\zeta) = eK_R\mathbf{F}_0,$$
$$K_R = \frac{\nu_F}{\nu_{eR}(\zeta)}K, \quad \Gamma_R = \frac{\nu_F}{\nu_{eR}(\zeta)}\Gamma,$$
$$\mathbf{F}_0 = -e\frac{\nu_F\mathbf{E}_A}{\nu_{eR}(\zeta)(1-\Gamma_R-K_R)} = -e\frac{\nu_F\mathbf{E}_A}{\tilde{\nu}_{eR}(\zeta)}, \tag{23}$$
$$\tilde{\nu}_{eR}(\zeta) = \nu_{eR}(\zeta)(1-\Gamma_R-K_R).$$

Here, $\tilde{\nu}_{eR}(\zeta) = [\tilde{\tau}_{eR}(\zeta)]^{-1}$ is the effective electron momentum relaxation rate. As seen from Eq. (23), the phonon subsystem drift related to normal scattering enhances the mutual electron–phonon drag and decreases the effective electron momentum relaxation rate. The parameters K and K_R characterize the influence of the nonequilibrium electron distribution on electrons through the drifting phonon system. It is evident that expressions for these parameters will be different for Herring's and Simons's relaxation mechanisms [see Eq. (17)]. The parameters $\Gamma = \tau_F/\tau_{e-ph-e}$ and $\Gamma_R = \Gamma\tau_{eR}/\tau_F$ characterize the influence of the nonequilibrium electron distribution on electrons through the diffusing phonon system. The parameter Γ_R is equal to the ratio of the resistive relaxation time τ_{eR} to the time τ_{e-ph-e} required for the momentum imparted by electrons to phonons to return to the electron subsystem.

To the first order in the degeneracy parameter, the solution to the set of equations for the functions $\mathbf{u}$, $\boldsymbol{\Lambda}(\varepsilon)$, and $\mathbf{Q}(\zeta)$ can also be expressed through the vector $\mathbf{F}$:

$$\mathbf{u} = \frac{1}{m_F\nu_F}\{\mathbf{F}(1 - J_1\Gamma D_\Phi) - e\Delta_n\},$$
$$\boldsymbol{\Lambda}(\zeta) = K(\zeta)\{\mathbf{F}(1 - J_1\Gamma D_\Phi)\} - e\boldsymbol{\Delta}_\Lambda,$$
$$\mathbf{Q}(\zeta) = \Gamma\{\mathbf{F}[1 - D_\Phi(J_1\Gamma - \ln(2))] - e\boldsymbol{\Delta}_Q\}, \tag{24}$$
$$\boldsymbol{\Delta}_Q = \frac{k_B}{e}\frac{\pi^2}{3}D_Q\nabla T,$$
$$\mathbf{F} = -e\frac{\nu_F}{\nu_{eR}}(\mathbf{E}_A + e\boldsymbol{\Delta}_F)\left\{1 - \Gamma_R - K_R + \Gamma_R D_\Phi\left(J_1\frac{\nu_{eeN}(\zeta)}{\nu_F} + \Gamma + K(\zeta) + \ln 2\right)\right\}^{-1},$$
$$\boldsymbol{\Delta}_F = \frac{\nu_{eeN}(\zeta)}{\nu_F}\boldsymbol{\Delta}_N + \Gamma\boldsymbol{\Delta}_Q + \boldsymbol{\Delta}_\Lambda, \tag{25}$$
$$D_Q = k_BT\frac{d}{d\varepsilon}[\ln(m(\varepsilon)\tau(\varepsilon)\Phi^{1/2}(\varepsilon))]_{\varepsilon=\zeta},$$

where

$$J_1 = \int_{-\infty}^{\infty} d\eta\left(-\frac{\partial f_0}{\partial \eta}\right)f_1(\eta) \cong 0.31, \; C_1 = J_1 + \ln(2) \approx 1.$$

Expressions (24) and (25) allow one to investigate the case of full mutual electron–phonon drag, where the electron and phonon drift velocities are so close to each other that $1 - \Gamma_K - K_R \ll (k_BT/\zeta)$. In this case, the conduction current is basically determined by the mutual electron–phonon drag. This limiting case demands a separate detailed analysis. For the more realistic case of $(k_BT/\zeta) \ll 1 - \Gamma_R - K_R$, which we will consider hereinafter, upon expansion of the denominator in Eq. (25) in powers of the small parameter, we find

$$\mathbf{F} = \frac{-e\nu_F}{\tilde{\nu}_{eR}(\zeta)}\left\{\mathbf{E}_A\left(1 - \frac{C_1\Gamma_R D_\Phi}{(1-\Gamma_R-K_R)}\right) + \boldsymbol{\Delta}_F\right\}. \tag{26}$$

In order to find the heat flux, it suffices to calculate the function $\mathbf{K}^>(\zeta)$ to zeroth order in the degeneracy parameter:

$$\mathbf{K}_0^>(\zeta) = -\frac{e}{2\nu_{eR}} \times \left\{\mathbf{E}_A(1-\Gamma_R-K_R)^{-1} + \frac{k_B\nu_{eR}}{e\nu_F}2\ln(2)\nabla T\right\}. \tag{27}$$

Substituting Eqs. (24)–(26) into Eqs. (21) and (18) gives $\boldsymbol{\Lambda}(\varepsilon)$, $\mathbf{u}$, and $\mathbf{Q}(\varepsilon)$ and, therefore, the function $\boldsymbol{\chi}(\varepsilon)$ in Eq. (14). This solution allows one to calculate the conduction current and the electron heat flux and to analyze the influence of normal quasiparticle scattering on the transport properties of degenerate semiconductors in both cases of strong and weak mutual electron–phonon drag.

4. CALCULATION OF THE ELECTRICAL CONDUCTIVITY AND THERMOPOWER

In order to calculate the conduction current **j**, we divide it into four parts proportional to nonequilibrium additions to the electron distribution function:

$$\mathbf{j} = -\frac{en_e}{m_F}\int_0^\infty d\varepsilon\left(-\frac{\partial f_0}{\partial\varepsilon}\right)\frac{\tilde{k}^3}{\tilde{m}(\varepsilon)}\boldsymbol{\chi}(\varepsilon) = \mathbf{j}_1 + \mathbf{j}_u + \mathbf{j}_\Lambda + \mathbf{j}_Q. \quad (28)$$

Substituting expressions (24)–(26) and (21) into Eq. (14) and then into Eq. (28), we obtain

$$\mathbf{j} = \sigma_{0F}\left\{\mathbf{E}_A + \frac{k_B\pi^2}{e}\frac{1}{3}D_j\nabla T - \frac{1}{e}[m_F\nu_{eeN}(\zeta)\mathbf{u} + \boldsymbol{\Lambda} + \mathbf{Q}(\zeta)]\right\}. \quad (29)$$

Here,

$$\sigma_{0F} = \frac{e^2n_e\tau_F}{m_F}, \quad D_j = k_BT\frac{d}{d\varepsilon}\left[\ln\left(\frac{k^3(\varepsilon)\tau(\varepsilon)}{m(\varepsilon)}\right)\right]_{\varepsilon=\zeta}.$$

The first two terms in braces give the current $\mathbf{j}_1$. The normal scattering enhances electron drag by phonons because of the phonon drift and the renormalization of the phonon relaxation rate caused by this drift [this rate is involved in expressions for $\tilde{A}_{ph}(\zeta)$ [see (16)]. The first term in the square brackets relates to the electron drift caused by electron–electron normal scattering. The term proportional to $\boldsymbol{\Lambda}$ defines the current $\mathbf{j}_\Lambda$ caused by the influence of nonequilibrium electron distribution on the electrons through the drifting phonon subsystem. The last term in the square brackets defines the mutual-drag current. Substituting Eq. (24) into Eq. (29) gives an expression for the conduction current, from which the kinetic coefficients σ_{xx} and β_{xx} are found to be

$$\sigma_{xx} = \tilde{\sigma}_{0R}\left\{1 - \frac{\Gamma_R D_\Phi C_1}{(1-\Gamma_R-K_R)}\right\}, \quad \tilde{\sigma}_{0R} = \frac{e^2n_e\tilde{\tau}_{eR}}{m_F},$$

$$\beta_{xx} = -\frac{k_B}{e}\left\{\sigma_{xx}\tilde{A}_{ph}(\zeta) + \frac{\pi^2}{3}\tilde{\sigma}_{0R}\left[(1-\Gamma_R-K_R)\times\frac{\nu_{eR}(\zeta)}{\nu_F}D_j + \Gamma D_Q + \frac{\nu_{eeN}(\zeta)}{\nu_F}D_N + \sum_\lambda K^\lambda D^\lambda_{e,ph}\right]\right\}. \quad (30)$$

Let us consider the renormalization of the electron relaxation rate due to the phonon subsystem drift in more detail:

$$\tilde{\nu}_{eR}(\zeta) = \nu_{eR}(\zeta)(1-\Gamma_R-K_R) = \nu_{eR}(\zeta) - \sum_\lambda\left\{\left\langle\frac{\nu^\lambda_{ph,e}(k_F,q)\nu^\lambda_{e,ph}(k_F,q)}{\nu^\lambda_{ph}(q)}\right\rangle_{z^\lambda_{2k}} - \psi^\lambda_{e,phN}\beta^{(H,S)}_{ph,eN}\right\}. \quad (31)$$

If $\nu_{phN}(q) \ll \nu_{phR}(q)$, the main contribution to the renormalization of the electron relaxation rate comes from the parameter Γ_R whereas the contribution of the phonon drift is relatively small ($K_R \ll \Gamma_R$). If the opposite inequality is true, $\nu_{phN}(q) \gg \nu_{phR}(q)$, then the phonon drift in sufficiently pure semiconductors may produce a significant decrease in the effective electron relaxation rate due to phonons and a change in the temperature dependence of the carrier mobility. This renormalization depends on the character of the phonon momentum relaxation due to *N* processes:

$$\tilde{\nu}^{(H,S)}_{eR}(\zeta) = \nu_{et} + \nu_{eeU} + \tilde{\nu}^{(H,S)}_{e,ph},$$

$$\tilde{\nu}^{(S)}_{e,ph} = \sum_\lambda\langle\nu^\lambda_{e,ph}(k_F,q)\rangle\left(1 - \frac{\langle\nu^\lambda_{ph,e}(q)\rangle}{\langle\nu^\lambda_{phR}(q)\rangle}\right),$$

$$\tilde{\nu}^{(H)}_{e,ph} = \sum_\lambda\langle\nu^\lambda_{e,ph}(k_F,q)\rangle \times\left(1 - \frac{\langle\nu^L_{ph,e}(q)\rangle + 2S^5_*\langle\nu^t_{ph,e}(q)\rangle}{\langle\nu^L_{phR}(q)\rangle + 2S^5_*\langle\nu^L_{phR}(q)\rangle}\right). \quad (32)$$

One can see from Eqs. (31) and (32) that the phonon subsystem drift increases the momentum imparted by phonons to electrons. This enhances the effect of mutual electron–phonon drag on the electric conductivity and causes renormalization of the phonon relaxation rate by the *N* processes involved in the thermoelectric coefficient β_{xx}. The addition of the first order in the degeneracy parameter to the electrical conductivity is caused by the mutual electron–phonon drag.

Now, let us consider the influence of normal quasiparticle scattering on thermopower in degenerate semiconductors. From the condition $j = 0$, we find

$$\alpha = -\frac{k_B}{e}\left\{\tilde{A}_{ph}(\zeta) + \frac{\pi^2}{3}\left[(1-\Gamma_R-K_R)\frac{\nu_{eR}(\zeta)}{\nu_F}D_j + \Gamma D_Q + \frac{\nu_{eeN}(\zeta)}{\nu_F}D_N + D_\Lambda\right]\right\} = \alpha_{ph} + \alpha_{\rm dif}. \quad (33)$$

One can see from Eq. (29) that both electron–electron and phonon–phonon normal scattering make contributions (D_N) and D_Λ, respectively) to the diffusion component of the thermopower. The phonon-drag ther-

mopower is affected by normal phonon scattering most significantly. In the extreme case of $\nu_{phN}(q) \ll \nu_{phR}(q)$ [$\nu_{ph}(q) \approx \nu_{phR}(q)$], where we have $\tilde{A}_{ph}(\zeta) = A_{ph}(\zeta)$, one can use the expression for the thermopower derived earlier in the one-parametrical approximation [1–12]. If $\nu_{phN}(q) \gg \nu_{phR}(q)$, normal phonon–phonon scattering and the phonon subsystem drift related to it may lead to a significant increase in the absolute value of the thermopower. It is noteworthy that the phonon component of thermopower α_{ph} is determined by the phonon momentum relaxation rate [renormalized by *N* processes, Eq. (10)], rather than by the total phonon relaxation rate $\nu^{\lambda}_{ph}(q)$, as advocated in [1–12]. In contrast to [20], we showed that the renormalization mentioned above and, correspondingly, α_{ph} are different for the cases of *N* process-induced phonon momentum redistribution within the branches of the vibrational spectrum (Simons's mechanism) and among the branches (Herring's mechanism):

$$\alpha^{(S,H)}_{ph} = -\frac{k_B}{e}\sum_{\lambda}\frac{m_F s^2_{\lambda}}{k_B T} \times \int_0^{z^{\lambda}_{2k}} dz^{\lambda}_q \frac{\nu^{\lambda}_{e,ph}(k_F, q)}{\nu^{\lambda}_{ph}(q)}(1 + \nu^{\lambda}_{phN}(q)\beta^{(S,H)}_{1\lambda}). \quad (34)$$

This is the most important result of this paper and has important practical applications. The point is that, in theoretical works using the one-parameter approximation (see [1–12, 24] and references therein) when interpreting experimental data on phonon-drag thermopower, the phonon relaxation rates due to *N* processes were included into the total rate $\nu^{\lambda}_{ph}(q)$ characterizing the resistive mechanisms of phonon scattering and, at $\nu_{phN}(q) \gg \nu_{phR}(q)$, these relaxation rates were considered as the dominant mechanism of long-wavelength phonon momentum relaxation [2–5]. However, from Eq. (34), it follows that in this extreme case, the relaxation rate $\nu_{phN}(q)$ is not involved in the phonon-drag thermopower and α_{ph} is determined solely by the frequency-average resistive phonon relaxation rate:

$$\alpha^{(S,H)}_{ph} = -\frac{k_B}{e}\sum_{\lambda}\frac{m_F s^2_{\lambda}}{k_B T}\int_0^{z^{\lambda}_{2k}} dz^{\lambda}_q \frac{\nu^{\lambda}_{e,ph}(k_F, q)}{\langle \nu_{phR}(q)\rangle^{(S,H)}_{z_{d\lambda}}},$$

$$\langle \nu_{phR}(q)\rangle^{(S)} = \langle \nu^{\lambda}_{phR}\rangle / J^{(4)}_{\lambda},$$

$$\langle \nu_{phR}(q)\rangle^{(H)} = \frac{\langle \nu^{L}_{phR}\rangle + 2S^5_* \langle \nu^{t}_{phR}\rangle}{J^{(4)}_L + 2S^3_* J^{(4)}_t}, \quad (34a)$$

$$J^{(4)}_{\lambda} = \int_0^{z_{d\lambda}} \frac{dz z^4 \exp(z)}{(\exp(z)-1)^2}.$$

Therefore, in interpreting experimental data, one has to take into account the phonon subsystem drift by using expressions (33) and (34). As for the conclusions made earlier in [1–12] concerning the temperature and field dependences of the phonon-drag thermopower, they must be revised.

5. CALCULATION OF THE ELECTRON AND PHONON HEAT FLUXES AND ANALYSIS OF THE ONSAGER RELATIONS

In order to calculate the electron heat flux $\mathbf{W}_e$,

$$\mathbf{W}_e = \frac{n_e}{m_F}\int_0^{\infty} d\varepsilon\left(-\frac{\partial f_0}{\partial \varepsilon}\right)(\varepsilon - \zeta)\frac{\tilde{k}^3}{\tilde{m}(\varepsilon)}\boldsymbol{\chi}(\varepsilon), \quad (35)$$

we substitute Eqs. (21) and (24)–(27) into Eq. (14) and then into Eq. (35). After integrating over the parameter ε, we obtain, in linear approximation in $(k_B T/\zeta)$,

$$\mathbf{W}_e = -L_0 T\sigma_{0F}\left\{\frac{e}{k_B}\left[\mathbf{E}D_j + \frac{\mathbf{E}_A}{1-\Gamma_R - K_R} \times\left(\frac{\nu_{eeN}(\zeta)}{\nu_{eR}}D_N + \sum_{\lambda}K^{\lambda}_R D^{\lambda}_{e,ph} + D_Q\Gamma_R\right)\right]\right. \quad (36)$$

$$\left. + [1 + \tilde{A}_{ph}(\zeta)D_A + \Gamma D_{\phi}C_2]\nabla T\right\},$$

where

$$L_0 = \frac{\pi^3}{3}\left(\frac{k_B}{e}\right)^2, \quad C_2 = \ln(2) - \frac{3}{\pi^2}J_3 \cong 0.577,$$

$$J_3 = \int_0^{\infty} d\eta\left(-\frac{\partial f_0}{\partial \eta}\right)\eta f_2(\eta) \cong 0.381,$$

$$D_A = k_B T\frac{d}{d\varepsilon}[\ln(m(\varepsilon)\tau(\varepsilon)\tilde{A}_{ph}(\varepsilon))]_{\varepsilon=\zeta}.$$

Comparing Eqs. (30) and (36), we can verify that the Onsager relations for the thermoelectric coefficients in the heat ($\mathbf{W}_e$) and charge ($\mathbf{j}$) fluxes do not hold. As shown in [12], the heat flux that is transported by phonons but caused by nonequilibrium electrons should be taken into account.

The phonon heat flux has three components:

$$\mathbf{W}_{ph} = \frac{1}{V}\sum_{\mathbf{q}\lambda}\hbar\omega_{q\lambda}\mathbf{v}_q^{\lambda}(g_{\lambda}^{(1)}(\mathbf{q}) + g_{\Delta u\lambda}(\mathbf{q}) + g_{\lambda}^{(2)}(\mathbf{q})) = \mathbf{W}_{ph1} + \mathbf{W}_{\Delta u} + \mathbf{W}_{ph,e}. \quad (37)$$

The heat flux W_{ph1} arises from both diffusion and drift of phonons caused by the temperature gradient. Taking phonon–phonon normal scattering into account, as is the case in the Callaway theory [13], leads to a renormalization of the phonon momentum relaxation rate:

$$\mathbf{W}_{ph1} = -\tilde{\kappa}_{ph}\nabla T,$$
$$\tilde{\kappa}_{ph}^{(H,S)} = \sum_{\lambda}\frac{k_B s_{\lambda}^2 q_{T\lambda}^3}{6\pi^2}\int_0^{z_d^{\lambda}} dz_q^{\lambda}\frac{(z_q^{\lambda})^4}{\tilde{\nu}_{ph}^{\lambda(H,S)}(q)}N_{q\lambda}^0(N_{q\lambda}^0+1). \quad (38)$$

Consistent generalization of the Callaway theory [13] by taking account of the difference between the longitudinal- and transverse-phonon contributions, as well as of the phonon momentum redistribution due to phonon–phonon normal scattering within branches (the Simons mechanism) and among branches (the Herring mechanism), is a new result of the present investigation. This result has an important practical application in the treatment of experimental data on the lattice heat conductivity of isotopically enriched crystals of germanium, silicon, and diamond, in which normal scattering plays an important role in the phonon momentum relaxation [25–27]. The point is that in theoretical calculations of the heat conductivity of such systems, the generalized Callaway model was applied [25], which assumes that the phonon momentum relaxation occurs independently for each branch of the phonon spectrum. Thus, this model corresponds to the Simons relaxation mechanism [22]. This approach is inadequate because, in actuality, the Herring mechanism dominates in the phonon relaxation due to the N processes in these systems, which causes a phonon momentum redistribution among different branches of the phonon spectrum. In this case, the drift contribution to the heat conductivity is different from that for the Simons mechanism [see Eqs. (11), (13)] and in treating experimental data [25–27] consistently, one must take into account the results of the present investigation.

The heat fluxes $\mathbf{W}_{\Delta u}$ and $\mathbf{W}_{ph,e}$ are due to the influence of the nonequilibrium electrons on the diffusion and drift of phonons. These fluxes are

$$\mathbf{W}_{\Delta u} = \frac{1}{V}\sum_{\mathbf{q},\lambda}s_{\lambda}^2\hbar\mathbf{q}g_{\Delta u\lambda}(\mathbf{q}) = \frac{k_B T}{m_F}\sum_{\lambda}\frac{(q_{T\lambda})^3\Psi_N^{\lambda}}{6\pi^2}\times\int_0^{\infty}d\varepsilon\left(-\frac{\partial f}{\partial\varepsilon}\right)\tilde{m}(\varepsilon)\beta_{ph,eN}^{(H,S)}(\varepsilon)\boldsymbol{\chi}(\varepsilon), \quad (39)$$

$$\mathbf{W}_{ph,e} = \frac{1}{V}\sum_{\mathbf{q},\lambda}s_{\lambda}^2\hbar\mathbf{q}g_{\lambda}^{(2)}(\mathbf{q}) = \frac{k_B T n}{m_F}\int_0^{\infty}d\varepsilon\left(-\frac{\partial f_0}{\partial\varepsilon}\right)\tilde{m}(\varepsilon)A_{ph}(\varepsilon)\boldsymbol{\chi}(\varepsilon). \quad (40)$$

The electron subsystem as being nonequilibrium relates not only to the action of an electric field and a temperature gradient but also to the electron drag by phonons. Hence, the fluxes in Eqs. (39) and (40) are due to both the nonequilibrium electrons and the influence of nonequilibrium phonons on phonons through the electron subsystem. These fluxes contribute both to the electron and phonon heat fluxes. Calculation gives

$$\mathbf{W}_{ph,e} + \mathbf{W}_{\Delta u} = \frac{k_B}{e}T\tilde{A}_{ph}(\zeta)\left\{\sigma_{xx}\mathbf{E}_A + \frac{k_B\pi^2}{e}\frac{\tilde{\sigma}_{0R}}{3}\times\left[(1-\Gamma_R-K_R)\frac{\nu_{eR}}{\nu_F}D_A + \frac{\nu_{eeN}}{\nu_F}D_N + \Gamma D_Q + D_{\Lambda}\right]\nabla T\right\}. \quad (41)$$

As in the analysis of the flux $\mathbf{W}_{ph,e}$ carried out in [19, 20], we include the diffusion and drift components of the heat flux in Eq. (41) into the total electron heat flux:

$$W_{e,tx} = \gamma_{xx}E_x - \kappa_{xx}^e\nabla_x T. \quad (42)$$

The terms proportional to $(\tilde{A}_{ph}(\zeta))^2\nabla T$ in Eq. (41) are related to the influence of nonequilibrium phonons on phonons through conductivity electrons and contribute to the phonon heat flux. As a result of this separation, the expressions for the kinetic coefficients can be written as

$$\gamma_{xx} = T\beta_{xx},$$
$$\kappa_{ph,xx} = \tilde{\kappa}_{ph} + \frac{3}{\pi^2}L_0 T\sigma_{xx}(\tilde{A}_{ph}(\zeta))^2,$$
$$\kappa_{xx} = L_0\sigma_{0F}T\left\{1 + D_{\Phi}\Gamma C_2 + 2\tilde{A}_{ph}(\zeta)D_A + \frac{2\tilde{A}_{ph}(\zeta)}{1-\Gamma_R-K_R}\left[\Gamma_R D_Q + \frac{\nu_{eeN}(\zeta)}{\nu_F(\zeta)}D_N + D_{\Lambda}\right]\right\}, \quad (43)$$

where β_{xx} is defined by Eq. (30). Thus, we verified through direct calculation that the Onsager relations for the thermoelectric coefficients β_{xx} and γ_{xx}, calculated in linear approximation in the degeneracy parameter with allowance for normal quasiparticle scattering, are fulfilled. It is noteworthy that the Onsager relations follow from the laws of thermodynamic irreversible processes and always have to be fulfilled. However, while solving kinetic equations and calculating transport properties, one assumes a number of approximations which can

break these relations. The fulfillment of the Onsager relations for the kinetic coefficients calculated above means that we have correctly taken account of the influence of the nonequilibrium electrons on electrons through the phonon subsystem, as well as of the influence of the nonequilibrium phonons on phonons through the conductivity electrons.

The electron heat conductivity is usually calculated under the condition $j = 0$. In this case, Eqs. (43), (30), and (33) give

$$\kappa_e = \kappa_{xx} - T\beta_{xx}\alpha = L_0\sigma_{0F}T\left\{1 + D_\Phi\Gamma C_2 + 2\tilde{A}_{ph}(\zeta)(D_A - D_j) - \frac{3}{\pi^2}(\tilde{A}_{ph}(\zeta))^2\frac{\sigma_{xx}}{\sigma_{0F}}\right\}. \quad (44)$$

We note that the mutual electron–phonon drag contributions, proportional to $[\tilde{A}_{ph}(\zeta)]^2$, in the total heat conductivity $\kappa = \kappa_{ph} + \kappa_e$ cancel each other:

$$\kappa = \tilde{\kappa}^0_{ph} + L_0\sigma_0 T \times \{1 + C_2\Gamma D_\Phi + 2\tilde{A}_{ph}(\zeta)(D_A - D_j)\}. \quad (45)$$

The Wiedemann–Franz relations are seen from Eqs. (30) and (44) not to hold. The effects of electron drag by phonons $[\tilde{A}_{ph}(\zeta)]$ and of their mutual drag (Γ) (both related to inelastic electron–phonon scattering), as well as normal quasiparticle scattering, decrease the effective Lorenz factor $L^* = L/L_0$. Neglecting the terms proportional to the degeneracy parameter, we obtain

$$L^* = \frac{\kappa_e}{L_0 T\sigma_{xx}} = \frac{\nu_{eR}}{\nu_F}\left\{1 - \Gamma_R - K_R - \frac{3}{\pi^2}(\tilde{A}_{ph}(\zeta))^2\right\}. \quad (46)$$

It is evident that the electron drag by phonons, their mutual drag, and normal quasiparticle scattering can produce an essential increase in the Lorenz factor L^* and must be taken into account in interpreting experimental data.

6. CONCLUSIONS

Thus, in this study, we solved a set of kinetic equations for electron and phonon distribution functions, taking into account the normal processes of electron–electron and phonon–phonon scattering in degenerate semiconductors. The kinetic coefficients are calculated in the linear approximation in the degeneracy parameter. The role of the mutual drag of electrons and phonons and of the normal quasiparticle scattering in the electrical resistance, thermopower, and heat conductivity was analyzed. Description of the nonequilibrium electron–phonon system in the framework of the three-parametrical approximation allowed the kinetic effects in semiconductors to be treated more correctly. It is shown that the phonon subsystem drift caused by normal processes enhances the effect of mutual electron–phonon drag on the electrical conductivity and significantly increases the phonon component of the thermopower if the phonon relaxation rate due to N processes is considerably higher than the resistive relaxation rate. In this case, the phonon-drag thermopower is determined by the frequency-average resistive phonon relaxation rate rather than by the phonon relaxation rate due to normal scattering [1–12]. Therefore, the results of earlier studies into phonon-drag thermopower in semiconductors [1–12] should be revised and a correct account of normal scattering should be taken. It is to be noted that direct inclusion of normal scattering into the resistive phonon momentum relaxation rate or, especially, the assumption of N processes to be the only resistive mechanism of phonon momentum relaxation is wrong.

We have shown that the renormalization of the effective phonon relaxation rate by normal phonon–phonon scattering is different in the cases when N processes redistribute the phonon momentum within each branch of the phonon spectrum (the Simons mechanism) and among different branches (the Herring mechanism). For this reason, the contribution of the phonon drift to both heat conductivity and phonon-drag thermopower is different for the Simons mechanism and that of Herring, which should be taken into account in treating the experimental data.

In the future, we plan to apply the theory developed here to analyze the lattice heat conductivity and thermopower in semiconductors with isotopic disorder. In isotopically enriched samples of Ge and Si and in artificial diamonds under sufficiently low temperatures, the resistive phonon relaxation processes turn out to be significantly frozen out and the phonon momentum relaxation is determined mainly by normal scattering [25–27].

In the present work, the influence of normal quasiparticle scattering on the mutual drag of phonons and electrons and on kinetic effects in semiconductors is consistently taken into account. However, inelastic electron–phonon collisions were allowed for only in calculating the collision integral $I_{e,ph}(f_0,\ g_\lambda(\mathbf{q}))$, whereas the collision integral $I_{e,ph}(\delta f_\mathbf{k},\ N^0_{q\lambda})$ was calculated in the approximation of elastic scattering and expressed through the relaxation rate. This approximation is quite satisfactory in calculating the electrical resistance but is not sufficient for calculating the thermal resistance at low temperatures [15]. At temperatures $T \ll \Theta_d$, vertical electron transitions [15] with small momentum transfer in electron–phonon collisions provide an effective mechanism of thermal resistance; therefore, one must also take into account inelastic collisions in calculating the collision integral $I_{e,ph}(\delta f_\mathbf{k},\ N^0_{q\lambda})$.

The following problems of the electron–phonon drag theory in degenerate semiconductors remain

unsolved: (1) the influence of inelastic electron–phonon scattering on the mutual drag of electrons and phonons and (2) normal scattering in semimetals with two types of charge carriers. We hope that the method for solving the set of integral equations for nonequilibrium electron–phonon systems developed in this paper will also prove useful in solving these problems.

ACKNOWLEDGMENTS

This study was supported by the Russian Foundation for Basic Research, project no. 00-02-16299.

REFERENCES

1. L. É. Gurevich, Zh. Éksp. Teor. Fiz. **16** (3), 193 (1946); **16** (5), 416 (1946).
2. A. I. Anselm, *Introduction to Semiconductor Theory* (Nauka, Moscow, 1978; Prentice-Hall, Englewood Cliffs, 1981).
3. V. M. Askerov, *Electronic Transport Phenomena in Semiconductors* (Nauka, Moscow, 1985).
4. I. M. Tsidil'kovskiĭ, *Thermomagnetic Effects in Semiconductors* (Fizmatgiz, Moscow, 1960; Academic, New York, 1962).
5. P. S. Zyryanov and M. I. Klinger, *Quantum Theory of Electron Transport Phenomena in Crystalline Semiconductors* (Nauka, Moscow, 1976).
6. F. J. Blatt, P. A. Schroeder, C. L. Foiles, and P. Greig, *Thermoelectric Power of Metals* (Plenum, New York, 1976; Metallurgiya, Moscow, 1980).
7. J. E. Parrott, Proc. Phys. Soc. London, Sect. B **70** (6), 590 (1957).
8. J. Appel, Z. Naturforsch. A **12** (5), 410 (1957); **13** (5), 386 (1958).
9. C. Herring, Phys. Rev. **96** (4), 1163 (1954); **111** (1), 36 (1958).
10. L. É. Gurevich and I. Ya. Korenblit, Fiz. Tverd. Tela (Leningrad) **6** (3), 856 (1964) [Sov. Phys. Solid State **6**, 661 (1964)].
11. I. G. Lang and S. T. Pavlov, Zh. Éksp. Teor. Fiz. **63** (4), 1495 (1972) [Sov. Phys. JETP **36**, 793 (1972)].
12. I. G. Kuleev, Fiz. Met. Metalloved. **87** (6), 5 (1999).
13. J. Callaway, Phys. Rev. **113** (4), 1046 (1959).
14. R. Berman, *Thermal Conduction in Solids* (Clarendon, Oxford, 1976; Mir, Moscow, 1979).
15. J. M. Ziman, *Electrons and Phonons* (Clarendon, Oxford, 1960; Inostrannaya Literatura, Moscow, 1962).
16. B. M. Mogilevskiĭ and A. F. Chudnovskiĭ, *Thermal Conductivity of Semiconductors* (Nauka, Moscow, 1972).
17. V. F. Gantmakher and Y. B. Levinson, *Carrier Scattering in Metals and Semiconductors* (Nauka, Moscow, 1984; North-Holland, New York, 1987).
18. M. Kaveh and N. Wiser, Adv. Phys. **33**, 257 (1984).
19. I. G. Kuleev, Fiz. Met. Metalloved. **90** (1), 14 (2000); **90** (6), 18 (2000).
20. I. G. Kuleev, Fiz. Tverd. Tela (St. Petersburg) **42** (11), 1952 (2000) [Phys. Solid State **42**, 2004 (2000)].
21. A. H. Wilson, *The Theory of Metals* (Cambridge Univ. Press, Cambridge, 1954).
22. S. Simons, Proc. Phys. Soc. London **82** (2), 401 (1963); **83** (3), 799 (1963).
23. C. Herring, Phys. Rev. **95** (4), 954 (1954).
24. Kh. M. Bikkin, A. T. Lonchakov, and I. I. Lyapilin, Fiz. Tverd. Tela (St. Petersburg) **42** (2), 202 (2000) [Phys. Solid State **42**, 207 (2000)].
25. M. Asen-Palmer, K. Bartkowski, E. Gmelin, *et al.*, Phys. Rev. B **56** (15), 9431 (1997).
26. J. R. Olson, R. O. Phol, J. W. Vandersande, *et al.*, Phys. Rev. B **47** (22), 14850 (1993).
27. T. Ruf, R. W. Henn, M. Asen-Palmer, *et al.*, Solid State Commun. **115** (1), 243 (2000).

Translated by D. Bayuk

Physics of the Solid State, Vol. 44, No. 2, 2002, pp. 235–240. Translated from Fizika Tverdogo Tela, Vol. 44, No. 2, 2002, pp. 226–231.

SEMICONDUCTORS AND DIELECTRICS

The Appearance of Structures of Excitons, Photons, and Biexcitons, Regular and Chaotic in Time, in Direct-Band Semiconductors

V. Z. Tronciu*, K. V. Shura, and A. Kh. Rotaru****

** Department of Physics, University of Durham, Durham DH1 3LE, United Kingdom*
e-mail: V.Z.Tronciu@durham.ac.uk
*** Moldova State University, ul. Mateevicha 60, Chisinau, MD 2009 Moldova*

Received May 18, 2001

Abstract—The dynamic properties of excitons and biexcitons in a ring cavity are studied. The nonlinearity of the problem is due to the direct binding of two excitons into a biexciton by virtue of the Coulomb attraction between them. A bifurcation analysis is carried out, revealing the points of Hopf bifurcations and period doubling. The effect of the cavity *Q* factor on the switching times is investigated. The possibility of experimental observation of the phenomena under study is discussed. © *2002 MAIK "Nauka/Interperiodica"*.

1. INTRODUCTION

Recently, special interest has arisen in investigating the appearance, control, and damping of chaotic self-oscillations. These phenomena, associated with excitons and biexcitons in condensed media, are of interest because of their giant optical nonlinearities at the long-wavelength edge of the fundamental absorption of the crystal, short relaxation times, small energies, and short switching times. This opens enormous prospects for investigation of fundamentally new optical phenomena involving excitons and biexcitons and for practical application of these phenomena mainly in optical data processing and in the development of a new generation of computers with optical logic.

In [1–3], we studied some nonlinear phenomena in a system of coherent (in terms of the Bogoliubov treatment) excitons and biexcitons at different quantum transitions. In particular, we developed a theory of optical bistability, regular and chaotic self-pulsations, induced optical phase transitions, and one- and two-photon stationary laser generation. Also, the theory describes the appearance of dissipative structures and the dynamic transient optical chaos, which is accompanied by the creation of a system of strange attractors in the phase space.

The theory of nonlinear and chaotic oscillations has been developed for the case when the systems of excitons, photons, and biexcitons under investigation are Hamiltonian and the corresponding effects appear within a time interval less than the characteristic relaxation time [4, 5].

It should be noted that for a system of coherent photons, excitons, and biexcitons, the nonlinear cooperative phenomena under investigation have been studied only with account of the giant oscillator strength of the exciton–biexciton transitions [6, 7] in the case of one- and two-photon creation of biexcitons. However, it was shown in [8–10] that there is another nonlinear process associated with biexciton creation due to Coulomb attraction between two excitons. Taking into account this fundamentally new mechanism of the exciton–biexciton rearrangement of the semiconductor spectra, which is due to the binding of two excitons into a biexciton by virtue of the Coulomb attraction, we studied [11] the stationary optical bistability and stability of the stationary states and determined the optical switching times between the branches of optical bistability. In addition, it was demonstrated that the appearance of nonlinear periodic and chaotic self-pulsations is also possible. However, a number of fundamental questions remained unsolved in [11]. For example, the scenario of the transition of the system to the dynamic-chaos regime was not described in detail, possible dynamic bifurcations were not revealed, the corresponding bifurcation diagrams were not plotted, and the power spectrum of the appearing oscillations was not found and studied.

This paper is devoted to eliminating these drawbacks and is a logical continuation of [11]. We carried out a bifurcation analysis, revealing the Hopf bifurcation points and period-doubling bifurcations. Also, we found the scenario of the transition to optical dynamic chaos and of the possible appearance of optical turbulence and determined the power spectrum of nonlinear self-pulsations. In the case when the external pumping is a parabolic function of time, the effect of the *Q* factor of the ring cavity on the dynamic optical bistability was studied. Finally, possible experimental observations of the effect under consideration are discussed.

1063-7834/02/4402-0235$22.00

2. STATEMENT OF THE PROBLEM AND FUNDAMENTAL EQUATIONS

Let a coherent monochromatic electromagnetic wave be incident on a ring cavity, in which a semiconductor specimen of length L is placed (Fig. 1), and let coherent excitons be generated in it. According to [8, 10], excitons can form biexcitons due to the Coulomb attraction between them. This process makes the problem nonlinear and is described by the term $\frac{1}{\sqrt{V}} Db^+aa$. For the ring cavity, the boundary conditions are

$$E(0, t) = \sqrt{T}E_I + RE(L, t - \Delta t)e^{iF},$$

$$E_T = \sqrt{T}E(L, t),$$

where E_I is the amplitude of the field at the entry into the cavity (the amplitude of the external pumping), E_T is the amplitude of the field at the cavity exit, $R = 1 - T$ is the reflection coefficient of mirrors *1* and *2* of the cavity, $\Delta t = \frac{L + 2l}{c_0}$ is the delay time due to the feedback, c_0 is the speed of light in vacuum, and $F = kL + k_0(2l + L)$ is the field phase shift in the cavity, with k_0 being the wave vector of the field in vacuum.

The Hamiltonian of the problem is the sum of the Hamiltonians of the free excitons, biexcitons, and the field and of the Hamiltonian describing the interaction of coherent excitons with the electromagnetic field and coherent biexcitons. Within this model, the latter Hamiltonian has the form

$$H_{\text{int}} = i\hbar g(aE^- - a^+E) + i\hbar D(ba^+a^+ - b^+aa), \quad (1)$$

where $a^+(b^+)$ is the exciton (biexciton) creation operator, g is the exciton–photon interaction constant, D is the constant of the direct binding of two excitons into a biexciton, and E^+ is the positive-frequency part of the electric field of the electromagnetic wave. Hereafter, we suppose the volume of the system to be equal to unity.

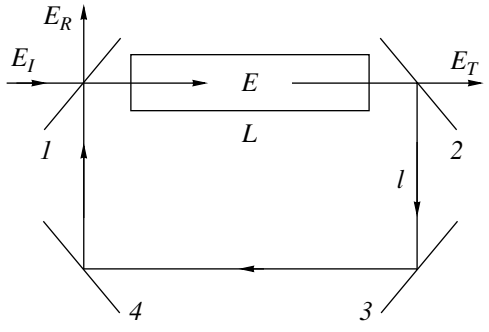

Fig. 1. Ring cavity: mirrors *1* and *2* are characterized by reflection coefficient R; the reflection coefficient of mirrors *3* and *4* is 100%. The distance between mirrors *1* and *2* is L, and the distance between mirrors *2* and *3* is l; E_I, E_R, and E_T are the amplitudes of the incident, reflected, and transmitted fields, respectively.

The equations of motion for the amplitudes of excitons a and biexcitons b have the form

$$\frac{da}{dt} = -i\omega_{\text{ex}}a - gE + 2Dba^+ - \gamma_{\text{ex}}a, \quad (2)$$

$$\frac{db}{dt} = -i\omega_{\text{biex}}b - Daa - \gamma_{\text{biex}}b, \quad (3)$$

where $\hbar\omega_{\text{ex}}(\hbar\omega_{\text{biex}})$ is the energy of the exciton (biexciton) creation and γ_{ex} and γ_{biex} are the exciton and biexciton damping constants, respectively, which determine the transition rate of quasiparticles from the coherent to incoherent modes and are considered to be phenomenological constants.

The equation of motion for the component of the electromagnetic field E is equivalent to the wave equation:

$$c_1^2\frac{\partial^2 E}{\partial z^2} - \frac{\partial^2 E}{\partial t^2} = i4\pi\hbar g\frac{\partial^2 a}{\partial t^2}, \quad (4)$$

where c_1 is the speed of field propagation through the semiconductor.

We represent the amplitudes of the excitons, biexcitons, and the field in the form of modulated plane waves:

$$a(z, t) = A'(z, t)e^{i(kz - \omega t)}, \quad b(z, t) = B'(z, t)e^{2i(kz - \omega t)}, \quad E(z, t) = E'(z, t)e^{i(kz - \omega t)}, \quad (5)$$

where ω and k are the carrier frequency and wave vector, respectively, and $A'(z, t)$, $B'(z, t)$, and $E'(z, t)$ are slowly varying amplitudes.

Hereafter, it is convenient to use the following dimensionless quantities:

$$X = \frac{E'}{E_a}; \quad B = \frac{B'}{B_a}; \quad A = \frac{A'}{A_a};$$

$$E_\delta = \frac{\gamma_{\text{biex}}^2}{gD}; \quad A_\delta = B_\delta = \frac{\gamma_{\text{biex}}}{D};$$

the optical-bistability constant $C = \alpha L/4T$, where $\alpha = 4\pi\hbar g^2\omega^2/c_1 k\gamma_{\text{ex}}$ and T is the transmission coefficient of the mirrors of the ring cavity (Fig. 1); the relative damping constant of excitons with respect to that of biexcitons $d = \gamma_{\text{ex}}/\gamma_{\text{biex}}$; the reduced biexciton energy $\delta_0 = (2\omega_{\text{ex}} - \omega_{\text{biex}})/\gamma_{\text{biex}}$; the dimensionless detuning from the exciton level $\delta_1 = (\omega - \omega_{\text{ex}})/\gamma_{\text{biex}}$; the damping of the electric field amplitude in the cavity (the cavity Q factor) $\sigma = C_1^2 kT/L\gamma_{\text{biex}}\omega$; the dimensionless time $\tau = \gamma_{\text{biex}}t$; and $\Delta_1 = (\omega^2 - c_1^2 k^2)/2\omega\gamma_{\text{biex}}$.

Taking into account the boundary conditions and using the mean-field approximation [12, 13], we obtain

a system of nonlinear differential equations, which describes the time evolution of coherent photons, excitons, and biexcitons:

$$\frac{dX_1}{d\tau} = -\Delta_1 X_2 - \frac{\sigma(1-R\cos F)}{T}X_1 - \frac{\sigma R\sin F}{T}X_2 + 2C\sigma A_1 + \sigma Y, \quad (6)$$

$$\frac{dX_2}{d\tau} = -\Delta_1 X_1 - \frac{\sigma(1-R\cos F)}{T}X_2 - \frac{\sigma R\sin F}{T}X_1 + 2C\sigma A_2, \quad (7)$$

$$\frac{dA_1}{d\tau} = -dA_1 - \delta_1 A_2 - X_1 + 2(B_1A_1 + B_2A_2), \quad (8)$$

$$\frac{dA_2}{d\tau} = -dA_2 - \delta_1 A_1 + X_2 + 2(B_2A_1 + B_1A_2), \quad (9)$$

$$\frac{dB_1}{d\tau} = -(2\delta_1 + \delta_0)B_2 - B_1 - A_1^2 + A_2^2, \quad (10)$$

$$\frac{dB_2}{d\tau} = -(2\delta_1 + \delta_0)B_1 - B_2 - 2A_1A_2, \quad (11)$$

where we took into account that X, A, and B are complex-valued quantities: $X_1 = \mathrm{Re}X$, $X_2 = \mathrm{Im}X$, $A_1 = \mathrm{Re}A$, $A_2 = \mathrm{Im}A$, $B_1 = \mathrm{Re}B$, and $B_2 = \mathrm{Im}B$. Detailed derivation of equations (6)–(11) is given in [11].

The system of nonlinear differential equations describes the dynamics of coherent quasiparticles in six-dimensional phase space and is the basis for investigation of the dynamics of coherent excitons, photons, and biexcitons with inclusion of the Coulomb binding of excitons into biexcitons. Solving the system of equations (6)–(11) exactly is a very complicated or even intractable problem.

Nonetheless, it should be noted that the evolution of solutions to the system of equations (6)–(11) essentially depends on the evolution of a small volume of the phase space of this system. Changes in the elementary six-dimensional phase volume V_0, each point of which moves according to Eqs. (6)–(11), are determined by the equation

$$\frac{dV_0}{d\tau} = -2\left[1 + d + \frac{\sigma(1-R\cos F)}{T}\right]V_0. \quad (12)$$

It follows from Eq. (12) that the six-dimensional phase volume of the system of equations (6)–(11) tends to zero as $\tau \longrightarrow \infty$ with a characteristic time equal to

$$\frac{1}{2}\left[1 + d + \frac{\sigma(1-R\cos F)}{T}\right]^{-1},$$

$$V_0(\tau) = V_0(0)\exp\left\{-2\left[1 + d + \frac{\sigma(1-R\cos F)}{T}\right]\tau\right\}. \quad (13)$$

However, this does not mean that any small volume of the phase space collapses into a point. It can spread over a surface, and the points of any element of the phase space are attracted to a subset whose dimensionality is smaller than the dimensionality of the original space.

Stationary states of the system, which relate the densities of the coherent excitons and biexcitons to the intensity of the electromagnetic field and the intensities of the field at the entrance to and exit from the cavity, can be easily found from Eqs. (6)–(11) [11].

If the stationary solutions are unstable, then the attractor in the phase space can be a limit cycle, sphere, or a strange attractor. They correspond to nonlinear periodic, quasi-periodic, or stochastic self-oscillations in the system.

3. COMPUTER EXPERIMENT. THE POSSIBILITY OF THE APPEARANCE OF STRUCTURES PERIODIC AND CHAOTIC IN TIME

Equations (6)–(11) belong to the class of nonlinear ordinary differential equations that describe open dynamic systems. There can be several stationary solutions to such equations. However, depending on the relationship between the parameters of the system, some of the stationary states may be unstable. For this reason, analysis of the solutions to Eqs. (6)–(11) implies answering the question of the stability of the stationary states. If part of the curve of the stationary state is unstable, nonlinear periodic or chaotic self-oscillations appear in the system.

The characteristic equation of system (6)–(11) is an algebraic sixth-degree equation and has the form

$$a_0\lambda^6 + a_1\lambda^5 + a_2\lambda^4 + a_3\lambda^3 + a_2\lambda^2 + a_1\lambda + a = 0, \quad (14)$$

where a_i are constants dependent on the parameters of the system.

Equation (14) has six roots $\lambda_i = \mathrm{Re}\lambda_i + i\,\mathrm{Im}\lambda_i$. Thus, the problem of stability of the stationary states is reduced to determining the positions of the roots in the complex λ plane. If all the roots are in the left half-plane, the stationary states are stable. In the case when at least one root is in the right half-plane, the stationary state is unstable. Using the Routh–Hurwitz criterion, it can be shown that at certain values of the parameters, a part of the stationary curve of the dependence $X_1(Y)$ corresponds to an unstable solution. In particular, Fig. 2 shows the stationary nonlinear dependence of the real

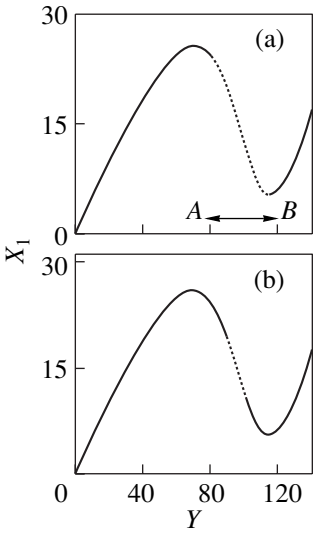

Fig. 2. Dependence of the real part of the amplitude of the transmitted field X_1 on the incident field amplitude Y for σ equal to (a) 1 and (b) 2 and for the parameter values $C = 5$, $\delta_0 = 5$, $F = 2\pi n$, and $\delta_1 = 10$. The dotted curves show unstable stationary states.

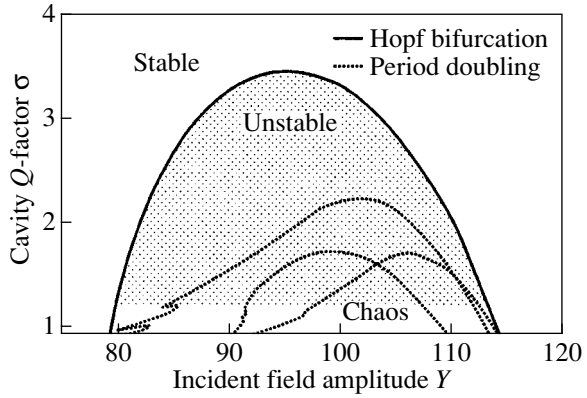

Fig. 3. Self-oscillation region in the plane of the cavity Q factor σ and incident field amplitude Y. The solid line corresponds to Hopf bifurcation points. The period-doubling bifurcations are represented by dotted lines.

part of the amplitude of the radiation X_1 emerging from the cavity on the incident radiation amplitude at the parameters $\sigma = 1$ (Fig. 2a) and 2 (Fig. 2b), $\delta_0 = 5$, $c = 5$, $F = 2\pi n$, $\Lambda_1 = 0$, and $\delta_1 = 10$. As seen from Fig. 2, instability windows, which are indicated by dotted lines, appear at these values of the parameters. The dimensions of the windows depend on the parameter σ. Hopf bifurcations correspond to points A and B. An increase in the parameter σ leads to merging of the bifurcation points at $\sigma > \sigma_{cr} = 3.45$ and disappearance of the instability windows.

Figure 3 shows the regions of self-pulsations in the (σ–Y) coordinate plane (cavity Q factor versus incident amplitude field diagram). The Hopf bifurcation line ($\mathrm{Re}\lambda = 0$) is obtained using the method of analytic continuation in a parameter [14]. This line is the boundary between the stable and unstable stationary states of the system. The shaded part of Fig. 3 is the region in which the system is unstable and nonlinear oscillations appear. The dotted lines show the regions of parameter values corresponding to oscillation period doubling in the system. Thus, nonlinear periodic self-pulsations occur along the boundary in the diagram of the system of coherent excitons, photons, and biexcitons and the corresponding phase trajectory is a limit cycle. As the representative point moves to the center of the instability window, oscillations become more complicated. A cascade of period-doubling bifurcations followed by a chaotic-oscillation regime and the appearance of a strange attractor is observed. In contrast to the Lorenz strange attractor associated with hops between the corresponding equilibrium states, the strange attractor, in our case, appears as a result of a complicated filling of six-dimensional phase space by nonintersecting phase trajectories.

It should be noted that bifurcation diagrams are important tools for studying the dynamic properties of nonlinear systems. Computer experiments indicate that various regimes of nonlinear oscillations can occur in a system of coherent excitons, photons, and biexcitons in the case where the nonlinearity is due to excitons being united into biexcitons. Figure 4 shows bifurcation diagrams at different values of the cavity Q factor. For $\sigma = 3$, the $\max X_1(Y)$ is a single-valued function over the entire instability region (Fig. 4a). It is seen from Fig. 4a that at incident field amplitudes $Y < Y(HB_1)$, the stationary state is a stable focus. This means that the system, having been disturbed from the equilibrium state, comes to equilibrium after several oscillations. At $Y = Y(HB_1) = 87$, the stable focus is transformed into an unstable focus. At $Y(HB_1) < Y < Y(HB_2)$, nonlinear periodic oscillations arise in the system and the phase trajectory goes to a stable limit cycle with time. Thus, a Hopf bifurcation, i.e., the transition of the system from the focus to a limit cycle, occurs. Analogous results are obtained for the motion of the representative point from B to A (Fig. 2). At $\sigma = 2$, the stationary states are stable focuses for $Y < Y(HB_1)$ and $Y > Y(HB_2)$ (Fig. 4b); the Hopf bifurcation occurs at $Y(HB_1) = 83$ and $Y(HB_2) = 41$. When the value of the incident field amplitude lies between $Y = Y(PD_{11}) = 96$ and $Y = Y(PD_{12}) = 106$, period doubling is observed. The first bifurcation of the period doubling takes place at $Y = Y(PD_{12})$. The cascade of period-doubling bifurcations corresponding to the transition of the system to the dynamic-chaos regime is shown in Fig. 4c. In this case, a strange attractor appears in the phase space.

Figure 5 shows a power spectrum of oscillations. At $Y = 99$, there is only one frequency f_0 in the original

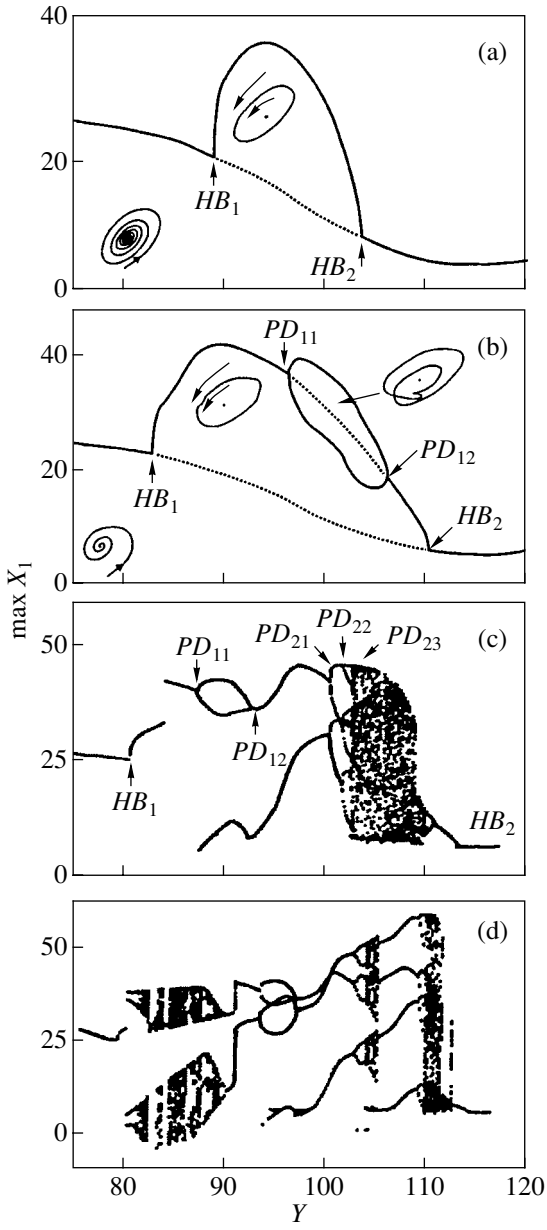

Fig. 4. Bifurcation diagrams at the cavity Q factor σ equal to (a) 3, (b) 2, (c) 1.4, and (d) 1. The other parameters are $C = 5$, $\delta_0 = 5$, $F = 2\pi n$, $\delta_1 = 10$, $d = 0.1$, $T = 0.01$, and $\Delta_1 = 0$.

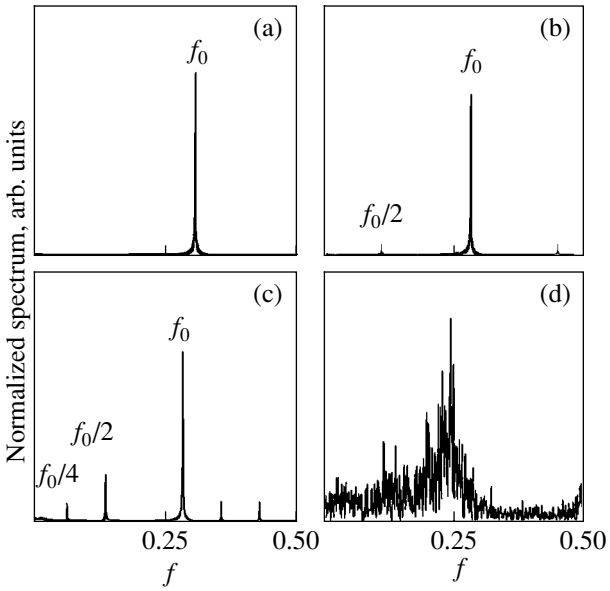

Fig. 5. Power spectrum of self-oscillations at the transition to the chaotic regime through period-doubling bifurcations for the incident field amplitude Y equal to (a) 99, (b) 102.3, (c) 103.3, and (d) 105. The other parameters are the same as in Fig. 4c.

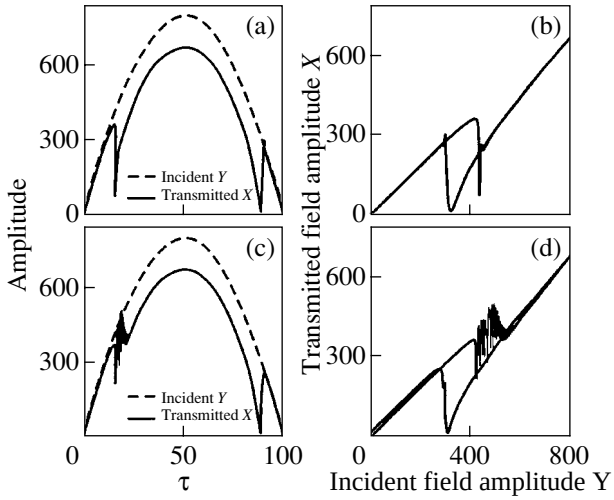

Fig. 6. The shape of the incident pulse Y (dashed line) and of the transmitted pulse X (solid line, $X = \sqrt{X_1^2 + X_2^2}$) for σ equal to (a) 10 and (c) 2. Panels (b) and (d) show the dynamic optical bistability. The parameter values are $C = 5$, $\delta_0 = 5$, $F = 2\pi n$, $\delta_1 = 30$, $d = 0.1$, $T = 0.01$, and $\Delta_1 = 0$.

spectrum (Fig. 5a). When the field strength becomes equal to $Y_1 = 102.3$, two lines with frequency $f_0/2$ appear in addition to the line at f_0 and the motion becomes doubly periodic (Fig. 5b). As Y increases further, a new subharmonic appears with frequency $f_0/4$. This indicates that the subharmonic with $f_0/2$ becomes unstable and a stable fourfold cycle appears (Fig. 5c). Finally, at $Y = 105$, the spectrum becomes continuous, a strange attractor appears in the phase space, and the motion of the system becomes chaotic (Fig. 5d).

The bifurcation diagram at $\sigma = 1$ (Fig. 4d) is more complicated. The chaotic behavior of the system is observed in different regions of the phase plane. It is of interest that, between the regions of chaotic regimes, there are regions with periodic self-oscillations.

It should be noted that in experimental studies on optical bistability, the dynamic optical bistability is observed when the time dependences of the pumping power and corresponding response of the system are

compared. We numerically solved the system of nonlinear differential equations (6)–(11) subject to the boundary conditions for a ring cavity in the case where the external pumping $Y(\tau)$ was a parabolic function of time. The results of this computer experiment are shown in Figs. 6a and 6b (for $\sigma = 10$) and Figs. 6c and 6d (for $\sigma = 2$). The other parameters are $F = 2\pi n = 5$, $\Delta_1 = 0$, $\delta_1 = 30$, $\delta_0 = 5$, $d = 0.1$, and $T = 0.01$. Figure 6a shows the time dependences of the electromagnetic fields incident on and emerging from the cavity for the case where the pulse duration is equal to $\tau = 100$ ($t = 100$ ps). It is seen that the pulse transmitted through the cavity is deformed. The dependence of the field amplitude emerging from the cavity on the incident field amplitude is shown in Fig. 6b. Dynamical optical bistability is seen to occur for a pulse traveling clockwise in the system of coherent excitons, photons, and biexcitons in this case. If the Q factor of the cavity is decreased, the switching will be accompanied by oscillations, which adversely affects the operation of a bistable element (Figs. 6c, 6d).

In conclusion, let us discuss possible experimental observations of the predicted effects. We made numerical estimates for CdS-type crystals in which $\hbar D = 10^{-9}$ eV cm$^{3/2}$, $\hbar g = 0.1$ eV cm$^{-1/2}$ V^{-1}, $\hbar\omega = 2$ eV, $\hbar c_0 k_0 \approx 2$ eV, $\hbar\gamma_{ex} = 10^{-5}$ eV, $\hbar\gamma_{biex} = 10^{-4}$ eV, $T = 0.01$, $L = 1$ μm, and $\hbar(2\omega - \omega_{biex}) = -0.04$ eV. The critical power at which the nonlinear phenomena under investigation can be observed is about $P \sim 40 \times 10^3$ W cm^{-2}. In this case, the concentrations of excitons and biexcitons are of the order of 10^{16} and 10^{14} cm^{-3}, respectively.

Thus, the numerical estimates enable one to conclude that it is possible to observe the phenomena under discussion and control self-pulsations which originate in the system of coherent excitons and biexcitons in semiconductors in the case where excitons unite into biexcitons.

ACKNOWLEDGMENTS

One of the authors (V.Z.T) thanks the Royal Society of the United Kingdom for financial support.

REFERENCES

1. V. A. Zalozh, S. A. Moskalenko, and A. Kh. Rotaru, Zh. Éksp. Teor. Fiz. **95**, 601 (1989) [Sov. Phys. JETP **68**, 338 (1989)].
2. V. A. Zalozh, A. Kh. Rotaru, and V. Z. Tronciu, Zh. Éksp. Teor. Fiz. **103**, 994 (1993) [JETP **76**, 487 (1993)].
3. V. A. Zalozh, A. Kh. Rotaru, and V. Z. Tronciu, Zh. Éksp. Teor. Fiz. **105**, 260 (1994) [JETP **78**, 138 (1994)].
4. A. Kh. Rotaru and K. V. Shura, Zh. Éksp. Teor. Fiz. **107**, 450 (1995) [JETP **80**, 240 (1995)].
5. A. Kh. Rotaru and K. V. Shura, Fiz. Tverd. Tela (Leningrad) **33**, 1973 (1991) [Sov. Phys. Solid State **33**, 1111 (1991)].
6. E. Hanamura, Solid State Commun. **12**, 951 (1973).
7. A. A. Gogolin and É. I. Rashba, Pis'ma Zh. Éksp. Teor. Fiz. **17**, 690 (1973) [JETP Lett. **17**, 478 (1973)].
8. A. L. Ivanov, H. Haug, and L. V. Keldysh, Phys. Rep. **296**, 236 (1998).
9. A. L. Ivanov and V. V. Panashchenko, Pis'ma Zh. Éksp. Teor. Fiz. **49**, 34 (1989) [JETP Lett. **49**, 39 (1989)].
10. A. L. Ivanov, L. V. Keldysh, and V. V. Panashchenko, Zh. Éksp. Teor. Fiz. **99**, 641 (1991) [Sov. Phys. JETP **72**, 359 (1991)].
11. A. Kh. Rotaru and V. Z. Tronciu, Fiz. Tverd. Tela (St. Petersburg) **40**, 1810 (1998) [Phys. Solid State **40**, 1641 (1998)].
12. H. M. Gibbs, *Optical Bistability: Controlling Light with Light* (Academic, Orlando, 1985; Mir, Moscow, 1988).
13. L. A. Lugiato, in *Theory of Optical Bistability*, Ed. by E. Wolf (North-Holland, Amsterdam, 1984), Progress in Optics, vol. XXI.
14. E. J. Doedel, A. R. Champneys, T. F. Fairgrieve, *et al.*, Auto 97 Continuation and bifurcation software for ordinary differential equations (March 1998).

Translated by A. Poushnov

Physics of the Solid State, Vol. 44, No. 2, 2002, pp. 241–247. Translated from Fizika Tverdogo Tela, Vol. 44, No. 2, 2002, pp. 232–238.

SEMICONDUCTORS AND DIELECTRICS

The Region of Existence of the Three-Dimensional Continuum Bipolaron

V. K. Mukhomorov

Institute of Agrophysics, Russian Academy of Agricultural Sciences, Grazhdanskiĭ pr. 14, St. Petersburg, 195220 Russia

e-mail: ivl@agrophys.spb.su

Received March 22, 2001; in final form, June 4, 2001

Abstract—The ranges of $\varepsilon^*/\varepsilon_\infty$ and of the electron–phonon coupling constant in which the three-dimensional bipolaron exists are determined. The limits of these ranges correspond to the emergence of the first bound state of two polarons. The criteria for the first bound state to arise are found by solving an integral equation, which corresponds to a Schrödinger equation describing internal vibrations of a bipolaron. The Hamiltonian describing these vibrations is separated from the complete Hamiltonian of the electron–phonon system by using the Bogoliubov–Tyablikov method of canonical transformations of coordinates. © *2002 MAIK "Nauka/Interperiodica".*

1. INTRODUCTION

In recent years, the existence of bipolarons has been the subject of numerous publications [1–9]. Experimentally, bipolarons have been observed in organic compounds [10–12], molten salts [13], and ammonia-based systems [14, 15]. In theoretical studies, the criterion for the formation of a bipolaron is based on the requirement of positiveness of its binding energy $\Delta F = 2F_p - F_{bp}$, where F_{bp} is the total energy of a singlet bipolaron and F_p is the total energy of a polaron in the ground 1*s* state. The energies are reckoned from the bottom of the conduction band. From this requirement, one commonly determines the limiting values of either the electron–phonon coupling constant or the dielectric constant of the polar medium for the region of existence of the three-dimensional bipolaron. However, the positiveness of the binding energy is a necessary but not sufficient condition. A bipolaron will arise if there is at least one bound state in the bipolaron potential well. This condition is of particular importance when the parameters of the system are close to their critical values and the bipolaron binding energy tends to zero.

In this paper, we determine the boundaries of the region of existence of the three-dimensional bipolaron from the condition of the emergence of the first bound state of two polarons in the bipolaron potential well. In order to solve this problem, one should first separate the Hamiltonian describing the ground state of the bipolaron from the complete Hamiltonian of the electron–phonon system and then find the Hamiltonian of the relative motion of two polarons in the bipolaron potential well. This problem can be solved using a canonical transformation of the coordinates and by going over to collective variables [16, 17], which enables one to separate the internal translation-invariant degrees of freedom from the motion of the system as a whole. In this case, the degeneracy with respect to the translation group is lifted and one can expand the initial Hamiltonian in powers of a small parameter and construct a successive-approximation scheme for calculating the energy and wave function.

2. RESULTS AND DISCUSSION

The Hamiltonian describing the states of two electrons in a polarizable medium in the effective-mass approximation is written in the standard form

$$H = -\frac{\hbar^2}{2m^*}(\nabla_{\mathbf{r}_1}^2 + \nabla_{\mathbf{r}_2}^2) + \sum_{\mathbf{f},\, j=1,2}(V_{\mathbf{f}} e^{i\mathbf{f}\mathbf{r}_j} b_{\mathbf{f}} - V_{\mathbf{f}}^* e^{-i\mathbf{f}\mathbf{r}_j} b_{\mathbf{f}}^+) + \frac{1}{2}\sum_{\mathbf{f}} \hbar\omega_{\mathbf{f}}(b_{\mathbf{f}}^+ b_{\mathbf{f}} + b_{\mathbf{f}} b_{\mathbf{f}}^+) + \frac{e^2}{\varepsilon_\infty |\mathbf{r}_1 - \mathbf{r}_2|}, \quad (1)$$

where

$$V_{\mathbf{f}} = i\frac{\hbar\omega_{\mathbf{f}}}{|\mathbf{f}|u^{1/2}}\left(\frac{4\pi\alpha}{\Omega}\right)^{1/2}, \quad u = \left(\frac{2m^*\omega_{\mathbf{f}}}{\hbar}\right)^{1/2};$$

m^* is the effective electron mass; $\alpha = e^2 u/2\varepsilon^*\hbar\omega_{\mathbf{f}}$ is the electron–phonon coupling constant; $\omega_{\mathbf{f}}$ is the frequency of longitudinal optical phonons; ε_∞ and ε_s are the high-frequency and static dielectric constants of the medium, respectively; $\varepsilon^{*-1} = \varepsilon_\infty^{-1} - \varepsilon_s^{-1}$; and Ω is the volume of the system. The summation is carried out over all vectors of the first Brillouin zone. Following [16, 17], we introduce a formally small parameter ξ such that $\omega_{\mathbf{f}} = \xi^2\nu_{\mathbf{f}}$. This approach is valid if $\alpha > 1$ [18].

It is convenient to go from the operators $b_{\mathbf{f}}$ and $b_{\mathbf{f}}^+$ to canonically conjugate variables of the phonon field, namely, to coordinates $q_{\mathbf{f}}$ and momenta $p_{\mathbf{f}}$:

$$b_{\mathbf{f}}^+ = (q_{-\mathbf{f}})/\xi - i\xi p_{\mathbf{f}}/\sqrt{2},$$
$$b_{\mathbf{f}} = (q_{\mathbf{f}}/\xi + i\xi p_{-\mathbf{f}})/\sqrt{2}. \quad (2)$$

Using Eqs. (2), Hamiltonian (1) is transformed into the form

$$H = -\frac{\hbar^2}{2m^*}(\nabla_{\mathbf{r}_1}^2 + \nabla_{\mathbf{r}_2}^2) + \sum_{\mathbf{f},\, j=1,2} W_{\mathbf{f}} e^{i\mathbf{f}\mathbf{r}_j} q_{\mathbf{f}}$$
$$+ \frac{1}{2}\sum_{\mathbf{f}} \hbar\nu_{\mathbf{f}}(q_{\mathbf{f}}q_{-\mathbf{f}} + \xi^4 p_{\mathbf{f}}p_{-\mathbf{f}}) + \frac{e^2}{\varepsilon_\infty|\mathbf{r}_1 - \mathbf{r}_2|}, \quad (3)$$

where we have introduced the notation

$$W_{\mathbf{f}} = \frac{i}{|\mathbf{f}|}\left(\frac{4\pi e^2\hbar\nu_{\mathbf{f}}}{\Omega\varepsilon^*}\right)^{1/2}.$$

Let us also introduce the new variables

$$\mathbf{r}_1 = \mathbf{R}_1 + \boldsymbol{\rho}_1, \quad \mathbf{r}_2 = \mathbf{R}_2 - \boldsymbol{\rho}_2, \quad (4)$$

where $\mathbf{R}_1$ and $\mathbf{R}_2$ are the position vectors of the centers of gravity of the polarization potential wells and $\boldsymbol{\rho}_1$ and $\boldsymbol{\rho}_2$ are position vectors of the electrons which describe high-frequency oscillations of the electrons in the polaron potential wells and are reckoned from the centers of gravity of the first and second polarons, respectively. It is convenient to go over to the position vector of the center of gravity of the system $\mathbf{R}$ and the relative position vector of the polarons $\boldsymbol{\rho}$ using the relations

$$\mathbf{r}_1 = \mathbf{R} + \frac{1}{2}\boldsymbol{\rho} - \boldsymbol{\rho}_1, \quad \mathbf{r}_2 = \mathbf{R} - \frac{1}{2}\boldsymbol{\rho} - \boldsymbol{\rho}_2. \quad (5)$$

Thus, the motion of the interacting polarons is represented as the sum of translation of the system as a whole and oscillations of the polarons (relative to each other) about their equilibrium positions. Instead of the variables $q_{\mathbf{f}}$, we introduce new phonon coordinates $Q_{\mathbf{f}}$, which describe quantum fluctuations of the phonon field about its classical values $u_{\mathbf{f}}(1)$ and $u_{\mathbf{f}}(2)$ [19]:

$$q_{\mathbf{f}} = \frac{e^{-i\mathbf{f}\mathbf{R}}}{2}[u_{\mathbf{f}}(1)e^{-i\mathbf{f}\boldsymbol{\rho}/2} + u_{\mathbf{f}}(2)e^{i\mathbf{f}\boldsymbol{\rho}/2}$$
$$+ \xi Q_{\mathbf{f}}(e^{i\mathbf{f}\boldsymbol{\rho}/2} + e^{-i\mathbf{f}\boldsymbol{\rho}/2})]. \quad (6)$$

Equation (6) allows one to separate out two independent classical components of the phonon field $u_{\mathbf{f}}(1)$ and $u_{\mathbf{f}}(2)$ that follow the moving electrons. These complex quantities are subject to the condition $u_{-\mathbf{f}} = u_{\mathbf{f}}^*$. Transforming coordinates (5) and (6), the translation coordinates are separated out and Hamiltonian (3) becomes explicitly invariant under the translation operators.

Let us go from the variables $\mathbf{r}_1$, $\mathbf{r}_2$, and $q_{\mathbf{f}}$ to the new variables $\mathbf{R}$, $\boldsymbol{\rho}$, $\boldsymbol{\rho}_1$, $\boldsymbol{\rho}_2$, and $Q_{\mathbf{f}}$ in Hamiltonian (3) and construct a self-consistent approximation scheme for solving the two-electron problem with allowance for the law of conservation of total momentum of the system. After changing the coordinates, the Hamiltonian is written as a power series in the small parameter ξ:

$$H = -\frac{\hbar^2}{2m^*}(\nabla_{\boldsymbol{\rho}_1}^2 + \nabla_{\boldsymbol{\rho}_2}^2) + \frac{1}{2}\sum_{\mathbf{f}}\{W_{\mathbf{f}}[M_{\mathbf{f}}(1,2)e^{i\mathbf{f}\boldsymbol{\rho}_1}$$
$$+ M_{\mathbf{f}}(2,1)e^{-i\mathbf{f}\boldsymbol{\rho}_2}] + \text{c.c.}\} + \frac{e^2}{\varepsilon_\infty|\boldsymbol{\rho} + \boldsymbol{\rho}_1 - \boldsymbol{\rho}_2|}$$
$$+ \frac{1}{2}\sum_{\mathbf{f}}\hbar\nu_{\mathbf{f}}(u_{-\mathbf{f}}(1)M_{\mathbf{f}}(1,2) + u_{-\mathbf{f}}M_{\mathbf{f}}(2,1))$$
$$+ \frac{\xi}{2}\sum_{\mathbf{f}}\{Q_{\mathbf{f}}W_{\mathbf{f}}[N_{\mathbf{f}}e^{i\mathbf{f}\boldsymbol{\rho}_1} + N_{\mathbf{f}}^* e^{i\mathbf{f}\boldsymbol{\rho}_2}] + \text{c.c.}$$
$$+ \hbar\nu_{\mathbf{f}}Q_{\mathbf{f}}(u_{-\mathbf{f}}(1)N_{\mathbf{f}} + u_{\mathbf{f}}(2)N_{\mathbf{f}}^*) + \text{c.c.}\}$$
$$+ \frac{\xi^2}{2}\sum_{\mathbf{f}}\left\{\hbar\nu_{\mathbf{f}}Q_{\mathbf{f}}Q_{-\mathbf{f}}(N_{\mathbf{f}} + N_{\mathbf{f}}^*)\right. \quad (7)$$
$$\left. + \left[P'_{\mathbf{f}} + \frac{2i\mathbf{f}}{\hbar}\mathbf{F}_{\mathbf{f}}(\mathbf{R},\boldsymbol{\rho})\right]\left[P'_{-\mathbf{f}} - \frac{2i\mathbf{f}}{\hbar}\mathbf{F}_{-\mathbf{f}}(\mathbf{R},\boldsymbol{\rho})\right]\right\}$$
$$+ \frac{i\xi^3}{2}\sum_{\mathbf{f}}\nu_{\mathbf{f}}\mathbf{f}\left\{\left[P'_{\mathbf{f}} + \frac{2i\mathbf{f}}{\hbar}\mathbf{F}_{\mathbf{f}}(\mathbf{R},\boldsymbol{\rho})\right]G_{-\mathbf{f}}(\boldsymbol{\rho}_1,\boldsymbol{\rho}_2)\right.$$
$$\left. - \mathbf{G}_{\mathbf{f}}(\boldsymbol{\rho}_1,\boldsymbol{\rho}_2)\left[P'_{\mathbf{f}} + \frac{2i\mathbf{f}}{\hbar}\mathbf{F}_{\mathbf{f}}(\mathbf{R},\boldsymbol{\rho})\right]\right\}$$
$$+ 2\xi^4\sum_{\mathbf{f}}\frac{\mathbf{f}\mathbf{f}}{\hbar}\mathbf{G}_{\mathbf{f}}(\boldsymbol{\rho}_1,\boldsymbol{\rho}_2)\mathbf{G}_{-\mathbf{f}}(\boldsymbol{\rho}_1,\boldsymbol{\rho}_2) + \ldots$$
$$= H_0 + \xi H_1 + \xi^2 H_2 + \xi^3 H_3 + \xi^4 H_4 + \ldots,$$

where we have introduced the notation

$$\mathbf{F}_{\mathbf{f}}(\mathbf{R},\boldsymbol{\rho}) = w_{\mathbf{f}}^*\mathbf{I} + z_{\mathbf{f}}^*\mathbf{J}, \quad \mathbf{G}_{\mathbf{f}} = 2\xi(y_{\mathbf{f}}^*\mathbf{P}_{\boldsymbol{\rho}_1} + x_{\mathbf{f}}^*\mathbf{P}_{\boldsymbol{\rho}_2}),$$
$$w_{\mathbf{f}}^* = \frac{1}{2}(y_{\mathbf{f}}^* + x_{\mathbf{f}}^*), \quad z_{\mathbf{f}}^* = y_{\mathbf{f}}^* - x_{\mathbf{f}}^*,$$
$$\mathbf{I} = 2\xi\mathbf{P}_R, \quad \mathbf{J} = 2\xi\mathbf{P}_\rho,$$
$$y_{\mathbf{f}}^* = \nu_{\mathbf{f}}^*(1)\exp(-i\mathbf{f}\boldsymbol{\rho}/2), \quad x_{\mathbf{f}}^* = \nu_{\mathbf{f}}^*(2)\exp(i\mathbf{f}\boldsymbol{\rho}/2),$$
$$\mathbf{P}_R = -i\hbar\partial/\partial\mathbf{R}, \quad \mathbf{P}_\rho = -i\hbar\partial/\partial\boldsymbol{\rho}, \quad P_{\mathbf{f}} = -i\partial/\partial Q_{\mathbf{f}},$$
$$N_{\mathbf{f}} = 1 + \exp(i\mathbf{f}\boldsymbol{\rho}), \quad N_{\mathbf{f}}^* = N_{-\mathbf{f}}, \quad (8)$$

$$M_{\mathbf{f}}(1,2) = u_{\mathbf{f}}(1) + u_{\mathbf{f}}(2)\exp(i\mathbf{f}\boldsymbol{\rho}),$$

$$M_{\mathbf{f}}(2,1) = u_{\mathbf{f}}(2) + u_{\mathbf{f}}(1)\exp(-i\mathbf{f}\boldsymbol{\rho}),$$

$$P'_{\mathbf{f}} = \exp(i\mathbf{f}\boldsymbol{\rho}/2)\left(P_{\mathbf{f}} - \mathbf{f}\nu^*_{\mathbf{f}}(1)\sum_{\mathbf{k}}\mathbf{k}M_{\mathbf{f}}(1,2)P_{\mathbf{k}}\right)$$

$$+ \exp(-i\mathbf{f}\boldsymbol{\rho}/2)\left(P_{\mathbf{f}} - \mathbf{f}\nu^*_{\mathbf{f}}(2)\sum_{\mathbf{k}}\mathbf{k}M_{\mathbf{f}}(2,1)P_{\mathbf{k}}\right)\ldots.$$

As is known [16, 17], the time-independent Schrödinger equation with Hamiltonian (7) exists only if $\langle\chi_0|H_1|\chi_0\rangle$ is equal to zero. From this condition, one can determine the unknown complex quantities $u_{\mathbf{f}}(1)$ and $u_{\mathbf{f}}(2)$, which are subject to six additional conditions [in order to average out the redundant degrees of freedom that are introduced by Eqs. (4) and (5)]:

$$\sum_{\mathbf{f}} f_\alpha \nu^*_{\mathbf{f}}(1)\left\{q_{\mathbf{f}}\exp\left[i\mathbf{f}\left(\mathbf{R} + \frac{1}{2}\boldsymbol{\rho}\right)\right] - u_{\mathbf{f}}(1)\right\} = 0,$$

$$\sum_{\mathbf{f}} f_\alpha \nu^*_{\mathbf{f}}(2)\left\{q_{\mathbf{f}}\exp\left[i\mathbf{f}\left(\mathbf{R} - \frac{1}{2}\boldsymbol{\rho}\right)\right] - u_{\mathbf{f}}(2)\right\} = 0, \quad (9)$$

$$\alpha = x, y, z.$$

Without loss of generality, the quantities $\nu_{\mathbf{f}}(i)$ and $u_{\mathbf{f}}(i)$ can be subject to the linear orthogonality conditions

$$\sum_{\mathbf{f}} f_\alpha f_\beta \nu^*_{\mathbf{f}}(1)[u_{\mathbf{f}}(1) + u_{\mathbf{f}}(2)\exp(-i\mathbf{f}\boldsymbol{\rho})] = \delta_{\alpha\beta},$$

$$\sum_{\mathbf{f}} f_\alpha f_\beta \nu^*_{\mathbf{f}}(2)[u_{\mathbf{f}}(2) + u_{\mathbf{f}}(1)\exp(-i\mathbf{f}\boldsymbol{\rho})] = \delta_{\alpha\beta}. \quad (10)$$

The quantities $u_{\mathbf{f}}(1)$ and $u_{\mathbf{f}}(2)$ are chosen to minimize the potential energy of renormalized phonons. Once the transformations indicated above are performed, the Schrödinger equation of the system under study can be expanded in powers of the parameter ξ:

$$(H - E)\Psi = (H_0 + \xi H_1 + \xi^2 H_2 + \xi^3 H_3 + \ldots - E)\Psi = 0. \quad (11)$$

The wave function Ψ and energy E are also sought in the form of perturbation series:

$$E = E_0 + \xi E_1 + \xi^2 E_2 + \xi^3 E_3 + \ldots, \quad (12a)$$

$$\Psi = \Psi_0 + \xi\Psi_1 + \xi^2\Psi_2 + \xi^3\Psi_3 + \ldots. \quad (12b)$$

Substituting Eqs. (12a) and (12b) into Eq. (11) and equating the coefficients of powers of ξ to zero yields the set of equations

$$(H_0 - E_0)\Psi_0 = 0, \quad (13a)$$

$$(H_0 - E_0)\Psi_1 = (E_1 - H_1)\Psi_0, \quad (13b)$$

$$(H_0 - E_0)\Psi_2 = (E_2 - H_2)\Psi_0 + (E_1 - H_1)\Psi_1, \ldots. \quad (13c)$$

The main term of the expansion is the Hamiltonian H_0, which carries important information about the system. The principal result of the electron–phonon interaction is the formation of a polarization potential well for each of the particles. Since, in the zeroth approximation, H_0 depends only on the variables $\boldsymbol{\rho}_1$ and $\boldsymbol{\rho}_2$ (and on the coordinate $\boldsymbol{\rho}$ as a parameter), the zeroth approximation Ψ_0 to the wave function can be written in a multiplicative form:

$$\Psi_0 = \chi_0(\boldsymbol{\rho}_1, \boldsymbol{\rho}_2; \boldsymbol{\rho})\Phi(\boldsymbol{\rho}, \mathbf{R}, Q_{\mathbf{f}}). \quad (14)$$

The ground state of the singlet bipolaron can be found either by solving the integro-differential equation (13a) or by using the variational principle and minimizing the functional corresponding to Eq. (13a). In the limiting long-wavelength optical phonon approximation ($\omega_{\mathbf{f}} = \omega_0$), the functional corresponding to the lowest energy electron state of the bipolaron has the form [19, 20]

$$\begin{aligned} E_0(\rho) = {} & -(\hbar^2/2m^*)\int\chi_0(\boldsymbol{\rho}_1, \boldsymbol{\rho}_2)(\nabla^2_{\boldsymbol{\rho}_1} + \nabla^2_{\boldsymbol{\rho}_2}) \\ & \times\chi_0(\boldsymbol{\rho}_1, \boldsymbol{\rho}_2)d\tau_1 d\tau_2 - (e^2/\varepsilon^*) \\ & \times\int\chi_0^2(\boldsymbol{\rho}_1, \boldsymbol{\rho}_2)\chi_0^2(\boldsymbol{\rho}'_1, \boldsymbol{\rho}'_2)\left\{|\boldsymbol{\rho}_1 - \boldsymbol{\rho}'_1|^{-1}\right. \\ & + |\boldsymbol{\rho}_1 - \boldsymbol{\rho} - \boldsymbol{\rho}'_1|^{-1} + |\boldsymbol{\rho}_2 - \boldsymbol{\rho} - \boldsymbol{\rho}'_2|^{-1} \\ & \left. + |\boldsymbol{\rho}_2 - \boldsymbol{\rho}'_2|^{-1}\right\}d\tau_1 d\tau_2 d\tau'_1 d\tau'_2 + (e^2/\varepsilon_\infty) \\ & \times\int\chi_0^2(\boldsymbol{\rho}_1, \boldsymbol{\rho}_2)|\boldsymbol{\rho}_1 - \boldsymbol{\rho} - \boldsymbol{\rho}_2|^{-1}d\tau_1 d\tau_2. \end{aligned} \quad (15)$$

As $\rho \longrightarrow \infty$, the energy $E_0(\rho)$ tends to twice the polaron energy. The choice of the trial wave function and minimization of this functional using the method of intermediate electron–phonon coupling strength [21] (under the assumption that the wave function is normalized and the virial theorem is valid for any fixed value of ρ) were made in [22]. In [20, 22], using the Heitler–London method and taking electron–electron correlations into account, it was shown that the three-dimensional singlet bipolaron is a two-center formation and that its total energy reaches a minimum at a finite equilibrium distance ρ_0, about which two bound polarons oscillate.

Using Eqs. (13), the first-order correction to the wave function is found to be

$$\Psi_1 = \chi_0(\boldsymbol{\rho}_1, \boldsymbol{\rho}_2; \boldsymbol{\rho})\Phi_1 + \sum_{j\neq 0}\frac{\langle\chi_j|H_1|\chi_0\rangle}{E_0 - E_j}\chi_j(\boldsymbol{\rho}_1, \boldsymbol{\rho}_2; \boldsymbol{\rho})\Phi_0, \quad (16)$$

Parameters involved in Eq. (24)

$\varepsilon^*/\varepsilon_\infty$	ρ_0, $\alpha^{-1}(\hbar/2m^*\omega_0)^{1/2}$	γ, $\alpha^2(2m^*\omega_0/\hbar)$	$-V_0$, $2\alpha^2\hbar\omega_0$	m_ρ, $\alpha^4 m^*$
1.00	5.0	3.65×10^{-2}	2.000×10^{-2}	0.02424
1.05	5.5	0.1357	1.250×10^{-2}	0.01953
1.08	5.75	0.2421	7.340×10^{-3}	0.01708
1.10	6.5	0.2833	1.0673×10^{-3}	0.01583
1.12	7.43	0.7940	2.5848×10^{-4}	0.01450

where Φ_1 is a function of coordinates $Q_\mathbf{f}$ (orthogonal to Φ_0).

Substituting the wave function given by Eqs. (12b) and (16) into Eq. (11) and replacing the vectors $\mathbf{F}_\mathbf{f}$ by their corresponding expressions, one can derive an equation describing the relative motion of the polarons with a reduced mass m_ρ and the motion of the bipolaron as a whole with an effective mass m_R, as well as the motion of new (renormalized) phonons:

$$\left\{\frac{\mathbf{P}_\rho^2}{2m_\rho}+\frac{\mathbf{P}_R^2}{2m_R}+E_0(\rho)+\frac{1}{2}\sum_\mathbf{f}\hbar\omega_\mathbf{f}(Q'_\mathbf{f}Q'_{-\mathbf{f}}+\Pi_\mathbf{f}\Pi_{-\mathbf{f}})\right.$$
$$\left.+\sum_j\frac{\langle\chi_0|H_1|\chi_j\rangle\langle\chi_j|H_1|\chi_0\rangle}{E_0-E_j}\right\}\Phi_0 = W(\boldsymbol{\rho},\mathbf{R},Q_\mathbf{f})\Phi_0, \quad (17)$$

where

$$Q'_\mathbf{f} = Q_\mathbf{f}N_\mathbf{f},$$

$$\Pi_\mathbf{f} = \frac{1}{2}[\pi'_\mathbf{f}(1)\exp(i\mathbf{f}\boldsymbol{\rho}/2)+\pi'_\mathbf{f}(2)\exp(-\mathbf{f}\boldsymbol{\rho}/2)],$$

$$\pi'_\mathbf{f}(1) = \pi_\mathbf{f}-\mathbf{f}\nu^*_\mathbf{f}(1)\sum_\mathbf{k}\mathbf{k}M_\mathbf{k}(1,2)\pi_\mathbf{k},$$

$$\pi'_\mathbf{f}(2) = \pi_\mathbf{f}-\mathbf{f}\nu^*_\mathbf{f}(2)\sum_\mathbf{k}\mathbf{k}M_\mathbf{k}(2,1)\pi_\mathbf{k}.$$

The momentum $\mathbf{P}_R$ canonically conjugate to the coordinate $\mathbf{R}$ is an integral of motion (the total momentum of the system). Since the dependence on $\mathbf{R}$ in Eq. (17) is due solely to the kinetic-energy operator, the equation of motion of the bipolaron center of gravity can be separated from Eq. (17). Therefore, the variable $\mathbf{R}$ is cyclic and related only to those translations of the bipolaron as a whole that are characterized by the effective mass m_R.

Since the dominant contribution to the sums over $\mathbf{f}$ comes from $|\mathbf{f}| \approx \xi^{-1}$, we can assume that $|\mathbf{f}||\boldsymbol{\rho}| \gg 1$; therefore, the terms involving $\exp(i\mathbf{f}\boldsymbol{\rho})$ can be omitted from Eq. (17), because the exponential is a rapidly oscillatory function. This makes it possible to separate the variables $\boldsymbol{\rho}$ and $Q_\mathbf{f}$ in Eq. (17) and to obtain an equation describing the relative motion of polarons characterized by the reduced mass m_ρ,

$$\left(\frac{\mathbf{P}_\rho^2}{2m_\rho}+E_0(\rho)\right)\chi(\rho) = W_\rho\chi(\rho). \quad (18)$$

The electronic term $E_0(\rho)$ plays the role of an interaction potential; it depends on the dielectric properties of the medium (through the ratio $\varepsilon^*/\varepsilon_\infty$) and on the electron–phonon coupling constant [22]. Analysis revealed that the binding energy of the bipolaron decreases with increasing ratio $\varepsilon^*/\varepsilon_\infty$; the maximum value of the latter (with constraint $\Delta F \geq 0$) is found to be 1.13 using the data from [19, 22, 23] or 1.15 using the data from [24].

Using the results of [22] and Eq. (18), one can find the critical value α_{cr} for the emergence of the first bound state in the bipolaron potential well for a fixed value of $\varepsilon^*/\varepsilon_\infty$. To do this, we take into account that the interaction potential between polarons $E_0(\rho)$ is closely approximated by a Gaussian $V_0\exp[-\gamma(\rho-\rho_0)^2]$ near its minimum. The zero in the energy scale is taken to be twice the polaron energy. The table lists the parameters of the interaction potential between the polarons near its minimum. As the ratio $\varepsilon^*/\varepsilon_\infty$ increases, the equilibrium distance between the polarons ρ_0 (characterizing the average size of the bipolaron) increases monotonically (table), which is natural because the interaction between the polarons becomes progressively weaker. It has been argued on occasion (see, e.g., [24–26]) that the bipolaron size can be characterized by the average distance $\langle\mathbf{r}_{12}\rangle$, which is, in fact, the spacing between the electrons in Eq. (1). However, the distances between the electrons and between the polarons are not one and the same. Moreover, the average distance $\langle\mathbf{r}_{12}\rangle$ was found in the above-mentioned papers to depend on the dielectric properties of the medium only slightly. Therefore, the results obtained in [24–26] lead to the paradoxical conclusion that, as $\varepsilon^*/\varepsilon_\infty$ increases, the bipolaron binding energy monotonically decreases, but the bipolaron size remains constant over the entire range of the $\varepsilon^*/\varepsilon_\infty$ values in question. Furthermore, in this scheme, the repulsion energy between the polarons tends to infinity as the polarons approach each other, although the distance r_{12} does not have to be zero when the centers of gravity of the polarons coincide ($\rho = 0$), because the distance between the electrons is given by $|\boldsymbol{\rho}_1-\boldsymbol{\rho}_2|$. The situation is similar to that in the model of a helium atom. It seems likely that the quantitative results obtained within the bipolaron model based on Hamiltonian (1), which involves only the coordinates $\mathbf{r}_1$ and $\mathbf{r}_2$, cannot describe some features of the three-dimensional bipolaron structure.

In order to find the critical value α_{cr} for a fixed value of $\varepsilon^*/\varepsilon_\infty$, we go from differential equation (18) to an integral equation. For this purpose, we make the substitution $\chi(\rho) = u(\rho)/\rho$ and introduce a new variable $x = \rho - \rho_0$. In this case, Eq. (18) becomes

$$\frac{d^2u}{dx^2} + \frac{2m_\rho}{\hbar^2}V_0 e^{-\gamma x^2}u + \frac{2m_\rho}{\hbar^2}W_\rho u = 0. \tag{19}$$

Taking into account that $u(x = 0) = u(x = \infty) = 0$ and using the integral relation

$$\int_{x_0}^{x} dx \int_{x_0}^{x} dx \ldots \int_{x_0}^{x} f(x)dx = \frac{1}{(n-1)!}\int_{x_0}^{x}(x-z)^{n-1}f(z)dz, \tag{20}$$

differential equation (19) is reduced to a Fredholm-type integral equation in a dimensional form,

$$u(x) = \int_0^x zu(z)\left(\frac{2m_\rho V_0}{\hbar^2\gamma}\exp(-z^2) + \frac{2m_\rho W_\rho}{\hbar^2\gamma}\right)dz + x\int_x^\infty u(z)\left(\frac{2m_\rho V_0}{\hbar^2\gamma}\exp(-z^2) + \frac{2m_\rho W_\rho}{\hbar^2\gamma}\right)dz. \tag{21}$$

Here, we have introduced a new variable $z = x\sqrt{\gamma}$. The first bipolaron bound state (whose energy lies below the values of the asymptotic Coulomb interaction potential between the polarons) arises at α_{cr}, which corresponds to W_ρ being equal to zero [27]. Substituting $u(z) = w(z)\exp(z^2/2)$ into Eq. (21), we obtain

$$w(z) = \frac{2m_\rho V_0}{\hbar^2\gamma}\int_0^\infty K(z,t)w(t)dt, \tag{22}$$

where the kernel of the integral equation has the form

$$K(z,t) = \begin{cases} t\exp[-(z^2+t^2)/2], & t < z \\ z\exp[-(z^2+t^2)/2], & t > z. \end{cases} \tag{23}$$

As the interaction potential increases in strength, the first bound state will arise when the trace of the kernel $T_j = \int_0^\infty K_j(z,z)dz$ in the jth iteration cycle of the successive approximations satisfies the inequality

$$T_j^{1/j} \geq \frac{\hbar^2\gamma}{2m_\rho V_0}. \tag{24}$$

For the kernel given by Eq. (23), the third iterate gives

$$T_3 = \frac{1}{4}\left(\frac{3\pi}{4\sqrt{2}} - \sum_{k=1}^{\infty}\sum_{n=0}^{\infty}\left(\frac{2}{3}\right)^{n+k+1}\frac{(n+k+1)!2^{n+k}n!k!}{(2n+1)!(2k+1)!}\right). \tag{25}$$

In deriving Eq. (25), we used the integral relation

$$K_j(z,t) = \int_0^\infty K_{j-1}(z,t)K(y,t)dy, \quad K_1(z,t) = K(z,t). \tag{26}$$

It was shown in [27, 28] that the iterations converge rather rapidly for the trace of the kernel. For this reason, we restrict ourselves to the first three iterations.

Using Eq. (24) and the values of parameters listed in the table, we determined the critical value of the electron–phonon coupling constant for a given value of $\varepsilon^*/\varepsilon_\infty$. The region of existence of the three-dimensional bipolaron is shown in the figure in the $(\varepsilon^*/\varepsilon_\infty, \alpha)$ coordinate plane; this region is above the solid curve. Analysis revealed that the relation between α_{cr} and $\varepsilon^*/\varepsilon_\infty$ has the form

$$\alpha_{cr} = 1/[2.7107 - 2.3789(\varepsilon^*/\varepsilon_\infty)]. \tag{27}$$

In the range up to $\alpha \approx 10$, this formula closely approximates the results obtained directly from Eq. (24). Discordance occurs in the range of $\varepsilon^*/\varepsilon_\infty > 1.1$, where the

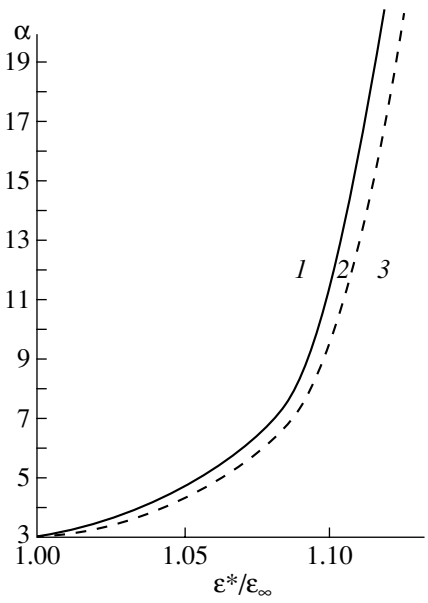

Regions of existence of the three-dimensional bipolaron: (*1*) stable states, (*2*) metastable states, and (*3*) unstable states.

formula underestimates α_{cr} by approximately 5%. It follows from Eq. (27) that three-dimensional bipolarons can exist in polar media with $\varepsilon^*/\varepsilon_\infty < 1.14$; the maximum value corresponds to $\alpha_{cr} \longrightarrow \infty$ and, as one might expect, is smaller than the critical value of 1.148 obtained in [29] from the condition of positiveness of the bipolaron dissociation energy. The published limiting values of $\varepsilon^*/\varepsilon_\infty$ for the existence of the bipolaron lie in the range from 1.16 [24, 26] to 1.8 [30] and appear to be overestimated, because those values were obtained by minimizing the total bipolaron energy functional without regard for the virial theorem. Analysis revealed that if the virial theorem is ignored when the bipolaron binding energy is calculated using the direct variational method, the results may be overestimated. At the same time, in variational calculations of the polaron energy, the virial theorem is automatically taken into account.

Using Eq. (27) and the definition of the parameter α involved in Hamiltonian (1), one can find an approximate relationship between the medium parameters that determines the region of existence of the three-dimensional bipolaron,

$$\left(\frac{e^4 m^*}{\hbar^3 \omega_0 \varepsilon^*}\right)^{1/2}\left(1.917 - 1.682\frac{\varepsilon^*}{\varepsilon_\infty}\right) \geq 1. \qquad (28)$$

Thus, our method for determining the region of existence of the three-dimensional singlet bipolaron allows one to find a relationship between the critical value of the electron–phonon coupling constant and the dielectric properties of the medium.

Let us compare the critical values of the parameters found in this paper with the corresponding values available in the literature. For example, in [31], the vibrational states of the three-dimensional bipolaron were directly calculated using the method of shifted $1/N$ expansion and it was shown that, if $\varepsilon^*/\varepsilon_\infty = 1.08$, a single bound state exists only for $\alpha = 7$. From the calculations performed in this paper, it follows that when $\varepsilon^*/\varepsilon_\infty = 1.08$, the first bound state arises at $\alpha_{cr} > 6.9$, which is consistent with the results of [31].

In the figure, the region above the solid curve corresponds to the values of the parameters of the dielectric medium and the electron–phonon coupling constant, for which there is at least one bipolaron bound state. In the region below the solid curve, there are no bound states of two polarons whose energy lies below the values of the asymptotic Coulomb interaction potential, though their binding energy can be positive ($\Delta F > 0$). However, there are metastable bipolaron states in the region between the solid and dashed curves, because the state of two polarons moving within the bipolaron potential well is separated from the states of free polarons by a potential barrier whose asymptotic behavior is similar to that of the Coulomb potential. Indeed, as can be seen from the expression for the Hamiltonian H_0, the interaction potential between the two polarons at distances larger than the bipolaron dimensions has the form

$$\begin{aligned} V &= V_1 + V_2, \\ V_1 &= e/\varepsilon_s\rho + e(\rho_{1z} - \rho_{2z})/2\varepsilon^{**}\rho^2 \\ &+ e(3\rho_{1z}^2 + 3\rho_{2z}^2 - \rho_1^2 - \rho_2^2)/4\varepsilon^{**}\rho^3 + \ldots, \\ V_2 &= e(\rho_{1x}\rho_{2x} + \rho_{1y}\rho_{2y} - 2\rho_{1z}\rho_{2z})/\varepsilon_\infty\rho^3, \end{aligned} \qquad (29)$$

where $\varepsilon^{**} = \varepsilon_\infty\varepsilon_s(\varepsilon_\infty + \varepsilon_s)^{-1}$ and ρ_{iz} is the z component of the vector $\boldsymbol{\rho}_i$. The z axis is directed along the line passing through the centers of gravity of the polarons. In the approximation where the electronic part of the wave function can be represented as the product of two one-electron wave functions with large distances between the polarons, we obtain the following expression for the interaction energy between the two polarons:

$$\Delta F \approx \frac{e^2}{\varepsilon_s\rho} - \frac{0.482e^4}{I_0\rho^2(\varepsilon^{**}\alpha_0\rho)^2}\left\{1 + \frac{1}{(\alpha_0\rho)^2}\right. \\ \left.\times\left[7.333 + \left(\frac{\varepsilon^{**}}{\varepsilon_\infty}\right)^2 23.14\right]\right\} + \ldots, \qquad (30)$$

where $I_0 = 0.322\alpha^2\hbar\omega$ is the ionization energy of a polaron, $\alpha_0 = 0.5/a_0^*$, and $a_0^* = \hbar^2\varepsilon^*/m^*e^2$ is the effective Bohr radius. We note that the leading term of the expansion in Eq. (30) has a Coulombic form.

The region of metastable states of the three-dimensional bipolaron is found by directly solving the Schröodinger equation (18) using the method of shifted $1/N$ expansion. This region lies between the solid and dashed curves. The boundary of the region of metastable states corresponds to smaller values of α than the boundary of the region of stable bipolaron states for the same values of $\varepsilon^*/\varepsilon_\infty$. This difference is especially significant when $\varepsilon^*/\varepsilon_\infty$ is close to its maximum value for which the bipolaron still exists. The dashed curve can be approximated by the equation

$$\alpha_{cr}^{meta} = 1/[2.6312 - 2.2936(\varepsilon^*/\varepsilon_\infty)]. \qquad (31)$$

Below the dashed curve, bipolarons do not exist for any value of the electron–phonon coupling constant. For alkali-halide crystals, the typical values of the parameters are $\varepsilon^*/\varepsilon_\infty \geq 1.1$ and $\alpha \approx 5$–6; in such media, even metastable bipolarons cannot exist. Three-dimensional bipolarons also cannot exist in La_2CuO_4, for which $\varepsilon^*/\varepsilon_\infty \approx 1.09$ and $\alpha \approx 4$–5 [32]. At the same time, in metal–ammonia systems, the values of the relevant parameters are $\varepsilon^*/\varepsilon_\infty = 1.08$ and $\alpha = 13.5$ and lie in the region of existence of the three-dimensional bipolaron. The continuum-bipolaron model was used by Mott [14] to explain the properties of electrons in ammonia. The formation of bipolarons in ammonia, in Mott's opinion,

explains the wide range of properties of the metal–ammonia systems, including the metal–insulator phase transitions. The hypothesis of the existence of three-dimensional bipolarons in such systems is substantiated by experimental optical studies [15], by investigations of the magnetic susceptibility [33, 34] and conductivity [35] (which revealed a sharp drop in the electrical resistivity by several orders of magnitude), and by electron spin resonance studies [36].

As can be seen from the figure, the upper limit of the range of $\varepsilon^*/\varepsilon_\infty \leq 1.13$–$1.145$ for the existence of the bipolaron, commonly cited in the literature, corresponds to the limit of very strong electron–phonon coupling $\alpha_{cr} \geq 21$. As the ratio $\varepsilon^*/\varepsilon_\infty$ is decreased, the range of values of the electron–phonon coupling constant within which three-dimensional bipolarons exist becomes progressively wider.

REFERENCES

1. A. S. Alexandrov and N. F. Mott, *Polarons and Bipolarons* (World Scientific, Singapore, 1995).
2. V. Cataudella, G. Iadonisi, and D. Ninno, Phys. Scr. T **39**, 71 (1991).
3. V. L. Vinetskiĭ, O. Meredov, and V. A. Yanchuk, Teor. Éksp. Khim. **25**, 641 (1989).
4. J. T. Devreese, G. Verbist, and F. M. Peeters, in *Polarons and Bipolarons in High-T_c Superconductors and Related Materials*, Ed. by E. K. H. Salje, A. S. Alexandrov, and W. Y. Leong (Cambridge Univ. Press, Cambridge, 1995), p. 75.
5. V. D. Lakhno, Usp. Fiz. Nauk **168**, 465 (1998) [Phys. Usp. **41**, 403 (1998)].
6. W. B. da Costa and F. M. Peeters, Phys. Rev. B **57**, 10569 (1998).
7. R. T. Senger and A. Ercelebi, Phys. Rev. B **60**, 10070 (1999).
8. G. Iadonisi, V. Cataudella, G. De Filippis, and D. Ninno, Europhys. Lett. **41**, 309 (1998).
9. N. F. Mott, in *Polarons and Bipolarons in High-T_c Superconductors and Related Materials*, Ed. by E. K. H. Salje, A. S. Alexandrov, and W. Y. Leong (Cambridge Univ. Press, Cambridge, 1995), p. 1.
10. J. C. Scott, P. Pfluger, M. T. Krounbi, and G. B. Street, Phys. Rev. B **28**, 2140 (1983).
11. K. F. Voss, C. M. Foster, L. Smilowitz, *et al.*, Phys. Rev. B **43**, 5109 (1991).
12. R. R. Chance, J. L. Bredas, and R. Silbey, Phys. Rev. B **29**, 4491 (1984).
13. E. S. Fois, A. Selloni, M. Parrinello, and R. Carr, J. Phys. Chem. **92**, 3268 (1988).
14. N. F. Mott, *Metal-Insulator Transitions* (Taylor & Francis, London, 1974; Nauka, Moscow, 1979).
15. J. Thompson, *Electrons in Liquid Ammonia* (Mir, Moscow, 1979).
16. N. N. Bogolyubov, Ukr. Mat. Zh. **2**, 3 (1950).
17. S. V. Tyablikov, Zh. Éksp. Teor. Fiz. **21**, 377 (1951).
18. A. S. Davydov, *Theory of Solid State* (Nauka, Moscow, 1976).
19. V. K. Mukhomorov, Phys. Status Solidi B **219**, 71 (2000).
20. V. K. Mukhomorov, Opt. Spektrosk. **55**, 246 (1983) [Opt. Spectrosc. **55**, 145 (1983)]; Khim. Fiz. **2**, 642 (1983).
21. S. I. Pekar and V. M. Buĭmistrov, Zh. Éksp. Teor. Fiz. **32**, 1193 (1957) [Sov. Phys. JETP **5**, 970 (1957)].
22. V. K. Mukhomorov, Opt. Spektrosk. **86**, 50 (1999) [Opt. Spectrosc. **86**, 41 (1999)].
23. A. V. Glushkov, Zh. Fiz. Khim. **64**, 1579 (1990).
24. G. Verbist, M. A. Smondyrev, F. M. Peeters, and J. T. Devreese, Phys. Rev. B **45**, 5262 (1992).
25. J. Adamowski, Phys. Rev. B **39**, 3649 (1989).
26. S. Sahoo, Phys. Lett. A **195**, 105 (1994).
27. R. Dutt and R. S. Gangopadhyay, Phys. Lett. A **109**, 4 (1985).
28. V. K. Mukhomorov, Fiz. Tverd. Tela (St. Petersburg) **42**, 1559 (2000) [Phys. Solid State **42**, 1602 (2000)].
29. S. Sil, A. K. Giri, and A. Chatterjee, Phys. Rev. B **43**, 12642 (1991).
30. T. K. Mitra, Phys. Lett. A **142**, 398 (1989).
31. G. Iadonisi, V. Cataudella, G. De Filippis, and V. K. Mukhomorov, Eur. Phys. J. B **18**, 67 (2000).
32. D. Reagor, A. Ahres, S.-W. Migliori, and Z. Fiks, Phys. Rev. Lett. **62**, 2048 (1989).
33. E. Huster, Ann. Phys. (Leipzig) **33**, 477 (1938).
34. S. Freed and N. Sugarman, J. Chem. Phys. **11**, 354 (1943).
35. I. M. Dmitrenko and I. S. Shchetkin, Pis'ma Zh. Éksp. Teor. Fiz. **18**, 497 (1973) [JETP Lett. **18**, 292 (1973)].
36. R. Catteral, Philos. Mag. **22**, 779 (1970).

Translated by Yu. Epifanov

Physics of the Solid State, Vol. 44, No. 2, 2002, pp. 248–254. Translated from Fizika Tverdogo Tela, Vol. 44, No. 2, 2002, pp. 239–245.

SEMICONDUCTORS AND DIELECTRICS

Superbright Photoluminescence of Er^{3+} Ions in Pseudoamorphous GaN Thin Films

A. A. Andreev

Ioffe Physicotechnical Institute, Russian Academy of Sciences, ul. Politekhnicheskaya 26, St. Petersburg, 194021 Russia

Received April 25, 2001; in final form, June 13, 2001

Abstract—High-intensity Er^{3+} photoluminescence at wavelength $\lambda = 1510$–1535 nm and with a quantum yield of up to 10% was revealed under nitrogen laser pumping ($\lambda = 327$ nm) in pseudoamorphous GaN films codoped by Er and oxygen. Because Er^{3+} ions do not have a resonant absorption level at this wavelength, the erbium ions are excited only via inter- and intraband recombination energy transfer. A distinctive feature of the Er^{3+} spectrum is its broadening caused by an appreciable contribution of "hot" transitions from the Stark components of the $^4I_{13/2}$ multiplet. At liquid-nitrogen temperature, this contribution is dominant. At 77 K, an instability of the spectrum in the form of optical noise was observed in the 1550- to 1570-nm region. Temperature quenching of the photoluminescence was virtually absent. The high Er^{3+} photoluminescence intensity was achieved through proper choice of the multistage (cumulative) anneal regime. © *2002 MAIK "Nauka/Interperiodica".*

1. INTRODUCTION

Investigation of Er^{3+} emission in semiconductors at the wavelength $\lambda = 1530$–1540 nm corresponding to the lowest losses in quartz fibers has acquired particular importance in connection with progress made in integrated optoelectronics and, accordingly, with the need to develop emitters that, on the one hand, would operate at an emission line having high temperature stability characteristic of rare-earth-doped solid-state lasers and, on the other, would provide the possibility of controlling the injection currents using radiation, as is the case with semiconductor light-emitting diodes [1, 2]. Despite the considerable progress made in this area over the past 10–15 years, the results obtained thus far do not give one grounds to maintain that a solution to this problem has been reached. Among the problems still unsolved are (i) selection of an optimum ligand environment of the erbium ion, which determines its optical activity; (ii) increasing the dopant ion density until optical gain at small lengths of the active element is reached; (iii) optimization of the excitation transfer mechanism from the semiconductor host to the erbium ion; and (iv) reduction of the various losses, including those caused by temperature quenching.

Until recently, studies of erbium incorporated into semiconductor hosts were carried out primarily on crystalline silicon (*c*-Si), amorphous silicon (*a*-Si), and, to a lesser extent, on III–V compounds of the arsenide–phosphide group. These studies culminated in the very important conclusion that the maximum optical activity of Er^{3+} is reached only in the case where the erbium ion is surrounded by ions with a large electronegativity. The best results were obtained empirically when codoping with oxygen. The necessity of employing an oxygen environment is connected with the fact that optical transitions inside the f^{11} erbium ion shell are dipole forbidden due to the electronic states having the same parity and only become possible when the crystal field of the environment (for instance, of the oxygen ligand, which is only weakly coupled with the *f* electrons) acts through *f*–*d* hybridization to produce Stark splitting of the f^{11} multiplets created by the spin–orbit interaction and, thus, lifts the degeneracy in parity. Group theory shows that a necessary condition for the lifting of parity degeneracy is the crystal field being noncentrosymmetric. Thus, the ligand should meet requirements relating not only to the electronegativity but also to the type of structural symmetry involved. It thus becomes clear that, in order to make erbium ions luminescent, one should dope a semiconductor not with erbium atoms but rather with ErO_x complexes; it is exactly this that is done presently using various technologies, more specifically, ion implantation with an implanted ion ratio Er/O ≈ 1/6–1/10 [1, 3] and molecular beam cosputtering, for instance, of Si and Er_2O_3 [4]. It has also been reliably established that the value of *x* in the ErO_x complex is approximately equal to or slightly less than six [5, 6]. Note, however, that the isolated complex ErO_6 is centrosymmetric and that the inversion symmetry can be broken only through interaction of the oxygen ligand with the host or through reduction of the oxygen coordination ($x < 6$). The need of introducing a large amount of oxygen gives rise to an acute problem of reaching the proper solubility of the ErO_x complexes without, at the same time, initiating defect formation and degrading the semiconducting properties of the host matrix. It has been shown that the Er concentration in *c*-Si cannot be higher than 5×10^{19} cm^{-3}.

1063-7834/02/4402-0248$22.00

For *a*-Si and AlGaAs, the Er density can be made as high as $(1–2) \times 10^{20}$ cm^{-3} [7, 8]. Despite some progress having been made in increasing the erbium solubility in classical semiconductors (Si, GaAs), the critical problem associated with the strong temperature quenching of the Er^{3+} luminescence, which reaches 10 to 100 times in the 77-to-293-K temperature interval [9, 10], remains unsolved. It was earlier established empirically [11] that temperature quenching decreases with increasing band-gap width E_g. For instance, already for *a*-Si : H with $E_g = 1.7$ eV, the quenching decreases by a few (3–5) times, which is a significant factor. For this reason, this work was aimed at studying wider band-gap semiconductors of the A^3N group, primarily gallium nitride with $E_g = 3.45$ eV. GaN and its solid solutions with InN and AlN have been used in recent years to develop injection lasers and light-emitting diodes operating in the high-energy region of the visible range [12]. This opens up new possibilities for the excitation of Er^{3+} through the absorption of photons created in the internal reemission of localized excitons and emitting impurity centers. Even the first experiments performed on doping *c*-GaN and *c*-AlN with Er^{3+} attested to the potential of these materials [13, 14].

This work proposes a new type of host matrix for Er^{3+}, namely, a pseudoamorphous *a-nc*-GaN thin-film material.

2. PREPARATION AND STRUCTURAL CHARACTERIZATION OF *a-nc*-GaN

Pseudoamorphous *a-nc*-GaN was prepared through magnetron reactive cosputtering of a metallic gallium target with small pellets of metallic erbium in an Ar + N_2 gas mixture with calibrated admission of O_2. Although nitrogen is in itself a strong electronegative species and, hence, was expected to form a sufficiently strong ligand field, subsequent experiments showed that the introduction of oxygen (with a flux $\approx 1.0 \times 10^{-2}$ cm^3/min) results in an enhancement of the Er^{3+} luminosity. The films were grown on fused-quartz substrates and polished silicon plates at temperatures of 300 to 480°C. The erbium concentration depended on the area of the erbium pellets, their position in the discharge zone, and the discharge current. The calculated concentration was 5.0×10^{20} cm^{-3}. Our experience, gained in erbium doping of *a*-Si : H and in monitoring the concentration with secondary-ion mass spectrometry, showed the calculational technique developed by us to yield sufficiently accurate results [15]. In some cases, the density of the Er–O bonds was checked experimentally by measuring the absorption associated with the 567-cm^{-1} IR-active vibrational mode, which corresponds to the Er–O bond. The Er–O bond density derived in this way was 5×10^{20} cm^{-3}. The x-ray diffraction pattern obtained by Kartenko (Ioffe Physicotechnical Institute) was an amorphous halo whose position corresponded to GaN. The film structure, however, was not totally amorphous. A high-resolution TEM study of the structure performed at the laboratory of Prof. H.P. Strunk (Erlangen, Germany) [16] clearly showed the film microstructure to be two-phase; namely, the films were amorphous matrices with embedded GaN microcrystallites of hexagonal symmetry 4–7 nm in size. The volume fraction of nanocrystallites in unannealed samples is ≈10%. After annealing at 750°C, the fraction of the nanocrystallites increases to 35% without an increase in their size. The dominant part being played by the amorphous host and the tendency to the formation of nanocrystallites under annealing are supported by the Raman spectra obtained by Davydov *et al.* [17]. The spectra exhibit diffuse phonon density distribution; the pattern is totally identical to the one observed for amorphous GaN produced by breaking up *c*-GaN through ion bombardment. In contrast, the annealed films clearly show an increase in the intensity of the LO(1) phonon mode, which is a measure of GaN crystallinity.

3. PHOTOLUMINESCENCE MEASUREMENT TECHNIQUE. ENERGY LEVELS AND SPECTRA OF Er^{3+} IN *a-nc*-GaN

The photoluminescence (PL) was measured on (i) a quartz prism monochromator equipped with an FEU-79 PM tube for operation in the UV and visible ranges and (ii) an 80×80-mm diffraction grating for the IR range, which operated in the third order and provided a resolution of ≈5 nm for an exit slit 0.4 mm wide. The best match with the input impedance of the low-noise amplifier was obtained using an InGaAs-based *pn* photodiode (sensitivity 25 μV/mW) as a radiation detector (provided by Karlina, Ioffe Physicotechnical Institute). The radiation source was an LGI-21 pulsed nitrogen laser ($\lambda = 327$ nm) producing 10-ns-long pulses with an average power of 3 mW. The laser radiation was passed through a set of color filters to suppress the concomitant narrow-line molecular-nitrogen spectrum. The amplification unit included a pulsed phase detector and a gated PL-response pulse measurement circuit with variable delay time, which provided the possibility of determining the excited-state lifetime, of isolating long-lived modes against the continuum background, and of obtaining time-resolved spectra. Figure 1 presents emission spectra of the trivalent erbium ion (Er^{3+}) in samples subjected to thermal annealing and possessing the highest brightness. The energy level diagram of the Er^{3+} ion is given in the inset on the right. The nitrogen laser (3.68 eV) excites electrons from the valence band to the conduction band. After thermalization to the band edge (3.4 eV), the energy of electrons is absorbed by localized excitons, forming a broad tail near the band edge, and is reemitted in the hard-blue region of the visible range. This reemission effect is enhanced by the Ce impurity, whose PL forms a broad maximum peaking at 2.8–2.7 eV and decaying at 2.4 eV. Thus, the upper levels $^4F_{7/2}$, $^4F_{5/2}$, $^4F_{3/2}$, and $^2H_{11/2}$ of the f^{11} elec-

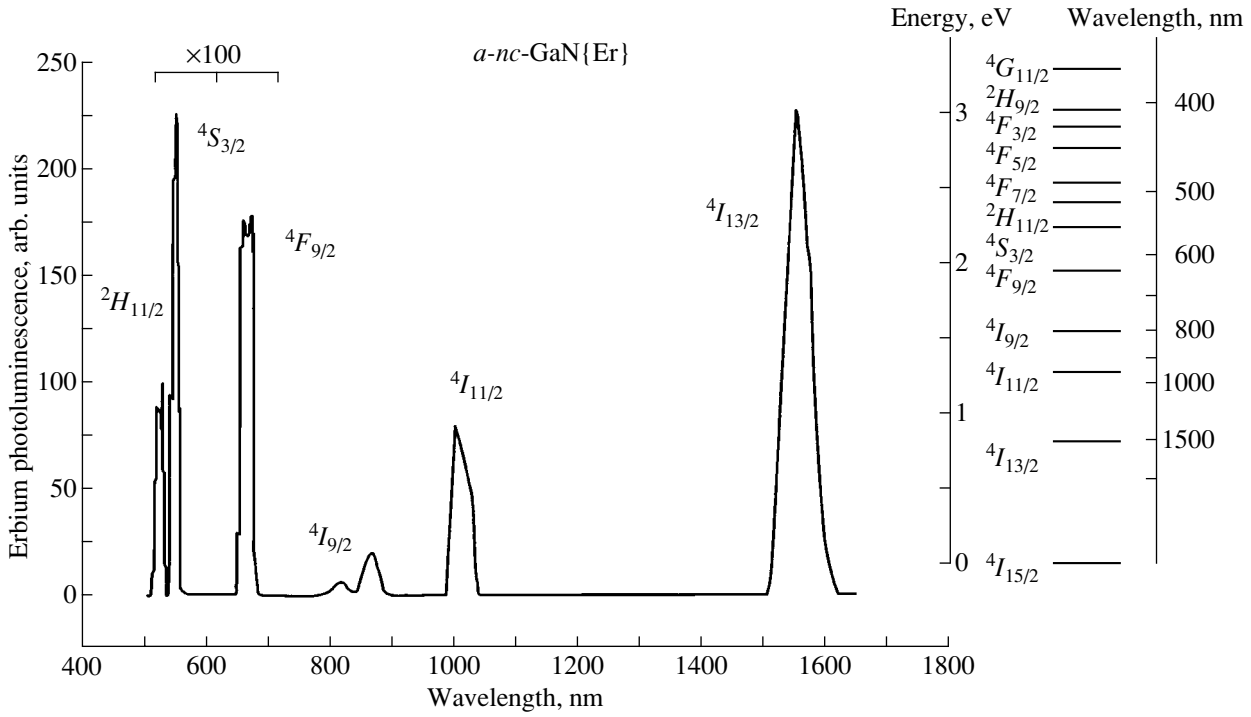

Fig. 1. Photoluminescence of Er^{3+} ions in *a-nc*-GaN within a broad wavelength range. The inset on the right shows the Er^{3+} f^{11}-shell multiplet without Stark splitting. The strongest peak (λ = 1535 nm) corresponds to the $^4I_{13/2} \longrightarrow {}^4I_{15/2}$ transition.

tron shell of the erbium ion fall in the energy range of intense photon pumping. The fact that the external quantum yield of the blue PL always decays in the course of erbium optical activation may serve as an argument for the internal reemission contributing to the excitation of erbium ions. It is appropriate to note here that the mechanism of direct optical excitation of erbium ions is not the only one operative in gallium nitride; this problem will be discussed later. The Er^{3+} multiplet radiation is reliably observed only at energies <2.5 eV, which correspond to the $^4S_{3/2}$ and lower states, and the transition intensity in the IR exceeds by approximately one-hundredfold the intensity of transitions $^4S_{3/2} \longrightarrow {}^4I_{15/2}$ in the green region. This latter observation gives one grounds to believe that the anti-Stokes luminescence originating from cooperative excitation may also contribute to the green radiation. Two $^4I_{11/2} \longrightarrow {}^4I_{15/2}$ quanta approximately correspond to the energy of the $^4S_{3/2} \longrightarrow {}^4I_{15/2}$ transition and can initiate it [10].

4. THERMAL ANNEALING AND OPTICAL ACTIVATION OF Er^{3+} TRANSITIONS

The 1535-nm emission measured immediately after film preparation was extremely weak, particularly in samples with $T_s \approx 300$°C. To optically activate erbium, we annealed the films thermally in consecutive 20-min cycles, with the anneal temperature in each cycle being higher by 25°C than that in the preceding one. The technique employed was that developed earlier in [15], but the anneal temperature range chosen was from 650 to 750°C. Annealing resulted in a substantial enhancement of the Er^{3+} PL intensity. This was accompanied by qualitative changes in the PL kinetics; namely, the rapidly decaying luminescence with a lifetime $\tau \approx 50$–100 μs was transformed into PL characterized by a bell-shaped curve with a rise time of up to 200 μs and a tail extending to ≈600 μs. Thus, the maximum τ_{p1}, which also corresponded to the maximum PL intensity, was ≈800–900 μs. An attempt to increase the number of anneal cycles, even without increasing the maximum temperature, brought about a decrease in the PL intensity, which followed a fairly abrupt pattern in some cases. The tendency to lose optical activity was more clearly pronounced in samples prepared at a higher T_s. The above process of optical activation of erbium can be connected only with the formation of a structurally optimal oxygen environment around the erbium ion. Obviously enough, this process is associated with the diffusion of oxygen and, possibly, of erbium and requires not only thermal activation but also a long period of time, during which the erbium complexes form and become stabilized and, apparently, find their place in the GaN structural network. The ErO_x-complex formation will be facilitated if atoms in the host undergo collective displacements of some kind under certain conditions, for instance, after an appropriate

temperature has been reached. In GaN, such a process can be expected to occur at temperatures from 650 to 700°C, because it is in this range that one observes partial dissociation of the compound accompanied by intense generation of nitrogen vacancies [12]. Obviously enough, the presence of vacancies in the nitrogen subsystem favors oxygen diffusion and, thus, rearrangement of the local structure around the erbium ions. Because Er is an extremely strong oxygen getter, the rearrangement of the local structure obviously involves its replacement by an oxygen environment. However, there is another factor which may favor the formation of an oxygen ligand. At temperatures from 650 to 750°C, the nucleation and growth of nanocrystallites are intensified, which is indicated in the electron microscopy data presented earlier. The role played by nanocrystallites in the activation of erbium ions remains unclear, but it may be conjectured that crystallite growth can be conducive to the formation of ErO_x complexes, for instance, at grain boundaries, which are known to act as sinks for oxygen and possess a certain freedom for chemical bonds. To fully understand the erbium activation process, it is also important to learn the reason for the abrupt loss of optical activity of Er^{3+} resulting from "overannealing." The presence of a critical stage in the activation process means that thermal annealing should not lead to its terminal stage. The terminal stage apparently corresponds to fully completed thermodynamic stabilization or to the formation of a chemically saturated ligand made up of six oxygen atoms. If, in order to reach the maximum PL, the annealing has to be stopped in an uncompleted stage, then the configuration of six oxygen atoms is apparently not optimal; therefore, in order to obtain the maximum optical response, the ligand must be partially incomplete and contain not six but, possibly, five oxygen atoms. Certain experimental evidence in support of this conclusion is presented in [6]. The ligand structure with an oxygen vacancy may be preferable for two reasons. The first of them is that an uncompleted complex has a broken symmetry, thus resulting in a loss of the center of inversion, and this, as pointed out before, is the necessary requirement imposed on the ligand. The second reason may be that a chemically unsaturated ErO_{6-z} complex interacts more strongly with the host, and this chemical coupling with the host acts as a bridge to transfer excitation energy from the matrix to the erbium ion. Such a coupling is called a bound defect in the literature [10]. In such a wide-band-gap material as GaN, a bound defect is capable of transferring the excitation energy from localized excitons in the conduction-band tail to Er^{3+}. An energy transfer effected in this way will be nonresonant. This nonresonant energy-transfer mechanism, combined with direct optical excitation via absorption of the host-emitted photons by the Er^{3+} resonant levels, accounts for the experimentally observed PL excitation function, which, while being basically monotonic, contains sharp resonant peaks [18].

5. PHOTOLUMINESCENCE OF Er^{3+} IONS AT λ = 1535 nm

By properly varying the technological parameters, both in the course of film deposition and under thermal annealing, we prepared a set of *a-nc*-GaN samples with different erbium-ion luminosities. Samples with high and maximum luminescence intensities appear to be the most interesting of this set. The other samples are of no importance. It should be stressed that there are no accepted standards for the Er^{3+} luminescence brightness. In this connection, we assume here that a high intensity corresponds to a level which is slightly above the mean statistical intensity quoted in the available publications. This level can be most simply defined in terms of its signal/noise ratio and was chosen to be 10^2. This parameter was estimated taking into account many additional factors, including the beam power and wavelength, the collecting power and resolution of the optical instrumentation, etc. The validity of this estimate was also checked using test measurements made on our samples and reference samples prepared by other researchers (including foreign groups) on other experimental setups.

Figure 2 presents reduced Er^{3+} spectra of samples with high (curve *1*) and maximum (curve *2*) brightness levels. The spectrum of the first sample has only one

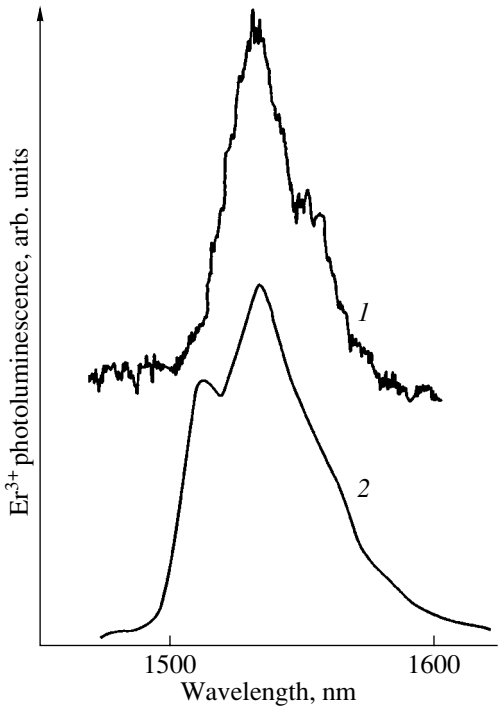

Fig. 2. Reduced room-temperature spectra of the $^4I_{13/2} \longrightarrow {}^4I_{15/2}$ transition of the Er^{3+} ion obtained on two *a-nc*-GaN samples with (*1*) a high and (*2*) the maximum brightness. The true brightness ratio of samples *1* and *2* is larger than 1 : 30.

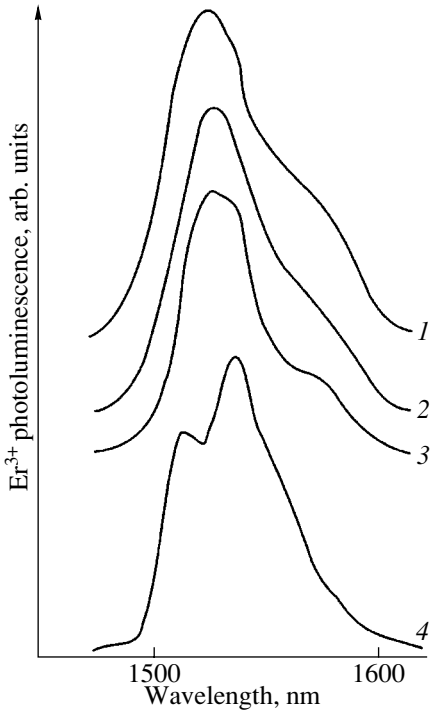

Fig. 3. Emission spectra of the $^4I_{13/2} \longrightarrow {}^4I_{15/2}$ transition of the Er^{3+} ion obtained (*1–3*) at 77 and (*4*) at 300 K on the maximum-brightness *a-nc*-GaN sample.

peak at $\lambda = 1535$ nm and an FWHM of 35 nm. This is a standard value for nonresonant excitation (327 nm). The sample with the maximum brightness exhibits two peaks, which are nearly equal in amplitude and correspond to $\lambda = 1510$ and 1535 nm. One may also observe a plateau-type curve with a flat or sloped top. The width of such a spectrum at half maximum is as large as 60 nm. The PL intensity ratio of the bright and superbright samples can be in the limit of 1 : 30. The enhancement in brightness is also accompanied by a change in the temperature dependence of the spectrum. The spectra of bright samples do not exhibit any noticeable changes under cooling to 77 K. Figure 3 presents spectra of superbright samples obtained at 77 K (curves *1–3*) and room temperature (curve *4*). All the spectra were measured at the same amplification. The approximate equality of the PL amplitudes implies that there is virtually no temperature quenching in the *a-nc*-GaN host. A comparison of the spectra taken at 77 and 300 K clearly shows that, at low temperatures, the spectral component corresponding to the 1510- to 1520-nm line becomes dominant. The presence in the Er^{3+} spectrum of such hot lines, i.e., of lines with photon energies higher than that of the main peak at 1535 nm, is not in itself a new observation. Hot lines were observed earlier as well [10, 18, 19]. However, we were the first to observe these lines with an amplitude comparable or even in excess of that of the main peak at 1535 nm. This peak corresponds to the transition from the ground (lowest) state of the $^4I_{13/2}$ multiplet to the ground (lowest) state of the $^4I_{15/2}$ multiplet. Radiation with a photon energy above the ground state of the $^4I_{13/2}$ multiplet can be connected either with transitions from the Stark-split states of the multiplet to the ground state of the $^4I_{15/2}$ multiplet or with the Er^{3+} ion being capable of occupying nonequivalent positions in the host. In the latter case, different configurations of the ligand and, accordingly, of the crystal field coexist. If the crystal field strength at different Er^{3+} sites differs strongly, one may expect local changes in the position of the lower state in the $^4I_{13/2}$ multiplet; this is what may bring about the multilevel pattern of the spectrum. The 1535 $\longrightarrow$ 1510-nm shift observed in this work is fairly large, and this indicates not some distortion of the ligand but rather a radical change in its configuration. Information available on the Stark splitting structure of the Er^{3+} multiplets [20] for erbium-doped oxides suggests that the lowest $^4I_{13/2}$ state can produce radiation with $\lambda \approx$ 1510 nm in a crystal field of O_h symmetry (rare-earth garnets). The garnet unit-cell structure is, however, too complex: it contains up to eight formula units; therefore, it is hard to conceive the arrangement of such bulky atomic formations, the more so, with there being high density already in the amorphous host. The presence of such structurally foreign inclusions would undoubtedly have been revealed by microstructural analysis. In this connection, the hypothesis of nonequivalent positions should be relegated to second place. We will discuss subsequently only the model that assumes hot transitions from the upper Stark levels of the $^4I_{13/2}$ multiplet.

In the section dealing with thermal annealing and erbium-ion optical activation, we considered the process of formation of an oxygen ligand around the erbium ion. The two following points should be stressed in connection with the ensuing discussion. (i) The ligand field in an oxygen-doped host is created by oxygen atoms. As a result, the erbium ion forms an ErO_{6-z} complex, with $z \approx 0$–1. (ii) If the local chemical composition in an amorphous host changes, its short-range order structure also changes because of the structural lability of the host, i.e., of there being no rigid constraints on the formation of a given short-range order. Therefore, the local structure of the ErO_{6-z} complex is determined primarily by the Er–O chemical bonds, whose thermodynamic energetics is higher than that of the other bonds that couple Er with the other components of the structural network of the amorphous gallium nitride host. As a result, the amorphous GaN host is, in first approximation, no more than a reservoir (a term taken from [5]) for the ErO_{6-z} complexes and only in the second approximation does the host act indirectly, via the oxygen bonds, on the local ligand field structure. This opens up a path to more labile structural self-organization of the erbium–oxygen complex. Only experimental investigation of the Stark spectra of spe-

cific hosts can apparently decide which ligand field symmetry is preferable in the given conditions. The weakly structured Stark spectra observed for high-brightness samples in the present work do not contain adequate information to warrant unambiguous conclusions to be made concerning the local symmetry of the erbium center. For this reason, we can venture here only tentative considerations. In accordance with [13], the erbium ion in III–V compounds lacks inversion symmetry and, hence, acquires optical activity if (i) it occupies positions on the cation sublattice, as well as at interstitial sites, and has T_d symmetry or (ii) if the erbium ion is interstitial and has C_{3v} symmetry. Because we did not have Stark spectra of amorphous hosts at our disposal, we carried out a comparative analysis of such spectra for the erbium-doped oxides in which Er^{3+} has different point symmetries [20–22]. It appears remarkable that the 1510-nm hot line combined with the 1532–1537 nm main transition was observed only for the C_{3v} erbium-center local symmetry [21]. While this still does not imply that this symmetry is realized in the amorphous GaN host, it does, nevertheless, suggest a promising direction for further studies.

Even though our arguments do not appear to be sufficiently convincing, we shall accept the Stark-based interpretation of the PL spectra of high-brightness samples. In this case, one has to explain the high intensity of the hot lines. The high hot-line intensity, which may even dominate over the main transition, is due to the approximately equal probabilities of photon emission from the state higher in energy and the lowest state of the multiplet; in other words, it is due to the excitation lifetimes being comparable for the higher and the lowest states of the multiplet. A study of the variation of the Er^{3+} emission spectrum with time within the time interval of radiation decay supports this conclusion. Figure 4 displays two spectra obtained with 50-μs-long gates delayed by 0 and 500 μs, respectively. While the relative hot-transition contribution to the total radiation is clearly seen to decrease as the $^4I_{13/2}$ multiplet is depleted, the λ = 1510-nm radiation does not disappear completely. It thus follows that the transition probability from the lowest $^4I_{13/2}$ state is indeed only insignificantly smaller than that from the nearest Stark levels. One cannot exclude the possibility that this situation is a consequence of the high density of the Er^{3+} ions.

The high Er^{3+} density can lead to aggregation of the ErO_{6-z} complexes. The coupling of the electronic *f* shells of Er^{3+} ions within such an aggregate may quite probably become manifest. This interaction creates new electronic configurations of the type of quantum dots, whose properties in this variant are totally unknown. It is clear, though, that the state-filling statistics in such a formation can change and that this will make the higher states more active, particularly under the high pulse pumping densities produced by an LGI-21 laser (1.6 kW). That this density is indeed high is supported by the generation of optical noise at liquid-nitrogen temperatures, which could be a forerunner of superluminescence. Figure 5 illustrates spectra containing optical noise. The noise region extends over the 1560- to 1570-nm wavelength range. Curve *2* even shows that the increase in noise intensity terminates in sharpening of the line. Instability of the spectrum is

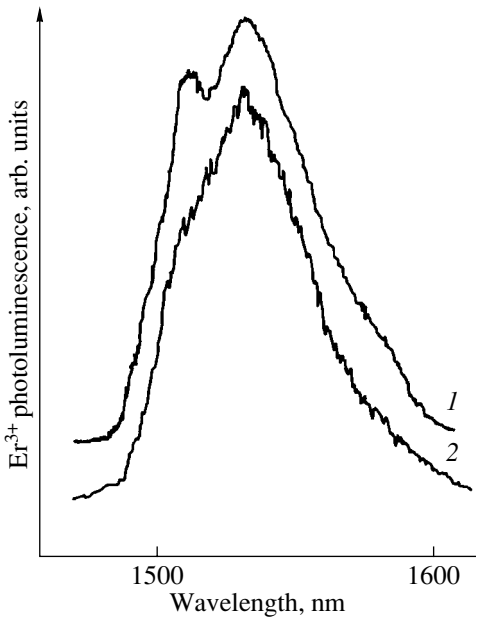

Fig. 4. Variation in the emission spectrum of the Er^{3+} ion in the *a-nc*-GaN host with time: (*1*) spectrum obtained with zero delay after the excitation pulse and (*2*) emission spectrum taken after 500 μs.

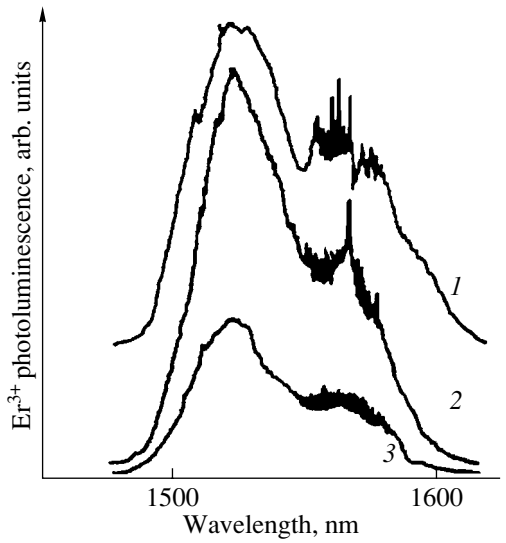

Fig. 5. Instability of the Er^{3+} emission spectrum and optical-noise generation (1550–1570 nm) in maximum-brightness samples. (*1–3*) Different spectrum measurements.

always observed to occur within a fixed wavelength range. If the radiation instability is indeed connected with a manifestation of spontaneous optical amplification, this means that the density of optically active erbium ions, at any rate in local regions, approaches the level at which partial self-synchronization of radiation becomes possible.

It does not appear possible at present to estimate experimentally the absolute magnitude of the quantum yield of samples with the maximum brightness, because the PL spatial distribution has not been studied. Nevertheless, an idea of the emission efficiency can be gained from the following parameters. The absolute time-averaged PL power reaching the power-calibrated photodetector within a 35° solid angle normal to the sample surface was 2.0 μW at a continuous equivalent radiation power of 1.5 mW with optical channel losses of 10 dB.

ACKNOWLEDGMENTS

The author is indebted to I.V. Korkin for development of the technological and measuring equipment.

REFERENCES

1. Y. H. Xie, E. A. Fitzgerald, and Y. J. Mii, J. Appl. Phys. **70** (6), 3223 (1991).
2. S. Coffa, G. Franzo, and F. Priolo, MRS Bull., 25 (1998).
3. A. Reittinger, J. Stimmer, and G. Abstreiter, Appl. Phys. Lett. **70** (18), 2431 (1997).
4. W.-X. Ni, K. B. Joelsson, C.-X. Du, *et al.*, Appl. Phys. Lett. **70** (25), 3383 (1997).
5. D. L. Adler, D. C. Jacobson, D. J. Eaglesham, *et al.*, Appl. Phys. Lett. **61** (18), 2181 (1992).
6. A. Terrasi, G. Franzo, S. Coffa, *et al.*, Appl. Phys. Lett. **70** (13), 1712 (1997).
7. M. S. Bresler, O. B. Gusev, V. Kh. Kudoyarova, *et al.*, Appl. Phys. Lett. **67** (24), 3599 (1995).
8. L. Kou, D. C. Hall, and H. Wu, Appl. Phys. Lett. **72** (26), 3411 (1998).
9. H. Ennen, J. Schneider, G. Pomrenke, and A. Axmann, Appl. Phys. Lett. **43** (10), 943 (1983).
10. A. Polman, J. Appl. Phys. **82** (1), 1 (1997).
11. P. N. Favennec, H. L. Harldon, D. Moutonnet, *et al.*, Mater. Res. Soc. Symp. Proc. **301**, 181 (1993).
12. S. Nakamura and G. Fasol, *The Blue Laser Diode (GaN Based Light Emitters and Lasers)* (Springer, Berlin, 1997), p. 129.
13. R. G. Wilson, R. N. Schwartz, C. R. Abernathy, *et al.*, Appl. Phys. Lett. **65** (8), 992 (1994).
14. D. M. Hansen, R. Zhang, N. R. Perkins, *et al.*, Appl. Phys. Lett. **72** (10), 1244 (1998).
15. A. A. Andreev, V. B. Voronkov, V. G. Golubev, *et al.*, Fiz. Tekh. Poluprovodn. (St. Petersburg) **33** (1), 106 (1999) [Semiconductors **33**, 93 (1999)].
16. S. B. Aldabergenova, M. Albrecht, A. A. Andreev, *et al.*, J. Non-Cryst. Solids **283** (1–3), 173 (2001).
17. V. Yu. Davydov, Yu. E. Kitaev, J. N. Goncharuk, *et al.*, J. Cryst. Growth **189/190**, 656 (1998).
18. Myo Thaik, U. Hommerich, R. N. Schwartz, *et al.*, Appl. Phys. Lett. **71** (18), 2641 (1997).
19. A. A. Andreev, V. G. Golubev, V. F. Masterov, *et al.*, Pis'ma Zh. Éksp. Teor. Fiz. **70** (12), 780 (1999) [JETP Lett. **70**, 797 (1999)].
20. A. A. Kaminskiĭ, *Laser Crystals* (Nauka, Moscow, 1975), p. 108.
21. V. T. Gabrieljan, A. A. Kaminskii, and L. Li, Phys. Status Solidi A **3**, K37 (1970).
22. J. B. Gruber, J. R. Henderson, M. Muramoto, *et al.*, J. Chem. Phys. **45**, 477 (1966).

Translated by G. Skrebtsov

Physics of the Solid State, Vol. 44, No. 2, 2002, pp. 255–259. Translated from Fizika Tverdogo Tela, Vol. 44, No. 2, 2002, pp. 246–250.

SEMICONDUCTORS AND DIELECTRICS

Electrical, Optical, and Photoelectric Properties of Electron-Irradiated Indium-Doped Cadmium Sulfide Single Crystals

G. E. Davidyuk*, V. A. Oksyuta*, and V. S. Manzhara**

** Volyn State University, pr. Voli 13, Lutsk, 44009 Ukraine*

e-mail: viktor@lab.univer.lutsk.ua

*** Institute of Physics, National Academy of Sciences, pr. Nauki 46, Kiev, 04050 Ukraine*

Received January 26, 2001; in final form, June 28, 2001

Abstract—The effect of irradiation by 1.2-MeV electrons to a dose $\Phi = 2 \times 10^{17}$ cm^{-2} on the electrical, optical, and photoelectric properties of In-doped CdS single crystals was studied. The experimental data obtained permit one to conclude that irradiation initiates decomposition of the supersaturated In solution in CdS, with the indium atoms at the sites of the cation sublattice being expelled by cadmium interstitial atoms. New slow-recombination centers were observed to exist in the irradiated CdS : In samples, with the maxima of optical quenching of the photoconductivity lying in the region of $\lambda_{M_1} = 0.75$ μm and $\lambda_{M_2} = 1.03$ μm. It is suggested that the new recombination centers are related to complexes containing cadmium vacancies and indium atoms.

1. INTRODUCTION

This paper reports on a study of the effect of electron irradiation on some electrical, photoelectric, and optical properties of indium-doped CdS single crystals. Published data on the mechanisms of defect formation in CdS compounds doped by Group-III elements are scarce.

The crystals to be studied were grown at the Institute of Single Crystals (Kharkov) from a melt of purified CdS powder in an inert-gas environment at a pressure of 1.86×10^7 Pa. The crystals were doped with indium during growth. Analysis showed the indium concentration in different samples to be $N_{\text{In}} \approx 10^{18}$ and $\approx 10^{19}$ cm^{-3}. The samples were irradiated by 1.2-MeV electrons (to a dose $\Phi = 2 \times 10^{17}$ cm^{-2}) on a linear accelerator. During the irradiation, the crystals were cooled by liquid-nitrogen vapor, such that their temperature did not rise above 290 K.

2. EXPERIMENTAL RESULTS

A feature specific to CdS : In single crystals is the existence of impurity maxima at $\lambda_M = 524$ nm, which disappear with decreasing temperature, in absorption and photoconductivity (PC) spectra taken at room temperature (curves *1*, *2*, peak I in Fig. 1). The displacement of the intrinsic photoconductivity peak II (Fig. 1) to shorter wavelengths with decreasing temperature agrees well with the increase in the band gap width E_g of single-crystal CdS under cooling.

Irradiation of CdS : In by electrons brings about the disappearance of impurity maxima in the absorption and PC spectra at $\lambda_M = 524$ nm. Moreover, the photosensitivity increases in the region of intrinsic photoconductivity (peak II) and decreases for $\lambda > 530$ nm (Fig. 1). It should also be pointed out that electron irradiation of doped samples results in a decrease in their

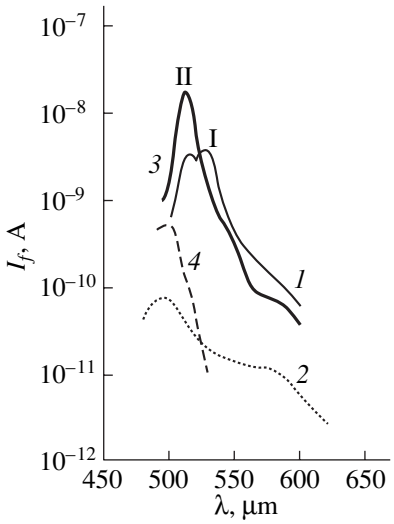

Fig. 1. Spectral response of the photoconductivity of CdS : In single crystals ($N_{\text{In}} = 10^{18}$ cm^{-3}) (*1*, *2*) unirradiated and (*3*, *4*) irradiated by electrons ($\Phi = 2 \times 10^{17}$ cm^{-2}) (*1*, *3*) at 290 and (*2*, *4*) 80 K.

1063-7834/02/4402-0255$22.00 © 2002 MAIK "Nauka/Interperiodica"

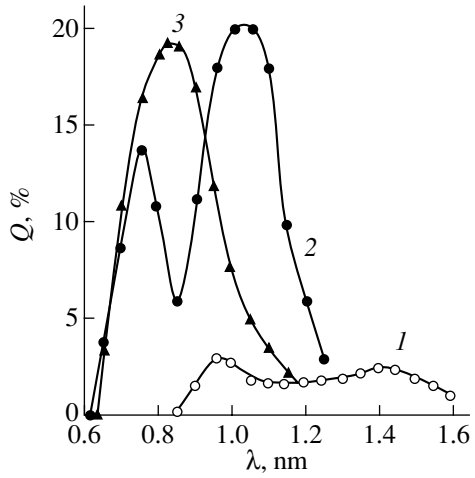

Fig. 2. Spectral response of the optical quenching of the photoconductivity of CdS : In single crystals ($N_{In} = 10^{18}$ cm^{-3}) (*1*) before irradiation and (*2*, *3*) after electron irradiation ($\Phi = 2 \times 10^{17}$ cm^{-2}) (*1*, *2*) at $T = 290$ and (*3*) 80 K.

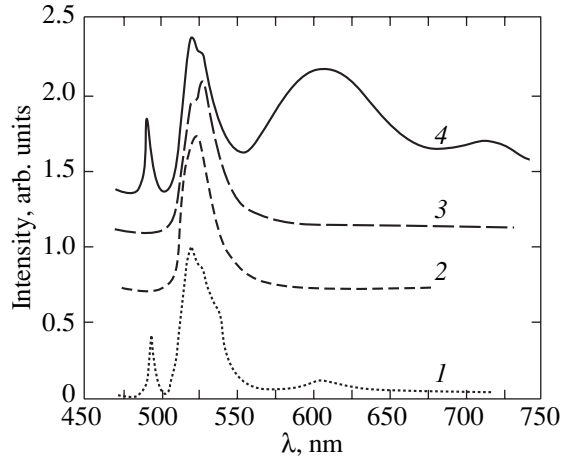

Fig. 3. Photoluminescence spectra of CdS (*1*) and CdS : In single crystals with In concentrations of (*2*) 10^{18} and (*3*, *4*) 10^{19} cm^{-3} measured at $T = 77$ K (*1*–*3*) before irradiation and (*4*) after electron irradiation to $\Phi = 2 \times 10^{17}$ cm^{-2}.

conductivity in the dark, while irradiation of undoped crystals gives rise to its decrease.

Before irradiation, the CdS : In samples under study exhibited a slight (up to 5%) optical quenching of photoconductivity (OPQ), well known from literature, with maxima at $\lambda_{M_1} = 0.9$–0.95 μm and $\lambda_{M_2} = 1.4$ μm (the latter disappears with decreasing temperature), which originate from centers associated with cadmium vacancies (V_{Cd}) in the ground and excited states [1, 2] (curve *1* in Fig. 2).

After irradiation, the OPQ spectral response changes radically (curves *2*, *3* in Fig. 2). First, the OPQ maxima grow in amplitude (by a factor of about five) and change position on the spectral curve. The new OPQ bands peak at $\lambda_{M_1} \approx 0.75$ μm and $\lambda_{M_2} \approx 1.03$ μm. The band peaking at $\lambda_{M_2} = 1.03$ μm disappears with decreasing temperature.

Irradiation of undoped CdS samples under the same conditions does not affect the position of the OPQ maxima at $\lambda_{M_1} = 0.9$ μm and $\lambda_{M_2} = 1.4$ μm, with only their amplitude increasing slightly (about twofold).

We recorded photoluminescence (PL) spectra not only of doped samples but also of undoped single crystals grown under the same conditions as CdS : In. The luminescence was excited by UV radiation ($\lambda = 365$ nm) from a DRSh mercury lamp on as-cleaved crystal surfaces.

At room temperature, a structureless green luminescence band (*G*-luminescence) was dominant in the spectra of both undoped and doped crystals. The band of undoped samples peaked at a wavelength $\lambda = 510$ nm. Introducing an In impurity broadens the emission band and reduces its intensity. Note that the position of the *G*-luminescence maximum in doped samples depends on the impurity concentration. As the In concentration increases, the emission maximum shifts toward short wavelengths to reach $\lambda_G = 500$ nm at $N_{In} = 10^{19}$ cm^{-3} (with its half-width increasing approximately twofold). At liquid-nitrogen temperature, the positions of the *G*-band maxima of both undoped and doped crystals almost coincide (irrespective of the actual impurity concentration).

Figure 3 presents PL spectra of the samples obtained at 77 K. The undoped crystals exhibited intense exciton emission bands (at $\lambda_M = 480$ nm) and *G* luminescence with well-pronounced phonon replicas (with the first zero-phonon maximum located at $\lambda_M \approx 514$ nm, curve *1*). The orange luminescence (*O* luminescence) at $\lambda_M = 604$ nm was weak. The intensity of the other emission bands was at the sensitivity limit of the detectors used. The doped samples ($N_{In} \approx 10^{18}$ cm^{-3}) revealed only a diffuse structureless *G*-luminescence band at $\lambda_M = 514$ nm (curve *2* in Fig. 3). As the In dopant concentration was increased to $N_{In} \approx 10^{19}$ cm^{-3}, an emission peak, which was absent at room temperature, appeared at $\lambda_M \approx 524$ nm (curve *3* in Fig. 3) against the background of a diffuse *G*-luminescence band.

After irradiation, the PL spectra of the doped samples acquire features characteristic of undoped CdS but with a different intensity distribution (curve *4* in Fig. 3). At room temperature, the *G*-luminescence band of the irradiated CdS : In crystals coincides in half-width and position with that of the undoped crystals. At liquid-nitrogen temperature, the *O* luminescence is seen to appear in the spectra of the irradiated CdS : In samples at $\lambda_M \approx 603$–604 nm; the *G*-luminescence band assumes the structure characteristic of undoped crys-

tals, with the first maximum lying at $\lambda_M \approx 514$ nm; and an exciton luminescence band (which was absent before irradiation) forms at $\lambda_M \approx 480$ nm. In strongly doped crystals, the PL band at $\lambda_M \approx 524$ nm disappears (curve *4* in Fig. 3). Note that, after irradiation, the emission intensity increases, with the intensity of the *G* luminescence in CdS : In becoming practically equal to that in CdS. In the IR region, a new and weak luminescence band appears in CdS : In at $\lambda_M \approx 1.2$ μm, which is not seen in the undoped samples, as well as in doped samples before irradiation.

3. DISCUSSION OF EXPERIMENTAL RESULTS

It is known [3] that In doped into a CdS single crystal enters the lattice as an impurity substituting for Cd on the cation sublattice to form shallow donor centers In_{Cd}. It is these centers that are apparently responsible for the additional extrinsic maxima in absorption and photoconductivity ($\lambda_M \approx 524$ nm) observed at room temperature in the CdS : In single crystals (peak I in Fig. 1). These maxima are due to photoexcitation of electrons from the valence band to the In_{Cd} donor centers, which are empty at room temperature, with subsequent thermal ionization to the conduction band. Two-step transitions of such kind are frequently observed in II–VI wide-band-gap semiconductors.

The ionization energy of the In_{Cd} center estimated by us from the position of the impurity maxima was found to be $E = (E_c - 0.06 \pm 0.02)$ eV, which is in agreement with the energy position of the In_{Cd} donor determined by other authors [1, 3]. As the temperature is lowered, electrons fill the donor centers and the probability of their thermal ionization to the conduction band decreases, as a result of which the impurity-absorption and photoconductivity peaks disappear. This gives rise to the formation of an additional PL band at $\lambda_M \approx 524$ nm (curve *3* in Fig. 3). It can apparently originate from the recombination of electrons (which occupy the In_{Cd} donor centers filled at low temperatures) with the valence-band holes. That the In_{Cd} donors are indeed responsible for the PL at $\lambda_M \approx 524$ nm is supported by the increase in intensity of this luminescence band with increasing In dopant concentration in CdS samples. Centers with such PL bands were also observed in CdS crystals doped by other impurities [2], which form shallow levels in the crystal band gap.

The reduced emission intensity, the absence of phonon replicas and the broadening of the dominant *G*-luminescence band, the shift of its maximum to shorter wavelengths (at room temperature), and the absence of exciton luminescence spectra (curves *2*, *3* in Fig. 3) indicate a high defect concentration in the doped samples, particularly at high dopant concentrations ($N_{In} = 10^{19}$ cm^{-3}).

The unit-cell parameters of CdS and CdS : In (determined with an HZG-4A x-ray diffractometer) are given in the table (shown in parentheses are data on the purest and structurally perfect CdS single crystals taken from [13]).

Unit-cell parameters of CdS and CdS : In single crystals ($N_{In} \approx 10^{19}$ cm^{-3})

CdS		CdS : n			
		before irradiation		after irradiation, $\Phi = 2 \times 10^{17}$ cm^{-2}	
a, Å	*c*, Å	*a*, Å	*c*, Å	*a*, Å	*c*, Å
4.1351 (4.1369)	6.7130 (6.7157)	4.1320	6.7100	4.1340	6.7125

As follows from the table, there is a slight difference between the cell parameters of the doped and undoped samples before irradiation, which decreases after irradiation of the doped samples. This argues for there being an improvement in the structure of doped samples in the course of irradiation.

It is known that the *G*-luminescence band at $\lambda_M \approx 514$ nm (at 77 K) originates from acceptors, which in this case are interstitial sulfur atoms (S_i) [4, 5]. The radiation is generated in the recombination of free electrons with holes trapped by S_i acceptors. The shift of the maximum in the *G*-luminescence band by 10 nm toward shorter wavelengths (compared to the undoped crystal) and the broadening of the luminescence band, which are observed at room temperature in CdS : In, can be assigned to a screening effect produced on the luminescence centers by the charged donors, which are In_{Cd} centers at high temperatures. Such phenomena are well known to occur in wide-band-gap crystal phosphors with high concentrations of dopants (or defects) [6, 7]. The gradual suppression of the screening effect on the S_i acceptors caused by the In_{Cd} donor centers, which become filled by electrons as the temperature is decreased, brings about a practical coincidence between the *G*-luminescence maxima of the doped and undoped crystals at 77 K (Fig. 3).

The mechanisms governing the interaction of native radiation defects with dopants have been most fully studied for silicon. It has been shown, in particular, that interstitial silicon atoms can interact with Group-III impurities differently, depending on the ratio of the atomic radii of the impurity (r_{imp}) and silicon atoms (r_{Si}) [8]. For $r_{imp} > r_{Si}$, the impurity atom is expelled from the lattice site by interstitial silicon. For $r_{imp} < r_{Si}$, there is no expulsion. For indium and cadmium atoms, we have $r_{In} > r_{Cd}$ [9]. If the mechanism operative in silicon is also realized in binary semiconductors, then one may expect part of the interstitial cadmium atoms (Cd_i) formed in the irradiation to substitute for In atoms occupying regular lattice sites, thus reducing the concentration of the In_{Cd} donor centers. The interstitial indium atoms (In_i) created in this process can interact

with other radiation-induced defects or escape through radiation-stimulated diffusion to various sinks (dislocations, twin boundaries, surface, and so on), which are always present in II–VI semiconductors. This conjecture provides a reasonable explanation for the disappearance of the extrinsic-absorption and photoconductivity maxima at $\lambda_M = 524$ nm and of the low-temperature PL band at $\lambda_M = 524$ nm in irradiated Cd : In single crystals. Because of the reduced probability of recombination of V_{Cd} with the Cd_i interstitials, which, after expelling In atoms out of the lattice sites, occupy their positions on the cadmium sublattice of the crystal, the concentration of the complexes associated with V_{Cd} is increased.

An improvement in the lattice structure in irradiated Cd : In single crystals (table) can apparently account for the appearance of exciton luminescence in these samples, the decrease in the emission line width, and for the *G* luminescence acquiring the characteristic properties of the corresponding band in undoped samples. The increase in the PL intensity and intrinsic photosensitivity in irradiated single crystals is explained, on the one hand, by the increase in the concentration of the slow recombination centers containing V_{Cd} (which is indicated by the increase in the OPQ intensity) and, on the other, by the decrease in the concentration of the centers responsible for the fast nonradiative recombination channel, which are known to be associated with lattice defects [10].

The improvement in the structure of doped samples produced by irradiation can be understood if we take into account that the solution of the In dopant in CdS (particularly at high concentrations $N_{In} = 10^{18}$–10^{19} cm^{-3}) can exist at room temperature in a supersaturated, metastable state; however, its decomposition is constrained by the limited diffusion rate of In atoms. By enhancing the diffusion of In atoms (through radiation-stimulated mechanisms), irradiation initiates decomposition of the supersaturated solution and removal of excess In atoms to various sinks and to the surface, thus purifying the bulk of the sample. There are reported observations of supersaturated solutions of Al and of other atoms in silicon whose decomposition can be initiated by carrier injection, which accelerates atomic diffusion [11].

In undoped crystals and CdS : In samples before irradiation, the V_{Cd} vacancies play the role of slow recombination centers (*r* centers), with quenching maxima in the region of $\lambda_{M_1} = 0.95$ μm and $\lambda_{M_2} = 1.4$ μm [1, 2]. Irradiation changes the nature of the slow recombination centers, which is indicated by a change in the position of the OPQ maxima associated with the ground and excited states of holes at the centers after irradiation ($\lambda_{M_1} = 0.75$ μm and $\lambda_{M_2} = 1.03$ μm, Fig. 2).

While our experimental data cannot answer the question as to the nature of the new *r* centers, it may be conjectured that these centers are associated with defect complexes containing V_{Cd} and In atoms. The formation of such complexes under irradiation of CdS : In is initiated by the enhanced mobility of In atoms and of the forming V_{Cd} vacancies. This conjecture is based on a number of observations. Recombination centers with a changed position of the OPQ maxima were observed only in irradiated doped crystals. Similar centers with slightly different positions of the OPQ maxima were also seen in irradiated Cu-doped CdS single crystals [12]. The formation of new *r* centers in CdS : In after irradiation in concentrations higher than that of V_{Cd} before irradiation results in an enhancement of OPQ and in a decrease in the dark electrical conductivity, because these centers, as with other slow-recombination centers, are acceptors.

It is known that V_{Cd} vacancies are responsible for the photoconductivity in the extrinsic region $\lambda \approx$ (550–600) nm in CdS [1]. Electron irradiation of CdS : In reduces the photosensitivity for wavelengths $\lambda >$ 530 nm (Fig. 1). This is evidence of a decrease in the V_{Cd} concentration, apparently as a result of their interaction with In atoms. It should be pointed out that irradiation of undoped CdS single crystals brings about an increase in the extrinsic photoconductivity due to an increase in the V_{Cd} concentration [13].

The *G* band and the *O* luminescence at $\lambda \approx 604$ nm are the dominant emission bands in irradiated CdS : In samples at 77 K. The *O* luminescence was not observed in doped crystals before irradiation. The increase in the *G*-luminescence intensity is apparently explained, in addition to other factors, by the formation of interstitial sulfur atoms under electron irradiation.

The nature of the *O* luminescence in CdS remains unclear. Most authors believe the Cd_i atoms to be responsible for it [14, 15], whereas others associate the formation of the *O*-luminescence centers with oxygen atoms [16]. We believe [17] that the *O* centers contain Cd_i atoms and some residual impurity, most probably oxygen, which is always present in the CdS lattice.

The increase in the *O*-luminescence intensity in irradiated CdS : In single crystals is connected with the increase in concentration of the Cd_i-containing complexes which did not recombine with the radiation-induced V_{Cd} vacancies that trapped In atoms.

The luminescence band at $\lambda_M = 1.2$ μm, which was observed only in irradiated CdS : In single crystals, should apparently be assigned to the recombination of free electrons with holes trapped by the new *r* centers, whose ground state is at a distance of 1.65 eV from the valence band.

REFERENCES

1. V. I. Gavrilenko, A. M. Grekhov, D. V. Korbutyak, and V. G. Litovchenko, *Optical Properties of Semiconductors: Handbook* (Naukova Dumka, Kiev, 1987), p. 392.

2. I. Schneider, W. C. Holten, T. L. Estle, and A. Rauber, Phys. Lett. **5**, 312 (1963).
3. *Physics and Chemistry of II–VI Compounds*, Ed. by M. Aven and J. S. Prener (North-Holland, Amsterdam, 1967; Mir, Moscow, 1970).
4. B. A. Kulp and R. H. Kelley, J. Appl. Phys. **31** (6), 1057 (1960).
5. I. B. Ermolovich, A. V. Lyubchenko, and M. K. Sheĭnkman, Fiz. Tekh. Poluprovodn. (Leningrad) **2** (11), 1639 (1968) [Sov. Phys. Semicond. **2**, 1364 (1968)].
6. A. M. Gurvich and M. A. Il'ina, in *Problems in Physics of II–VI Compounds* (Vilnius, 1972), Vol. 2, p. 325.
7. A. M. Gurvich, *Introduction to the Physical Chemistry of Phosphor Crystals* (Vysshaya Shkola, Moscow, 1982), p. 182.
8. V. V. Emtsev and T. V. Mashovets, *Impurities and Point Defects in Semiconductors* (Radio i Svyaz', Moscow, 1981), p. 185.
9. *Properties Inorganic Compounds: Handbook*, Ed. by A. I. Efimov *et al.* (Khimiya, Leningrad, 1983), p. 15.
10. N. E. Korsunskaya, J. V. Markevich, T. V. Torchinskaya, and M. K. Seinkman, Phys. Status Solidi A **60** (2), 565 (1980).
11. B. N. Mukashev, Kh. A. Abdulin, and Yu. V. Torelkinskiĭ, Usp. Fiz. Nauk **170**, 143 (2000).
12. A. P. Galushka, G. E. Davidyuk, N. S. Bogdanyuk, *et al.*, Fiz. Tekh. Poluprovodn. (Leningrad) **10** (4), 778 (1976) [Sov. Phys. Semicond. **10**, 463 (1976)].
13. G. E. Davidyuk, N. S. Bogdanyuk, V. T. Mak, and V. V. Bozhko, Fotoélektronika, No. 3, 7 (1990).
14. B. A. Kulp, Phys. Rev. **125** (6), 1865 (1962).
15. I. B. Ermolovich, G. I. Matvievskaya, and M. K. Sheĭnkman, Fiz. Tekh. Poluprovodn. (Leningrad) **9** (5), 1620 (1975) [Sov. Phys. Semicond. **9**, 1070 (1975)].
16. N. K. Morozova, A. V. Morozov, I. A. Karetnikov, *et al.*, Fiz. Tekh. Poluprovodn. (St. Petersburg) **28** (10), 1699 (1994) [Semiconductors **28**, 944 (1994)].
17. G. E. Davidyuk, V. S. Manzhara, N. S. Bogdanyuk, *et al.*, Fiz. Tekh. Poluprovodn. (St. Petersburg) **31** (4), 390 (1997) [Semiconductors **31**, 326 (1997)].

Translated by G. Skrebtsov

Physics of the Solid State, Vol. 44, No. 2, 2002, pp. 260–265. Translated from Fizika Tverdogo Tela, Vol. 44, No. 2, 2002, pp. 251–256.

SEMICONDUCTORS AND DIELECTRICS

The Influence of Structural Features on the Thermal Conductivity of Polycrystalline Zinc Sulfide

N. V. Lugueva and S. M. Luguev

Institute of Physics, Dagestan Scientific Center, Russian Academy of Sciences, ul. 26 Bakinskikh komissarov 94, Makhachkala, 367003 Dagestan, Russia

e-mail: kamilov@datacom.ru

Received May 24, 2001

Abstract—The thermal conductivity of single-crystal zinc sulfide and optically transparent zinc sulfide polycrystals differing in crystal grain size and density is experimentally investigated in the temperature range 80–400 K. It is shown that the thermal conductivity of polycrystalline samples substantially depends on the crystal grain size and the defect concentration in the grain-boundary layers. In zinc sulfide samples with a grain size of 1 μm, excess thermal resistance due to phonon scattering by grain boundaries is observed at temperatures $T < 130$ K. It is demonstrated that, at higher temperatures ($T > 210$ K), the heat transfer is associated not only with transverse phonon modes but also with longitudinal phonon modes and the role of the latter modes increases with an increase in temperature. © *2002 MAIK "Nauka/Interperiodica".*

1. INTRODUCTION

Zinc sulfide is widely used in optical instrument production owing to its transparency in the IR spectral range. For some practical purposes, polycrystalline materials based on zinc sulfide are more preferable to single-crystal zinc sulfide [1]. In commercial production, optical polycrystalline ZnS-based materials are usually prepared by recrystallization compaction of a finely disperse powder under vacuum or through vapor deposition of raw materials. Compared to the PO-2 samples produced by vapor deposition, the KO-2 samples prepared using recrystallization compaction possess better mechanical properties but a slightly worse transparency, especially in the short-wavelength optical range [2, 3]. Reliable data on the thermal conductivity coefficient κ of polycrystalline zinc sulfide samples prepared by recrystallization compaction or vapor deposition are required to optimize the procedures and techniques of producing high-quality optical polycrystalline ZnS-based materials and to solve problems in engineering. Moreover, the data on the thermal conductivity and its temperature dependence can provide a deeper insight into both the mechanism of heat transfer and the influence of structural features on the thermal conductivity coefficient κ of zinc sulfide materials.

In our earlier work [4], we revealed that the thermal conductivity of the KO-2 optical polycrystalline material produced by vacuum recrystallization compaction of a finely disperse zinc sulfide powder is considerably less than that of single-crystal zinc sulfide. The thermal conductivity coefficients determined in [4] for the KO-2 material were 3.9 (at 80 K) and 1.6 (at 300 K) times less than those obtained by Slack [5] for single-crystal zinc sulfide at the same temperatures. A preliminary analysis allowed us to assume that the low thermal conductivity of the KO-2 material, as compared to single-crystal zinc sulfide, is associated with specific features in the defect structure of polycrystalline ceramics. In this respect, the aim of the present work was to investigate in detail the mechanisms of heat transfer in optical polycrystalline ZnS-based materials in relation to their structural features, temperature, crystal grain size, and the presence of linear and bulk defects in the crystal structure.

The present paper reports on the results of careful investigations into the thermal conductivities of the KO-2 material, polycrystalline zinc sulfide samples prepared by vapor deposition, and single-crystal zinc sulfide.

2. SAMPLES AND EXPERIMENTAL TECHNIQUE

The KO-2 samples were prepared by vacuum recrystallization compaction of a finely disperse ZnS powder (zinc sulfide for optical ceramics; particle size, 25 nm). The grain size in the samples was equal to 1–2 μm. The relative densities of the KO-2(1) and KO-2(2) samples amounted, respectively, to 0.998 and 0.991 of the density of the ZnS single crystal. The PO-2 samples consisted of crystallites 1–3 mm in size, and their density was equal to the density of the ZnS single crystal. The samples to be studied were cut from bulk disks and had the form of rods with a circular or rectangular cross section 20 mm^2 in area and 22–24 mm in height. According to x-ray diffraction analysis, the KO-2 and PO-2 samples and the ZnS single crystal had a cubic structure (β-ZnS sphalerite).

The thermal conductivity coefficients κ were measured by the absolute stationary method in the temper-

ature range 80–400 K under vacuum. The experimental setup used was similar to the A-type instrument described in [6]. In the temperature range 160–250 K, the κ coefficients were also measured under quasi-stationary conditions with the use of supercooled ethanol as a cooling agent. The temperature drift was no more than 0.5 K/h. The necessity of performing these measurements was dictated by the specific features revealed in the temperature dependences $\kappa(T)$ obtained for the samples under stationary thermal conditions at fixed temperatures of the cooling agent. These features will be discussed below. The relative error in measurements for both temperature regimes did not exceed 2% at low temperatures and 3% in the temperature range 300–400 K.

3. RESULTS AND DISCUSSION

Figure 1 displays the experimental temperature dependences of the thermal conductivity coefficient for the samples studied in the present work. For comparison, the data on the thermal conductivity coefficient obtained by Slack [5] for the ZnS single crystal and the results of our earlier measurements made in [4] for the KO-2 sample are also shown in Fig. 1. It can be seen from this figure that our data for the ZnS single crystal virtually coincide with the results obtained in [5]. Moreover, the κ coefficients measured for the KO-2 samples in the present work are in close agreement with those determined earlier in [4]. The thermal conductivity of the KO-2 sample is substantially less than that of the PO-2 sample and the ZnS single crystal over the entire temperature range covered. The thermal conductivities of the PO-2 sample and the ZnS single crystal are close to each other in magnitude and exhibit similar temperature dependences. The κ coefficients measured under stationary (when the measuring instrument was placed in the cooling agent at a fixed temperature) and quasi-stationary conditions also coincide to within the limits of experimental error. For convenience, the experimental data on the thermal conductivity coefficients for the KO-2 and PO-2 samples and the ZnS single crystal are represented in the form of temperature dependences of the thermal resistivity ($W = 1 / \kappa$). It is seen from Fig. 2 that the dependences $W(T)$ for the PO-2 samples and the ZnS single crystal in the temperature range studied are parallel straight lines with inflection points at a temperature of approximately 210 K. The thermal resistivity of the KO-2 samples is considerably greater in magnitude compared to that of the PO-2 samples and the ZnS single crystal. In the temperature range 130–400 K, the dependence $W(T)$ for the KO-2 samples also exhibits a linear behavior with an inflection point at 210 K. However, at $T < 130$ K, this dependence deviates from linear behavior, most likely, due to the specific features observed in phonon scattering.

Let us now consider the contributions to heat transfer mechanisms that can be responsible for (1) the low thermal conductivity coefficients κ observed in the

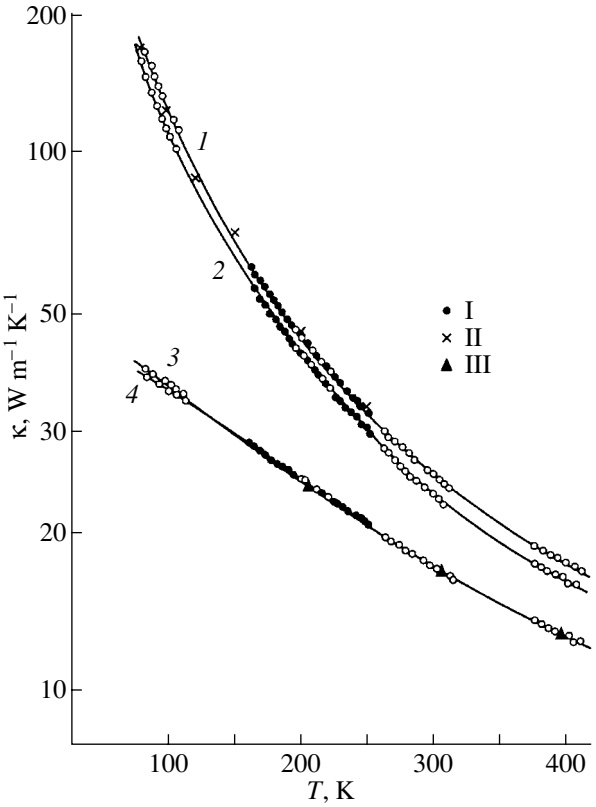

Fig. 1. Temperature dependences of the thermal conductivity coefficient κ for zinc sulfide samples with different structures: (*1*) single-crystal zinc sulfide, (*2*) PO-2 polycrystal, and (*3*, *4*) KO-2 polycrystals of different porosities. Points I indicate the temperature dependence of the κ coefficient measured under quasi-stationary conditions. Points II represent the κ coefficients obtained by Slack [5] for the ZnS single crystal. Points III correspond to the κ coefficients determined in our earlier work [4] for the KO-2 sample.

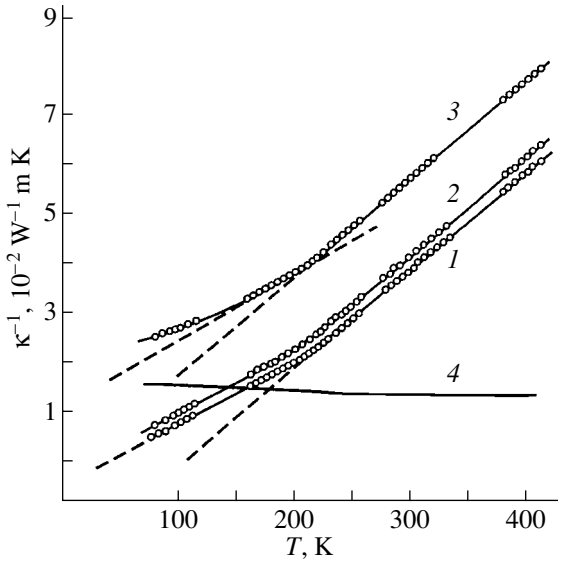

Fig. 2. Temperature dependences of the thermal resistivity ($W = 1/\kappa$) for ZnS samples with different structures. The numbering of curves *1–3* is the same as in Fig. 1. (*4*) Temperature dependence of the difference between the thermal resistivities of the KO-2 and PO-2 samples.

experiment with the KO-2 polycrystalline samples (even though their optical transparency is rather high) as compared to those obtained for the PO-2 polycrystalline samples and the ZnS single crystal, (2) the appearance of excess thermal resistance in the KO-2 samples at $T < 130$ K, and (3) the changes observed in the slope of the temperature dependence of the thermal resistivity for the KO-2 and PO-2 samples and the ZnS single crystal at a temperature of approximately 210 K.

Analysis of the possible contributions to the κ coefficient for the samples studied in the temperature range 80–400 K shows that zinc sulfide possesses a high electrical resistivity. Hence, the electron-assisted heat transfer can be ignored in the temperature range covered. Estimates demonstrate that, despite the optical transparency of the samples under investigation, the photon component of thermal conductivity κ_{phot} is negligibly small even for the ZnS single crystals. According to the estimates made in our recent work [7] for polycrystalline zinc sulfide samples, the photon component κ_{phot} at 300 K accounts for 0.006% of the total thermal conductivity. Therefore, the thermal conductivity coefficients κ obtained in the experiment with our samples are determined by the heat transfer through crystal lattice vibrations.

As regards the role played by acoustic and optical phonons in the heat transfer in zinc sulfide samples, their contributions are quite different. The contribution of optical phonons is insignificant in the temperature range 80–400 K. This is explained by the fact that the characteristic temperatures of transverse and longitudinal optical phonons in this compound are equal to 426 and 477 K, respectively [8]. Consequently, the transverse and longitudinal optical phonon modes are excited only at high temperatures in the studied range. For this reason and owing to the low group velocity, the optical phonons cannot contribute significantly to the heat transfer at temperatures below room temperature. Thus, the acoustic phonons make a dominant contribution to the heat transfer in zinc sulfide samples in the temperature range 80–400 K.

Now, we discuss the mechanisms responsible for the decrease in the heat transfer in zinc sulfide samples. In the temperature range 80–400 K, the thermal conduction in ZnS single crystals is limited primarily by the mechanisms associated with three-phonon umklapp processes and phonon scattering by point and linear (one-dimensional) defects existing in real crystals. In the PO-2 and KO-2 polycrystals, the heat transfer can also be limited by two-dimensional defects (grain boundaries). Moreover, the heat transfer in the KO-2 polycrystals can be hindered by bulk defects (pores), because the densities of the KO-2(1) and KO-2(2) samples are 0.2 and 0.9% less than those of the PO-2 samples and the ZnS single crystal. The preparation of the KO-2 samples through hot compaction can be accompanied by the formation of small-sized vacuum pores [9]; therefore, the density of these samples decreases. We estimated the contribution of pores to the observed decrease in the thermal conductivity of the KO-2 samples according to the formula proposed by Skorokhod [10] for materials of low porosity, that is,

$$\kappa = \kappa_0\left(1 - \frac{3}{2}P\right), \tag{1}$$

where κ_0 is the thermal conductivity coefficient for a reference material whose porosity is equal to zero and P is the porosity of the material under investigation. These calculations demonstrated that the thermal conductivity coefficients for the KO-2(1) and KO-2(2) porous samples at 300 K amount, respectively, to 0.3 and 1.3% of the κ coefficient for the reference sample of zero porosity. Hence, it follows that the low thermal conductivity of the KO-2 samples as compared to the PO-2 and single-crystal ZnS samples cannot be provided by the micropores alone in the KO-2 samples.

In polycrystalline samples, grain boundaries and surface layers of grains always contain a large amount of defects [9]. These defects distort the crystal lattice, strongly scatter phonons, and increase the thermal resistance of the samples. The role of grain boundaries and defects in phonon scattering can be judged from the estimates of the mean free path of phonons for each type of scattering processes. By using the data on the thermal conductivity coefficient, the mean free path l of phonons can be estimated from the formula

$$l = \frac{3\kappa}{C_V(v)}, \tag{2}$$

where κ is the experimental thermal conductivity coefficient, C_V is the specific heat at constant volume, and v is the mean velocity of sound. In our calculations, the values of C_V and v for ZnS were taken from [11] and [12], respectively. The phonon mean free paths thus obtained for the studied samples are shown in Fig. 3. Since the phonon scattering observed in our samples involves phonon–phonon scattering processes and phonon scattering by defects and grain boundaries, the mean free path of phonons can be represented in the following form:

$$l = (l_{ph}^{-1} + l_d^{-1} + l_b^{-1})^{-1}, \tag{3}$$

where l_{ph} is the mean free path associated with phonon–phonon scattering, l_d is the mean free path of phonons in phonon scattering by defects, and l_b is the mean free path of phonons in phonon scattering by grain boundaries. The mean free path associated with phonon–phonon scattering processes in zinc sulfide can be evaluated from the relationship [13]

$$l_{ph} = \frac{a}{\beta\gamma T}, \tag{4}$$

where a^3 is the volume per atom in the crystal, β is the thermal expansion coefficient, and γ is the Grüneisen parameter. In our calculations, the values of β and γ for

zinc sulfide were taken from [8, 14]. The mean free path l_b was calculated using the expression [15]

$$l_b = 1.12F\sqrt{d}, \quad (5)$$

where d is the grain cross section and F is the relative fraction of phonons involved in diffuse scattering by grain boundaries. According to Noguera and Wasim [15], the relative phonon fraction F for ZnS is equal to 0.58. The temperature dependences of the calculated mean free paths l_{ph} and l_b for the samples under investigation are displayed in Fig. 3. When calculating the mean free path l_b, the grain sizes were taken equal to 1 and 2 μm, which correspond to the grain sizes in the KO-2 samples.

It can be seen from Fig. 3 that, in zinc sulfide polycrystals with a grain size of 1 μm, the contributions of the phonon–phonon scattering and phonon scattering by grain boundaries to the mean free path of phonons are comparable to each other in magnitude even at 130 K. A further decrease in the temperature leads to an increase in the relative contribution of the phonon scattering by grain boundaries to the limitation of both the mean free path of phonons and the thermal conductivity. This explains the observed deviation of the $W(T)$ dependence for the KO-2 polycrystalline sample (Fig. 2) from linear behavior in the low-temperature range (i.e., the additional increase in the thermal resistance). In zinc sulfide polycrystals with a grain size $d >$ 5 μm, the contribution of the phonon scattering by grain boundaries to the limitation of the phonon mean free path in the temperature range covered becomes negligibly small.

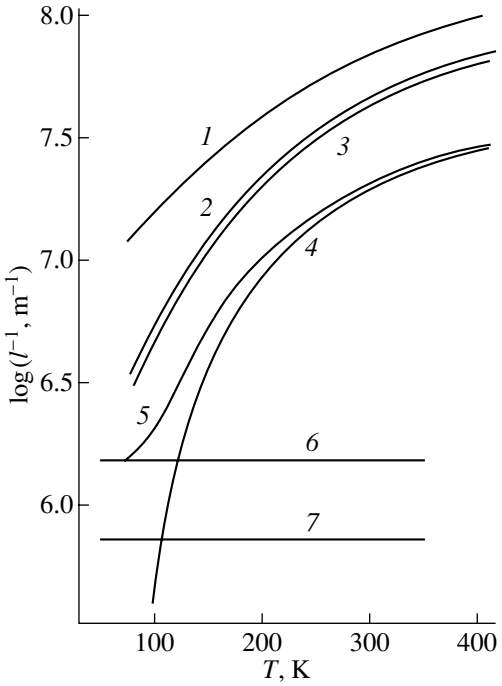

Fig. 3. Temperature dependences of the mean free path of phonons in (*1*) KO-2, (*2*) PO-2, and (*3*) single-crystal ZnS samples. Temperature dependences of the (*4*) calculated mean free path of phonons (l_{ph}) in phonon–phonon scattering, (*5*) calculated mean free path of phonons in the KO-2 sample with inclusion of phonon–phonon scattering and phonon scattering by grain boundaries, and the mean free path of phonons in grain-boundary scattering for the KO-2 samples with grain sizes of (*6*) 1 and (*7*) 2 μm.

The phonon mean free path associated with phonon scattering by defects was determined from relationship (3). As is seen from Fig. 3, the phonon scattering by defects substantially contributes to the limitation of the phonon mean free path in the studied samples. The calculations demonstrate that the contribution of the phonon scattering by defects to the thermal resistance increases when changing over from single-crystal zinc sulfide to the KO-2 polycrystalline sample. The thermal resistance observed even in the zinc sulfide single crystals due to phonon scattering by defects can, most likely, be associated with the presence of impurities (in particular, iron ions) in the samples. These impurities involved in II–VI compounds are efficient scattering centers of phonons [5] and decrease their mean free path. In the PO-2 and, especially, KO-2 crystalline samples, it is also necessary to take into account the contribution of the phonon scattering by defects in grain-boundary layers to the thermal resistance. Owing to the small size of the grains, the concentration of these defects in the KO-2 samples is substantially higher than that in the PO-2 samples. Correspondingly, their contribution to the thermal resistance is appreciably larger in the KO-2 samples than in the PO-2 samples. As can be seen from Fig. 2, the excess thermal resistance due to a larger amount of defects in the vicinity of grain boundaries in the KO-2 samples as compared to that in the PO-2 samples is virtually temperature independent, which is consistent with the existing theory of phonon scattering by defects [16].

As was noted above, the temperature dependences $W(T)$ for the KO-2, PO-2, and single-crystal ZnS samples exhibit a change in the slope (inflection point) at a temperature of approximately 210 K. Devyatkova and Smirnov [17] also observed an inflection point in the dependence $W(T)$ near the Debye temperature θ for lead and cadmium chalcogenides and alkali halide compounds. Logachev *et al.* [18] obtained a similar inflection point in the theoretically calculated dependence $W(T)$ for NaCl. The mean Debye temperature for acoustic phonon modes contributing to heat transfer in zinc sulfide can be determined from the relationship [19]

$$\bar{\theta} = \left[\frac{2}{3}\theta_{TA}^2 + \frac{1}{3}\theta_{LA}^2\right]^{\frac{1}{2}}, \quad (6)$$

where θ_{TA} and θ_{LA} are the Debye temperatures for transverse and longitudinal acoustic phonons, respectively. The Debye temperature $\bar{\theta}$ calculated from formula (6) for ZnS is equal to 206 K (in our calculations,

Table 1. Coefficients *B* and *C* characterizing the temperature dependences of the thermal resistivity for the KO-2 and PO-2 samples and single-crystal ZnS

Material	B, 10^{-5} m/W		C, 10^{-3} m K/W	
	$T < 200$ K	$T > 240$ K	$T < 200$ K	$T > 240$ K
KO-2	13.8	20.4	12.6	–2.3
PO-2	14.1	20.2	–4.9	–17.2
Single-crystal ZnS	13.9	20.1	–5.6	–19.6

Table 2. Debye temperature, Grüneisen parameter, and the γ^2/θ^3 ratio for transverse and longitudinal acoustic branches of zinc sulfide

Phonons	θ, K	γ	γ^2/θ^3, 10^{-8} K^{-3}
TA	131	0.21	1.96
LA	306	1.33	6.17

the temperatures θ_{TA} and θ_{LA} were taken from [8]). Thus, inflection points in the experimental dependences of the thermal resistivity for the KO-2, PO-2, and single-crystal ZnS samples are observed at the Debye temperature. At temperatures above and below the Debye temperature, the dependence $W(T)$ can be represented by the relationship

$$W = BT + C. \quad (7)$$

Table 1 lists the coefficients *B* and *C*, which were determined from the experimental data. The quantity $BT = W_0$ is the thermal resistivity of a defect-free ZnS crystal. The coefficient *B*, which determines the slope of the linear dependence $W(T)$, characterizes the material and is identical (within the limits of experimental error) for the studied samples in each temperature range (above and below the Debye temperature). It is known that, in the case when the heat transfer is provided by acoustic phonons and three-phonon umklapp processes are dominant in the phonon scattering, the thermal resistivity of the defect-free crystal can be represented in the following form [20]:

$$W_0(T) = A\frac{\gamma^2 T}{n^{1/3} M a \bar{\theta}^3}, \quad (8)$$

where *A* is constant, *M* is the mean atomic mass, and *n* is the number of atoms per unit cell. A comparison of formulas (7) and (8) shows that the coefficient *B* is proportional to γ^2/θ^3. Since the slope of the straight line $W(T)$ is determined by the *B* coefficient, the observed change in the slope is caused by the change in this coefficient, i.e., by the change in the γ^2/θ^3 ratio. It should be noted that the values of γ and θ differ for different acoustic branches. Therefore, the γ^2/θ^3 ratio (and, hence, the *B* coefficient) can vary with a change in the contribution of the longitudinal and transverse acoustic phonons to heat transfer. The calculated ratios γ^2/θ^3 are given in Table 2. This table also presents the values of γ and θ (taken from [8]) for transverse and longitudinal acoustic branches of zinc sulfide, which were used in calculations of the γ^2/θ^3 ratios. It is seen from Table 2 that the γ^2/θ^3 ratio for transverse phonons is approximately three times less than that for longitudinal phonons. Consequently, an increase in the contribution of longitudinal acoustic phonons to the heat transfer should be accompanied by an increase in the *B* coefficient and, correspondingly, by a change in the slope of the dependence $W(T)$. In zinc sulfide, all transverse acoustic phonons are excited at 210 K (for the transverse acoustic branch, $\theta = 131$ K). A further increase in the temperature brings about excitation of longitudinal acoustic phonons for which $\theta = 306$ K. Thus, as the temperature increase, the role played by longitudinal phonons in the heat transfer in zinc sulfide increases, which leads to an increase in the *B* coefficient. It follows from Table 1 that, in the experimental dependences $W(T)$ for the KO-2, PO-2, and single-crystal ZnS samples, the magnitude of the *B* coefficient in the high-temperature range ($T > 240$ K) is larger than that in the low-temperature range. Therefore, the change in the slope of the dependence $W(T)$ for ZnS-based materials in the high-temperature range can be explained by the increase in the contribution of longitudinal acoustic phonons to the heat transfer. This inference is confirmed by the data obtained in the study of the thermal conductivity coefficient for ZnS under uniform compression [7].

The coefficient *C* in formula (7) characterizes impurities (their amount and the phonon scattering cross section) contained in a particular sample and, as a rule, is positive. In our experiment, the coefficient *C* is negative for all the samples studied, except for the KO-2 sample at low temperatures. This can be explained by the fact that the zinc sulfide samples contain oxygen ion impurities substituting for sulfur in the crystal lattice. Since the ionic and covalent radii of oxygen are less than those of sulfur [21], an increase in the oxygen concentration in zinc sulfide samples leads to a decrease in the mean atomic mass and the lattice parameter; consequently, the thermal conductivity increases insignificantly [22]. Therefore, oxygen impurities acts as defects that decrease the thermal conduction and increase the thermal resistance of the crystal lattice.

4. CONCLUSION

Thus, the results of the experimental investigation allowed us to conclude that the relatively low thermal conductivity of fine-grained zinc sulfide (the KO-2 sample) as compared to single-crystal ZnS is associated with strong phonon scattering by defects in the grain-boundary layers. The ZnS polycrystals with a grain size of 1 μm are characterized by size effects, namely, the mean free path of phonons at low temperatures

becomes comparable to the grain size and an increase in the phonon scattering by grain boundaries with a decrease in the temperature gives rise to an excess thermal resistance in these samples at $T < 130$ K. The change observed in the slope of the temperature dependence of the thermal resistivity for the studied samples near the Debye temperature is caused by an increase in the contribution of longitudinal acoustic phonons to heat transfer at high temperatures.

ACKNOWLEDGMENTS

We are grateful to G.N. Dronova for supplying the samples used in our investigations.

REFERENCES

1. F. K. Volynets, Opt.-Mekh. Prom-st. **11**, 39 (1978).
2. S. V. Buldina, G. N. Dronova, and S. V. Zhukova, in *Crystalline Optical Materials* (Informtekhnika, Moscow, 1992), p. 49.
3. V. N. Savushkin, G. V. Anan'eva, S. M. Volynskaya, T. I. Merkulyaeva, and I. A. Mironov, in *Crystalline Optical Materials* (Informtekhnika, Moscow, 1992), p. 51.
4. N. V. Lugueva, G. N. Dronova, and S. M. Luguev, Opt.-Mekh. Prom-st. **10**, 30 (1983).
5. G. A. Slack, Phys. Rev. B **6** (10), 3791 (1972).
6. E. D. Devyatkova, A. V. Petrov, I. A. Smirnov, and B. Ya. Moĭzhes, Fiz. Tverd. Tela (Leningrad) **2** (4), 738 (1960) [Sov. Phys. Solid State **2**, 681 (1960)].
7. N. V. Lugueva, N. L. Kramynina, and S. M. Luguev, Fiz. Tverd. Tela (St. Petersburg) **43** (2), 222 (2001) [Phys. Solid State **43**, 231 (2001)].
8. D. N. Talwar, M. Vandevyver, K. Kunc, and M. Zigone, Phys. Rev. B **24** (2), 741 (1981).
9. J. P. Suchet, *Chemical Physics of Semiconductors* (Van Nostrand, London, 1965; Metallurgiya, Moscow, 1969).
10. V. V. Skorokhod, Poroshk. Metall., Nos. 1–2, 53 (1995).
11. H. M. Kagaya and T. Soma, Phys. Status Solidi B **134** (2), K101 (1986).
12. D. N. Chung and W. R. Buessem, J. Appl. Phys. **38** (6), 2535 (1967).
13. R. Berman, *Thermal Conduction in Solids* (Clarendon Press, Oxford, 1976; Mir, Moscow, 1979).
14. T. Soma, Solid State Commun. **34** (12), 927 (1980).
15. A. Noguera and S. M. Wasim, Solid State Commun. **50** (4), 483 (1984).
16. V. S. Oskotskiĭ and I. A. Smirnov, *Defects in Crystals and Thermal Conduction* (Nauka, Leningrad, 1972).
17. E. D. Devyatkova and I. A. Smirnov, Fiz. Tverd. Tela (Leningrad) **4** (9), 2507 (1962) [Sov. Phys. Solid State **4**, 1836 (1962)].
18. Yu. A. Logachev, B. Ya. Moĭzhes, and A. S. Skal, Fiz. Tverd. Tela (Leningrad) **12** (10), 2791 (1970) [Phys. Solid State **12**, 2251 (1970)].
19. G. A. Slack and P. Andersson, Phys. Rev. B **26** (4), 1873 (1982).
20. G. A. Slack, in *Solid State Physics* (Academic, New York, 1979), Vol. 34, p. 1.
21. B. F. Ormont, *Introduction to Physical Chemistry and Crystal Chemistry of Semiconductors* (Vysshaya Shkola, Moscow, 1982).
22. A. I. Anselm, *Introduction to Semiconductor Theory* (Nauka, Moscow, 1978; Prentice-Hall, Englewood Cliffs, 1981).

Translated by O. Borovik-Romanova

Physics of the Solid State, Vol. 44, No. 2, 2002, pp. 266–273. Translated from Fizika Tverdogo Tela, Vol. 44, No. 2, 2002, pp. 257–264.

SEMICONDUCTORS AND DIELECTRICS

Electronic Structure, X-ray Spectra, and Magnetic Properties of the $LiCoO_{2-\delta}$ and Na_xCoO_2 Nonstoichiometric Oxides

V. R. Galakhov*, V. V. Karelina, D. G. Kellerman**, V. S. Gorshkov**, N. A. Ovechkina*, and M. Neumann*****

**Institute of Metal Physics, Ural Division, Russian Academy of Sciences, ul. S. Kovalevskoĭ 18, Yekaterinburg, 620219 Russia*
e-mail: galakhov@ifmlrs.uran.ru
***Institute of Solid-State Chemistry, Ural Division, Russian Academy of Sciences, ul. Pervomaĭskaya 91, Yekaterinburg, 620219 Russia*
****Universität Osnabrück, D-49069 Osnabrück, Germany*

Received June 18, 2001

Abstract—This paper reports on a study of the magnetic susceptibility, x-ray photoelectron, and x-ray emission spectra of the $LiCoO_{2-\delta}$ and Na_xCoO_2 nonstoichiometric oxides. The valence-band structure of $LiCoO_2$ was analyzed. The hole concentration in the oxygen 2*p* band of $LiNiO_2$ and $LiCoO_2$ was derived from measurements of the O *K*α emission spectra. Measurements of Co 2*p* and Co *3s* photoelectron spectra showed that the Co^{3+} ions reside in the low-spin state with $S = 0$. The deficiency of oxygen in the $LiCoO_{2-\delta}$ reduced oxides gives rise to the formation of divalent cobalt ions. The deficiency of the alkali metal in Na_xCoO_2 initiates the formation of holes in the oxygen 2*p* band while not changing the electronic configuration d^6 of the cobalt-ion ground state. © *2002 MAIK "Nauka/Interperiodica".*

1. INTRODUCTION

$LiCoO_2$ complex oxide has a layered structure, with the Li and Co ions ordered in alternating (111) planes. The existence of planes containing only lithium ions provides a possibility of complete deintercalation of the alkali metal and, thus, application of this compound as a cathode material in chemical storage batteries. The ground state of the Co^{3+} ions can be written as $t_{2g\uparrow}^3 t_{2g\downarrow}^3 e_g^0$; their nonmagnetic character was established by Bongers [1]. Estimates of van Elp [2] showed $LiCoO_2$ to be an insulator with a band gap of 2.7 ± 0.3 eV.

The valence band of $LiCoO_2$ stoichiometric oxide was studied using x-ray photoelectron spectroscopy (XPS) in [2–4]. The O 1*s* x-ray absorption spectra (XAS) were measured in [5], and in [4], XPS studies of $LiCoO_2$ stoichiometric oxide were complemented by O *K*α and Co *L*α x-ray emission (XES) measurements.

The $LiCoO_2$ band structure was calculated in [6]. The studies of XPS spectra of the inner Co 2*p* levels of $LiCoO_2$ performed in [2, 3] led to controversial conclusions. According to [2], $LiCoO_2$ is a charge-transfer insulator with the energy required for charge transfer from the oxygen to the metal ion $\Delta = 4.0$ eV and its ground state is strongly covalent with 47% of the d^6 configuration, 44% of the $d^7\underline{L}$ configuration, and 9% of the $d^8\underline{L}^2$ configuration. Here, $\underline{L}$ denotes a hole in the 2*p* shell of oxygen appearing as a result of electron transfer from an oxygen ion to a cobalt ion and $\underline{L}^2$ corresponds to two holes in the oxygen shell.

An opposite conclusion was arrived at in [3]. Kemp and Cox [3] obtained $\Delta = -0.5$ eV for the charge transfer energy. Whence it follows that $LiCoO_2$ belongs to the class of insulators with negative charge transfer energy, similar to $LiNiO_2$, $NaCuO_2$, and $SrFeO_3$ [7].

To obtain charge neutrality in oxides deficient in an alkali metal, such as Li_xCoO_2 and Na_xCoO_2 ($x < 1$), these oxides should also have, in addition to Co^{3+}, tetravalent Co^{4+} ions. As shown in measurements of the Co 2*p* and O 1*s* x-ray absorption spectra of deintercalated samples of Li_xCoO_2 ($x = 1$, 0.69, 0.57, 0.46) [8], charge compensation takes place due to holes in the O 2*p* band of oxygen, rather than as a result of the formation of tetravalent cobalt. According to [8], the structure of the Co 2*p* absorption spectra in deintercalated oxides is in agreement with the calculated multiplet of the Co^{3+} ion in the low-spin state and the O 1*s* spectrum exhibits a peak near the conduction-band bottom, which indicates the formation of doping holes in the 2*p* band of oxygen.

In this work, we present new data on the magnetic properties and electronic structure of both stoichiometric $LiCoO_2$ and of $LiCoO_{2-\delta}$ and Na_xCoO_2 nonstoichiometric compounds. It is shown how subjecting $LiCoO_2$ samples to an environment with different partial oxygen pressure brings about the formation of Co^{2+} ions.

2. EXPERIMENTAL

Single-phase, homogeneous $LiCoO_2$ was prepared by sintering a mixture of Co_3O_4 and Li_2CO_3 in air at a temperature of 850°C for 25 h, followed by slow cooling. The $LiCoO_2$ prepared in this way was additionally annealed in two different environments, namely, in oxygen and in mixtures of helium and oxygen with fixed partial pressures of oxygen ($\log p_{O_2}$ = –1.85, –2.85, and –3.1). All the anneals were made at 750°C. X-ray phase analysis showed that after such a treatment, all samples retained the crystal structure of $LiCoO_2$. The dependence of the lattice parameters on the partial pressure of oxygen is presented in Table 1. It should be pointed out that $LiCoO_2$ annealed at higher temperatures and lower partial pressures of oxygen becomes unstable and decomposes with the formation of CoO or Co_3O_4.

Na_xCoO_2 oxide was synthesized using the solid-phase method from sodium oxalate $Na_2C_2O_4$ and cobalt oxide Co_3O_4. Annealing was performed in a flow of oxygen at a temperature of 850°C for 150 h, with intermediate grinding of the mixture to homogenize the samples. X-ray phase analysis showed that the compound thus obtained is isostructural with $Na_{0.71}CoO_2$.

The magnetic susceptibility was measured in the 300–1000-K temperature range using the Faraday method in fields of up to 10 kOe and in the 4-to-300-K range with a SQUID magnetometer (Quantum Design) at 1000 Oe.

The XPS spectra were obtained on a PHI 5600 Multitechnique System x-ray photoelectron spectrometer with monochromatized Al $K\alpha$ radiation. Samples pressed into pellets were studied after their breakage in a high vacuum. The spectrometer was calibrated against the Au 4*f* line (binding energy 84.0 eV). The spectrometer energy resolution estimated from the valence-band spectrum of gold foil was 0.35–0.40 eV. The sample charging and the associated line shift toward higher energies were taken into account in reference to the C 1*s* line, whose energy was taken equal to 285.0 eV.

The Co $L\alpha$ and O $K\alpha$ x-ray emission spectra were measured on an RSM-500 x-ray spectrometer under electron excitation. The Co $L\alpha$ spectra were obtained in second-order reflection, with instrumental broadening of about 0.8 eV. The O $K\alpha$ spectra were taken in first-order reflection, with an instrumental line width of approximately 1 eV. The error in determining the energy position of the spectral maxima was ±0.2 eV. The V $L\alpha$ line of metallic vanadium (511.3 eV [9]) was used for calibration of the O $K\alpha$ spectra. The Co $K\alpha$ lines were calibrated against the Ni *Ll*, η, and Ni $L\alpha$ lines (with the peaks at 742.7, 762, and 851.5 eV, respectively [9]).

Table 1. Lattice parameters of $LiCoO_{2-\delta}$ samples prepared under different conditions

Sample/oxygen pressure	*a*, Å	*c*, Å
$LiCoO_2$ (synthesis in oxygen)	2.8103 ± 0.0002	14.027 ± 0.004
$LiCoO_{2-\delta}$ ($\log p_{O_2}$ = –1.85)	2.8147 ± 0.0002	14.039 ± 0.005
$\log p_{O_2}$ = –2.85	2.8153 ± 0.0002	14.047 ± 0.005
$\log p_{O_2}$ = –3.1	2.8159 ± 0.0002	14.049 ± 0.005
Na_xCoO_2	2.833 ± 0.001	10.88 ± 0.01

3. RESULTS

3.1. Magnetic Properties of $LiCoO_{2-\delta}$ and Na_xCoO_2

It was established that annealing of $LiCoO_2$ at low partial pressures of oxygen gives rise to oxygen nonstoichiometry. The nonstoichiometry of an object manifests itself distinctly in magnetic susceptibility measurements. The magnetic susceptibility of stoichiometric $LiCoO_2$ is a temperature-independent quantity because the trivalent cobalt Co^{3+} resides in the low-spin state $t_{2g\uparrow}^3 t_{2g\downarrow}^3 e_g^0$ and, hence, its magnetic moment is zero. The presence of oxygen defects in $LiCoO_2$ and of the associated paramagnetic centers, which are Co^{2+} ions [10], should result in an increase in the magnetic susceptibility and in its becoming temperature-dependent. As seen from the data presented in Fig. 1, the magnetic susceptibility of stoichiometric $LiCoO_2$ measured in an oxygen environment (curve *1*) is practically temperature-independent up to $T \sim 750$ K.

At the same time, the susceptibility of $LiCoO_{2-\delta}$ with defects prepared at low partial pressures of oxygen and measured under conditions close to those in which it was synthesized depends distinctly on temperature (curve *2* in Fig. 1) and, within the 4- to 500-K range, can be described by the Curie–Weiss law:

$$\chi = \chi_0 + C/(T + \Theta), \quad (1)$$

where χ_0 is the temperature-independent part including the contribution from diamagnetism and the van Vleck paramagnetism, *C* is the Curie constant, and Θ is the Weiss constant. For $LiCoO_{2-\delta}$ annealed at $\log p_{O_2}$ = –3.1, we have χ_0 = 0.000145 cm³/mol, *C* = 0.40 cm³ K/mol, and Θ = –106.3 K, which corresponds to a content of about 2% Co^{2+} ions or 1% vacant oxygen positions. This result does not contradict thermogravimetric data if we assume Co^{2+} to be in the high-spin state *S* = 3/2. The assumption of the low-spin state of the Co^{2+} impurity ions (*S* = 1/2) would have led to unjustifiably high concentrations of the divalent cobalt.

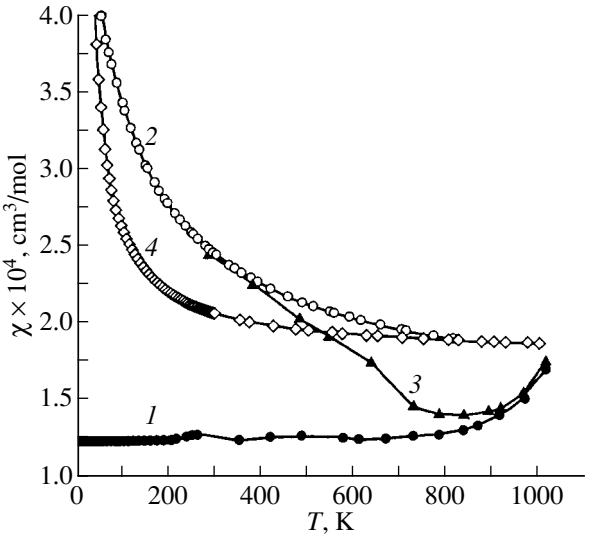

Fig. 1. Temperature dependence of the magnetic susceptibility of $LiCoO_2$ prepared at different oxygen pressures: (*1*) $LiCoO_2$ annealed in oxygen; (*2*) annealing at $\log p_{O_2}$ = –3.1 and measurements in vacuum; (*3*) annealing at $\log p_{O_2}$ = –3.1 and measurements in oxygen; and (*4*) temperature dependence of the magnetic susceptibility of Na_xCoO_2.

Susceptibility measurements on the nonstoichiometric sample in an oxygen environment (curve *3* in Fig. 1) showed that the defect concentration decreases in the 300- to 750-K range, which becomes manifest in a drop in the susceptibility. Note the remarkably low temperature at which oxygen exchange with the gas phase, causing oxidation of the nonstoichiometric sample, becomes possible.

The magnetic susceptibility of Na_xCoO_2 displayed in Fig. 1 fits well to the Curie–Weiss law with the parameters $\chi_0 = 1.78 \times 10^{-4}$ cm^3/mol and $\Theta = -0.36$ K. The effective magnetic moment per cobalt ion is very small, $0.26\mu_B$. A question arises as to the nature of the paramagnetic centers. It may be conjectured that in Na_xCoO_2, as in $LiCoO_2$, the crystal field also stabilizes the low-spin state of Co^{3+}. Otherwise, the magnetic moment per cobalt ion would have been substantially higher.

Based on the charge neutrality condition, the chemical formula of Na_xCoO_2 should be written as $Na_x^{1+}Co_{1-x}^{4+}Co_x^{3+}O_2^{2-}$. In this case, the experimentally observed paramagnetic centers could be formally assigned to the presence of Co^{4+} ions. Taking into account the stoichiometric coefficient, the magnetic moment per such a center is

$$\mu(Co^{4+}) = \frac{\mu(Co)}{\sqrt{1-x}} = 0.48\mu_B. \quad (2)$$

One may also conceive another variant, namely, that the paramagnetic centers are not Co^{4+} ions but rather an equivalent number of exchange-coupled Co^{3+}–O^{1-} pairs and that the magnetic moment of $0.48\mu_B$ relates to such a pair. This situation was analyzed for the case of $Li_xNi_{1-x}O_2$ [11].

3.2. X-Ray Photoelectron and Emission Spectra of the $LiCoO_2$ Valence Band

Figure 2 presents an XPS valence-band spectrum and XES O $K\alpha$ and Co $L\alpha$ spectra of $LiCoO_2$. The XES spectra are shown reduced to a common energy scale based on the electron binding energies of the O 1*s* and Co $2p_{3/2}$ levels. For convenience of comparison, the XPS and O $K\alpha$ XES spectra were resolved into constituent Gaussians. The background arising from secondary-electron scattering approximated with the Shirley method was subtracted from the photoelectron spectrum.

Near the Fermi level, the Co 3*d* states are concentrated, which follows from the fact that maximum *A* and component *B* of the XPS spectrum coincide with the maximum of the x-ray Co $L\alpha$ emission spectrum. The Co 3*d* states provide a dominant contribution to the photoelectron spectrum at the excitation energy equal to 1486.7 eV. The peak with the binding energy of 21.6 eV relates to the O 2*s* states. The binding-energy region from 0 to 10 eV includes the O 2*p* states, with the maximum of the distribution at 5 eV, as determined from the position of the O $K\alpha$ emission spectrum (the energy of the maximum is 525.2 eV on the photon energy scale). The Co 3*d* and O 2*p* states are in the same energy interval, which implies their strong hybridization.

To analyze the features present in the spectra, we shall use the density-of-states function of $LiCoO_2$ calculated in the density-functional approximation by Czyzyk *et al.* in [6]. A comparison of experimental spectra with the calculations reveals that the strongest peak *A* and the *B* feature derive from the t_{2g} orbital. Considered in the simplified scheme of molecular orbitals for an octahedral field, where only the ligand *p* orbitals and the metal *d* orbitals are included, the t_{2g} level is antibonding. However, if we take into account the existence of the other two oxygen states and of the states of lithium, the t_{2g} orbitals will begin to contribute to chemical bonding, with a substantial degree of covalency [6]. The XPS feature *C*, according to the calculations of [6], is due to the t_{1u} orbitals, which derive primarily from the O 2*p* states (see the correlation with the maximum in the O $K\alpha$ spectrum, curve *b*), with a slight admixture of the Co 4*p* states. Band *D*, next in order, forms from the hybridized O 2*p*–Co 3*d* (e_g) states. Finally, band *E* reflects hybridization of the Co 4*s* and *p* states (the a_{1g} and t_{1u} orbitals) with the O 2*p* states. As seen from Fig. 2, the *D* and *E* features manifest themselves in the O $K\alpha$ spectrum (shoulder *c*, which is not

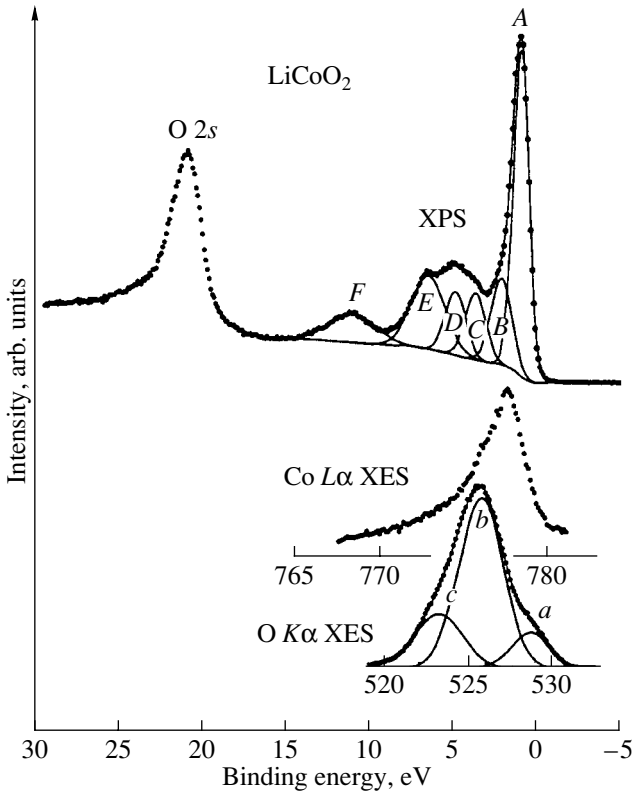

Fig. 2. X-ray valence-band photoelectron spectrum and x-ray O $K\alpha$ and Co $L\alpha$ emission spectra of $LiCoO_2$. The XES spectra are reduced to a common energy scale based on the binding energies of the inner-level electrons.

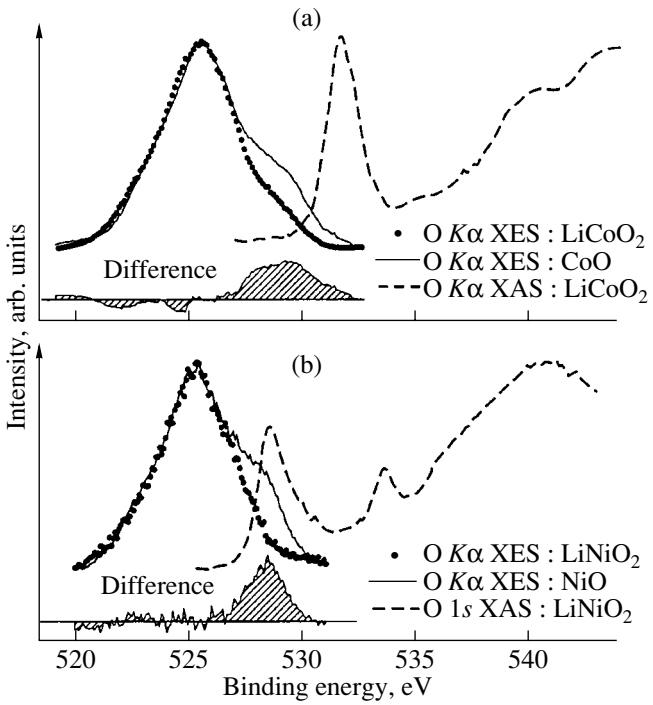

Fig. 3. (a) X-ray O $K\alpha$ emission spectra (XES) of $LiCoO_2$ and CoO and an O 1*s* absorption spectrum (XAS) of $LiCoO_2$. The O 1*s* absorption spectrum is reproduced from [5]. The hatched area is a difference spectrum obtained by subtracting the spectrum of $LiCoO_2$ from the O $K\alpha$ spectrum of CoO. (b) O $K\alpha$ XES spectra of $LiNiO_2$ and NiO and an O 1*s* XAS spectrum of $LiNiO_2$. The O 1*s* absorption spectrum is reproduced from [11]. A difference spectrum (hatched region) obtained by subtracting the $LiNiO_2$ spectrum from the O $K\alpha$ spectrum of NiO is also shown.

split off, apparently, because of the low resolution of the XES spectrum).

The *F* satellite at 11.5 eV cannot be interpreted in terms of band-structure calculations, because it forms due to the presence of a poorly screened Co 3*d* hole (the $3d^5$ final states). This satellite can be reproduced only by using multiconfigurational cluster calculations [2, 3].

Thus, the XPS features *A*–*E* originate from the states in which the hole created in photoemission is screened as a result of electron transfer from the oxygen 2*p* band to form a $3d^6\underline{L}$ final-state configuration and the *F* satellite is characterized by a $3d^5$ configuration.

3.3. Hole Concentration in the Oxygen 2p Band in $LiCoO_2$

$LiCoO_2$ and $LiNiO_2$ oxides are structural analogs. However, while the 3*d*-metal ions in $LiCoO_2$ are trivalent, the Ni ions in $LiNiO_2$ retain the ground-state electronic configuration $3d^8$, which corresponds to holes in the oxygen 2*p* band. This was shown experimentally in [11] using O 1*s* absorption spectra in the $Li_xNi_{1-x}O$ system. According to these data, 70% of all doping holes in $LiNiO_2$ are localized at the oxygen atoms. It appears natural to expect that variations in the filling of the O 2*p* band will become manifest not only in the absorption spectra but also in the oxygen $K\alpha$ emission spectra.

Figure 3a displays O $K\alpha$ emission spectra of $LiCoO_2$ and CoO and an O 1*s* absorption spectrum of $LiCoO_2$ taken from [5]. For convenience of comparison, the CoO spectrum is shifted by 0.5 eV toward higher photon energies to match its maximum with that of the $LiCoO_2$ spectrum. This comparison is suggested by the fact that the spectra are identical in the low photon energy domain and differ only at high energies, near the Fermi level.

In a similar manner, Fig. 3b shows the O $K\alpha$ spectra of $LiNiO_2$ and NiO. The O 1*s* absorption spectrum of $LiNiO_2$ was taken from [11]. As in the preceding case, the NiO spectrum is displaced by 0.5 eV toward higher photon energies. The hatched regions in both figures show the result of subtraction of the spectra of the monoxides from those of the lithium samples.

The two systems differ appreciably. The difference spectrum of the NiO–$LiNiO_2$ system matches closely,

in position, the first peak of the absorption spectrum, which, according to [11], is due to doping holes. The intensity of this peak grows with Li concentration in the $Li_xNi_{1-x}O$ system and reaches a maximum for $LiNiO_2$.

In the case of CoO–$LiCoO_2$, the difference spectrum and the maximum in the absorption spectrum do not coincide in energy and, hence, are of different nature. The maximum in the $LiCoO_2$ absorption spectrum corresponds to the upper Hubbard band (the final states in the $3d^7$ configuration). It may be conjectured that the difference in the filling of the O 2*p* states between CoO and $LiCoO_2$ is due to covalency effects, namely, to charge transfer from oxygen to the metal.

According to [2], the ground-state wave function of CoO can be written as

$$|g\rangle = \alpha_0|d^7\rangle + \alpha_1|d^8\underline{L}\rangle + \alpha_2|d^9\underline{L}^2\rangle. \quad (3)$$

Here, $\underline{L}$ and $\underline{L}^2$ reflect the presence of one and two holes in the oxygen 2*p* band, respectively, and the coefficients in the wave function expansion are $\alpha_0^2 = 0.79$, $\alpha_1^2 = 0.20$, and $\alpha_2^2 = 0.01$. This means that the number of electrons in the oxygen 2*p* band in CoO is given by the relation [4]

$$N_{O2p}(\text{CoO}) = 6 - (\alpha_1^2 + 2\alpha_2^2) = 5.78. \quad (4)$$

We assume that the number of electrons in the 2*p* band of oxygen, in the purely ionic limit, is six and that charge transfer from the ligand to the metal reduces the filling of the oxygen band.

The ratio of the integral intensities of the O *K*α spectra of $LiCoO_2$ and CoO normalized as shown above is 0.958. This means that in $LiCoO_2$, there are $0.958 \times 5.78 = 5.54$ electrons or 0.46 holes per oxygen ion.

Calculations of the configuration interaction in $LiCoO_2$ carried out in [2] give, for the ground-state wave function of $LiCoO_2$, the expression

$$|g\rangle = \alpha_0|d^6\rangle + \alpha_1|d^7\underline{L}\rangle + \alpha_2|d^8\underline{L}^2\rangle, \quad (5)$$

with the coefficients $\alpha_0^2 = 0.47$, $\alpha_1^2 = 0.44$, and $\alpha_2^2 = 0.09$. This means that the oxygen ions donate a $\Delta N = \alpha_1^2 + 2\alpha_2^2 = 0.62$ electron to each metal ion. If we assume that the Li–O bond is fully ionic, then the 2*p* band of the oxygen ion will have 0.31 holes. This number is in good agreement with our figure extracted from the O *K*α spectral intensity.

In the case of NiO, the ground-state wave function can be written as

$$|g\rangle = \alpha_0|d^8\rangle + \alpha_1|d^9\underline{L}\rangle + \alpha_2|d^{10}\underline{L}^2\rangle. \quad (6)$$

The α_1^2 lies within the 0.176–0.21 limits, and the α_2^2 lies in the range from 0.005 to 0.006 [12–14]. The experimentally found intensity ratio of the O *K*α spectra of $LiNiO_2$ and NiO is 0.88. Using the coefficients α_1^2 and α_2^2, we find 0.88–0.89 holes per ion in the oxygen 2*p* band.

Note the difference between the holes in $LiNiO_2$ and $LiCoO_2$. In the $LiNiO_2$ oxide, the holes in the oxygen band are doping and delocalized, whereas in the oxygen band of $LiCoO_2$, the holes are covalent, localized at definite atoms, and determine the covalent contribution to the Co–O chemical bond. The difference between the doping and covalent holes was considered in detail using NiO in [15].

3.4. X-Ray Photoelectron Spectra of the Inner Levels of $LiCoO_{2-\delta}$ and Na_xCoO_2

3.4.1. Co 2*p* spectra. The shape of XPS spectra of the inner metal levels in oxides is known to be sensitive to the electronic structure of the compounds, including the valence state of the transition-metal ion and the degree of covalency of the metal-oxygen bond [16]. We shall consider the Co 2*p* spectra, which, as will be seen later, vary substantially depending on the stoichiometry of the $LiCoO_{2-\delta}$ oxide.

Figure 4 shows Co 2*p* XPS spectra of $LiCoO_{2-\delta}$ samples with different stoichiometries, Co_3O_4, Na_xCoO_2, single-crystal CoO, and metallic Co. Also presented is a spectrum of $LiCoO_2$ bombarded by 4.5-eV argon ions. The Co 2*p* spectrum of CoO is reproduced from [17].

In addition to the two spin–orbit components, Co $2p_{3/2}$ and $2p_{1/2}$, the spectra exhibit satellites due to the charge transfer effect. While the main line (*A*) is characterized primarily by the $2p^53d^7\underline{L}$ configuration of the final state in photoemission, the *C* satellite should correspond to the sum of the $2p^53d^6$ and $2p^53d^8\underline{L}^2$ configurations.

The *C* satellite in the spectra of the stoichiometric $LiCoO_2$ is 9.5 eV distant from the Co $2p_{3/2}$ maximum, and the similar Co $2p_{1/2}$ satellite is separated by 10 eV from the Co $2p_{1/2}$ maximum. Oxygen deficiency results in a shift of the spectral maxima toward higher binding energies and in the formation of an additional satellite (*B*), which is about 4.5 eV away from the main spectral line. The intensity of this satellite increases with decreasing oxygen content.

The appearance of the additional satellite *B* can be assumed to originate from the formation of Co^{2+} ions. After the bombardment of $LiCoO_2$ by argon ions, the spectrum changes substantially and almost coincides with that of single-crystal CoO, in which the cobalt ions are divalent. This means that the samples prepared in oxygen-deficient conditions contain Co^{2+} ions. It should be pointed out that the spectra of reduced samples cannot be resolved into a simple sum of the spectra of CoO and stoichiometric $LiCoO_2$. However, the 2%

content of the Co^{2+} ions found from the magnetic susceptibility measurements on the $LiCoO_{2-\delta}$ sample prepared at a partial oxygen pressure $\log p_{O_2} = -3.1$ is hardly capable of effecting such a strong change in the XPS Co 2*p* spectrum. In our opinion, the reason for this difference is as follows.

The magnetic susceptibility measurements relate to the bulk of the sample. The thickness of the layer analyzed using XPS is measured in tens of nanometers. The spectra were obtained on a sample broken in vacuum. The sample breaks, however, over grain boundaries, where the content of divalent cobalt is apparently higher than that in the grain bulk. Therefore, the change in the spectra induced by oxygen deficiency is substantially larger than follows from magnetic susceptibility data.

Nonstoichiometry on the oxygen sublattice shifts not only the Co 2*p* levels but also those of the other lines toward higher binding energies (Table 2). This effect cannot be accounted for by the chemical shift; it should be assigned to the shift of the Fermi level within the band gap. This shift can be caused by the formation of impurity levels inside the band gap. It should be pointed out that impurity levels in nonstoichiometric $LiCoO_{2-\delta}$ are quite probable, because the escape of oxygen from a cell gives rise to the formation of additional XPS lines, which indicate the appearance of nonstructural oxygen.

The Co 2*p* XPS spectrum of Na_xCoO_2 virtually does not differ from the spectrum of stoichiometric $LiCoO_2$. This means that the ground-state electronic configuration in Na_xCoO_2 is the same as in $LiCoO_2$, namely, d^6. The deficiency of the alkali metal ions is compensated by a change in the population of the 2*p* oxygen band. Interaction of the spins of holes in the 2*p* oxygen band with those of the 3*d* electrons apparently brings about the formation of local magnetic moments and, hence, a change in the behavior of the magnetic susceptibility.

$LaCoO_3$, in which all cobalt ions are trivalent, may serve as an analog of $LiCoO_2$. Substitution of divalent strontium ions for the trivalent ions of lanthanum in the $La_{1-x}Sr_xCoO_3$ oxide should produce tetravalent cobalt ions. In the limit of $x = 1$ (the $SrCoO_3$ compound), cobalt should be tetravalent, according to the simple ion model.

Studies of x-ray absorption spectra by Potze *et al.* [18] revealed that the ground state of $SrCoO_3$ is an intermediate-spin state ($t_{2g}^4 e_g^1$, $S = 3/2$). However, the dominant configuration is $d^6\underline{L}$ rather than d^5, because the charge transfer energy $\Delta < 0$. This statement agrees not only with the results of photoelectron and absorption studies [19] but also with magnetic susceptibility data [20].

3.4.2. Co 3*s* spectra. A change in the satellite structure occurring during reduction can also be seen in the 3*s* spectra. The 3*s* levels in transition-metal compounds are known to exhibit exchange splitting. The magnitude of this splitting is proportional to $(2S + 1)$, where S is the local spin of the 3*d* electrons in the ground state. In

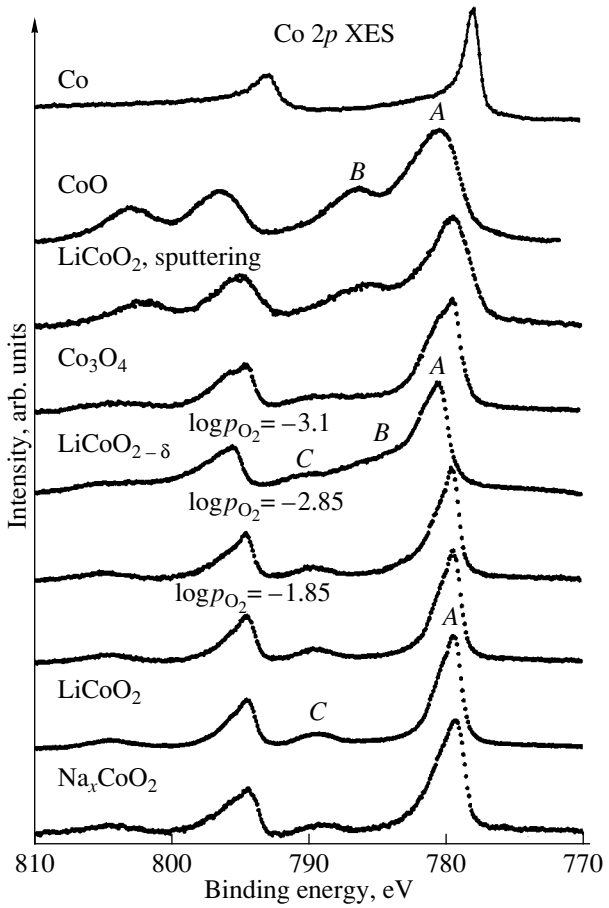

Fig. 4. Co 2*p* XPS spectra of CoO, Co_3O_4, stoichiometric $LiCoO_2$, $LiCoO_{2-\delta}$ annealed at partial oxygen pressures $\log p_{O_2} = -1.85$, -2.85, and -3.1 and of Na_xCoO_2. Also shown are the spectra of $LiCoO_2$ subjected to argon ion milling and of metallic Co.

Table 2. Binding energies of inner-shell electrons, eV

Sample/oxygen pressure	Co 2*p*	Co 3*p*	Co 3*s*	O 1*s*	Li 1*s*
CoO	780.4	59.9	101.9	529.5	–
Co_3O_4	779.9	61.3	102.7	530.1	–
$LiCoO_2$	779.4	60.8	102.3	529.1	54.1
$LiCoO_{2-\delta}$ ($\log p_{O_2} = -1.85$)	779.5	60.7	102.3	529.1	54.0
$\log p_{O_2} = -2.85$	779.6	60.7	102.3	529.1	54.1
$\log p_{O_2} = -3.1$	780.5	61.9	103.4	530.2	55.0
Na_xCoO_2	779.2	59.9	102.1	528.7	–

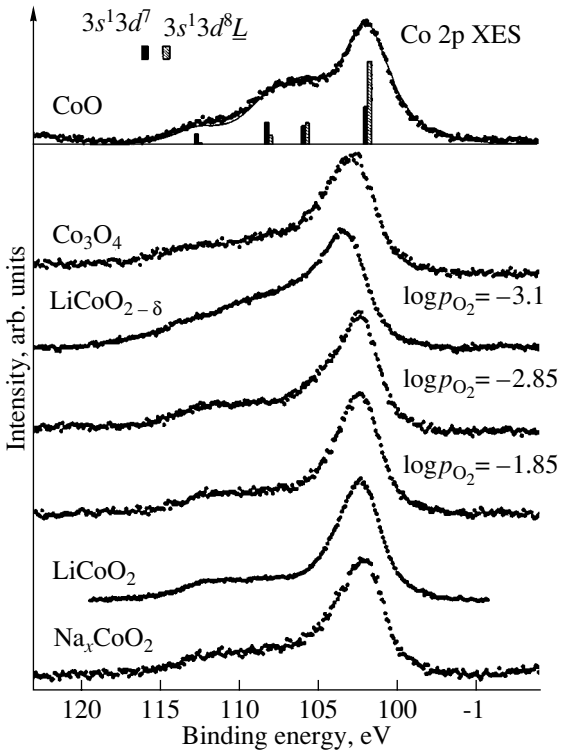

Fig. 5. Co 3*s* XPS spectra of CoO, Co_3O_4, stoichiometric $LiCoO_2$, $LiCoO_{2-\delta}$ annealed at partial oxygen pressures $\log p_{O_2} = -1.85$, -2.85, and -3.1, and of Na_xCoO_2. Also shown for CoO are line spectra showing the contributions of the $3s^13d^7$ and $3s^13d^8\underline{L}$ final states to the formation of the main spectral lines and satellites. The solid line was obtained by broadening the line spectra.

addition to the exchange interaction, charge transfer processes also play an important role.

Figure 5 shows spectra of the CoO monoxide, which were drawn taking into account satellites by using a simple two-level model [21, 22] assuming a mixture of the $3s^13d^7$ and $3s^13d^8\underline{L}$ configurations in the final state. The calculation was carried out for the following parameters: the charge transfer energy $\Delta = 2.9$ eV, the Coulomb interaction energy between the hole at the 3*s* level and 3*d* electrons $U_{sd} = 6.0$ eV, and the transfer integral $T = 2.9$ eV. The Co 3*s* spectrum of single-crystal CoO was obtained in [18]. The calculated line spectra of the $3s^13d^8\underline{L}$ configuration are shown by a dashed line; those of the $3s^13d^7$ configuration, by a solid line. The envelope is the result of a transformation of line spectra into a mixture of a Lorentzian and a Gaussian. Each configuration splits into a high- and a low-spin component.

The low-spin $3d^6$ configuration ($S = 0$) of stoichiometric $LiCoO_2$ does not split. However, the Co 3*s* spectrum exhibits a satellite structure in the region from 105 to 115 eV. This structure can be explained in terms of the charge transfer concept if one takes into account the $3d^6$, $3d^7\underline{L}$, and $3d^8\underline{L}^2$ configurations.

The Co 3*s* XPS spectra of Na_xCoO_2 virtually do not differ from those of stoichiometric $LiCoO_2$ (Fig. 5). Hence, the ground state of Na_xCoO_2 can be represented as a sum of the ground states of the Co^{3+} trivalent ion and the formally tetravalent Co^{4+} ion:

$$|g\rangle = (1-x)|d^6\rangle + x|d^6\underline{L}\rangle. \quad (7)$$

Here, $d^6\underline{L}$ denotes the ground-state configuration for the formally tetravalent cobalt. The ground-state configuration of a truly tetravalent cobalt should look the same as d^5. However, assuming a high-spin ground state, the presence of the d^5 configuration should result in exchange splitting between the ^7S and ^5S components of the XPS spectra of about 6.2–6.5 eV, which is not observed for Na_xCoO_2.

4. CONCLUSIONS

Thus, we have carried out studies of the electronic structure; magnetic properties of the $LiCoO_{2-\delta}$ and Na_xCoO_2 nonstoichiometric oxides, including measurement of soft O $K\alpha$ and Co $L\alpha$ x-ray emission spectra; and XPS spectra of the valence band and of the inner Co 2*p* and 3*s* levels. The results obtained permit the following conclusions to be drawn:

(1) The valence state of cobalt ions in $LiCoO_2$, according to measurements of the Co 2*p* XPS spectra, is 3+.

(2) The Co 3*s* XPS spectrum of $LiCoO_2$ does not exhibit exchange splitting, which confirms the low-spin configuration ($S = 0$) of the ground state.

(3) The holes created in the substitution of lithium for cobalt are localized in the Co 3*s* band.

(4) According to our estimates, the number of holes in the oxygen 2*p* band, which are due to the covalency of the cobalt–oxygen bond, is 0.46 per oxygen atom.

(5) The O 2*p* states in $LiCoO_2$, which are responsible for the O $K\alpha$ XES spectra, lie closer to the Fermi level than those in CoO, which implies a stronger Co-3*d*–O-2*p* hybridization in $LiCoO_2$ compared with CoO.

(6) Oxygen deficiency in reduced $LiCoO_{2-\delta}$ oxides gives rise to the formation of divalent cobalt ions.

(7) Deficiency of the alkali metal in Na_xCoO_2 results in the formation of holes in the oxygen 2*p* band, i.e., in the $3d^6\underline{L}$ ground-state configuration.

ACKNOWLEDGMENTS

This study was support by the Russian Foundation for Basic Research, project nos. 99-03-32503 and 00-15-96575.

REFERENCES

1. P. F. Bongers, Ph.D. Thesis (University of Leiden, The Netherlands, 1957).
2. J. van Elp, J. L. Wieland, H. Eskes, *et al.*, Phys. Rev. B **44** (12), 6090 (1991).
3. J. P. Kemp and P. A. Cox, J. Phys.: Condens. Matter **2** (48), 9652 (1990).
4. V. R. Galakhov, E. Z. Kurmaev, S. Uhlenbrock, *et al.*, Solid State Commun. **99** (4), 221 (1996).
5. F. M. F. de Groot, M. Abbate, J. van Elp, *et al.*, J. Phys.: Condens. Matter **5**, 2277 (1993).
6. M. T. Czyžyk, R. Potze, and G. A. Sawatzky, Phys. Rev. B **46** (7), 3729 (1992).
7. T. Mozokawa, A. Fujimori, H. Namatame, *et al.*, Phys. Rev. Lett. **67** (12), 1638 (1991).
8. L. A. Montoro, M. Abbate, and J. M. Rosolen, Electrochem. Solid-State Lett. **3** (9), 410 (2000).
9. J. A. Bearden, Rev. Mod. Phys. **39**, 1 (1967).
10. V. S. Gorshkov, D. G. Kellerman, and V. V. Karelina, Zh. Fiz. Khim. **73** (6), 1041 (1999).
11. P. Kuiper, K. Kruizinga, J. Ghijsen, *et al.*, Phys. Rev. Lett. **62** (2), 221 (1989).
12. G. van der Laan, J. Zaanen, and G. A. Sawatzky, Phys. Rev. B **33** (6), 4253 (1986).
13. J. van Elp, H. Eskes, P. Kuiper, and G. A. Sawatzky, Phys. Rev. B **45** (4), 1612 (1992).
14. A. Tanako and J. Takeo, J. Phys. Soc. Jpn. **63** (7), 2788 (1994).
15. S. Hüfner, P. Steiner, I. Sander, *et al.*, Z. Phys. B **83** (2), 185 (1991).
16. G. van der Laan, G. Westa, C. Haas, and G. Sawatzky, Phys. Rev. B **23** (9), 4369 (1981).
17. S. Uhlenbrock, Doktordissertation (Universität Osnabrück, Germany, 1994).
18. R. H. Potze, G. A. Sawatzky, and M. Abbate, Phys. Rev. B **51** (11), 11501 (1995).
19. T. Saitoh, T. Mizokawa, A. Fujimori, *et al.*, Phys. Rev. B **56** (3), 1290 (1997).
20. H. Taguchi, M. Shimada, and M. Koizumi, J. Solid State Chem. **29** (2), 221 (1979); **33**, 169 (1980).
21. V. R. Galakhov, S. Uhlenbrock, S. Bartkowski, *et al.*, http://xxx.lanl./gov/abs/cond-mat/9903354.
22. V. R. Galakhov, L. D. Finkelstein, D. A. Zatsepin, *et al.*, Phys. Rev. B **62** (8), 4922 (2000).

Translated by G. Skrebtsov

Physics of the Solid State, Vol. 44, No. 2, 2002, pp. 274–277. Translated from Fizika Tverdogo Tela, Vol. 44, No. 2, 2002, pp. 265–268.

SEMICONDUCTORS AND DIELECTRICS

Oscillator Strength of Electron-Type Color Centers in KCl Single Crystals Irradiated with Electrons and Protons

M. M. Mikhaĭlov, V. M. Ardyshev, and M. V. Belyakov

Tomsk State University of Control Systems and Radioelectronics, Tomsk, 634050 Russia

Received January 16, 2001

Abstract—The absorption spectra of KCl single crystals irradiated with electrons and protons at energies of 15 and 100 keV and a particle flux ranging from 5×10^{12} to 10^{15} cm^{-2} are investigated. The absorption bands attributed to simple (F, F_a, K) and complex (M, R_2, R_4, N) color centers are identified in the spectra. The correlation dependences of the absorption coefficients for M, R_2, and R_4 centers on the absorption coefficient of F centers and the correlation dependences of the absorption coefficients for R_2 and R_4 centers on the absorption coefficient of M centers are established. The oscillator strengths are calculated for M, R_2, and R_4 color centers. © *2002 MAIK "Nauka/Interperiodica".*

1. INTRODUCTION

Alkali halide crystals are model objects in solid-state radiation physics. In the 1950s–1970s, considerable attention was given to the investigation of the regularities observed in the generation and accumulation of different-type color centers in these crystals. The results obtained at that time are currently used in the radiative study of materials. Earlier, we investigated the combined effects of different radiations (effects of additivity, synergetic effects, etc.) on materials used in space technology under conditions of simultaneous or sequential action of protons and electrons with energies of tens and hundreds of kiloelectron-volts [1]. However, it is difficult to elucidate the mechanisms of the accumulation of color defects under the above conditions and their influence on the degradation of the performance characteristics for actual materials with a complex composition and a complex structure. In recent years, these studies have been performed with alkali halide crystals [2–4]. Despite the large number of works dealing with the accumulation of color centers in alkali halide crystals, some of the parameters and coefficients necessary for the calculations have either not been determined or are contradictory [5, 6]. In particular, the oscillator strengths of complex electron-type color centers remain unknown. This hampers the calculation of their concentration and interpretation of the results. The purpose of the present work was to analyze the correlations between the absorption coefficients at maxima of F, M, R_2, and R_4 color centers and to estimate the oscillator strengths of these centers in KCl single crystals irradiated with electrons and protons.

2. EXPERIMENTAL TECHNIQUE

The procedures of preparation and irradiation of the samples with protons and electrons, *in situ* recording of the induced absorption spectra under vacuum (at the site of irradiation of the samples), decomposition of the spectra into individual components on the basis of available data on the location of the maximum (K_m) and the half-width ($H_{1/2}$) of the spectral bands attributed to simple and complex defects, and the irradiation conditions were described earlier in [4–6]. The energies of the protons and electrons were equal to 15 and 100 keV, the particle flux density was 3×10^{11} cm^{-2} s^{-1}, and the particle flux for different samples was varied from 5×10^{12} to 10^{15} cm^{-2}. The energy and the flux of particles were chosen in such a way as to obtain the relationships between the absorption coefficients of different-type color centers in the maximum permissible range. The accuracy of measuring the absorption coefficient was no worse than 1% in the UV and visible ranges and no worse than 4% in the near-IR range of the spectrum [7].

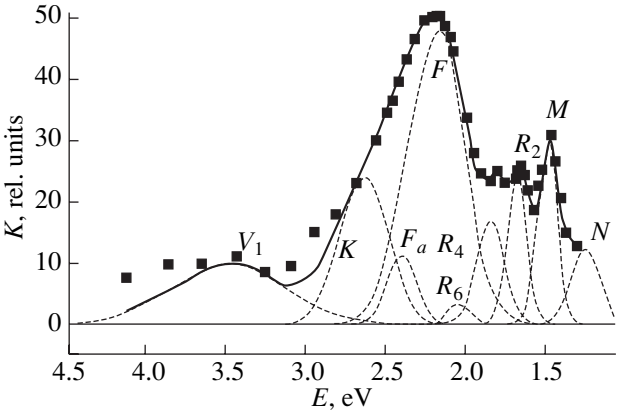

Fig. 1. Experimental (points) and calculated (solid line) absorption spectra and absorption bands of intrinsic point defects (dashed lines) of a KCl single crystal irradiated with protons at an energy of 100 keV and a flux of 8.6×10^{14} cm^{-2}.

3. RESULTS

Figure 1 displays the experimental absorption spectrum of the KCl single crystal irradiated with protons and the dependence $K = f(E)$ calculated from the superposition of individual absorption bands (dashed lines). The bands associated with the F, F_a, M, N, R_2, R_4, R_6, K, and V_1 absorption centers are resolved in the spectra. The calculated and experimental data are in good agreement. Similar spectra were obtained at different fluxes of electrons and protons, i.e., at different color center concentrations and absorption coefficients. The accumulation kinetics and the relationships between the absorption coefficients were analyzed only for F, M, R_2, and R_4 centers.

The dependences of the absorption coefficients at maxima of the absorption bands assigned to M, R_2, and R_4 centers on the absorption coefficient at a maximum of the band attributed to F centers are shown in Fig. 2. It can be seen that, under the given irradiation conditions, these dependences have two portions. In the first portion, when the absorption coefficient at a maximum of the band attributed to F centers (K_F) is less than 30 rel. units, the dependences of the absorption coefficients at maxima of the bands associated with the M, R_2, and R_4 color centers (the K_M, K_{R_2}, and K_{R_4} coefficients) on the absorption coefficient K_F can be represented by the linear function

$$K_M, K_{R_2}, K_{R_4} = AK_F. \quad (1)$$

In the second portion ($K_F > 30$ rel. units), these dependences can be described by the power law

$$K_M, K_{R_2}, K_{R_4} = BK_F^n. \quad (2)$$

Figure 3 depicts the dependences of K_{R_2} and K_{R_4} on the absorption coefficient K_M at a maximum of the band assigned to M centers. These dependences can be well approximated by the linear function

$$K_{R_2}, K_{R_4} = CK_M. \quad (3)$$

The table presents the parameters A, B, and C determined by the least-squares method according to the data shown in Figs. 2 and 3.

4. DISCUSSION

According to modern concepts, F color centers in alkali halide crystals are considered anionic vacancies with a trapped electron, M centers consist of two F centers located in the adjacent anionic vacancies, and R_2 and R_4 color centers are treated as three neighboring F centers differently oriented in the lattice.

Reasoning from the described structure, it can be assumed that there is a correlation between the concentrations or the absorption coefficients of the aforementioned centers. This assumption is supported by the

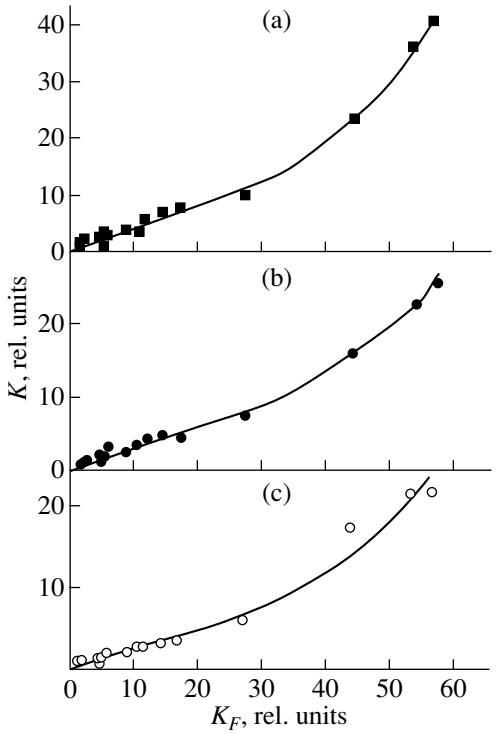

Fig. 2. Dependences of the absorption coefficient at maxima of the bands attributed to (a) M, (b) R_2, and (c) R_4 centers on the absorption coefficient at a maximum of the band assigned to F color centers of the irradiated KCl single crystals.

experimental dependences of the absorption coefficients K_M, K_{R_2}, and K_{R_4} on the absorption coefficients K_F and K_{R_2} and the experimental dependence of the absorption coefficient K_{R_4} on the absorption coefficient K_M. It should be noted that two (linear and power) portions in the dependences of the absorption coefficients K_M, K_{R_2}, and K_{R_4} on K_F have never been previously observed. In our opinion, this behavior of the dependences is due to the contribution of the surface to the accumulation of color centers under irradiation.

Earlier, the absorption spectra of irradiated KCl single crystals were always recorded in the atmosphere. In the case when the energy of charged particles is not

Correlation parameters and oscillator strengths of different-type color centers in KCl crystals irradiated with electrons and protons

Color center type	Parameter				Oscillator strength
	A	B	n	C	
M	0.44	1.5×10^{-2}	2.00	–	0.45 ± 0.15
R_2	0.31	6.1×10^{-2}	1.48	0.64	0.34 ± 0.07
R_4	0.20	9.9×10^{-3}	1.88	0.44	0.6 ± 0.2

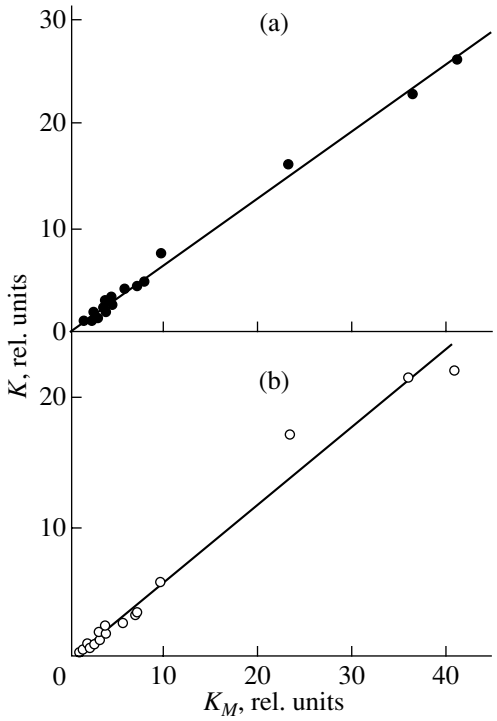

Fig. 3. Dependences of the absorption coefficient at maxima of the bands attributed to (a) R_2 and (b) R_4 centers on the absorption coefficient at a maximum of the band assigned to *M* color centers of the irradiated KCl crystals.

very high, a considerable amount of color centers is generated in the near-surface layer and on the surface. Consequently, they can transform or decay upon interaction with atmospheric oxygen. In our case, the absorption spectra were recorded under vacuum; therefore, the contribution of the surface color centers to their total concentration was taken into account.

Under the assumption that, in a KCl single crystal exposed to irradiation with electrons and protons, color defects are generated as a result of the decay of electron excitations [8], the correlation dependences can be obtained from the following system of equations:

$$\frac{dN_{EV}}{dt} = G_{EE} - \frac{N_{EE}}{\tau_{EE}} - \alpha N_{EV} N_V, \quad (4)$$

$$\frac{dN_F}{dt} = \alpha N_{EE} N_V, \quad (5)$$

$$\frac{dN_M}{dt} = \beta\left(\frac{N_F}{N_0}\right)\alpha N_{EE} N_V, \quad (6)$$

$$\frac{dN_R}{dt} = \gamma\left(\frac{N_M}{N_0}\right)\alpha N_{EE} N_V. \quad (7)$$

Here, N_{EE} is the concentration of electron excitations (*EE*); N_F, N_M, and N_R are the concentrations of the *F*, *M*, and *R* color centers, respectively; N_V and N_0 are the concentrations of anionic vacancies and anions, respectively; $G_{EE} = \sigma_i N_0 J$ is the generation term (where σ_i is the ionization cross section and J is the particle flux density); τ_{EE} is the lifetime of electron excitations with respect to unsaturated sinks; α is the coefficient of electron trapping in an anionic vacancy; and β and γ are the configurational factors.

The factors N_F/N_0 and N_M/N_0 determine the probability that the *F* and *M* centers will be generated in the vicinity of the already existing *F* and *M* color centers, respectively. From expressions (4) and (5) with allowance made for expression (3), the relationships $N_M \sim N_F^2$ and $N_R \sim N_F^3$ are derived under the assumption that the color defects are generated throughout the bulk of the irradiated sample.

The experimental results (Figs. 2, 3, table) disagree with these relationships (taking into account the proportionality of the color center concentration to the absorption coefficient at a maximum of the absorption band). This disagreement can be explained by the fact that the mechanisms of color-center generation in alkali halide crystals (including KCl crystals) under irradiation with electrons and protons at energies up to 100 keV differ from those realized under irradiation with high-energy particles.

The dependences of the absorption coefficients for *M*, R_2, and R_4 centers on the absorption coefficient of *F* color centers (Fig. 2) can be conventionally separated into two portions. The first portion ($K_F < 30$ rel. units) corresponds to a more rapid increase in the absorption coefficient K_F with an increase in the irradiation time, i.e., to conditions under which the saturation of K_F is still not attained. This portion is linear for the dependences of the absorption coefficients of all three color centers on the absorption coefficient K_F. It can be assumed that, under these irradiation conditions, the *M*, R_2, and R_4 color centers are generated independently of the *F* centers.

For $K_F > 30$ rel. units, the experimental results cannot be approximated by a linear function. This indicates that the mechanisms of generation of *M*, R_2, and R_4 color centers differ for the first and second portions; i.e., they depend on the *F*-center concentration.

The power character of the dependences K_M, K_{R_2}, $K_{R_4} = BK_F^n$ indicates the complex formation of *M* and *R* centers from the *F* centers. For the *M* color centers, the exponent *n* is equal to 2. This agrees with the known concepts on the structure of the *M* color center consisting of two *F* centers [6, 7]. For the R_2 and R_4 centers, the *n* exponent not only differs from 3 but is less than 2.

Most likely, these values of the *n* exponent are associated with the influence of the surface on the relaxation processes of electron excitations. Under the chosen irradiation conditions, the defective layer is located in the immediate vicinity of the surface (irradiated with

15-keV protons). Therefore, the linear character of the dependences K_M, K_{R_2}, $K_{R_4} = AK_F$ suggests that the contribution from the recombination of electron excitations at the surface levels to the concentration of accumulated color centers is significant.

We determined the oscillator strengths f for these color centers from the experimental data and the Smakula formula [6] by assuming that the changes in K_M, K_{R_2}, and K_{R_4} are caused by the increase in concentration of the relevant defects rather than by the changes in the oscillator strength. The results obtained are presented in the table.

In the case when the oscillator strength f for F centers is taken to be 0.8 [6], the oscillator strength for M centers is equal to $0.56f$. This value is close to 2/3 of the oscillator strength f given in [9]. It should be noted that the f values differ for R_2 and R_4 centers, which is probably reflects their configurations being different in the KCl lattice.

5. CONCLUSIONS

The results obtained in this work can be summarized as follows:

(1) The dependences of the absorption coefficients at maxima of the bands attributed to F, M, R_2, and R_4 color centers in KCl single crystals on the conditions of irradiation with electrons and protons at energies of 15 and 100 keV are determined.

(2) It is found that the dependences of the absorption coefficients at maxima of the bands associated with the M, R_2, and R_4 centers on the absorption coefficient at a maximum of the band assigned to the F centers have two portions described by linear and power functions.

(3) It is established that the dependences of the absorption coefficients at maxima of the bands attributed to R_2 and R_4 centers on the absorption coefficient at a maximum of the band associated with the M centers exhibit a linear character.

(4) The oscillator strengths of the M, R_2, and R_4 color centers in KCl single crystals are estimated at 0.45 ± 0.15, 0.34 ± 0.07, and 0.6 ± 0.2, respectively.

REFERENCES

1. M. M. Mikhaĭlov, *Optical Degradation Forecasting for Temperature Control Coatings of Space Vehicles* (Nauka, Novosibirsk, 1999).
2. M. M. Mikhaĭlov and V. M. Ardyshev, Fiz. Tverd. Tela (St. Petersburg) **40** (11), 2015 (1998) [Phys. Solid State **40,** 1823 (1998)].
3. M. M. Mikhaĭlov, V. M. Ardyshev, and M. V. Belyakov, Fiz. Khim. Obrab. Mater., No. 5, 31 (1998).
4. M. M. Mikhaĭlov and V. M. Ardyshev, Fiz. Khim. Obrab. Mater., No. 3, 9 (1999).
5. L. G. Kositsin, M. M. Mikhaĭlov, and N. Ya. Kuznetsov, Prib. Tekh. Éksp. **4**, 176 (1985).
6. I. A. Parfianovich and É. É. Penzina, *Electron-Type Color Centers in Ionic Crystals* (Vost.-Sib. Knizhnoe Izd., Irkutsk, 1977).
7. A. A. Vorob'ev, *Color Centers in Alkali Halide Crystals* (Tomsk. Gos. Univ., Tomsk, 1968).
8. V. M. Lisitsin, Izv. Tomsk. Politekh. Univ. **303** (2), 7 (2000).
9. C. Z. van Doorn, Phys. Rev. Lett. **4** (3), 236 (1960).

Translated by O. Moskalev

Physics of the Solid State, Vol. 44, No. 2, 2002, pp. 278–281. Translated from Fizika Tverdogo Tela, Vol. 44, No. 2, 2002, pp. 269–271.

SEMICONDUCTORS AND DIELECTRICS

Magnetic-Field-Controlled Polarized Luminescence of $Y_3Al_5O_{12}$–Tb and $Y_3Al_5O_{12}$–Ho Garnets

U. V. Valiev, U. R. Rustamov, and B. Yu. Sokolov

National University of Uzbekistan, Tashkent, 700174 Uzbekistan

Received May 24, 2001

Abstract—The circularly polarized luminescence spectra of $Y_3Al_5O_{12}$–Tb and $Y_3Al_5O_{12}$–Ho garnets are analyzed in the wavelength ranges of the $^5D_4 \longrightarrow {}^7F_5$ transition in the Tb^{3+} ion and the $^5S_2 \longrightarrow {}^5I_8$ transition in the Ho^{3+} ion. It is found that the intensities of the orthogonal circularly polarized components of the series of luminescence lines attributed to the studied garnets differ substantially. The results obtained are interpreted in terms of the mixing of the Tb^{3+} and Ho^{3+} electronic states in an external magnetic field. © *2002 MAIK "Nauka/Interperiodica".*

1. INTRODUCTION

Earlier [1], it was shown that, under certain conditions, the mixing of the electronic states of the Kramers rare-earth ion in an external magnetic field leads to considerable changes in the oscillator strengths of the $4f \longrightarrow 4f$ transitions. For example, the difference between the integrated intensities of the orthogonal circularly polarized components of the secondary emission lines attributed to the $^4S_{3/2} \longrightarrow {}^4I_{15/2}$ transition in the Er^{3+} ion in the $Y_3Al_5O_{12}$–Er garnet was found to be ~15% in the magnetic field $H = 10$ kOe. A more noticeable modulation of the luminescence intensity due to the mixing effect can be expected for non-Kramers Tb^{3+} and Ho^{3+} ions in garnets, because the mixing of electronic states in a magnetic field H plays the decisive role in the formation of the magnetization-dependent properties of crystals containing these ions [2]. Our measurements demonstrated that the magnetic field strongly affects the intensity of circularly polarized components of the secondary emission lines associated with the radiative transitions in Tb^{3+} and Ho^{3+} ions in the $Y_3Al_5O_{12}$ matrix but leaves the spectral location of these lines virtually unchanged; in other words, we deal here with field-controlled luminescence of the garnets under investigation.

2. SAMPLES AND MEASUREMENT PROCEDURE

The experiments were performed with $Y_3Al_5O_{12}$–Tb and $Y_3Al_5O_{12}$–Ho single crystals in which the content of rare-earth ions was ~5 wt %. We analyzed the circularly polarized luminescence spectra and the spectra of the degree of magnetic circular polarization of the luminescence (MCPL) attributed to the $^5D_4 \longrightarrow {}^7F_5$ transition in the Tb^{3+} ion and the $^5S_2 \longrightarrow {}^5I_8$ transition in the Ho^{3+} ion. Both excitation and observation of the luminescence were carried out using the transmission method in a magnetic field up to 10 kOe with the longitudinal magnetization with respect to the direction of light propagation. The degree of magnetic circular polarization of luminescence can be defined by the formula $P = (I_+ - I_-)/(I_+ + I_-)$, where I_+ and I_- are the intensities of two orthogonal circularly polarized components of the luminescence line. The value of P was measured according to a procedure involving polarization modulation of the secondary emission by a piezoelectric modulator [1, 3]. In the spectral measurements, the optical resolution was ~1 cm^{-1} for the spectra of I_+ and I_- and ~2 cm^{-1} for the P dispersion. In all the experiments, the relative error in measuring the quantities I_+, I_-, and P was no more than 5%.

Since the $^5S_2$ multiplet structure of the Ho^{3+} ion was unknown, we examined the optical absorption spectra of the holmium yttrium aluminate garnet in the vicinity of the $^5I_8 \longrightarrow {}^5S_2$ transition. In order to determine the location of the actual $^5S_2$ multiplet sublevels, we used the available data on crystalline splitting of the ground $^5I_8$ multiplet of the Ho^{3+} ion in the $Y_3Al_5O_{12}$ matrix [4].

3. RESULTS AND DISCUSSION

The circularly polarized luminescence spectra and the spectra of the degree of magnetic circular polarization of the luminescence associated with the $^5D_4 \longrightarrow {}^7F_5$ transition in the terbium yttrium aluminate garnet are displayed in Figs. 1 and 2, respectively. Judging from the luminescence lines (*1–4*) shown in Figs. 1 and 2, the $Y_3Al_5O_{12}$–Tb garnet is characterized by a high degree of magnetic circular polarization of the luminescence. For example, its magnitude at $H = 5$ kOe and $T = 90$ K reaches ~0.4 (line *2*). Note that, even at low tem-

1063-7834/02/4402-0278$22.00

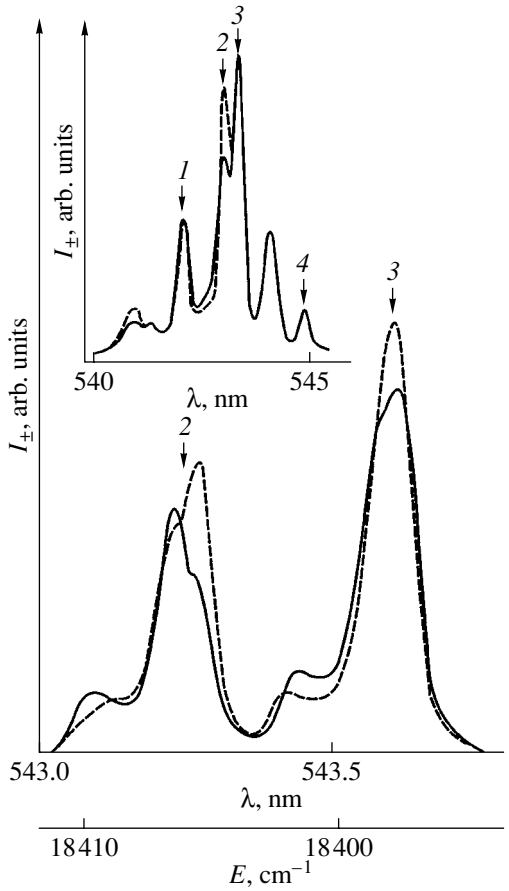

Fig. 1. A fragment of the circularly polarized luminescence spectrum of the $Y_3Al_5O_{12}$–Tb garnet at T = 90 K in the magnetic field H = 5 kOe. The solid and dashed lines correspond to the intensities of the left-hand and right-hand circularly polarized luminescence components, respectively. The inset shows the circularly polarized luminescence spectrum of the $Y_3Al_5O_{12}$–Tb garnet at T = 300 K and H = 10 kOe (the solid and dashed lines represent the orthogonal MCPL components).

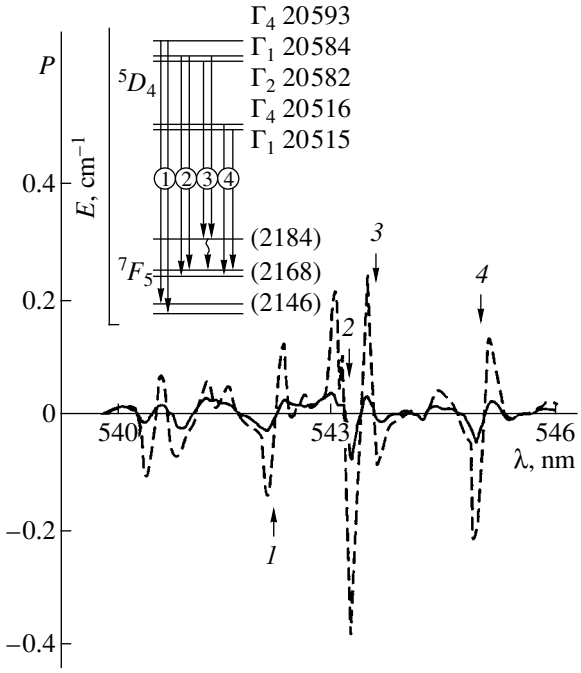

Fig. 2. Spectrum of the degree of magnetic circular polarization of luminescence in the $Y_3Al_5O_{12}$–Tb garnet in the magnetic field H = 5 kOe at temperatures T = 300 K (solid line) and T = 90 K (dashed line). At the upper left of the figure, the scheme of the $^5D_4 \longrightarrow {}^7F_5$ magnetooptically active transitions in the Tb^{3+} ion is shown (the energy spectrum of the $^5D_4$ multiplet is taken from [9]). The parenthetic numbers are the experimental energies of the $^7F_5$ multiplet sublevels. Mixing in the field H of the $^7F_5$ multiplet states is shown by a wavy line. Numerals at the arrows denote the numbering of the corresponding luminescence lines.

peratures under paramagnetic saturation conditions, the typical P value for rare-earth compounds is approximately equal to 10^{-1} [5, 6].

As can be seen from Fig. 1, there exists a substantial difference in the spectra of orthogonal circularly polarized luminescence components of line *2*. For this luminescence line, the integrated intensities I_+ and I_- at any temperature in the magnetic field H = 10 kOe differ by a factor of approximately 1.4. It is clearly seen from the spectra measured at T = 90 K that line *2* has a doublet structure and that the magnetic field most strongly affects the intensities I_+ and I_- of the long-wavelength component of the doublet (Fig. 1). At the same time, the difference between the intensities I_+ and I_- for line *3* becomes noticeable only at low temperatures. A similar difference in the spectra of the I_+ and I_- intensities is observed for line *4* at T = 90 K (this line is not shown in Fig. 1). As regards line *1*, its orthogonal circularly polarized luminescence components at T = 90 K (and at room temperature) are equal in intensity and only slightly differ in energy.

It is known that the energy shift of the components I_+ and I_- of the luminescence line is attributed to the Zeeman splitting of states involved in the radiative transition. Moreover, admixing of other closely spaced electronic states of the rare-earth ion in a magnetic field H to the states participating in the optical transition leads to a difference in the oscillator strengths of the orthogonal components of the corresponding luminescence line, and this difference does not depend on the temperature T. On the other hand, the difference in the thermal equilibrium population of the electronic states involved in the radiative transition results in a temperature dependence of the difference $(I_+ - I_-)$. On this basis and with allowance made for the specific behavior of the dispersion and temperature dependences of the A, B, and C terms in the MCPL spectra [7, 8] (Fig. 2), we can conclude that, in the MCPL spectra of the $Y_3Al_5O_{12}$–Tb garnet, lines *1* and *2* are associated with the singlet–quasi-doublet transitions, whereas lines *3*

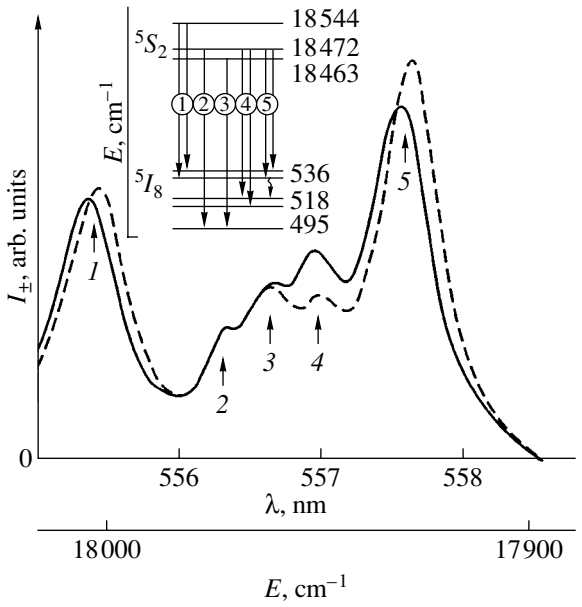

Fig. 3. A fragment of the circularly polarized luminescence spectrum of the $Y_3Al_5O_{12}$–Ho garnet at T = 300 K in the magnetic field H = 10 kOe. Notations are the same as in Fig. 1. At the upper left of the figure, the scheme of the $^5S_2 \longrightarrow {}^5F_8$ radiative transitions in the Ho^{3+} ion is shown (notations are the same as in Fig. 2).

and *4* are attributed to either the quasi-doublet–singlet transitions or the quasi-doublet–quasi-doublet transitions.

By using the results of our analysis of the spectra shown in Figs. 1 and 2 and the available data on the energy spectrum of the $^5D_4$ multiplet in the Tb^{3+} ion in the $Y_3Al_5O_{12}$ matrix [9], we constructed a scheme for the $^5D_7 \longrightarrow {}^7F_5$ magnetooptic radiative transitions (see Fig. 2). In this case, the magnetooptically actual $^5D_4$ multiplet states were treated as states of the quasi-doublets Γ_2, Γ_1 and Γ_1, Γ_4 and the singlet Γ_4.

Thus, according to the above model of the $^5D_4 \longrightarrow {}^7F_5$ transition, the considerable change in the intensities I_+ and I_- of the longer-wavelength component of line *2* in the magnetic field is associated with a strong admixing of the states of the most closely spaced singlet level of the Tb^{3+} ion to the upper sublevel of the quasi-doublet (E = 2168 cm^{-1}) involved in the $^7F_5$ multiplet.[1]

A qualitatively similar situation is observed for a series of transitions between the $^5S_2$ and $^5I_8$ multiplet states of the Ho^{3+} ion in the $Y_3Al_5O_{12}$–Ho garnet. Figure 3 shows a fragment of the circularly polarized luminescence spectrum of the $Y_3Al_5O_{12}$–Ho garnet in the wavelength range of the $^5S_2 \longrightarrow {}^5I_8$ transition. It can be seen that the integrated intensities I_+ and I_- for lines *1*, *4*, and *5* differ considerably even at room temperature (a similar difference is observed for the MCPL spectrum at T = 90 K). The difference in the spectra of I_+ and I_- for lines *1*, *4*, and *5* has defied explanation within the model of a quasi-doublet–singlet transition under the assumption that the difference $(I_+ - I_-)$ is associated with the difference in the thermal equilibrium population of the quasi-doublet components. In this case, according to [7, 8], we can write the following relationship: $[(I_+ - I_-)/(I_+ + I_-)] \approx g\beta H/\beta T$, where g is the g factor of the quasi-doublet, β is the Bohr magneton, and k is the Boltzmann constant. In order to obtain the observed difference $(I_+ - I_-)$ for lines *1*, *4*, and *5* at T = 300 K, we assume that the quasi-doublet is characterized by an improbably large g factor. This, in turn, should lead to more pronounced Zeeman splitting of the corresponding luminescence lines as compared to that determined in the experiment.

The scheme of $^5S_2 \longrightarrow {}^5I_8$ radiative transitions in the Ho^{3+} ion is shown in Fig. 3. The scheme was constructed based on the results of MCPL measurements in the $Y_3Al_5O_{12}$–Ho garnet and the data on the energy spectrum of the $^5S_2$ multiplet, which were obtained from the optical absorption spectra of the $Y_3Al_5O_{12}$–Ho garnet. As follows from this scheme, the mixing of the states of two quasi-doublets located in the upper part of the ground multiplet of the Ho^{3+} ion in a magnetic field H results in a noticeable difference between the oscillator strengths of transitions *1*, *4*, and *5* in the orthogonal polarization.

4. CONCLUSION

The results obtained allowed us to conclude that the strong effect of the magnetic field on the oscillator strengths of the $4f \longrightarrow 4f$ transitions is a rather common phenomenon in rare-earth systems with a quasi-doublet structure of the energy spectrum. The contribution of the mixing, which is usually ignored, can play a significant role in magnetooptics of these systems in the vicinity of the corresponding lines of absorption or luminescence.

ACKNOWLEDGMENTS

This work was supported by the International Association of Assistance for the promotion of cooperation with scientists from the New Independent States of the former Soviet Union (INTAS), project no. 097-0366.

[1] The noticeable difference in the spectra of I_+ and I_- for line *2* cannot be explained by mixing of the $^5D_4$ multiplet states, because, according to [8], a similar effect was not observed in the MCPL spectra of the $Y_3Al_5O_{12}$–Tb garnet upon the $^5D_4 \longrightarrow {}^7F_6$ transition in the Tb^{3+} ion.

REFERENCES

1. Sh. U. Abdullaev, U. V. Valiev, and B. Yu. Sokolov, Opt. Spektrosk. **87** (3), 419 (1999) [Opt. Spectrosc. **87**, 386 (1999)].
2. A. K. Zvezdin, V. M. Matveev, A. A. Mukhin, and A. I. Popov, *Rare Earth Ions in Magnetic-Ordered Crystals* (Moscow, 1985).
3. U. V. Valiev, T. Asilov, and R. A. Salyukov, Prib. Tekh. Éksp. **4**, 87 (1994).
4. V. Nekvasil, Phys. Status Solidi B **94**, K41 (1979).
5. E. L. Ivchenko, E. V. Maksimov, and V. N. Medvedev, Opt. Spektrosk. **47** (6), 1096 (1979) [Opt. Spectrosc. **47**, 609 (1979)].
6. V. S. Zapasskiĭ and P. P. Feofilov, Opt. Spektrosk. **41** (6), 1051 (1976) [Opt. Spectrosc. **41**, 620 (1976)].
7. V. S. Zapasskiĭ and P. P. Feofilov, Usp. Fiz. Nauk **116** (1), 41 (1975) [Sov. Phys. Usp. **18**, 323 (1975)].
8. Sh. U. Abdullaev, U. V. Valiev, D. R. Dzhuraev, and V. Nekvasil, Opt. Spektrosk. **84** (3), 471 (1998) [Opt. Spectrosc. **84**, 412 (1998)].
9. R. Baurer, J. Heber, and D. Mateika, Z. Phys. B **64**, 201 (1986).

Translated by N. Korovin

Physics of the Solid State, Vol. 44, No. 2, 2002, pp. 282–285. Translated from Fizika Tverdogo Tela, Vol. 44, No. 2, 2002, pp. 272–274.

SEMICONDUCTORS AND DIELECTRICS

Specific Features of Anion Transfer in HoF_3 Crystals at High Temperatures

N. I. Sorokin*, B. P. Sobolev*, and M. W. Breiter**

** Shubnikov Institute of Crystallography, Russian Academy of Sciences, Leninskiĭ pr. 59, Moscow, 117333 Russia*

*** Technical University, Vienna, Austria*

Received June 14, 2001

Abstract—The anionic conductivity of HoF_3 single crystals with a β-YF_3 structure (orthorhombic crystal system, space group *Pnma*) is investigated over a wide range of temperatures (323–1073 K). The unit cell parameters of HoF_3 crystals are as follows: $a = 0.6384 \pm 0.0009$ nm, $b = 0.6844 \pm 0.0009$ nm, and $c = 0.4356 \pm 0.0005$ nm. It is revealed that the conductivity anisotropy of the HoF_3 crystals is insignificant over the entire temperature range covered. The crossover from one mechanism of ion transfer to another mechanism is observed near the critical temperature $T_c \approx 620$ K. The activation enthalpy of electrical conduction is found to be $\Delta H_1 = 0.744$ eV at $T < T_c$ and $\Delta H_2 = 0.43$ eV at $T > T_c$. The fluorine vacancies are the most probable charge carriers in HoF_3 crystals. The fluorine ionic conductivities at temperatures of 323, 500, and 1073 K are equal to 5×10^{-10}, 5×10^{-6}, and 2×10^{-3} S cm^{-1}, respectively. © *2002 MAIK "Nauka/Interperiodica".*

1. INTRODUCTION

Fluoride materials with a high F^- anion mobility belong to the important class of superionic conductors. Over recent years, a great variety of new superionic materials of different stricture types have been developed, including rare-earth trifluorides RF_3 (where R is a rare-earth element) with a β-YF_3 orthorhombic structure (space group *Pnma*) [1–4]. As far as we know, no works have dealt with the electrical properties of RF_3 orthorhombic crystals at high temperatures. The sole exception is the study carried out by O'Keeffe [1] in the frequency range from 1 to 10 kHz for YF_3 and LuF_3 crystals prepared through molten-salt crystallization. However, knowledge of the electrical properties of RF_3 orthorhombic crystals over a wide temperature range is essential both to the understanding of the specific mechanisms of anionic conduction in these materials and for their practical use in superionic solid devices. In the present work, the high-temperature (up to 1073 K) anion transfer in HoF_3 single crystals was investigated by impedance spectroscopy at frequencies ranging from 0.1 to 10^7 Hz.

2. EXPERIMENTAL TECHNIQUE

The HoF_3 single crystals were grown by planar crystallization from the melt at the Shubnikov Institute of Crystallography, Russian Academy of Sciences. The procedure of crystal growth was described earlier in [4]. The crystals were free from scattering inclusions of oxygen-containing phases and had a β-YF_3 structure, as was confirmed by x-ray diffraction. The unit cell parameters of the HoF_3 single crystal are as follows: $a = 0.6384 \pm 0.0009$ nm, $b = 0.6844 \pm 0.0009$ nm, and $c = 0.4356 \pm 0.0005$ nm.

The samples were prepared in the form of wafers of typical size: the surface area was 5×5 mm and the thickness was equal to 1 mm. The surfaces of the single-crystal samples were subjected to optical finishing and ultrasonic cleaning in acetone (Bransonic 221). The quality of the samples were checked using a Zeiss KL1500-Z optical microscope. The thermal analysis was performed on a Setaram DTA/TG 92-12 instrument at a rate of 5–10 K/min in a flow of gaseous nitrogen in the temperature range from 293 to 1073 K.

The electrical properties were investigated by the loss tangent method with a Solarton 1260 impedometer in the frequency range from 10^{-1} to 10^7 Hz at a voltage of 30 mV. The impedance of the crystals was measured in a flow of gaseous N_2 nitrogen at temperatures ranging from 323 to 1073 K. The electrodes were fabricated from a silver paste and provided blocking of F^- ions. The experimental setup was described in detailed in [5]. The parameters of the anion transfer were calculated according to the formula $\sigma T = A\exp(-\Delta H/kT)$, where ΔH is the activation enthalpy of electrical conduction.

Under normal experimental conditions at high temperatures, the pyrohydrolysis occurring at the surface of HoF_3 single crystals resulted in the formation of a conducting film. This hampered correct determination of the bulk resistivity. Figure 1 shows typical results of the electrical measurements performed without resorting to special precautions. The pyrohydrolysis of HoF_3 single crystals can be caused by the presence of water traces in the ambient atmosphere. In our experiments, we took special precautions, such as ultrasonic cleaning

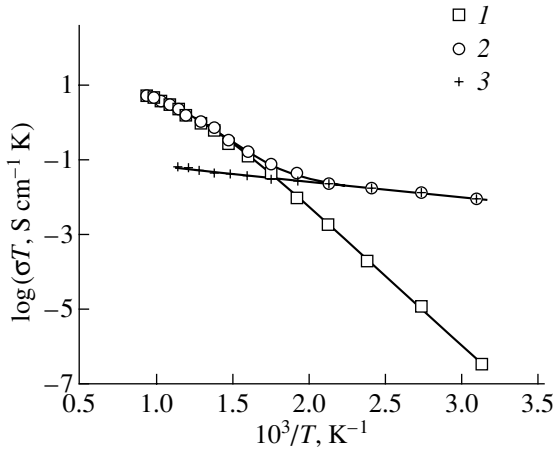

Fig. 1. Effect of pyrohydrolysis on the electrical conductivity of the HoF_3 single crystal: (*1*) heating, bulk resistivity R_b; (*2*) cooling, impedance $R_b + R_f$; and (*3*) cooling, resistivity of the film R_f.

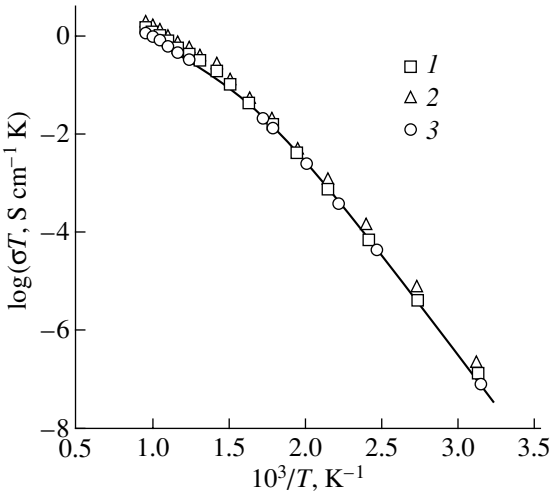

Fig. 2. Temperature dependence of the anionic conductivity for HoF_3 single crystals: (*1*) the sample aligned parallel to the *b* axis, (*2*) the sample oriented normally to the *b* axis, and (*3*) the unoriented sample.

of the samples, measurements in a flow of purified nitrogen and in a wider frequency range in order to separate the contribution of the bulk resistivity of the single crystal from the contribution of the resistivity of the film, and others. These efforts made it possible to carry out high-temperature investigation of the electrolytic properties of HoF_3 single crystals.

3. RESULTS AND DISCUSSION

Figure 2 displays the temperature dependences of the ionic conductivity of the HoF_3 single-crystal samples in different orientations. For all the samples under investigation, the reproducibility of the results upon heating and cooling was quite reasonable. No thermal effects were observed in the thermograms of the samples in the temperature range from 293 to 1073 K. After thermal cycling, the powder diffraction patterns of HoF_3 also showed no traces of other phases. The dependences $\sigma(T)$ at the critical temperature $T_c \approx 620$ K can be divided into two linear portions in accordance with different mechanisms of ion transfer. It should be noted that the activation enthalpy of electrical conduction decreases in the high-temperature range. As was demonstrated earlier in [3], the dependence $\sigma(T)$ for β-YF_3 crystals also has two portions (see Fig. 1 in [3]). Table 1 presents the preexponential factors A and the activation enthalpies of electrical conduction ΔH for differently oriented samples of HoF_3 single crystals. Our data on the parameters of the anion transfer in HoF_3 single crystals slightly differ from those obtained by Trnovcova *et al.* [6] for these crystals but are in good agreement with the parameters determined by the same authors [3, 4, 6, 7] for orthorhombic crystals RF_3 (R = Tb, Er, and Y) measured at temperatures no higher than 923 K (Table 2). The conductivity anisotropy in HoF_3 and β-YF_3 crystals is insignificant and can be ignored (Tables 1, 2).

The results of structural investigations [8] indicate a similarity between structural motifs of the tysonite-type and orthorhombic rare-earth trifluorides. The nominally pure tysonite-type rare-earth trifluorides RF_3 (R = La–Nd) are characterized by the formation of Schottky defects (vacancies V_F and V_{La}), among which the V_F^+ fluorine vacancies are the mobile defects responsible for the high ionic conductivity $\sigma \sim 10^{-6}$ S cm^{-1} at 293 K [9]. As in the case of RF_3 tysonite-type trifluorides, the experimental data on ion transfer in the RF_3 orthorhombic crystals can be consistently interpreted under the assumption that the electrical conduction in these compounds occurs through the vacancy mechanism. According to Trnovcova *et al.* [3], the V_F vacancies in β-YF_3 crystals are the structural defects that most probably contribute to the anionic conduction. The activa-

Table 1. Parameters A and ΔH for HoF_3 single crystals

Orientation	ΔT, K	ΔH, eV	log(A, S cm^{-1} K)
Sample 1, $\parallel b$	323–623	0.737	4.61
	623–1073	0.45	2.34
Sample 1, $\perp b$	323–623	0.745	5.14
	623–1073	0.43	2.78
Sample 2, $\parallel b$	323–623	0.765	5.14
	623–1073	0.37	2.15
Sample 2, $\perp b$	323–623	0.722	4.65
	623–1073	0.45	2.49
Sample 3 (unoriented)	323–623	0.750	4.72
	623–1073	0.43	2.14

Table 2. Electrical characteristics of orthorhombic single crystals RF_3 (R = Tb, Ho, Er, and Y)

RF_3	Orientation	$\sigma_{500\,K}$, S/cm	ΔH, eV	References
TbF_3	[010]	1×10^{-5}	0.74	[6]
HoF_3	$\parallel b$	4×10^{-6}	0.75	This work
	$\perp b$	7×10^{-6}	0.73	This work
	Unoriented	3×10^{-6}	0.75	This work
	"	1×10^{-5}	0.64	[6]
ErF	"	1×10^{-6}	0.74	[4, 7]
β-YF_3	[101]	2×10^{-6}	0.71	[6]
	[010]	3×10^{-6}	0.71	[6]
	Unoriented	2×10^{-6}	0.70	[3]

tion enthalpy of electrical conduction ΔH = 0.74 eV, which was determined for HoF_3 crystals in the present work, is rather close to the enthalpy of migration of fluorine vacancies $\Delta H \approx 0.70$ eV [3] in β-YF_3 crystals.

Making allowance for the small coefficients of cation diffusion in trifluorides, we can assume that the kink observed in the dependence $\sigma(T)$ at the critical temperature $T_c \approx 620$ K reflects a crossover from one mechanism of anionic conduction in HoF_3 crystals to another. It should be noted that orthorhombic rare-earth trifluorides, like the tysonite-type trifluorides [10], obey the following relationship: $\Delta H_2 < \Delta H_1$, where ΔH_1 and ΔH_2 are the activation enthalpies of electrical conduction at $T < T_c$ and $T > T_c$, respectively. This suggests that the V_F vacancies at different crystallographic positions contribute to the mechanism of ion transfer.

The LaF_3 tysonite structure (space group $P\bar{3}c1$, number of formula units z = 6) contains three fluorine sublattices, namely, the F_1, F_2, and F_3 sublattices, in which the number of anions per unit cell is determined by the relationship $F_1 : F_2 : F_3 = 12 : 4 : 2$. Note that, along the c axis in the tysonite structure, the F_1 ions are located in puckered anionic layers and the F_2 and F_3 ions occupy planar cationic–anionic layers. When interpreting the electrical properties of tysonite crystals, the F_2 and F_3 ions are often considered to be combined into a common subsystem, $F_{2,3}$ (at $F_2 = F_3$, the trigonal tysonite-type structure with the space group $\bar{3}c1$ and z = 6 transforms into the hexagonal tysonite-type structure with the space group $P6/mmm$ and z = 2). Consequently, we obtain the ratio $F_1 : F_2 = 2 : 1$. In the β-YF_3 structure (space group $Pmma$, z = 4) [11, 12], the anionic layers formed by the F_3 ions and the cationic–anionic layers containing F_2 ions are arranged along the b axis. The number of anions per unit cell in the β-YF_3 structure is determined by the ratio $F_1 : F_{2,} = 2 : 1$. At $T < T_c$, the anion transfer in the β-YF_3 structure predominantly proceeds, first, in one fluorine subsystem (most probably, in the F_1 subsystem) and, then, in two subsystems simultaneously, including the F_2 sublattice. As the critical temperature T_c is approached, the fluorine vacancies are involved in active exchange between the anionic subsystems. At $T > T_c$, the anion transfer occurs through all the fluorine sites.

However, the anionic conductivity of HoF_3 crystals at 1073 K reaches only 2×10^{-3} S cm^{-1}. This value is considerably less than the electrical conductivity of RF_3 tysonite-type trifluorides ($\sigma \sim 1$ S cm^{-1}). The large difference between the F^- ionic conductivities in orthorhombic and tysonite-type lanthanide-containing trifluorides can be explained in terms of crystal chemistry [13]. The characteristic coordination polyhedron of R^{3+} ions can be considered a trigonal prism with different degrees of distortion that determines the minimum coordination number to be equal to six. The mutual arrangement of these prisms leads to an increase in the coordination number to nine in structures of the β-YF_3 type and to 11 in structures of the tysonite type.

The tysonite-type hexagonal structure with high symmetry is composed of layers that are located normally to the c axis and consist of regular trigonal prisms. The prisms are alternately occupied by La and F atoms in accordance with a structural motif similar to that in the MoS_2 compound. In this structure, fluorine atoms can occupy two different positions: vertices of the polyhedra and the centers of the prisms built up of like ions. However, the latter situation is not typical of ionic structures. Hence, it is these fluorine positions at the centers of the prisms that appear to be vacant after the heterovalent isomorphous replacement of R^{3+} by Ca^{2+} (Sr^{2+}, Ba^{2+}). Upon transition to the trigonal modification with low symmetry, the fluorine atoms are displaced insignificantly, which, in turn, results in a distortion of the trigonal prisms.

In structures with a β-YF_3 orthorhombic lattice, the fluorine atoms are located only at vertices of coordination polyhedra, namely, distorted trigonal prisms. This impedes the generation of anionic vacancies (charge carries) and, consequently, the formation of MF_2 solid solutions (M = Ca, Sr, and Ba) in orthorhombic trifluorides. The above treatment in terms of crystal chemistry is supported by the close values of the activation enthalpy of low-temperature (at $T < T_c$) anion transfer in the HoF_3 crystal ($T_c \approx 620$ K, $\Delta H_1 = 0.74$ eV) and the tysonite-type solid solutions $Ho_{0.77}Ca_{0.23}F_{2.77}$ ($T_c \approx 685$ K, $\Delta H_1 = 0.7$ eV [14]) and $Ho_{0.75}Sr_{0.25}F_{2.75}$ ($T_c \approx 670$ K, $\Delta H_1 = 0.6$ eV [15]).

ACKNOWLEDGMENTS

We are grateful to V.S. Sidorov and P.P. Fedorov for providing the crystals used in our measurements.

This work was supported by the L. Meitner Austrian Foundation, grant no. M00231-CHE.

REFERENCES

1. M. O'Keeffe, Science **180**, 1276 (1973).
2. A. I. Livshits, V. M. Buznik, P. P. Fedorov, and B. P. Sobolev, *Nuclear Magnetic Resonance in Crystals* (Inst. Fiziki Sib. Otd. Akad. Nauk SSSR, Krasnoyarsk, 1978), p. 90.
3. V. Trnovcova, P. P. Fedorov, B. P. Sobolev, *et al.*, Kristallografiya **41** (4), 731 (1996) [Crystallogr. Rep. **41**, 694 (1996)].
4. V. Trnovcova, P. P. Fedorov, M. D. Valkovskii, *et al.*, Ionics **3**, 313 (1997).
5. N. I. Sorokin and M. W. Breiter, Solid State Ionics **99**, 241 (1997).
6. V. Trnovcova, L. Mitas, C. Jeskova, *et al.*, in *Extended Abstracts of the VI International Conference on Solid State Ionics, Garmisch-Partenkirchen, Germany, 1987*, p. 165.
7. V. Trnovcova, F. Hanic, A. N. Smirnov, *et al.*, in *Proceedings of the International Conference "Engineering Ceramics-92," Bratislava, Slovakia, 1993*, p. 183.
8. L. S. Garashina, B. P. Sobolev, V. B. Aleksandrov, and Yu. S. Vishnyakov, Kristallografiya **25** (2), 294 (1980) [Sov. Phys. Crystallogr. **25**, 171 (1980)].
9. A. Sher, R. Sobolev, K. Lee, and M. W. Muller, Phys. Rev. B **144** (2), 593 (1966).
10. N. I. Sorokin and B. P. Sobolev, Kristallografiya **39** (5), 889 (1994) [Crystallogr. Rep. **39**, 810 (1994)].
11. A. Zalkin and D. H. Templeton, J. Am. Chem. Soc. **75**, 2453 (1953).
12. B. P. Sobolev, L. S. Garashina, P. P. Fedorov, *et al.*, Kristallografiya **18** (4), 751 (1973) [Sov. Phys. Crystallogr. **18**, 473 (1973)].
13. L. S. Garashina, R. M. Zakalyukin, E. A. Krivandina, *et al.*, in *Proceedings of the II National Crystal Chemical Conference, Chernogolovka, Russia, 2000*, p. 163.
14. N. I. Sorokin, M. V. Fominykh, E. A. Krivandina, *et al.*, Fiz. Tverd. Tela (St. Petersburg) **41** (4), 638 (1999) [Phys. Solid State **41**, 573 (1999)].
15. N. I. Sorokin, M. V. Fominykh, E. A. Krivandina, *et al.*, Kristallografiya **41** (2), 310 (1996) [Crystallogr. Rep. **41**, 292 (1996)].

Translated by O. Borovik-Romanova

Physics of the Solid State, Vol. 44, No. 2, 2002, pp. 286–293. Translated from Fizika Tverdogo Tela, Vol. 44, No. 2, 2002, pp. 275–282.

DEFECTS, DISLOCATIONS, AND PHYSICS OF STRENGTH

Deep Levels of Nitrogen Vacancy Complexes in Graphite-like Boron Nitride

S. N. Grinyaev, F. V. Konusov, and V. V. Lopatin

Research Institute of High-Voltage Equipment, Tomsk Polytechnical University, Tomsk, 634050 Russia

e-mail: kabyshev@hvd.tpu.ru

Received April 5, 2001

Abstract—This paper presents the results of a theoretical study of deep nitrogen vacancy levels and of small clusters of nitrogen di- and trivacancies, including the nearest neighbor defects in one layer of graphite-like boron nitride, made using the model-pseudopotential and supercell methods. The calculated spectra and oscillator strengths were used to interpret the local bands of optical absorption, luminescence, and photoconductivity in pyrolytic boron nitride before and after irradiation by fast neutrons, protons, and carbon ions (50–150 keV). The shallow activation levels of thermally stimulated luminescence and conductivity existing before and arising after irradiation were identified. © *2002 MAIK "Nauka/Interperiodica".*

1. INTRODUCTION

Despite the continued interest in boron nitride as a multifunctional material with properties stable against extremal external factors [1, 2], the nature of its intrinsic and extrinsic defects still has not been sufficiently studied. At the same time, because of the specific technology of preparation employed, the boron nitride samples obtained contain defects that differ in character and give rise to significant features in its physical properties. For instance, defects present in the pyrolytic boron nitride *h*-BN produce a red shift of the optical absorption edge, change the conduction type, and give rise to a fine structure in the electron paramagnetic resonance (EPR) spectrum. The variety of defects and of their complexes make identification of the deep levels they create difficult and require experimental and theoretical studies to be carried out with the use of different techniques.

The nitrogen vacancy V_N plays a particular part among defects, because pyrolytic *h*-BN of stoichiometric composition is characterized by a noticeable deficiency of nitrogen, a factor associated with its extremely high temperature of synthesis (~2300 K) and small V_N binding energy, which is indicated in studies of its close analogs, *w*-GaN and *w*-InN [3–5]. The electronic states of localized centers in boron nitride were earlier investigated in the tight-binding approximation [6, 7] using the Hückel method [8, 9] and the augmented plane wave method [10]. In the cubic modification *c*-BN, the unrelaxed neutral nitrogen vacancy creates a completely filled, *s*-like state near the valence-band (VB) top and a partially filled, *p*-type resonant state at the conduction-band (CB) edge [10].

Graphite-like *h*-BN is characterized by sp^2 bond hybridization, which brings about modification of the deep levels produced by V_N. The three dangling bonds created by the nitrogen vacancy form, in the band gap of *h*-BN, a filled singlet state A_1 and a twofold degenerate state *E* with one unpaired electron [6, 7].

A comparison of the results obtained using different methods validates the approximations employed. In particular, recent studies made using the pseudopotential method revealed [3, 4] the existence of resonance states created by a neutral nitrogen vacancy in the VB (a singlet) and the CB (a quasi-triplet) of *w*-GaN, which is at odds with earlier tight-binding calculations [11, 12] placing the singlet state near the CB. The reason for these discrepancies lies in the small magnitude of the splitting between the deep levels, which was obtained using the tight-binding method for anion vacancies and is due, as is the case with other compounds [13, 14], to the limited extent of the basis used and to neglection of essential interactions. Because the defect states in three-dimensional *h*-BN have thus far been investigated only using the tight-binding method, it becomes obvious that studies based on more precise approximations are needed.

The present work is a study of the deep nitrogen-vacancy levels in *h*-BN using the pseudopotential and supercell (SC) methods similar to [15]. This approach provides a satisfactory description of the electronic spectrum of both a perfect and a defected crystal. We consider here, in addition to a single nitrogen vacancy, small clusters of the di- and trivacancies of nitrogen, including the nearest neighbor defects. Formation of such complexes is made possible by the high V_N concentration and fairly high cluster binding energy [3]. The calculated spectra and oscillator strengths offer a basis for interpretation of the optical characteristics of the pyrolytic *h*-BN.

1063-7834/02/4402-0286$22.00

2. METHOD OF CALCULATION

The deep-level calculation was carried out with a sufficiently large SC ($4 \times 4 \times 2$) containing 128 atoms, which permitted us to reduce the dispersion of the impurity band (for comparison, the SCs used in [3–5] contained 32, 72, and 64 atoms, respectively) and to study the states of complex defects. The cell was enlarged along the hexagonal axis by a smaller number of times than in the layer plane because of the relatively weak interlayer coupling in *h*-BN [16].

According to [17], the valence-band top of perfect *h*-BN lies at the symmetry point *H* of the Brillouin zone, the conduction band bottom lies at the *M* point, and the width of the indirect band gap is 4.65 eV. At the Γ point, the highest filled state of symmetry Γ_5' lies 0.9 eV below the top of the VB. The band dispersion along the hexagonal axis (in particular, along the *U* line connecting the symmetry points *L* and *M*) is weak.

The electronic spectrum and the wave functions of a defected crystal were found on the basis of the 30 lowest Bloch states of a perfect *h*-BN crystal using the model-pseudopotential method [17]. The nitrogen vacancies were placed at the anion sites of the perfect lattice, and the lattice distortion and relaxation effects were neglected. The deep levels were identified with the states of a defected crystal for a zero superlattice wave vector. The Γ, *L*, *M*, and *A* points and the points on the *R*, *S*, *T*, and Σ lines of the Brillouin zone of the perfect crystal are equivalent to the Γ point of the superlattice. Similar to [15], the potential of the neutral nitrogen vacancy was constructed from the nitrogen pseudopotential screened by the dielectric permittivity [18], the pseudopotential being determined from experimental data and the results of *ab initio* band-structure calculations.

To test the method, we calculated the deep levels created by a single nitrogen vacancy in the more well studied crystals *w*-GaN and *c*-BN. The band structure and wave functions of perfect *w*-GaN were calculated using the pseudopotential method [18]. The deep levels of a single nitrogen vacancy were determined using the SC ($4 \times 4 \times 2$) approximation. The localized singlet *s*-like state A_1 and the quasi-triplet *p*-like state, both associated with V_N in *w*-GaN, were found to be, in accordance with [4], resonance states lying in the VB and CB. When transformed to the wurtzite structure, the sphalerite state T_2 splits into A_1 and *E* states, so that the lowest singly occupied A_1 state is 0.2 (0.8) eV above the CB bottom and the upper empty state *E* is 0.4 (0.5) eV distant from it (the data in parentheses are from [4]). The band structure of the perfect *c*-BN was calculated using the model-pseudopotential method [17], and the deep levels of a single V_N vacancy were found using the SC ($4 \times 4 \times 4$) approach. The parameters of the model pseudopotentials [$V_0(B) = 0$, $R_m(B) = 2.5$, $\beta(B) = -15$, $\beta(N) = -15$, $V_0(N) = -4.8$, $R_m(N) = 2.15$ in $\hbar = m = e = 1$ atomic units] were derived from the condition that the calculated band spectrum of *c*-BN be similar to the spectrum obtained from the LMTO-TB-NO-ES approximation [10]. In this case, the energies of the deep levels of a perfect nitrogen vacancy in *c*-BN [$\varepsilon(A_1) = 0.95$ eV, $\varepsilon(T_2) = 5.34$ eV relative to the VB top, Γ_{15}^v] are also in accordance with [10]. Because the position of the deep levels depends directly on the defect potential, the agreement obtained with the results of *ab initio* calculations made for crystals with different structure validates the nitrogen vacancy potential model employed.

3. RESULTS OF THE CALCULATION

The calculated deep levels of defected *h*-BN near the band gap are displayed in Fig. 1. A single neutral nitrogen vacancy creates, in the band gap, two deep levels split off from the VB. The energy of the lowest A_1 level is $\varepsilon = 3.75$ eV (here and subsequently, the energies are referenced relative to the VB top), and this level has one unpaired electron, so that the nitrogen vacancy is a donor. The unoccupied level *E* lies near the CB bottom ($\varepsilon = 4.41$ eV). An analysis of the coefficients of expansion of the localized states in wave functions of the perfect crystal showed that both levels derive primarily from the lowest CB states at the *L* and *M* points, with the π states (antisymmetric relative to the layer plane) contributing to the A_1 level. The character of localization of the deep-level functions is seen from the charge density map (Fig. 2). The density maxima of state A_1 in the cross section parallel to the hexagonal axis lie near the nearest and next-to-nearest neighbor boron atoms. The wave function of state A_1 in the layer plane is zero. The charge density of the *E* level is localized at the dangling bonds. The wave functions of both levels fall off in the direction of the hexagonal axis and vanish at the midpoint between the layers.

The results obtained for a single nitrogen vacancy differ from the data quoted in [6], according to which the lower A_1 level is about 1 eV above the VB and is

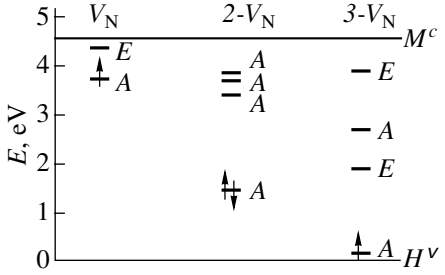

Fig. 1. Diagram of *h*-BN deep levels with one (V_N), two ($2\text{-}V_N$), and three ($3\text{-}V_N$) nitrogen vacancies. The energies are reckoned from the VB top. Solid horizontal lines are the limits of the band gap. The arrows show the filling of the highest level occupied by electrons.

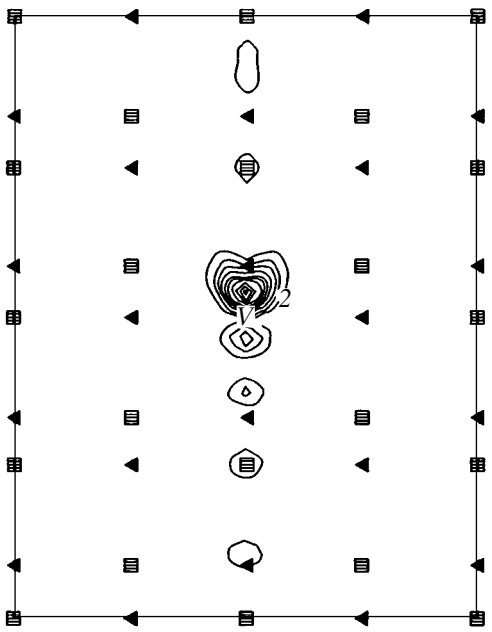

Fig. 2. Charge density map of the lower A_1 deep level of a single nitrogen vacancy in the (*yz*) plane. The squares show the position of the nitrogen atoms, the triangles show the positions of the boron atoms, and *V* identifies the nitrogen vacancy. The densities are given in units of e/Ω_0, where Ω_0 is the supercell volume.

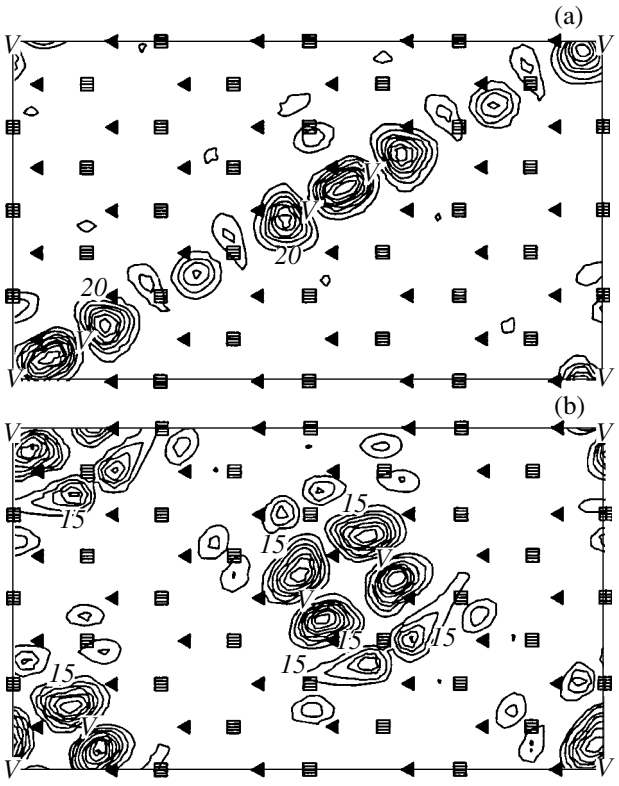

Fig. 3. Charge density map of the deep nitrogen divacancy levels in the (*xy*) plane: (a) A_1 (ε = 1.41 eV) and (b) A_1 (ε = 3.71 eV).

fully occupied and the *E* level is distant by ~2.5 eV from it and contains one electron. The reason for this discrepancy is probably due to the difference in the strength of the defect potential. Calculations made with a renormalized V_N potential showed that the energy level diagram presented in [6] can be reproduced if one takes a stronger nitrogen-vacancy potential (by about a factor of two). In this case, however, one does not reach agreement with the *ab initio* calculations of the V_N levels for *c*-BN [10] and *w*-GaN [4].

It is known that the antisymmetric character of the partially occupied A_1 state of a single nitrogen vacancy does not account for the structure of the 10 resonance peaks observed in the EPR spectrum of pyrolytic *h*-BN [19, 20]. These features are believed to be connected with the hyperfine interaction between the spin moment of the unpaired electron and the moments of the three boron atoms surrounding the nitrogen vacancy. The breakdown of the antisymmetry of the A_1 state required for the features mentioned above to occur is caused by other defects, for instance, by the effect of interlayer carbon atoms, as postulated in the model of the *F* center [20], which creates a nonzero electron density around the boron atoms and a finite spin interaction. We will show later that nitrogen vacancy complexes can play a similar role.

The symmetry of the nitrogen divacancy made up of nearest neighbor in-plane defects (2-V_N) is lower than that of a single vacancy. As a result of interaction between the states of two nitrogen vacancies, the divacancy creates four one-dimensional states in the band gap of *h*-BN. The lower A_1 level (ε = 1.41 eV) is fully occupied and derives from the states of the upper valence σ^+ band; its charge density is oriented along the line connecting the vacancies and reaches a maximum midway between them (Fig. 3). The deep levels next in energy are empty. The wave function of the third level (ε = 3.71 eV) consists of almost the same σ^+ states but is localized primarily on the dangling bonds. The character of the density distribution in the vertical plane for the first and third divacancy levels can be reproduced by following, in analogy, the data for the single vacancy and Fig. 3. The second (ε = 3.42 eV) and fourth (ε = 3.85 eV) levels of the divacancy are derived from the π states of the VB and CB; therefore, their charge densities in the layer plane are zero. The defects located in adjacent layers affect one another only weakly. The energy levels of a divacancy made up of such defects are nearly degenerate (the splitting < 0.1 eV) and are close to those of a single nitrogen vacancy.

The nitrogen trivacancy (3-V_N), which consists of three nearest neighbor V_N defects lying at the vertices of an equilateral triangle in the plane of one layer, creates four levels in the band gap of *h*-BN. The lower A_1 level is occupied by one electron and lies near the VB top (ε = 0.15 eV); therefore, the nitrogen trivacancy is an acceptor. The wave function of this level is derived

from the VB σ^- states, and the charge density maxima are localized on the dangling bonds and at the 3-V_N center. Because of this state being symmetric, the unpaired electron has a small but finite probability density of residing near the boron nuclei (Fig. 4); therefore, the nitrogen trivacancy can act as a paramagnetic center. The influence of defect complexes on EPR signals was observed in [21]. The E level (ε = 1.88 eV), which is unoccupied by electrons, derives from the σ^+ states of the VB. The levels A_1 (ε = 2.70 eV) and E (ε = 3.93 eV) derive from the π states of the VB and CB and have zero densities in the layer plane.

Thus, because the states of single defects are strongly coupled, complexes consisting of nearest neighbor nitrogen vacancies create a series of deep levels extending over the band gap of *h*-BN. As the clusters grow in size, the energy of the highest filled level decreases and the defect center changes its character from the donor type of single vacancy to the acceptor type for trivacancy.

The above deep levels can manifest themselves in various physical properties. In particular, optical transitions involving these levels can produce features in the spectral response. The interband transition intensity depends on the momentum-operator matrix elements. As follows from a calculation of these matrix elements, the strongest transitions from the deep levels in a single nitrogen vacancy and its clusters occur when the light waves are polarized perpendicular to the hexagonal axis. In a single vacancy, such transitions are possible from the upper VB states to the deep levels. The transition energies are $\varepsilon(\Gamma_5' \longrightarrow A_1)$ = 4.6 eV and $\varepsilon(\Gamma_5' \longrightarrow E)$ = 5.3 eV. The transition connecting deep levels with an energy $\varepsilon(A_1 \longrightarrow E)$ = 0.7 eV is also allowed. In the nitrogen divacancy, transitions between all deep levels (from one to another) and between them and the L_1 state at the CB bottom are strong. The transitions from the lowest A_1 filled level (ε = 1.41 eV) to the upper deep levels have energies of 2.0, 2.3, and 2.4 eV, and the transition energy to the CB bottom ($A_1 \longrightarrow L^c$) is 3.2 eV. In the nitrogen trivacancy, transitions from the Γ_5' and A_3 states of the upper VB can take place only to the lower deep levels of A_1 (ε = 0.15 eV) and E (ε = 1.88 eV) with energies of 1.1 and 2.8 eV, respectively. The energy of the allowed transition connecting these deep levels is 1.7 eV. The transitions occurring between unfilled deep levels next in energy and states at the CB bottom at the L point are also strong.

4. COMPARISON OF THE CALCULATIONS WITH THE EXPERIMENTALLY OBSERVED ENERGY LEVELS

The parameters of the localized defect states with energy ε < 1.5 eV were determined from the temperature dependences (T = 300–650 K) of the thermally stimulated conductivity (TSC) and luminescence (TSL) [22]. The density of deep states $N(\varepsilon)$ was estimated from the spectral response of the absorption coefficient $\alpha(h\nu)$ derived from diffuse-reflection spectra (T = 300 K, $h\nu$ = 1.5–6.2 eV) [23]. To establish the form of the spectral distribution in energy and type of optical transition, the $\alpha(h\nu)$ coefficient was approximated by the Urbach rule $\alpha \sim \exp(h\nu/E_U)$ and the power law $\alpha h\nu \sim (h\nu - E_g)^m$, which, under some simplifying assumptions, describe interband transitions (m = 1/2 and 2 correspond to direct and indirect allowed transitions, respectively) [24].

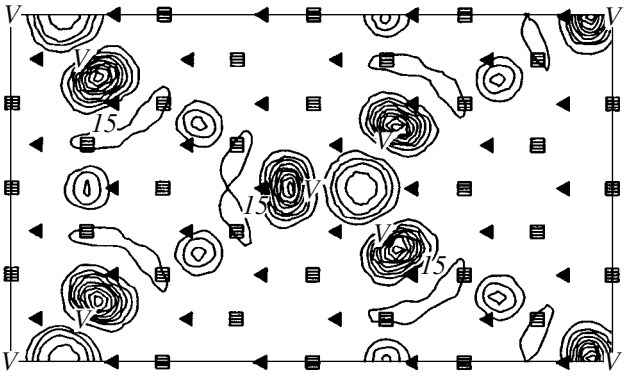

Fig. 4. Charge density map of the lowest A_1 deep level of the nitrogen trivacancy (ε = 0.15 eV) in the (xy) plane.

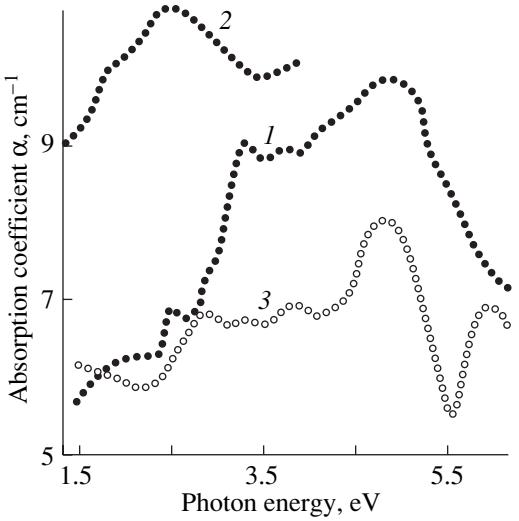

Fig. 5. Spectral response of the absorption coefficient of boron nitride at 300 K measured (*1*) before and (*2*) after reactor-neutron irradiation to a fluence $\Phi = 4.6 \times 10^{17}$ cm^{-2} and (*3*) after annealing of the neutron-irradiated material ($\Phi = 1.1 \times 10^{19}$ cm^{-2}) at T_{an} = 2000 K.

Analysis of the spectra of pyrolytic BN indicates a continuous distribution of energy states localized in the band gap (Fig. 5). Near the fundamental absorption edge, the $\alpha(h\nu)$ dependence follows, as is the case with

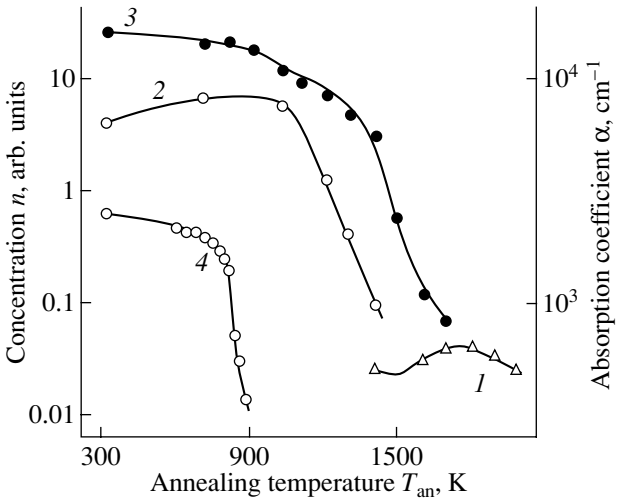

Fig. 6. Effect of thermal treatment on (*1*, *4*) the paramagnetic-center concentration *n* and (*2*, *3*) absorption coefficient α of reactor-neutron irradiated BN to a fluence Φ equal to (*1*) 3×10^{18}, (*2*) 5×10^{17}, (*3*) 1×10^{19}, and (*4*) 5×10^{18} cm^{-2}. $h\nu$ is equal to (*2*) 1.9 and (*3*) 2.5 eV.

most materials, the Urbach rule ($h\nu$ = 4.0–4.5 eV, E_U = 0.7–0.9 eV). That the values of E_U characterizing the density of states in the tails of the VB and CB are larger than the figures obtained for other dielectrics [24] is due to the defects of technological origin affecting the absorption edge considerably. The band-gap width estimated in terms of the models of allowed direct (E_{gd}) and indirect (E_{gi}) transitions was found to be 4.1–4.2 and 2.9–3.5 eV, respectively, which differs from the theoretical values E_{gd} = 5.27 eV and E_{gi} = 4.65 eV from [17]. This discrepancy is due to the hierarchical structure of the ceramic [25] and the effect of the defect levels distributed near the energy band edges [22]. In addition to a continuous spectrum of states, one also observed monoenergetic shallow (ε < 1.5 eV) [22] and deep optical levels. The latter were deduced from the spectral response of luminescence, $I(h\nu)$; they are also seen as local bands in the absorption spectra (Fig. 5). The absorption center concentration was calculated using Smakula's formula.

The local absorption band centered on ε_i = 3.85 eV is most clearly seen in a material with a deficiency of nitrogen atoms (1–3 wt %) (curve *1* in Fig. 5). Following fast-neutron irradiation and annealing in vacuum at $T_{an} \geq 1300$ K, the band at 3.85 eV becomes additionally localized (curve *3* in Fig. 5), which correlates with a growth in concentration of the induced paramagnetic (V_N–3B[11]) centers, which were identified by EPR spectrometry [21]. The dose and anneal dependences of the concentration of paramagnetic V_N (curve *1* in Fig. 6) are similar to those of the concentration of the absorption centers with energies of 3.85 eV. The above observations suggest that the 3.85-eV band is due to electron transitions from the VB to the energy levels of a single vacancy of technological and/or radiation origin. However, the band center energy (3.85 eV) and the calculated transition energies (ε = 4.6 and 5.3 eV) between the VB top (Γ'_{5v}) and the vacancy levels *A* and *E* do not coincide. One also cannot overlook the contribution of the $\Gamma'_{5v} \longrightarrow A$ transitions (ε = 4.6 eV) to the broad absorption peak at ε_i = 4.8 eV (Fig. 5). A more probable origin of this peak is the decrease in the absorption coefficient for ε > 4.8 eV caused by a contribution to the reflection coefficient of the photoluminescence (PL), which is excited intensely in this spectral region [8].

The 3.85-eV absorption band can be tentatively assigned to indirect transitions from the upper VB states (H^v) to the *A* vacancy level (ε = 3.75 eV). The intensity of such indirect transitions is weak in a crystal containing only nitrogen vacancies; however, the intensity can increase in a realistic material because of the effect of intra- and intercrystallite defects (average crystallite size, ~50 nm [25]) with energy levels (concentration $N = 10^{18}$–10^{19} cm^{-3}) distributed continuously over energy (ε = 0.3–1.5, 3.6–4.8 eV). Analysis of the absorption [23] and luminescence [22] characteristics confirms the strong influence of interdefect interaction on the parameters of the monoenergetic levels of single defects. Indirect transitions $H^v \longrightarrow A$ (ε = 3.75 eV) can also be favored by the electron–phonon coupling. By analogy with the above discussion of absorption transitions and taking into account the diagram of the activation-recombination transitions proposed in [22], the intense x-ray luminescence band observed at ε = 3.6 eV in an *n*-type material can be assigned to recombination transitions of holes from the upper VB states (H^v) to the *A* level of the vacancy (ε = 3.75 eV). The indirect character of such transitions is in accordance with the observation that temperature quenching (*T* = 300–600 K) affects the luminescence intensity only insignificantly [22]. The (*p*-type) photoconductivity level at ε_i = 3.9 eV (table) can also be identified with the $H^v \longrightarrow A$ transitions.

The TSL and TSC donor monoenergetic levels with energies of 0.7–1.0 and 1.0–1.3 eV [22] (0.7 and 1.0 eV, according to [8]), which donate thermally ionized electrons (*T* = 300–600 K) to the CB, should be identified with the vacancy level *A* (table). That the activation energies of the donor levels 0.7–1.0 and 1.0–1.3 eV do not coincide with the energy position of level *A* relative to the CB bottom (ε = 4.65 – 3.75 = 0.9 eV) is due both to the interaction of defects with vacancies and to the differences between the thermal and optical ionization processes, as well as to the change in the vacancy charge state (the vacancy level shift in the III–V compounds is estimated, for instance, in [26] as 0.1–0.2 eV). Analysis of the parameters of the TSL activation donor levels with ε = 0.9–1.3 eV (table), which were revealed in a material irradiated with heavy high-energetic particles, permits one to assign them to radia-

Nitrogen-vacancy-complex levels, transition energies, luminescence activation energies (ε), and energy positions of optical band centroids (ε_i) in pyrolytic BN before and after irradiation by neutrons (*), protons (**), and carbon ions (***)

Defect	Notation of level (energy ε, eV)	Transition energy (ε, eV) and notation	ε, eV	Absorption		Photoconductivity ε_i, eV	Luminescence	
				ε_i, eV	N, cm^{-3}		ε_i, eV	I, arb. units
V_N	E(4.41)	0.7	0.7–1.2					
		($A \longrightarrow E$)						
	A(3.75)		1.0–1.2**					
			0.9–1.1*					
		3.75		3.85	5×10^{18}	3.9	3.6	0.05
		($H^V \longrightarrow A$)						
				3.85*	1×10^{19}			
		4.6		4.80	3×10^{19}			
		($\Gamma'_{5V} \longrightarrow A$)						
		5.3						
		($\Gamma'_{5V} \longrightarrow E$)						
2-V_N	A(3.85)	2.0		1.9***	$(0.9–3) \times 10^{20}$	(1.8–2.0)***	2.1–2.2*	
		($A \rightleftharpoons A$)						
	A(3.71)	2.3		2.5***	$(3–5) \times 10^{20}$	(2.2–2.4)***	2.5*	1.0
		($A \rightleftharpoons A$)						
	A(3.42)	2.4		(2.2–2.4)***	$(2–5) \times 10^{20}$		(1.5–2.3)***	1–0.3
		($A \rightleftharpoons A$)						
	A(1.41)	3.2					3.2*	1.0
		(CB $\longrightarrow A$)						
		0.8	(0.8–1.0)***					
		($A \longrightarrow$ CB)						
3-V_N	A(0.15)	0.15	0.1–0.2*					
		($H^V \longrightarrow A$)						
	A(0.15)	1.1	0.9–1.1*					
		($\Gamma'_{5V} \longrightarrow A$)						
	E(1.88)	2.8		2.85*	$(3–5) \times 10^{19}$			
		($\Gamma'_{5V} \longrightarrow E$)						
				2.9***	1.5×10^{20}	2.9***		
		2.77					3.0*	0.5
		(CB $\longrightarrow E$)						
	A(2.70)	1.73		1.9***	$(0.9–3) \times 10^{20}$			
		($A \longrightarrow E$)						
		1.95						
		($A \longrightarrow$ CB)						
	E(3.93)	0.72	(0.2–0.4*)					
		($E \longrightarrow$ CB)						

tion-induced nitrogen-vacancy levels, which, unlike the V_N of technological origin, are located inside the crystallites rather than near the grain boundaries.

Based on the correlation between the dose and annealing dependences of the optical density (curves *2*, *3* in Fig. 6) and the concentration of complex paramag-

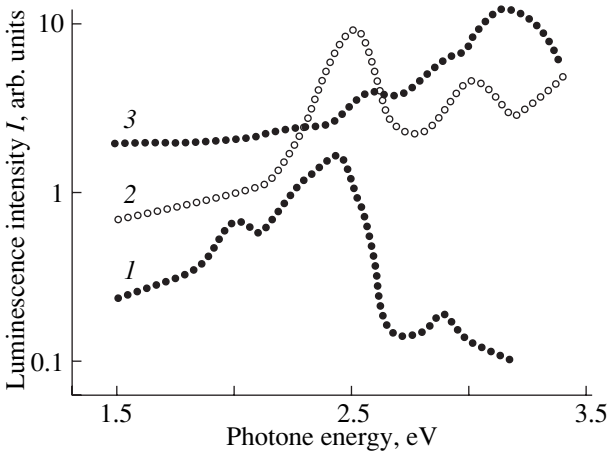

Fig. 7. Spectral response of the intensity of (*1*) thermo- and (*2*, *3*) photoluminescence at $h\nu = 3.7$ eV of boron nitride (*1*) irradiated by x-rays (50 keV, 0.2 Mrad) and (*2*) annealed ($T_{an} = 2000$ K) after reactor-neutron irradiation to Φ equal to 10^{18}–10^{19} and (*3*) $\Phi > 10^{19}$ cm^{-2}.

netic centers (curve *4* in Fig. 6) [21], the absorption bands at $\varepsilon_i = 1.9$ and 2.5 eV (curve *2* in Fig. 5), revealed after neutron irradiation ($\Phi = 10^{15}$–3×10^{18} cm^{-2}), were tentatively assigned to complex multivacancy complexes (MVC). The variation in the parameters of the 2.5-eV PL band after annealing ($T_{an} \geq 1500$ K) with increasing neutron fluence relative to the parameters of the TSL band in the original BN, which is close in energy (curves *1*–*3* in Fig. 7), and the behavior of the neutron-induced PL bands at 2.1–2.2 and 2.25–2.42 eV [27] with annealing give one grounds to suggest that the above bands are associated with electron transitions between the MVC energy levels. An analysis of the changes in the electrophysical [28, 29] and optical properties [30, 31] induced by ion irradiation and thermal treatment showed that anion vacancy complexes produce the strongest effect among all defects. The peaks of the ion-induced absorption at 2.2–2.4 eV and the peaks in the excitation spectrum of *n*-type photoconductivity at 1.8–2.0 and 2.2–2.4 eV were tentatively assigned in [31] to electron transitions from the ground states of the anion vacancy clusters to the CB. The above absorption, photoconductivity-excitation, and emission bands in the irradiated material should be identified taking into account the closeness of their centers to the energies of the calculated transitions (2.0, 2.3, 2.4 eV), with the transitions connecting the upper *A* (3.85, 3.71, and 3.42 eV) and the lower *A* (1.41 eV) states of the 2-V_N divacancy (table). The 3.2-eV transition from the *A* level (1.41 eV) to the CB is not seen in the optical spectra as a local band, probably because the competing electronic transitions form a strong absorption peak at 3.3 ± 0.15 eV in the original material (curve *1* in Fig. 5). One cannot, however, exclude the possibility that the strong PL peak at 3.2 ± 0.2 eV (curve *3* in Fig. 7), which becomes manifest after neutron irradiation and annealing, can be assigned to electrons being transferred from the CB to the divacancy level *A* (1.41 eV). The intensity redistribution in the PL spectra (curves *2*, *3* in Fig. 7) can be accounted for by a change in the level population of the divacancies, which results from their interaction as they build up with increasing fluence. The upper divacancy levels *A* (3.85, 3.71, 3.42 eV) act as traps for electrons transferred to the CB during thermally stimulated ionization (T = 300–500 K) of the luminescence donor levels, which are seen at $\varepsilon = 0.1$–0.5 eV [32]. The depth of the *A* levels (3.85 and 3.71 eV) with respect to the CB bottom is 0.8 and 0.94 eV, which is close to the activation energy of the donor levels, 0.8–1.0-eV; these levels are populated to a considerable extent [32] and were assigned [31] to anion vacancy clusters.

Thermal activation spectroscopy also revealed thermally activated acceptor levels in irradiated BN, which, when ionized, deliver holes to the VB [30, 32]. The correlation between the energy and kinetic parameters of (*p*-type) TSC and TSL permits one, with due account of the results of [22], to establish that the luminescence levels lie above the VB top by 0.1–0.2 eV (T = 300–500 K) and by 0.9–1.1 eV (T = 500–600 K). Taking into account the position of the acceptor levels of luminescence in the band gap and calculations, they can be identified with the lower *A* level (0.15 eV) of the trivacancy acting as an acceptor. The allowed electronic transition ($\varepsilon = 1.1$ eV) from the Γ'_{5v} point to the *A* level can be associated with a thermally activated transition with energy $\varepsilon > 0.9$ eV to levels of strongly populated traps, and the assumed transition $H^v \longrightarrow A$ (0.15 eV) is connected with the activation of shallow ($\varepsilon < 0.2$ eV), weakly populated levels.

The local absorption band at 2.85 ± 0.15 eV (curve *3* in Fig. 5), which is seen clearly in the $\alpha(h\nu)$ spectrum after annealing at $T_{an} \geq 1500$ K, can be due to transitions with energy $\varepsilon = 2.8$ eV from the VB (the Γ'_{5v} state) to the *E* level (1.88 eV); this is confirmed by the correlation between the dose dependences of the paramagnetic-center concentration [21] and optical density. The local bands of additional absorption, 2.9 ± 0.2 eV, and of induced photosensitivity, 2.9 ± 0.1 eV [30], which appeared after ion irradiation and were found to grow in intensity with increasing ion fluence, are also probably associated with the $\Gamma'_{5v} \longrightarrow E$ transitions (1.88 eV); however, the shift of the absorption-band maximum from 2.9 to 2.6 eV, observed to occur for $\Phi \geq 10^{17}$ cm^{-2} and after thermal treatment, and the structure of this band are apparently caused by the effect of the implanted impurity atoms on the population of the trivacancy levels. The PL band centered on $\varepsilon_i = 3.0 \pm 0.15$ eV (curve *2* in Fig. 7) (2.73–3.1 eV in [27]) may partially derive from electron transitions from the CB to the *E* level ($\varepsilon = 1.88$ eV) of the trivacancy (table).

The 1.9 ± 0.25-eV absorption band of the irradiated material may have contributions from the allowed electron transitions with energy $\varepsilon = 1.73$ eV between the trivacancy levels *A* (0.15 eV) and *E* (1.88 eV) and/or from the strong transitions ($\varepsilon = 1.95$ eV) from the *A* level (2.70 eV) to the CB states at the *L* point. The similarity between the annealing-temperature dependences of the optical density of the 1.9-eV band (curve *2* in Fig. 6) and of the concentration of unstable complex paramagnetic centers (curve *4*, Fig. 6) supports this band identification. The trivacancy levels *E* (3.93 eV) and *A* (2.70 eV) should act as traps for electrons excited to the CB from shallow donor levels ($\varepsilon = 0.2$–0.4 eV) of thermoluminescence ($T = 300$–500 K).

Thus, a comparison of the calculated levels of the nitrogen vacancy and of its small clusters with the characteristics of band-gap states in original and irradiated pyrolytic BN, which were revealed by thermal-activation and optical spectroscopy, has permitted us largely to confirm the important part played by the nitrogen vacancy and its complexes in the formation of the activation, recombination, absorption, and photoconductivity levels. The donor levels of activation with an energy 0.7–1.2 eV relative to the CB bottom can be identified with single vacancies of radiation or technological origin. The absorption band at 3.85 eV and the luminescence band at 3.6 eV (the interdefect or electron–phonon coupling) are formed in indirect electron transitions between the VB and the vacancy level *A*. The electronic transitions involving divacancy or trivacancy levels are most clearly seen in the stage of incomplete annealing of multivacancy paramagnetic centers in neutron-irradiated BN. These levels play the part of deep traps of nonequilibrium electrons and holes, which govern thermoluminescence.

ACKNOWLEDGMENTS

This study was supported by the program "Universities of Russia—Fundamental Research," project no. 06.01.05.

REFERENCES

1. G. V. Samsonov, *Nitrides* (Naukova Dumka, Kiev, 1969).
2. *EMIS Datareviews Series*, No. 11: *Properties of Group III Nitrides*, Ed. by J. H. Edgar (Kansas State University, 1994).
3. J. Neugebauer and C. G. van de Walle, Phys. Rev. B **50** (11), 8067 (1994).
4. P. Boguslawski, E. L. Briggs, and J. Bernholc, Phys. Rev. B **51** (23), 17255 (1995).
5. C. Stampfl, C. G. van de Walle, D. Vogel, *et al.*, Phys. Rev. B **61** (12), 7846 (2000).
6. A. M. Dobrotvorskij and R. A. Evarestov, Phys. Status Solidi B **66** (1), 83 (1974).
7. R. A. Évarestov, E. A. Kotomin, and A. N. Ermoshkin, *Models of Point Defects in Solids* (Zinatne, Riga, 1983).
8. A. Katzir, J. T. Suss, A. Zunger, and A. Halperin, Phys. Rev. B **11** (6), 2370 (1975).
9. A. Zunger and A. Katzir, Phys. Rev. B **11** (6), 2378 (1975).
10. V. A. Gubanov, Z. V. Lu, B. M. Klein, and C. Y. Fong, Phys. Rev. B **53** (8), 4377 (1996).
11. D. W. Jenkins and J. D. Dow, Phys. Rev. B **39**, 3317 (1989).
12. D. W. Jenkins, J. D. Dow, and M. H. Tsai, J. Appl. Phys. **72**, 4130 (1992).
13. W. Potz and D. K. Ferry, Phys. Rev. B **31**, 968 (1985).
14. E. S. Ho and J. D. Dow, Phys. Rev. B **27**, 1115 (1983).
15. S. N. Grinyaev and G. F. Karavaev, Fiz. Tekh. Poluprovodn. (St. Petersburg) **31** (5), 545 (1997) [Semiconductors **31**, 460 (1997)].
16. S. N. Grinyaev and V. V. Lopatin, Fiz. Tverd. Tela (St. Petersburg) **38** (12), 3576 (1996) [Phys. Solid State **38**, 1948 (1996)].
17. S. N. Grinyaev and V. V. Lopatin, Izv. Vyssh. Uchebn. Zaved., Fiz. **35** (2), 27 (1992).
18. L. Bellaiche, S.-H. Wei, and A. Zunger, Phys. Rev. B **54** (24), 17568 (1996).
19. M. B. Khusidman and V. S. Neshpor, Zh. Éksp. Teor. Khim. **3** (2), 270 (1967).
20. A. W. Moore and L. S. Singer, J. Phys. Chem. Solids **33**, 343 (1972).
21. A. V. Kabyshev, V. M. Kezkalo, V. V. Lopatin, *et al.*, Phys. Status Solidi A **126**, K19 (1991).
22. V. V. Lopatin and F. V. Konusov, J. Phys. Chem. Solids **53** (6), 847 (1992).
23. A. V. Kabyshev, F. V. Konusov, and V. V. Lopatin, Fiz. Tverd. Tela (St. Petersburg) **37** (7), 1981 (1995) [Phys. Solid State **37**, 1079 (1995)].
24. *Amorphous Semiconductors*, Ed. by M. H. Brodsky (Springer, New York, 1979; Mir, Moscow, 1982).
25. V. S. Dedkov, Yu. F. Ivanov, V. V. Lopatin, and B. N. Sharupin, Kristallografiya **38** (2), 217 (1993) [Crystallogr. Rep. **38**, 248 (1993)].
26. M. J. Puska, J. Phys.: Condens. Matter **1**, 7347 (1989).
27. O. A. Plaksin, V. A. Stepanov, P. A. Stepanov, *et al.*, J. Nucl. Mater. B **233–237**, 1355 (1996).
28. A. V. Kabyshev and V. V. Lopatin, Poverkhnost, No. 7, 86 (1994).
29. A. V. Kabyshev, F. V. Konusov, and V. V. Lopatin, Poverkhnost, No. 8, 34 (1996).
30. A. V. Kabyshev, F. V. Konusov, and V. V. Lopatin, Fiz. Khim. Obrab. Mater., No. 6, 21 (1997).
31. A. V. Kabyshev, F. V. Konusov, and V. V. Lopatin, Izv. Vyssh. Uchebn. Zaved., Fiz. **43** (3), 85 (2000).
32. A. V. Kabyshev, F. V. Konusov, and V. V. Lopatin, Poverkhnost, No. 5, 9 (2000).

Translated by G. Skrebtsov

Physics of the Solid State, Vol. 44, No. 2, 2002, pp. 294–299. Translated from Fizika Tverdogo Tela, Vol. 44, No. 2, 2002, pp. 283–288.

DEFECTS, DISLOCATIONS, AND PHYSICS OF STRENGTH

Motion of a Helium Atom through a Comparable-Diameter Channel in the Frenkel–Kontorova Model

E. V. Kalashnikov* and B. Z. Pevzner**

** Institute of Problems in Machine Science, Russian Academy of Sciences, Vasil'evskiĭ ostrov, Bol'shoĭ pr. 61, St. Petersburg, 199178 Russia*

e-mail: Kev@ipme.ru

*** Grebenshchikov Institute of Silicate Chemistry, Russian Academy of Sciences, ul. Odoevskogo 24/2, St. Petersburg, 199155 Russia*

e-mail: pevbor@omen.ru

Received March 19, 2001; in final form, May 22, 2001

Abstract—The motion of a helium atom through a channel with a diameter comparable to the diameter of this atom is investigated. Such channels are observed in materials of the quartz type. The inclusion of the local law of momentum conservation in the analysis of the interaction between the He atom and the atoms forming the channel wall makes it possible to reduce the problem to one-dimensional motion similar to the motion of a dislocation in the Frenkel–Kontorova model. In the model proposed here, the activation energy of the complex formed by the He atom and the displacements of atoms of the channel wall is calculated. The obtained energy is expressed in terms of the shear modulus of the material forming the channel and the helium atom polarizability, which depends on the state of the helium atom. © *2002 MAIK "Nauka/Interperiodica"*.

1. INTRODUCTION

The motion of helium atoms through thin channels is of considerable interest in the study of nanostructures [1, 2] and mechanical properties of materials [3, 4]. The penetration of He atoms into a crystal and their motion were studied experimentally and theoretically in terms of dynamic dislocation-assisted diffusion in [3]. This phenomenon as a new mechanism of the influence of the surroundings on the physical and mechanical properties of solids is of athermal nature and is observed only in a crystalline material plastically deformed in a gaseous or liquid medium, whose particles penetrate into the surface layer of the material through nucleating or moving dislocations. It has been proven, in particular in [5], that helium transport at $T \leq 300$ K occurs predominantly through dislocation tubes. (The dislocation tube diameter is 0.6–1 nm.)

The diffusion of helium through channels in zeolites was considered in [6, 7]. The channel diameter (0.5–5 nm) usually exceeds the diameter of an He atom (0.18–0.24 nm, according to different authors [2, 8–10]).

However, the situation when an He atom moves through a channel whose diameter is comparable with the diameter of this atom is completely different. Such channels are observed in crystalline materials of the quartz type. The structural unit in such materials is an SiO_4 tetrahedron [11]. The SiO_4 tetrahedrons are arranged so that they form long channels 0.24–0.26 nm in diameter (Fig. 1) [11].

It was observed long ago by Ioffe [12] that the diffusion of light ions (Na^+, K^+) takes place mainly through these channels [12, 13]. It was assumed that He atoms can also move through such channels relatively freely. This process must be characterized by a large diffusion coefficient and a high penetrability. However, experiments show that helium diffusion in such open crystalline structures formed by regular channels is 5–10 orders of magnitude lower than that in disordered glasslike structures [14, 15]. Thus, an open ordered structure is virtually impermeable for He, in contrast to a disordered structure.

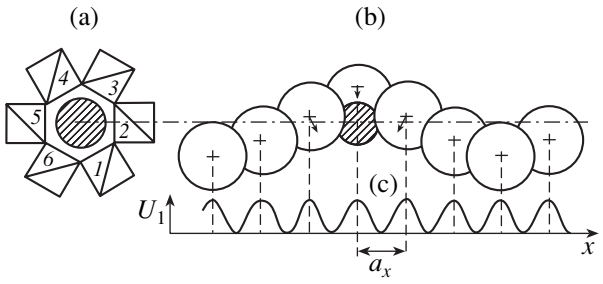

Fig. 1. Schematic diagram of a channel formed by SiO_4 tetrahedrons: (a) transverse and (b) longitudinal sections of the channel and (c) potential $\mathcal{U}_1$. Numerals in (a) denote tetrahedrons; the relative height of the silicon atom at the center of each next tetrahedron is larger by 1/3; the He atom is hatched. Arrows in (b) indicate the displacements of the oxygen atoms nearest to the He atom in the channel.

1063-7834/02/4402-0294$22.00 © 2002 MAIK "Nauka/Interperiodica"

It should be borne in mind, however, that a real channel in materials of the quartz type is formed not by the edges of the tetrahedrons but by oxygen atoms whose ionic radii are large (≈0.12 nm) [9] and almost overlap the geometrical diameter of the channel. In this case, a helium atom is in direct contact with the atoms forming the channel wall and pushes them apart during its motion through the channel. Therefore, in order to determine the behavior of a helium atom in a small-diameter channel, one must also know the character of motion of the atoms forming the channel wall. In the general case, this problem is three-dimensional. It will be proved below, however, that a system consisting of an He atom and atoms of the wall can be described in terms of a one-dimensional model similar to the Frenkel–Kontorova model proposed for describing the motion of a dislocation in a one-dimensional crystal. Using this model, we can determine the activation energy involved in the diffusion coefficient.

This work is devoted to an analysis of the motion of an He atom in a channel with a diameter comparable to the diameter of this atom and to the evaluation of the activation energy for such motion.

2. MODEL AND EQUATIONS OF MOTION

A channel in quartz along the optical axis *C* [0001] is formed by the edges of SiO_4 tetrahedrons [13, 16] (Fig. 1a). Oxygen atoms occupy positions at the corners of a tetrahedron. Thus, the channel wall is formed by a helical chain consisting of *n* oxygen atoms (Fig. 1b). The number *n* is infinitely large. Therefore, we can assume that the silicon atom in a tetrahedron is screened by oxygen atoms and a helium atom in the channel interacts only with the oxygen atoms, causing local deformation of the channel walls (Fig. 1b). The oxygen atoms forming the channel wall are displaced in this case through a distance $\boldsymbol{\xi}_n$ from their equilibrium positions $\mathbf{a}_n$. The change in the separation between the *n*th and $(n-1)$th atoms in the chain caused by these displacements can be written (in the components along the *x* axis) in the form

$$x_n - x_{n-1} - a_x = na_x + \xi_{nx} - (n-1)a_x - \xi_{n-1,x} - a_x = \xi_{nx} - \xi_{n-1,x}.$$

Consequently, the force (for definiteness, its component along the *x* axis) acting on the *n*th atom of such a chain is given by

$$F_{n,x} = -\alpha_c[(\xi_{n,x} - \xi_{n-1,x}) - (\xi_{n+1,x} - \xi_{n,x})] = \alpha_c[\xi_{n+1,x} + \xi_{n-1,x} - 2\xi_{n,x}],$$

where α_c is the elastic interaction constant between the oxygen atoms forming the channel wall.

Similar forces are exerted on the helium atom by the chain. A helium atom in such a chain is surrounded by three atoms of the spiral (Fig. 1b). We assume that the He atom interacts elastically and pairwise independently with each nearest neighbor atom of the wall. Consequently, the elastic force exerted on the He atom by the surroundings of *z* atoms is equal to the sum of these forces; the *x* component of this force is

$$F_{\gamma x} = -\alpha_\gamma[(\gamma_{1,x} - \xi_{nx}) - (\xi_{n+1,x} - \gamma_{1,x}) + (\gamma_{2,x} - \xi_{n+1,x}) - (\xi_{n+2,x} - \gamma_{2,x}) + (\gamma_{3,x} - \xi_{n+2,x}) - (\xi_{n,x} - \gamma_{3,x})]. \quad (1)$$

Here, γ_m is the displacement vector of the He atom (m = 1–3) and α_γ is the elastic interaction constant between the helium atom and oxygen atoms (it will be proved below that this quantity is determined by the polarizability of the helium atom).

Since neither of the elastic forces acting between the *n*th atom, the He atom, and the $(n+1)$th atom has any preference over the other forces, we assume that

$$\gamma_{1,x} = \gamma_{2,x} = \gamma_{3,x} = \gamma_x. \quad (2)$$

In this case, the *x* component of force (1), which is exerted on the helium atom by the wall, is given by

$$F_{\gamma x} \simeq \alpha_\gamma(z/2)[\xi_{n+1,x} + \xi_{nx} - 2\gamma_x]. \quad (3)$$

A transition of the He atom to another (adjacent) position in the channel causes displacements of atoms of the wall, making way for the He atom. Subsequently, the wall atoms return to their initial positions under the action of the periodic crystal field. This periodic field (presented in Fig. 1c) also acts on the moving He atom. In this case, the potential of this field has the form

$$\mathcal{U}_1 = A[1 - \cos(2\pi\gamma_x/a_x)]. \quad (4)$$

The displacement of the He atom along the channel is described by a system of $3(n+1)$ differential equations:

$$\begin{cases} md^2\gamma_x/dt^2 = -\partial\mathcal{U}/\partial\gamma_x = -2\pi A a_x^{-1}\sin(2\pi\gamma_x/a_x) \\ \quad + (z/2)\alpha_\gamma(\xi_{n+1,x} + \xi_{n,x} - 2\gamma_x) \\ md^2\gamma_j/dt^2 = -\partial\mathcal{U}/\partial\gamma_j \\ \quad = (z/2)\alpha_\gamma(\xi_{n+1,j} + \xi_{n,j} - 2\gamma_j), \quad j = y, z \\ Md^2\xi_{n,j}/dt^2 = \alpha_c(\xi_{n+1,j} + \xi_{n-1,j} - 2\xi_{n,j}) \\ \quad + (z/2)\alpha_\gamma(\xi_{n+1,j} + \xi_{n,j} - 2\gamma_j), \quad j = x, y, z. \end{cases} \quad (5)$$

Here, *M* is the mass of an oxygen atom, *m* is the mass of the helium atom, index *n* labels oxygen atoms in the channel, index *j* denotes the components of the displacement vectors $\boldsymbol{\xi}$ and $\boldsymbol{\gamma}$ ($j = x, y, z$), and potential $\mathcal{U}$ is the sum of the potential of elastic forces corresponding to the force $F_{\gamma,x}$ in Eq. (3) and the potential $\mathcal{U}_1$ given by Eq. (4). Both potentials play the role of an external field relative to the He atom.

The system of equations (5) shows that in order to determine the law of motion of the He atom, we must know the behavior of the *n* oxygen atoms forming the channel wall. In turn, the displacements $\boldsymbol{\xi}_n$ of oxygen

atoms are caused by displacements of the helium atom in the channel. The first equation in system (5) is similar to the Frenkel–Kontorova equation [17, 18]. The form of this equation is a consequence of the application of potential (4), which was first introduced by Taylor to describe the plastic deformation of a crystal [19]. The similarity between the first equation in system (5) and the Frenkel–Kontorova equation suggests a possible way to solve the system.

3. REDUCTION OF THREE-DIMENSIONAL MOTION TO THE ONE-DIMENSIONAL CASE

In accordance with the idea put worth by Frenkel and Kontorova [17, 18], we assume that a helium atom and the perturbation (displacements of oxygen atoms) caused by it propagate at a constant velocity v. Then, a complex consisting of the He atom and the displacements of wall atoms passes to an adjacent position in the time $\tau = a_x/v$ and the displacements ξ_n of the atoms of the channel wall change insignificantly. This is equivalent to the conditions $\xi_n(t) = \xi_{n+1}(t + \tau)$ and $\xi_{n+1}(t) = \xi_n(t - \tau)$. We expand the amplitudes of displacements in a power series in τ and, to the second-order terms, write $\xi_{n\pm1,x} = \xi_{n,x}(t \pm \tau) = \xi_{n,x}(t) \pm (d\xi_{n,x}/dt)\tau + (d^2\xi_{n,x}/dt^2)\tau^2/2!$. In this case, the first parenthetical expression in Eq. (5) for the displacements of atoms of the wall has the form $\xi_{n+1,x} + \xi_{n-1,x} - 2\xi_{n,x} = (d^2\xi_{n,x}/dt^2)\tau^2$.

In connection with the subsequent transformation of the system of equations (5), it should be noted that expression (1) can be regrouped, taking into account relation (2), so that the expression for displacements in the parentheses acquires a more conventional form and becomes equal to $(\xi_{n+1,x} + \xi_{n-1,x} - 2\gamma_x)$. Further, we assume that the amplitude ξ_n of the displacement of a wall atom during time τ does not exceed the amplitude γ of the displacement of the He atom. (This assumption is equivalent to the local law of momentum conservation in the interaction of the He atom with the oxygen atoms; see [9].) In this case, the displacements in the parentheses in Eqs. (1), (3), and (5) can be represented in an analogous form, $\xi_{n+1,x} + \xi_{n-1,x} - 2\gamma_x \simeq \tau^2(d^2\gamma_x^2/dt^2)$. A similar equality is also valid for the y and z components.

As a result, the system of equations of motion (5) of an He atom in a channel and of the channel itself acquires the form

$$\begin{cases} m^* d^2\gamma_x/dt^2 = -2\pi A a_x^{-1}\sin(2\pi\gamma_x/a_x) \\ M^* d^2\gamma_{n,x}/dt^2 = (z/2)\alpha_\gamma\tau^2(d^2\gamma_x/dt^2) \\ m^* d^2\gamma_j/dt^2 = 0 \\ M^* d^2\xi_{n,j}/dt^2 = (z/2)\alpha_\gamma\tau^2(d^2\gamma_j/dt^2), \quad j = y, z. \end{cases} \tag{6}$$

This system can be reduced to a system of equations for one-dimensional motion of the helium atom and n atoms of the channel wall:

$$\begin{cases} m^* d^2\gamma_x/dt^2 = -2\pi A a_x^{-1}\sin(2\pi\gamma_x/a_x) \\ M^* d^2\xi_{n,x}/dt^2 = (z/2)\alpha_\gamma\tau^2(d^2\gamma_x/dt^2). \end{cases} \tag{7}$$

Here, $M^* = M - \alpha_c\tau^2$ is the effective mass of an oxygen atom and m^* is the effective mass of the helium atom,

$$m^* = m - (z/2)\alpha_\gamma\tau^2. \tag{8}$$

The second equation in system (7) is the law of momentum conservation in local form (index n for $\xi_{n,x}$ indicates this locality),

$$d/dt[M^*(d\xi_{n,x}/dt) + (m^* - m)(d\gamma_x/dt)] = 0, \tag{9}$$

and leads to the following relation between the displacements of the He atom and of one of the atoms in the channel wall:

$$\begin{aligned} \gamma_x &= (M^*\xi_{n,x} - q_x\tau)/(m - m^*) \\ &= 2(M^*\xi_{n,x} - q_x\tau)/(z\alpha_\gamma\tau^2), \end{aligned} \tag{10}$$

where $q_x = M^*(d\xi_{n,x}/dt) + (m^* - m)(d\gamma_x/dt) = \text{const}$. It can be seen from Eq. (10) that γ_x can be expressed in terms of the quantities $\xi_{n,x}$. In particular, for $q_x = 0$, we have $\gamma_x = 2M^*\xi_{n,x}/(z\alpha_\gamma\tau^2)$. For this reason, we introduce the notation $\gamma_x = \gamma_{x,n}$. (The condition $q_x = 0$ only leads to a phase shift in the motion of the He atom relative to oxygen atoms and does not affect the basic results concerning the evaluation of the energy of this motion.)

Relation (9) makes it possible to reduce the entire system of equations (7) to a one-dimensional equation of motion of the nth atom in a chain, which was derived by Frenkel and Kontorova:

$$m^* d^2\gamma_{x,n}/dt^2 = -2\pi A a_x^{-1}\sin(2\pi\gamma_{x,n}/a_x). \tag{11}$$

In our case, this equation describes the motion of an atom in a chain consisting of n atoms of He. Such a chain is of virtual nature and arises as a result of the transition of the He atom and of the wall atom displacements accompanying it to an adjacent position in the channel. The potential energy of the elastic interaction between He atoms in such a chain,

$$\mathcal{U}_1 = \alpha_\gamma(z/2)\Sigma_n(\gamma_{x,n} - \gamma_{x,n-1})^2/2 \tag{12}$$

is determined by the interaction constant α_γ of He atoms with oxygen atoms in the channel wall defined in Eq. (1). The entire chain moves in the field $\mathcal{U}_2 = A\Sigma_n(1 - \cos 2\pi\gamma_{n,x}/a_x)$ determined by the superposition of sinusoidal potentials created by displacements of the He atom at each of the n atoms of the channel wall.

In the subsequent analysis, we will be interested in the process associated with the activation of the motion of the He atom through the channel. This process is equivalent to the activation of a perturbation in a virtual

chain composed of He atoms. For this reason, we assume that the initial conditions are the same as in [17, 18]:

$$\gamma_{n,x} = 0, \quad d\gamma_{n,x}/dt = 0. \tag{13}$$

In the next section, we present the relations required for evaluating the energy of the chain. These relations coincide (except for the substitution $\alpha \longrightarrow z\alpha_\gamma/2$) with the relations derived by Frenkel and Kontorova.

4. BASIC RELATIONS

Integrating Eq. (11) with initial conditions (13), we find the velocity of an He atom in the channel (in the chain of He atoms),

$$d\gamma_{x,n}/dt = \pm 2(-A/m^*)^{1/2}\sin(\pi\gamma_{x,n}/a_x), \tag{14}$$

and its displacement, viz., the Frenkel–Kontorova soliton (kink) [20],

$$\gamma_{n,x} = (2a_x/\pi) \times \arctan(C\exp[\pm 2\pi(\sqrt{-A/m^*}t)/a_x]), \tag{15}$$

where constant C can be determined from the initial conditions (13). Then, the time taken by an He atom of effective mass m^* to traverse the distance a_x is

$$T = (a_x/2\pi)(-m^*/A)^{1/2}. \tag{16}$$

It follows from Eq. (15) that the uniform motion of a complex consisting of the He atom and the displacements of wall atoms is characterized by a negative value of the effective mass in Eq. (8), $m^* < 0$.

We assume that the velocity v of the helium atom moving in the channel does not exceed the sound velocity c in the chain of oxygen atoms. In this case, the effective mass m^* can be written in the form

$$m^* = m[1-(c/v)^2]. \tag{17}$$

From Eqs. (17) and (16), we find the length of the channel region perturbed by the He atom: $\lambda = vT = \lambda_0[1-(v/c)^2]^{1/2}$, where $\lambda_0 = (a_x^2/2\pi)(z\alpha_\gamma/2A)^{1/2}$. The quantity λ_0 depends strongly on the state of the helium atom and may change from fractions of a nanometer to several tens of nanometers. This is due to the dependence of α_γ on the polarizability of the He atom [see Eq. (20)].

The interaction of helium atoms in the virtual chain is determined by the interaction constant α_γ. If the value of α_γ is small or equal to zero, then a virtual chain composed of He atoms does not arise, in accordance with Eqs. (8) and (12). The effective mass m^* of the helium atom becomes positive, and the quantity $\gamma_{n,x}$ given by Eq. (15) is an oscillating function of time. This means that the He atom in this case can perform only oscillatory motion.

The total energy of the virtual chain of helium atoms is given by

$$E = U + K = -4A(\alpha_\gamma z\tau^2/2m^*)\Sigma_n \sin^2(\pi\gamma_{n,x}/a_x). \tag{18}$$

Here, the potential energy U is equal to the sum of $\mathcal{U}_1$ given by Eq. (12) and $\mathcal{U}_2$, while K is the kinetic energy calculated with the help of formula (14). Passing in Eq. (18) from summation to integration and carrying out standard operations [17, 18], we obtain an expression for the total energy of the chain of helium atoms in the relativistic form: $E = E_0/1-(v/c)^{21/2}$, where E_0 is the rest energy of the chain,

$$E_0 = (4a_x/\pi)(\alpha_\gamma zA/2)^{1/2}. \tag{19}$$

This quantity sets the lower limit on the range of values of energy E sufficient for an He atom to move through the channel. For energies lower than E_0, the motion of an He atom through the channel is impossible. The upper boundary value of E is set by the condition that the velocity of an He atom in the channel does not exceed the velocity of sound propagation in the oxygen chain (in quartz).

Thus, for an He atom to be able to move through the channel, its energy must lie in a certain range. The energy E_0 is the minimum energy above which a virtual chain arises and its perturbation can propagate even if this minimum energy is exceeded only slightly. Therefore, E_0 is the activation energy for a perturbation propagating in the virtual chain (or, equivalently, in complexes consisting of the He atom and the displacements of atoms of the channel wall). Let us now evaluate E_0 from independent data.

5. ACTIVATION ENERGY

Expression (19) for the quantity E_0 incorporates three different characteristics. One of them (α_γ) corresponds to the He atom, and another (a_x) characterizes the crystalline structure of the channel. The third characteristic (A) is the maximum value of the interaction potential between the helium atom and an oxygen atom.

Let us determine α_γ. The displacements ξ_n of the oxygen atoms forming the channel wall are caused by the moving He atom and lead to violation of the equilibrium distribution of charges in SiO_4 tetrahedrons. Local dipole moments arise and attain values of the order of the product of the electron charge and the diameter of the atom. The electric field induced in this case is of the order of the intra-atomic field. This local field $\mathcal{E}(r)$ acts on the He atom and induces a dipole moment in it, $p_{\text{ind}} = ed = \beta\mathcal{E}$, where β is the polarizability of the He atom, e is the electron charge, and d is the displacement of an electron in the atom. Here, we assume that the field $\mathcal{E}$ is uniform over the He-atomic-

size region. The potential energy of the induced dipole in this field is $V_{pot} = (1/2)\mathscr{E}p_{ind} = (1/2)(p_{ind}/\beta)p_{ind} = (p_{ind})^{1/2}/2\beta = (ed)^2/2\beta$. On the other hand, the potential energy is equal to the elastic energy due to the displacement of the He atom, $V_{pot} = \alpha_\gamma d^2/2$. The equality of these two energies gives

$$\alpha_\gamma = e^2/\beta. \quad (20)$$

The polarizability β of the He atom depends on its state. In particular, if He is in the ground state 1^1S_0, its polarizability is $\beta = 0.0203$ nm^3 [21, 22]. If, however, the He atom is in one of the metastable states 2^1S_0 or 2^3S_1, its polarizability is 11.8 or 4.67 nm^3, respectively.

Now, we determine the value of A using the result obtained by Indenbom [23]. Let the lattice parameters be a_y along the normal to the plane of Fig. 1 and a_z in the direction lying in this plane and perpendicular to a_y and a_x. Comparing the displacement of oxygen atoms with a uniform shear strain of the crystal in the x direction, we find the shear modulus $G = A4\pi^2 a_z/a_x^3 a_y$. This leads to the following expression for the amplitude of the potential in Eq. (4) in terms of observable quantities: $A = Ga_x^3 a_y/4\pi^2 a_z$. Therefore, the activation energy in Eq. (19) can be written in the form

$$E_0 = (2e/\pi^2)\sqrt{(z/2)(G/\beta)a_x^5 a_y/a_z}. \quad (21)$$

Let us estimate the value of this quantity for quartz. We assume that a_y and a_z in Eq. (14) are of the same order of magnitude ($a_y/a_z \approx 1$). Further, $e = 1.6 \times 10^{-19}$ Pa, $G = 39.1 \times 10^9$ Pa [16], $\beta(2^3S_1) = 4.67$ nm$^3 = \beta_1$ and $\beta(1^1S_0) = 0.0203$ nm$^3 = \beta_2$ [10, 21, 22]; the value of a_x can be determined from the channel geometry (Fig. 1) and the separation between the oxygen atoms in a tetrahedron [15], which is equal to 0.265 nm. In this case, we have from Eq. (21) $E_0 = (2e/\pi^2)\sqrt{(z/2)(G/\beta)a_x^5}$. The activation energy (for different values of the polarizability of the He atom) is found to be

$$E_0(\beta_2) = 6.18 \text{ eV}, \quad E_0(\beta_1) = 0.4 \text{ eV}.$$

The value of $E_0(\beta_2)$ is comparable to the values of energy typical of chemical compounds. With such an activation energy, a helium atom cannot move through the channel. However, an excited He atom has an activation energy one order of magnitude lower. Therefore, an excited He atom can move quite freely through the channel. In connection with such a large difference in the values of activation energy, we note that the experimentally determined activation energy for the diffusion of He atoms in quartz has a considerable spread: the value of this quantity is 0.54 eV according to [24], while in [25], this quantity is reported to be 1 eV and becomes even higher at lower temperatures.

6. DISCUSSION

In the present work, the motion of a helium atom through a channel whose diameter is comparable with the diameter of this atom is considered. This problem can be solved only numerically, because the state of the atoms of the channel wall must be taken into account. In this case, it is difficult to find an appropriate functional relation between the activation energy and the parameters characterizing the channel and the He atom. However, the inclusion of the short-range order (the number z) and the approximation of the elastic interaction of the He atom with the surroundings followed by the inclusion of the local law of momentum conservation in this interaction made it possible to reduce the problem to the one-dimensional Frenkel–Kontorova model. In this case, however, the He atom in the channel of comparable diameter cannot be regarded as an independent particle any longer. Instead, a chain of He atoms with a new interatomic interaction potential (12), which is completely controlled by the polarizability of the He atom, should be considered. The chain of these atoms is virtual by nature; it should be dealt with each time the helium atom and the displacements of oxygen atoms accompanying it move to an adjacent position in the channel.

It is important that, in order for a helium atom to be able to move through the channel, the atom necessarily interacts with local electric fields. Such fields arise as a result of displacements of the oxygen atoms forming the channel wall and are found to be strong enough to polarize the helium atom. On the other hand, the polarizability of the helium atom strongly depends on its quantum state and determines, to a considerable extent, the conditions of motion of the atom through the channel.

Indeed, if an He atom is in the ground state, its polarizability is extremely small and the atom virtually does not move through the channel. The length λ_0 of the channel region involved in the interaction with the He atom in this case is ~3 nm. The He atom is strongly bound and oscillates. The activation energy is high and considerably exceeds any energy of the chemical bond between oxygen atoms and between an oxygen atom and a silicon atom [15]. In other words, the He atom in the ground state can move only if the channel is destroyed. In addition, if we disregard the other quantum states of He, the value of λ_0 can reach as high as ~10^7 nm.

However, being in a metastable state, the He atom becomes capable of moving freely along the channel. The length λ_0 of the channel region involved in the motion is ~0.2 nm in this case. The most important excited state of He is 2^3S_1. This state is a long-lived one with a lifetime of 6×10^5 s [10].

Summarizing our results, we note that an He atom in a channel with comparable diameter is strongly bound and cannot move if it is in the ground state. If, however,

the He atom is in an excited (in particular, a long-lived) state, it can easily move through the channel. However, such a motion occurs only if the energy of the atom lies in a certain range.

ACKNOWLEDGMENTS

The authors are grateful to O.V. Klyavin for fruitful discussions of the problem.

This work was supported by the Swiss National Science Foundation, grant no. 7SUPJ062127.

REFERENCES

1. J. F. Shackelford, J. Non.-Cryst. Solids **49**, 19 (1982).
2. J. F. Shackelford, J. Non.-Cryst. Solids **49**, 299 (1982).
3. O. V. Klyavin, Fiz. Tverd. Tela (St. Petersburg) **35**, 513 (1993) [Phys. Solid State **35**, 261 (1993)].
4. O. V. Klyavin, *Physics of Plasticity of Crystals at Helium Temperatures* (Nauka, Moscow, 1987).
5. O. V. Klyavin, N. P. Likhodedov, and A. N. Orlov, Fiz. Tverd. Tela (Leningrad) **28**, 156 (1986) [Sov. Phys. Solid State **28**, 84 (1986)].
6. E. G. Derouane, J.-M. Andre, and A. A. Lucas, J. Catal. **110**, 58 (1988).
7. A. V. Kiselev, A. A. Lopatkin, and A. A. Shulga, Zeolites **5**, 261 (1985).
8. R. H. Doremus, *Glass Science* (Wiley, New York, 1973), p. 133.
9. L. Pauling, *The Nature of the Chemical Bond and the Structure of Molecules and Crystals* (Cornell Univ. Press, Ithaca, 1940; Gostekhizdat, Moscow, 1947).
10. Yu. P. Raizer, *Gas Discharge Physics* (Nauka, Moscow, 1987; Springer-Verlag, Berlin, 1991).
11. A. G. Betekhtin, *Mineralogy* (Leningrad, 1950), pp. 424–429.
12. A. F. Ioffe, *Crystal Physics* (ONTI, Moscow, 1923).
13. E. H. Snow and P. Gibbs, J. Appl. Phys. **35**, 2368 (1964).
14. B. A. Mamyrin and I. N. Tolstikhin, *Helium Isotops in Nature* (Elsevier, Amsterdam, 1984).
15. V. K. Leko, Fiz. Khim. Stekla **19**, 673 (1993).
16. A. V. Shubnikov, *Quartz and Its Application* (Akad. Nauk SSSR, Moscow, 1940).
17. T. A. Kontorova and Ya. I. Frenkel', Zh. Éksp. Teor. Fiz. **8**, 89 (1938).
18. Ya. I. Frenkel', *Introduction to the Theory of Metals* (Gostekhizdat, Moscow, 1950).
19. G. I. Taylor, Proc. R. Soc. London, Ser. A **145**, 362 (1934).
20. A. S. Davydov, *Solitons in Molecular Systems* (Naukova Dumka, Kiev, 1988; Kluwer, Dordrecht, 1991).
21. H. A. Bethe and E. E. Salpeter, *Quantum Mechanics of One- and Two-Electron Atoms* (Academic, New York, 1957; Fizmatgiz, Moscow, 1960).
22. K. T. Chang and R. P. Hurst, Phys. Rev. **152**, 35 (1966).
23. V. L. Indenbom, Kristallografiya **3**, 197 (1958) [Sov. Phys. Crystallogr. **3**, 193 (1958)].
24. R. M. Barrer and D. E. Vaughan, Trans. Faraday Soc. **63**, 2275 (1967).
25. T. W. Trull, M. D. Kurz, and W. J. Jenkins, Earth Planet. Sci. Lett. **103**, 241 (1991).

Translated by N. Wadhwa

Physics of the Solid State, Vol. 44, No. 2, 2002, pp. 300–301. Translated from Fizika Tverdogo Tela, Vol. 44, No. 2, 2002, pp. 289–290.

DEFECTS, DISLOCATIONS, AND PHYSICS OF STRENGTH

Dislocation-Induced Internal Friction of a Material with Vacancies in Weak Magnetic Field Pulses

O. I. Datsko

Donetsk Physicotechnical Institute, National Academy of Sciences of Ukraine, Donetsk, 83114 Ukraine

Received May 7, 2001; in final form, July 10, 2001

Abstract—It is found that the form of the amplitude dependence of low-frequency internal friction in a quenched and aged aluminum sample (99.999% pure) changes under the effect of weak magnetic field pulses ($H \geq 10^5$ A/m): the general level of internal friction increases. This effect is attributed to the influence of a magnetic field on the structural complex formed by a dislocation and point defects (the role of point defects is played by vacancies). © *2002 MAIK "Nauka/Interperiodica".*

It was demonstrated earlier [1–3] that the level of dislocation-induced internal friction (IF) in technically pure materials in a nonequilibrium metastable state changes under the action of pulses of a weak ($H \leq 10^5$ A/m) magnetic field (WMFP). On the other hand, the IF level in a deformed (nonaged) material or a material with a high degree of purity does not change under the action of WMFP. In other words, the effect takes place when dislocations are pinned by impurity atoms and is absent for dislocations free of impurity atoms. The observed changes in the IF level were attributed to the influence of WMFP on structural complexes of the dislocation–point defect type containing magnetically active states excited by WMFP and were explained as resulting from a change in the strength of interaction of dislocations with impurity atoms located at dislocations and hampering their motion.

According to the ideas developed in [4, 5], a magnetic field affects structural complexes such as dislocation–paramagnetic pinning centers, whose role can be played by impurity atoms of paramagnetic elements or vacancies. Consequently, we can expect that if in a material saturated with vacancies, the vacancies play the role of paramagnetic centers located at dislocations, then the dislocation-induced IF will vary as a result of the action of WMFP; otherwise, no effect will be observed. This communication aims at comparing the changes in dislocation-induced IF under the action of WMFP in a material saturated with vacancies blocking dislocations and in a material unsaturated with vacancies.

The object of our investigations was Al, for which it is known that (1) deformation-induced vacancies vanish upon recrystallization [6]; (2) the concentration of vacancies increases upon quenching [7]; (3) quenching-induced vacancies block dislocations as a result of ageing of the material [7] and vanish upon tempering [8, 9]; and (4) after quenching, the level of amplitude-dependent dislocation-induced IF becomes lower; this is due to vacancies moving towards dislocations and blocking them upon quenching, because the dislocations become fixed [7].

In order to reduce the effect of impurity atoms as point defects blocking dislocations, we used aluminum of a high-purity grade (99.999%). Samples in the form of wires in diameter 3 mm and a working part length of 40 mm were obtained through hydraulic pressing; they had a recrystallized structure and, hence [6], were characterized by a low concentration of vacancies. In order to increase the concentration of vacancies, a sample was heated to 600°C, held at this temperature for an hour, and then quenched in water. For dislocations to be blocked by vacancies, the quenched sample was subjected to ageing at room temperature for 24 h [7]. For decreasing the concentration of vacancies, the quenched and aged sample was tempered by heating to 300°C and held for 1.5 h at this temperature [8, 9].

The sample was subjected to the action of WMFP under the following conditions: the magnetic field amplitude was 3×10^5 A/m, the pulse leading-edge time was 10^{-4} s, the pulse repetition rate was 0.5 Hz, and the time of action was up to 5 min.

The internal friction was measured using an inverse torsion pendulum with an oscillation frequency of approximately 1 Hz. The dependence of IF on the deformation amplitude, which varied from 2×10^{-5} to 12×10^{-5}, was determined. The total time of measurements did not exceed 5 min, and the error was within 10%. A decrease in the amplitude was not accompanied by any IF hysteresis. The IF magnitude was measured before and during the action of WMFP first in the initial recrystallized sample (with a reduced vacancy concentration), then in the quenched and aged sample (with an elevated concentration of vacancies), and, finally, in the tempered sample (with a lowered concentration of vacancies).

1063-7834/02/4402-0300$22.00 © 2002 MAIK "Nauka/Interperiodica"

The experiments proved that the IF of the material in the initial recrystallized state is characterized by an elevated magnitude and a well-defined amplitude dependence (figure, curve *1*). The action of WMFP on the sample does not modify the amplitude dependence of IF (curve *2*).

This result indicates that structural complexes of the dislocation–pinning center type have no magnetically active states excited by WMFP (the role of the pinning centers is probably played by the nodes corresponding to the intersection of dislocations).

The amplitude dependence of the IF of the material in the quenched and aged state is characterized by a lower IF level and by a stronger amplitude dependence (curve *3*). The observed changes in IF as a result of quenching and ageing of the sample (curves *1*, *3*) are similar to those described in [7]. These changes indicate that dislocations in the material have been pinned by new pinning centers in the form of point defects (vacancies) and that the number of dislocation segments breaking away from pinning centers has increased. The action of WMFP on a quenched and aged sample elevates the general IF level and suppresses the amplitude dependence (curve *4*), which indicates the emergence of magnetically active WMFP-induced states in structural complexes of the dislocation–pinning center type as a result of quenching and ageing of the material. In other words, WMFP affect structural complexes of the dislocation–point defect type, in which vacancies play the role of paramagnetic point defects. This effect is manifested in the depinning of dislocations from vacancies.

The amplitude dependence of the IF of the material in the tempered state after quenching and ageing is characterized by an elevated general level and a weak amplitude dependence (curve *5*). The observed changes in the IF as a result of tempering of a quenched and aged sample (curves *3*, *5*) indicate that dislocations have broken away from point defects (vacancies) in the material and the number of dislocation segments breaking away from pinning centers has decreased. The action of WMFP on a tempered sample does not alter the amplitude dependence of IF (curve *6*). This indicates that the magnetically active states excited by WMFP in structural complexes of the dislocation–pinning center type have disappeared as a result of tempering of the quenched and aged material.

The results obtained by us indicate that (1) the nature of the amplitude dependence of IF is changed upon the action of WMFP on the material in the case when dislocations are pinned by vacancies and remains unchanged when dislocations are free of vacancies; (2) the physics of the observed changes in the amplitude dependence of the IF in the material may be associated with the magnetically active state excited by WMFP in a structural complex of the dislocation–point defect (vacancies) type; and (3) the effect can be explained as resulting from a change in the interaction energy between dislocations and vacancies blocking them upon the action of WMFP on a material saturated with vacancies.

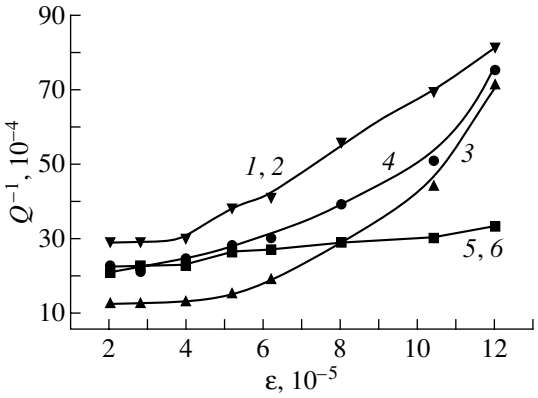

Amplitude dependences of the IF in aluminum (99.999%): (*1*, *3*, *5*) under ordinary conditions of measurements and (*2*, *4*, *6*) during the action of WMFP for (*1*, *2*) the initial recrystallized, (*3*, *4*) quenched and aged, and (*5*, *6*) tempered states of the material.

REFERENCES

1. O. I. Datsko, V. I. Alekseenko, and A. D. Shakhova, Fiz. Tverd. Tela (St. Petersburg) **38** (6), 1799 (1996) [Phys. Solid State **38**, 992 (1996)].
2. O. I. Datsko and V. I. Alekseenko, Fiz. Tverd. Tela (St. Petersburg) **39** (7), 1234 (1997) [Phys. Solid State **39**, 1094 (1997)].
3. O. I. Datsko, V. I. Alekseenko, and A. L. Brusova, Fiz. Tverd. Tela (St. Petersburg) **41** (11), 1985 (1999) [Phys. Solid State **41**, 1821 (1999)].
4. Yu. I. Golovin and R. B. Morgunov, Izv. Ross. Akad. Nauk, Ser. Fiz. **61** (5), 850 (1997).
5. Ya. B. Zel'dovich, A. L. Buchachenko, and E. L. Frankevich, Usp. Fiz. Nauk **155** (1), 3 (1988) [Sov. Phys. Usp. **31**, 385 (1988)].
6. R. W. Balluffi, J. S. Koehler, and R. O. Simmons, in *Proceedings of a Symposium on Recovery and Recryslallization of Metals, New York, 1962* (Interscience, New York, 1963; Metallurgiya, Moscow, 1966).
7. A. H. Cottrell, in *Proceedings of the Symposium on Vacancies and Other Point Defects in Metals and Alloys, Harwell, 1957* (Inst. of Metals, London, 1958; Metallurgizdat, Moscow, 1961).
8. T. Federighi, in *Proceedings of the International Conference on Lattice Defects in Quenched Metals, Argon, 1964* (Academic, New York, 1965; Atomizdat, Moscow, 1969).
9. H. Kimura and R. Maddin, in *Proceedings of the International Conference on Lattice Defects in Quenched Metals, Argon, 1964* (Academic, New York, 1965; Atomizdat, Moscow, 1969).

Translated by N. Wadhwa

Physics of the Solid State, Vol. 44, No. 2, 2002, pp. 302–307. Translated from Fizika Tverdogo Tela, Vol. 44, No. 2, 2002, pp. 291–296.

DEFECTS, DISLOCATIONS, AND PHYSICS OF STRENGTH

Analysis of Dynamic Dislocation-Assisted Penetration of Helium into Tin and Cadmium Deformed by Stretching in Liquid Helium

O. V. Klyavin, B. A. Mamyrin, L. V. Khabarin, and Yu. M. Chernov

Ioffe Physicotechnical Institute, Russian Academy of Sciences,
ul. Politekhnicheskaya 26, St. Petersburg, 194021 Russia
e-mail: mamyrin.mass@pop.ioffe.rssi.ru

Received July 11, 2001

Abstract—Curves describing the liberation of helium from Sn single crystals deformed by stretching in liquid ^{3}He and ^{4}He and from Cd polycrystals in ^{4}He are analyzed. It is found that the stress–strain diagrams for Sn are in qualitative agreement with the concentration of helium in the samples. The peaks in the amount of He liberated from Cd and Sn at temperatures both below and above the melting point are found to be of different types. The reasons for this difference are investigated, and the assumption concerning the existence of a chemical bond between helium atoms and structural defects of the metals under investigation is formulated. © *2002 MAIK "Nauka/Interperiodica".*

1. INTRODUCTION

This article continues an analysis of the physical mechanism of the influence of the ambient on the physical and mechanical properties of solids, in particular, the phenomenon of dislocation-assisted dynamic diffusion (DADD), viz., the penetration of particles of a gaseous or liquid medium into crystalline materials through nucleating and moving dislocations [1–3]. The DADD effect was observed for a model medium of liquid helium. Single crystals of CsI, LiF, and NaCl [2, 3], as well as polycrystals of metals (In, Zn, Pb, Cu [4], Al [5], Ti [6]), were investigated. It was found that these materials contain considerable amounts of helium after deformation in a liquid helium medium. The processes of helium liberation from samples deformed to different degrees are studied to determine the amount of helium and the type of traps confining helium atoms in these materials at various temperatures.

An analysis of LiF crystals [4] deformed in liquid helium (T = 4.2–1.3 K) revealed various types of traps and migration routs for He atoms in these objects. The general nature of the DADD phenomenon was also confirmed for a heavy-water medium [7], whose molecules penetrate in different amounts and to different depths into the surface layer of LiF crystals, depending on the type of dislocations (edge or screw dislocations) and on the degree of plastic deformation. The penetration of the surroundings not only into crystalline but also into amorphous materials was discovered for amorphous eutectic films of $Pd_{84.5}$–$Si_{15.5}$ and N_{78}–Si_8–B_{14} [8] deformed by stretching in a liquid ^{3}He or ^{4}He medium. It was found that the quantity of He atoms is in one-to-one correspondence with the number and length of plastic shifts in these materials. Curves describing the liberation of helium from amorphous films are obtained for a wide temperature range up to their melting point. An analysis of these curves led us to assume the existence of a chemical bond between helium atoms and structural defects formed in the course of plastic deformation. Thus, the physical mechanism of the DADD phenomenon typical of crystalline materials and amorphous films gives rise to the effect of mechanochemical penetration of helium atoms through dynamically excited defects of their atomic structure, where plastic shear strains are formed and develop.

The present work aims at extending the range of materials with different types of crystal lattice in order to discover and study the DADD effect in these materials under deformation in liquid helium.

2. EXPERIMENTAL TECHNIQUE

We used Sn (99.998%) single crystals (with a body-centered tetragonal lattice), as well as polycrystalline Cd (99.8%) with an hcp lattice. The samples of Sn ($25 \times 4.5 \times 1.5$ mm) with the $\langle 110 \rangle$ orientation ensuring their maximum plasticity in the slip system $\{100\}\langle 010 \rangle$ were deformed by stretching at a strain rate $\dot{\varepsilon} = 10^{-4}$ s^{-1} in liquid ^{4}He (T = 4.2 K) to strains ε = 0.7, 3, 4.6, and 11% and in ^{3}He (T = 1.8–0.6 K) to strains ε = 0.9 and 6.4% at a rate $\dot{\varepsilon} = 10^{-3}$ s^{-1}. Cadmium samples ($21 \times 3 \times 0.7$ mm) were stretched (at $\dot{\varepsilon} = 10^{-4}$ s^{-1}) to rupture (ε = 7%) in liquid ^{4}He (T = 4.2 K). The He concentration in the deformed samples was determined using the mass-spectrometric method. The liberation of helium from

1063-7834/02/4402-0302$22.00

tin samples was analyzed after five-year holding at 300 K to find out whether helium is preserved in tin after its deformation in liquid helium and prolonged storage of this metal at $T = 300$ K, which is close to its recrystallization temperature ($T_r \approx 0.5T_s \approx 255$ K). Cadmium samples were investigated five days after rupture testing at 4.2 K. We used a mass spectrometer with a ^{4}He sensitivity of $\sim 10^9$ atoms and a ^{3}He sensitivity of $\sim 10^5$ atoms [9]. Deformed samples were cut into pieces using the electric spark technique. We analyzed the working length of the samples, as well as the transition regions to their vanes and the neck region.

The curves describing helium extraction from deformed tin and cadmium samples were obtained through dynamic annealing of the samples at a rate of 7 K/min in the temperature range $T = 300$–800 K. In Sn single crystals, we measured the helium concentration as a function of strain at 4.2 K. The obtained curves were compared with the stress–strain diagram of the samples.

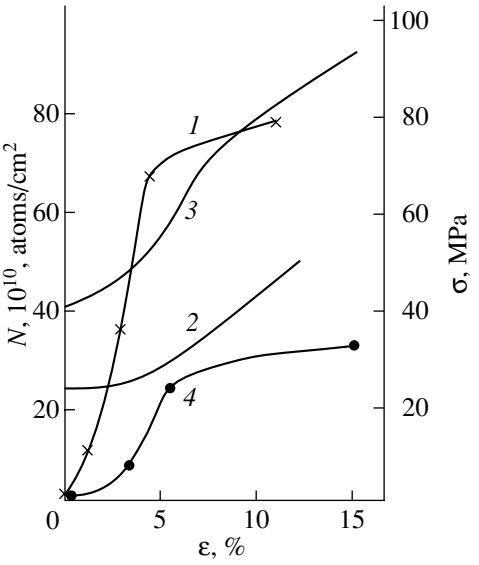

Fig. 1. Dependence of the concentration N of ^{4}He atoms in samples of (*1*) Sn single crystals and (*4*) Al polycrystals [5] on their strain and the stress–strain diagrams for (*2*) Sn and (*3*) Al at $T = 4.2$ K.

3. EXPERIMENTAL RESULTS

3.1. Tin

We measured the concentration of helium (N, atoms/cm^2) in samples deformed in liquid helium to various strains (ε) at $T = 4.2$ K, as well as in undeformed parts of the samples. It was found that the He concentration in the vanes was approximately two orders of magnitude lower ($\sim 5 \times 10^9$ atoms/cm^2) than that after deformation of tin in liquid helium ($\sim (1\text{–}8) \times 10^{11}$ atoms/cm^2). The obtained $N(\varepsilon)$ dependence is represented by curve *1* in Fig. 1 and compared with a typical stress–strain diagram $\sigma(\varepsilon)$ for tin single crystals at $T = 4.2$ K (curve *2*). It can be seen that the two curves exhibit saturation and correlate qualitatively. However, the shapes of the curves differ considerably at the initial stages of deformation. A similar form of the $N(\varepsilon)$ and $\sigma(\varepsilon)$ dependences was obtained by us earlier for polycrystalline aluminum [5] deformed by stretching in liquid ^{3}He at $T = 0.6$ K. In our opinion, the observed difference between the curves can be explained as follows. At the initial stage, the plastic deformation of a crystalline body is determined by the emergence and dynamic growth of and a sharp increase in the number of slip bands (lines) [10]; this is accompanied by the formation of a dislocation density gradient in the surface layer of the material [11]. This process can be described by an S-shaped curve [12]. Upon a further increase in strain, the dynamic increase in the length and number of plastic shifts slows down abruptly due to their intersection, interaction with grain boundaries and subblocks, and the formation of deformation boundaries, which pass through the entire cross section of the sample. This leads to a deceleration of shifts and, as a result, to an intense hardening of the material. The number of slip bands virtually does not increase in this case, and the plastic deformation is associated mainly with the multiplication of dislocations through the mechanism of their cross slip [13]. A comparison of the stress–strain curves with the curves describing the liberation of helium from tin and aluminum shows (Fig. 1) that, for both types of metals, helium atoms intensely penetrate into the material mainly in the easy-slip region (up to $\varepsilon \sim 5\%$), where the hardening rate is low. At this stage, plastic deformation in these metals occurs through nucleation and a sharp increase in the number (density) of slip bands moving at high velocities. The kinetics of the process of shear deformation described above was observed in LiF crystals for which the emergence and development of slip bands in the vicinity of and beyond the yield point were filmed directly in liquid helium [14–16]. In tin single crystals, this process occurs with a very low hardening rate as compared to polycrystalline aluminum, for which the hardening rate is much higher due to the presence of grain boundaries in it (cf. curves *2*, *3* in Fig. 1 for $\varepsilon < 5\%$). For this reason, the difference in the shape of the stress–strain diagram and the curve describing the change in He concentration for aluminum was much smaller than that for tin (cf. curves *2*, *3* and *1*, *4*).

With increasing ε, the velocities of slip bands (lines) decrease by several orders of magnitude for the reasons described above, leading to a decrease in the amplitudes of vibrations of atoms in the cores of moving dislocations [17] and, hence, to a decrease in the amount of helium absorbed by dislocations. It should also be borne in mind that helium penetrates only into a thin surface layer of the deformed tin sample and not into the bulk due to the presence of impurity stoppers and the accumulation of deformation-induced stoppers at

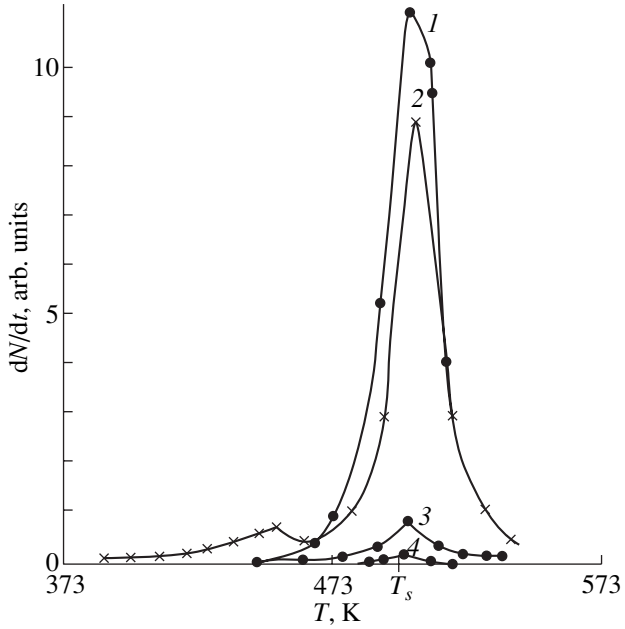

Fig. 2. Curves describing the relative liberation rate of ^{3}He atoms from Sn single crystals deformed at T = 1.8–0.6 K: curves *1–3* correspond to transition regions near the vanes (ε = 0.9%) and curve *4* corresponds to the middle part of the sample (ε = 6.4%). ^{3}He concentration N (10^9 atoms/cm^2) equal to (*1*) 63, (*2*) 40, (*3*) 4.6, and (*4*) 0.3.

which moving dislocations are pinned. In addition, a transition from the multiplication of dislocations by Frank–Read sources at the initial stage of plastic deformation of tin to multiplication through the cross-slip mechanism for large values of ε also sharply reduces the velocities of dislocations due to their deceleration at obstacles. Helium atoms can also be liberated from the surface layers of samples as a result of their subsequent deformation [18], which is accompanied by an increase in the total density of dislocations and an increase in the number of mobile dislocations, as well as by an enhancement in their interaction and annihilation in view of the presence of image forces in the surface layer of the deformed material [11]. These factors lead to a considerable decrease in the intensity of He penetration into moving dislocations and, hence, to a suppression of the $N(\varepsilon)$ dependence.

We also obtained helium extraction curves for tin samples deformed in liquid ^{3}He (T = 0.6 K, Fig. 2) and in liquid ^{4}He (T = 4.2 K, Fig. 3). The shape of the curves for both types of atoms was qualitatively the same. The position of the main peak in the helium liberation rate virtually coincides with the melting point of tin (T_s = 505 K). However, the helium liberation curves for samples deformed in ^{4}He are more extended along the temperature scale. We can attribute this effect to the difference in the physical properties of ^{4}He and ^{3}He atoms that determine the depth of their penetration into the metal being deformed. This difference is indirectly confirmed by the results obtained in [19], where it is shown that the change in the density of screw dislocations in the surface layer of LiF crystals compressed to the yield point in liquid ^{3}He (T = 3 K) extends up to a depth of 50 μm, as compared to 25 μm in the case of deformation in liquid ^{4}He (T = 4.2 K).

It is important to note that the liberation of helium takes place not only in the vicinity of and at the melting

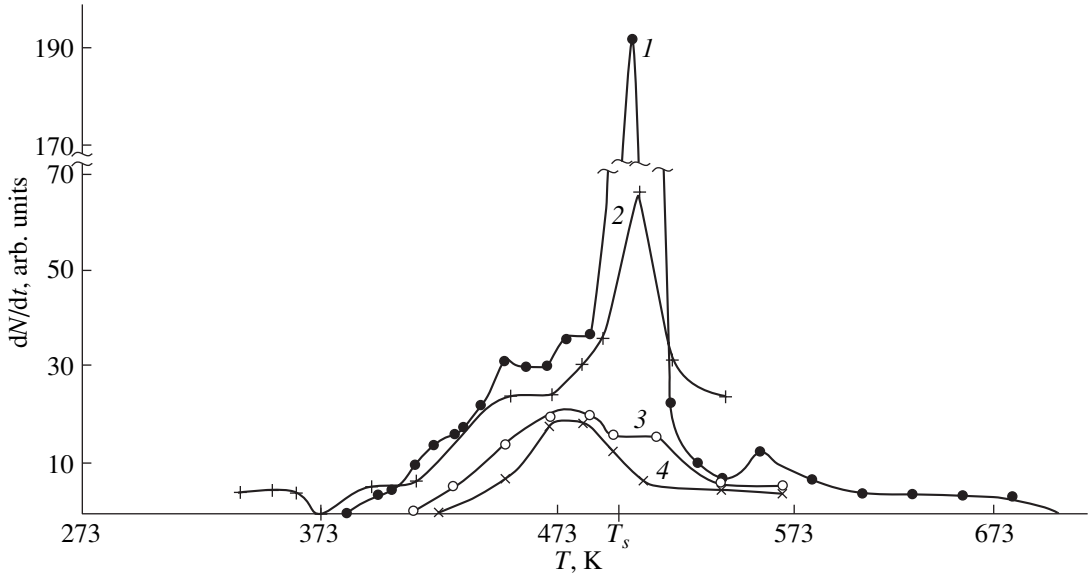

Fig. 3. Curves describing the relative liberation rate of ^{4}He atoms from Sn single crystals deformed at T = 4.2 K, ε = 7.6%: curves *1* and *2* correspond to transition regions near the vanes, and curves *3* and *4* correspond to the middle part of the sample. ^{4}He concentration N (10^9 atoms/cm^2) equal to (*1*) 137, (*2*) 57, (*3*) 15.2, and (*4*) 14.8.

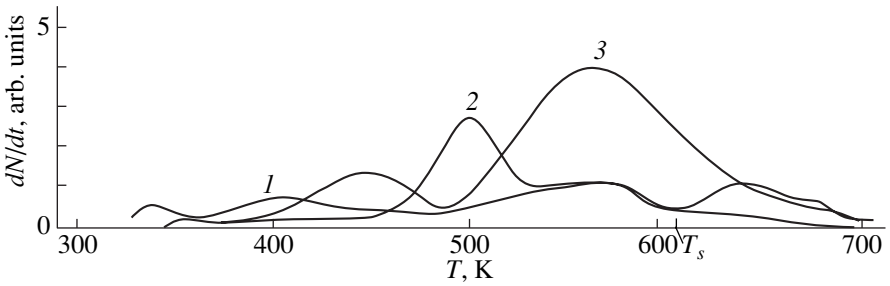

Fig. 4. Curves describing the relative liberation rate of ^{4}He from polycrystalline Cd deformed by ε = 7% at T = 4.2 K for different parts of the sample: curve *1* corresponds to the middle part of the sample; curve *2*, to transition regions near the vanes; and curve *3*, to the necks. Helium concentration N (10^{11} atoms/cm^2) equal to (*1*) 1.4, (*2*) 6.8, and (*3*) 5.9.

point for tin but also at $T > T_s$ in both cases of ^{4}He and ^{3}He (cf. Figs. 2, 3). Apparently, in both cases, helium atoms are in very deep traps due to chemical bonding with structural defects of the deformed tin samples. This bonding was observed using helium defectoscopy for LiF crystals [20]. The energy of interaction of He atoms with the cations of the lattice attained values of –0.45 eV, which is 30 times larger in magnitude than the van der Waals interaction energy typical of inert gases. In addition, the probability of coagulation of helium penetrating into tin crystals (into bubbles of various sizes, which can evolve from a melt of this metal with a high activation energy) through the DADD mechanism increases at high temperatures.

3.2. Cadmium

A cadmium sample deformed to rupture (ε = 7%) at T = 4.2 K was then cut mechanically into 12 pieces. The helium concentration in the working cross section of the sample was in the limits $N = (1–8) \times 10^{11}$ atoms/cm^2 and amounted, on the average, to $\bar{N} = 3.5 \times 10^{11}$ atoms/cm^2. In the transition zones of the sample, the concentration was $N = (21–110) \times 10^{11}$ atoms/cm^2 and $\bar{N} = 42 \times 10^{11}$ atoms/cm^2, while in both necks of the sample, the concentration was $N = (19–29) \times 10^{11}$ atoms/cm^2 and $\bar{N} = 24 \times 10^{11}$ atoms/cm^2. Thus, the helium concentration in the working cross section was found to be smaller by a factor of roughly 12 than that in the transition zone and by a factor of 7 than that in neck. The observed difference in the values of $\bar{N}$ in different parts of the Cd sample is primarily due to the values of plastic strain in these parts being different. Indeed, the value of ε in a neck is much larger than that in the middle part of the sample due to the presence of concentrated strain; for this reason, the amount of helium in a neck is considerably larger (by a factor of 7). However, the values of $\bar{N}$ in the regions of transition to the vanes were (by a factor of 1.7) higher than those in the neck. This can be explained as follows. A considerable fraction of helium absorbed by dislocations in the neck region is lost due to the formation of numerous micro- and macrocracks in it [16]. These cracks lead to a sharp increase in the area of free surface in the neck and, hence, facilitate the evolution of helium from the bulk, which is also stimulated by the emergence of He-containing dislocations at the fresh surface on account of the image forces aiding this process. In the sample transition region near a grip, the amount of plastic strain is much smaller than that in the working cross section and, even more so, than that in a neck. It should be noted, however, that in this transition region, all slip elements corresponding to the entire strain range in the sample (ε = 0–7%) are present. In the major part of the cross section adjoining the working region of the sample, slip bands oriented in the basal planes do not overlap and do not interact with grain boundaries in view of their low deformation. In this case, helium atoms penetrating into slip bands remain in them and do not evolve in the course of sample deformation; consequently, the largest amount of helium is accumulated in slip bands.

The curves of the helium liberation rate from cadmium were obtained for two batches of samples (for different parts), with a low and a high concentration N of ^{4}He atoms (Figs. 4, 5). Let us consider the liberation of helium from different parts of the samples with a small value of N. It can be seen from Fig. 4 that peaks are observed in a wide temperature range (T = 340–700 K); the main peaks lie at $T < T_s$, but liberation of helium also occurs at $T > T_s$. All the peaks are quite broad and smooth. This fact indicates the presence of a wide spectrum of energy traps for helium atoms. The main peaks can be attributed to the following temperatures: the middle part of the sample (curve *1*) is characterized by the presence of two low-temperature peaks ($T \approx 340$, 410 K), which are not observed for the necks and the transition regions of the sample, and a high-temperature peak ($T \approx 570$ K) typical of all the parts of the samples investigated by us. The low-temperature peaks are due to there being a large number of microcracks in the necks; this facilitates the evolution of helium from the bulk and surface traps upon sample heating and holding at 300 K. In the middle part, where fracture of the material is virtually absent, helium is

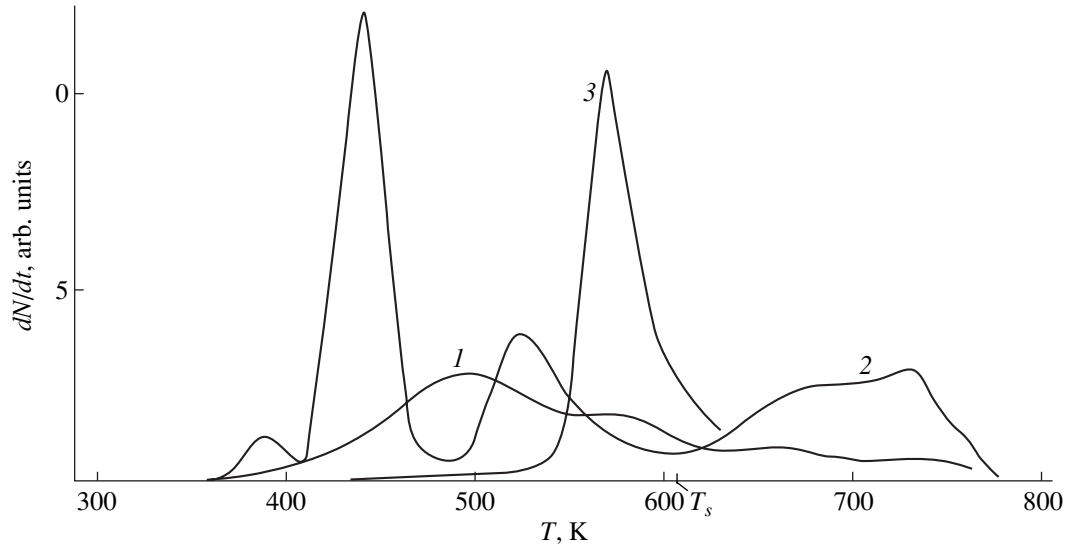

Fig. 5. The same as in Fig. 4 for a larger number of ^{4}He atoms in different parts of the sample: (*1*) middle part, (*2*) transition regions near the vanes, and (*3*) necks. Helium concentration N (10^{12} atoms/cm^2) equal to (*1*) 0.82, (*2*) 61, and (*3*) 2.9.

partially preserved in surface traps. Only two high-temperature peaks were observed in the necks at $T < T_s$ ($T \approx$ 450, 570 K). The transition regions of the sample containing the largest amount of helium (curve *2*) are characterized by the presence of three high-temperature peaks in the amount of liberated helium ($T \approx$ 500, 570, 640 K). There is also a small peak at $T > T_s$ (T = 670 K).

The extraction curves for a high helium concentration are presented in Fig. 5. The curves are characterized by the presence of sharper and higher (in amplitude) peaks in the helium liberation rate over a wider temperature range as compared to that for the low value of N (cf. Figs. 4, 5). These peaks are observed for $T < T_s$ ($T \approx$ 380, 430, 520, 570 K), as well as for $T > T_s$ ($T \approx$ 680, 730 K). The last two blurred peaks overlap and are observed for the transition regions of the sample. The reason for their emergence can be associated with the liberation of helium bubbles of various sizes from the cadmium melt. The effect of the cadmium oxide film through which helium atoms can diffuse also cannot be ruled out.

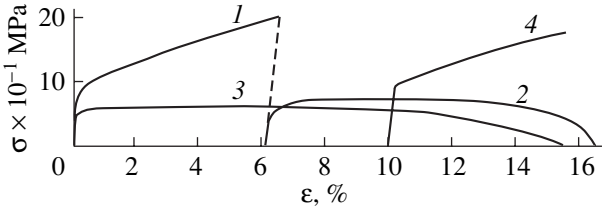

Fig. 6. Stress–strain curves for polycrystalline Cd (99.98%) at (*1*) 4.2 and (*2*) 300 K after deformation to ε = 6% at 4.2 K and at (*3*) 300 and (*4*) 4.2 K after deformation to ε = 10% at 300 K.

A comparison of the curves corresponding to small and large values of N indicates that the height and sharpness of the helium liberation rate peaks and the amount of helium liberated at $T > T_s$ increase significantly upon an increase in N. Thus, an increase in the helium concentration in different parts of the samples considerably affects the character of helium extraction and distribution over various types of traps formed in the course of plastic deformation of cadmium, as well as during its recrystallization upon heating from 4.2 to 300 K.

The traps for helium atoms in deformed samples of tin and cadmium are regions of plastic strain. The quantity and variety of traps are determined by many factors, such as lattice type, initial defect and impurity structure, and degree of plastic deformation (dislocation density, number of deformation-induced vacancies, and the intensity of formation of subboundaries and vacancy pores), as well as by the recrystallization of these metals leading to a radical change in their substructure upon heating from 4.2 K and holding at 300 K. For example, the removal of low-temperature hardening of cadmium is so significant that the stress–strain diagram obtained at 300 K (curve *1* in Fig. 6) after preliminary deformation through 6% at 4.2 K (curve *2* in Fig. 6) virtually coincides with curve *3* obtained at 300 K. Preliminary stretching of Cd by 10% at 300 K practically does not change its stress–strain diagram at 4.2 K (cf. curves *2*, *4*). The processes described above lead to a redistribution of helium in the bulk of samples deformed in liquid helium and to the accumulation of helium atoms in bubbles located in vacancy pores, as well as in the boundaries of blocks and grains. The fact that the temperature range corresponding to the liberation of helium from tin single crystals is narrower than that in the case of cadmium

(cf. Figs. 2–5) is probably due to their prolonged five-year holding at the recrystallization temperature ($T_r \approx$ 255 K), as a result of which helium atoms are redistributed over deeper energy traps. In order to identify the various types of helium traps and to determine their activation parameters, special experiments on the dynamic annealing of samples at various rates after their deformation in liquid helium are required.

4. CONCLUSIONS

Thus, it is found that tin single crystals stretched in liquid ^{3}He and ^{4}He contain helium, which is preserved after a five-year holding at 300 K. The amplitudes of the helium liberation rate peaks in the regions close to T_s and above this temperature decrease sharply upon a decrease in the total concentration of helium in deformed samples. A qualitative correlation is established between the stress–strain diagram for tin single crystals deformed in liquid ^{3}He and the curves describing the helium concentration in this metal as a function of the amount of metal strain. Peaks on the curves describing helium liberation from polycrystalline cadmium deformed to fracture at 4.2 K are observed in a wide range of temperatures below and above the melting point for cadmium. As the helium concentration in deformed samples increases, the height of the peaks increases significantly and the temperature range of helium liberation becomes wider. The emergence of high-temperature peaks of the helium liberation rate from tin and cadmium at $T \geq T_s$ indicates the mechanochemical penetration of helium into these metals. This effect is probably associated with the formation of a chemical bond between helium atoms and structural defects appearing during plastic deformation of the metals under investigation in liquid helium.

ACKNOWLEDGMENTS

The authors are grateful to S.N. Golyandin and V.S. Yudenich for their help and to V.G. Bengus, S.É. Shumilin, and V.V. Pustovalov for supplying the tin samples deformed in liquid helium.

This work was supported by the Russian Foundation for Basic Research, project no. 99-03-32536.

REFERENCES

1. O. V. Klyavin, B. A. Mamyrin, L. V. Khabarin, and Yu. M. Chernov, Fiz. Tverd. Tela (Leningrad) **18** (5), 1281 (1976) [Sov. Phys. Solid State **18**, 736 (1976)].
2. O. V. Klyavin, N. P. Likhodedov, and A. N. Orlov, Prog. Surf. Sci. **33** (4), 259 (1990).
3. O. V. Klyavin, Fiz. Tverd. Tela (St. Petersburg) **35** (3), 513 (1993) [Phys. Solid State **35**, 261 (1993)].
4. O. V. Klyavin, B. A. Mamyrin, L. V. Khabarin, *et al.*, Fiz. Tverd. Tela (Leningrad) **24** (7), 2001 (1982) [Sov. Phys. Solid State **24**, 1143 (1982)].
5. O. V. Klyavin, B. A. Mamyrin, L. V. Khabarin, and Yu. M. Chernov, Izv. Ross. Akad. Nauk, Ser. Fiz. **63** (9), 1876 (1999).
6. O. V. Klyavin, B. A. Mamyrin, L. V. Khabarin, and Yu. M. Chernov, in *Proceedings of the International Workshop "Topical Problems of Strength," Tambov, 1998*; Vestn. Tambovs. Gos. Univ. **3** (3), 211 (1998).
7. G. I. Shvets, O. V. Klyavin, and A. G. Banshchikov, Fiz. Nizk. Temp. **27** (9), 2618 (1985) [Sov. J. Low Temp. Phys. **27**, 1570 (1985)].
8. O. V. Klyavin, B. A. Mamyrin, L. V. Khabarin, *et al.*, Fiz. Tverd. Tela (St. Petersburg) **42** (7), 1256 (2000) [Phys. Solid State **42**, 1294 (2000)].
9. B. A. Mamyrin, Yu. A. Akulov, L. V. Khabarin, and V. S. Yudenich, Prib. Tekh. Éksp., No. 2, 151 (1982).
10. A. V. Stepanov, *Bases of Practical Strength of Crystals* (Nauka, Moscow, 1974).
11. V. P. Alekhin, *Physics of Strength and Plasticity of Surface Layers of Materials* (Nauka, Moscow, 1983).
12. V. Z. Bengus, T. P. Kovalenko, and V. A. Kuklev, Dokl. Akad. Nauk SSSR **247** (6), 1372 (1979) [Sov. Phys. Dokl. **24**, 672 (1979)].
13. B. I. Smirnov, *Dislocation Structure and Hardening of Crystals* (Nauka, Leningrad, 1981).
14. O. V. Klyavin and A. V. Nikiforov, *Dynamics of Dislocations* (Naukova Dumka, Kiev, 1975).
15. O. V. Klyavin and A. V. Nikiforov, Fiz. Tverd. Tela (Leningrad) **18** (3), 1167 (1976) [Sov. Phys. Solid State **18**, 672 (1976)].
16. O. V. Klyavin, *Physics of Plasticity of Crystals under Helium Temperatures* (Nauka, Moscow, 1987).
17. W. G. Hoover, N. E. Hoover, and W. C. Moss, J. Appl. Phys. **50**, 829 (1979).
18. Yu. A. Akulov, I. N. Zimkin, O. V. Klyavin, *et al.*, Fiz. Tverd. Tela (Leningrad) **32** (5), 1537 (1990) [Sov. Phys. Solid State **32**, 899 (1990)].
19. O. V. Klyavin, Yu. M. Chernov, N. N. Pravdina, and I. I. Rykova, Fiz. Tverd. Tela (Leningrad) **20** (10), 3100 (1978) [Sov. Phys. Solid State **20**, 1787 (1978)].
20. A. Ya. Kupryazhkin and A. Yu. Kurkin, Fiz. Tverd. Tela (St. Petersburg) **35** (11), 3003 (1993) [Phys. Solid State **35**, 1475 (1993)].

Translated by N. Wadhwa

Physics of the Solid State, Vol. 44, No. 2, 2002, pp. 308–311. Translated from Fizika Tverdogo Tela, Vol. 44, No. 2, 2002, pp. 297–300.

MAGNETISM AND FERROELECTRICITY

The Influence of Interatomic Distances on Magnetic Ordering in *R*MnSi Compounds (*R* = La, Y, Sm, and Gd)

S. A. Nikitin*, T. I. Ivanova*, Yu. A. Ovchenkova*, M. V. Maslennikova*, G. S. Burkhanov, and O. D. Chistyakov****

** Moscow State University, Vorob'evy gory, Moscow, 119899 Russia*

*** Baĭkov Institute of Metallurgy, Russian Academy of Sciences, Leninskiĭ pr. 49, Moscow, 117334 Russia*

e-mail: ivanova@rem.phys.msu.su

Received May 15, 2001

Abstract—Magnetic ordering in the *R*MnSi (*R* = La, Y, Sm, and Gd) compounds is investigated. It is found that the type of magnetic ordering depends on the $d_{Mn–Mn}$ distance between manganese atoms inside the magnetic layers located in the planes perpendicular to the *c* axis. This inference is based on the results of studies performed with SmMnSi and GdMnSi compounds in which the distances between manganese atoms are close to the critical value $d_{Mn–Mn}$ that corresponds to the crossover between ferromagnetic and antiferromagnetic ordering in *R*MnSi compounds. The introduction of lanthanum and yttrium atoms into the rare-earth sublattice leads to an increase and a decrease in the unit cell size, respectively, and brings about magnetic phase transitions in the compounds under investigation. © *2002 MAIK "Nauka/Interperiodica".*

1. INTRODUCTION

Over the last decade, rare-earth and transition metal triple silicides—a new class of magnetically ordered materials—have attracted the particular attention of many researchers [1–6]. Compounds *R*MnSi (where *R* is a rare-earth element) are magnets with two magnetic sublattices, namely, rare-earth and manganese sublattices, in which magnetic atoms are located in layers separated by silicon layers alternating in the following order: *R*–Si–Mn_2–Si–*R*. As a rule, the manganese sublattice is characterized by a substantial localized magnetic moment (1.5–3 μ_B) and has an ordered structure at relatively high temperatures. The magnetic ordering in *R*MnSi compounds should be considered with due regard for different types of exchange interactions, including the *R*–*R*, *R*–Mn, and Mn–Mn interactions. It should be noted that the type of magnetic ordering in the *R*MnSi compounds and the magnitude and sign of the exchange integral inside the manganese sublattice essentially depend on the Mn–Mn interatomic distance within the magnetic layers located in the basal plane of the tetragonal crystal lattice. For example, it was found that the manganese layers in $La_{1-x}Y_xMnSi$ compounds with a sole magnetic subsystem are characterized by antiferromagnetic ordering when the $d_{Mn–Mn}$ distance inside the manganese layers exceeds a certain value, i.e., $d_{Mn–Mn} > 2.88$ Å, and by ferromagnetic ordering when $d_{Mn–Mn} < 2.85$ Å. Moreover, the character of exchange coupling between manganese layers also correlates with the Mn–Mn distances inside these layers [7].

The purpose of the present work was to reveal a correlation between the $d_{Mn–Mn}$ distances (both inside and between the manganese layers) and the type of magnetic ordering in the *R*MnSi (*R* = Sm and Gd) compounds upon the corresponding substitution in the rare-earth sublattice.

2. SAMPLE PREPARATION AND EXPERIMENTAL TECHNIQUE

The experiments were performed with *R*MnSi (*R* = Sm, Y, La, and Gd) alloys produced in an electric arc furnace by melting a batch on a water-cooled copper hearth with a tungsten electrode in a purified argon atmosphere. The alloys prepared were subjected to homogenizing annealing in evacuated sealed silica tubes at a temperature of 800–850°C for 100 to 150 h. The chemical composition of the studied compounds was determined by x-ray fluorescence analysis. The single-phase state of the samples was checked against an x-ray powder diffraction analysis on a DRON-3 diffractometer (CuK_α radiation). Analysis of the x-ray powder diffraction patterns demonstrated that the polycrystalline compounds were in a single-phase state and had a simple tetragonal structure of the CeFeSi type. The lattice parameters of the samples were calculated from the x-ray diffraction patterns to within an accuracy $\Delta a = \pm 0.001$ Å and $\Delta c = \pm 0.003$ Å.

The specific magnetization of the compounds studied in this work was measured in static magnetic fields (up to 13.5 kOe) in the temperature range 77–350 K. The procedure of magnetic measurements was described in detail in [8].

1063-7834/02/4402-0308$22.00 © 2002 MAIK "Nauka/Interperiodica"

3. EXPERIMENTAL RESULTS

In order to solve the posed problem, we studied samples of the SmMnSi and GdMnSi compounds in which gadolinium and samarium were partially replaced by nonmagnetic rare-earth elements, namely, yttrium and lanthanum.

The ferromagnetic ordering in the GdMnSi compound at temperatures below the Curie point T_C = 310 K (Fig. 1) was revealed earlier in the study of the temperature and field dependences of the specific magnetization σ [1]. At temperatures close to the Curie point T_C, the dependence of H/σ on σ^2 exhibits a linear behavior characteristic of ferrimagnetic and ferromagnetic ordering. These findings allow us to make the inference that the magnetic moments of the manganese and gadolinium sublattices are ferrimagnetically ordered at $T < T_C$.

The substitution of lanthanum for gadolinium leads to noticeable changes in the magnetic phase transitions in $La_{1-x}Gd_xMnSi$ compounds. For example, the $La_{0.5}Gd_{0.5}MnSi$ compound undergoes two transitions: an antiferromagnetic–ferrimagnetic transition at T_1 = 100 K and a ferrimagnetic–paramagnetic transition at T_C = 180 K (Fig. 1). An increase in the gadolinium concentration ($x > 0.5$) brings about an increase in the magnetic moment of the gadolinium sublattice, whereas the exchange interaction between gadolinium and manganese ions remains antiferromagnetic. This results in breaking of the antiferromagnetic exchange coupling between manganese sublattices whose magnetic moment is aligned antiparallel to the magnetic moment of the gadolinium sublattice. Consequently, the interaction between the manganese and gadolinium sublattices leads to ferrimagnetic ordering in the $La_{1-x}Gd_xMnSi$ compounds. The appearance of antiferromagnetism in the studied compounds with concentrations in the range $0.5 < x < 0.6$ can be explained by the fact that, as the temperature decreases below T_1 ($T < T_1$), the negative exchange interaction between the manganese layers becomes stronger than the exchange interaction between the manganese and gadolinium layers. As a result, the manganese sublattices undergo antiferromagnetic ordering at temperatures below T_1. The positive paramagnetic Curie temperature θ_p indicates that the positive exchange interaction inside the manganese and gadolinium layers dominates over the negative exchange interaction between these layers.

The substitution of yttrium for gadolinium results in a decrease in the magnetization of the $Gd_{0.7}Y_{0.3}MnSi$ compound. As can be seen from Fig. 1, the temperature dependence of the magnetization of the $Gd_{0.7}Y_{0.3}MnSi$ compound is similar to the curve $\sigma(T)$ for GdMnSi, even though the inflection point is not observed in the latter case. Therefore, it can be concluded that the introduction of yttrium in small amounts only slightly affects the magnetic ordering in the $Gd_{0.7}Y_{0.3}MnSi$ compound, which remains a ferrimagnet at $T < T_C$ (T_C = 260 K).

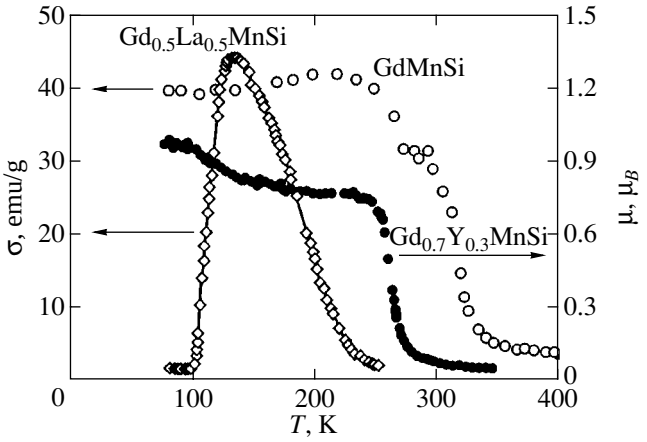

Fig. 1. Temperature dependences of the magnetization for GdMnSi and $Gd_{0.7}Y_{0.3}MnSi$ compounds in a field of 1.5 kOe and for the $Gd_{0.5}La_{0.5}MnSi$ compound in a field of 2 kOe.

Let us now consider the temperature dependences of the magnetization for the $Sm_{1-x}R_xMnSi$ (R = La and Y) compounds in the magnetic field H = 10 kOe (Fig. 2).

The results of complex investigations into the structural, magnetic, and electrical properties of the SmMnSi compound were reported in [9]. The temperature dependence of the magnetization of the SmMnSi compound exhibits an anomalous behavior. This manifests itself in a considerable temperature hysteresis, two magnetic phase transitions, and a magnetic compensation point (Fig. 2a). Similar anomalies are also observed in the temperature dependences of the electrical resistivity and thermal expansion. This behavior of the magnetization can be explained in the framework of the following model. In the manganese sublattice, a weak ferromagnetic moment μ_{Mn} arises at $T < T_N$ (T_N = 240 K is the Néel temperature). In the samarium sublattice, the ferromagnetic moment of the manganese sublattice induces a magnetic moment μ_{Sm} whose orientation is opposite to that of the μ_{Mn} magnetic moment. As the temperature decreases, the μ_{Sm} magnetic moment increases more rapidly compared to the μ_{Mn} moment. At the temperature T_k = 215 K, the μ_{Sm} magnetic moment becomes equal to the μ_{Mn} magnetic moment. As a consequence, the magnetic compensation occurs in the SmMnSi compound. A decrease in temperature results in a drastic decrease in the coercivity of this compound. An external magnetic field of 10 kOe is insufficient for magnetization reversal of the studied sample in the temperature range 130–220 K, and the magnetic moment in this field becomes negative. At $T <$ 130 K, the antiferromagnetic ordering of the manganese sublattices leads to a first-order phase transition to the antiferromagnetic phase with zero spontaneous

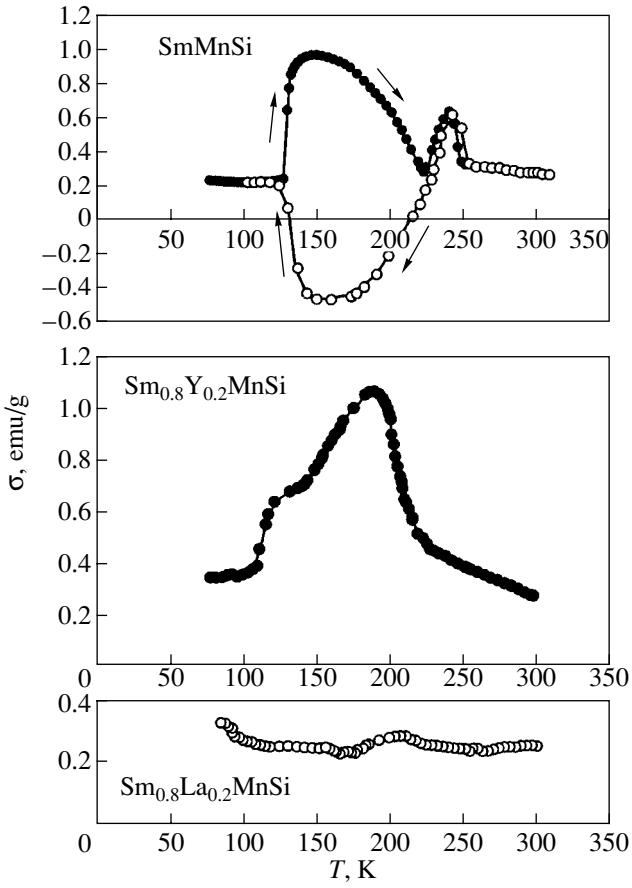

Fig. 2. Temperature dependences of the magnetization for SmMnSi, $Sm_{0.8}Y_{0.2}MnSi$, and $Sm_{0.8}La_{0.2}MnSi$ compounds.

magnetic moment. In order to reveal a correlation between the sign of the exchange integral in the manganese sublattices and the interatomic distances $d_{Mn–Mn}$, we determined the parameters of the tetragonal lattice and the types and temperatures of magnetic ordering in the compounds under investigation (see table).

The introduction of yttrium into the rare-earth sublattice results in an insignificant decrease in the interatomic distances in the $Sm_{0.8}Y_{0.2}MnSi$ compound. The magnetic ordering in this compound is similar to that observed in the initial SmMnSi sample, and the temperatures of magnetic phase transitions from the antiferromagnetic to the noncollinear phase (T_1) and from the noncollinear antiferromagnetic to the paramagnetic phase (T_N) are slightly shifted toward the low-temperature range (Fig. 2). No considerable temperature hysteresis (with negative magnetization), which is characteristic of the SmMnSi compound, was observed for the $Sm_{0.8}Y_{0.2}MnSi$ compound in a magnetic field of 10 kOe.

The above investigation into the magnetic properties of the $Sm_{0.8}La_{0.2}MnSi$ sample revealed that this compound is an antiferromagnet whose magnetization and magnetic susceptibility reach a maximum at the Néel temperature $T_N = 195$ K.

4. DISCUSSION

A comparison of the data on the magnetic properties and the crystal structure of the *R*MnSi compounds shows that the type of magnetic ordering depends on the $d_{Mn–Mn}$ interatomic distances inside the manganese layers located in the basal planes perpendicular to the tetragonal axis *c* (see table). For the SmMnSi and GdMnSi compounds, these distances are close to the critical value $d_{Mn–Mn}$ that corresponds to a crossover between ferromagnetic and antiferromagnetic ordering in *R*MnSi compounds. Specifically, the SmMnSi and $Sm_{0.8}Y_{0.2}MnSi$ compounds with interatomic distances larger than the critical value exhibit antiferromagnetic ordering at temperatures $T < T_N$. It can be assumed that, in the substituted compounds $Sm_{0.8}Y_{0.2}MnSi$ and

Unit cell parameters *a* and *c*, interatomic distances $d_{Mn–Mn}$ inside Mn layers, and types and temperatures of magnetic ordering in *R*MnSi (*R* = La, Y, Sm, and Gd) compounds

Compound	*a*, Å	*c*, Å	$d_{Mn–Mn}$, Å	Type and temperature of magnetic ordering	
$Sm_{0.8}La_{0.2}MnSi$	4.051(4)	7.198(6)	2.864	Antiferromagnetic	$T_N \approx 195$ K
SmMnSi	4.044(4)	7.159(7)	2.860	Antiferromagnetic	$T_1 = 130$ K
				Angular phase	$T_N = 250$ K
$Sm_{0.8}Y_{0.2}MnSi$	4.033(2)	7.133(6)	2.852	Antiferromagnetic	$T_1 = 115$ K
				Angular phase	$T_N = 205$ K
$Gd_{0.5}La_{0.5}MnSi$	4.11	7.275	2.906	Antiferromagnetic	$T_1 = 100$ K
				Ferrimagnetic	$T_C = 180$ K
$Gd_{0.7}Y_{0.3}MnSi$	4.052	7.005	2.865	Ferrimagnetic	$T_C = 260$ K
$Gd_{0.7}Sm_{0.3}MnSi$	4.013(4)	7.172(7)	2.838	Ferrimagnetic	$T_C = 295$ K
GdMnSi	4.016(1)	7.160(1)	2.840	Ferrimagnetic	$T_C = 310$ K

$Sm_{0.8}La_{0.2}MnSi$ at low temperatures ($T < 77$ K), there arises a magnetic ordering with two components of the μ_{Mn} magnetic moment of the manganese ion: one component is directed along the [001] tetragonal axis and the other component is aligned with the (001) basal plane. It is quite possible that this ordering leads to the formation of a noncollinear structure in these compounds.

For the GdMnSi, $Gd_{0.7}Y_{0.3}MnSi$, and $Gd_{0.7}Sm_{0.3}MnSi$ compounds, the $d_{Mn–Mn}$ distances are shorter than the critical distance (2.85 Å). These compounds are characterized by a ferrimagnetic ordering with strong magnetization.

The substitution of lanthanum for gadolinium brings about an increase in the $d_{Mn–Mn}$ distance and an enhancement of the exchange interaction in the manganese subsystem. As a consequence, the substituted compounds $La_{1-x}Gd_xMnSi$ ($x < 0.5$) undergo two transitions, namely, a paramagnetic–ferrimagnetic transition at the Curie temperature T_C and a ferrimagnetic–antiferromagnetic transition at the lower temperature T_1. For example, in the $La_{0.5}Gd_{0.5}MnSi$ compound, the $d_{Mn–Mn}$ distance is equal to 2.906 Å (i.e., this distance exceeds a critical value of 2.85 Å) and the antiferromagnetic state is observed in the low-temperature range (at $T < 100$ K).

In compounds with a magnetic rare-earth sublattice, the interaction between the rare-earth and manganese sublattices (the *R*–Mn interaction) should substantially affect the magnetic ordering. Since the difference between the exchange energies of the manganese sublattices in the antiferromagnetic and ferrimagnetic states is insignificant, the *R*–Mn exchange interaction that increases with a decrease in temperature results in ferromagnetic–antiferromagnetic phase transitions.

ACKNOWLEDGMENTS

This work was supported by the Russian Foundation for Basic Research (project no. 00-02-17862) and the State Program of Support for Leading Scientific Schools of the Russian Federation (project no. 00-15-96695).

REFERENCES

1. S. A. Nikitin, O. V. Nekrasova, I. T. Ivanova, *et al.*, Fiz. Tverd. Tela (Leningrad) **33** (6), 1640 (1991) [Sov. Phys. Solid State **33**, 923 (1991)].
2. R. Welter, G. Venturini, and B. Malaman, J. Alloys Compd. **206**, 55 (1994).
3. R. Welter, G. Venturini, E. Ressouche, and B. Malaman, J. Alloys Compd. **210**, 273 (1994).
4. A. Szytula, *Crystal Structures and Magnetic Properties of RTX Rare Earth Intermetallics* (Jagiellonian Univ. Press, Krakow, 1998).
5. S. A. Nikitin, T. I. Ivanova, I. A. Tskhadadze, *et al.*, J. Alloys Compd. **280** (1), 16 (1998).
6. S. A. Nikitin, I. A. Tskhadadze, A. V. Morozkin, and Yu. D. Seropegin, J. Magn. Magn. Mater. **196** (1), 632 (1999).
7. I. Ijjaali, R. Welter, G. Venturini, *et al.*, J. Alloys Compd. **270**, 63 (1998).
8. Yu. A. Ovchenkova, Candidate's Dissertation in Physics and Mathematics (Mosk. Gos. Univ., Moscow, 2000).
9. S. A. Nikitin, I. A. Tskhadadze, M. V. Makarova, and A. V. Morozkin, J. Phys. D **32** (6), L23 (1999).

Translated by O. Borovik-Romanova

Physics of the Solid State, Vol. 44, No. 2, 2002, pp. 312–314. Translated from Fizika Tverdogo Tela, Vol. 44, No. 2, 2002, pp. 301–303.

MAGNETISM AND FERROELECTRICITY

The Influence of Neutron and Proton Irradiation on the Magnetization of Biotite

U. Abdurakhmanov, A. B. Granovskiĭ*, A. A. Radkovskaya*, M. Kh. Usmanov**, Sh. M. Sharipov**, and V. P. Yugaĭ****

** Moscow State University, Vorob'evy gory, Moscow, 119899 Russia*

*** Higher Fire-Fighting School, Tashkent, Uzbekistan*

Received June 1, 2001

Abstract—This paper reports on the results of investigations into the field dependences of the magnetization for biotite in the initial state, after heat treatment at a temperature of 1000°C for 15 min, and after irradiation with 14-MeV neutrons at a dose of 1.2×10^{13} cm^{-2} or with 3-MeV protons at a dose of 2.2×10^{14} cm^{-2}. It is demonstrated that the magnetization of biotite drastically increases after neutron and proton irradiation. This effect can be associated with the formation of oxide melt at radiation-induced thermal peaks and the freezing of high-temperature phase states corresponding to magnetite or magnetite–hematite solid solutions. © *2002 MAIK "Nauka/Interperiodica".*

1. INTRODUCTION

Considerable interest expressed by researchers in radiation effects in biotite is motivated by the possible use of this mineral as a natural indicator of radioactive radiation. In particular, the use of biotite as a tracking detector has lent impetus to comparative investigation into the influence of proton irradiation and heat treatment on the Mössbauer spectra of this material [1]. It was found that, upon proton irradiation and heat treatment under vacuum, the Mössbauer spectra of the biotite samples change in a similar manner. Earlier [2, 3], we undertook comparative studies of the influence of neutron and proton irradiation and heat treatment on the magnetization of biotite. It was revealed that neutron and proton irradiation and the heat treatment lead to substantial changes in the magnetization of biotite but produce opposite effects: exposure to neutron and proton radiation brings about an increase in the magnetization, whereas the heat treatment causes a decrease in the magnetization of biotite. The drastic change in the magnetization of biotite under neutron and proton irradiation can be used for examining sites of radiative disasters, along with the use of magnetic traces of thermal effects in biotite for examining fire sites [4–6]. In our recent work [7], we analyzed the experimental dependences of the magnetic susceptibility of biotite on the temperature and time of heat treatment and considered the possible physicochemical processes responsible for these dependences. Now, we return to the discussion of the nature of radiation effects in biotite. It should be noted that, when studying radiation effects in solids, the use of neutrons rather than protons is more adequate, because this provides a more uniform distribution of radiation damages over the crystal lattice in samples with sizes commonly used under laboratory conditions.

2. INTERPRETATION OF THE EFFECT OF NEUTRON IRRADIATION

As is known, the heat treatment of biotite at temperatures above 500°C results in an irreversible change in the magnetic susceptibility [8].Therefore, it can be expected that the change observed in the magnetization of biotite under neutron irradiation [2, 3] is also associated with thermal processes.

In our previous works [7, 9], we investigated and interpreted the effect of heat treatment on biotite. It was assumed that the heating of biotite is accompanied by a number of physicochemical processes that are responsible for the dependence of the magnetic susceptibility of this mineral on the temperature and time of the heat treatment. These processes are as follows: (1) the oxidation of Fe^{2+} ions to the trivalent state, (2) the formation of submicroinhomogeneous regions through the aggregation of a certain part of the Fe^{3+} ions around vacancies and subsequent transformation of these ions into the spin-paired state, and (3) the formation of the hematite phase at high temperatures and the precipitation of Fe_2O_3 hematite particles upon cooling.

The observed change in the magnetization of biotite under neutron irradiation cannot be caused merely by the first process. In actual fact, the magnetic moment of Fe^{3+} ions is equal to 5.9 μ_B; i.e., this value is only 10% greater than the magnetic moment of Fe^{2+} ions (5.4 μ_B). Therefore, the transformation of even all the biotite Fe^{2+} ions into the trivalent state does not provide the observed change in the magnetization (at a maximum

dose of 3.5×10^{13} cm^{-2}, the change in the magnetization in an external magnetic field with a strength of 18 kOe was as high as approximately 50%).

The same situation is also true for the second process. The formation of spin-paired states in submicroinhomogeneous regions results in the fact that the magnetic moments of ions in these states do not contribute to the magnetization. Consequently, under neutron irradiation, the total magnetization of biotite should decrease rather than increase.

The third process also cannot be responsible for the observed change in the magnetization of biotite. At a temperature of 4.2 K, hematite is a pure antiferromagnet with the total magnetic moment equal to zero. Therefore, the formation of the hematite phase in biotite samples upon high-temperature treatment should lead to a decrease in the magnetization measured at 4.2 K rather than to an increase (a number of magnetic moments of iron atoms are antiferromagnetically ordered and do not participate in the magnetization process).

Thus, the physicochemical processes occurring in biotite under neutron irradiation differ from the processes responsible for the behavior of the magnetic susceptibility of this mineral upon heat treatment. In order to elucidate these processes, we analyzed the field dependences of the magnetization for biotite in different states (see figure).

The field dependence of the magnetization measured at 4.2 K in the biotite sample in the initial state (prior to the action of external factors) indicates that this sample contains a paramagnetic phase (a linear portion in the magnetization curve) and a magnetically ordered phase with a nonzero total magnetic moment (a nonlinear portion in the magnetization curve in the range of low external magnetic field strengths). It can be seen from the figure that, upon heat treatment, the content of the magnetically ordered phase in the samples remains unchanged (the extensions of the linear portions in the magnetization curves for biotite prior to and after the heat treatment intersect the ordinate axis at the same point). Exposure of biotite to neutron radiation leads to an increase in the content of the magnetically ordered phase with a nonzero total magnetic moment in the biotite samples (the magnetization at the point of intersection between the ordinate axis and the extension of the linear portion in the magnetization curve for the sample subjected to neutron irradiation is higher than the magnetization at the intersection point for the sample in the initial state). This increase in the content of the magnetically ordered phase can be interpreted in the framework of the thermal peak model.

According to thermal peak concepts, neutron irradiation can lead to an instantaneous release of a sufficiently high energy for melting to occur in a certain volume of the biotite lattice [10]. Owing to the very short lifetime of the thermal peak, the oxide melt thus formed should cool very quickly, which, in turn, brings about

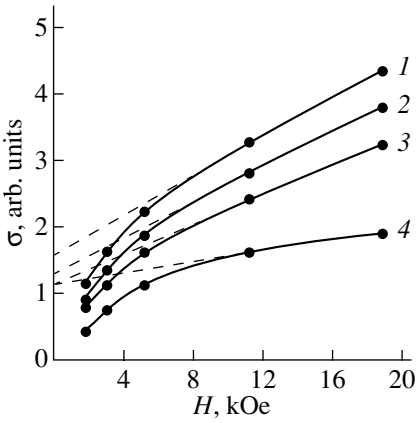

Field dependences of the magnetization σ for biotite at 4.2 K: (*1*) after irradiation with neutrons at an energy of 14 MeV and a dose of 1.2×10^{13} cm^{-2}, (*2*) after irradiation with protons at an energy of 3 MeV and a dose of 2.2×10^{14} cm^{-2}, (*3*) in the initial state, and (*4*) after heat treatment at 1000°C for 15 min.

the freezing of high-temperature phase states in the sample.

As follows from the phase diagram of the Fe–O system, the Fe_3O_4 magnetite is characterized by an extended homogeneity region at high temperatures and large oxygen contents [11]. Hence, the observed increase in content of the magnetically ordered phase in biotite and, correspondingly, the increase in magnetization of biotite under neutron irradiation can be explained by the formation of the magnetite phase and the precipitation of magnetite particles in the biotite samples. This assumption is also confirmed by the results of investigations into the radiation effects in biotite samples subjected to proton irradiation, which will be discussed below. Note that the aforementioned oxidation of the Fe^{2+} ions to the Fe^{3+} state can also make a certain contribution (no more than 10%) to the change in the magnetization of the biotite under consideration.

It should be noted that, depending on the partial content of oxygen over the oxide melt and its cooling rate, the magnetically ordered phase formed under neutron irradiation can involve a magnetite–hematite solid solution. In this solid solution, hematite forms an oxygen-deficient phase and magnetite forms an oxygen-excessive phase. According to the phase diagram of the Fe–O system, the magnetite region decreases with a decrease in the temperature, whereas the region corresponding to the magnetite–hematite solid solution increases. Thus, the lower the temperature of existence of the frozen phase, the higher the hematite content in this phase. Recall that the thermal processes occurring in biotite during heat treatment at 900–1000°C bring about the formation of the magnetically ordered phase. This phase involves hematite and is responsible for the drastic increase in the magnetic susceptibility of biotite

samples subjected to heat treatment [7, 9]. However, the hematite component in the phase formed in biotite under neutron irradiation does not contribute to the magnetization at 4.2 K, because, at this temperature, hematite is a pure antiferromagnet.

3. INTERPRETATION OF THE EFFECT OF PROTON IRRADIATION

It can be seen from the figure that, as in the case of neutron irradiation, the magnetization of the biotite sample irradiated with 3-MeV protons also increases considerably due to the increase in the content of the magnetically ordered phase.

Reasoning from the similarity between the changes observed in the Mössbauer spectra of the biotite samples irradiated with protons and heat treated under vacuum, Kotlicki *et al.* [1] drew the conclusion that these changes can be associated with the oxidation of the Fe^{2+} ions to the Fe^{3+} state at thermal peaks. It is evident that, under proton irradiation, the aforementioned oxidation reaction proceeds in parallel with other processes occurring in biotite in the course of heat treatment. This reaction, together with the other processes, is responsible for the irreversible change in the magnetic susceptibility of this mineral. However, the substantial increase in the magnetization of biotite under proton irradiation is similar to that observed in this material under neutron irradiation and defies explanation only in terms of the oxidation of Fe^{2+} ions at thermal peaks for the reasons considered in the above analysis of neutron irradiation.

For the same reasons as in the interpretation of the effect of neutron irradiation, the change observed in the magnetization of the biotite samples under proton irradiation can also be attributed to the freezing of the magnetite phase and the precipitation of magnetite particles.

Note that the data obtained in [1] confirm the above interpretation of the effect of proton (and neutron) irradiation on the magnetization of biotite. Indeed, the Mössbauer spectra measured in [1] at high radiation doses and liquid-nitrogen temperatures are characterized by the contribution of the magnetically ordered phase, and the lines attributed to this phase coincide in position with the corresponding lines in the spectrum of magnetite. Moreover, the x-ray diffraction patterns recorded in [1] also contain the lines assigned to magnetite.

Thus, the effect of proton irradiation on the magnetization and the Mössbauer spectra of biotite should be considered with due regard for both the oxidation of Fe^{2+} ions to the Fe^{3+} state and the process involving the formation of oxide melt at thermal peaks and the freezing of the high-temperature phase states corresponding to magnetite or magnetite–hematite solid solutions.

REFERENCES

1. A. Kotlicki, N. B. Olsen, and J. S. Olsen, Radiat. Eff. **28**, 1 (1976).
2. M. Kh. Usmanov, V. P. Yugaĭ, A. B. Granovskiĭ, *et al.*, Dokl. Akad. Nauk UzSSR, No. 8, 31 (1989).
3. A. B. Granovskiĭ, L. V. Navalikhin, V. E. Rode, *et al.*, Fiz. Tverd. Tela (Leningrad) **32**, 2479 (1990) [Sov. Phys. Solid State **32**, 1439 (1990)].
4. M. Kh. Usmanov, Pozharovzryvobezopasnost' **4**, 24 (1997).
5. N. N. Brushlinskiĭ, A. V. Danilov, K. M. Muminov, *et al.*, Pozharovzryvobezopasnost' **4**, 95 (1998).
6. N. N. Brushlinsky, A. V. Danilov, K. M. Muminov, *et al.*, Fire Technol. **33** (3), 195 (1997).
7. M. Kh. Usmanov, V. P. Yugaĭ, U. Abdurakhmanov, and Sh. M. Sharipov, in *Proceedings of the Scientific and Practical Conference, Higher Fire-Fighting School, Ministry of Internal Affairs of Uzbekistan, Tashkent, 2000.*
8. A. A. Aminov, A. V. Danilov, L. A. Skachkova, *et al.*, Dokl. Akad. Nauk UzSSR, No. 8, 31 (1988).
9. M. Kh. Usmanov, V. P. Yugai, Sh. M. Sharipov, and U. Abdurakhmanov, in *Proceedings of the Eurasian Conference on Nuclear Science and Its Application, Izmir, Turkey, 2000*, p. 311.
10. B. T. Kelly, *Irradiation Damage to Solids* (Pergamon, Oxford, 1966; Atomizdat, Moscow, 1970).
11. Yu. D. Tret'yakov, *Thermodynamics of Ferrites* (Khimiya, Leningrad, 1967), p. 304.

Translated by O. Borovik-Romanova

Physics of the Solid State, Vol. 44, No. 2, 2002, pp. 315–317. Translated from Fizika Tverdogo Tela, Vol. 44, No. 2, 2002, pp. 304–306.

MAGNETISM AND FERROELECTRICITY

Magnetic-Field-Induced Valence Transition in $EuNi_2(Si_{1-x}Ge_x)_2$ in Fields up to 500 T

V. V. Platonov*, O. M. Tatsenko*, V. D. Selemir*, and M. Shiga**

** All-Russia Scientific-Research Institute of Experimental Physics, Sarov, Nizhegorodsk oblast, 607188 Russia*

***Kyoto University, Sakyo-ku, Kyoto 606-01, Japan*

e-mail: Platonov@ntc.vniief.ru

Received June 1, 2001

Abstract—The critical fields of the valence transition induced by a magnetic field in the $EuNi_2(Si_{1-x}Ge_x)_2$ (x = 0.5–0.75) compound in an intermediate valence state are measured. The magnetic-field-induced valence transition is observed in the low-concentration range down to x = 0.5. It is demonstrated that the critical field increases linearly with a decrease in the germanium concentration. © *2002 MAIK "Nauka/Interperiodica"*.

1. INTRODUCTION

A number of compounds containing Ce, Sm, Eu, Tm, and Yb ions have a variable valence. This is associated with the location of the $4f$ level near the Fermi level. Among these systems, the $EuNi_2(Si_{1-x}Ge_x)_2$ [1] and $EuPd_2Si_2$ [2] compounds are characterized by a substantial change in the valence under external actions.

A mixed-valence state is observed in $EuNi_2Si_2$ and $EuNi_2Ge_2$ solid solutions. In the $EuNi_2Si_2$ compound, the Eu^{3+} ion with a $4f^6$ configuration is nonmagnetic. In the $EuNi_2Ge_2$ compound, the magnetic moment of the Eu^{2+} ion with a $4f^7$ configuration is equal to $7\mu_B$. For $EuNi_2(Si_{1-x}Ge_x)_2$ compounds, the magnetic field can induce a valence transition from a predominantly trivalent state to a predominantly bivalent state. This transition is accompanied by a jump in the magnetic moment, which was observed by Wada *et al.* [1] in the concentration range $0.75 \le x \le 0.82$ close to the range of magnetic ordering. Antiferromagnetic ordering with the Eu^{2+} stable state occurs at higher concentrations ($x \ge 0.85$), whereas the nonmagnetic phase is observed when $x \le 0.70$.

Since investigation into the magnetic phenomena of interest in the low-concentration range calls for the application of magnetic fields above 100 T, they are not clearly understood. In the present work, we determined the critical fields of induced valence transitions in the $EuNi_2(Si_{1-x}Ge_x)_2$ compound in an intermediate valence state with concentrations x = 0.75, 0.70, 0.65, 0.6, and 0.50.

2. SAMPLES AND EXPERIMENTAL TECHNIQUE

The measurements of the magnetic susceptibility were carried out at liquid-helium temperatures in magnetic fields up to 600 T. The samples were put at our disposal by Dr. M. Shiga. These samples were prepared by zone melting in an argon atmosphere. The single-phase state of the samples was checked using x-ray diffraction analysis and measurements of the temperature dependence of the magnetic susceptibility. The quality of the samples was discussed thoroughly in [1]. In order to ensure against heating in a pulsed magnetic field, the $EuNi_2(Si_{1-x}Ge_x)_2$ single crystals were crushed in a porcelain mortar to powder with a grain size of less than 100 μm. In this case, the heating of the samples in a maximum field did not exceed 6 K.

The magnetic susceptibility was measured with a force-balance transducer consisting of a pair of well-compensated induction coils connected in opposition. A PÉTV-2 wire 71 μm in diameter was dropped in helical flutes of two caprolan cores 2 mm in diameter (N = 9 turns). The degree of compensation of the coils was tested using a high-frequency magnet. The total coil areas defined as NS (where S is the area of one turn and N is the number of turns) differed from each other by no more than 2%. A hole 1.6 mm in diameter was drilled in one of the cores to mount the sample under investigation. In the case when the sample is inserted into one of the coils, the measured signal is proportional to the derivative of the magnetic moment of the sample: $V(H) \propto dM/dt + KdH/dt$. The coefficient K depends on the precision of the coil compensation in the absence of the sample and, in an ideal case, should be equal to zero. This cannot be achieved in experiments, specifically with superhigh magnetic fields when the rate of change in the magnetic field dM/dH reaches approximately 16 T/s. However, if the phase transition occurs in a narrow range of magnetic fields and the derivative dM/dH exceeds the compensation coefficient K, the dependence $M(H)$ can be calculated to a sufficiently high accuracy. In this case, the quantity dH/dt should be measured with a separate transducer.

1063-7834/02/4402-0315$22.00 © 2002 MAIK "Nauka/Interperiodica"

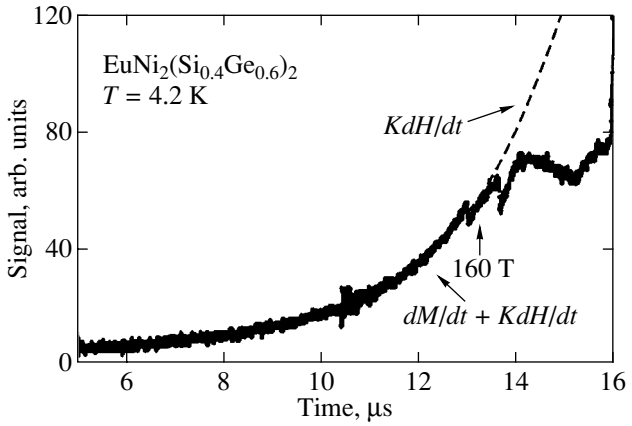

Fig. 1. Time dependences of the differential magnetic susceptibility and the derivative of the magnetic field for the $EuNi_2(Si_{0.4}Ge_{0.6})_2$ sample.

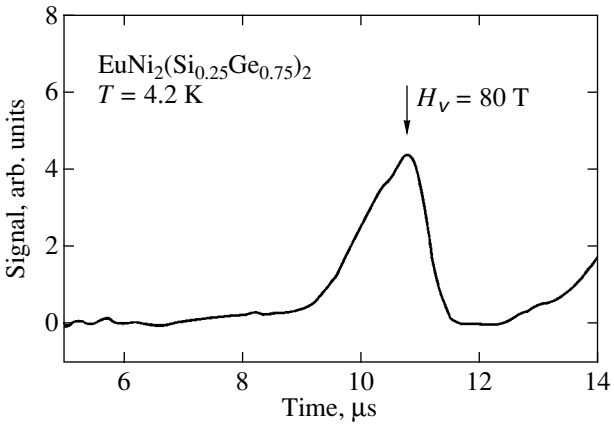

Fig. 2. Dependence of the differential magnetic susceptibility for the $EuNi_2(Si_{0.25}Ge_{0.75})_2$ sample.

In order to produce magnetic fields with an induction up to 500 T, we used an MK-1 magnetic cumulation generator [3]. The limiting fields achieved with this generator can be as high as 1000 T. In this work, such high fields were not needed and most attention was concentrated on the smoothness of the magnetic field pulse and efficiency in the use of the working volume. For this reason, the MK-1 generator was used in a single-cascade mode without intermediate inner cascades. From four to eight samples were measured in a single experiment. The initial magnetic field ($B \approx 16$ T) was generated in a thin-wall multilayer multifilar solenoid with a capacitor bank discharge $W = 2$ MJ. The magnetic flux trapped into the conducting cylinder was compressed by the products of explosion down to a diameter of 20 mm. The compression time for the magnetic field was approximately equal to 16 μs. The effective volume at a maximum magnetic field was considered a cylinder with a diameter of approximately 20 mm and a length of approximately 100 mm. The samples and transducers used for measuring the magnetic field were mounted on a glass-textolite plate and were then placed in helium of a flow cryostat. The magnetic field was measured using a set of one-turn inductive transducers (from 0.6 to 14.0 mm in diameter) wound with PÉTV-2 wire. The signals were recorded on Tektronix-784 and Tektronix-744 four-trace oscilloscopes with a resolution of 2 ns per point.

3. RESULTS AND DISCUSSION

3.1. Figure 1 shows typical oscillograms of signals taken from the inductive transducer measuring the magnetic field and the transducer measuring the differential magnetic susceptibility dM/dt. At the germanium concentration $x = 0.6$, the oscillogram displays two sharp peaks. It should be noted that only one broad peak is usually observed, as can be seen, for example, from Fig. 2 for the sample with the germanium concentration $x = 0.75$. Judging from the shape of the curve for the magnetic susceptibility anomaly, this transformation is a first-order transition. The jump in the magnetic susceptibility decreases with a decrease in the germanium concentration.

The sample with the germanium concentration $x = 0.75$ served as a reference sample, because it was used in similar measurements performed in a solenoid with a long pulse of the magnetic field [1]. The results obtained for the critical field ($H_v = 80$ T) and the induced valence transition range agree well with the data reported in [1]. Figure 3 represents the critical fields of the valence transition for the $EuNi_2(Si_{1-x}Ge_x)_2$ compound in the concentration range from 0.82 to 0.5 according to our data and the data taken from [1]. It can be seen that the critical field $H_v(x)$ increases linearly with a decrease in the germanium concentration.

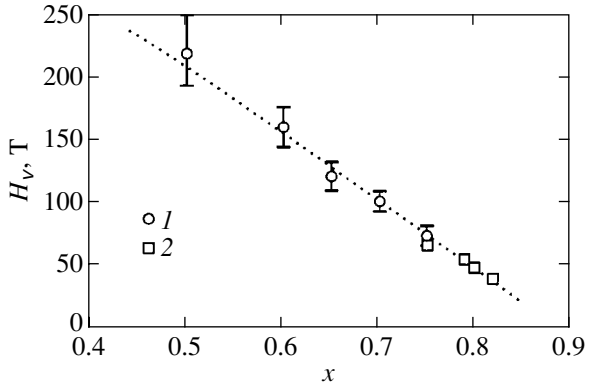

Fig. 3. Dependence of the critical field of the magnetic-field-induced valence transition in the $EuNi_2(Si_xGe_{1-x})_2$ compound on the germanium concentration at $T = 4.2$ K according to (*1*) our data and (*2*) the data taken from [1].

3.2. The magnetic properties of $EuNi_2(Si_{1-x}Ge_x)_2$ compounds depend on the occupancy of the Eu bivalent and trivalent states. A schematic diagram of the energy levels for Eu is shown in Fig. 4. In the case when the magnetic field is equal to zero and the temperature is low, the electrons reside in the conduction band whose energy coincides with the energy of the nonmagnetic state $J = 0$ for the Eu^{3+} ion. The energy difference between the ground and excited states for both Eu^{3+} and Eu^{2+} ions is sufficiently large. In terms of Boltzmann statistics, we can calculate the occupation probability of the level $J = 7/2$ in the range of measured temperatures at which the metamagnetic transition is observed. It is found that the occupation probability does not exceed 10^{-4}. Mitsuda *et al.* [4] proposed the interconfigurational fluctuation (ICF) model for explaining the spontaneous occupation of magnetic states. They introduced the effective temperature and considered the relationship between the splitting of the level $J = 7/2$ and the occupancy of the Eu^{2+} p_2 state: $E_{ex} = E_0(1 - \alpha p_2)$, where α and E_0 are the parameters. The occupation probability for the 7/2 level in a magnetic field due to Zeeman splitting is determined by the expression

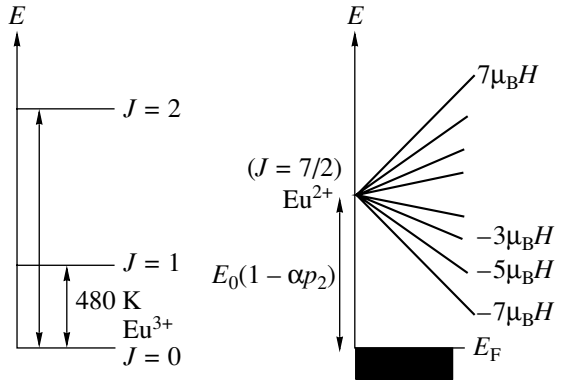

Fig. 4. Schematic diagram of energy levels in the $EuNi_2(Si_{1-x}Ge_x)_2$ compound in a magnetic field.

$$p_2 = p_3 \frac{\sum_{j_z=-7/2}^{7/2} \exp[-E_0(1-\alpha p_2) + g_2\mu_B J_z H]/kT^*}{1 + \sum_{j_z=-1}^{1} \exp[-480k + g_3\mu_B J_z H]/kT^* + \sum_{j_z=-2}^{2} \exp[-1330k + g_3\mu_B J_z H]/kT^*},$$

where p_3 is the occupation probability of the Eu^{3+} state and g_2 and g_3 are the Landé splitting factors for Eu^{2+} and Eu^{3+}, respectively. The proper choice of the parameters α and E_0 can provide a jump in the magnetic susceptibility whose width decreases with a decrease in the temperature and an increase in the magnetic field. This formula adequately describes the experimental results with the following parameters: $\alpha = 1.05$, $E_0 = 700$–2000 K, and $T_f = 500$ K. The value of E_0 is dependent on the germanium concentration.

4. CONCLUSION

Thus, the results of measurements of the magnetic susceptibility in $EuNi_2(Si_xGe_{1-x})_2$ compounds in superhigh magnetic fields confirmed the occurrence of the magnetic-field-induced valence transitions in the low-concentration range down to $x = 0.5$. The critical field H_v increases linearly with a decrease in the concentration x over the entire range of concentrations. The curves of the magnetic transitions are adequately described in terms of the ICF model.

ACKNOWLEDGMENTS

This work was supported by the Ministry of Atomic Energy of the Russian Federation.

REFERENCES

1. H. Wada, A. Nakamura, A. Mitsuda, *et al.*, J. Phys.: Condens. Matter **9**, 7913 (1997).
2. E. V. Sampathkumaran, L. C. Gupta, R. Vjiayaraghavan, *et al.*, J. Phys. C **14**, L237 (1981).
3. A. I. Pavlovskiĭ and R. Z. Lyudaev, in *Problems of Modern Experimental Science and Technology*, Ed. by A. P. Aleksandrov (Nauka, Leningrad, 1984), p. 206.
4. A. Mitsuda, H. Wada, M. Shiga, *et al.*, Phys. Rev. B **55**, 12474 (1997).

Translated by O. Moskalev

Physics of the Solid State, Vol. 44, No. 2, 2002, pp. 318–323. Translated from Fizika Tverdogo Tela, Vol. 44, No. 2, 2002, pp. 307–311.

MAGNETISM AND FERROELECTRICITY

Temperature Effect on the Elastic Properties of Yttrium Garnet Ferrite $Y_3Fe_5O_{12}$

Yu. A. Burenkov and S. P. Nikanorov

Ioffe Physicotechnical Institute, Russian Academy of Sciences, Politekhnicheskaya ul. 26, St. Petersburg, 194021 Russia
e-mail: s.nikanorov@pop.ioffe.rssi.ru

Received June 19, 2001

Abstract—The Young's moduli along the [100] and [110] crystallographic directions and the shear modulus along the [100] direction in a high-purity yttrium garnet ferrite single crystal are measured in the temperature range from 20 to 600°C. All the independent elastic constants are calculated for this temperature range. The behavior of the elastic moduli and elastic anisotropy factor is analyzed in the vicinity of the critical temperature of the magnetic phase transition. © *2002 MAIK "Nauka/Interperiodica".*

1. INTRODUCTION

Yttrium garnet ferrite $Y_3Fe_5O_{12}$ is an interesting material, because it exhibits the properties of an antiferromagnet owing to the type of ordering of spin magnetic moments and the microproperties of a ferromagnet. Moreover, this material is of importance in microwave technology. However, the elastic properties of yttrium garnet ferrite have not been adequately investigated. Knowledge of these characteristics is necessary both to the understanding of the role played by magnetoelastic coupling in oscillation and wave processes occurring in magnetically ordered materials and to the elucidation of the mechanism of transition from an antiferromagnetic state to a paramagnetic state near the Curie temperature T_C.

Gibbons and Chirba [1] were the first to measure the Young's modulus E for polycrystalline yttrium garnet ferrite. According to their measurements, the E modulus at room temperature is equal to 200.5 GPa. Clark and Strakna [2] studied single-crystal yttrium garnet ferrite containing the following impurities (wt %): Pb < 0.2, Al < 1, Si < 1, Mn < 0.01, and Cu < 0.001. It was found that, at room temperature, the velocities of longitudinal acoustic waves along the directions [100] $V_{l[100]}$ and [110] $V_{l[110]}$ are equal to 7.209×10^5 and 7.153×10^5 cm s^{-1}, respectively, and the velocity $V_{t[100]}$ of the transverse acoustic wave is 3.843×10^5 cm s^{-1}. In [2], the authors used the theoretical density $\rho = 5170$ kg/m^3 to calculate the elastic moduli $C_{11} = 269$ GPa, $C_{12} = 107.7$ GPa, and $C_{44} = 76.4$ GPa. Moreover, the previously unpublished results of MacSkimin's measurements of the longitudinal wave velocity (7.17×10^5 cm s^{-1}) and the transverse wave velocity (3.87×10^5 cm s^{-1}) were reported in [2]. Elastic moduli close to the data presented in [2] were obtained by Bateman [3], who used the MacSkimin interference method to measure longitudinal and transverse wave velocities in an yttrium garnet ferrite single crystal of higher purity (Pb < 0.1%, Si < 0.01%, Al < 0.25%, Mn < 0.01%, Cu < 0.001%, and Ca < 0.005%). The elastic moduli C_{ij} and the thermoelastic constants $T_{ij} = dC_{ij}/(C_{ij}dT)$ for yttrium garnet ferrite single crystals at room temperature were determined by Haussuhl *et al.* [4]. Kamilov and Aliev [5] measured the V_l velocities along the [100] and [110] directions in the temperature range from 260 to 300°C and analyzed the character of the phase transition in the vicinity of the Curie point.

The aforementioned data and other information on the properties of yttrium garnet ferrites were collected and presented in [6]. As can be seen from the available data, the elastic properties of yttrium garnet ferrites have been thoroughly investigated only at room temperature. At higher temperatures, independent elastic moduli have not been investigated despite the fact that the temperature dependences of these parameters in the vicinity of the Curie point T_C can provide additional information on the mechanism of magnetic phase transition. The phase transition near the Curie point was investigated in [5] but only for longitudinal waves propagating along two directions.

The aim of the present work was to investigate the temperature dependences of all independent elastic constants that provide comprehensive description of the elastic anisotropy of yttrium garnet ferrite over a wide temperature range, including the Curie point T_C.

2. SAMPLES AND EXPERIMENTAL TECHNIQUE

Young's and shear moduli were measured by the resonance method with an instrument producing electrostatic excitation of longitudinal and torsional vibrations in the samples. The accuracy of measurements was 0.12%. The general principle of operation of the instrument used was described earlier in [7]. The rela-

tive error in determining the modulus for the same sample with a change in temperature, which is determined by the accuracy of measuring the resonance frequency, was equal to 10^{-4}%. However, the error in measuring the resonance frequency at high temperatures and, especially, in the magnetic phase transition range was considerably larger due to the increase in resonance attenuation in the sample.

All the samples used in our experiments were cut from the same single-crystal ingot grown on a $Gd_3Fe_5O_{12}$ substrate in a crystallizer [8]. The initial materials were of high-purity grade and contained the following impurities (wt %): Pb < 0.2 and Si, Mn, Cu, Co, Ni, Ca, and Cr < (1–2) × 10^{-4}. The samples were prepared in the form of rectangular rods $4 \times 4 \times 15$ mm in size. The sample length was measured on an IZA-2 horizontal comparator with an accuracy of 0.01 mm. The sample density ($\rho = 5150$ kg/m^3) at room temperature was determined by hydrostatic weighing. For acoustic measurements, electrodes were produced by cementing an aluminum foil 10 μm thick with the use of a BF-2 adhesive onto two opposite faces and onto the end of the sample. In order to improve the heat exchange and to prevent oxidative processes, the measurements were performed in a gaseous helium atmosphere at a pressure of 1.013×10^5 Pa.

The resonance frequencies were measured at different temperatures upon heating (direct run) from 20 to 600°C and cooling (back run) of the sample. However, for the most part, the experimental data at different temperatures were obtained upon slow heating of the sample from room temperature at a rate of about 2 K/min. Each resonance frequency was measured after reaching a steady-state temperature. The measurements of torsional frequencies of samples at the instant of resonance at high temperatures presented severe difficulties associated with a large attenuation background. For this reason, we failed to measure the torsional vibrations upon cooling (back run). The resonance frequencies of the longitudinal and torsional vibrations in the samples fell in the ranges 200–208 and 113–117 kHz, respectively. The Young's moduli E_{100} and E_{110} and the shear modulus G_{100} were calculated from the resonance frequencies ν of longitudinal and torsional vibrations oriented along the [100] and [110] directions at each steady-state temperature.

The elastic moduli were determined using the formula for the resonance frequency of a rod: $\nu = [n/(2L)](M/\rho)^{1/2}$, where n is the harmonic number, i.e., the number of half-waves being along the sample length at resonance (in our case, $n = 1$); L is the sample length at room temperature; and M is the elastic modulus.

The Young's moduli were calculated with correction for thermal expansion. The Young's modulus is defined by the relationship

$$E = 4\rho L^2 \nu_l^2 / [n^2(1 + \Delta L/L)],$$

where ν_l is the natural frequency of longitudinal vibrations of the sample at resonance and $\Delta L/L$ is the elongation per unit length of the sample due to thermal expansion in the temperature range from room temperature to the temperature of measurement.

The measurements of torsional vibrations were performed with samples of square section that were orientated along the cube axis [100]. The shear modulus was calculated from the formula used in calculating the Young's modulus but with allowance for the fact that the square section of the sample under torsion becomes nonplanar [9]; that is,

$$G_{100} = 4.742\rho L^2 \nu_t^2 / [n^2(1 + \Delta L/L)],$$

where ν_t is the natural frequency of torsional vibrations at resonance.

The data on the linear expansion coefficient $\alpha(T)$ required for calculating the moduli E and G were taken from [10].

By using the data on elastic moduli E_{100}, E_{110}, and G_{100} at different temperatures and the standard relationships [9], we calculated the adiabatic elastic constants S_{11}, S_{12}, and S_{44}; the elastic moduli C_{11}, C_{12}, and $C_s = (C_{11} - C_{12})/2$; and the elastic anisotropy factor $A = 2C_{44}/(C_{11} - C_{12})$.

3. RESULTS AND DISCUSSION

Table 1 presents the elastic constants S_{ij}, elastic moduli C_{ij}, and elastic anisotropy factors A at room temperature which were obtained in this work and those taken from [2–4]. It can be seen that the results of our measurements at room temperature are in agree-

Table 1. Elastic constants, elastic moduli, and density of yttrium garnet ferrite at room temperature

T, °C	S_{11}	$-S_{12}$	S_{44}	C_{11}	C_{12}	C_{44}	A	ρ, kg/m^3	Reference
	TPa^{-1}			GPa					
23	4.821	1.378	13.089	269.00	107.70	76.40	0.9472	5170	[2]
25	4.917	1.436	13.055	268.00	110.60	76.60	0.9733	5170	[3]
20	4.865	1.416	12.903	270.10	110.90	77.50	0.9736	5188	[4]
20	4.979	1.487	13.316	269.38	114.75	75.10	0.9713	5150	This work

Table 2. Elastic constants, elastic moduli, and elastic anisotropy factors for yttrium garnet ferrite at different temperatures

T, °C	S_{11}	$-S_{12}$	S_{44}	C_{11}	C_{12}	C_{44}	A
	TPa^{-1}			GPa			
20	4.979	1.487	13.316	269.38	114.75	75.10	0.9713
100	5.038	1.508	13.436	266.80	114.04	74.72	0.9744
150	5.077	1.520	13.512	264.72	113.14	74.01	0.9765
200	5.122	1.531	13.591	262.09	111.78	73.58	0.9790
250	5.172	1.543	13.679	259.06	110.12	73.11	0.9817
260	5.182	1.544	13.695	258.38	109.71	73.02	0.9822
270	5.192	1.546	13.714	257.69	109.28	72.92	0.9827
275	5.197	1.547	13.724	257.34	109.06	72.87	0.9828
280	5.202	1.548	13.734	256.99	108.84	72.81	0.9829
285	5.207	1.548	13.744	256.62	108.59	72.76	0.9830
290	5.202	1.549	13.735	257.15	109.01	72.81	0.9830
295	5.198	1.549	13.726	257.53	109.31	72.85	0.9830
300	5.195	1.548	13.719	257.66	109.34	72.89	0.9830
310	5.200	1.548	13.733	257.13	108.94	72.82	0.9828
320	5.207	1.547	13.748	256.48	108.42	72.74	0.9826
335	5.219	1.548	13.774	255.58	107.80	72.60	0.9826
350	5.232	1.551	13.800	254.76	107.34	72.46	0.9830
400	5.278	1.562	13.888	252.28	106.08	72.01	0.9850
450	5.324	1.574	13.976	249.79	104.80	71.55	0.9870
500	5.371	1.586	14.068	247.37	103.62	71.08	0.9891
550	5.419	1.598	14.158	244.91	102.40	70.63	0.9912
600	5.468	1.610	14.250	242.46	101.17	70.18	0.9934
			Extrapolated values				
750	5.620	1.646	14.532	234.96	97.32	68.82	1.0000

ment with the data obtained by other authors. Note that the elastic anisotropy factor for yttrium garnet ferrite is considerably closer to unity than that for the majority of materials with a cubic crystal lattice.

The values of S_{ij}, C_{ij}, and A at different temperatures are listed in Table 2. The temperature dependences of the Young's and shear moduli measured upon heating (direct run) and cooling (back run) of the studied samples are depicted in Fig. 1. It is seen that no hysteresis is observed in the curves $E(T)$ and $G(T)$ upon heating–cooling thermocycling. This indicates that the yttrium garnet ferrite lattice is stable to heat. In the ferrimagnetic phase ($T < T_C$), the dependences $E(T)$ and $G(T)$ exhibit a smooth behavior with a change in temperature. However, these dependences in the ferrimagnetic phase are essentially nonlinear. Most likely, this behavior is caused by the effect of zero-point quantum-mechanical vibrations [9, 11] at temperatures below the Debye temperature (near 267°C [6]) and structural transformations of the yttrium garnet ferrite lattice. As the transition temperature is approached, there arise elastic and magnetostrictive strains due to changes in the orientation of local magnetization vectors. This leads to an additional decrease in the elastic moduli. Note that the Curie temperature T_C of the magnetic phase transition can be determined from magnetic measurements using the thermodynamic coefficient method, from the complex susceptibility of the paraprocess, polarized neutron diffraction, and other independent measurements. According to different authors [5, 6], the Curie temperature of yttrium garnet ferrite lies in the range from 275 to 287°C. As is known, the T_C temperature increases with a decrease in the impurity content in the crystals [12]. The temperature dependences of the elastic moduli indicate that the T_C temperature of high-purity yttrium garnet ferrite is equal to 285°C. It should be noted that, in our experiments, no temperature shift of the minima in the curves $E(T)$ and $G(T)$ at the Curie point is observed upon cooling of the samples (the direct and back runs coincide).

At temperatures close to T_C (in a narrow temperature range from 285 to 300°C), the elastic moduli exhibit an anomalous behavior characteristic of a magnetic phase transition. In this critical range, an increase

in the temperature leads to an increase in the Young's moduli E_{100} and E_{110} and the shear moduli G_{100} by 0.453, 0.441, and 0.135 GPa, respectively.

It is known that the critical change in the acoustic wave velocity is virtually independent of the vibrational frequency (up to 10^5–10^6 Hz) and follows a logarithmic or power dependence on the temperature [5]. Our measurements demonstrate that, as the T_C temperature is approached, the change in the velocity of sound in the paramagnetic phase is determined by the relationship $\Delta V/V = \varepsilon^{-n}$, where n is the critical exponent and $\varepsilon = (T - T_C)/T_c$ is the reduced temperature ranging from 9×10^{-4} to 10^{-2}. This can be seen from Fig. 2, which displays the dependence of $\Delta V/V$ on the reduced temperature ε in the log–log coordinates for longitudinal and transverse waves propagating along the [100] direction. The change in the velocity in the critical range was determined by extrapolating the temperature dependence of $\Delta V/V$ from the paramagnetic phase to the anomalous region. It follows from Fig. 2 that the critical exponent n is equal to 0.15 for longitudinal and transverse waves. This exponent falls in the theoretical exponent range $0 \le n \le 0.66$ [13]. However, the critical exponent we determined is substantially less than that obtained in [5] from measurements of the velocity and absorption. According to the theoretical work by Bennet [13], it can be expected that the exponent for the velocity will be less than that for the attenuation. The difference in the exponents obtained in the present work and in [5] can also be associated with the different contents of impurities and defects in the studied samples, which manifests itself in higher velocities of sound in our work.

Bennet [13] proved that the change in the elastic wave velocity in the vicinity of the T_C temperature depends on the type of propagating wave and the type of spin–phonon interaction. For an antiferromagnet in the paramagnetic phase, the shift in the angular frequency of an elastic wave due to the interaction with a spin system near the T_C temperature can be represented by the relationship

$$\Delta\omega(\lambda, \mathbf{q}) = \Delta V\mathbf{q} = -[S_\lambda^2\mathbf{q}/2MV(\lambda)A^2] f_a(\lambda, \beta), \quad (1)$$

where the wave vector $\mathbf{q} \longrightarrow 0$ tends to zero, S_λ^2 is the coupling coefficient of phonons with the spin system independent of the wave vector, λ is the wavelength, M is the magnetic ion mass, $\beta = 1/kT$, f_a is the temperature-dependent function, and A is a constant [13].

In the case when the interaction of phonons with the spin system is determined by the volume magnetostriction, the coupling coefficient S_λ^2 for the longitudinal wave with the wave vector $\mathbf{q} = q(\sin\theta\cos\varphi + \sin\theta\sin\varphi + \cos\theta)$ and the polarization $\mathbf{e}_l = \mathbf{q}/q$ has the form

$$(S_\lambda^2)_l = 6Q^2d^2, \quad (2)$$

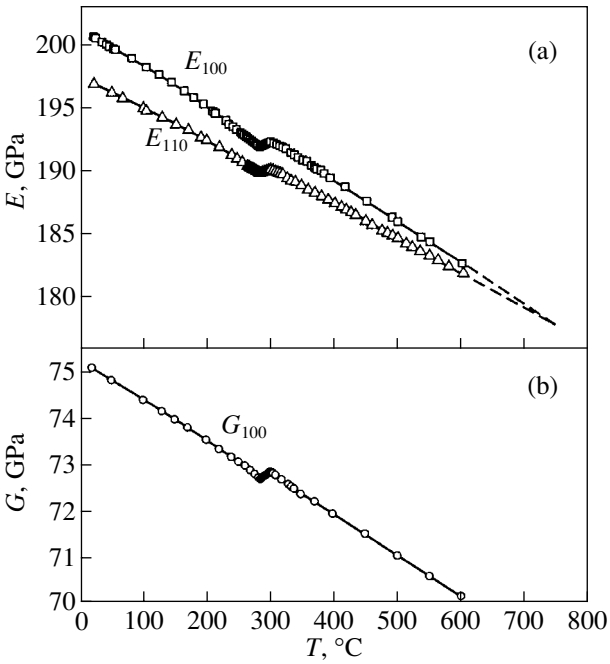

Fig. 1. Temperature dependences of the (a) Young's and (b) shear moduli for yttrium garnet ferrite.

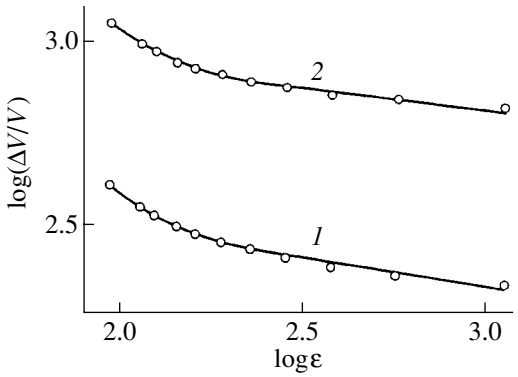

Fig. 2. Dependences of the relative decrease ($\Delta V/V$) in the velocity of (*1*) longitudinal and (*2*) transverse waves along the [100] direction in the critical range on the reduced temperature in the log–log coordinates.

where q, θ, and φ are the coordinates in a spherical coordinate system for a crystal with an axis aligned along the Z axis; d is the lattice parameter; and Q is the force coupling coefficient in the case of volume magnetostriction. From relationship (2), it follows that the decrease in the velocity of sound in the vicinity of the T_C temperature is independent of the wave propagation direction.

For a transverse wave with the polarization $\mathbf{e}_t = -\sin\varphi + \cos\varphi$, the coupling coefficient can be written as

$$(S_\lambda^2)_t = (3/2)Q^2\sin^2\theta\sin^2\varphi\cos^2\varphi. \quad (3)$$

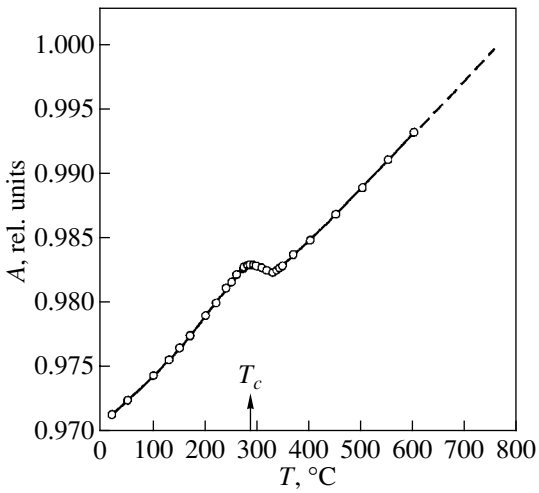

Fig. 3. Temperature dependence of the elastic anisotropy factor for yttrium garnet ferrite.

From formula (3), when the transverse wave propagates along one of the crystal axes, we have $(S_\lambda^2)_t = 0$ and, according to expression (1), the shift in the velocity near the T_C temperature is also equal to zero.

If the phonon–magnon interaction is associated with single-ion magnetostriction, the coupling coefficients are represented by the relationships

$$(S_\lambda^2)_l = 3G_{11}^2\{\cos^2\varphi(\cos^2\varphi - \sin^2\varphi) + \sin^4\varphi(\cos^4\varphi - \sin^2\varphi\cos^2\varphi + \sin^4\varphi)\} + 4G_{44}^2\sin^2\theta(\cos^2\theta + \sin^2\theta\cos^2\varphi\sin^2\varphi) \quad (4)$$

for the longitudinal wave and

$$(S_\lambda^2)_t = 9G_{11}^2\sin^2\theta\sin^2\varphi\cos^2\varphi + G_{44}\{\cos^2\theta + \sin^2\theta(\cos^2\varphi - \sin^2\varphi)^2\} \quad (5)$$

for the transverse wave. Here, G_{11} and G_{44} are the force coupling coefficients for the single-ion magnetostriction interaction.

In the case of single-ion magnetostriction, the anomaly in the temperature dependence of the shear wave velocity near the T_C temperature in the paramagnetic phase, according to formula (5), is nonzero and should be of the same order of magnitude as the anomaly observed for longitudinal waves.

The experimental data count in favor of the single-ion magnetostriction. In actual fact, relative changes in the shear moduli that determine the transverse wave velocities along the [100] and [110] directions are nonzero in the vicinity of the T_C temperature: $\Delta C_{44}/C_{44} = 0.0031$ and $\Delta C_s/C_s = 0.0033$. The small difference between the anomalies in the temperature dependences of the shear moduli near the T_C temperature can be explained by the fact that the crystal is almost elastically isotropic. In this case, the elastic anisotropy factor A is equal to 0.983.

Another indication of the single-ion magnetostriction in the crystal is the anisotropy of the anomalous decrease in the longitudinal wave velocity in the vicinity of the T_C temperature. As follows from relationships (4) and (5), the ratio of coupling coefficients for the waves propagating along the [100] and [110] directions is equal to $3G_{11}^2/[(1/16)^2(3G_{11}^2 + 4G_{44}^2)]$. According to expression (2) for the volume magnetostriction, the anisotropy of the aforementioned anomaly for longitudinal waves should be absent. This anisotropy was observed in [5]. Our measurements demonstrate that the relative decrease in the elastic modulus responsible for the longitudinal wave velocity along the [100] direction is associated with critical fluctuations of the spin system in the vicinity of the Curie point and can be determined from the following ratio: $\Delta C_{11}/C_{11} = 0.0092$. The shift in frequency of the longitudinal wave along the [110] direction is determined as follows: $\Delta[0.5(C_{11} + C_{12} + 2C_{44})]/[0.5(C_{11} + C_{12} + 2C_{44})] = 0.0083$.

Thus, the anomalies in the elastic properties in the vicinity of the critical temperature are associated with the contribution of the single-ion mechanism of spin-lattice interaction.

At temperatures above the critical range ($T >$ 300°C), the elastic moduli in the paramagnetic phase almost linearly decrease with an increase in the temperature in accordance with the quasi-harmonic elasticity theory [9, 11].

The temperature dependence of the elastic anisotropy factor is plotted in Fig. 3. It is seen from this figure that, in the ferrimagnetic phase, unlike the paramagnetic phase, the A factor increases more rapidly with an increase in the temperature. The extrapolation of the dependence $A(T)$ indicates that the crystal becomes elastically isotropic ($A = 1$) at 750°C.

In conclusion, it should be noted that the experimental results obtained in this work for the elastic properties of yttrium garnet ferrite are of importance not only in physical acoustics. These data can prove be useful both in evaluating the wear resistance of articles and thermoelastic stresses arising during the growth of single crystals and epitaxial films and in solving certain problems of phase transitions.

ACKNOWLEDGMENTS

We are grateful to Yu.K. Petrene for supplying the samples used in our measurements and B.K. Kardashev for his participation in discussions of the results and valuable remarks.

REFERENCES

1. D. F. Gibbons and V. G. Chirba, Phys. Rev. **110** (3), 770 (1958).
2. A. E. Clark and R. E. Strakna, J. Appl. Phys. **32** (6), 1172 (1961).
3. T. B. Bateman, J. Appl. Phys. **37** (5), 2194 (1966).
4. S. Haussuhl, D. Mateika, and W. Tolksdorf, Z. Naturforsch. A **31** (3–4), 390 (1976).
5. I. K. Kamilov and Kh. K. Aliev, Zh. Éksp. Teor. Fiz. **65** (5), 1911 (1973) [Sov. Phys. JETP **38**, 954 (1973)].
6. *Acoustical Crystals: A Handbook*, Ed. by M. P. Shaskol'skaya (Nauka, Moscow, 1982).
7. Yu. A. Burenkov, S. P. Nikanorov, and A. V. Stepanov, Izv. Akad. Nauk SSSR, Ser. Fiz. **35**, 525 (1971).
8. B. V. Zaĭtsev, S. Sh. Gendelev, A. G. Titova, and V. G. Kurilenko, Élektron. Tekh., Ser. 7: Ferritovaya Tekh., No. 4 (16), 10 (1968).
9. S. P. Nikanorov and B. K. Kardashev, *Elasticity and Dislocation Inelasticity of Crystals* (Nauka, Moscow, 1985).
10. S. Geller, G. P. Espinosa, and P. B. Crandall, J. Appl. Crystallogr. **2**, 86 (1969).
11. G. Leibfried and W. Ludwig, *Theory of Anharmonic Effects in Crystals* (McGraw-Hill, New York, 1961; Inostrannaya Literatura, Moscow, 1963).
12. R. M. Bozorth, *Ferromagnetism* (Van Nostrand, New York, 1951; Inostrannaya Literatura, Moscow, 1956).
13. H. S. Bennet, Phys. Rev. **181** (2), 978 (1969).

Translated by O. Borovik-Romanova

Physics of the Solid State, Vol. 44, No. 2, 2002, pp. 324–332. Translated from Fizika Tverdogo Tela, Vol. 44, No. 2, 2002, pp. 312–320.

MAGNETISM AND FERROELECTRICITY

Vortices and Magnetic Structures of the Target Type in a Two-Dimensional Ferromagnet with Anisotropic Exchange

A. B. Borisov, S. A. Zykov, N. A. Mikushina, and A. S. Moskvin

Institute of Metal Physics, Ural Division, Russian Academy of Sciences, ul. S. Kovalevskoĭ 18, Yekaterinburg, 620219 Russia

e-mail: borisov@imp.uron.ru

Received July 2, 2001

Abstract—Various types of magnetic structure in a two-dimensional Heisenberg ferromagnet are considered in a continuum approximation. The effect of anisotropic exchange and single-ion anisotropy on the vortex structure is analyzed. A new type of static magnetic structure ("target") is predicted and investigated in an easy-plane ferromagnet. © *2002 MAIK "Nauka/Interperiodica".*

1. INTRODUCTION

In the last two decades, there has been an increasing interest in solitons, vortices, and other nonlinear excitations in low-dimensional magnets. The important role played by these excitations and their influence on the occurrence of long-range order; various magnetic phase transitions, including topological transitions; and responses to external fields have been noticed by many researchers (see, for example, [1–3]). These problems are not only of academic interest but are a matter of practical importance. Recently, a large class of quasi-one-dimensional (1D) and quasi-two-dimensional (2D) magnets was discovered in which the magnetic interactions in crystallographic planes are by far stronger than the interactions between planes. These materials include layered magnets, intercalated compounds (such as $CoCl_2$), and a quite wide class of high-temperature superconducting basic systems (La_2CuO_4, $Sr_2CuO_2Cl_2$, $YBa_2Cu_3O_6$) [4].

A peculiar property of quasi-two-dimensional systems is their high sensitivity not only to relatively weak interactions between planes but also to various kinds of magnetic anisotropy, both local (single-ion) and nonlocal (two-ion). Allowance for the second-order magnetic anisotropy results in a well-known generalization of a classical two-dimensional isotropic *XY* Heisenberg model with the Hamiltonian

$$H = -J\sum_{j,k}(S_j^xS_{j+k}^x + S_j^yS_{j+k}^y + \lambda S_j^zS_{j+k}^z) - K\sum_j (S_j^z)^2, \quad (1)$$

which describes the interaction of classical spins S_j on a lattice. Here, $J > 0$ is the exchange integral; the spin vector S_j is represented in the form $\{S_j^x + iS_j^y, S_j^z\} = S_0\{\sin\theta_j\exp(i\Phi_j), \cos\theta_j\}$, and its orientation is determined by the polar (θ_j) and azimuthal (Φ_j) angles; λ is the anisotropic exchange constant (generally, $0 < \lambda < \infty$); K is the single-ion anisotropy constant; the index j numbers lattice sites; and the summation over k includes only nearest neighbors. The *XY* symmetry implies that, in the range of λ values indicated above, the ground state of the system is infinitely degenerate with respect to the spin rotation angle in the *XY* plane. This model includes both the isotropic Heisenberg model ($\lambda = 1$) and the *XY* model ($\lambda = 0$).

It is well known that in 2D systems described by Hamiltonian (1), there are not only ordinary spin waves but also topological excitations, namely, vortices, which are responsible for a topological phase transition in the *XY* model [5] and make an important contribution to thermodynamics of the isotropic Heisenberg model. The structure and dynamics of vortices in model (1) (and in its continual approximation) and their contribution to the dynamic structure factor in the approximation of a free vortex gas were investigated in [2, 6] in the case where there is no local magnetic anisotropy ($K = 0$). Numerical simulations show that, in the interval $0 < \lambda < \lambda_c$, where $\lambda_c = 0.72$ for a square lattice and $\lambda_c = 0.86$ for a hexagonal lattice, the energy of an in-plane (IP) vortex in the configuration

$$S_z = 0, \quad \Phi = q\varphi + \Phi_0 \quad (q \in Z) \quad (2)$$

with topological charge q is less than the energy of an out-of-plane (OP) vortex with spins going out of the easy plane [6]. In the continual approximation for model (1), such vortices are characterized by a monotonically decreasing radial-symmetric distribution of

the spin component S_z perpendicular to the easy plane, which is subject to the boundary conditions

$$\begin{aligned} S_z &\longrightarrow \pm S_0 \quad \text{for} \quad r \longrightarrow 0, \\ S_z &\longrightarrow 0 \quad \text{for} \quad r \longrightarrow \infty. \end{aligned} \tag{3}$$

The aim of the present work is to investigate the structure of vortices and other topological defects in a quasi-two-dimensional ferromagnet with anisotropic exchange with allowance for the local second-order magnetic anisotropy energy and for magnetic dipole interactions. In Section 2, we present the tenants of the microscopic theory of spin anisotropy in systems based on 3*d* and 4*f* elements, as this is of great importance in substantiating the model proposed. In Section 3, we consider magnetization vortices in an easy-plane ferromagnet with anisotropic exchange and local magnetic anisotropy. Section 4 is devoted to an analysis of magnetic structures of the target type in an anisotropic ferromagnet.

2. MICROSCOPIC ORIGIN OF SPIN ANISOTROPY

The microscopic origin of the two-ion anisotropy, characterized by the parameter λ, for compounds based on 3*d* elements is associated with long-range ($\propto 1/R^3$) magnetic dipole interaction and short-range quasi-dipole relativistic exchange interaction, or anisotropic exchange, which is a combination of exchange and spin–orbital interactions [7–9]:

$$\hat{V}_{ex} = -\sum_{i,k} \hat{j}_{i,k}(s_i s_{i+k}), \quad \hat{V}_{so} = \sum_i \zeta_{nl}(i)(l_i s_i). \tag{4}$$

Here, $\hat{j}_{i,k}$ is the exchange integral, which is an orbital operator in the general case, and ζ_{nl} is the one-electron spin–orbital coupling constant. For the sake of simplicity, we omitted the summation over all electrons of multielectron atoms.

The anisotropic exchange in a pair of ions is a third-order effect in perturbation theory, and it can be schematically represented as a sum of several terms,

$$\begin{aligned} V_{an}(1,2) \propto \frac{V_{so}(1)V_{ex}(12)V_{so}(2)}{\Delta E^2} + \frac{V_{so}(1)V_{so}(2)V_{ex}(12)}{\Delta E^2} \\ + \frac{V_{so}(1)V_{ex}(12)V_{so}(1)}{\Delta E^2} + \frac{V_{so}(1)V_{so}(1)V_{ex}(12)}{\Delta E^2}, \end{aligned} \tag{5}$$

adding terms with a change $1 \longrightarrow 2$ and Hermitian conjugate terms. For ions 1 and 2 with spins $S_1 = S_2 = 1/2$, the anisotropic exchange has a rather simple bilinear form of quasi-dipole interaction and, in fact, is reduced to an anisotropic Heisenberg interaction (1). For ions 1 and 2 with spins $S_1(S_2) > 1/2$, the anisotropic exchange contains additional non-Heisenberg terms with second- or even third-rank tensor spin operators [9] of the type

$$\begin{aligned} V_{an}^{22} &\propto \sum_{i,k} (S_i S_{i+k}) S_i^z S_{i+k}; \\ V_{an}^{31} &\propto \sum_{i,k} (S_i S_{i+k}) [(S_i^z)^2 + (S_{i+k}^z)^2], \end{aligned} \tag{6}$$

whose contribution can be comparable in magnitude to the quasi-dipole contribution. The anisotropic exchange parameter λ can be estimated using the relationship suggested by Moriya [7]:

$$|\lambda - 1| \approx \left(\frac{\Delta g}{g}\right)^2,$$

where Δg is the deviation of the g factor from the purely spin value $g \approx 2$. However, in reality, the Moriya relationship has a very limited area of application and it would be more correct to use a more general relationship [9],

$$|\lambda - 1| \approx \eta\left(\frac{\xi_{3d}}{\Delta E}\right)^2, \tag{7}$$

where ξ_{3d} is the one-electron spin–orbit coupling constant ($\xi_{3d} \sim 0.01$–0.1 eV); ΔE is an average energy of the excited 3*d* ion states, which are mixed with the ground state due to spin–orbit interaction ($\Delta E \geq 1$ eV); and $\eta \sim 1$–10 is a numerical parameter. Examples of numerical model calculations of two-ion anisotropy for a number of 3*d*-element compounds are presented in [9]. On the whole, the anisotropic exchange in these compounds is relatively small, so that usually $|\lambda - 1| \leq 0.1$.

The second-order single-ion local anisotropy in the compounds based on 3*d* elements is due to both the spin–orbit interaction and low-symmetry crystal field. As a rule, the single-ion anisotropy energy in these systems is far less in magnitude than the exchange energy but is comparable to, or even exceeds, the two-ion anisotropy energy in most cases. The important feature of the single-ion anisotropy is that it occurs only for spins $S \geq 1$.

In magnets based on rare-earth 4*f* elements and described by effective Hamiltonian (1), the constant λ can vary in wide limits ($0 < \lambda < \infty$) and the single-ion anisotropy energy can considerably exceed the exchange energy. The classical long-range magnetic dipole interaction can be taken into account by introducing a demagnetizing field.

3. MAGNETIZATION VORTICES IN EASY-PLANE FERROMAGNETS WITH ANISOTROPIC EXCHANGE

3.1. Main Equations of the Model

The magnetization distribution in nonuniform magnetic structures arising in anisotropic ferromagnets with Hamiltonian (1) can be found in a continual approximation by minimizing the classical energy with the density

$$W = \frac{\alpha}{M_0^2} \times \left[(\nabla M_x)^2 + (\nabla M_y)^2 + \lambda (\nabla M_z)^2 + \frac{\varepsilon}{l_0^2} M_z^2 \right] - \frac{1}{2}\mathbf{RM}, \quad (8)$$

$$\varepsilon = \pm 1,$$

where $\alpha = JS^2$ is the exchange interaction parameter, $M_0 = g\mu_B S_0/a^2$, and

$$\frac{\varepsilon}{l_0^2} = \frac{4(1-\lambda) - K/J}{a^2},$$

where l_0 is the effective magnetic length and the parameter $\varepsilon = \pm 1$ defines the sign of the effective anisotropy constant $4(1-\lambda)J - K$.

The demagnetizing field **R** satisfies the magnetostatics equations

$$\begin{aligned} \mathrm{curl}\mathbf{R} &= 0, \\ \mathrm{div}[4\pi\mathbf{M} + \mathbf{R}] &= 0. \end{aligned} \quad (9)$$

We consider the structure of nonlocalized vortices (according to the terminology used in [4, 5]), in which the magnetization does not tend to a constant vector at large distances. For the case when demagnetizing fields **R** are absent and $\lambda = 1$, the structure of such vortices is discussed in detail in monograph [5]. It is known that for small distances $r \ll l_0$, the function $\theta(r)$ is determined by the exchange interaction and coincides with the well-known instanton solution (the Belavin–Polyakov skyrmion) [10]

$$\theta = 2\arctan[C\exp(q\ln(r/l_0))], \quad (10)$$

and the expression for the azimuthal angle coincides with Eq. (2). Using model (8), we consider the simplest vortex static configurations in the form

$$\theta = \theta(r), \quad \Phi = \varphi + \Phi_0, \quad (11)$$

where r and φ are the polar coordinates ($x = r\cos\varphi$, $y = r\sin\varphi$) in the XY plane. It can be easily seen that in this case, the demagnetizing field is a local function of the magnetization [11]:

$$\begin{aligned} R_x &= -4\pi M_x \cos\Phi_0, \quad R_y = -4\pi M_y \cos\Phi_0, \\ R_z &= 0. \end{aligned} \quad (12)$$

We take the constant Φ_0 to be equal to $\pi/2$, which corresponds to the minimum in the static magnetic field energy RM/2. Therefore, the static magnetic field $R = 0$ and is not taken into account in what follows. For arbitrary values of $q \neq 1$, the demagnetizing field is expressed through the scalar potential ψ ($\mathbf{R} = -\mathrm{grad}\psi$), which satisfies the Poisson equation $\Delta\psi = 4\pi\mathrm{div}\mathbf{M}$. In this case, the Landau–Lifshitz equation is invariant under simultaneous spatial and spin rotations, as in the theory of liquid crystals [12]. Therefore, at $q \neq 1$, the function $\theta = \theta(r, \varphi, z)$ has a different form (than at $q = 1$); it will be discussed below. From Hamiltonian (8) and Eq. (11), we obtain an ordinary differential equation for the function $\theta(r)$:

$$\begin{aligned} &(\cos^2\theta + \lambda\sin^2\theta)\left(\theta_{rr} + \frac{\theta_r}{r}\right) \\ &= \sin\theta\cos\theta\left((1-\lambda)\theta_r^2 + \frac{1}{r^2} - \frac{\varepsilon}{l_0^2}\right). \end{aligned} \quad (13)$$

3.2. Easy-Axis Ferromagnet

We show now that in the easy-axis ferromagnet ($\varepsilon = -1$), there is no localized vortex structures that are regular at the origin of coordinates and approach the ground state at infinity; i.e., we show that the boundary-value problem with the boundary conditions

$$\theta \longrightarrow 0, \quad \theta'(r) < \infty \quad \text{for} \quad r \longrightarrow 0, \quad (14)$$

$$\theta \longrightarrow \pi, \quad \theta'(r) \longrightarrow 0 \quad \text{for} \quad r \longrightarrow \infty \quad (15)$$

has no solution. For this purpose, we introduce the quantity

$$F(r) = \frac{1}{2}\left[\frac{(\cos^2\theta + \lambda\sin^2\theta)r^2\theta_r^2}{1 + r^2/l_0^2} + \cos^2\theta\right], \quad (16)$$

which is proportional to the energy density in the absence of anisotropy ($l_0 \longrightarrow \infty$). Then, according to Eq. (13), its derivative is negative,

$$F'(r) = -\frac{(\cos^2\theta + \lambda\sin^2\theta)r^3\theta_r^2}{(1 + r^2/l_0^2)^2} < 0, \quad (17)$$

and the function $F(r)$ decreases monotonically for $0 < \lambda < \infty$. However, with the nonsingular boundary conditions of (14), the values of $F(r)$ at $r \longrightarrow 0$ and $r \longrightarrow \infty$ coincide,

$$\lim_{r\to 0} F(r) = \lim_{r\to\infty} F(r) = 1/2, \quad (18)$$

which is in contradiction with the fact that $F(r)$ is a monotonic decreasing function. Consequently, there are no nonsingular vortex solutions subject to the boundary conditions of (14) and the Belavin–Polyakov skyrmion structure (10) drastically changes in the presence of any negligibly small easy-axis anisotropy.

3.3. Easy-Plane Ferromagnetic

Now, we discuss solutions to nonlinear equation (13) for an easy-plane magnet ($\varepsilon = 1$) with nonsingular boundary conditions

$$\theta \longrightarrow 0 \text{ for } r \longrightarrow 0, \quad \theta \longrightarrow \pi/2 \text{ for } r \longrightarrow \infty. \quad (19)$$

It can be easily shown (linearizing Eq. (13) at large r near $\theta = \pi/2$) that the vortex approaches a limit at large distances (for $\lambda \neq 0$) exponentially:

$$\theta \longrightarrow \pi/2 - C_1 K_{i/\sqrt{\lambda}}\left(\frac{r}{l_0\sqrt{\lambda}}\right) \longrightarrow \pi/2 - \frac{\tilde{C}_1}{\sqrt{r}}\exp\left(-\frac{r}{l_0\sqrt{\lambda}}\right) \text{ for } r \longrightarrow \infty, \quad (20)$$

where $K_i/\sqrt{\lambda}$ is a Macdonald function of the order $i/\sqrt{\lambda}$.

In the particular case $\lambda = 0$, Eq. (13) is factorized and has an exact solution. One can easily verify that at $\varepsilon = 1$, the solution is

$$\sin\theta = 1 \quad (r \geq r_1),$$
$$\sin\theta = \frac{J_1(r/l_0)}{J_1(r_1/l_0)} \quad (r \leq r_1) \quad (21)$$

[where r_1 is the first maximum of the Bessel function of the first order $J_1(r/l_0)$]; it is continuous, together with its first derivative, and describes a localized *OP* vortex in the *XY* model.

In the general case of an easy-plane magnet with a given l_0 value, the nonlinear boundary-value problem for Eqs. (13) and (19) has a solution only for discrete values of $\theta'(0)$.

We integrated Eq. (13) for various λ values using the shooting method. Figure 1 shows, as an example, the phase diagram of a solution found for $\lambda = 0.8$. The phase trajectories leaving the points $[\theta(0) = 0, \theta'(0) = \theta'_1]$ and $[\theta'(0) = 0, \theta'(0) = \theta'_2]$ terminate at the focuses $[\theta(\infty) = 0, \theta'(\infty) = 0]$ and $[\theta(\infty) = \pi, \theta'(\infty) = 0]$, respectively, as $r \longrightarrow \infty$. Therefore, the interval $\theta'_1 < \theta'(0) < \theta'_2$, in which there is a single trajectory with $\theta(\infty) \longrightarrow \pi/2$ and $\theta'(\infty) \longrightarrow 0$, can be determined very accurately. The functions $\theta(r)$ calculated using the shooting method for different λ values are presented in Fig. 2. It can be seen from Fig. 2 that, with increasing λ (starting from the value $\lambda = 0$), the vortex becomes more localized near the origin of coordinates and approaches the equilibrium value $\theta = \pi/2$ far from the origin more slowly, in accordance with Eq. (20).

The *OP* vortex energy depends on the system dimension L as $\ln L$, because the energy density contains the term $\sin^2\theta/r^2$, which results in logarithmic divergence of the integral in the expression for the magnet energy for an arbitrary law of $\theta(r)$ approaching $\pi/2$.

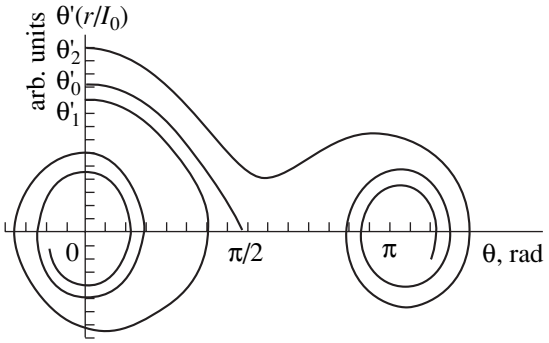

Fig. 1. Phase diagrams of solutions illustrating the shooting method: a search for a solution with the appropriate asymptotics at $r \longrightarrow \infty$.

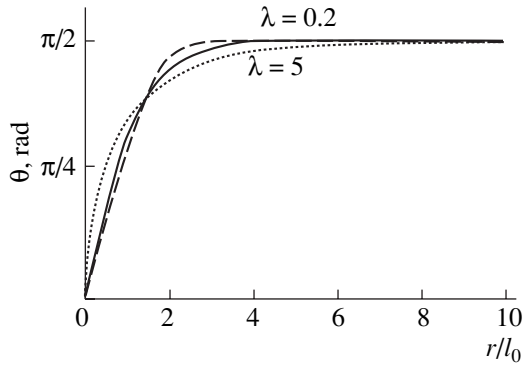

Fig. 2. Profiles of $\theta(r)$ functions for regular solutions calculated using the shooting method. The solid line corresponds to a vortex without anisotropic exchange.

The exact value differs from the value $2\pi\alpha\ln(L/l_0)$ by a term which is limited at $L \longrightarrow \infty$. For convenience, we represent the dependence of the energy E_{OP} on the system dimension and on the parameters λ and l_0 in the form

$$E_{OP} = 2\pi\int_0^L Wrdr = 2\pi\alpha\ln\left(\frac{B(\lambda)L}{l_0}\right). \quad (22)$$

The $B(\lambda)$ dependence is shown in Fig. 3. We compare the *OP*-vortex energy with the energy

$$E_{IP} = 2\pi\alpha\ln(L/r_0)$$

of the in-plane vortex defined by Eq. (2). Here, r_0 is the cutoff radius, which is of the order of several lattice constants. It is clear that the *OP* vortex is energetically favored under the condition

$$\frac{l_0}{r_0} > B(\lambda), \quad (23)$$

which implies a quite complex relationship between the two-ion and single-ion anisotropy parameters. Indeed,

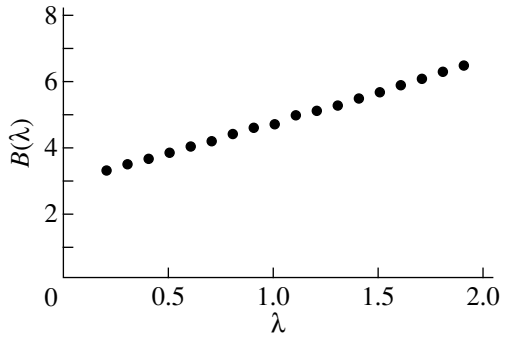

Fig. 3. $B(\lambda)$ graph for regular solutions.

the left-hand side of inequality (23) is determined by the effective magnetic length, i.e., by the effective magnetic anisotropy constant, whilst the right-hand side is determined only by the two-ion anisotropy constant. The presence of the parameter r_0 in Eq. (23) makes a direct comparison of the criterion for the transformation of the *IP* to the *OP* vortex, which we derived in the continuous model, with the corresponding criterion derived in the lattice model complicated [6]. If only the contribution from the anisotropic exchange interaction to magnetic anisotropy is taken into account, then $l_0 = a/2\sqrt{1-\lambda}$ (at $0 < \lambda < 1$), $r_0 \approx a$, and the *OP* vortex is stable at small positive values of $(1 - \lambda)$ [6], i.e., within the model with quasi-isotropic exchange. In the general case, the *OP*-vortex energy depends on the relation between the single-ion and two-ion magnetic anisotropy contributions in a complicated way, which allows one to consider the structure of stable topological defects in real magnets as a result of competition between the two contributions to magnetic anisotropy.

4. MAGNETIC STRUCTURES OF THE TARGET-TYPE IN AN EASY-PLANE FERROMAGNET WITH ANISOTROPIC EXCHANGE

In this section, we predict and analyze a new type of vortex structure, namely, structures of the static leading center type or the target. Spatial structures of the target type are observed in distributed active media and are the most widespread dissipative structures [13, 14]. In self-oscillating active media, the simplest type is represented by a source of spreading concentric phase waves. Dynamical structures of the pacemaker type in magnetically ordered media (easy-axis magnets) were first described in [15, 16]. They were also observed by other researchers, for example, in [17–21]. These spatial structures persisted after switching of the alternating magnetic field, thereby approaching the thermal equilibrium state in a sufficiently large time interval. This fact suggests that these structures are topological defects in magnetically ordered media and their theoretical study is of undeniable interest. Attempts to investigate them theoretically were made in [22–26].

For an analytical description of a system of radial-symmetric domain structures, we use singular solutions to Eq. (13) subject to the boundary conditions

$$\theta(\infty) \longrightarrow \frac{(2N+1)\pi}{2}, \quad N \in Z,$$
$$\theta'(0) \sim \frac{1}{r} \text{ unlimited function.} \tag{24}$$

These solutions we also further call vortex structures of the magnetic target type, as the dependence of their magnetization on the azimuthal angle Φ is also determined by Eq. (2), which is typical of vortices. The behavior of the magnetization near the singular-vortex core is dictated by the exchange interaction, which is invariant under scale transformations ($r \longrightarrow r/\beta$). Therefore, it is convenient to introduce a new extending variable $R = \ln(r/l_0)$, in terms of which Eq. (13) takes a simple form,

$$(\cos^2\theta + \lambda\sin^2\theta)\theta_{RR} = \sin\theta\cos\theta((1-\lambda)\theta_R^2 + 1 - e^{2R}). \tag{25}$$

We consider the asymptotic behavior and classification of the singular vortices at $r \longrightarrow 0$. In this limit, one can neglect the magnetic anisotropy energy, assuming $l_0 \longrightarrow \infty$ in Eq. (13), and reduce the solution $\theta(R)$ to quadratures:

$$R - R_0 = \int_{\theta(R_0)}^{\theta(R)} \frac{\sqrt{\cos^2\theta + \lambda\sin^2\theta}\,d\theta}{\sqrt{k^2 - \cos^2\theta}} \quad (0 < k < 1), \tag{26}$$

$$R - R_0 = k\int_{\theta(R_0)}^{\theta(R)} \frac{\sqrt{\cos^2\theta + \lambda\sin^2\theta}\,d\theta}{\sqrt{1 - k^2\cos^2\theta}} \quad (0 < k < 1). \tag{27}$$

4.1. Target-Type Structure in Easy-Plane Magnets with Isotropic Exchange Interaction

We consider a target-type structure in magnets with isotropic exchange interaction ($\lambda = 1$). In this case, $\theta(r)$ is expressed in terms of the elliptic functions

$$\cos\theta(R) = k\,\mathrm{sn}(R - R_0, k) \quad (0 < k < 1), \tag{28}$$

$$\cos\theta(R) = \mathrm{sn}\left(\frac{R - R_0}{k}, k\right) \quad (0 < k < 1). \tag{29}$$

Here, R_0 and k are constants of integration.

Note that the parameter k characterizes the periodic magnetization distribution (as a function of R) near the target center. The transition ($\lambda \longrightarrow 1$) from the anisotropic case of Eqs. (26) and (27) to the isotropic case of Eqs. (28) and (29) does not change the parameter k.

These solutions are singular at $r \longrightarrow 0$: $\theta'(r) \sim 1/r$ ($0 < k < 1$); they coincide with the well-known Belavin–Polyakov solution (10) at $k \longrightarrow 1$, which is the separatrix solution to the pendulum equation (25) at $\lambda = 1$ and

$l_0 \longrightarrow \infty$. Equation (28) describes R-periodic oscillations of the magnetization near zero: $-k \le \cos\theta(R) \le k$. Solution (29), which we will discuss below, describes a system of concentric ring-shaped domains (in the variable R), i.e., a magnetic target. The two consecutive centers of domain boundaries, at the points r_{n+1} and r_n, are related through the formula $r_{n+1} = r_n \exp[2kK(k)]$, where $K(k)$ is a total elliptic integral of the first kind. The domain width

$$d_n = d_0 e^{2nkK(k)} \tag{30}$$

depends on the k value and increases with distance from the target center, because $kK(k)$ is a monotonic increasing positive function of k.

As already mentioned, the solution found is singular and detailed analysis is required to estimate its contribution to the thermodynamics of two-dimensional systems. However, in real magnets, the nucleation of spiral- and target-type magnetic structures occurs, as a rule, on defects of a nonmagnetic nature. In this case, the target core radius coincides with the defect radius b and the solution found for small values of r is valid at $r > b$. At distances $r \sim l_0$, the magnetic anisotropy energy essentially influences the target structure. One might expect the singular vortex magnetization to coincide approximately with the in-plane vortex magnetization given by Eq. (2), namely, $S_z \approx 0$ and $\Phi = \varphi + \Phi_0$ in the region $r_c < r < \infty$, where r_c depends on the parameter k. In this case, $r_c(k)$ must be an increasing function of k^{-1}, because the average anisotropy energy per unit area of the nth domain

$$\frac{2\int_{r_n}^{r_{n+1}} W r dr}{r_{n+1}^2 - r_n^2}, \tag{31}$$

where $r_n = l_0 \exp[2nkK(k)]$ increases with decreasing k for configuration (2) at $n \longrightarrow \infty$. In addition, the parameter k, which characterizes the magnetization behavior near the vortex core [Eqs. (26)–(29)] must assume discrete values for which the $\theta(r)$ remains localized at large distances. These qualitative considerations are substantiated by numerical calculations performed with the shooting method.

To illustrate the shooting method, we present phase trajectories of the solutions at $\lambda = 1$ in Fig. 4. It can be seen that, at a given value $\theta(l_0) = \theta_0$ lying in the interval $[\theta'_1(l_0), \theta'_2(l_0)]$, there is a single phase trajectory, which terminates at the point $\theta = (2N + 1)\pi/2$. We fixed the value $\theta(r = l_0)$ and found the values $\theta'_1(l_0)$ and $\theta'_2(l_0)$ at which the solutions of the Cauchy problem for Eq. (25) with the initial conditions $\theta(l_0) = \theta_0$, $\theta'_{1,2}(l_0)$ exhibited asymptotic behavior $\theta(\infty) \longrightarrow N\pi$, $\theta'(\infty) \longrightarrow 0$ and $(\theta(\infty) \longrightarrow (N + 1)\pi$, $\theta'(\infty) \longrightarrow 0$, respectively. Having found these $\theta'_{1,2}(l_0)$ values, we took the $\theta'(l_0)$ value in the interval $[\theta'_1(l_0), \theta'_2(l_0)]$ at the next step of the calculations. Decreasing the interval $\theta'_1(l_0) < \theta'(l_0) < \theta'_2(l_0)$ for $\theta'(l_0)$, we arrived at the only $\theta'(l_0)$ value at which boundary condition (24) was fulfilled with the required extent of precision. Next, using the obtained values $\theta(l_0)$ and $\theta'(l_0)$, we solved the Cauchy problem for Eq. (25) in the interval $r \le l_0$ and found the magnetization near the vortex core. The resulting numerical solution was well approximated by formula (27) at $r \ll l_0$ with the particular k value. A graph of one of the solutions is presented in Figs. 5 and 6.

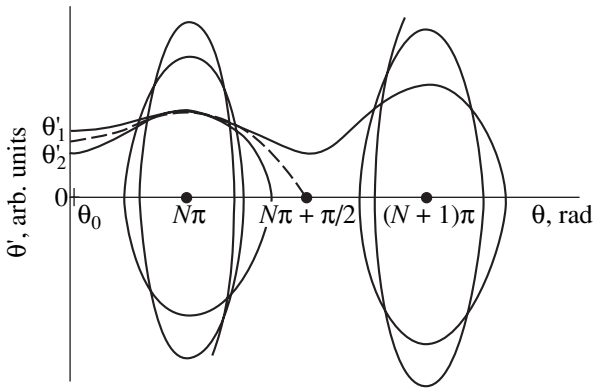

Fig. 4. Phase diagrams of solutions illustrating the shooting method.

Using the obtained numerical solutions, one can analyze the influence of anisotropy on the target structure. Note that in traditional magnetooptical experiments, for a wide class of magnets, the scale for identification of the spatial magnetic structure does not exceed the typical magnetic length l_0. Therefore, we shall further only discuss the target structure at $r > l_0$ and determine the N value involved in Eq. (24) as

$$N = \left[\frac{\theta(\infty) - \theta(l_0) - \pi/2}{\pi}\right], \tag{32}$$

where $[x]$ denotes the integer part of the variable x. To estimate the magnetization at $r < l_0$, it is helpful to find the average value $\overline{M}_z = 2M_0 \int_0^{l_0} \cos\theta r dr / l_0^2$ in the region $r < l_0$. It appears that the sign of $\overline{M}_z$ coincides with the sign of M_z in the preceding ring with respect to the ring where the $\theta(l_0)$ is found. In Fig. 7, we present the dependence of the ring width d_n on the ring index n for a target consisting of $N = 15$ rings. Here and further, the rings are numbered starting from the distance $r = l_0$. A domain is determined as a region wherein $|M_z| > 0.7M_0$. To estimate the localization of the singular vortex, it is helpful to present the dependence of the radius of the last ring R_l on the parameter k (Fig. 8). As can be seen, the vortex localization region decreases in size with

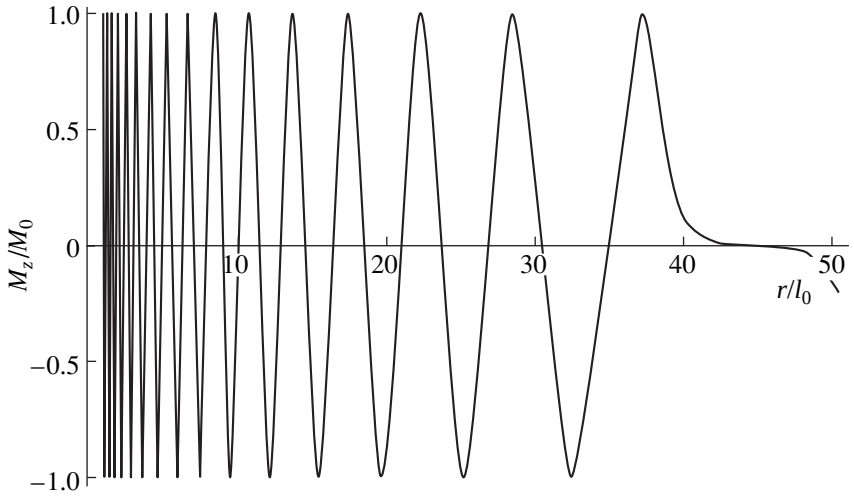

Fig. 5. Graph of a target-type solution with fifteen rings in dimensionless coordinates (r/l_0).

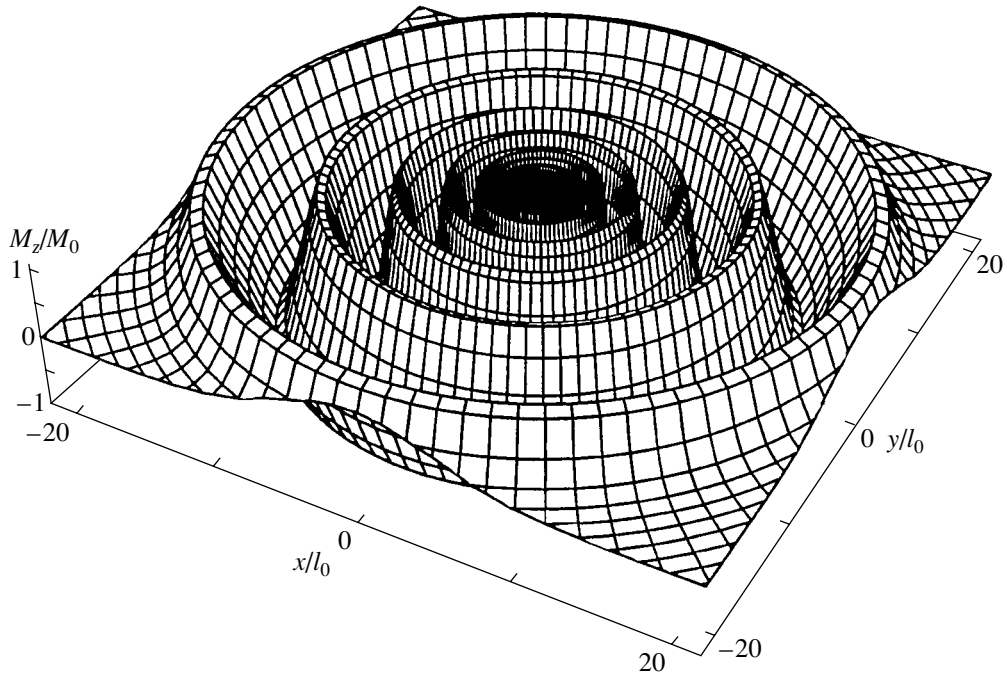

Fig. 6. Graph of a target-type solution with fifteen rings on a plane for the dimensionless magnetization $M_z(x/l_0, y/l_0)/M_0$.

increasing k and coincides with the localization region of the regular vortex at $k \longrightarrow 1$. A numerical calculation also shows that, for $1 < N < 15$, excluding the two outer rings, the domain width is described by formula (30), which is valid only in the exchange approximation. This dependence is indicated in Fig. 7 by a solid line. A similar formula is also valid for the domain-wall width. Thus, the anisotropy results in the widening of several outer domains and in infinite spreading of the last domain.

4.2. Target-Type Structure in Easy-Plane Magnets with Anisotropic Exchange

In the presence of exchange anisotropy, the solution to integral equation (27) is expressed in terms of an

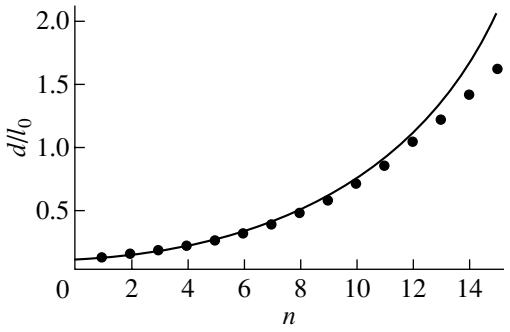

Fig. 7. Dependence of the dimensionless ring width on the ring index for a solution with fifteen rings. The solid curve is approximation (30).

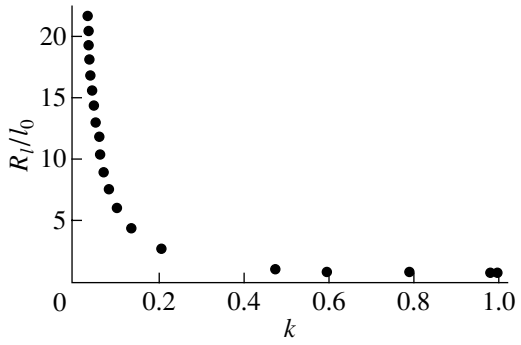

Fig. 8. Dimensionless radius of the last ring R_l/l_0 as a function of the parameter k.

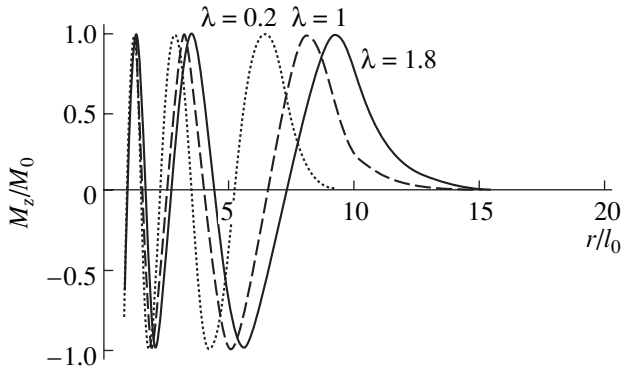

Fig. 9. Profiles $M_z(r)$ of a target for different values of λ in normalized variables.

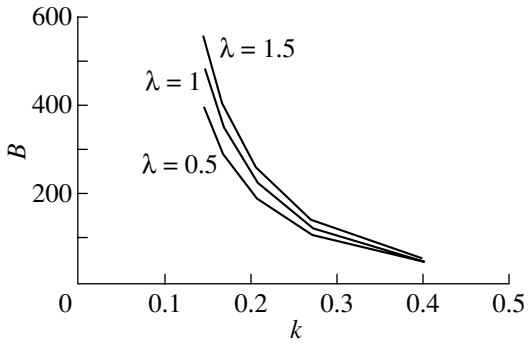

Fig. 10. Dependence of $\ln B(\lambda, k)$ on k for different values of λ.

incomplete elliptic integral of the third kind. Therefore, the asymptotic behavior of the singular vortex at $r \longrightarrow 0$ cannot be described analytically. Solutions (27) are periodic in R space, with the period

$$T(k, \lambda) = 4k \int_0^{\pi/2} \frac{\sqrt{\cos^2\theta + \lambda \sin^2\theta}\, d\theta}{\sqrt{1 - k^2 \cos^2\theta}}, \qquad (33)$$

which is a monotonical increasing function of both the parameter k and the anisotropy exchange parameter λ One can easily show that at $\lambda = 0$, there are no bounded solutions for M_z with a singular derivative. For the other λ values, the magnetic target structure does not differ qualitatively from the case of $\lambda = 1$. In Fig. 9, we display M_z component profiles obtained through numerical integration of Eq. (25) using the shooting method. It is seen that with increasing λ (at a fixed k value), the singular-vortex localization region increases in size, which is in agreement with the asymptotic behavior (20).

Due to the target singular behavior at small distances, its energy depends logarithmically on the cutoff radius r_0. This dependence can be found using the magnetization asymptotic behavior at $r \longrightarrow 0$ described by Eq. (27). In this approximation, the exchange interaction energy is expressed as an integral over the variable R of the periodic function

$$w = \frac{(1 - k^2 \cos(2\theta))\sqrt{\cos^2\theta + \lambda \sin^2\theta}}{k\sqrt{1 - k^2 \cos^2\theta}} \qquad (34)$$

with period $T(\lambda, k)$. The integral of w over a large number of periods can be approximately represented as the product of w averaged over a period

$$I(\lambda, k) = \frac{4 \int_0^{\pi/2} w\, d\theta}{T(\lambda, k)} \qquad (35)$$

using the length of the interval of integration. Therefore, one might expect the singular vortex energy to contain the term

$$E_s = 2\pi\alpha I(\lambda, k) \ln\left(\frac{l_0}{r_0}\right). \qquad (36)$$

Indeed, numerical simulations show that the energy of a magnetic target with anisotropic exchange E_{targ} consists of two terms,

$$E_{\text{targ}} = 2\pi\alpha \ln\left(B(\lambda, k)\frac{L}{l_0}\right) + E_s. \quad (37)$$

The term proportional to $\ln L$ is due to the magnetization asymptotic behavior at infinity. The dependence of $\ln B(\lambda, k)$ on k is presented in Fig. 10 for different λ values. As one might expect, the energy of a magnetic target increases monotonically with parameter λ, because $I'(\lambda) > 0$ and $B'(\lambda) > 0$ for $0 < \lambda < \infty$.

5. CONCLUSIONS

Thus, we have considered various vortex configurations in a 2D ferromagnet with allowance for single-ion and two-ion anisotropy (anisotropic exchange). In an easy-axis ferromagnet ($\varepsilon = -1$), there are no localized vortex structures that are regular at the origin of coordinates and approach the ground state at infinity. For an easy-plane ferromagnet, the behavior of the z component of magnetization in the vortex at large distances from the center is exponential, $M_z \propto \exp(-r/r_c)/\sqrt{r}$, with $r_v = l_0\sqrt{\lambda}$. Using the shooting method, we calculated the z-component of magnetization in the vortex at different values of the anisotropy parameters. The *OP*-vortex energy in an easy-plane ferromagnet ($\varepsilon = +1$) depends on both the effective magnetic length l_0 and the anisotropic exchange parameter λ and, consequently, on the relation between the contributions from single-ion and two-ion magnetic anisotropy. We predicted and analyzed the structure of a new class of vortex configurations, namely, a target of the leading-static-center type, in easy-plane magnets with isotropic and anisotropic exchange. The new solutions are singular, with the energy dependent logarithmically on the system size and on the effective magnetic length. In real magnets, vortices of the magnetic-target type will be formed on defects and can significantly contribute to the thermodynamics of the system. A consideration of the nucleation mechanism of the magnetic target [26] is of undeniable interest but is beyond the framework of the present work.

REFERENCES

1. *Nonlinearity in Condensed Matter*, Ed. by A. R. Bishop, R. Ecke, and S. Gubernatis (Springer, Berlin, 1993).
2. *Nonlinear Coherent Structures in Physics and Biology*, Ed. by K. H. Spatchek and F. G. Martens (Plenum, New York, 1994).
3. *Fluctuation Phenomena: Disorder and Nonlinearity*, Ed. by A. R. Bishop, S. Jiménez, and L. Vázquez (World Scientific, Singapore, 1995).
4. B. A. Ivanov and A. K. Kolezhuk, Fiz. Nizk. Temp. **21** (4), 355 (1995) [Low Temp. Phys. **21**, 275 (1995)].
5. A. M. Kosevich, B. A. Ivanov, and A. S. Kovalev, *Nonlinear Waves of Magnetization. Dynamic and Topological Solitons* (Naukova Dumka, Kiev, 1983).
6. M. E. Gouvea, G. M. Wysin, F. G. Mertens, and A. R. Bishop, Phys. Rev. B **39** (1), 1840 (1989).
7. T. Moriya, Phys. Rev. **120**, 91 (1960).
8. K. Yosida, J. Appl. Phys. **39**, 511 (1960).
9. A. S. Moskvin, I. G. Bostrem, and M. A. Sidorov, Zh. Éksp. Teor. Fiz. **104**, 2499 (1993) [JETP **77**, 127 (1993)].
10. A. A. Belavin and A. M. Polyakov, Pis'ma Zh. Éksp. Teor. Fiz. **22**, 503 (1975) [JETP Lett. **22**, 245 (1975)].
11. A. Hubert and A. Bogdanov, Phys. Status Solidi B **186**, 527 (1994).
12. S. A. Sonin, *Introduction to Physics of Liquid Crystals* (Nauka, Moscow, 1983).
13. A. Yu. Loskutov and A. S. Mikhaĭlov, *Introduction to the Synergetics* (Nauka, Moscow, 1990).
14. M. C. Cross and H. C. Hohenberg, Rev. Mod. Phys. **65**, 851 (1993).
15. H. Dötsch and H. J. Schmitt, Appl. Phys. Lett. **24**, 442 (1974).
16. H. Dötsch, AIP Conf. Proc. **29**, 78 (1976).
17. V. V. Randoshkin and V. V. Sigachev, in *Proceedings of the XVII All-Union Conference on Physics of Magnetic Phenomena, Donetsk State University, Donetsk, 1985*, p. 131.
18. A. P. Ges', V. V. Fedotova, A. K. Bogush, and T. A. Gorbachevskaya, Pis'ma Zh. Éksp. Teor. Fiz. **52**, 1079 (1990) [JETP Lett. **52**, 476 (1990)].
19. G. S. Kandaurova, Dokl. Akad. Nauk SSSR **308** (6), 1364 (1989) [Sov. Phys. Dokl. **34**, 918 (1989)].
20. G. S. Kandaurova, Dokl. Akad. Nauk **331** (4), 428 (1993) [Phys. Dokl. **38**, 342 (1993)].
21. G. S. Kandaurova, Fiz. Met. Metalloved. **79** (1), 158 (1995).
22. I. E. Dikshteĭn, F. V. Lisovskiĭ, U. G. Mansvetova, and E. S. Chizhik, Zh. Éksp. Teor. Fiz. **100**, 1606 (1991) [Sov. Phys. JETP **73**, 888 (1991)].
23. F. V. Lisovskiĭ, U. G. Mansvetova, E. P. Nikolaeva, and A. V. Nikolaev, Zh. Éksp. Teor. Fiz. **103**, 213 (1993) [JETP **76**, 116 (1993)].
24. V. N. Mal'tsev and N. M. Fakhrutdinov, Fiz. Met. Metalloved. **88** (1), 17 (1999).
25. A. F. Gal'tsev and Yu. I. Yalyshev, Fiz. Met. Metalloved. **85** (4), 5 (1998).
26. Yu. L. Gobov and G. A. Shmatov, Fiz. Met. Metalloved. **78** (1), 39 (1994).

Translated by N. Kovaleva

Physics of the Solid State, Vol. 44, No. 2, 2002, pp. 333–337. Translated from Fizika Tverdogo Tela, Vol. 44, No. 2, 2002, pp. 321–324.

MAGNETISM AND FERROELECTRICITY

Magnetic Birefringence of Light in Hematite

I. Sh. Akhmadullin, V. A. Golenishchev-Kutuzov, S. A. Migachev, and M. F. Sadykov

Kazan Physicotechnical Institute, Russian Academy of Sciences, Kazan, 420029 Tatarstan, Russia

e-mail: iakhm@kfti.knc.ru

Received January 10, 2001; in final form, July 2, 2001

Abstract—Peculiarities in the propagation of IR radiation in the easy-plane antiferromagnet α-Fe_2O_3 are investigated. In the geometry of the Cotton–Mouton effect, magnetic birefringence is measured and magnetooptical constants are estimated. © *2002 MAIK "Nauka/Interperiodica".*

1. INTRODUCTION

Easy-plane antiferromagnets of the hematite type are interesting due to their peculiar magnetoelastic (ME) and magnetooptical (MO) properties [1, 2]. In its own right, analysis of the ME and MO properties provides more comprehensive information on the magnetic structure, exchange interactions, and phase transitions in such systems. According to the results reported in a series of recent publications, these materials can be used, for example, for controlling optical and acoustic beams. The additional possibility of controlling the magnetic-field for such media [1] is of special importance. However, MO properties have not been studied comprehensively. This is due to the fact that the optical transparency region for hematite lies in the IR range ($\lambda > 1.2$ μm). This informational gap can be filled by obtaining accessible sources of monochromatic radiation in the IR region (semiconductor lasers).

Magnetic birefringence in hematite was discovered by Pisarev *et al.* [3], who established that this effect emerges above the Morin temperature $T_M \approx 260$ K. In subsequent publications, magnetic birefringence induced by uniaxial mechanical stresses [4] and in the vicinity of the Morin temperature [5] was investigated. In those works, only the terms quadratic in the antiferromagnetism vector **L** were taken into account in the permittivity tensor ε_{ij} in Eq. (1) [6], while the terms linear in L and in the magnetic field H were disregarded. The effects of the linear and quadratic (in the magnetic field) contributions to ε_{ij} were considered in [7], where these terms were assumed to appear due to the dependence of magnetization M on the magnetic field H.

Linear magnetic birefringence in crystals that are not antiferromagnets is normally an effect quadratic in H or M [8]. In easy-plane antiferromagnets of the hematite type, which are characterized by the order parameters L and M ($M \ll L$) [6], the power expansion of the ε_{ij} tensor in these parameters contains terms of the form $L_iH_j \gg M_iH_j$ typical of antiferromagnets with D_{3d} symmetry [1, 2]. For this reason, one can expect, for example, a magnetic field dependence of the birefringence $\Delta n = \sqrt{\varepsilon} \propto \sqrt{LH}$ to be associated with the antiferromagnetic order parameter L. In view of such premises, a detailed analysis of the MO properties of hematite is essential for revealing peculiarities associated with the order parameter L. In our opinion, it is necessary to analyze the magnetic field dependence of Δn in order to find the actual parameters that determine the permittivity tensor for hematite in the presence of a magnetic field.

2. EXPERIMENTAL TECHNIQUE AND RESULTS OF MEASUREMENTS

A block diagram of the experimental setup is shown in Fig. 1. The source of IR radiation was a semiconductor laser of the ILPN-206-1 type ($\lambda = 1.35$ μm). The power supply made it possible to modulate radiation with a frequency of 512 Hz; the reference frequency from the power supply was fed to a synchronous V9-2 detector. The system of lenses forming the objective made it possible to obtain a light beam with a relatively plane wave front. Light was directed through a quartz plate, a polarizer, and a diaphragm to samples under

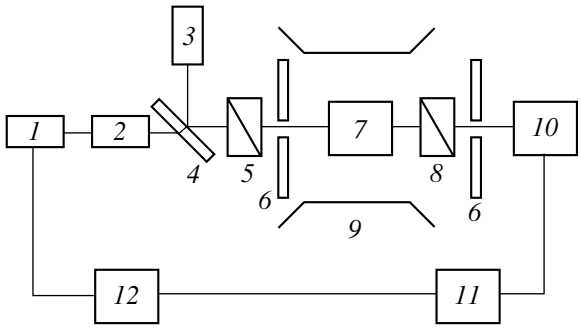

Fig. 1. Block diagram of the setup: (*1*) laser emitter, (*2*) objective, (*3*) He–Ne laser, (*4*) quartz plate, (*5*) polarizer, (*6*) iris diaphragm, (*7*) sample, (*8*) analyzer, (*9*) electromagnet, (*10*) photodetector, (*11*) synchronous detector, and (*12*) power supply of the semiconductor laser.

1063-7834/02/4402-0333$22.00 © 2002 MAIK "Nauka/Interperiodica"

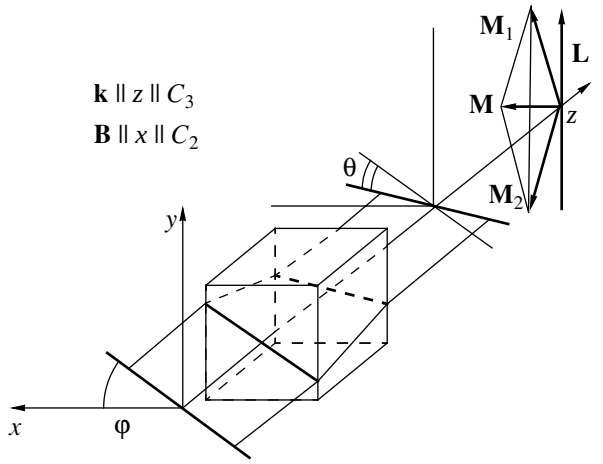

Fig. 2. Experimental geometry: φ is the angle between the polarization plane of incident light and the direction of the magnetic induction vector **B**, θ is the angle of rotation of the polarization plane of emerging light relative to the polarization plane of incident light, and $\mathbf{M}_1$ and $\mathbf{M}_2$ are the magnetizations of the sublattices.

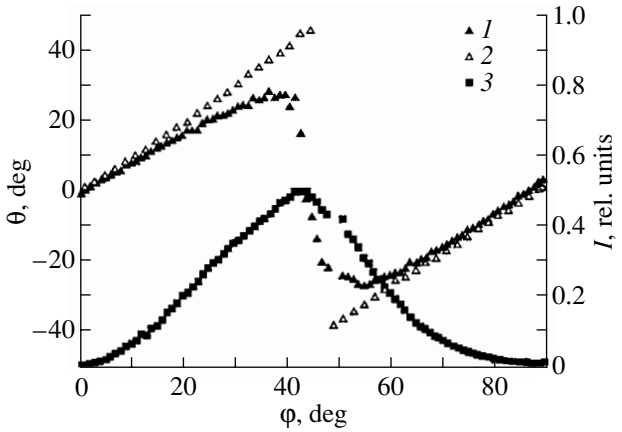

Fig. 3. Dependence of the angle of rotation θ on the angle φ between the polarization plane of incident light and the direction of the induction vector of the constant external magnetic field for air gaps in a magnet (*1*) 50 and (*2*) 13 mm wide; symbols *3* correspond to the relative intensity of light at the input of the photodetector; $B = 0.71$ T.

investigation mounted in the gap of an electromagnet. Samples had antireflection coated faces with a deviation from parallelism of the order of 20″. The orientation of the crystallographic axes of the crystal was determined to within 0.3° using x-ray diffraction analysis. The sample length along the direction of light propagation was 0.057 or 0.62 cm. The size of a thinner sample was chosen such that the phase difference for light emerging from the sample was smaller than π/2. The sample orientation in the gap of the magnet was controlled with the help of an adjusting He–Ne laser, which allowed us to minimize the contribution to birefringence associated with the deviation from parallelism between the direction of light propagation and the optical axis of the crystal.

The light beam emerging from the sample passed through an analyzer and the second diaphragm to the input of a photodetector. The sensitive element of the detector was a single-element photoresistor with a cooling system and thermal stabilization on the basis of the Peltier effect. The detected signal was amplified by high-precision operational amplifiers of the K140UD17A type with a controllable gain factor up to 10^5 fed to a synchronous detector.

The magnetic field induction was varied from 0 to 2.1 T. The construction of the magnet allowed us to vary the width of the air gap and to control the position of the pole pieces to attain a higher uniformity of the magnetic field. The experiments were made with two values of the gap width (50 and 13 mm). In the former case, the magnetic field nonuniformity was characterized by a gradient of up to 3–4 mT/cm. In the latter case, the uniformity of the created magnetic field was much better, which was monitored with the help of an NMR meter of magnetic induction of the Sh1-1 type.

We analyzed the linearly polarized light transmitted along the axis $z \parallel C_3$. In our experiments, we registered the angle θ of rotation of the optical polarization plane at the sample exit as a function of angle φ between the polarization plane of incident light and the magnetic field direction (Fig. 2). (In the case of elliptical polarization of the emerging light, the difference φ – θ was determined by the angle between the semimajor axis of the ellipse and the magnetic field.) The wave vector **k** was parallel to the triad axis of the crystal. The external magnetic field **B** was directed along one of the binary axes. All measurements were made at room temperature ($T \sim 295$ K).

Figure 3 shows the dependences of the angle θ of rotation of the polarization plane on angle φ for a higher (curves *2*) and lower (curve *1*) uniformity of the magnetic field **B**. For a more uniform magnetic field, this dependence is almost linear in the intervals 0°–40° and 50°–90°; field nonuniformity violates the linearity of this dependence (Fig. 3). It should be noted that the polarization of emerging light in our experiments varies with angle φ: it is linear for φ = 0° and 90°, circular for φ = 45°, and elliptical for intermediate values. This is confirmed by the variation of the intensity of transmitted light from the minimum value for nearly complete absorption of linearly polarized light by crossed polarizers to the maximum value in the case of circularly polarized light at the sample exit (curve *3* in Fig. 3). Figure 4 shows the measured dependence of the angle of rotation θ on the magnitude of a highly uniform magnetic field for a fixed angle φ = 22.5° (curve *1*).

3. DISCUSSION

The ME and MO properties of easy-plane antiferromagnets in the ordered phase are determined by two

order parameters, viz., the total magnetization vector **M** and the antiferromagnetism vector **L** [6]:

$$\mathbf{M} = \mathbf{M}_1 + \mathbf{M}_2, \quad \mathbf{L} = \mathbf{M}_1 - \mathbf{M}_2,$$

where $\mathbf{M}_i$ is the magnetization of sublattices (i = 1, 2) in the noncollinear phase [1, 2].

Hematite has the $I^+3^+2^-$ structure, and the antiferromagnetism vector **L** above the Morin temperature ($T_M \approx 260$ K) lies in the easy-magnetization plane at right angles to the triad axis [1, 6]. The experimental geometry is such that the magnetic induction vector **B** also lies in the easy magnetization plane and $\mathbf{L} \perp \mathbf{B}$ if the field magnitude exceeds the threshold value $B_S \sim 0.15$ T at which the crystal acquires a monodomain structure. If we choose vector **B** along the x axis and vector **L** along the y axis in the easy plane, then the expansion of the permittivity tensor into a power series in the antiferromagnetism vector **L** to within L^2 terms can be presented in the form [1]

$$\begin{aligned}
\varepsilon_{xx} &= \varepsilon_\perp + \alpha_{14}BL + \alpha_{12}L^2,\\
\varepsilon_{yy} &= \varepsilon_\perp - \alpha_{15}BL + \alpha_{11}L^2,\\
\varepsilon_{zz} &= \varepsilon_\parallel + \alpha_{34}BL + \alpha_{31}L^2,\\
\varepsilon_{xy} &= (i\alpha_0 - \alpha_{18}L)B_z, \quad \varepsilon_{xz} = -\alpha_{68}LB_z,\\
\varepsilon_{yz} &= -i\alpha_1 B + i\alpha_2 L - \alpha_{61}L^2 - \alpha_{64}LB_z.
\end{aligned} \tag{1}$$

Here, $\varepsilon_\parallel$ and $\varepsilon_\perp$ are the dielectric constants along the triad axis (z axis) and perpendicular to it, respectively, in a zero magnetic field and α_{ij} and α_k are the MO constants. When deriving Eqs. (1), we assumed that the crystal is optically transparent, which imposes the self-conjugation condition on the permittivity tensor ε_{ij}: $\varepsilon_{ji} = \varepsilon_{ij}^*$. In Eqs. (1), the terms proportional to the spontaneous magnetization M_S are not written explicitly (they are obtained through the substitution $B \longrightarrow M$) but are taken into account in the renormalization of coefficients α_{ij} [1].

The dependence of off-diagonal terms of tensor ε_{ij} on the z component B_z of the magnetic induction is worth noting. For $B_z = 0$, we have $\varepsilon_{xy} = 0$ and light in the crystal is linearly polarized [2], in contrast to elliptical polarization for $B_z \neq 0$ [2].

In the above experimental geometry, when light propagates along axis $z \parallel C_3$, the normal modes have the form

$$n_{1,2}^2 = \frac{1}{2}[(\Omega_{xx} + \Omega_{yy}) \pm \sqrt{(\Omega_{xx} - \Omega_{yy})^2 + 4\Omega_{xy}^2}], \tag{2}$$

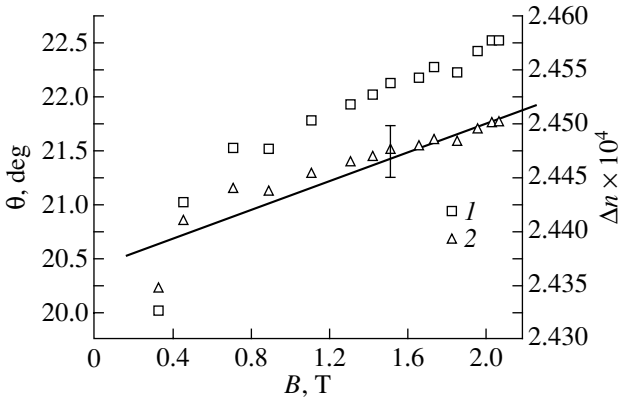

Fig. 4. Dependences of (*1*) the angle of rotation θ and (*2*) the magnetic-field-induced birefringence Δn for a fixed angle $\varphi = 22.5°$ on the magnitude of a highly uniform magnetic field. The solid line describes the approximation of the experimental results by the linear $\Delta n(B)$ dependence using the least squares technique.

$$\begin{pmatrix} E_x \\ E_y \end{pmatrix}_1 = \frac{1}{1+\alpha^2}\begin{pmatrix} |\alpha| \\ -\dfrac{|\alpha|}{\alpha^*} \end{pmatrix}\exp i(\omega t - k_1 z),$$

$$\begin{pmatrix} E_x \\ E_y \end{pmatrix}_2 = \frac{1}{1+\alpha^2}\begin{pmatrix} 1 \\ \alpha \end{pmatrix}\exp i(\omega t - k_2 z), \tag{3}$$

$$\alpha = \frac{2\Omega_{xy}}{2\Omega_{xx} - [(\Omega_{xx} + \Omega_{yy}) + \sqrt{(\Omega_{xx} - \Omega_{yy})^2 + 4\Omega_{xy}^2}]}, \tag{4}$$

where $\Omega_{xx} = \varepsilon_{xx} - \varepsilon_{xz}^2/\varepsilon_{zz}$, $\Omega_{yy} = \varepsilon_{yy} - \varepsilon_{yz}^2/\varepsilon_{zz}$, and $\Omega_{xy} = \varepsilon_{xy} - \varepsilon_{xz}\varepsilon_{yz}^*/\varepsilon_{zz}$; $n_{1,2}$ are the refractive indices; $k_i = n_i\omega/c$; ω is the frequency; and c is the velocity of light. In this case, the Jones matrix [2, 9] has the form

$$\begin{pmatrix} E_x \\ E_y \end{pmatrix}_{z=h} = \begin{pmatrix} \cos(\delta) - i\sin(\delta)\cos\chi & -i\sin(\delta)\sin\chi^* \\ -i\sin(\delta)\sin\chi & \cos(\delta) + i\sin(\delta)\cos\chi \end{pmatrix} \times \begin{pmatrix} E_x \\ E_y \end{pmatrix}_{z=0}, \tag{5}$$

where $\sin\chi = 2\alpha/(1+\alpha^2)$, $\cos\chi = (1-\alpha^2)/(1+\alpha^2)$, h is the crystal thickness, $2\delta = h(k_1 - k_2)$ is the phase difference between the normal modes in Eqs. (2) and (3), and $\alpha = \alpha' + i\alpha''$. It follows from Eqs. (1), (3), and (4) that the normal modes in Eq. (3) are linearly polarized for $B_z = 0$; otherwise, they are polarized elliptically.

If linearly polarized light with its polarization vector forming an angle φ with the magnetic induction vector

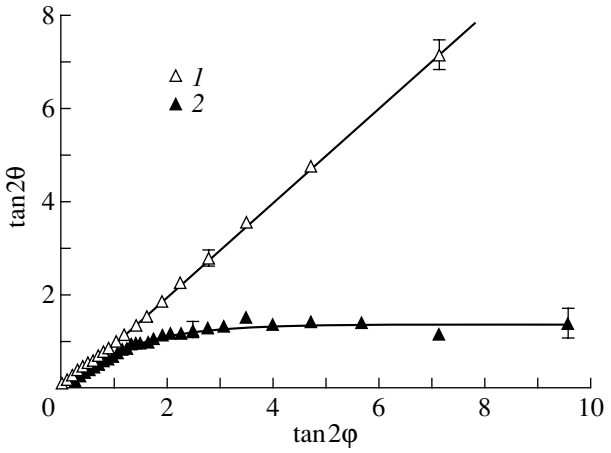

Fig. 5. Dependence of $\tan 2\theta$ on $\tan 2\varphi$ for (*1*) a uniform and (*2*) nonuniform magnetic field ($B = 0.71$ T).

is incident on the crystal along the z axis, we can find the angle θ of rotation of the polarization plane of emerging light from Eq. (5):

$$\tan[2(\varphi - \theta)] = \frac{a + b\tan 2\varphi}{c + d\tan 2\varphi}, \qquad (6)$$

where

$$a = \sin\chi''\sin 2\delta + 2\sin\chi'\cos\chi\sin^2\delta,$$

$$b = \cos^2\delta + \sin^2\delta(\sin^2\chi' - \sin^2\chi'' - \cos^2\chi),$$

$$c = \cos^2 x + \sin^2\chi\cos 2\delta,$$

$$d = 2\sin\chi'\cos\chi\sin^2\delta - \sin\chi''\sin 2\delta.$$

If $\alpha' = 0$, $\varphi = 0$, and $\sin\chi'' \ll 1$, then expression (6) is transformed into the formula given in [2]. Let us consider the following two cases.

(a) **Linear polarization** ($B_z = 0$). In this case, $\alpha = 0$; i.e., normal modes in Eq. (3) are linearly polarized and we obtain, instead of Eq. (6), the following expression for the angle θ of rotation of the polarization plane:

$$\tan[2(\varphi - \theta)] = \cos 2\delta\tan 2\varphi, \qquad (7)$$

$$2\delta \cong \frac{\pi h}{\lambda n_0}[(\alpha_{12} - \alpha_{11})L^2 + (\alpha_{14} + \alpha_{15})LB], \qquad (8)$$

$$n_0 = \sqrt{\varepsilon_\perp} = 2.84.$$

Expression (7) coincides with the expression derived in [10] and correctly describes the dependence presented in Fig. 5 (curve *1*). It should be noted that the dependence of the angle of rotation of the polarization plane on the magnetic field in the easy plane is determined only by the phase difference given by Eqs. (8). The phase difference is $2\delta = 2\pi h(n_1 - n_2)/\lambda$; it follows hence from Eq. (7) that the dependence of birefringence Δn on the magnetic field B can be represented in the form

$$\Delta n = \frac{\lambda}{2\pi h}\arccos\left[\frac{\tan 2(\varphi - \theta)}{\tan 2\varphi}\right] + \frac{\lambda}{h}, \qquad (9)$$

where the term λ/h takes into account the additional phase shift of 2π emerging in the thick sample as compared to the thin sample.

Our experimental results are presented in Fig. 4 (curve *2*), demonstrating the measured magnetic-field dependence of the birefringence Δn induced by a highly uniform magnetic field for a fixed angle $\varphi = 22.5°$. The solid line in this figure presents the results of fitting of the experimental results on birefringence using the least squares technique. This allowed us to determine the values of the constants appearing in formula (8):

$$(\alpha_{12} - \alpha_{11})L^2 \approx 3.1 \times 10^{-4},$$

$$(\alpha_{14} + \alpha_{15})L \approx 8.35 \times 10^{-10}\mathrm{T}^{-1}.$$

Substituting the value of L equal to 0.1740 T (from [11]) into this formula, we obtain

$$\alpha_{12} - \alpha_{11} \approx 1.02 \times 10^{-2}\mathrm{T}^{-2},$$

$$\alpha_{14} + \alpha_{15} \approx 4.8 \times 10^{-9}\mathrm{T}^{-2}.$$

In a magnetic field $B < B_S$, the monodomain structure of the crystal becomes damaged. Although the antiferromagnetism vector within each domain differs from zero, the resultant vector $\mathbf{L} \longrightarrow 0$ and, hence, the phase difference 2δ also vanish. In addition, for the magnetic fields used in our experiments, the magnitude of the antiferromagnetism vector is independent of field B, because the value of L is determined by the exchange fields B_E (which are of the order of 10^3 T). The terms proportional to magnetization M,

$$M = \frac{M_S + \chi B}{1 + 4\pi\chi},$$

(where $\chi \ll 1$ is the magnetic susceptibility and $M_S < L$ is the spontaneous magnetization of a crystal with a monodomain structure) make a small contribution to the renormalization of parameters a_{ij} [1, p. 57] by virtue of the above inequalities.

(b) **Elliptical polarization** ($B_z \neq 0$). In this case, as follows from Eq. (1), we have $\varepsilon_{xy} \neq 0$ (i.e., $\alpha \neq 0$) and the normal modes in Eq. (3) are elliptically polarized. For this reason, we are dealing in this case with elliptical birefringence and rotation of the polarization plane. The dependence of the angle of rotation of the polarization plane on angle φ is given by the general expression of (6). It can be seen from Eq. (6) that the dependence of $\tan[2(\varphi - \theta)]$ on $\tan 2\varphi$ is nonlinear. This nonlinearity appears due to the nonzero factor d being proportional to $\varepsilon_{xy} \sim B_z$. In contrast to case (a), the dependence of the angle of rotation of the polarization plane on the

magnetic field in the easy plane is determined not only by the phase difference but also by the dependence of ε_{xy} on the z component B_z of the magnetic field. The experimental results are presented in Fig. 5 (curve *2*). The solid curve presents the results of fitting experimental data with formula (6) using the least squares technique for $B_z = 5.5$ mT. In the present case, this value apparently characterizes the magnetic-field nonuniformity in the bulk of the sample.

REFERENCES

1. E. A. Turov, *Kinetic, Optical, and Acoustical Properties of Antiferromagnets* (Ural. Otd. Akad. Nauk SSSR, Sverdlovsk, 1990).
2. G. A. Smolenskiĭ, R. V. Pisarev, and I. G. Siniĭ, Usp. Fiz. Nauk **116** (2), 231 (1975) [Sov. Phys. Usp. **18**, 410 (1975)].
3. R. V. Pisarev, I. G. Siniĭ, and G. A. Smolenskiĭ, Pis'ma Zh. Éksp. Teor. Fiz. **9**, 294 (1969) [JETP Lett. **9**, 172 (1969)].
4. V. S. Merkulov, E. G. Rudashevskiĭ, H. Le Gall, and C. Leycuras, Zh. Éksp. Teor. Fiz. **75** (2), 628 (1978) [Sov. Phys. JETP **48**, 316 (1978)].
5. V. S. Merkulov, E. G. Rudashevskiĭ, H. Le Gall, and C. Leycuras, Zh. Éksp. Teor. Fiz. **80** (1), 161 (1981) [Sov. Phys. JETP **53**, 81 (1981)].
6. I. M. Dzyaloshinskiĭ, Zh. Éksp. Teor. Fiz. **32** (6), 1547 (1957) [Sov. Phys. JETP **5**, 1259 (1957)].
7. V. S. Merkulov, Kristallografiya **28** (3), 421 (1983) [Sov. Phys. Crystallogr. **28**, 249 (1983)].
8. E. A. Turov, Zh. Éksp. Teor. Fiz. **92** (5), 1886 (1987) [Sov. Phys. JETP **65**, 1060 (1987)].
9. Yu. M. Fedorov, A. A. Leksikov, and A. E. Aksenov, Fiz. Tverd. Tela (Leningrad) **26** (1), 220 (1984) [Sov. Phys. Solid State **26**, 128 (1984)].
10. M. Born and E. Wolf, *Principles of Optics* (Pergamon, Oxford, 1969; Nauka, Moscow, 1973).
11. E. A. Turov, Zh. Éksp. Teor. Fiz. **98** (2), 655 (1990) [Sov. Phys. JETP **71**, 365 (1990)].

Translated by N. Wadhwa

Physics of the Solid State, Vol. 44, No. 2, 2002, pp. 338–344. Translated from Fizika Tverdogo Tela, Vol. 44, No. 2, 2002, pp. 325–331.

MAGNETISM AND FERROELECTRICITY

Domain-Wall Mechanism of Nucleation in a Magnetic Structural Phase Transition in La_2CuO_4

M. A. Shamsutdinov* and V. N. Nazarov**

**Bashkortostan State University, ul. Frunze 32, Ufa, Bashkortostan, 450074 Russia*

***Institute of Molecular and Crystal Physics, Russian Academy of Sciences, Ufa, Bashkortostan, 450075 Russia*

Received April 5, 2001; in final form, July 9, 2001

Abstract—The structure of domain walls and new-phase nucleation are investigated in a four-sublattice antiferromagnet (AFM) of the La_2CuO_4 type placed in a magnetic field which initiates an AFM–weak-ferromagnet (WFM) magnetic structural phase transition. The critical fields for nucleus growth are found in the case of two types of domain walls present. The magnetization curve is calculated and a two-step mechanism is proposed for the AFM–WFM phase transition observed in La_2CuO_4. *© 2002 MAIK "Nauka/Interperiodica".*

1. INTRODUCTION

In the last decade, four- (and more) sublattice antiferromagnets have attracted the attention of investigators. Among such antiferromagnets is La_2CuO_4, belonging to space group D_{2h}^{18}. In La_2CuO_4, three types of antiferromagnetic (AFM) structures can exist: $(I^+2_x^+2_y^-\tau^-)$ with the antiferromagnetism vector $\mathbf{L}_1 = \mathbf{M}_1 - \mathbf{M}_2 - \mathbf{M}_3 + \mathbf{M}_4$, $(I^+2_x^+2_y^-\tau^+)$ with $\mathbf{L}_2 = \mathbf{M}_1 - \mathbf{M}_2 + \mathbf{M}_3 - \mathbf{M}_4$, and $(I^+2_x^+2_y^+\tau^-)$ with $\mathbf{L}_3 = \mathbf{M}_1 + \mathbf{M}_2 - \mathbf{M}_3 - \mathbf{M}_4$, where $\mathbf{M}_i$ (i = 1–4) are the sublattice magnetizations [1–4]. The antiferromagnet La_2CuO_4 consists of alternating Cu–O layers, each of which contains two nearly collinear magnetic sublattices. The interaction between the sublattices of adjacent Cu–O layers is weaker than that between the sublattices of the same layer. The magnetic properties of La_2CuO_4 can be described in terms of the ferromagnetism ($\mathbf{m}_j$) and antiferromagnetism ($\mathbf{l}_j$) vectors of adjacent layers (j = 1, 2) [5]: $\mathbf{m}_{1,2} = (\mathbf{M}_{1,3} + \mathbf{M}_{2,4})/2M_0$ and $\mathbf{l}_{1,2} = (\mathbf{M}_{1,3} - \mathbf{M}_{2,4})/2M_0$, where M_0 is the saturation magnetization of the magnetic sublattices. The vectors $\mathbf{l}_1$ and $\mathbf{l}_2$ are parallel to the Cu–O layers, while the vectors $\mathbf{m}_1$ and $\mathbf{m}_2$ are normal to these layers. In the structure with $\mathbf{L}_1$, the vectors $\mathbf{m}_1$ and $\mathbf{m}_2$ are nonzero (because of the intralayer Dzyaloshinskiĭ interaction) and antiparallel to each other. The resultant ferromagnetism vector $\mathbf{m} = \mathbf{m}_1 + \mathbf{m}_2$ is zero in the absence of an external magnetic field (pure AFM state [2]). In the structure with $\mathbf{L}_2$, the vectors $\mathbf{m}_1$ and $\mathbf{m}_2$ are parallel and the resultant ferromagnetism vector $\mathbf{m}$ is nonzero, which corresponds to a weakly ferromagnetic (WFM) state. The transition between the AFM and WFM structures occurs in a magnetic field perpendicular to the Cu–O layers, i.e., directed along the $2y$ axis [1–3, 6]. Upon this transition, the direction of $\mathbf{m}_2$ is reversed, because the sublattice magnetizations $\mathbf{M}_3$ and $\mathbf{M}_4$ reverse their directions. Symmetry analysis reveals [3] that this transition is the $I^+2_x^+2_y^-\tau^- \longrightarrow I^+2_x^+2_y^-\tau^+$ magnetic structural phase transition. According to the conductivity measurements in an increasing magnetic field, this transition occurs in two steps. The reason for such behavior of the conductivity as a function of magnetic field cannot be explained in terms of the modern theory of first-order phase transitions [7].

In our previous paper [8], we investigated the structure and steady-state dynamics of the interphase boundary separating the AFM and WFM states (i.e., the $\mathbf{L}_1$ and $\mathbf{L}_2$ states) in La_2CuO_4. It is well known [9–11] that, in two-sublattice antiferromagnets, the interphase boundaries separating the AFM and WFM states are 90° walls and their formation involves rotation of the magnetizations of all magnetic sublattices. Such an interphase boundary can arise as a result of dissociation of an AFM 180° wall into two 90° walls. In La_2CuO_4, the interphase boundary separating the AFM and WFM states is formed through a 180° rotation of the magnetizations of only two of the four magnetic sublattices. However, the mechanisms of formation of a nucleus of the new magnetic phase and of the interphase boundary in four-sublattice antiferromagnets of the La_2CuO_4 type during the magnetic structural phase transition remain unclear.

The objective of this paper is to investigate the domain-wall (DW) mechanism of new-phase nucleation in a four-sublattice antiferromagnet placed in a magnetic field $\mathbf{H}$ initiating the magnetic structural phase transition. We also analyze the features of the magnetization curve in the case where there are two types of nuclei and explain the two-step character of the $I^+2_x^+2_y^-\tau^- \longrightarrow I^+2_x^+2_y^-\tau^+$ magnetic structural phase transition in an increasing magnetic field.

1063-7834/02/4402-0338$22.00 © 2002 MAIK "Nauka/Interperiodica"

2. THE STRUCTURE OF A DOMAIN WALL IN A WEAK MAGNETIC FIELD $\mathbf{H} \parallel 2_y$

We start from the free-energy density [12] written in a coordinate frame with axes $y \parallel 2_y$ and $x \parallel 2_x$ (see [3, Fig. 23]):

$$W = 2M_0\Bigg\{\sum_{j=1}^{2}\Big(\frac{1}{2}H_e\mathbf{m}_j^2 + H_D[\mathbf{m}_j\mathbf{l}_j]_z + \frac{1}{2}(H_{AY}l_{jy}^2 - H_{AX}l_{jx}^2) - \mathbf{H}\mathbf{m}_j + \frac{1}{4}\alpha M_0(\partial l_j/\partial x_i)^2\Big) + h_e l_1 l_2 - h_a(l_{1z}l_{2z} - l_{1x}l_{2x}) + H_D'(m_{1z}l_{2y} - m_{1y}l_{2z} + m_{2z}l_{1y} - m_{2y}l_{1z})\Bigg\}, \quad (1)$$

where H_e and h_e characterize the intra- and interlayer interactions, respectively; H_D and H_D' characterize the intra- and interlayer Dzyaloshinskiĭ interactions, respectively; α is the exchange stiffness parameter; H_{AY} and H_{AX} are the tetragonal and orthorhombic anisotropy fields, respectively; h_a is the interlayer anisotropy field; and $\mathbf{H}$ is an external magnetic field.

The ground state can be found by minimizing the energy in Eq. (1), which gives the following two possible AFM structures:

$$I^+2_x^+2_y^-\tau^-,\ \mathbf{l}_2 \uparrow\downarrow \mathbf{l}_1 \uparrow\uparrow x,$$
$$H \le H_1 = H_D + H_D' + H_e(H_{AX} + h_e + h_a)/(H_D + H_D') \quad (2a)$$
$$I^+2_x^+2_y^-\tau^+,\ \mathbf{l}_2 \uparrow\uparrow \mathbf{l}_1 \uparrow\uparrow x,$$
$$H \ge H_1 = -((H_D - H_D')^2 + H_e(H_{AX} - h_e - h_a))/(H_D + H_D'). \quad (2b)$$

The first structure corresponds to the AFM state with $\mathbf{L}_1$; the second structure, to the WFM state with $\mathbf{L}_2$. The stability regions of the WFM and AFM phases overlap. The transition between these phases occurs abruptly (first-order phase transition) when the external field becomes equal to $H = H_\tau$, where

$$H_\tau = [H_e(h_e + h_a) + 2H_DH_D']/(H_D + H_D'),$$

which is determined by the equality of the energies of the two phases. According to [2], $H_\tau \approx 30$ kOe. In oxygen-enriched La_2CuO_4 crystals, the phase-transition field decreases, $H_\tau \longrightarrow 0$ [13, 14].

Four types of AFM domain walls can exist in La_2CuO_4 [5]. Two of them are formed through a rotation of the vectors $\mathbf{l}_1$ and $\mathbf{l}_2$ in the Cu–O plane, while in the other two, these vectors deviate from the Cu–O plane. It was shown in [15] that the latter two types can occur only in strong external magnetic fields directed along the z axis. In this paper, we consider much lower fields directed along the $2y$ axis; therefore, only the case of antiferromagnetism vectors rotated in the Cu–O planes is discussed.

Let θ_1 and θ_2 be the deviation angles of the vectors $\mathbf{l}_1$ and $\mathbf{l}_2$ from their directions in the ground state, respectively: $\mathbf{l}_j = (-1)^{j+1}(\cos\theta_j,\ 0,\ \sin\theta_j)$. Then, the Euler equations which determine the minimum of the energy in Eq. (1) have the form

$$\beta_2\frac{d^2\theta_+}{d\xi^2} - \beta_2\sin\theta_+\cos\theta_- + (\delta_1 - \delta_2)\sin\theta_+ - 2h\sin\Big(\frac{\theta_-}{2}\Big)\cos\Big(\frac{\theta_+}{2}\Big) = 0,$$
$$\beta_2\frac{d^2\theta_-}{d\xi^2} - \beta_2\sin\theta_-\cos\theta_+ - (\delta_1 + \delta_2)\sin\theta_- - 2h\sin\Big(\frac{\theta_+}{2}\Big)\cos\Big(\frac{\theta_-}{2}\Big) = 0, \quad (3)$$

where $\theta_\pm = \theta_1 \pm \theta_2$, $\xi = z\sqrt{\beta_2/\alpha}$, $\beta_2 = 2[H_{AX} + (H_D^2 + H_D'^2)/H_e]/M_0$, $\delta_1 = 2(h_e - h_a)/M_0$, $\delta_2 = 2(h_e + h_a + 2H_DH_D'/H_e)/M_0$, and $h = 2(H_D + H_D')H/H_eM_0$.

We consider the case where the antiferromagnetism vectors rotate in the Cu–O plane in such a way that, in a zero field, they always remain antiparallel to each other (A-DW [5]). In low fields $h \ll (\delta_1, \delta_2) \ll \beta_2$, the angles θ_1 and θ_2 can be written as

$$\theta_1 = \theta_0 + \vartheta_1 + \psi_1 + \dots, \quad \theta_2 = \theta_0 - \vartheta_2 - \psi_2 + \dots. \quad (4)$$

Here, the zeroth terms correspond to the rotation of the antiferromagnetism vectors in the DW in the absence of interlayer interactions and of an external magnetic field and satisfy the equation

$$\frac{d^2\theta_0}{d\xi^2} - \sin\theta_0\cos\theta_0 = 0. \quad (5)$$

A solution to this equation subject to the boundary conditions $\theta_0(\xi \longrightarrow -\infty) = 0$, $\theta_0(\xi \longrightarrow \infty) = \pi$, and $d\theta_0/d\xi = 0$ has the form

$$\sin\theta_0 = 1/\cosh\xi. \quad (6)$$

The equations for the first-order corrections are

$$\hat{L}(\vartheta_1 - \vartheta_2) = 2\frac{\delta_2 - \delta_1}{\beta_2}\frac{\tanh\xi}{\cosh\xi}, \quad \hat{L}(\vartheta_1 + \vartheta_2) = 0, \quad (7)$$

where $\hat{L} = -d^2/d\xi^2 + 1 - 2\cosh^2\xi$.

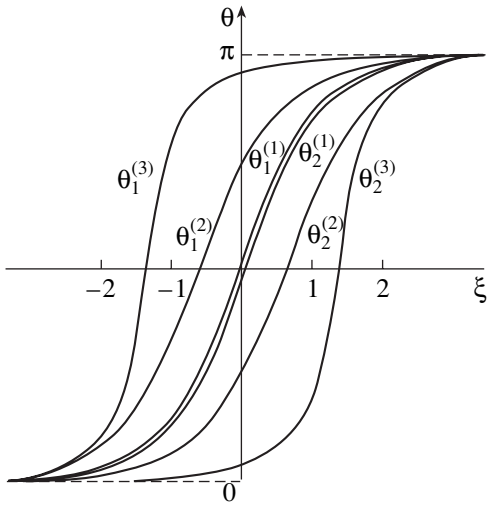

Fig. 1. Coordinate dependence of θ_1 and θ_2 for $H = 0.1H_\tau$ [curves $\theta_1^{(1)}$, $\theta_2^{(1)}$], $0.9H_\tau$ [$\theta_1^{(2)}$, $\theta_2^{(2)}$], and $0.99H_\tau$ [$\theta_1^{(3)}$, $\theta_2^{(3)}$].

A solution to the first equation of set (7) describes distortions of the structure given by Eq. (6) that are due to interlayer interactions; this solution has the form

$$\vartheta_1 - \vartheta_2 = \frac{\delta_2 - \delta_1}{2\beta_2} \times \int_{-\infty}^{\infty} \frac{\exp(i\eta\xi)}{(1+\eta^2)\cosh\pi\eta/2}(\tanh\xi - i\eta)d\eta. \quad (8)$$

The second equation of set (7) has a solution

$$\vartheta_1 + \vartheta_2 = \frac{C}{\cosh\xi}, \quad (9)$$

where C is a constant. This solution describes the shift of the θ_1 and θ_2 distributions relative to each other. The constant C is found from the equation for the second-order corrections, which is written as

$$\hat{L}(\psi_1 + \psi_2) = -\left(2(\vartheta_2 - \vartheta_1)\frac{\tanh\xi}{\cosh\xi} + \frac{\delta_1 + \delta_2}{\beta_2}\right)\frac{C}{\cosh\xi} - \frac{h}{\beta_2}\frac{2}{\cosh\xi}. \quad (10)$$

This equation has a solution if

$$C = -\frac{3h}{\delta_1 + 2\delta_2}. \quad (11)$$

If the vectors $\mathbf{l}_1$ and $\mathbf{l}_2$ cease to be antiparallel when rotating in the domain wall (*E*-DW [5]), then the constant C, characterizing the shift of the centers of the θ_1 and θ_2 distributions relative to each other in a magnetic field, is given by Eq. (11) with $-\delta_1$ in place of δ_1.

Thus, in a zero magnetic field, the θ_1 and θ_2 distributions in the DW (i.e., the rotation of the sublattice magnetizations) are described by Eq. (6) as before. In an external magnetic field $\mathbf{H} \parallel 2_y$, adjacent Cu–O layers differ in energy, because at the DW center, the magnetization of one Cu–O layer is parallel to the external field while the magnetization of the other Cu–O layer is antiparallel. Therefore, the centers of the θ_1 and θ_2 distributions in adjacent Cu–O layers are shifted by C relative to each other. Figure 1 shows the dependences of the angles θ_1 and θ_2 on the coordinate as calculated numerically from Eqs. (3) for an *A*-DW.

3. THE DOMAIN-WALL STRUCTURE AND NUCLEATION IN MAGNETIC FIELDS IN THE VICINITY OF THE MAGNETIC STRUCTURAL TRANSITION

Now, we consider the mechanism of formation of an interphase boundary separating the AFM and WFM phases in a field $\mathbf{H} \parallel 2_y$. With allowance for the results obtained above, the θ_1 and θ_2 distributions are taken in the form

$$\sin\theta_1 = 1/\cosh\left(\frac{z}{\Delta} - \frac{q}{2}\right), \quad \sin\theta_2 = \pm 1/\cosh\left(\frac{z}{\Delta} + \frac{q}{2}\right), \quad (12)$$

where Δ and q are variational parameters. The parameter Δ is the characteristic scale of inhomogeneity and $q/2$ is the shift of the centers of the θ_1 and θ_2 distributions in the magnetic field. The upper sign corresponds to the case where the vectors $\mathbf{l}_1$ and $\mathbf{l}_2$ remain antiparallel to each other when rotating in the DW in the field $H = 0$ (*A*-DW), and the lower sign corresponds to the case where the antiparallelism is destroyed (*E*-DW). The DW energy as a function of q and Δ is

$$E_W = 2M_0^2\Delta\left(\beta_2 + \frac{\alpha}{\Delta^2} \mp \delta_1\frac{q}{\sinh q} + \delta_2 q\coth q - hq\right). \quad (13)$$

Minimizing the DW energy with respect to q and Δ gives the dependences of the DW energy and the effective DW thickness,

$$\Delta_{\text{eff}} = (\pi + q)\Delta, \quad (14)$$

on the external magnetic field. In low fields ($H \ll H_\tau$), the shift of the centers of the θ_1 and θ_2 distributions relative to each other is found to be

$$q = \frac{3h}{2\delta_2 \pm \delta_1}. \quad (15)$$

The quantity q is identical to the parameter C found in the preceding section [see Eq. (11)]. The DW energy

and the effective DW thickness (for $H \ll H_\tau$) are

$$E_W = 4M_0^2\sqrt{\alpha(\beta_2 \mp \delta_1 + \delta_2)} \times\left(1 - \frac{3h^2}{4(\beta_2 \mp \delta_1 + \delta_2)(\pm\delta_1 + 2\delta_2)}\right),$$

$$\Delta_{\text{eff}} = \left(\pi + \frac{3h}{2\delta_2 \pm \delta_1}\right)\sqrt{\frac{\alpha}{\beta_2 \mp \delta_1 + \delta_2}}.$$

Figure 2 shows the effective thickness and the energy of the *A*-DW and *E*-DW as functions of the external field over a wide range of *H* values. It is seen from Fig. 2a that as $H \longrightarrow H_n^{(A,E)}$, the DW thickness tends to infinity. This means that the AFM domain wall is split into two interphase boundaries in such fields.

As shown in [5], both DWs are stable at $H = 0$. The energy of the *E*-DW is higher than that of the *A*-DW. In a magnetic field, the difference in the energy of these DWs decreases. As the external magnetic field increases and approaches a critical value $H_n^{(E)}$, the *E*-DW energy tends to twice the interphase boundary energy [8]. The field $H_n^{(E)}$ corresponds to the formation of a nucleus of the WFM phase and is equal to H_τ, the field at which the first-order phase transition occurs between the AFM and WFM phases. In the case of the *A*-DW, the field at which a new-phase nucleus arises is equal to $H_n^{(A)} = 1.06H_\tau$. It is seen from Fig. 2 that in a narrow range $0 \le (H - H_\tau) \le 0.06H_\tau$, two different states of the *A*-DW with different thicknesses and energies correspond to one value of the magnetic field. (The dashed curves in Fig. 2 correspond to unstable states.)

Thus, the *E*-DW, which is metastable (at $\delta_1 > 0$), is split into two interphase boundaries when the external field becomes equal to the first-order phase transition field H_τ. The *A*-DW has a minimum energy and is split in an external field equal to $H_n^{(A)}$, which is only slightly higher than H_τ. It should be noted that in La_2CuO_4, the critical field $H_n^{(A)}$ is significantly lower than the field in which the AFM phase becomes unstable, $H_1 = 5.5H_\tau$. In actual practice, in fields close to H_τ, the fluctuation mechanism of the first-order phase transition can be partially blocked; the transition from the AFM to the WFM phase can also occur through the DW mechanism of nucleation in that case.

It is notable that at $\delta_1 > 0$ ($h_e > h_a$), the thickness of the DW (and, hence, the WFM-phase nucleus thickness) increases continuously in the case of the *E*-DW and discontinuously in the case of the *A*-DW (Fig. 2a). At $\delta_1 < 0$ ($h_e < h_a$), the situation is reversed. For this reason, the field dependences of the magnetization in the *A*-DW and *E*-DW are different (Fig. 3). It is seen from Fig. 3 that, in an external magnetic field, the magnetization becomes nonzero, with its maximum being at the

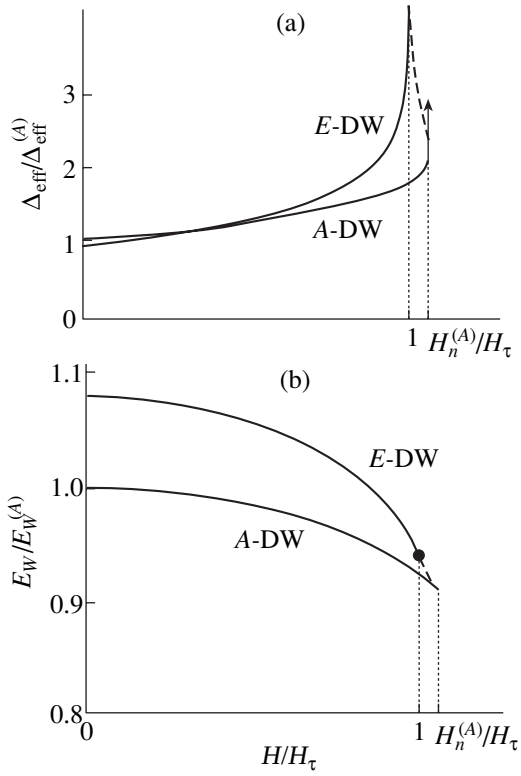

Fig. 2. Dependences of (a) the thickness and (b) energy of domain walls on the external magnetic field.

DW center; that is, the state with $\mathbf{L}_2$ arises. As the field is increased, the region where the magnetization has a maximum increases in size and, at a certain critical value H_n, occupies the entire volume of the sample. The magnetization process is continuous in the case of the *E*-DW and discontinuous in the case of the *A*-DW. The magnitude of the magnetization $M_y = 2M_0(m_{1y} + m_{2y})$ tends to the value

$$M_y^0 = M_S + \chi H \tag{16}$$

everywhere over the sample. Here, $M_S = 4M_0(H_D + H_D')/H_e$ is the WFM moment and $\chi = 4M_0/H_e$ is the AFM susceptibility.

Thus, DWs of both the *E*-DW and *A*-DW types can be considered as nuclei of a new, WFM phase with the vector $\mathbf{L}_2$ and structure $I^+2_x^+2_y^-\tau^+$ arising in the AFM phase with the vector $\mathbf{L}_1$ and structure $I^+2_x^+2_y^-\tau^-$. The WFM phase will grow in volume through the splitting of an AFM domain wall into two interphase boundaries and their moving farther apart [8].

4. THE MAGNETIZATION CURVE

The difference in the fields $H_n^{(A)}$ and $H_n^{(E)}$, at which interphase boundaries are formed in the case of *A*-DWs and *E*-DWs, respectively, can manifest itself in the

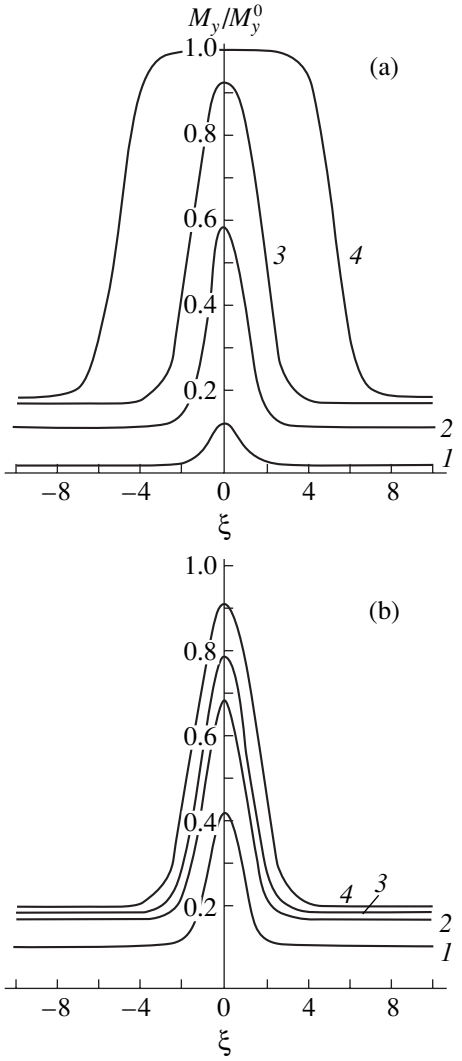

Fig. 3. Magnetization distribution in the central region of a DW for different values of the external field (a) for *E*-DW: $H = 0.1H_\tau$ (curve *1*), $0.55H_\tau$ (*2*), $0.9H_\tau$ (*3*), and $0.99H_\tau$ (*4*); and (b) for *A*-DW: $H = 0.1H_\tau$ (curve *1*), $0.5H_\tau$ (*2*), $0.9H_\tau$ (*3*), and $H_n^{(A)}$ (*4*).

shape of the magnetization curve. Let us find the dependence of the magnetization on the external magnetic field. Taking the average of the resultant magnetization over a magnetic-structure period, we find

$$\langle M_y^{(A,E)}\rangle = \frac{M_S}{2}\frac{\Delta}{D} \times \ln\frac{\coth D/\Delta\coth q/2+1}{\coth D/\Delta\coth q/2-1} + \chi H, \quad (17)$$

where D is the domain width. Figure 4 shows the field dependence of the average resultant magnetization,

$$\langle M_y\rangle = \Delta N_A\langle M_y^{(A)}\rangle + \Delta N_E\langle M_y^{(E)}\rangle,$$

where $\langle M_y^{(A)}\rangle$ and $\langle M_y^{(E)}\rangle$ are the average magnetizations in blocks containing *A*-DWs and *E*-DWs, respectively, and ΔN_A and ΔN_E are the volume fractions of these blocks. At $\delta_1 = 0$ ($h_a = h_e$), as seen from Fig. 4a, the growth of a nucleus of the WFM phase proceeds in one step in the field $H_n^{(A)} = H_n^{(E)} = H_n = H_\tau$. In this case, the *A*-DW and *E*-DW are identical and have the same energy. As the parameter δ_1 increases, the $H_n^{(A)}$ corresponding to the formation of a WFM-phase nucleus increases (Figs. 4b, 4c). For this reason, the sample is magnetized in two steps and the magnetization curve exhibits two jumps, the first of which occurs at $H_n^{(E)}$; the second, at $H_n^{(A)}$.

Figure 5 presents the magnetization curve calculated with allowance for the coercive force acting on the interphase boundary with the structure [8]

$$\theta_+ = \theta_0 + \vartheta_1 + \ldots, \quad \theta_- = -\theta_0 + \psi_1 + \ldots,$$

$$\sin\theta_0 = 1/\cosh((z+z_0)\sqrt{\beta_2(0)/\alpha}).$$

Here, ϑ_1, $\psi_1 \ll \theta_0$ and z_0 is the shift of the interphase boundary at equilibrium. For the sake of simplicity, the coercive force is assumed to be due to the inhomogeneous anisotropy constant β_2 taken to be

$$\beta_2 = \beta_2(0)\left(1 - \Delta\beta_2\cos\frac{2\pi}{d}z\right), \quad (18)$$

where d is the characteristic scale of inhomogeneity of the anisotropy constant. Interphase boundaries break away from defects when the field is equal to $H_c^{(E)}$ and $H_c^{(A)}$ given by

$$H_c^{(A,E)} = H_n^{(A,E)} + \sqrt{\alpha\beta_2(0)}\Delta\beta_2\frac{M_0H_e}{(H_D+H_D')}\frac{\pi\lambda}{d\sinh\lambda}, \quad (19)$$

where $\lambda = \pi^2/d\sqrt{\alpha/\beta_2(0)}$. It is seen from Eq. (19) that, as $\Delta\beta_2$ increases, the fields $H_c^{(E)}$ and $H_c^{(A)}$ become progressively higher in comparison with the phase transition field H_τ. In the presence of a coercive force, the magnetization in an increasing field also reaches saturation in two steps (Fig. 5). When the field is decreased and becomes equal to H_τ, corresponding to the first-order phase transition, the magnetization drops in a jump, because interphase boundaries arise at $H = H_\tau$ [8] and the AFM phase increases sharply in volume through their motion. The magnetization curve in Fig. 5 is calculated for $\Delta\beta_2 = 0.1$. Figure 5b corresponds to the interlayer interaction fields taken from [16]; for this case, $H_c^{(E)} = 1.14H_\tau$ and $H_c^{(A)} = 1.20H_\tau$. The magnetization curve in Fig. 5c is calculated for $\delta_1 = \delta_2$; in this case, $H_c^{(E)} = 1.14H_\tau$ and $H_c^{(A)} = 1.34H_\tau$. We note that

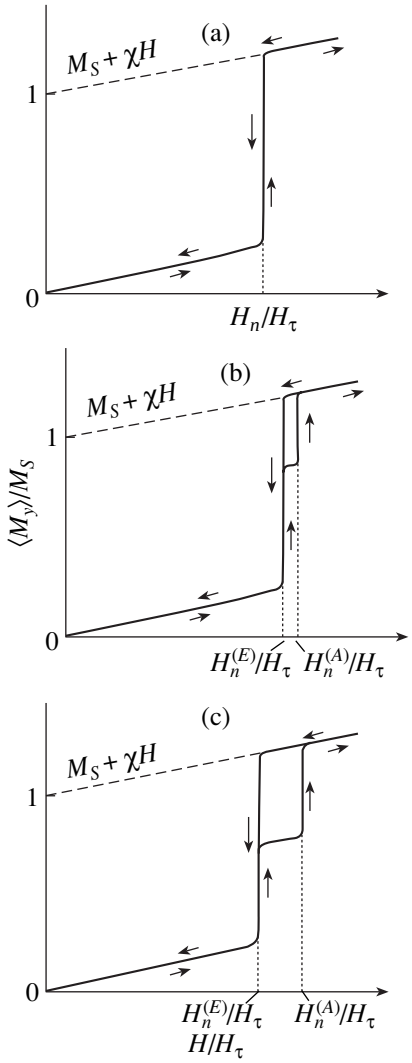

Fig. 4. Calculated magnetization curve in the absence of a coercive force: (a) $\delta_1 = 0$, (b) $\delta_1 \neq 0$ ($\delta_1 < \delta_2$), and (c) $\delta_1 = \delta_2$.

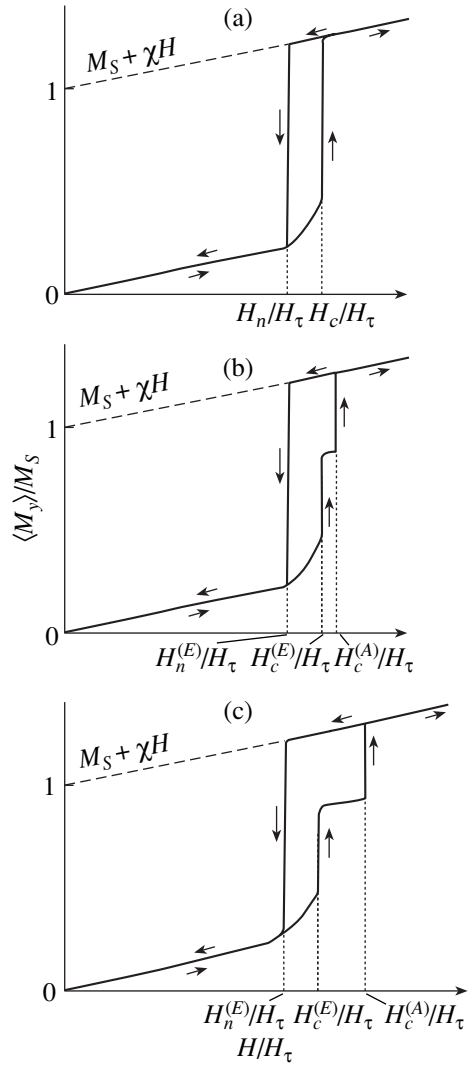

Fig. 5. Magnetization curve calculated with allowance for the coercive force for $\Delta\beta_2 = 0.1$ and the same values of δ_1 as in Fig. 4.

these results correspond to $h_e \geq h_a$. When $h_e < h_a$, the field $H_n^{(E)}$ required for a nucleus to arise is higher than $H_n^{(A)}$ and, therefore, the field $H_c^{(E)}$ corresponding to the break-away of an interphase boundary from defects is higher than $H_c^{(A)}$.

The magnetization curve calculated by us is similar in character to the experimental field dependence of the conductivity reported in [7], according to which the AFM–WFM phase transition proceeds in two steps in an increasing field and in one step in a decreasing field. Two hypotheses were proposed for explaining the fact that the observed AFM–WFM phase transition proceeds in two steps. One of them involved more complex magnetic structures, because the approach that was based on Eq. (1) for the energy failed to explain this fact. The other hypothesis was based on an inhomogeneous model according to which the phase transition occurs in successive jumps in two spatially separated parts of the sample. However, the assumption of the existence of such spatially separated regions was not substantiated in [7] in the framework of the well-known model of the magnetic structure of the compounds under study [2, 3, 12].

In constructing the magnetization curve, we assumed that a sample consists of a great number of regions of two types containing *A*-DWs and *E*-DWs, respectively. This assumption is justified, because the difference in the energy of these two types of DWs is small (less than 8% in the case of the parameters of La_2CuO_4 presented in [16]) and the stability regions of these DWs overlap [8]. In terms of the DW mechanism of formation of a WFM-phase nucleus considered above, the transition to the WFM state first occurs at

$H_c^{(E)}$ in the regions where *E*-DWs are dominant. When the field is increased to $H = H_c^{(A)}$, the transition to the WFM phase occurs in the remaining regions of the sample. In this model, the relative difference in the magnitude of the fields in which new-phase nuclei arise and interphase boundaries begin to break away from defects is equal to

$$\Delta h = \frac{H_c^{(A)} - H_c^{(E)}}{H_\tau} = \frac{H_n^{(A)} - H_n^{(E)}}{H_\tau}.$$

Here, Δh depends on the value of δ_1. For example, at $\delta_1 = \delta_2 \ll \beta_2$, we have $\Delta h \approx 0.2$. For the values of parameters corresponding to La_2CuO_4 [16] ($\delta_1 \neq \delta_2$), $\Delta h = 0.06$. According to experimental data on conductivity [7], the relative difference between the fields in which the AFM–WFM phase transition proceeds in two steps is $\Delta h \approx 0.2$ at $T = 77$ K. We see that the theory agrees with the experimental data.

5. CONCLUSIONS

Thus, the fact that the AFM–WFM phase transition proceeds in two steps [7] in an increasing field can be interpreted in terms of the model of the magnetic structure of lanthanum cuprate proposed earlier (see, e.g., [2, 3, 12]) if the new-phase nucleation is assumed to be governed by the domain-wall mechanism and if one takes into account that there are two types of stable DWs (*A*-DWs and *E*-DWs) with nearly equal energies.

Therefore, we can make the inference that, in a four-sublattice antiferromagnet, a magnetic structural phase transition in a magnetic field can proceed through the domain-wall mechanism of formation of new-phase nuclei and interphase boundaries. The DW mechanism of new-phase nucleation in a four-sublattice antiferromagnet of the La_2CuO_4 type differs essentially from that in two-sublattice antiferromagnets. The difference is in the fact that the magnetization of one pair of sublattices rotates in one half of the DW, while the magnetization of the other pair rotates in the other half of the DW. The WFM-phase nucleus that arises at the center of the AFM domain wall is characterized by the antiferromagnetism vector $\mathbf{L}_2$ and the structure $I^+2_x^+2_y^-\tau^+$. (Far from the DW, the AFM state is characterized by the antiferromagnetism vector $\mathbf{L}_1$ and the structure $I^+2_x^+2_y^-\tau^-$.) The critical fields for the formation of a WFM-phase nucleus are different for *E*-DWs and *A*-DWs, which is the reason for the two-step character of the AFM–WFM phase transition observed in the experiments.

ACKNOWLEDGMENTS

This study was supported by the Russian Foundation for Basic Research (project no. 01-02-17373) and the Ministry of Education of the Russian Federation (project no. 97-0-7.3-1).

REFERENCES

1. T. Thio, T. R. Thurston, and N. W. Preyer, Phys. Rev. B **38** (1), 905 (1988).
2. A. S. Borovik-Romanov, A. I. Buzdin, N. M. Kreĭnes, and S. S. Krotov, Pis'ma Zh. Éksp. Teor. Fiz. **47** (11), 600 (1988) [JETP Lett. **47**, 697 (1988)].
3. E. A. Turov, *Kinetic, Optical, and Acoustical Properties of Antiferromagnets* (Ural. Otd. Akad. Nauk SSSR, Sverdlovsk, 1990).
4. I. S. Smirnova, Physica B (Amsterdam) **262**, 247 (1999).
5. V. G. Bar'yakhtar, A. L. Sukstanskiĭ, and D. A. Yablonskiĭ, Fiz. Tverd. Tela (Leningrad) **32** (4), 1231 (1990) [Sov. Phys. Solid State **32**, 723 (1990)].
6. H. E. Viertiö and N. E. Bonesteel, Phys. Rev. B **49** (9), 6088 (1994).
7. K. L. Dudko, N. V. Gapon, V. N. Savitskiĭ, and V. V. Solov'ev, Fiz. Nizk. Temp. **21** (3), 270 (1995) [Low Temp. Phys. **21**, 205 (1995)].
8. M. A. Shamsutdinov and V. N. Nazarov, Fiz. Tverd. Tela (St. Petersburg) **43** (2), 265 (2001) [Phys. Solid State **43**, 274 (2001)].
9. M. M. Farztdinov, *Physics of Magnetic Domains in Antiferromagnets and Ferrites* (Nauka, Moscow, 1981).
10. A. I. Mitsek, P. F. Gaidanskii, and V. N. Pushkar, Phys. Status Solidi **38**, 69 (1970).
11. V. G. Bar'yakhtar, A. E. Borovik, and V. A. Popov, Zh. Éksp. Teor. Fiz. **62** (6), 2233 (1972) [Sov. Phys. JETP **35**, 1169 (1972)].
12. V. G. Bar'yakhtar, V. M. Loktev, and D. A. Yablonskiĭ, Preprint ITF-88-81R (Kiev, 1998).
13. A. A. Nikonov, O. E. Parfenov, and A. A. Zakharov, Pis'ma Zh. Éksp. Teor. Fiz. **66** (3), 159 (1997) [JETP Lett. **66**, 165 (1997)].
14. A. A. Nikonov and O. E. Parfenov, Pis'ma Zh. Éksp. Teor. Fiz. **72** (11), 797 (2000) [JETP Lett. **72**, 550 (2000)].
15. M. A. Shamsutdinov, V. N. Nazarov, and A. A. Khalfina, J. Magn. Magn. Mater. **214** (1–2), 139 (2000).
16. V. N. Krivoruchko and T. E. Primak, Fiz. Nizk. Temp. **19** (8), 871 (1993) [Low Temp. Phys. **19**, 620 (1993)].

Translated by Yu. Epifanov

Physics of the Solid State, Vol. 44, No. 2, 2002, pp. 345–352. Translated from Fizika Tverdogo Tela, Vol. 44, No. 2, 2002, pp. 332–339.

MAGNETISM AND FERROELECTRICITY

Thermodynamics and Kinetics of Switching of Ferroelastic Ferroelectrics at Its Initial Stage

S. A. Kukushkin* and M. A. Zakharov**

**Institute of Problems of Mechanical Engineering, Russian Academy of Sciences, Vasil'evskiĭ ostrov, Bol'shoĭ pr. 61, St. Petersburg, 199178 Russia*

e-mail: ksa@math.ipme.ru

***Novgorod State University, Novgorod, 173003 Russia*

Received May 31, 2001

Abstract—Thermodynamics and kinetics of switching of ferroelastic ferroelectrics (FFs) are studied at the initial (weak-metastability) stage. It is shown that in the switching of a uniaxial FF, the role of the electric field and mechanical stress simultaneously applied to the FF is analogous to that of supersaturation or supercooling of solutions and melts in the process of a conventional phase transition. The dependence of the critical size of a domain on the strength of the switching field is derived. In the space of domain sizes, the dependence of the steady flux of repolarized and redeformed nuclei on the applied field is determined and the time required for this steady flux to set in (latent time) and the time during which this flux is steady are estimated. © *2002 MAIK "Nauka/Interperiodica".*

1. INTRODUCTION

Ferroelastic ferroelectrics (FFs) have widespread application as light valves and optical switches, logic and memory elements, and materials for use as capacitors and piezoelectric elements [1, 2]. FFs have no center of symmetry above the phase-transition point and, therefore, exhibit a piezoelectric effect in the paraelectric phase [3]. For this reason, the spontaneous deformation that arises in them below the Curie point is due to the piezoelectric effect rather than to electrostriction, as in pure ferroelectrics, and, hence, its magnitude is proportional to the spontaneous polarization. Another characteristic feature of FFs is that the domains that are formed in the lower symmetric phase can change their orientation under the action of an externally applied field of a certain strength and direction. As is the case with conventional ferroelectric crystals, the FF switching is accompanied by the occurrence of a switching current. However, the switching of FFs also has specific features associated with a linear relation between the deformation and polarization. For example, because of this relation, polarization reorientation in FFs is accompanied by deformation reorientation. Experimental and theoretical studies of the switching process in ferroelectrics and related materials (see, e.g., [4–11]) are an important field of the physics of dielectric crystals and of the theory of structural phase transitions.

A rigorous kinetic theory of switching processes in uniaxial ferroelectric crystals was constructed in [12–14]. It was shown that the role of the electric field in switching processes is analogous to that of supersaturation or supercooling in conventional phase transitions. The switching process is a first-order phase transition, and its time evolution can be divided into several stages. In the initial stage, fluctuation nucleation of the new phase occurs and a steady flux of nuclei of reversed polarization is established. However, the system as a whole is not affected by these new-phase nuclei and its thermodynamic parameters remain unchanged. In the next stage, characterized as the basis of the switching process, nuclei become so large in number that the electric field in the ferroelectric is changed (i.e., the extent of "supersaturation" decreases). Coalescence of new-phase nuclei occurs in the third, final stage.

FF switching can be considered in a similar manner, thereby generalizing the theory developed in [12–14].

The objective of this paper is to describe the thermodynamics and kinetics of the initial stage of FF switching. We restrict our consideration to uniaxial FFs (Rochelle salt $KNaC_4H_4O_6 \cdot 4H_2O$, potassium dihydrogen phosphate KH_2PO_4, etc.); the switching process in multiaxial FFs, such as sodium trihydrogen selenite $NaH_3(SeO_3)_2$, is not considered in this paper.

In Section 2, the thermodynamics of FF switching is considered; we outline the concepts and terminology of the theory and show that the role of the combined electric field and mechanical stress in the switching of uniaxial FFs is analogous to that of supersaturation or supercooling in conventional first-order phase transitions. In Section 3, the kinetics of FF switching at its initial stage is investigated; a nonequilibrium distribution function in the domain size (number of unit cells) of repolarization and redeformation is introduced and the corresponding Fokker–Planck–Zel'dovich kinetic equation is written out; the critical domain size is calculated as a function of the switching field. Finally, in

Section 4, the basic parameters of the kinetics of FF switching at its initial stage, such as the diffusion coefficient in the space of domain sizes and the steady flux of repolarized and redeformed nuclei, are determined and the time required for this steady flux to set in and the time during which this flux is steady are estimated.

2. THERMODYNAMICS OF SWITCHING

We consider an L-thick slab of an FF in a spatially homogeneous (single-domain) state below the Curie point. It is assumed that spontaneous polarization arises only along one of the crystal axes and that the spontaneous deformation is no more than a shear and is associated with rotation about the same crystal axis. The x axis is taken to be along the polarization vector. In other directions, the FF is assumed to exhibit no anomalies in its dielectric and mechanical properties. Under these assumptions, the spontaneous polarization of the uniaxial FF is completely determined by the x component P_x of the polarization vector and the spontaneous deformation is the yz shear component U_{yz} of the deformation tensor. The FFs with such electromechanical properties are typified by Rochelle salt crystals (a $222 \longrightarrow 2$ symmetry change).

If an electric field and mechanical stress are simultaneously applied to the crystal under study, then its incomplete thermodynamic potential at a temperature near the Curie point can be written in the form [3]

$$\Phi = \Phi_0(p, T) + \frac{1}{2}\alpha(T - T_c)\eta^2 + \frac{1}{4}\beta\eta^4 - a_1\eta E_x - a_2\eta\sigma_{yz}, \quad (1)$$

where η is the order parameter for the ferroelastic–ferroelectric phase transition (it transforms like a component of a second-rank tensor and, simultaneously, like a component of a vector); $\Phi_0(p, T)$ is the part of the thermodynamic potential that is independent of the order parameter; p and T are the pressure and temperature of the ambient medium, respectively; α and β are coefficients of the power series expansion of the thermodynamic potential in η; T_c is the Curie temperature; E_x is the x component of the electric field; and σ_{yz} is the yz component of the stress tensor.

Minimizing the thermodynamic potential (1), we obtain a relation between the order parameter and the applied field and stress,

$$\alpha(T - T_c)\eta + \beta\eta^3 = a_1E_x + a_2\sigma_{yz}. \quad (2)$$

Using the thermodynamic potential (1), the electrical and mechanical equations of state for a unit volume of the FF are found to be

$$P_x = -\left(\frac{\partial\Phi}{\partial E_x}\right)_{T, \sigma_{yz}} = a_1\eta,$$
$$U_{yz} = -\left(\frac{\partial\Phi}{\partial\sigma_{yz}}\right)_{T, E_x} = a_2\eta, \quad (3)$$

where the equilibrium value of the order parameter is given by Eq. (2). The x component of the polarization vector and the yz component of the deformation tensor are subject to the obvious condition [3]

$$\frac{P_x}{a_1} = \frac{U_{yz}}{a_2}.$$

It follows from Eq. (2) that in the absence of external fields and stresses ($E_x = 0$, $\sigma_{yz} = 0$), the higher symmetry phase ($\eta = 0$) is stable above the Curie point. We will study FF switching in the temperature range below the Curie point, where the order parameter of the stable (lower symmetry) phase of the FF is nonzero and, hence, the polarization and deformation are also nonzero. The equilibrium values of the order parameter are equal to

$$\eta_{1, 20} = \pm\sqrt{\frac{\alpha(T - T_c)}{\beta}}, \quad (4)$$

and, therefore, the spontaneous polarization and deformation in the lower symmetry phase are

$$P_{x, 1, 20} = a_1\eta_{1, 20} = \pm a_1\sqrt{\frac{\alpha(T - T_c)}{\beta}},$$
$$U_{yz}^{1, 20} = a_2\eta_{1, 20} = \pm a_2\sqrt{\frac{\alpha(T - T_c)}{\beta}}. \quad (5)$$

The boundaries of the stability region of the uniaxial FF are found from the condition $a_1(\partial E_x/\partial\eta)_T + a_2(\partial\sigma_{yz}/\partial\eta)_T = 0$ (cf. [15]) to be

$$\eta_{1, 2s} = \pm\sqrt{\frac{\alpha(T - T_c)}{3\beta}},$$
$$P_{x1, 2s} = a_1\eta_{1, 2s} = \pm a_1\sqrt{\frac{\alpha(T - T_c)}{3\beta}}, \quad (6)$$
$$U_{yz}^{1, 2s} = a_2\eta_{1, 2s} = \pm a_2\sqrt{\frac{\alpha(T - T_c)}{3\beta}}.$$

In describing first-order phase transitions in solutions, the quantity called supersaturation plays an important role. In [12–14], an analogous quantity called repolarization was introduced in constructing a consistent theory of polarization reversal in uniaxial ferroelectrics. In this paper, in describing the switching kinetics of uniaxial FFs, we introduce the quantity

$$\Delta\eta = |\eta - \eta_{10}|, \quad (7)$$

which is similar to repolarization and will be referred to as repolarization–redeformation (RR). In addition, we define the relative RR as

$$\xi_\eta = \left|\frac{\eta}{\eta_{10}} - 1\right| = \frac{|\eta| - |\eta_{10}|}{|\eta_{10}|} = \frac{\Delta\eta}{\eta_{10}}. \quad (8)$$

Using the quantities defined in Eqs. (7) and (8) and the dependences of the spontaneous polarization and spontaneous deformation on the order parameter given by Eq. (3), one can determine the repolarization, introduced in the theory of polarization reversal in uniaxial ferroelectrics [12–14], and the redeformation as

$$\begin{aligned} \Delta P \equiv |P_x - P_{x10}| &= a_1|(\eta - \eta_{10})| = a_1\Delta\eta, \\ \xi_P \equiv \left|\frac{P_x}{P_{x10}} - 1\right| &= \xi_\eta, \\ \Delta U \equiv |U_{yz} - U_{yz}^{10}| &= |a_2(\eta - \eta_{10})| = a_2\Delta\eta, \\ \xi_U \equiv \left|\frac{U_{yz}}{U_{yz}^{10}} - 1\right| &= \xi_\eta, \end{aligned} \quad (9)$$

where ΔP and ξ_P are the repolarization and the relative repolarization, respectively, and ΔU and ξ_U are the redeformation and the relative redeformation, respectively. It should be noted that in a uniaxial FF, the relative repolarization, the relative redeformation, and the relative RR are equal in value.

If the electric field and mechanical stress applied to the crystal are weak enough, then the RR and the relative RR can easily be found as functions of these external fields. For this purpose, we expand the left-hand side of Eq. (2) in powers of $(\eta - \eta_{10})$,

$$\begin{aligned} \alpha(T - T_c)\eta + \beta\eta^3 &\approx [\alpha(T - T_c) + 3\beta\eta_{10}](\eta - \eta_{10}) \\ &= 2\alpha(T - T_c)(\eta - \eta_{10}) = a_1E_x + a_2\sigma_{yz}, \end{aligned}$$

and find that

$$\Delta\eta = \frac{a_1E_x + a_2\sigma_{yz}}{2\alpha(T_c - T)}, \quad (10)$$

$$\xi_\eta = \frac{a_1E_x + a_2\sigma_{yz}}{2\alpha(T_c - T)\eta_{10}}. \quad (11)$$

Therefore, the role of the combined electric field and mechanical stress in FF switching is analogous to that of supersaturation or supercooling in conventional phase transitions.

Below the Curie point, according to [3], the dielectric susceptibility is $\chi_{xx}^{T,\sigma_{yz}} = a_1^2/2\alpha(T_c - T)$ and the elastic compliance is $s_{yzyz}^{T,E_x} = a_2^2/2\alpha(T_c - T)$. Therefore, Eqs. (10) and (11) can be represented in the form

$$\Delta\eta = \frac{\chi_{xx}^{T,\sigma_{yz}}E_x}{a_1} + \frac{s_{yzyz}^{T,E_x}\sigma_{yz}}{a_2}, \quad (12)$$

$$\begin{aligned} \xi_\eta &= \left(\frac{\chi_{xx}^{T,\sigma_{yz}}E_x}{a_1} + \frac{s_{yzyz}^{T,E_x}\sigma_{yz}}{a_2}\right)\frac{1}{\eta_{10}} \\ &= \frac{\chi_{xx}^{T,\sigma_{yz}}E_x}{P_{x10}} + \frac{s_{yzyz}^{T,E_x}\sigma_{yz}}{U_{yz}^{10}}. \end{aligned} \quad (13)$$

Using Eqs. (9), one can also derive analogous expressions for the repolarization and redeformation:

$$\begin{aligned} \Delta P &= a_1\Delta\eta = \chi_{xx}^{T,\sigma_{yz}}E_x + \frac{a_1s_{yzyz}^{T,E_x}\sigma_{yz}}{a_2}, \\ \Delta U &= a_2\Delta\eta = \frac{a_2\chi_{xx}^{T,\sigma_{yz}}E_x}{a_1} + s_{yzyz}^{T,E_x}\sigma_{yz}. \end{aligned} \quad (14)$$

The quantity $\xi_\eta^{\max} = |\eta_{1s}/\eta_{10} - 1|$ is the maximum attainable value of the relative RR. At $\xi_\eta > \xi_\eta^{\max}$, the initial orientation of the polarization and deformation in the lower symmetry phase becomes absolutely unstable and spontaneous switching of the polarization and deformation occurs in the FF.

In terms of the thermodynamic description presented above, one can make a qualitative comparison between the features of uniaxial FF, uniaxial ferroelectric, and intrinsic ferroelastic switching. For example, the domain switching in a uniaxial FF can be performed by applying either an electric field (as is the case with pure ferroelectrics) or a mechanical stress (loading), as in pure ferroelastics. In this respect, the application of an electric field along the polar axis is equivalent to the application of a shearing stress [1]. In the general case, a uniaxial FF can be switched by applying an electric field and a stress simultaneously. On the other hand, the crystal under study is initially in a spatially homogeneous (single-domain) state and can be thought of as both a ferroelectric and a ferroelastic domain (elastic twin), because a uniaxial FF is a uniaxial ferroelectric and, at the same time, an intrinsic ferroelastic. Therefore, when the relative RR in a ferroelastic-ferroelectric domain reaches its maximum value and the intrinsic order parameter η is reversed, the ferroelectric and ferroelastic domains are both switched simultaneously. In other words, when a uniaxial single-domain FF crystal is switched, the polarization and deformation in the lower symmetry phase are reversed. This process is accompanied by the occurrence of both polarization- and deformation-switching currents.

It should be noted that the term "ferroelastic-ferroelectric domain" has not come into wide use and needs clarification. This term is used in the context of the classification of FFs as complete and incomplete. Apparently, this classification was first introduced by Gridnev and coworkers (see, e.g., [16, 17]), who experimentally investigated relaxation processes in various FFs, among them uniaxial ones. It is well known that in uniaxial FFs (termed complete), the ferroelastic domains coincide

with ferroelectric ones, while in multiaxial (incomplete) FFs, a ferroelastic domain has a substructure formed by ferroelectric domains. We apply the term ferroelastic–ferroelectric domain to a spatially homogeneous complete FF.

In concluding this section, it should be noted that in the framework of the thermodynamics of uniaxial FF switching, one can also describe the switching of both uniaxial ferroelectrics (as in [12]) and intrinsic ferroelastics. In these two particular cases, the order parameter can be specified. In intrinsic ferroelectric phase transitions [$\sigma_{yz} = 0$ in Eq. (1)], the order parameter is the polarization, which transforms like a vector component. In an intrinsic ferroelastic phase transition [$E_x = 0$ in Eq. (1)], the order parameter is the deformation and transforms like a component of a second-rank tensor. In these two cases, the analog of the extent of supersaturation is the electric field and the mechanical stress, respectively.

We are now in a position to study the kinetics of uniaxial FF switching at its initial stage in the framework of the thermodynamic description presented above.

3. SWITCHING KINETICS AT THE INITIAL STAGE IN THE REGION OF WEAK INSTABILITY

When describing the kinetics of uniaxial FF switching, it is convenient to introduce, in addition to the order parameter η, polarization P_x, and deformation U_{yz} used above, the corresponding (specific) quantities η_ω, p_x, and u_{yz} for a unit cell of the crystal:

$$\begin{aligned} \eta_\omega &= \eta\omega, \quad p_x = P_x\omega = a_1\eta_\omega, \\ u_{yz} &= U_{yz}\omega = a_2\eta_\omega, \end{aligned} \tag{15}$$

where ω is the unit-cell volume.

We consider domains as being composed of unit cells of a crystal characterized by the order parameter η_ω, polarization p_x, and deformation u_{yz}. A domain of volume V_d contains $n = V_d/\omega$ unit cells and is characterized by the order parameter, polarization, and deformation defined as

$$\begin{aligned} \eta_n &= \eta_\omega n, \quad P_{xn} = p_x n = a_1\eta_n, \\ U^n_{yz} &= u_{yz} n = a_2\eta_n. \end{aligned} \tag{16}$$

As in [12], we introduce the size distribution function of domains $f(n, t)$ normalized to the number of domains $N(t)$ per unit volume of the crystal. The kinetic equation describing the process of nucleation of the new phase in the case of $n \gg 1$ has the form [12]

$$\begin{aligned} &\frac{\partial f(n,t)}{\partial t} \\ &= \frac{\partial}{\partial n} W_{n,n+1}\left[\frac{1}{k_B T}\frac{\partial R_{\min}}{\partial n} f(n,t) + \frac{\partial f(n,t)}{\partial n}\right], \end{aligned} \tag{17}$$

where $f(n, t)$ is the size distribution function of repolarized and redeformed domains, $W_{n,n+1}$ is the diffusion coefficient of reversed nuclei in the space of domain sizes, $R_{\min}(n)$ is the minimum work done by the system to create a nucleus, and $\partial R_{\min}/\partial n$ is the change in the minimum work caused by a change in the number of unit cells in a domain whose size does not exceed its critical value, $n < n_c$ (n_c is the size of a critical nucleus in equilibrium with the medium). Depending on their size, the nuclei can be divided into two classes: nuclei with $n < n_c$ and nuclei with $n > n_c$. The former nuclei decay, whereas the latter grow in size, because the repolarization and the redeformation of the medium are not large enough for the former nuclei to exist but are sufficiently large for the latter nuclei to grow. The difference in behavior of subcritical and supercritical nuclei is due to the positive surface energy of arising nuclei; this energy plays a decisive role in any first-order phase transition.

At the initial stage of FF switching, the system does not respond to the formation of the new phase and the thermodynamic parameters of the system remain unchanged. Therefore, it will suffice to solve Eq. (17) for the steady-state case and find the steady flux of arising nuclei of the switched phase. For this purpose, one has to calculate the diffusion coefficient $W_{n,n+1}$, the minimum work $R_{\min}(n)$ done to create a nucleus, and the critical nucleus size n_c. To find these quantities, characterizing the initial stage of FF switching, we employ the method developed in [12].

Following [12], it is easy to show that the minimum work done to create a new-phase nucleus of size n with order parameter η_n, polarization P_{xn}, and deformation U^n_{yz} in a uniaxial FF at fixed values of the pressure and temperature can be written as

$$\begin{aligned} R_{\min}(n) &= \Delta(W + p_0 V - T_0 S - E_{xn}P_{xn} - \sigma^n_{yz}U^n_{yz}) \\ &\quad + (E_{xn} - E_{x0})P_{xn} + (\sigma^n_{yz} - \sigma^0_{yz})U^n_{yz} - \mu_0 n \\ &\equiv \Delta(W + p_0 V - T_0 S - [a_1 E_{xn} + a_2\sigma^n_{yz}]\eta_n) \\ &\quad + [a_1(E_{xn} - E_{x0}) + a_2(\sigma^n_{yz} - \sigma^0_{yz})]\eta_n - \mu_0 n, \end{aligned} \tag{18}$$

where ΔW, ΔV, and ΔS are the total changes in the energy, volume, and entropy of the nucleus on its formation, respectively, and p_0, T_0, and μ_0 are the pressure, temperature, and chemical potential of the medium, respectively. Here and henceforth, quantities with the index zero are related to the medium and quantities without this index are related to a nucleus. The first term in Eq. (18) is the thermodynamic potential of a nucleus of size n with combined internal field and stress $(a_1 E_{xn} + a_2\sigma^n_{yz})$ and can be written as

$$\begin{aligned} \phi(\eta_n) &= \Delta(W + p_0 V - T_0 S \\ &\quad - [a_1 E_{xn} + a_2\sigma^n_{yz}]\eta_n) = \tilde{\mu} n, \end{aligned} \tag{19}$$

where $\tilde{\mu}$ is the chemical potential per unit cell of a new-phase nucleus of size n (including the surface tension energy).

In order to find the chemical potential of a nucleus of the repolarized and redeformed phase with allowance for the surface tension energy, one should make an assumption as to the shapes of the ferroelastic-ferroelectric nuclei. As in [12], we assume that the new-phase nuclei arising in the process of uniaxial FF switching merge instantaneously into a cylindrical domain with a constant height $H \sim \omega^{1/3}$ and variable radius and that the interfaces between old-phase and new-phase domains are parallel to the polar axis of the crystal (the x axis). It should be noted that a domain wall being parallel to the polar axis of the FF is a necessary condition of continuity of the tangential component of the electric-field strength at the nucleus–medium interface. For a cylindrical nucleus of reversed polarization and strain, the surface energy is $W_s = 2(\pi H\omega)^{1/2}\sigma n^{1/2}$, where σ is the surface tension coefficient of the domain wall.

With allowance for the surface tension, the chemical potential of a new-phase nucleus of size n is

$$\tilde{\mu}(a_1E_{xn} + a_2\sigma_{yz}^n, p, T) = \left(\frac{\partial\phi(\eta_n)}{\partial n}\right)_{E_x, \sigma_{yz}, p, T} = \mu(a_1E_{xn} + a_2\sigma_{yz}^n, p, T) + \frac{(\pi H\omega)^{1/2}\sigma}{n^{1/2}}, \quad (20)$$

where the terms $\mu(a_1E_{xn} + a_2\sigma_{yz}^n, p, T)$ and $(\pi H\omega)^{1/2}\sigma/n^{1/2}$ are the contributions from the bulk energy and surface energy of the nucleus, respectively, to the chemical potential.

Using Eqs. (18)–(20), we find the minimum work $\tilde{R}_{\min}$ done to create a new-phase nucleus whose size is close to critical:

$$\tilde{R}_{\min} = \left(\frac{\partial R_{\min}}{\partial n}\right)_{E_x, \sigma_{yz}, p, T} = (\tilde{\mu} - \mu) + [a_1(E_{xn} - E_{x0}) + a_2(\sigma_{yz}^n - \sigma_{yz}^0)]\frac{\partial\eta_n}{\partial n} \quad (21)$$

$$= (\tilde{\mu} - \mu) + [a_1(E_{xn} - E_{x0}) + a_2(\sigma_{yz}^n - \sigma_{yz}^0)]\eta_\omega,$$

where η_ω is the specific order parameter defined by Eq. (15) [see also Eq. (16)].

The equilibrium value of the order parameter (and, hence, the equilibrium values of the deformation and polarization) of the nucleus–medium system is determined by the condition

$$\tilde{\mu}(a_1E_{xn} + a_2\sigma_{yz}^n, p, T) = \mu(a_1E_{xn} + a_2\sigma_{yz}^n, p, T) + \frac{(\pi H\omega)^{1/2}\sigma}{n^{1/2}} = \mu_0(a_1E_{xn} + a_2\sigma_{yz}^n, p, T). \quad (22)$$

On the other hand, the equilibrium magnitude of the combined field and stress $a_1\tilde{E}_x + a_2\tilde{\sigma}_{yz}$ in the nucleus–medium system (in the case of an infinitely large nucleus, $n \longrightarrow \infty$) is found from the condition

$$\mu(a_1\tilde{E}_x + a_2\tilde{\sigma}_{yz}) = \mu_0(a_1\tilde{E}_x + a_2\tilde{\sigma}_{yz}). \quad (23)$$

We subtract Eq. (23) from Eq. (22) and expand the result around the point $a_1\tilde{E}_x + a_2\tilde{\sigma}_{yz}$ in powers of the small deviation $(a_1E_{xn} + a_2\sigma_{yz}^n - a_1\tilde{E}_x - a_2\tilde{\sigma}_{yz})/(a_1\tilde{E}_x + a_2\tilde{\sigma}_{yz})$. Keeping only the first term of the power series, we find the basic part of the nucleus size distribution to be

$$\left(\frac{\partial\mu}{\partial[a_1E_x + a_2\sigma_{yz}]}\right)_{a_1\tilde{E}_x + a_2\tilde{\sigma}_{yz}} \times (a_1E_{xn} + a_2\sigma_{yz}^n - a_1\tilde{E}_x - \tilde{\sigma}_{yz}) + \frac{(\pi H\omega)^{1/2}\sigma}{n^{1/2}} = \left(\frac{\partial\mu_0}{\partial[a_1E_x + a_2\sigma_{yz}]}\right)_{a_1\tilde{E}_x + a_2\tilde{\sigma}_{yz}} \times (a_1E_{xn} + a_2\sigma_{yz}^n - a_1\tilde{E}_x - \tilde{\sigma}_{yz}). \quad (24)$$

Note that

$$-\left(\frac{\partial\mu}{\partial[a_1E_x + a_2\sigma_{yz}]}\right)_{a_1\tilde{E}_x + a_2\tilde{\sigma}_{yz}} = \eta_\omega^{(2)}, \quad -\left(\frac{\partial\mu_0}{\partial[a_1E_x + a_2\sigma_{yz}]}\right)_{a_1\tilde{E}_x + a_2\tilde{\sigma}_{yz}} = \eta_\omega^{(1)}, \quad (25)$$

where $\eta_\omega^{(1)}$ and $\eta_\omega^{(2)}$ are the specific order parameters of the medium and nucleus, respectively, and $\eta_\omega^{(1)} = -\eta_\omega^{(2)}$. Introducing the notation $\eta_\omega^{(1)} = -\eta_\omega$, we obtain from Eq. (24)

$$2(a_1E_{xn} + a_2\sigma_{yz}^n - a_1\tilde{E}_x - a_2\tilde{\sigma}_{yz})\eta_\omega = \frac{(\pi H\omega)^{1/2}\sigma}{n^{1/2}}, \quad n^{1/2} = \frac{(\pi H\omega)^{1/2}\sigma}{2(a_1E_{xn} + a_2\sigma_{yz}^n - a_1\tilde{E}_x - a_2\tilde{\sigma}_{yz})\eta_\omega}. \quad (26)$$

For the FF in the equilibrium state, we have $a_1\tilde{E}_x + a_2\tilde{\sigma}_{yz} = 0$. When the FF is in a switching field, the size of a critical nucleus (which is in equilibrium with the medium) is determined by the condition $a_1E_{xn_c} + a_2\sigma_{yz}^{n_c} = a_1E_{x0} + a_2\sigma_{yz}^0$, from which one can find

$$n_c^{1/2} = \frac{(\pi H\omega)^{1/2}\sigma}{2\eta_\omega(a_1E_{x0} + a_2\sigma_{yz}^0)}. \quad (27)$$

Dropping the index zero, which indicates that the field and stress are related to the medium, we write

$$n_c^{1/2} = \frac{(\pi H\omega)^{1/2}\sigma}{2\eta_\omega(a_1E_x + a_2\sigma_{yz})}. \quad (28)$$

Substituting Eqs. (15), we rewrite Eq. (28) in the final form

$$n_c^{1/2} = \frac{(\pi H\omega)^{1/2}\sigma}{2(p_xE_x + u_{yz}\sigma_{yz})}. \quad (29)$$

Formulas (28) and (29) give the number of unit cells in a critical nucleus of the repolarized and redeformed phase in a uniaxial FF. These expressions are similar to the corresponding formulas giving the number of unit cells in critical nuclei that arise in solutions, melts, and uniaxial ferroelectrics [12]. The magnitude of the linear combination $a_1E_x + a_2\sigma_{yz}$ of the electric field and stress is an analog of the extent of supersaturation or supercooling.

The minimum work done to create a cylindrical critical nucleus is [12]

$$R_{\min}(n_c) = (\pi H\omega)^{1/2}\sigma n_c^{1/2}. \quad (30)$$

On the other hand, the minimum work done to create a nucleus whose size is close to that of a critical nucleus can be represented in the following form using Eq. (22):

$$\tilde{R}_{\min} = \left(\frac{\partial R_{\min}}{\partial n}\right)_{E_x,\,\sigma_{yz},\,p,\,T}$$

$$= \mu_0(a_1E_{xn} + a_2\sigma_{yz}^n, p, T) - \mu_0(a_1E_{x0} + a_2\sigma_{yz}^0, p, T)$$

$$-(a_1E_{xn} + a_2\sigma_{yz}^n - a_1E_{x0} - a_2\sigma_{yz}^0)\eta_\omega$$

$$= \left(\frac{\partial\mu_0}{\partial(a_1E_x + a_2\sigma_{yz})}\right)_{a_1E_{x0} + a_2\sigma_{yz}^0 \approx a_1E_{xn} + a_2\sigma_{yz}^n} \quad (31)$$

$$\times(a_1E_{xn} + a_2\sigma_{yz}^n - a_1E_{x0} - a_2\sigma_{yz}^0)$$

$$-(a_1E_{xn} + a_2\sigma_{yz}^n - a_1E_{x0} - a_2\sigma_{yz}^0)\eta_\omega$$

$$= -2(a_1E_{xn} + a_2\sigma_{yz}^n - a_1E_{x0} - a_2\sigma_{yz}^0)\eta_\omega,$$

where η_ω is the specific order parameter of the medium. Substituting Eq. (15) into Eq. (31), we obtain

$$\tilde{R}_{\min} = -2p_x(E_{xn} - E_{x0}) - 2u_{yz}(\sigma_{yz}^n - \sigma_{yz}^0). \quad (32)$$

Formulas (29) and (32), derived for a uniaxial FF, are also applicable to uniaxial ferroelectrics and intrinsic ferroelastics. For example, in the case of a pure ferroelectric, Eqs. (29) and (32) are reduced to the formulas $n_c^{1/2} = (\pi H\omega)^{1/2}\sigma/2p_xE_x$ and $\tilde{R}_{\min} = -2p_x(E_{xn} - E_{x0})$ respectively, derived in [12] for this case. For a pure ferroelastic, Eqs. (29) and (32) take the form $n_c^{1/2} = (\pi H\omega)^{1/2}\sigma/2u_{yz}\sigma_{yz}$ and $\tilde{R}_{\min} = -2u_{yz}(\sigma_{yz}^n - \sigma_{yz}^0)$.

Now, we calculate the basic characteristics of the initial stage of FF switching.

4. THE MAIN CHARACTERISTICS OF THE INITIAL STAGE OF THE FERROELASTIC–FERROELECTRIC SWITCHING

We calculate the diffusion coefficient in the space of domain sizes, the steady flux of repolarized and redeformed nuclei, the time required for this steady flux to set in, and the time during which this flux will be steady.

In order to calculate the diffusion coefficient in the domain-size space, we use kinetic equation (17). We note that the quantity $(W_{n,\,n+1}/k_BT)(\partial R_{\min}/\partial n)$ in this equation is the growth rate of nuclei of size n; that is,

$$\frac{dn}{dt} = -W_{n,\,n+1}\frac{1}{k_BT}\frac{\partial R_{\min}}{\partial n}. \quad (33)$$

On the other hand, the nucleus growth rate can be written as

$$\frac{dn}{dt} = [\beta(a_1E_{xn} + a_2\sigma_{yz}^n) - \beta(a_1E_{x0} - a_2\sigma_{yz}^0)]S, \quad (34)$$

where $\beta(a_1E_{xn} + a_2\sigma_{yz}^n)$ is the flux of unit cells with reversed polarization and deformation that merge with the cylindrical domain at its lateral surface, $\beta(a_1E_{x0} + a_2\sigma_{yz}^0)$ is the reverse unit-cell flux due to dissolution of the domain, $a_1E_{xn} + a_2\sigma_{yz}^n$ is the linear combination of the electric field and stress in an imaginary medium in equilibrium with a domain of size n, $a_1E_{x0} + a_2\sigma_{yz}^0$ is the linear combination of the electric field and stress in the FF under study, and $S = 2(\pi H\omega)^{1/2}n^{1/2}$ is the area of the lateral surface of the cylindrical domain.

The equilibrium unit-cell flux is equal to

$$\beta_0 = N_s\nu\exp(-V_0/k_BT), \quad (35)$$

where ν is the oscillation frequency of atoms in the unit cells situated at the domain surface; V_0 is the height of the energy barrier (in the absence of an external field) separating two adjacent domains that are in symmetrical positions but whose order parameters have opposite directions; and N_s is the number of unit cells at the domain surface, which is roughly equal to $N_s \sim 1/\omega^{2/3}$, where $\omega^{2/3}$ is the area occupied by a unit cell at the domain surface.

When an electric field and a stress are applied to the FF, the barrier height V_0 is changed; it decreases to a value of $V_0 - \eta_\omega(a_1E_x + a_2\sigma_{yz})$ for the unit cells of a domain with the order parameter aligned with the field

but becomes higher and equal to $V_0 + \eta_\omega(a_1E_x + a_2\sigma_{yz})$ for the unit cells of a domain whose order parameter is in opposition to the field. Therefore, the oppositely directed unit-cell fluxes through a domain wall become unequal. The unit-cell flux from the medium is $\beta(a_1E_{xn} + a_2\sigma_{yz}^n) = \beta_0\exp[\eta_\omega(a_1E_{xn} + a_2\sigma_{yz}^n)/k_BT]$, while the unit-cell flux from a nucleus of critical size is equal to $\beta(a_1E_{x0} + a_2\sigma_{yz}^0) = \beta_0\exp[\eta_\omega(a_1E_{x0} + a_2\sigma_{yz}^0)/k_BT]$. If $\eta_\omega(a_1E_x + a_2\sigma_{yz}) \ll k_BT$, then the above exponentials can be expanded in a Taylor series. Keeping only the linear terms and substituting into Eq. (34), we obtain the following expression for the growth rate of the lateral surface of a domain with $n > n_c$:

$$\frac{dn}{dt} = 2(\pi H\omega)^{1/2}\beta_0 \times \frac{2\eta_\omega(a_1E_{xn} + a_2\sigma_{yz}^n - a_1E_{x0} - a_2\sigma_{yz}^0)}{k_BT}n^{1/2}. \quad (36)$$

By comparing Eq. (36) with Eqs. (33) and (31), one can obtain

$$D_n \equiv W_{n,n+1} = 2(\pi H\omega)^{1/2}\beta_0 n^{1/2}; \quad (37)$$

therefore, for a nucleus of critical size, we have

$$D_{n_c} = 2(\pi H\omega)^{1/2}\beta_0 n_c^{1/2}. \quad (38)$$

This formula gives the diffusion coefficient in the domain-size space. We note that Eq. (38) is similar to the expression for the diffusion coefficient derived in the theory of switching of uniaxial ferroelectrics in [12].

Using Eq. (30) for the minimum work done to create a nucleus of critical size and Eq. (38) for the diffusion coefficient in the domain-size space, the steady flux of repolarized and redeformed domains can be found to be [12]

$$I = \frac{N_v\pi^{1/4}\beta_0(H\omega)^{3/4}\sigma^{1/2}}{\sqrt{2}n_c^{1/4}\sqrt{k_BT}}\exp\left(-\frac{(\pi H\omega)^{1/2}\sigma n_c^{1/2}}{k_BT}\right), \quad (39)$$

where N_v is the number of unit cells in the crystal, which is roughly estimated to be $N_v \approx 1/\omega$.

Substituting Eq. (29) for the critical size n_c into Eq. (39), the flux of reversed domains is found as a function of the applied electric field and stress:

$$I = \frac{N_v\beta_0(H\omega)^{1/2}(\eta_\omega[a_1E_x + a_2\sigma_{yz}])^{1/2}}{\sqrt{k_BT}} \times \exp\left(-\frac{\pi H\omega\sigma^2}{2k_BT\eta_\omega[a_1E_x + a_2\sigma_{yz}]}\right) = \frac{N_v\beta_0(H\omega)^{1/2}(p_xE_x + u_{yz}\sigma_{yz})^{1/2}}{\sqrt{k_BT}} \times \exp\left(-\frac{\pi H\omega\sigma^2}{2k_BT(p_xE_x + u_{yz}\sigma_{yz})}\right). \quad (40)$$

Taking the logarithm of this expression gives

$$\ln I = \ln K - \frac{1}{2}\ln(a_1E_x + a_2\sigma_{yz}) - \frac{\pi H\omega\sigma^2}{2k_BT\eta_\omega(a_1E_x + a_2\sigma_{yz})}, \quad (41)$$

where

$$K = \frac{N_v\beta_0(H\omega\eta_\omega)^{1/2}}{\sqrt{k_BT}}.$$

Since the logarithm is a slowly varying function, the second term in Eq. (41) can be considered to be independent of the field and stress in the first approximation. In this case, Eq. (41) takes a form convenient for making estimates from experimental data:

$$\ln I = \text{const} - \frac{\pi H\omega\sigma^2}{2k_BT\eta_\omega(a_1E_x + a_2\sigma_{yz})}, \quad (42)$$

where const stands for the first two terms in Eq. (41).

Now, we estimate the time required for the steady flux of new-phase nuclei to set in and the time during which this flux will be steady. In the region of $n < n_c$, the flux of nuclei is determined primarily by heterophase fluctuations. Therefore, the flux becomes steady upon passing through the size range of width δn_0 near the critical value of the nucleus size. The width of this range is given by [18]

$$\delta n_0 = \left(-\frac{1}{2k_BT}\frac{\partial^2 R_{\min}(n)}{\partial n^2}\right)^{-1/2}. \quad (43)$$

Using Eq. (43), we find that the time during which the steady flux of nuclei sets in is equal to [12]

$$t \sim \frac{(\delta n_0)^2}{W_{n,n+1}} = \frac{4k_BTn_c}{\pi H\omega\beta_0\sigma}. \quad (44)$$

Substituting Eq. (29) for n_c into Eq. (44) yields

$$t \sim \frac{k_BT\sigma}{\beta_0(p_xE_x + u_{xy}\sigma_{yz})^2}. \quad (45)$$

Thus, the time required for the steady flux to set in varies in inverse proportion to the square of the linear combination of the applied electric field and stress.

In order to estimate the time during which the flux of nuclei will be steady, one should take into account that the time required for a nucleus to pass through a region of width δn_0 near the critical point in the domain-size space is much shorter than the time during

which a nucleus of critical size emerges from this region; that is,

$$\frac{(\delta n_0)^2}{W_{n,n+1}} \ll \frac{\delta n_0}{(dn_c/dt)}. \quad (46)$$

The formulas derived above for the quantities characterizing the initial stage of uniaxial FF switching can be used to calculate analogous switching parameters of uniaxial ferroelectrics in an external electric field ($\sigma_{yz} = 0$) and intrinsic ferroelastics subjected to external stresses ($E_x = 0$).

5. CONCLUSIONS

In closing, we specify the principal results of this work and point out some lines of further investigation of FF switching. In this paper, we developed a kinetic theory for the initial stage of uniaxial FF switching and calculated the main characteristics of this process. The results can also be used to describe the switching of uniaxial ferroelectrics and intrinsic ferroelastics. However, the results of this work are inapplicable to the basic stage of FF switching (not considered here), in which the polarization and deformation reversal involve the main body of the FF and the thermodynamic parameters of the system are changed. It is also of interest to theoretically investigate the switching of multiaxial ferroelectrics and related materials characterized by a multicomponent order parameter. These subjects will be considered in the future.

ACKNOWLEDGMENTS

This study was supported in part by the Russian Foundation for Basic Research (project no. 99-03-32768), the Russian Federal Center “Integration” (project no. A0151), and CONACYT (grant no. 32208).

REFERENCES

1. G. A. Smolenskiĭ and N. N. Kraĭnik, *Ferroelectrics and Antiferroelectrics* (Nauka, Moscow, 1968).
2. M. E. Lines and A. M. Glass, *Principles and Applications of Ferroelectrics and Related Materials* (Oxford Univ. Press, Oxford, 1977; Mir, Moscow, 1981).
3. B. A. Strukov and A. P. Levanyuk, *Physical Principles of Ferroelectric Phenomena in Crystals* (Nauka, Moscow, 1995).
4. D. Damjanovic, Rep. Prog. Phys. **61**, 1267 (1998).
5. J. F. Scoff, Ferroelectr. Rev. **1**, 1 (1998).
6. V. Ya. Shur and E. L. Rumyantsev, Ferroelectrics **191**, 319 (1997).
7. V. Ya. Shur, E. L. Rumyantsev, V. P. Kuminov, *et al.*, Fiz. Tverd. Tela (St. Petersburg) **41** (1), 126 (1999) [Phys. Solid State **41**, 112 (1999)].
8. N. A. Pertsev and A. G. Zembilgotov, J. Appl. Phys. **78** (10), 6170 (1995).
9. N. A. Pertsev, A. G. Zembilgotov, and A. K. Tagantsev, Ferroelectrics **223**, 79 (1999).
10. E. V. Balashova, V. V. Lemanov, and G. A. Pankova, Fiz. Tverd. Tela (St. Petersburg) **43** (7), 1275 (2001) [Phys. Solid State **43**, 1328 (2001)].
11. V. V. Lemanov, S. N. Popov, V. V. Bukhurin, and N. V. Zaĭtseva, Fiz. Tverd. Tela (St. Petersburg) **43** (7), 1283 (2001) [Phys. Solid State **43**, 1336 (2001)].
12. S. A. Kukushkin and A. V. Osipov, Fiz. Tverd. Tela (St. Petersburg) **43** (1), 80 (2001) [Phys. Solid State **43**, 82 (2001)].
13. S. A. Kukushkin and A. V. Osipov, Fiz. Tverd. Tela (St. Petersburg) **43** (1), 88 (2001) [Phys. Solid State **43**, 90 (2001)].
14. S. A. Kukushkin and A. V. Osipov, Fiz. Tverd. Tela (St. Petersburg) **43** (2), 312 (2001) [Phys. Solid State **43**, 325 (2001)].
15. L. D. Landau and E. M. Lifshitz, *Course of Theoretical Physics*, Vol. 8: *Electrodynamics of Continuous Media* (Nauka, Moscow, 1982; Pergamon, New York, 1984).
16. S. A. Gridnev, B. M. Darinskii, and V. S. Postnikov, Ferroelectrics **14**, 583 (1976).
17. S. A. Gridnev and B. M. Darinskii, Phys. Status Solidi A **47**, 379 (1978).
18. V. V. Slezov and Yu. Schmelzer, Fiz. Tverd. Tela (St. Petersburg) **36** (2), 353 (1994) [Phys. Solid State **36**, 193 (1994)].

Translated by Yu. Epifanov

Physics of the Solid State, Vol. 44, No. 2, 2002, pp. 353–357. Translated from Fizika Tverdogo Tela, Vol. 44, No. 2, 2002, pp. 340–343.

MAGNETISM AND FERROELECTRICITY

Studies of the Thermodynamic Properties of the Ordered Perovskites Pb_2CdWO_6 and Pb_2YbTaO_6 within a Broad Temperature Range

M. V. Gorev*, I. N. Flerov*, V. S. Bondarev*, and Ph. Sciau**

** Kirenskiĭ Institute of Physics, Siberian Division, Russian Academy of Sciences, Akademgorodok, Krasnoyarsk, 660036 Russia*

e-mail: gorev@iph.krasn.ru

*** CEMEC-CNRS, 31055 Toulouse, France*

Received June 26, 2001

Abstract—This paper reports on measurements of the specific heat of Pb_2CdWO_6 made at temperatures ranging from 80 to 750 K and of Pb_2YbTaO_6 within the 350- to 700-K temperature range. First-order phase transitions from the cubic phase at 677.3 and 581 K, respectively, were observed, and their thermodynamic characteristics were determined. The entropy change on the phase transitions is close to $R\ln 4$ for both compounds. The results obtained are discussed in terms of the model of position disordering of the lead ions. It was established that below 350 K, Pb_2CdWO_6 can exist in two states, stable and metastable, depending on the sample thermal prehistory. *© 2002 MAIK "Nauka/Interperiodica".*

Many perovskite-like oxygen compounds with a three-dimensional framework of corner-sharing octahedra undergo various sequences of phase transitions with decreasing temperature which entail the formation of a superstructure; however, only in some of them have incommensurate modulated structures been revealed. Only a few such compounds are thus far known to exist among the $Pb_2B'B''O_6$ mixed perovskites, in particular, Pb_2ScTaO_6 [1], Pb_2CoWO_6[2, 3], Pb_2CdWO_6 [4], and, possibly, Pb_2YbTaO_6 [5, 6]. The reasons for the incommensurate phase formation and the phase transitions of this type remain poorly studied.

This paper presents the results of a study on the specific heat of two ordered perovskites, Pb_2CdWO_6 and Pb_2YbTaO_6, carried out within a broad temperature range with the purpose of determining the thermodynamic parameters of the phase transitions and the behavior of these compounds in the temperature regions where anomalies in the dielectric properties are observed.

The occurrence of the antiferroelectric-II–antiferroelectric-I and antiferroelectric-I–paraelectric cubic phase transitions (at 370 and 683 K, respectively) in Pb_2CdWO_6 was first reported in [7], with the lower temperature phase found to be pseudomonoclinic. In a later x-ray study [4], only one phase transition, at 683 K, was detected; in contrast to [7], no appreciable changes in the unit-cell parameters were observed to occur near 370 K. In the higher temperature phase, the compound has an fcc structure $Fm\bar{3}m$ ($Z = 4$), which is characteristic of ordered mixed perovskites. Below the phase-transition point, the x-ray diffractograms were interpreted as corresponding to a pseudoorthorhombic unit cell [$a_0 = a_c$, $b_0 = (b_c + c_c)/2$, $c_0 = (b_c - c_c)/2$] similar to the unit cell of the lower temperature phase of Pb_2CoWO_6 [3, 8]. In this phase, one observes additional weak reflections, which were assigned in [4] to incommensurate distortions.

The Pb_2YbTaO_6 compound was also reported [5, 6, 9] to undergo two phase transitions which proceed in the following sequence: cubic paraelectric ($Fm\bar{3}m$)–antiferroelectric at $T_1 = 558$ K and antiferroelectric–ferroelectric ($Pcm2_1$?) at $T_2 \approx 450$ K. The anomaly in the dielectric permittivity at T_2 is very weak, and noticeable dispersion is observed.

The samples for investigation were prepared through solid-state synthesis from a stoichiometric mixture of the starting oxides. The mixture was heated in a gold ampule and kept at a high temperature for several hours. The quality and purity of the samples were verified on a Siemens-D-5000 x-ray diffractometer. A diffractometric analysis showed the sample to contain neither the starting substances used in the solid-state synthesis nor foreign phases [4]. It was also established that there is no disorder in the distribution of the Cd^{2+} and W^{6+} ions, nor in the Yb^{3+} and Ta^{5+} ions occupying positions at the centers of the corresponding octahedra [4].

The heat capacity of Pb_2CdWO_6 was measured in the 80- to 370-K temperature range with an adiabatic calorimeter in the discrete and continuous heating modes. The powder sample, 4.297 g in mass, employed earlier in structure refinement measurements [4], was

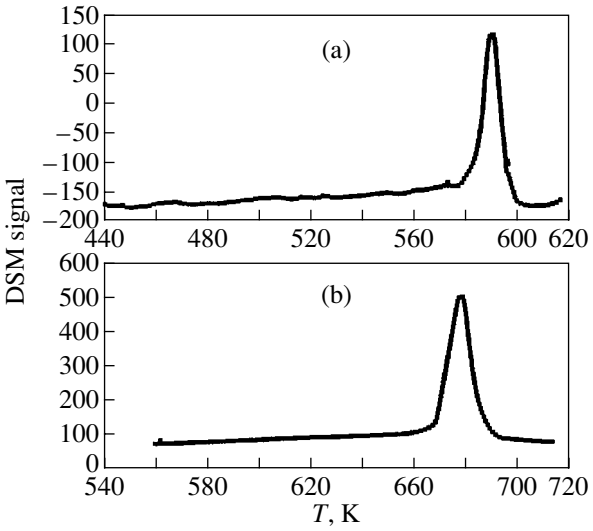

Fig. 1. DSM-2M microcalorimetric traces obtained on (a) Pb_2CdWO_6 and (b) Pb_2YbTaO_6.

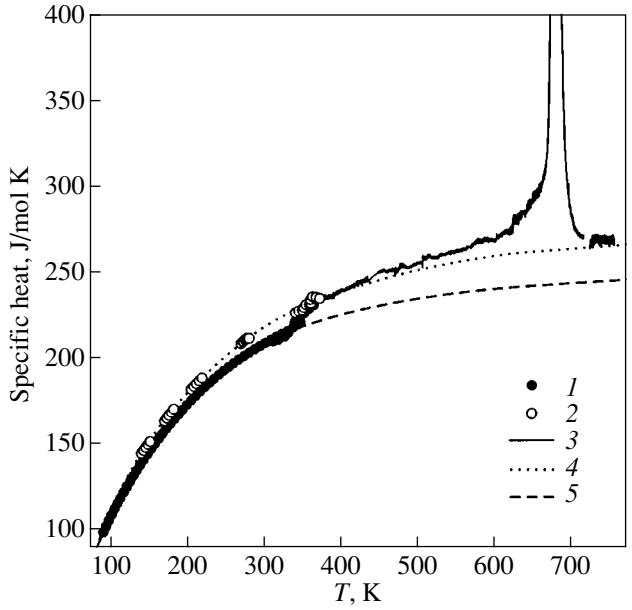

Fig. 2. Specific heat of Pb_2CdWO_6 measured within a broad temperature range: (*1*) first series of measurements; (*2*) the second series and subsequent measurements; (*3*) DSM measurements made at high temperatures; and (*4*, *5*) lattice specific heat.

placed in an indium container which was sealed in a helium environment. The container heat capacity was measured in a separate experiment. The scatter of experimental points from a smoothened curve did not exceed 0.5%.

In the 330- to 770-K range, the heat capacities of Pb_2CdWO_6 and Pb_2YbTaO_6 were measured with a differential scanning microcalorimeter on a computerized DSM-2M setup. The samples were 0.588 and 0.410 g in mass, respectively. The error inherent in this method (~5%) is substantially larger than that in an adiabatic calorimeter.

The results obtained on samples of Pb_2CdWO_6 and Pb_2YbTaO_6 with the differential scanning microcalorimeter are presented in Fig. 1. Pb_2CdWO_6 exhibited only one noticeable anomaly, with a maximum at 677 K (Fig. 1a). In Pb_2YbTaO_6, the anomaly is observed at 581 K (Fig. 1b). Neither of the crystals revealed any substantial anomalies in the temperature regions where structural changes were reported in [5, 7, 9] to take place. This is possibly associated with the insufficiently high sensitivity of the DSM method and the smallness of the thermal effect of this phase transition in Pb_2YbTaO_6, a factor pointed out in [5]. The enthalpy changes at the high-temperature phase transitions in Pb_2CdWO_6 and Pb_2YbTaO_6 were found to be 6800 ± 300 and 6250 ± 350 J/mol, respectively.

Figure 2 displays the results obtained in a study of the heat capacity of Pb_2CdWO_6. The specific heat does not exhibit anomalous behavior up to 330 K. When heated above 330 K, the sample reveals a stepwise increase in the specific heat by ~5% within a narrow (~10 K) temperature range (curve *1* in Fig. 2). The values of the low-temperature specific heat obtained in repeated measurements were found to be higher than those obtained in the first series. No changes in $C_p(T)$ near 330 K were presently found (curve *2* in Fig. 2). The two levels of the specific heat obtained in different series of measurements below this temperature imply that a sample can reside in two possible states. Attempts were made to act on the state of the sample through thermal cycling and by maintaining it at liquid-nitrogen and room temperature for 14 days. Subsequent measurements showed, however, that this does not restore the specific heat to its original value of below 330 K. It may be conjectured that the equilibrium state corresponding to the lower value of the specific heat is reached as a result of aging, which is caused by prolonged storage of the sample at room temperature. Effects of aging, which influence the behavior of the dielectric properties in perovskite-like compounds, were reported in [10]. In our case, the sample was maintained at room temperature for several years before the beginning of the calorimetric measurements. The nonequilibrium state may have arisen after the sample was heated above 330 K (above the temperature of storage) and have persisted under subsequent cooling. To investigate this phenomenon, we will repeat the specific-heat measurements made on the same sample following prolonged (about a year) storage at room temperature.

The anomaly of the specific heat associated with the phase transition from the cubic phase is observed in scanning-microcalorimeter measurements at 677.3 K

(curve *3* in Fig. 2), which is slightly lower than the value quoted in [4].

The results of the first series of measurements below 320 K and of the repeated experiment with the adiabatic calorimeter from 140 to 360 K were treated using a combination of the Debye and Einstein functions:

$$C_L(T) = A\left(\frac{T}{\Theta_D}\right)^3 \int_0^{\frac{\Theta_D}{T}} x^4 \frac{\exp(x)}{(\exp(x)-1)^2} dx + B\left(\frac{\Theta_E}{T}\right)^2 \frac{\exp\left(\frac{\Theta_E}{T}\right)}{\left(\exp\left(\frac{\Theta_E}{T}\right)-1\right)^2}. \quad (1)$$

The relations derived in this treatment are plotted in Fig. 2 (curves *4*, *5*). Extrapolation of the relation obtained in the repeated series of measurements to the high-temperature region reveals good agreement with the data obtained from scanning microcalorimetry above the phase-transition temperature. In our opinion, this observation, as well as the good fit of the data in the temperature range near 370–400 K, is evidence of a fairly good agreement between the results obtained with the two experimental methods and provides grounds for their combined treatment.

It should be pointed out that when extrapolated to the high-temperature domain, the specific heat [described by Eq. (1)] derived from the original experiments in the 80- to 320-K range tends to the classical value following from the Dulong–Petit law. The values of the specific heat found at high temperatures in the second series of measurements lie above this level. The reason for this remains unclear. We stress once more that DSM measurements of the specific heat are made with an error of about 5%. The systematic error can increase at high temperatures.

The anomalous specific heat associated with the phase transition from the cubic phase is observed in Pb_2CdWO_6 within a fairly broad temperature range, as wide as ~150 K below the transition temperature and ~15–20 K above it. The integrated thermodynamic characteristics of the phase transition were derived from the anomalous part of the specific heat $\Delta C_p(T) = C_p(T) - C_L(T)$, where, for the lattice specific heat $C_L(T)$, we used results obtained by fitting the low-temperature specific heat with Eq. (1). The phase-transition specific enthalpy $\Delta H = \int \Delta C_p(T) dT$ is 7320 ± 360 J/mol, which slightly exceeds the value extracted from the DSM measurements themselves (6800 ± 300 J/mol). The specific entropy of the phase transition, calculated by integrating the $\Delta C_p(T)/T$ function, is plotted in Fig. 3. The total change in the specific entropy is ΔS = 11.1 ± 0.6 J/mol K ≈ 1.33*R*. Also shown in Fig. 3 is the change in the specific entropy of Pb_2YbTaO_6, ΔS = 10.9 ± 0.6 J/mol K, which was derived from the DSM measurements.

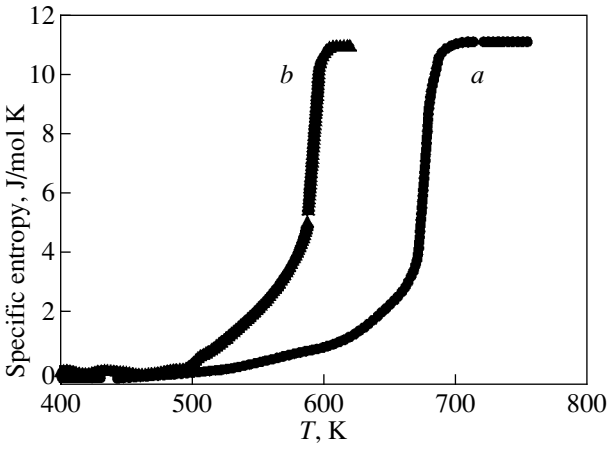

Fig. 3. Temperature dependence of the excess specific entropy: *a*—Pb_2CdWO_6 and *b*—Pb_2YbTaO_6.

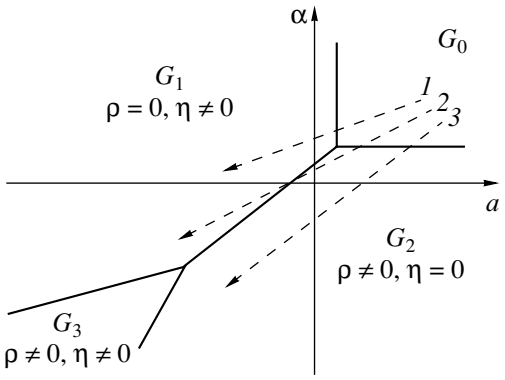

Fig. 4. Phase diagram constructed on the α–*a* plane in the model of [15, 16]. $G_0(Fm\bar{3}m)$ is the praphase, G_1 is a commensurate phase, and G_2 and G_3 are incommensurate phases.

The value of ΔS obtained in this work for both compounds is large and close to *R*ln4, which is in accordance with our earlier data on the related compounds Pb_2CoWO_6 and Pb_2MgWO_6, which also undergo transitions from the cubic to a pseudoorthorhombic phase [11, 12]. Such a large change in the entropy indicates a substantial role being played by ordering processes in the phase-transition mechanism.

Judging from structural data on the $Pb_2B'B''O_6$ ordered perovskites [13, 14], Pb ions have the largest temperature parameter in the cubic phase if we assume them to occupy the 8*c* positions. In the distorted phase, this parameter is of normal magnitude if the phase is pseudoorthorhombic. This provided grounds for the assumption that lead ions in the cubic phase are positionally disordered [14]. There are three models of pos-

sible disorder which consider the lead-ion displacements from the 8*c* position in the [100]-, [110]-, and [111]-type directions.

Symmetry considerations leave six equally probable positions for the lead ions in the first model, twelve in the second, and four in the third. A refinement of the Pb_2CoWO_6 and Pb_2MgWO_6 structures made within these models yields the following results [13, 14]. The lowest value of the *R* factor for Pb_2CoWO_6 was obtained in the case of lead disordered over twelve positions (the [110] model). For Pb_2MgWO_6, all the models considered yielded very close values of the *R* factor, making it difficult to give preference to any one of them. In the distorted phase, the lead ions are displaced primarily along the [100]-type directions of the pseudocubic unit cell. This may occur as a result of complete lead-atom ordering in the [100] model and should be accompanied by an entropy change $\Delta S = 2R\ln 6 = R\ln 36$. In the [110] model, the lead should remain partially disordered over two or four positions in the distorted phase in order to provide the experimentally observed mean displacements. The specific entropy is changed in this case by $\Delta S = 2R\ln(12/4) = R\ln 9$ or $2R\ln(12/2) = R\ln 36$. In the [111] model, only two of the four possible lead-ion positions should remain in the distorted phase, thus changing the entropy by $\Delta S = 2R\ln(4/2) = R\ln 4$.

The values of ΔS determined by us agree only with the [111] model; the entropy changes calculated within the other models far exceed those observed in all the $Pb_2B'B''O_6$ compounds studied in this work and in [11, 12].

Some $Pb_2B'B''O_6$ compounds revealed soft modes in the inelastic neutron and Raman scattering spectra [15, 16]. One may thus conjecture that the phase-transition mechanism in these compounds involves both lead ordering and oxygen-atom displacements. Processes of the first kind provide the major contribution to the entropy change. That the values of ΔS found in all the compounds studied are close to $R\ln 4$ suggests the same lead-disordering type to be operative in the cubic phase.

Studies of the Pb_2CoWO_6 compound suggest a phenomenological model of phase transitions to incommensurate and commensurate phases [17]. It was proposed in [17] that an incommensurate phase arises at T_1 as a result of soft mode condensation at the point $k_1 = (k_x, k_x, 2\pi/a)$ in the Brillouin zone. At T_2, additional x-ray reflections appear, which correspond to the wave vector $k_2 = (0, 0, 2\pi/a)$ (the *X* point of the Brillouin zone). Reflections of the two types coexist within a broad (~100 K wide) temperature region. The thermodynamic potential has the form [17]

$$F = \frac{\alpha}{2}\rho^2 + \frac{\beta}{4}\rho^4 + \frac{a}{2}(\eta_1^2 + \eta_3^2) + \frac{b_1}{4}(\eta_1^4 + \eta_3^4) + \frac{b_2}{2}\eta_1^2\eta_3^2 + \frac{c}{6}(\eta_1^6 + \eta_3^6) + \delta\rho^2(\eta_1^2 + \eta_3^2), \quad (2)$$

where ρ is the magnitude of the order parameter of the incommensurate phase and η_1 and η_3 are the nonzero components of the order parameter corresponding to the ferroelectric phase. The coefficient δ describes the interaction of the two order parameters. To include the possibility of first-order transitions associated with these two order parameters, one has to add a term of the sixth power in ρ to the potential in Eq. (2) [18]. Depending on the actual values of the coefficients of the potential in Eq. (2), one may conceive various sequences of phase transitions: cubic paraelectric $G_0 \longrightarrow$ commensurate G_1 ($\rho = 0$, $\eta \neq 0$), cubic $G_0 \longrightarrow$ incommensurate G_2 ($\rho \neq 0$, $\eta = 0$), and cubic $G_0 \longrightarrow$ incommensurate G_2 ($\rho \neq 0$, $\eta = 0$) $\longrightarrow$ incommensurate G_3 ($\rho \neq 0$ $\eta \neq 0$) $\longrightarrow$ commensurate G_1 ($\rho = 0$, $\eta \neq 0$). The thermodynamic paths for these transition sequences are shown in Fig. 4 in a schematic phase diagram in α–*a* coordinates (the thermodynamic-potential parameters) by lines *1*, *2*, and *3*, respectively. The first sequence is likely to be realized in Pb_2MgWO_6, where one phase transition to the commensurate phase G_1 is observed [14]. In Pb_2CoWO_6 with a larger cation, the intermediate incommensurate phase G_2 becomes stable in the 258- to 304-K temperature range. In Pb_2CdWO_6, with a still larger cation, the region of stability of the intermediate incommensurate phase G_2 broadens and, according to our studies, no transition to the G_1 or G_3 phase occurs, at least down to 80 K. As for Pb_2YbTaO_6, the above phase diagram is also applicable to description of the phase-transition sequences in this compound, because, as reported in [5], its intermediate phase is incommensurate.

ACKNOWLEDGMENTS

This study was supported by the Russian Foundation for Basic Research, project no. 00-15-96790.

REFERENCES

1. C. A. Randall, S. A. Markgraf, A. S. Bhalla, and K. Baba-Kishi, Phys. Rev. B **40**, 413 (1989).
2. H. Tamura, Ferroelectrics **21**, 449 (1978).
3. Ph. Sciau, K. Krusche, P. A. Buffat, and H. Schmid, Ferroelectrics **107**, 235 (1990).
4. Ph. Sciau and D. Grabille, in *Aperiodic'94*, Ed. by G. Chapuis and W. Paciorek (World Scientific, Singapore, 1995), pp. 460–464.
5. E. S. Gagarina, V. V. Demidova, V. V. Eremkin, *et al.*, Kristallografiya **44** (2), 281 (1999) [Crystallogr. Rep. **44**, 247 (1999)].
6. N. Yasuda and J. Konda, Ferroelectrics **158**, 405 (1994).
7. Yu. V. Roginskaya and Yu. N. Venevtsev, Kristallografiya **10** (3), 341 (1965) [Sov. Phys. Crystallogr. **10**, 275 (1965)].

8. G. Baldinozzi, Ph. Sciau, and P. A. Buffat, Solid State Commun. **86** (9), 541 (1993).
9. V. A. Isupov and N. N. Kraĭnik, Fiz. Tverd. Tela (Leningrad) **6**, 3713 (1964) [Sov. Phys. Solid State **6**, 2975 (1964)].
10. H. Fan, L. Zhang, and X. Yao, J. Phys.: Condens. Matter **12**, 4381 (2000).
11. I. N. Flerov, M. V. Gorev, and Ph. Sciau, Fiz. Tverd. Tela (St. Petersburg) **41** (9), 1686 (1999) [Phys. Solid State **41**, 1544 (1999)].
12. I. N. Flerov, M. V. Gorev, and Ph. Sciau, J. Phys.: Condens. Matter **12** (5), 559 (2000).
13. G. Baldinozzi, Ph. Sciau, and J. Lapasset, Phys. Status Solidi A **133** (1), 17 (1992).
14. G. Baldinozzi, Ph. Sciau, M. Pinot, and D. Grabille, Acta Crystallogr. B **51**, 668 (1995).
15. G. Baldinozzi, Ph. Sciau, and A. Bulou, J. Phys.: Condens. Matter **7**, 8109 (1995).
16. W. Bührer, W. Brixel, and H. Schmid, in *Phonons 85* (World Scientific, Singapore, 1985), p. 325.
17. F. Maaroufi, P. Toledano, H. Schmid, *et al.*, Ferroelectrics **79**, 295 (1988).
18. Yu. M. Gufman and E. S. Larkin, Fiz. Tverd. Tela (Leningrad) **22** (2), 463 (1980) [Sov. Phys. Solid State **22**, 270 (1980)].

Translated by G. Skrebtsov

Physics of the Solid State, Vol. 44, No. 2, 2002, pp. 358–360. Translated from Fizika Tverdogo Tela, Vol. 44, No. 2, 2002, pp. 344–346.

MAGNETISM AND FERROELECTRICITY

Thermally Stimulated Electron Emission in the Paraelectric Phase of Triglycine Sulfate Crystals Heated at a High Rate

A. A. Sidorkin, A. S. Sidorkin, O. V. Rogazinskaya, and S. D. Milovidova

Voronezh State University, Universitetskaya pl. 1, Voronezh, 394693 Russia

e-mail: sidorkin@dom.vsu.ru

Received May 15, 2001

Abstract—Thermally stimulated electron emission is experimentally observed in ferroelectric triglycine sulfate (TGS) crystals in a temperature range whose upper limit is 10–15 K above the Curie point. Samples of a nominally pure and a chromium-doped TGS crystal, heated at different constant rates $q = dT/dt$, are investigated. It is shown that an increase in the heating rate results in increased emission current density over the entire temperature range investigated. The temperature at which emission arises depends only slightly on the rate q. At the same time, the temperature at which emission ceases increases monotonically with increasing q; if q is less than 1 K/min, this temperature is below the Curie point, while at q = 4–5 K/min, this temperature becomes as large as 60–65°C, which is more than 15°C above the Curie point. In chromium-doped TGS crystal, the electron emission onset temperature is close to that of pure TGS, but the width of the temperature range over which emission is observed in the paraelectric phase is approximately two times less than in the case of pure TGS heated at the same rate. The emission disappearance below the Curie point (in the ferroelectric phase) at low q is explained as a result of full emptying of the electron traps under slow heating. The reason for the occurrence of emission above the Curie point is related to the charges that shield the spontaneous polarization and, because of their slow relaxation, persists in the paraelectric phase. © *2002 MAIK "Nauka/Interperiodica"*.

1. INTRODUCTION

One of the most powerful methods of disclosing the nature of electron emission observed experimentally is to investigate the emission kinetics. In the case of ferroelectrics, investigations of the kinetics of thermally stimulated electron emission (TSEE) were carried out in [1], where the influence of sample heating rate on the TSEE was also considered. Main attention was focused in [1] on the magnitude of the emission signal. In the present work, we investigate not only this effect but also the influence of the heating rate of ferroelectric triglycine sulfate (TGS) crystals on the magnitude and limits of the temperature range in which the TSEE is observed. It is shown experimentally that at a sufficiently high heating rate, emission occurs at temperatures essentially above the Curie point.

2. EXPERIMENTAL TECHNIQUE AND RESULTS

In the present study, the electron emission current density j_{em} was measured using a standard technique (described in [2]) in a vacuum of 6.5×10^{-3} Pa. The samples of nominally pure and chromium-doped TGS crystal (1 mol % in solution) used were polar *Y* cuts with an area of 20 mm^2 and a thickness of 1 mm. The heating rate of the samples $q = dT/dt$ was varied from 0.1 to 0.4 K/min. The temperature of the samples was measured using a copper–constantan thermocouple and controlled through simultaneous measurement of the capacity of another TGS crystal sample. The temperature of samples in different experiments was varied in the range from 20 to 65°C. The temperature was measured accurate to 5%.

The results of our investigation are the following. The TSEE occurs in a limited temperature range depending on the sample heating rate $q = dT/dt$. The lower temperature limit virtually does not depend on the heating rate q (Figs. 1a–1d). The magnitude of an emission signal increases approximately linearly with q (Fig. 2). The most interesting effect is the variation in the upper temperature limit. As one can see from Figs. 1a–1d and 3, this limit increases approximately in proportion to the sample heating rate. The temperature at which the electron emission ceases can be either above or below T_c depending on the value of q. At q = 0.5 K/min, the upper temperature limit for electron emission from the pure TGS crystal is 45–46°C, which is below the Curie point. At q = 4–5 K/min, this limit reaches 60–65°C; i.e., the electron emission is observed in a temperature range 10–15°C above the Curie point.

In the chromium-doped TGS crystal, the situation is qualitatively similar to that in the pure crystal, the difference being that, in this case, the width of the temperature range over which electron emission is observed in

the paraelectric phase is smaller; in particular, for q = 4.5 K/min, this width is 4–5 K.

For both nominal pure and doped TGS samples, a decrease in the total number of emitted electrons is observed with an increase in the sample heating rate (Fig. 4).

The observed thermionic emission of the investigated ferroelectric crystals can be attributed to autoelectron emission from shallow surface electronic states in the total field of the charges due to the spontaneous polarization of free charges and their compensation. This total field becomes nonzero, because the balance of the mentioned fields is upset when the Curie point is approached and the spontaneous polarization decreases. As a result, electron emission occurs from electron-trapping surface states [2].

Within this model, the emission current density is

$$j_{em}(T) = en(T)W(T), \quad (1)$$

where $n(T)$ is the surface density of occupied surface electron states at a given temperature,

$$W(T) = \frac{2\sqrt{2mA}\zeta}{mS}\exp\left(-\frac{4\sqrt{2m}A^{3/2}}{\hbar eE}\right) \quad (2)$$

is the ionization probability (per unit time) of an electron at the energy level A of a surface trapping center in the field E, ζ is the width of the electron-trapping well, and S is the area of the ferroelectric-sample surface involved in the electron emission.

The $n(T)$ dependence is defined by the equation

$$dn = -nWdt. \quad (3)$$

Substituting $dt = dT/q$ and taking account of the boundary conditions $n(T = T_0) = n_0$ [T_0 is the temperature at the beginning of the heating, $E(T = T_0) = 0$], we obtain (at q = const)

$$n = n_0\exp\left\{-\frac{1}{q}\int_{T_0}^{T} WdT\right\}. \quad (4)$$

The position of the emission current maximum is found from the condition $\partial j_{em}/\partial T = 0$, which, together with Eqs. (1)–(4), leads to the expression

$$W(T_m) = q\frac{E^*}{E^2(T_m)}\frac{\partial E}{\partial T}\bigg|_{T = T_m}, \quad (5)$$

where T_m is the temperature corresponding to the emission current maximum, $E(T)$ is the temperature dependence of the total (effective) field producing ionization of impurity centers, and

$$E^* = \frac{4}{3}\frac{\sqrt{2m}A^{3/2}}{\hbar e}. \quad (6)$$

As follows from Eq. (5), $W(T_m)$ is proportional to q. For the sake of simplicity, when performing integration in Eq. (4), one can assume W to be constant and put it

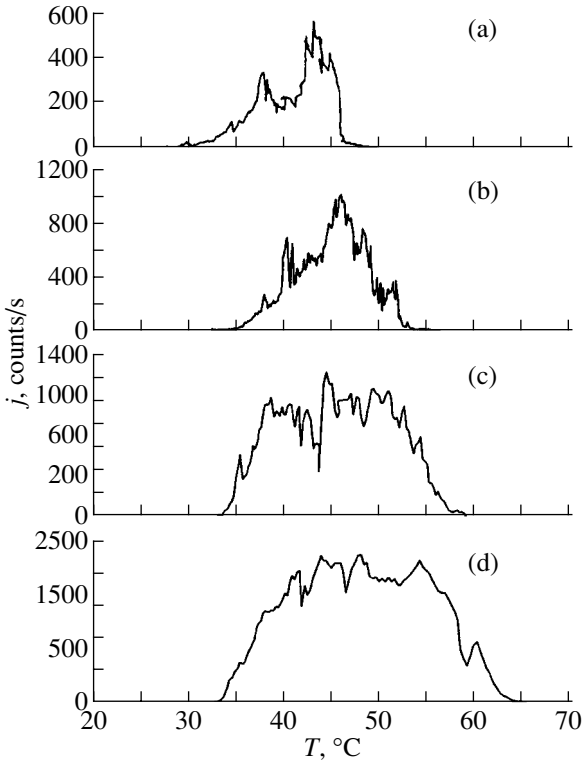

Fig. 1. Dependence of the emission current density on temperature for a pure TGS monocrystal heated at a rate q equal to (a) 0.3, (b) 1.1, (c) 2.1, and (d) 3.5 K/min.

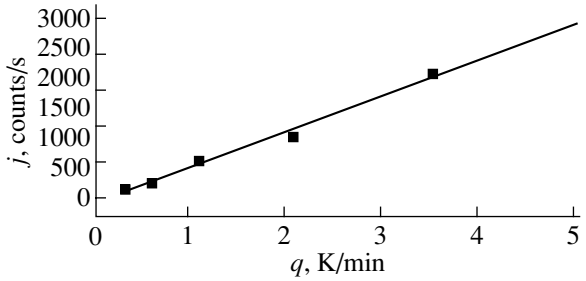

Fig. 2. Dependence of the maximal emission current density on the heating rate for a pure TGS monocrystal.

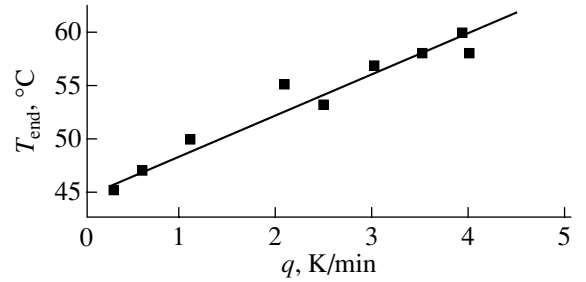

Fig. 3. Dependence of the emission disappearance temperature on the heating rate for a pure TGS monocrystal.

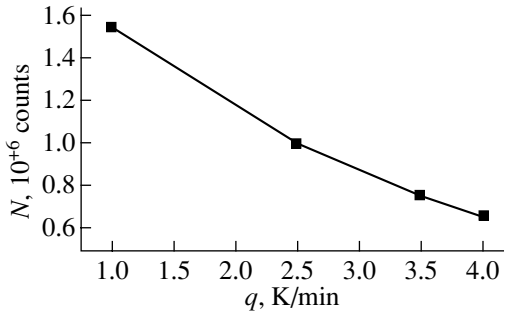

Fig. 4. Dependence of the total number of emitted electrons on the heating rate for a pure TGS monocrystal.

equal to $W(T_m)$. In this case, n becomes independent of q and the emission current maximum is found to be

$$j_{\max}^{\mathrm{em}} = en(T_m)\frac{E^*}{E^2(T_m)}\left.\frac{\partial E}{\partial T}\right|_{T=T_m} q, \qquad (7)$$

which is linear in the heating rate q, in accordance with the experimental data presented in Fig. 2.

The emission will cease when either the occupied electron-trapping states become empty or the total field of the charges due to spontaneous polarization and of the charges compensating them (the factor producing emission) vanishes. If the emission ceases below the Curie point, the first reason is more probable. Indeed, compensating charges can disappear only after the charges due to spontaneous polarization have vanished if the heating rate is very small. The charges due to spontaneous polarization exist up to T_c, and the capacity of the compensating charges to react swiftly to changes and, therefore, to a decrease in the effective field (which causes electron emission) down to a critical magnitude is limited by the Maxwell relaxation time.

The assumption that the traps become entirely empty in the case corresponding to Fig. 1a can be verified by comparing the total charge Q of emitted electrons with the analogous charges in the cases corresponding to the other panels of Fig. 1. In order to calculate the charge Q, one has to replace the temperature scale of Fig. 1 with a time scale and then calculate the area under the corresponding curve or, alternatively, to simply divide the area under the curves in Fig. 1 by the heating rate. A comparison of Figs. 1a, 1d, and 4 shows that the charge of emitted electrons at high heating rates is always less than that at low rates, which justifies our assumption.

The occurrence of electron emission above T_c also confirms the assumption concerning the nature of charges active in emission (that the compensating charges rather than the spontaneous-polarization charges are responsible for emission). Furthermore, the increase in the temperature at which emission ceases in the paraelectric phase with increasing heating rate can be related to the compensating charges persisting up to this temperature as a result of the fairly long Maxwell relaxation time τ.

Near the phase transition, the resistivity of a TGS crystal is about $10^{12}\ \Omega\ \mathrm{cm}^{-1}$ and the permittivity ε is of the order of 10^3, which gives, for the Maxwell relaxation time of compensating charges $\tau = \varepsilon/4\pi\sigma$, a value of the order of 10^3 s [3]. The product of τ and the heating rate 3.5 K/min gives 10°C for the width of the temperature range over which these charges exist, which agrees with the estimate of 10–15°C, following from Fig. 1d, for the width of the temperature range over which emission occurs in the paraelectric phase.

The decrease in the width of the temperature range of emission in the paraelectric phase in the case of the chromium-doped TGS crystal is due to a decrease in the Maxwell relaxation time of compensating charges, which was observed in [4] and related to an increase in the conductivity of the doped material [5].

Thus, the obtained results show that the temperature at which electron emission ceases in ferroelectrics is not a constant and does not necessarily coincide with the Curie point T_c, in contrast to common opinion. This temperature can be both below and above T_c, and in the latter case, the electron emission in the paraelectric phase of TGS can persist over a temperature range more than 15°C wide. The disappearance of the emission below T_c is caused by the complete emptying of electron traps involved in emission at relatively low sample heating rates. The persistence of electron emission in the nonpolar phase confirms the presence of charges that compensate charges due to spontaneous polarization involved in emission and is related to the fairly long Maxwell relaxation time of the former charges.

ACKNOWLEDGMENTS

This study was supported by the Netherlands Organization for Scientific Research (NWO) in the framework of the program “Nonlinear Dielectric Films for Nanotechnology” and by the Russian Foundation for Basic Research, project no. 01-02-16828.

REFERENCES

1. A. S. Sidorkin, A. M. Kostsov, and V. S. Zal’tsberg, Fiz. Tverd. Tela (Leningrad) **27** (7), 2200 (1985) [Sov. Phys. Solid State **27**, 1320 (1985)].
2. A. M. Kostsov, A. S. Sidorkin, V. S. Zal’tsberg, and S. P. Gribkov, Fiz. Tverd. Tela (Leningrad) **24**, 3436 (1982) [Sov. Phys. Solid State **24**, 1952 (1982)].
3. A. A. Sidorkin, S. D. Milovidova, O. V. Rogazinskaya, and A. S. Sidorkin, Fiz. Tverd. Tela (St. Petersburg) **42** (4), 725 (2000) [Phys. Solid State **42**, 743 (2000)].
4. A. S. Sidorkin, O. V. Rogazinskaya, S. D. Milovidova, *et al.*, Izv. Ross. Akad. Nauk, Ser. Fiz. **64** (9), 1763 (2000).
5. M. S. Tsedrik, *Physical Properties of Crystals from the Triglycine Sulfate Family* (Nauka i Tekhnika, Minsk, 1986).

Translated by D. Bayuk

Physics of the Solid State, Vol. 44, No. 2, 2002, pp. 361–364. Translated from Fizika Tverdogo Tela, Vol. 44, No. 2, 2002, pp. 347–350.

MAGNETISM AND FERROELECTRICITY

The Influence of Low X-ray Doses on the Properties of Chromium-Doped Triglycine Sulfate

L. N. Kamysheva, S. N. Drozhdin, and O. M. Golitsyna

Voronezh State University, Universitetskaya pl. 1, Voronezh, 394693 Russia

Received May 18, 2001

Abstract—The influence of low x-ray doses on pulsed polarization switching in triglycine sulfate crystals at different chromium impurity concentrations is investigated. It is demonstrated that the activation field α in the temperature range 20.0°C–T_c ambiguously depends on the radiation dose for pulses of switching currents of different polarities. It is found that the unipolarity associated with the presence of chromium ions in impurity triglycine sulfate crystals decreases as a result of the interaction between radiation-induced and impurity defects. © *2002 MAIK "Nauka/Interperiodica".*

1. INTRODUCTION

The majority of studies dealing with pulsed polarization switching in triglycine sulfate crystals (see monographs [1–3] and references therein) have been performed with nominally pure crystals. Specific features of the polarization switching properties of triglycine sulfate crystals containing defects of different origins have been thoroughly investigated in a number of works (see, for example, [4]) predominantly through visualization of the domain structure with the use of nematic liquid crystals. However, in all these works, consideration was not given to either the dependence of polarization switching properties and important parameters of crystals (such as the activation field, domain-wall mobility, etc.) on the defect concentration or the problems concerning interaction between impurity defects and defects induced by hard electromagnetic radiation in the crystal.

Investigation into the aforementioned properties and phenomena is a topical problem (because defects play an essential role in the formation of the internal field and its associated unipolarity in the crystal) and has a specific feature. This feature lies in the fact that irradiation of the crystal, on the one hand, generates additional radiation defects that act as impurity defects and, on the other hand, should substantially affect the impurity subsystem, which, in turn, can cause unpredictable changes in the crystal properties. Moreover, when used in practice, impurity triglycine sulfate crystals may be exposed to hard electromagnetic radiation. In this case, it is necessary to know the behavior of the operational characteristics of these crystals.

The influence of low radiation doses (no higher than 300–500 kR) on the crystal properties is of special interest. Under these conditions, there can exist effects not observed at high radiation doses, as was demonstrated earlier in [5–8] for KH_2PO_4 crystals and nominally pure triglycine sulfate. In the present work, we analyzed the influence of low x-ray doses on the pulsed polarization switching in Cr^{3+}-doped triglycine sulfate crystals with the aim of elucidating the behavior of unipolarity in these crystals upon introduction of radiation defects.

2. SAMPLE PREPARATION AND EXPERIMENTAL TECHNIQUE

Crystals of triglycine sulfate with Cr^{3+} were grown at a temperature below the Curie point from a solution containing the $Cr_2(SO_4)_3 \cdot 6H_2O$ salt (1 mol %). Although the chromium impurity content was not determined, it differed for different samples due to inhomogeneous distribution of impurities throughout the bulk of the crystal [9]. The degree of imperfection and the degree of unipolarity were estimated from the internal bias field E_i. The field E_i and the coercive field E_c were determined from the dielectric hysteresis loops at frequencies of 50 and 300 Hz. For the studied samples, the initial values of E_i and E_c differed. The samples were prepared in the form of plane-parallel plates from a polar cut (~0.3 cm^2 in area and ~0.1 cm thick) with vacuum-deposited silver electrodes. The samples were exposed to CuK_α characteristic radiation with an energy of 30 eV at a dose rate $N_d \approx 240$ kR/h along the polar axis of the crystal at room temperature. For each sample, the dose was gradually accumulated with a step of 20 kR.

The pulsed polarization switching was examined using the procedure described earlier in [10, 11]. The frequency of passing bipolar pulses of the polarization switching field was 300 Hz. The activation field α was determined from the relationship $i_{max} = i_{max\alpha}\exp(-\alpha/E)$, where i_{max} is the maximum value of the switching current pulse and E is the strength of the polarization switching field.

1063-7834/02/4402-0361$22.00 © 2002 MAIK "Nauka/Interperiodica"

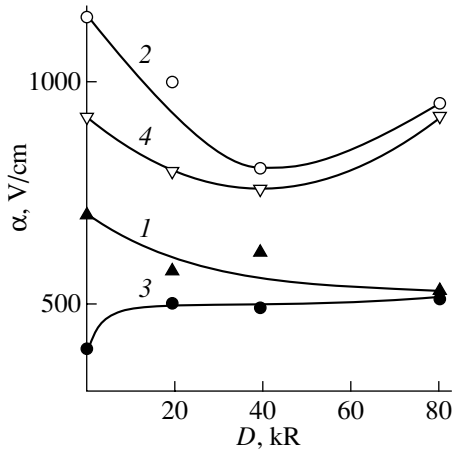

Fig. 1. Dependences of the activation field in (*1*, *3*) weak and (*2*, *4*) strong fields for the impurity triglycine sulfate crystal on the x-ray dose for (*1*, *2*) positive and (*3*, *4*) negative pulses of polarization switching current at $T = 40°C$ and $E_i = 100$ V/cm.

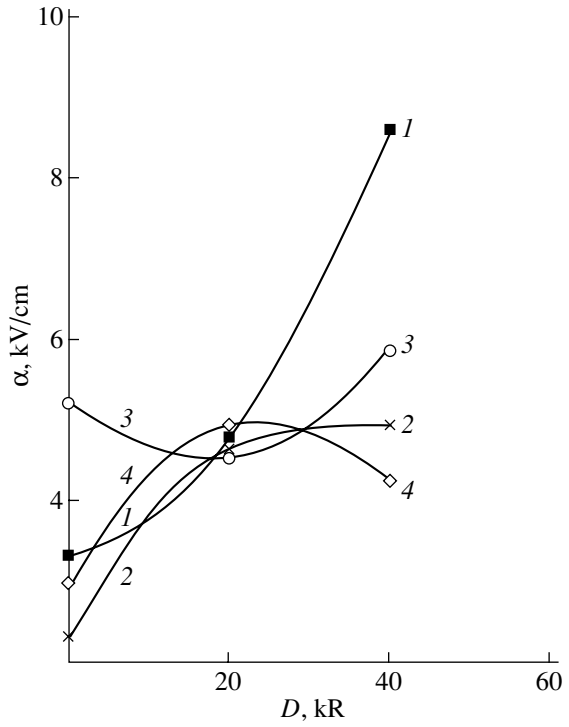

Fig. 2. Dependences of the activation field in (*1*, *3*) weak and (*2*, *4*) strong fields for the impurity triglycine sulfate crystal on the x-ray dose for (*1*, *2*) positive and (*3*, *4*) negative pulses of polarization switching current at $T = 40°C$ and $E_i = 300$ V/cm.

The polarization switching current pulses of opposite polarities, which were observed for the crystals under investigation, exhibited a pronounced asymmetry due to the internal bias field induced by the chromium impurity.

The direction of the internal field and the preferred direction of macroscopic polarization in the samples were determined from independent measurements of the static pyroelectric coefficient. It was revealed that, in the case when the directions of the polarization switching and internal fields coincide, the polarization switching current pulse has a lower value of i_{max} and a longer duration τ_s compared to those obtained for the mutually opposite orientation of these fields. According to the terminology introduced earlier in [10], a current pulse with the above characteristics is considered to be positive: $i^+_{max} < i^-_{max}$ and $\tau^+_s > \tau^-_s$.

3. RESULTS AND DISCUSSION

For the samples with initial values of $E_i \le 100$ V/cm, the activation fields in strong electric fields α_2 are higher than those in weak electric fields α_1 ($\alpha_2 > \alpha_1$). This is characteristic of nominally pure triglycine sulfate crystals [10, 11] and suggests that the switching in the weak and strong electric fields predominantly occurs through different mechanisms of changes in the domain structure under the action of a polarization switching field. For the samples with a pronounced unipolarity, the situation changes qualitatively: the values of α_1 (weak fields) become larger than α_2 (strong fields) over the entire temperature range covered. This relationship holds for samples with initial values of $E_i \ge 300$ V/cm in which the chromium impurity content is rather high (heavily doped samples). In contrast with this, the samples with fields $E_i < 100$ V/cm are treated as lightly doped samples.

In the case of low chromium impurity content (Fig. 1), the effect of the initial (impurity) unipolarity manifests itself in the difference between the values of $\alpha_1^{+,-}$ and $\alpha_2^{+,-}$, which were determined from the parameters of the positive and negative pulses of the switching current.

Under irradiation with an increasing dose, the values of α_2^+ and α_2^- (α_1^+ and α_1^-) approach each other. This apparently indicates that the internal field created by the chromium impurity is partially destroyed under x-ray irradiation. This assumption is also supported by the observed disappearance of the asymmetry of current pulses with an increase in the x-ray dose.

The above regularities are also observed for heavily doped samples. As can be seen from Fig. 2, the activation fields α_1 and α_2 are considerably higher than those for the samples with low fields E_i. The second feature of the curves depicted in Fig. 2 resides in the fact that, for the positive pulse, the activation fields α_1 and α_2 only slightly differ at $D = 0$ and virtually coincide at $D = 20$ kR. Further evolution in the activation fields α_1 and α_2 proceeds in such a manner that the field α_1^+ increases rapidly with an increase in the radiation dose,

whereas the field α_2^+ varies only slightly and remains lower than α_1^+. As regards the activation fields α_1 and α_2 for the negative pulse, they strongly differ at zero dose. However, after the first exposure to x-ray radiation (D = 20 kR), the field α_1^- decreases against the background of a noticeable increase in a_2^-. Under further irradiation (D = 40 kR), the situation changes qualitatively: $\alpha_1^- > a_2^-$.

The coincidence of the activation fields $\alpha_1^{+,-}$ and $\alpha_2^{+,-}$ for pulses of different polarities suggests that the initial unipolar state changes at a dose of ~20 kR. This indicates that no polarization switching mechanism is dominant in a given field E ($\alpha_1 = \alpha_2$). Further exposure to radiation only stabilizes the unipolar state created by the impurity ions.

This rather unexpected result is also confirmed by the behavior of the switched charge under x-ray radiation. It is clearly seen from Fig. 3 that an increase in the radiation dose is accompanied by an increase in the charge switched in the pulsed (curve *1*) and sinusoidal (curve *2*) electric fields.

The results shown in Figs. 1–3 allow us to argue that the chelate complex of chromium biglycine sulfate, which is responsible for the formation of the unipolar state in the Cr^{3+}-doped triglycine sulfate crystal [12], is rather sensitive to irradiation. Even low radiation doses lead to breaking of intermolecular bonds in the structure of triglycine sulfate crystals [13] and apparently cause decomposition of the chelate complex. In turn, this leads to softening of the polarization switching conditions for a crystal with a low initial internal field.

This assumption is corroborated by the dose dependences of the coercive field measured at a frequency of 50 Hz (Fig. 3; curves *3*, *4*). Note that the dependence $E_c(D)$ exhibits a minimum for radiation doses at which $\alpha^+ \approx \alpha^-$. The dependences $E_i(D)$ measured at a frequency of 300 Hz are less pronounced. The internal bias field, which was measured from the dielectric hysteresis loops, turned out to be less sensitive to irradiation. More specifically, the decrease in the internal field E_i for the same maximum dose was no greater than 10%. This value is comparable to the error in determining the fields E_c and E_i from the dielectric hysteresis loops.

In our earlier work [10], we proved that the ratio between α_1 and α_2 can differ depending on the chromium impurity content in triglycine sulfate crystals (depending on E_i) and varies from $\alpha_2 > \alpha_1$ to $\alpha_2 < \alpha_1$ with an increase in the internal field. The temperature T_0 (at which $\alpha_2 = \alpha_1$) shifts to the phase transition temperature with an increase in the internal field. A similar situation also occurs when radiation-induced defects serve as a source of unipolarity. Figure 4 illustrates the change in the ratio between the activation fields in weak and strong fields from $\alpha_1 < \alpha_2$ to $\alpha_1 > \alpha_2$ for nominally pure triglycine sulfate (curve *1*) and Cr^{3+}-doped triglycine sulfate (curve *2*) crystals with a low initial unipolarity after x-ray irradiation with an increasing dose. It is evident from Fig. 4 that this ratio changes in the same manner as the T_0 temperature varies with an increase in

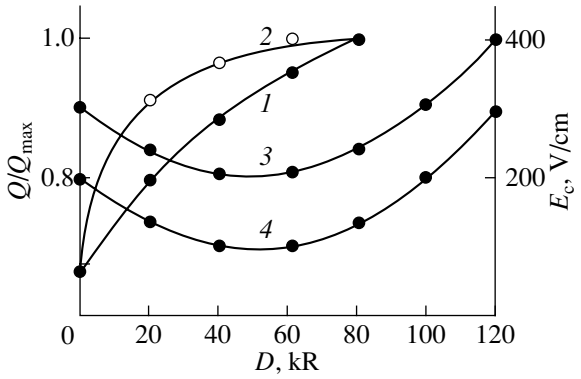

Fig. 3. Dependences of the switched charge Q/Q_{max} on the x-ray dose according to the data on (*1*) pulsed polarization switching and (*2*) dielectric hysteresis loops (Q_{max} is the switched charge at the x-ray dose D = 80 kR and T = 40°C). Dependences of the coercive field on the x-ray dose for the impurity triglycine sulfate crystal at temperatures of (*3*) 25 and (*4*) 35°C. E_i = 100 V/cm.

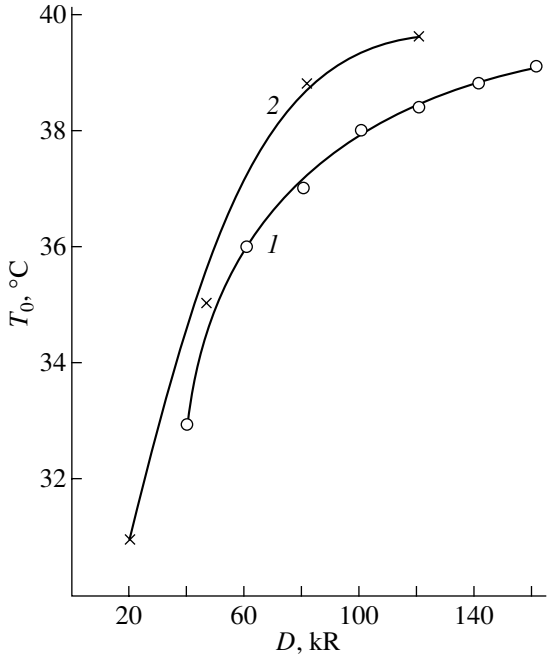

Fig. 4. Dependences of the temperature T_0 ($\alpha_1 > \alpha_2$ at $T < T_0$ and $\alpha_1 < \alpha_2$ at $T > T_0$) on the x-ray dose for (*1*) nominally pure triglycine sulfate and (*2*) Cr^{3+}-doped triglycine sulfate crystals.

the radiation dose, i.e., with an increase in the concentration of radiation-induced defects.

4. CONCLUSION

The main conclusion drawn in this work is as follows: low x-ray doses (no higher than 100 kR) can partially destroy the unipolar state created by chromium impurities in triglycine sulfate crystals. These doses can lead to an increase in the switched part of the macroscopic polarization.

REFERENCES

1. E. V. Peshikov, *Radiation Effect on Ferroelectrics* (Fan, Tashkent, 1972).
2. J. C. Burfoot and G. W. Taylor, *Polar Dielectrics and Their Applications* (Univ. of California Press, Berkeley, Calif., 1979; Mir, Moscow, 1981).
3. M. E. Lines and A. M. Glass, *Principles and Applications of Ferroelectrics and Related Materials* (Oxford Univ. Press, Oxford, 1977; Mir, Moscow, 1981).
4. L. I. Dontsova, N. A. Tikhomirova, and L. A. Shuvalov, Kristallografiya **39** (1), 158 (1994) [Crystallogr. Rep. **39**, 140 (1994)].
5. L. N. Kamysheva, N. A. Burdanina, O. K. Zhukov, *et al.*, Izv. Akad. Nauk SSSR, Ser. Fiz. **34** (12), 2612 (1970).
6. L. N. Kamysheva, S. D. Milovidova, and A. S. Sidorkin, J. Phys. Soc. Jpn., Suppl. B **49**, 24 (1980).
7. L. N. Kamysheva, S. N. Drozhdin, and O. M. Serdyuk, Zh. Tekh. Fiz. **58** (8), 1607 (1988) [Sov. Phys. Tech. Phys. **33**, 971 (1988)].
8. B. A. Strukov, S. A. Taraskin, Song Young Von, *et al.*, Izv. Akad. Nauk, Ser. Fiz. **57** (6), 12 (1993).
9. M. S. Tsedrik, *Physical Properties of Crystals from the Triglycine Sulfate Family* (Nauka i Tekhnika, Minsk, 1986).
10. L. N. Kamysheva, O. A. Kosareva, S. N. Drozhdin, and O. M. Golitsyna, Kristallografiya **40** (1), 93 (1995) [Crystallogr. Rep. **40**, 82 (1995)].
11. L. N. Kamysheva, O. M. Golitsyna, S. N. Drozhdin, *et al.*, Fiz. Tverd. Tela (St. Petersburg) **37** (2), 388 (1995) [Phys. Solid State **37**, 209 (1995)].
12. W. Windsch, Izv. Akad. Nauk SSSR, Ser. Fiz. **39** (5), 914 (1975).
13. A. T. Dem'yanchuk, Author's Abstracts of Candidate's Dissertation (Kiev, 1976).

Translated by N. Korovin

Physics of the Solid State, Vol. 44, No. 2, 2002, pp. 365–372. Translated from Fizika Tverdogo Tela, Vol. 44, No. 2, 2002, pp. 351–358.

MAGNETISM AND FERROELECTRICITY

Slow Polarization Processes in Relaxor Ferroelectrics

V. V. Gladkiĭ, V. A. Kirikov, and T. R. Volk

Shubnikov Institute of Crystallography, Russian Academy of Sciences, Leninskiĭ pr. 59, Moscow, 117333 Russia
e-mail: glad@ns.crys.ras.ru

Received June 7, 2001

Abstract—The general features of the slow polarization kinetics in relaxor ferroelectrics, observed and studied by us in the specific example of crystals of barium–strontium niobate (SBN) solid solutions of various compositions and of lead magnesium niobate (PMN), are considered. The dielectric hysteresis loops and spectra of the polarization relaxation time distribution in quasi-static and static electric fields were found to reveal characteristic anomalies related to a random internal electric field in the bulk of a relaxor ferroelectric. Such a field caused by structural disorder accounts for the anomalously broad spectrum of potential barriers for domain walls. The part played by free charge carriers in the formation of giant barriers is demonstrated. The paper presents some quantitative data characterizing the specific features of the structure and physical properties of the relaxors. © *2002 MAIK "Nauka/Interperiodica".*

1. INTRODUCTION

Relaxor ferroelectrics (relaxors), to which oxide solid solutions with perovskite [1–3] or tungsten bronze [2, 3] structure belong, are essentially inhomogeneous systems with a disordered structure and a number of unique physical properties. Unlike conventional homogeneous ferroelectrics, the phase transition and the anomalies in the properties of relaxors are broadened over a wide temperature region (the Curie region) and the dielectric, piezoelectric, pyroelectric, electrooptical, and nonlinear optical characteristics are extremely large in magnitude and only weakly temperature-dependent. In particular, the high dielectric permittivity ε exhibits a smooth maximum and a noticeable low-frequency dispersion at a temperature T_m [1–3].

The unique features in the physical properties of relaxors make them promising piezoelectric and optical materials [4, 5]. A new area of interest could be optical-frequency conversion by ferroelectric domains in barium–strontium niobate, which is made possible by the needle-shaped domain structure characteristic of these crystals [6–8].

Viewed solely from the standpoint of application, all relaxors have, apparently, a common shortcoming which consists in the irreproducibility of their properties and in the degradation of their parameters after exposure to an electric field. This lends particular importance to a comprehensive investigation of the processes involved in the evolution of the polarization, which affects virtually all the most significant physical characteristics. The anomalous dielectric properties of the relaxors have been studied heretofore primarily in low-frequency electric fields [1–3, 9]. This communication offers a brief overview of our recent works [10–12] and of some new results bearing on the specific features in the dielectric properties of relaxors in the infralow-frequency range, down to 10^{-5} Hz.

We immediately stress the radical difference between the $PbMg_{1/3}Nb_{2/3}O_3$ (PMN) and $Sr_xBa_{1-x}Nb_2O_6$ (SBN) crystals studied here. As is well known, in the absence of an electric field, the classical ferroelectric relaxor PMN does not undergo a phase transition from the relaxor to the ferroelectric state, which is accompanied by a change in the symmetry and by the nucleation of ferroelectric domains [1, 3]. In contrast, SBN crystals do transfer to the 4*mm* polar phase [13]. The diffuseness of the maximum of ε and its frequency dispersion in SBN are much less pronounced than those in PMN and become practically insignificant in some compositions. Nevertheless, the specific features of the polarization observed by us are characteristic of both types of crystals, which apparently permits one to assume the observed anomalies to be common for all ferroelectric relaxors.

2. THE CRYSTALS STUDIED

Relaxors have a convenient feature in that their properties can be varied by properly varying the chemical composition. For instance, increasing the Sr concentration in SBN [2, 3, 14] and doping it with rare-earth elements [5] considerably reduces the temperature T_m, increases the diffuseness of the phase transition, and makes the properties characteristic of relaxors more clearly pronounced. For the study, we chose SBN crystals with $x = 0.61$ doped with La and Ce to concentrations of 0.44 and 0.023 at. %, respectively, SBN : (La + Ce); with Nd to a concentration of 0.7–0.8 at. %, SBN : Nd; with Cr to a concentration of 2.2×10^4 ppm, SBN : Cr; and a PMN crystal. This particular choice of the crystals was motivated by the following considerations:

1063-7834/02/4402-0365$22.00

SBN : (La + Ce) has a strongly diffuse maximum of ε at a comparatively low temperature, T_m = 310–314 K, i.e., well-pronounced relaxor characteristics. For $T < T_m$, its electrical resistivity $\rho \geq 10^{13}$ Ω cm. SBN : Nd with T_m = 340 K has a considerably smaller $\rho \geq 10^{11}$ Ω cm for $T < T_m$ and, thus, is a convenient subject in studying the effect of polarization screening by free charge carriers; as will be shown later, this part played in the formation of giant barriers for domain walls is essential. The temperature T_m = 244 K of SBN : Cr is the lowest among all known SBNs, and $\rho \geq 10^{13}$ Ω cm at $T \cong T_m$, thus making it possible to study the observed anomalies electrometrically for $T > T_m$. For the PMN crystal, T_m = 269 K and $\rho \geq 10^{13}$ Ω cm in the vicinity of T_m.

3. EXPERIMENTAL TECHNIQUE

The evolution of the crystal polarization P with time t in static or slowly varying fields E was studied using compensation electrometry. The basic unit of the measuring setup is an equal-arm bridge, with one arm including the sample, the second including a reference capacitance C, and the third and fourth including the sources of reference (V) and of compensating $\nu(t)$ voltages. A V7-29 electrometer serving as a null indicator was connected to the bridge diagonal. The voltage across the diagonal was compensated using an IBM PC and peripheral units. The dependence of the compensating voltage $\nu(t)$ on time was reproduced in real time. The maximum sensitivity of the bridge was 20 μV in voltage and 2×10^{-9} μC in charge (at C = 10 pF). A detailed description of the computerized measuring setup for recording the P relaxation is given in [15]; for the hysteresis loops in [11].

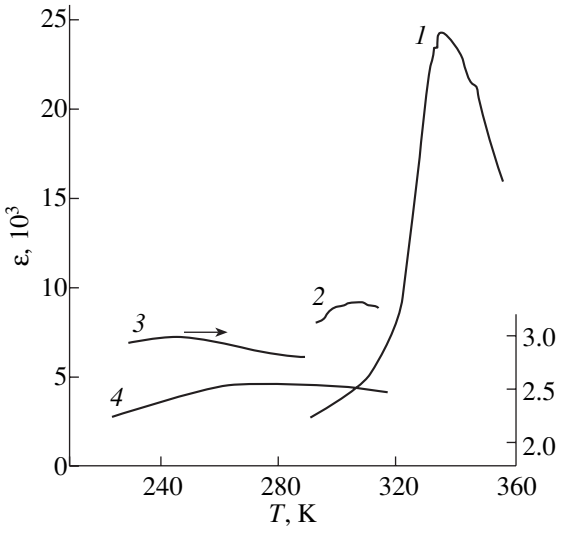

Fig. 1. Temperature dependences of permittivity ε of the relaxors (*1*) SBN : Nd, (*2*) SBN : (La + Ce), (*3*) SBN : Cr, and (*4*) PMN.

If the field applied to the sample is $E \neq 0$, then the contributions to $\nu(t)$ come, generally speaking, not only from the polarization P but also from the sample electrical conductivity 1/ρ; i.e., $\nu(t) = SP(t)/C + ESt/\rho C$, where S is the sample electrode area. For dielectrics with a high ρ (as a rule, not less than 10^{12} Ω cm), the inequality $Et/\rho \ll P(t)$ holds, in which case the second term in $\nu(t)$ can be neglected, yielding $P(t) = C\nu(t)/S$. If, however, ρ is so small that the inequality fails, one must correct the quantity $\nu(t)$, needed to calculate $P(t)$, for the electrical conductivity, thus reducing the accuracy of P determination. For the above crystals, this correction is essential only for the SBN : Nd composition. The electrical conductivity, which increases under crystal heating, places a constraint on the temperature range in which the application of electrometry gives reliable results. Therefore, we succeeded in measuring P with sufficient accuracy within a temperature range including T_m only for the SBN : Cr crystal, which has the lowest T_m = 244 K.

Quasi-static dielectric hysteresis loops were measured in electric fields E with a period of ~1 h. The polarization relaxation processes were recorded in static fields over several hours, and the smallest possible electrical resistivity was estimated after the relaxation had practically come to an end and the $\nu(t)$ dependence had become a straight line, $\nu(t) = ESt/\rho C$. The permittivity was measured using the standard bridge method at a frequency of 1 kHz.

4. RESULTS AND DISCUSSION

4.1. Quasi-Static Dielectric Hysteresis Loops

The maxima of ε in the crystals under study spread out over a broad temperature region (a feature which is characteristic of relaxors, Fig. 1) and have a low-frequency dispersion (not shown in the figure).

The quasi-static dielectric hysteresis loops of the dependence of polarization P on electric field E have an unusual shape (Fig. 2). Unlike the loops observed in a conventional homogeneous ferroelectric (Fig. 2a), the initial loop cycles of all relaxors do not close and do not reproduce one another and the amplitude of P decreases. After a few cycles of slow polarization reversal, the polarization amplitude stops decreasing and all the subsequent loop trajectories coincide; in other words, they become reproducible, as usual.

The diffuseness of the ε maximum in temperature and the irreproducibility of the first few loop trajectories are, apparently, interconnected phenomena. In other words, the anomalous shape of the hysteresis loop of a relaxor is also its characteristic feature. All the relaxor loops presented in Fig. 2 were obtained at temperatures below T_m (for PMN, below the field-induced ferroelectric phase transition [16]). The loop for SBN : Nd was constructed with due inclusion of cor-

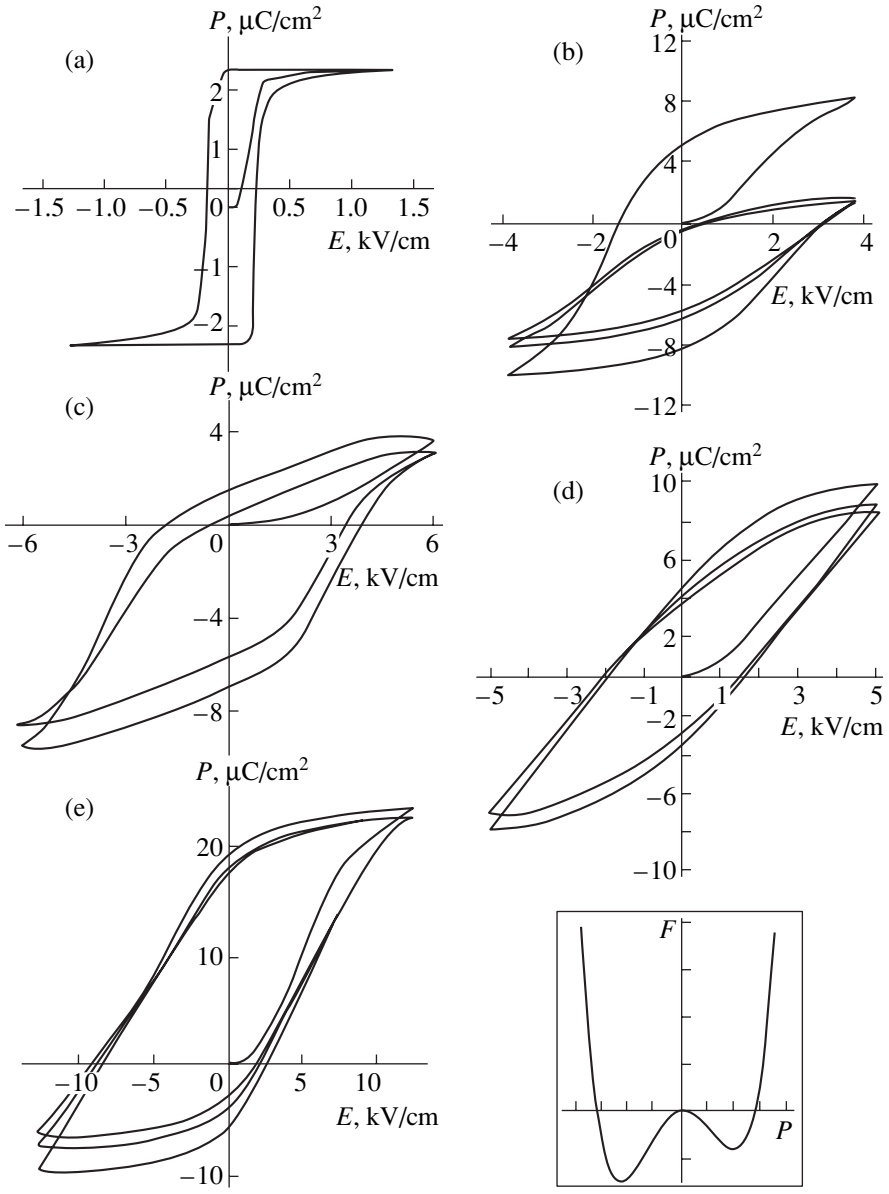

Fig. 2. Quasi-static dielectric hysteresis loops of (a) TGS and the relaxors (b) SBN : (La + Ce), (c) SBN : Nd, (d) SBN : Cr, and (e) PMN obtained at 293, 274, 273, 206, and 210 K, respectively. Inset: local free energy F plotted vs. P.

rections for the electrical conductivity (Fig. 2c). In the SBN : Cr crystals, the field dependences of polarization were studied within the temperature range including T_m. The hysteresis loop and its characteristic anomalies (Fig. 2) persist up to temperatures 30 K above T_m, with the loop amplitude falling off smoothly with temperature [17].

The existence of loops for $T > T_m$, which is characteristic of relaxor ferroelectrics, is in qualitative agreement with estimates of the local spontaneous polarization made within the same wide temperature range from the temperature dependences of birefringence and thermal expansion of undoped SBN [18]. The hysteresis loop anomalies are in accordance with present ideas concerning the polar structure of the relaxors [3]. Disordered distribution of some ions gives rise to internal electric fields E_i lowering the local symmetry; the local free energy F should be an asymmetric double-minimum function of P, namely, $F = -\alpha P^2 + \beta P^4 - (E_i + E)P$, where α and β are constants and E is the external field (inset to Fig. 2). The field E_i, the depth of the minima, and the height of the barrier separating these minima are distributed in a random manner in the relaxor volume within a broad range of values. As a result, before field application, one part of the volume resides in the metastable state and the other is in the stable state,

which corresponds to shallow and deep minima, respectively. When an alternating ac field E of a certain amplitude is applied, the shape of the F function becomes distorted, the barriers are lowered, and relaxation to stable states with deep minima is accelerated. The reverse process virtually does not occur if $|E| < |E_i|$. In other words, part of the relaxor volume is not involved in the subsequent polarization switching (remains frozen) and the amplitude of P in the repeating cycles of E variation falls off gradually down to the value of the total polarization of the part of the volume in which the condition $|E| > |E_i|$ holds. Obviously enough, the total reproducible polarization switching of the crystal as a whole, with coinciding loop cycles, is possible only in fields E in excess of the maximum level E_i, which is apparently quite high.

4.2. Polarization Switching in Ferroelectric Relaxors

An idea of the height of the barriers separating the stable and metastable states, as well as more detailed information on the shape of the relaxor hysteresis loops, can be gained by studying the polarization kinetics in static electric fields E. Figure 3 presents the results of the measurement and analysis of the dependence of polarization P on time t made for different values of E for the relaxors SBN : (La + Ce) [11], SBN : Cr [17], and the homogeneous ferroelectric TGS [15].

Note the following main differences in the P relaxation between TGS and the relaxors. In TGS, the internal field $E_i = 0$ everywhere, the free energy F is a symmetric function of P for $E = 0$, and the spontaneous polarization $P_s = (\alpha/2\beta)^{1/2}$ and the coercive field $E_c = (2\alpha/3)[(2\alpha/3)/\beta]^{1/2}$ (which coincides with the half-width of the hysteresis loop) are clearly defined. In external fields $E > E_c$, polarization proceeds in an avalanche manner, whereas for $E < E_c$, polarization is a thermally activated slow process, practically without a jump in P at the instant of E application. The equilibrium polarization P_e is always equal to P_s and does not depend on the magnitude of E. The rate of relaxation grows with E. Thus, when an external field of any magnitude is applied to a homogeneous ferroelectric, the polarization reaches the same level $P_e = P_s$, albeit with different kinetics.

In relaxors placed in a field E larger or smaller than the half-width of the loop, the polarization P changes initially in a jump, to vary thereafter in a thermally activated manner (insets to Fig. 3). The jumps ΔP observed to occur at any value of E indicate the absence of a distinct coercive field E_c in the relaxor; its magnitude is different in different parts of the crystal. An increased E polarizes a larger volume of the crystal, and the jump ΔP naturally increases. As will be shown later, relaxors also do not have a distinct equilibrium polarization P_e; more specifically, to each external field corresponds a certain value of P_e which increases with E (Fig. 3).

In all crystals, the slow thermally activated stage of relaxation follows a power-law course,

$$p(t) = (P_e - P(t))/(P_e - P_0) = 1/(1 + t/a)^n, \quad (1)$$

where P_0 is the original polarization (at $t = 0$) and a, n, and P_e are fitting parameters.

Assuming the relaxation centers to be independent, their contribution can be considered additive, so that

$$p(t) = \int_0^\infty f(\tau)\exp(-t/\tau)d\tau, \quad (2)$$

where $f(\tau)$ is a normalized distribution function of the relaxation times τ. One may find it more convenient to use a dimensionless distribution function g of $\ln\tau$ or of the barrier energy $U = kT\ln(\tau/\tau_0)$ (τ_0 is a kinetic coefficient):

$$g = \tau f(\tau) = (1/\Gamma(n))(a/\tau)^n\exp(-a/\tau), \quad (3)$$

where $\Gamma(n)$ is the gamma function and τg is related to $p(t)$ through the Laplace transform [19].

In analysis of the experimental data, power law (1) is preferable to the well-known empirical Kohlrausch relation $p(t) \sim \exp(-t/\tau)^\beta$, where $\beta < 1$, which, as can be readily verified, also reasonably accurately describes our results obtained over long periods of time. First, Eq. (1) better reproduces the experimental behavior at short times (dp/dt is finite for $t \longrightarrow 0$). Second, relation (1) corresponds to a simple distribution function $f(\tau)$ in Eq. (2) for any value of a and n [15].

Note that the power relation (1) is apparently of a universal nature, because under some conditions it describes nonexponential forms observed frequently to hold in inhomogeneous systems. For instance, $p(t) \sim 1/t^n$ for $t \gg a$, $p(t) \sim 1 - (n/a)t$ for $t \ll a$, and $p(t) \sim 1 - n\ln(1 + t/a)$ for $n \ll 1$ [12]. Equation (1) also describes the relaxation in $K_{1-x}Li_xTaO_3$ mixed crystals in the glassy state [20].

The measured values of P were least squares fitted by power relation (1) with free fitting parameters a, n, and P_e using the standard technique. The solid lines in Fig. 3 plot our calculations, and the circles are experimental points. The deviation of the experimental values of P from the calculations does not exceed 0.5%. Note that the errors in determination of the parameters (Table 1) decrease with increasing time interval of the relaxation measurement [21].

Let us consider the difference between the $g(\ln\tau)$ spectra with maxima $g_{\max}$ at $\tau_m = a/n$ obtained for TGS and the relaxors. For TGS studied in weak fields $E < E_c$, the spectrum g becomes more narrow and shifts toward short τ with increasing E, thus exhibiting a trend in the values of U of all barriers to decrease and become closer in magnitude as E approaches E_c (Fig. 3a). Relaxors do not demonstrate such a distinct dependence of the spectral shape on E within a field interval.

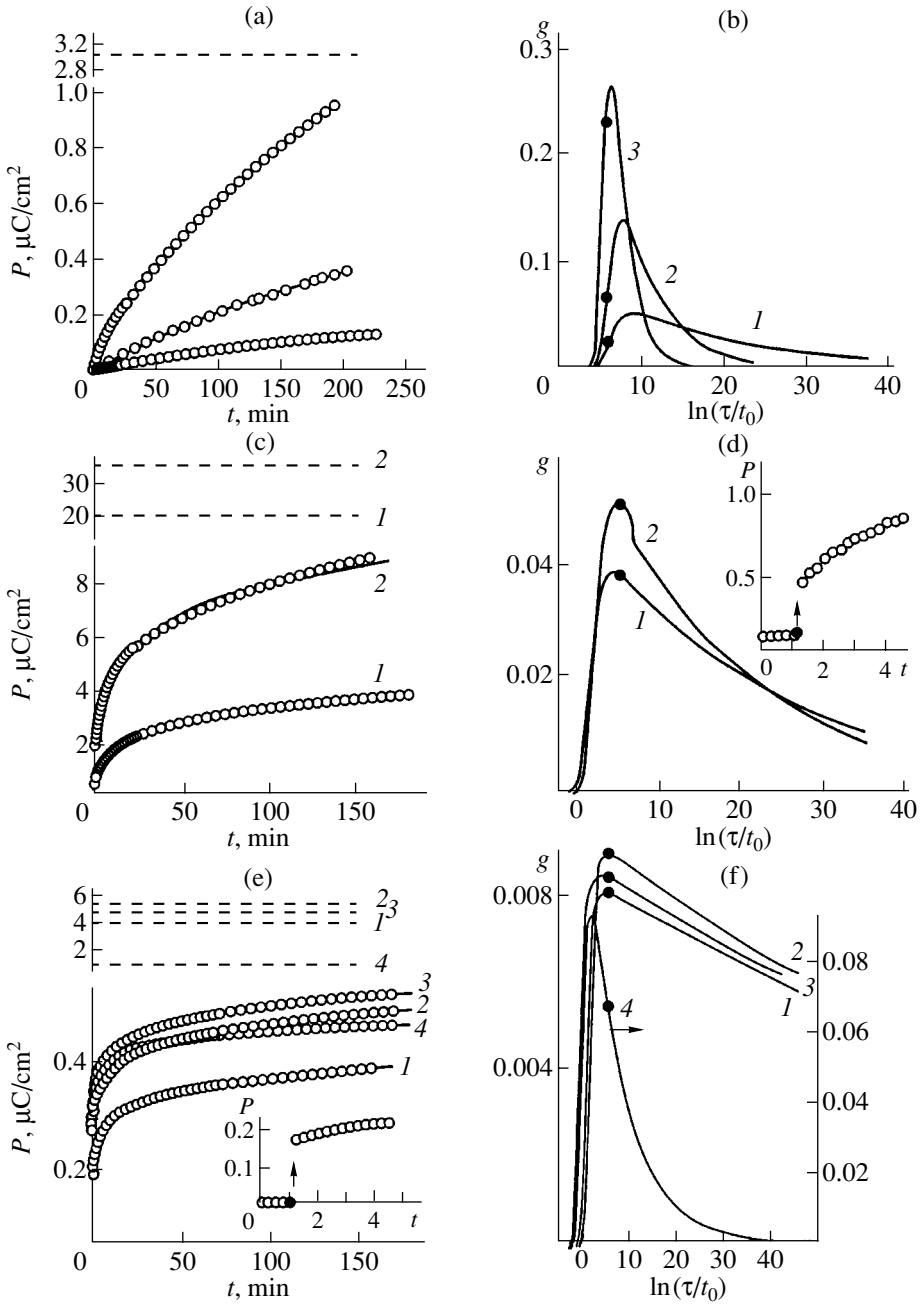

Fig. 3. (a, c, e) Polarization relaxation $P(t)$ and (b, d, f) spectra $g(\ln\tau)$ obtained at different fields E and temperatures T on (a, b) TGS and the relaxors (c, d) SBN : (La + Ce) and (e, f) SBN : Cr. (a, b) E is equal to (*1*) 5.6, (*2*) 16, and (*3*) 25 V/cm and T = 293 K; (c, d) E is equal to (*1*) 300 and (*2*) 600 V/cm and T = 274 K; and (e, f) E = 430 V/cm and T is equal to (*1*) 205, (*2*) 236, (*3*) 249, and (*4*) 268 K; t_0 = 1 min. Solid lines are calculated results, and circles are experimental results. Dashed lines are equilibrium values P_e. Insets show the beginning of the relaxor polarization processes (the jumps in P are identified by arrows).

Although the fraction of the polarized volume within which the E_c fields assume different values naturally increases with increasing E, the contributions of slow processes to the polarization may accidentally turn out to be the same and the spectra may almost coincide (Fig. 3b). Heating a relaxor above T_m shifts the g spectrum toward short τ and narrows it, which means that the relaxation processes become faster (Fig. 3c). The points in the spectra specify values of τ equal to the maximum relaxation measurement times t_{max}. The spectra measured for $\tau > t_{max}$ were obtained by extrapolating the available data to longer times. As demonstrated by SBN : Nd, relaxors may have giant values of τ; for example, for $\ln(\tau/t_0) = 10$, where t_0 = 1 min, we have τ = 15 days, and for $\ln(\tau/t_0) = 30$, we have τ = 10 years.

Table 1. Parameters of P relaxation and of spectra $g(\ln\tau)$ in the polarization of TGS, SBN : (La + Ce) and SBN : Cr crystals

Crystal	T, K	E, V/cm	P_e, μC/cm^2	a, min	n	τ_m, min
TGS	293	5.6	3.0	240 ± 10	0.063 ± 0.002	3800 ± 270
		16	3.0	270 ± 10	0.22 ± 0.03	1225 ± 85
		25	3.0	224 ± 8	0.60 ± 0.02	380 ± 30
SBN : (La + Ce)	273	300	4.50 ± 0.02	3.724 ± 0.012	0.045 ± 0.001	82.2 ± 0.3
		400	6.97 ± 0.02	4.35 ± 0.013	0.038 ± 0.001	114.5 ± 0.4
		600	8.60 ± 0.013	4.80 ± 0.007	0.058 ± 0.001	82.70 ± 0.2
SBN : Cr	205	430	4.03 ± 0.01	0.88 ± 0.05	0.010 ± 0.0002	88.0 ± 7
	236		5.34 ± 0.01	1.66 ± 0.09	0.009 ± 0.0002	184 ± 14
	249		4.82 ± 0.01	0.37 ± 0.04	0.0089 ± 0.0002	42 ± 5
	267.7		0.67 ± 0.001	0.54 ± 0.05	0.132 ± 0.001	4.1 ± 0.4

Table 2. Parameters of P relaxation and of spectra $g(\ln\tau)$ in the depolarization of SBN : (La + Ce) and SBN : Nd crystals

Impurity	T, K	E, V/cm	P_e, μC/cm^2	a, min	n	τ_m, min
La : Ce	274	500	1.217 ± 0.003	0.82 ± 0.06	0.273 ± 0.004	3.0 ± 0.3
		650	1.874 ± 0.004	0.38 ± 0.02	0.157 ± 0.001	2.40 ± 0.14
		800	2.866 ± 0.006	0.094 ± 0.004	0.081 ± 0.001	1.16 ± 0.06
Nd	273	1000	1.3 ± 0.1	2.0 ± 0.3	0.012 ± 0.0004	167 ± 30
		2000	13.20 ± 0.06	2.92 ± 0.13	0.022 ± 0.0003	133 ± 7

4.3. Effect of Electrical Conductivity on the Relaxation Processes

To correctly estimate the polarization P, one has to subtract the linear-in-time contribution to the measured compensating voltage $\nu(t)$ due to the electrical conductivity (see Section 3). This contribution is significant, and it introduces a noticeable error in the determination of P only in the case of SBN : Nd [12]. For this reason, the $\nu(t)$ curves which fairly rapidly became straight lines due to conductivity in the course of polarization of SBN : Nd were not analyzed.

The part played by electrical conductivity in relaxation processes manifests itself clearly in depolarization measurements. In this case, $E = 0$ and the electrical conduction through the sample, which masks the relaxation, is absent, thus allowing a sufficiently precise analysis of the experimental data to be made. Figure 4 presents P relaxation curves obtained under depolarization in SBN : (La + Ce) and SBN : Nd. The depolarization was measured after the crystals had been polarized in various fields E for 5 min. As in the case of polarization (Fig. 3), the process starts with a jump ΔP, after which it becomes thermally activated and strictly follows a power-law behavior described by Eq. (1). The solid lines in Fig. 4 are plots of Eq. 1, and the circles are experimental data. The dashed lines are the equilibrium values P_e, which are higher, the larger the polarizing field.

The spectra g for the thermally activated stages of relaxation were calculated using Eq. (3) with the parameters listed in Table 2. The points in the spectra identify the time to which the depolarization was measured. The spectra $g(\ln\tau)$ of SBN : Nd are wider and contain giant relaxation times, despite the high prepolarization fields employed.

The reason for the giant times τ and barrier energy U may lie in the screening of the polarized regions in the crystal by free carriers [12]. Indeed, as follows from straightforward estimates, the screening times $\tau_{sc} = \varepsilon\rho/4\pi$ are 1000 and 10 min for the SBN : (La + Ce) and SBN : Nd, respectively (τ_{sc} was estimated using the data on the static permittivity $\varepsilon = 4\pi P/E$ given in Fig. 2). Hence, the relaxation measurement time ~120 min is long enough for the inhomogeneously polarized regions in the low-resistivity SBN : Nd relaxor to become screened and this process is accompanied by the formation of inhomogeneously distributed fields E_{sc} of the screening charge. This increases the height of the potential barriers, relaxation times, and equilibrium values of P_e (crystal memory). Note that screening may also account for the large width of the dielectric hysteresis loops of the SBN : Nd relaxor.

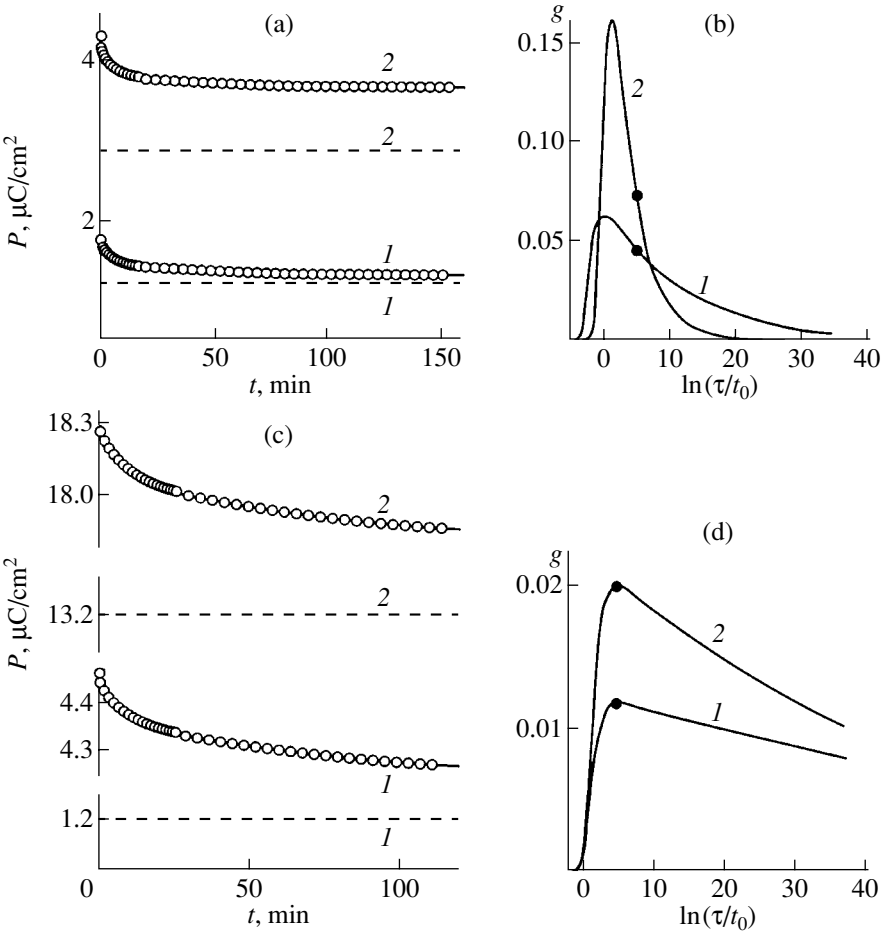

Fig. 4. Depolarization and spectra $g(\ln\tau)$ for the relaxors (a, b) SBN : (La + Ce) and (c, d) SBN : Nd. (a, b) The polarizing field E is equal to (*1*) 500 and (*2*) 800 V/cm; and (c, d) E is equal to (*1*) 1000 and (*2*) 2000 V/cm, t_0 = 1 min. Solid lines are calculated results, and circles are experimental results. Dashed lines are equilibrium values P_e.

4.4. Temperature Dependence of the Relaxor Relaxation Parameters

An idea of the temperature dependence of the parameters may be gained from an inspection of Fig. 5, which presents measured values of the jump ΔP observed in SBN : Cr with the application of E, the equilibrium polarization P_e, and the relaxation time $\tau_m = a/n$ corresponding to the maximum of the distribution function g. Similar to the properties measured in alternating fields, these parameters vary smoothly with temperature. The jump ΔP occurring in a weak field grows slowly and monotonically with temperature, because the energies U of an ever increasing number of barriers approach zero, while P_e and τ_m pass through maxima near T_m, with the time τ_m decreasing by a factor of approximately 30 as the crystal is heated by 20 K above T_m, which likewise argues for the decrease in the barrier height. The maxima of P_e and of τ_m become ever smoother as the polarizing field E increases [17]. These features correlate with the temperature dependences of the hysteresis loop parameters. As the temperature is lowered, the hysteresis loop anomalies become less distinct for the external fields employed due to the increase in the potential barriers [10, 11]; as the temperature

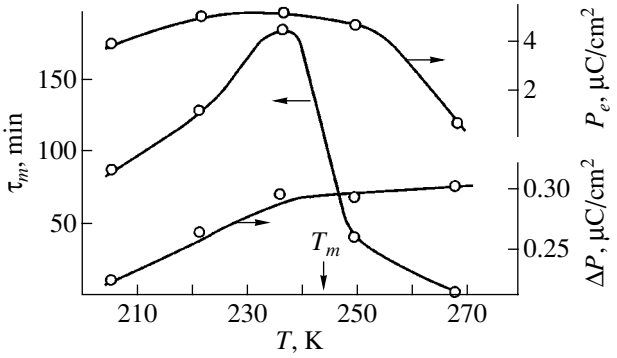

Fig. 5. Temperature dependences of the parameters ΔP, P_e, and τ_m of P relaxation and spectra of $g(\ln\tau)$ obtained for an electric field E = 430 V/cm near the T_m point of the SBN : Cr relaxor.

increases, the anomalies also become less pronounced as a result of the decrease in the polarization [17].

5. CONCLUSIONS

Thus, all the relaxor ferroelectrics studied (SBN of various compositions, PMN) have been found to exhibit similar anomalies in the polarization kinetics, which manifest themselves in specific features in the dielectric hysteresis loops (the first few loop cycles are open and do not reproduce, the absence of a distinct coercive field and equilibrium polarization) and in broad spectra of the potential-barrier distribution exhibiting giant amplitudes. These anomalies are a signature and a measure of structural disorder in relaxors. The anomalies are only observed in static and quasistatic electric fields and have not been revealed before, apparently, because of the measurements having been performed on overly short time scales. The results obtained can account for the irreproducibility of the various properties of relaxors known from the literature, as well as permit one to relate it to partial freezing of the polarization after application of an external factor (an electric field). Studies on the polarization kinetics in other ferroelectrics also show that similar indications of structural disorder, albeit less pronounced, can also be observed in conventional homogeneous crystals. In contrast to the rectangular profile, the slim shape of hysteresis loops seen in traditionally employed low-frequency electric fields is the clearest indication of the absence of a distinct coercive field in a given sample [21, 22].

The main results presented in this paper can be used to characterize various inhomogeneous materials with long-lived metastable states.

ACKNOWLEDGMENTS

The authors are indebted to L.I. Ivleva (Institute of General Physics, Russian Academy of Sciences) and R. Pankrath (Physical Department of the Osnabrück University, Germany) for providing SBN crystals of various compositions, S.G. Lushnikov (Ioffe Physicotechnical Institute, Russian Academy of Sciences) for the PMN crystal, and S.V. Nekhlyudov for setting up the equipment.

This study was supported by the Russian Foundation for Basic Research, project nos. 99-02-17303 and 00-02-16624.

REFERENCES

1. G. A. Smolenskiĭ, V. A. Bokov, V. A. Isupov, N. N. Kraĭnik, R. E. Pasynkov, and M. S. Shur, *Ferroelectrics and Antiferroelectrics* (Nauka, Leningrad, 1971), p. 355.
2. M. E. Lines and A. M. Glass, *Principles and Applications of Ferroelectrics and Related Materials* (Oxford Univ. Press, Oxford, 1977; Mir, Moscow, 1981).
3. L. E. Cross, Ferroelectrics **76**, 241 (1987).
4. R. R. Neurgaonkar, J. R. Oliver, W. K. Cory, *et al.*, Ferroelectrics **160**, 265 (1994).
5. T. R. Volk, V. Yu. Salobutin, L. I. Ivleva, *et al.*, Fiz. Tverd. Tela (St. Petersburg) **42** (11), 2066 (2000) [Phys. Solid State **42**, 2129 (2000)].
6. S. Kawai, T. Ogawa, H. S. Lee, *et al.*, Appl. Phys. Lett. **73** (6), 768 (1998).
7. A. A. Kaminskiĭ, J. García Sole, S. N. Bagaev, *et al.*, Kvantovaya Élektron. (Moscow) **25** (12), 1059 (1998).
8. J. J. Romero, D. Jaque, J. García Sole, and A. A. Kaminskii, Appl. Phys. Lett. **78** (14), 1961 (2001).
9. F. M. Salaev, L. S. Kamzina, and N. N. Kraĭnik, Fiz. Tverd. Tela (St. Petersburg) **34** (6), 999 (1992) [Sov. Phys. Solid State **34**, 983 (1992)].
10. V. V. Gladkiĭ, V. A. Kirikov, S. V. Nekhlyudov, *et al.*, Pis'ma Zh. Éksp. Teor. Fiz. **71** (1), 38 (2000) [JETP Lett. **71**, 24 (2000)].
11. V. V. Gladkiĭ, V. A. Kirikov, S. V. Nekhlyudov, *et al.*, Fiz. Tverd. Tela (St. Petersburg) **42** (7), 1296 (2000) [Phys. Solid State **42**, 1334 (2000)].
12. V. V. Gladkiĭ, V. A. Kirikov, T. R. Volk, and L. I. Ivleva, Zh. Éksp. Teor. Fiz. **120** (3), 678 (2001) [JETP **93**, 596 (2001)].
13. P. B. Jamieson, S. C. Abrahams, and J. L. Bernstein, J. Chem. Phys. **48**, 5048 (1968).
14. Yu. S. Kuz'minov, *Ferroelectric Crystals for Laser Emision Control* (Nauka, Moscow, 1982), p. 400.
15. V. V. Gladkiĭ, V. A. Kirikov, S. V. Nekhlyudov, and E. S. Ivanova, Fiz. Tverd. Tela (St. Petersburg) **39** (11), 2046 (1997) [Phys. Solid State **39**, 1829 (1997)].
16. Z.-G. Ye and H. Schmid, Ferroelectrics **145**, 83 (1993).
17. V. V. Gladkiĭ, V. A. Kirikov, E. V. Pronina, *et al.*, Fiz. Tverd. Tela (St. Petersburg) **43** (11), 2052 (2001) [Phys. Solid State **43**, 2140 (2001)].
18. A. S. Bhalla, R. Guo, L. E. Cross, *et al.*, Phys. Rev. B **36** (4), 2030 (1987).
19. V. I. Ditkin and A. P. Prudnikov, *Handbook of Operation Calculus* (Vysshaya Shkola, Moscow, 1965), p. 466.
20. F. Allberici, P. Doussineau, and A. Levelut, J. Phys. I **7** (2), 329 (1997).
21. V. V. Gladkiĭ, V. A. Kirikov, E. S. Ivanova, and S. V. Nekhlyudov, Fiz. Tverd. Tela (St. Petersburg) **41** (3), 499 (1999) [Phys. Solid State **41**, 447 (1999)].
22. V. V. Gladkiĭ and V. A. Kirikov, Fiz. Tverd. Tela (St. Petersburg) **43** (1), 111 (2001) [Phys. Solid State **43**, 113 (2001)].

Translated by G. Skrebtsov

Physics of the Solid State, Vol. 44, No. 2, 2002, pp. 373–378. Translated from Fizika Tverdogo Tela, Vol. 44, No. 2, 2002, pp. 359–364.

LATTICE DYNAMICS AND PHASE TRANSITIONS

Normal Vibrational Modes in Benzil Crystals

M. A. Ivanov*, V. A. Kimasov*, and Yu. F. Markov**

** Institute of Physics, St. Petersburg State University, ul. Pervogo maya 100, Petrodvorets, 198904 Russia*

*** Ioffe Physicotechnical Institute, Russian Academy of Sciences, ul. Politekhnicheskaya 26, St. Petersburg, 194021 Russia*

e-mail: Yu.Markov@pop.ioffe.rssi.ru

Received July 5, 2001

Abstract—A group-theoretical analysis of the vibrational spectrum of benzil crystals was carried out. The selection rules and normal coordinates were found. Raman scattering spectra of benzil single crystals were studied in polarized light within a broad temperature range from 100 K to the melting point (T_m = 96°C). The experimental data were found to correlate with theory. The temperature dependences of the spectral-line half-widths were used to separate the observed vibrations into translational and librational modes, and the correspondence between the experimentally observed vibrations and their normal coordinates was established in some cases.

1. INTRODUCTION

Benzil $(C_6H_5–CO)_2$, whose molecules consist of two phenyl rings and two CO groups, is an interesting representative of organic compounds. At room temperature, these crystals have trigonal (rhombohedral) symmetry $D_3^{4,6}$ ($P3_{1,2}21$) with three molecules (formula units) in a unit cell (see, for instance, Fig. 1) [1, 2]. Quartz has the same symmetry (space group) at room temperature, which accounts for benzil being frequently called "organic quartz." When cooled down to T_c = 83.5 K, benzil crystals undergo a structural phase transition from the higher temperature trigonal phase to the monoclinic C_2^2 ($P2_1$) phase [3]. This transition is assumed to be triggering; in other words, the lattice becomes unstable at the center of the Brillouin zone (the Γ point), which is accompanied by a softening of the acoustic (TA) and optical (TO) phonon modes in the Brillouin [4] and Raman [5] spectra, respectively, and this induces an instability at the *M* point of the Brillouin zone edge of the paraelastic phase through order parameter interaction [6]. This ferroelastic triggering phase transition brings about a unit-cell doubling, an $M \longrightarrow \Gamma$ folding of the Brillouin zone, and spontaneous deformation. Benzil (organic quartz) is a model organic crystal for use in studying the general aspects of lattice dynamics and structural phase transitions.

The purpose of this work was to study Raman spectra of benzil single crystals for $T > T_c$ up to the melting point; to obtain information on the temperature behavior of phonon modes, including their frequencies and half-widths; to separate the experimentally observed vibrations into translational and librational modes; and to determine their normal coordinates.

2. NORMAL VIBRATIONAL MODES OF BENZIL CRYSTALS

The unit cell of benzil crystals contains three molecules (Z = 3) located along the threefold screw axis (Fig. 1), with the C_2 axis of each of the molecules coinciding with the corresponding C_2 axis of the crystal. The spectra exhibit three acoustic vibration modes of A_2 and E symmetry (twofold degenerate) and $6Z – 3 = 15$ external optical vibration modes, some of which are of

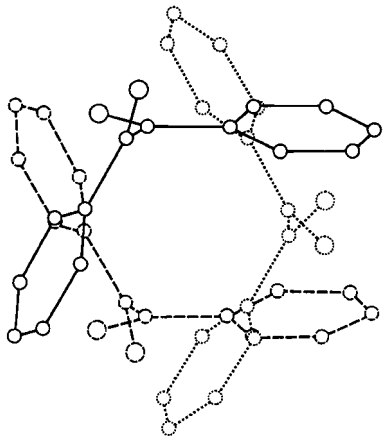

Fig. 1. Projection of the primitive cell of a benzil crystal on the (001) plane [1, 2]. The small circles are carbon atoms, and the large ones are oxygen atoms; the inequivalent $C_6H_5COCOC_6H_5$ molecules displaced by 1/3 period along the C_3 screw axis are denoted by different (solid, dashed, and dotted) lines.

1063-7834/02/4402-0373$22.00

the translational and the remaining, of the orientational, type. Group-theoretical consideration made in the rigid-molecule approximation (with each molecule assumed to displace or rotate as a whole) yielded decomposition of the representation of external optical vibrations (Γ_{ext}), including vibrations of the translational (Γ_{tr}) and orientational (Γ_{or}) types, into irreducible representations of the D_3 point symmetry group (the Brillouin zone center):

$$\begin{aligned}\Gamma_{ext} &= 2A_1 + 3A_2 + 5E,\\ \Gamma_{tr} &= A_1 + A_2 + 2E,\\ \Gamma_{or} &= A_1 + 2A_2 + 3E.\end{aligned} \tag{1}$$

Thus, two vibration modes of symmetry $A_1(xx, yy, zz)$ and five twofold degenerate vibration modes of symmetry $E(xx, yy, xz, yz, xy)$ are Raman active and three vibration modes of symmetry $A_2(z)$ and five of symmetry $E(x, y)$ are active in IR absorption (reflection). Group-theoretical analysis (see, e.g., [7]) also permits one to find the eigenvectors for the above acoustic and external optical vibrations:

$$\begin{aligned}&A_1:\ x_1 - 2x_2 + x_3 - \sqrt{3}y_1 + \sqrt{3}y_3,\\ &l_x^1 - 2l_x^2 + l_x^3 - \sqrt{3}l_y^1 + \sqrt{3}l_y^3;\\ &A_2:\ z_1 + z_2 + z_3,\quad x_1 - x_3 + \frac{\sqrt{3}}{3}y_1 - 2\frac{\sqrt{3}}{3}y_2 + \frac{\sqrt{3}}{3}y_3,\\ &l_z^1 + l_z^2 + l_z^3,\quad l_x^1 - l_x^3 + \frac{\sqrt{3}}{3}l_y^1 - 2\frac{\sqrt{3}}{3}l_y^2 + \frac{\sqrt{3}}{3}l_y^3;\\ &E_x:\ x_1 + x_2 + x_3,\\ &y_1 - y_3 + \frac{\sqrt{3}}{3}x_1 - 2\frac{\sqrt{3}}{3}x_2 + \frac{\sqrt{3}}{3}x_3,\\ &z_1 - z_3,\quad l_x^1 + l_x^2 + l_x^3,\\ &l_y^1 - l_y^3 + \frac{\sqrt{3}}{3}l_x^1 - 2\frac{\sqrt{3}}{3}l_x^2 + \frac{\sqrt{3}}{3}l_x^3,\quad l_z^1 - l_z^3;\\ &E_y:\ y_1 + y_2 + y_3,\\ &x_1 - x_3 - \frac{\sqrt{3}}{3}y_1 + 2\frac{\sqrt{3}}{3}y_2 - \frac{\sqrt{3}}{3}y_3,\\ &\frac{\sqrt{3}}{3}z_1 - 2\frac{\sqrt{3}}{3}z_2 + \frac{\sqrt{3}}{3}z_3,\quad l_y^1 + l_y^2 + l_y^3,\\ &l_x^1 - l_x^3 - \frac{\sqrt{3}}{3}l_y^1 + 2\frac{\sqrt{3}}{3}l_y^2 - \frac{\sqrt{3}}{3}l_y^3,\\ &\frac{\sqrt{3}}{3}l_z^1 - 2\frac{\sqrt{3}}{3}l_z^2 + \frac{\sqrt{3}}{3}l_z^3,\end{aligned} \tag{2}$$

where x_i, y_i, z_i and l_x^i, l_y^i, l_z^i (i = 1–3) are displacements of the centers of gravity of the molecules and their rotation angles about the *x*, *y*, and *z* axes, respectively.

Figure 2 shows all the above normal modes. The fully symmetric A_1 vibrations consist of the translational and orientational vibration modes [the first and second polynomials in Eq. (2), respectively]. In the first case, all three inequivalent molecules [shifted by 1/3 period with respect to one another along the $C_3(z)$ screw axis] are displaced in the (001) plane, each along its C_2 axis with the same amplitude (translation), and in the second case, all molecules rotate in phase (libration), each about its C_2 axis (Fig. 2a). The displacements $z_1 + z_2 + z_3$ (A_2 symmetry, Fig. 2c) and $x_1 + x_2 + x_3$, $y_1 + y_2 + y_3$ (E symmetry, Figs. 2e, 2h) relate to acoustic vibrations. The IR-active optical vibrations A_2 are in-phase translations perpendicular to the C_2 axes of molecules in the (001) planes, molecular librations about these translation directions, and in-phase librations about the *z* axis (Figs. 2b, 2c). The eigenvectors of the twofold-degenerate vibration modes of the E symmetry (E_x, E_y) in Eqs. (2) are also displayed. These modes involve translations in the (001) planes (Figs. 2d, 2g) and along the C_3 axis (Figs. 2f, 2i) and orientational vibrations in the planes perpendicular to the directions of these translations (Figs. 2d, 2f, 2g, 2i), as well as about the *x* and *y* directions (Figs. 2e, 2h).

3. EXPERIMENTAL TECHNIQUE

Raman scattering measurements on benzil single crystals were performed on a DILOR-Z24 triple-grating Raman spectrometer, with argon and helium–neon lasers of a low variable power (50–200 mW) used for pumping. Low-power operation was chosen to avoid local heating and possible surface damage of the slightly yellow crystals used. Our samples were high-quality benzil single crystals grown from solutions in different solvents (ether, alcohol, xylene, etc.) with $5 \times 5 \times 10$-mm edges along the *x*, *y*, and *z* axes, respectively. The *z* axis of the samples is taken along the optical axis of the crystals, i.e., along the screw axis C_3. The temperature dependences of the spectra were measured in closed-flow Cryogenic cryostats capable of maintaining the temperature to within ~0.1 K.

4. EXPERIMENTAL RESULTS

We studied Raman spectra of oriented benzil single crystals in polarized light over a broad temperature range, from low temperatures ($T > T_c$) up to the melting point (96°C). Main attention was focused on studying external optical vibrations (lattice modes) whose frequencies lie in the low-frequency domain, ~0–100 cm^{-1}. Figure 3 presents typical Raman spectra obtained at a few fixed temperatures for the most characteristic polarizations (*zz* vibrations of the A_1 symmetry, *yz* and

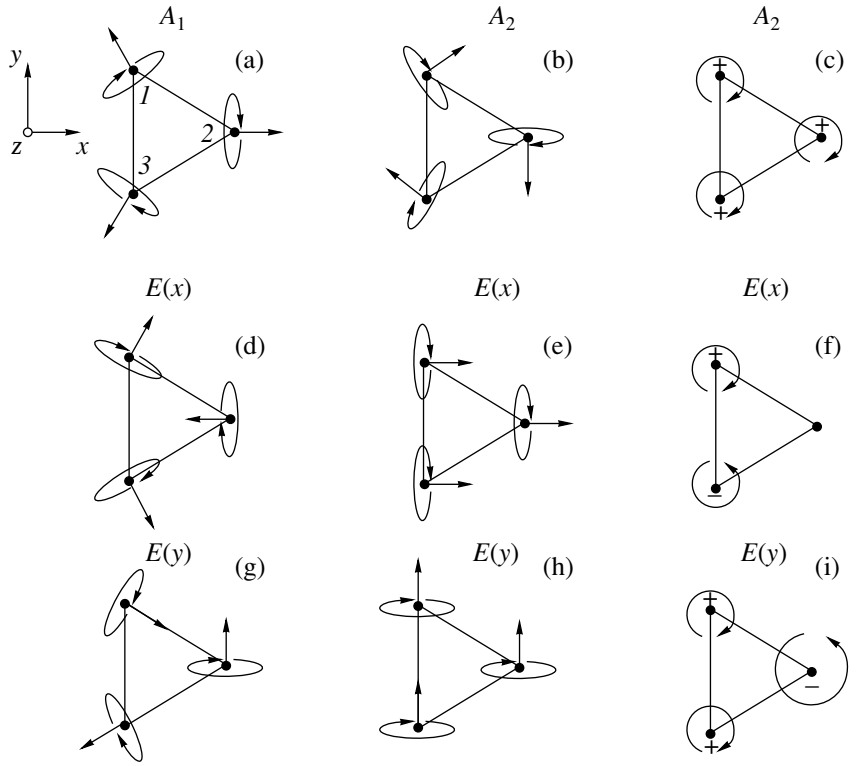

Fig. 2. Eigenvectors of the fundamental lattice vibrations of benzil crystals of symmetry (a) A_1, (b, c) A_2, and (d, g; e, h; f, i) E. The straight arrows [or +(–) in the case of displacements along the C_3 axis perpendicular to the plane of the figure] specify the displacements of the centers of gravity of the molecules (filled circles) in translational vibrations; the displacements in orientational vibrations are denoted by arrows lying on the ellipses (circles).

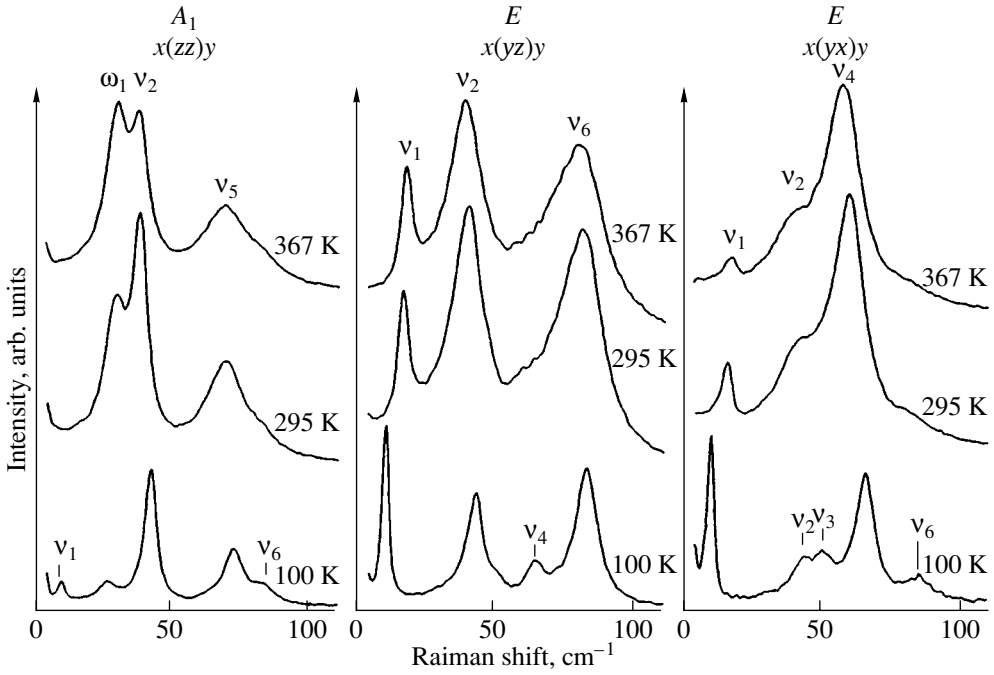

Fig. 3. Low-frequency (lattice) Raman spectra of benzil crystals obtained at different temperatures and polarizations.

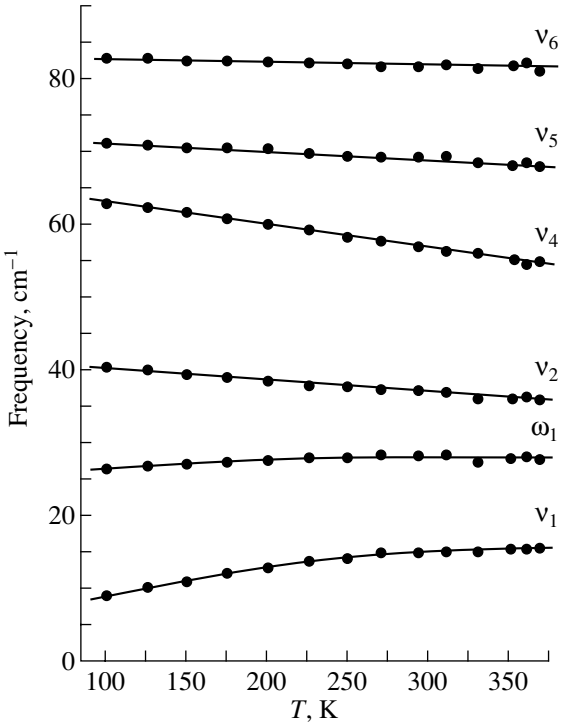

Fig. 4. Temperature dependences of the phonon (vibration) frequencies of the Raman spectrum of benzil crystals. Points are experiment; solid lines are drawn through the experimental points to aid the eye.

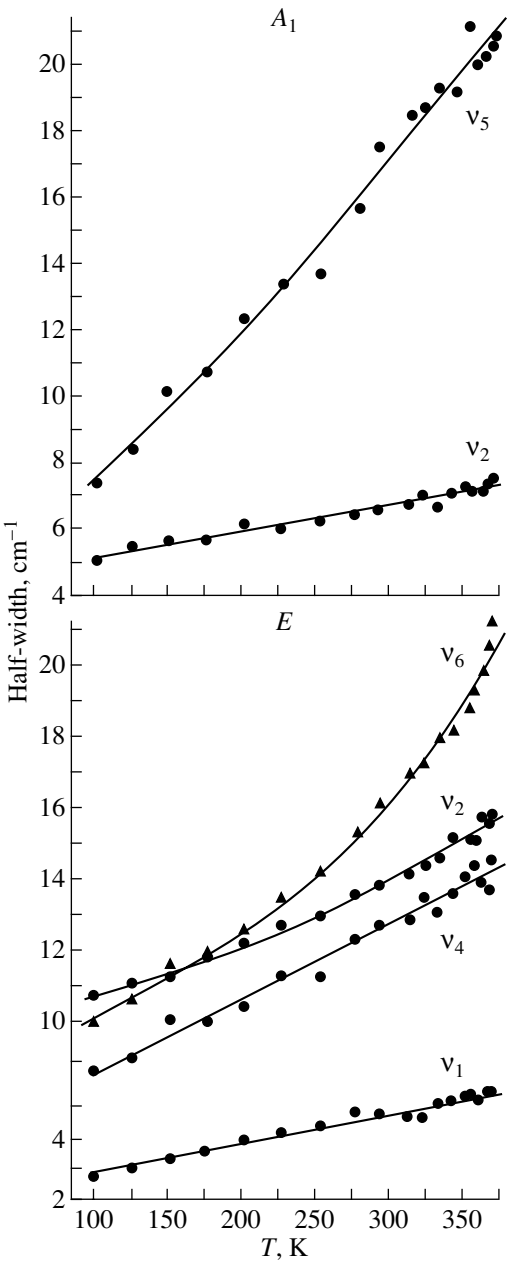

Fig. 5. Temperature dependences of the half-widths of lines of the A_1 and E vibration modes in the benzil Raman spectrum. Solid lines are fits to experimental dependences.

yx twofold-degenerate vibrations of the *E* symmetry). One clearly sees a temperature evolution of the spectra under heating, which consists in a frequency decrease, line broadening, and an increase in the integrated intensity. The *x*(*zz*)*y* geometry reveals three vibration modes of symmetry A_1, whose room-temperature frequencies (20°C) are 29 cm^{-1} (ω_1), 38 cm^{-1} (ν_2), and 70 cm^{-1} (ν_5). The first mode exhibits an anomalously strong temperature dependence of intensity compared to the other lines, which is seen clearly from Fig. 3, and relates to second-order Raman scattering. The two other modes are fundamental vibrations. In the *x*(*yz*)*y* and *x*(*yx*)*y* geometries, one clearly observes four twofold-degenerate vibration modes of symmetry *E* with room-temperature frequencies of 16 (ν_1), 38 (ν_2), 58 (ν_4), and 82 cm^{-1} (ν_6), with the fifth vibration mode of this symmetry lying at 47 cm^{-1} (ν_3) being observed only under strong cooling, starting from 200 K (Fig. 3, T = 100 K). Thus, the theory is in full agreement with experimental data, because we succeeded in observing all the fundamental vibration modes predicted by group theory, namely, two modes of the A_1 symmetry and five of the *E* symmetry.

Figures 4 and 5 display the temperature dependences of the frequencies and half-widths of the lines corresponding to these modes. The vibration frequencies are seen to smoothly decrease under heating up to the melting point (96°C). Only the two lowest energy vibration modes behave anomalously, with the frequencies increasing with temperature. Such an anomalous temperature behavior is characteristic of soft modes. The half-widths of the spectral lines also behave differently: in some cases, the temperature dependence is strictly linear, while in others, one observes a clearly pronounced exponential course, which is seen particularly clearly near the melting point. The latter dependence is characteristic of librational modes, while the former is usually observed for translational vibrations.

5. DISCUSSION OF RESULTS

The study of the temperature dependence of the frequencies and half-widths of the low-frequency Raman lines of molecular crystals, performed in the region of normal lattice vibrations (<100 cm^{-1}), was aimed at interpretation of the observed spectra. An attempt was made to associate the observed vibrations with translations or librations and to assign the corresponding normal coordinates to the experimental spectral lines. The broadening of the fundamental vibrational bands in crystals is connected with the possibility of excitation decay, which is due to the anharmonic interaction of the given vibration mode with lattice phonons. Taking into account the third-order anharmonicity, the broadening (half-width) should depend linearly on temperature, $\Delta\omega = \alpha T$, whereas for much less probable fourth-order processes, the broadening is proportional to the temperature squared [8].

Vibrations of the orientational type are characterized by a stronger temperature dependence of the half-width, which originates from the orientational wave being modulated by random reorientations of molecules in the crystal (see, for instance, [9]). In molecular crystals, the bonding forces acting inside molecular groups far exceed the intermolecular forces responsible for the condensed state of the matter. In this case, the potential barrier for molecular reorientation can be relatively low, which may give rise to orientational melting, plasticity, and second-order phase transitions. In the case of a low potential barrier, there is always a certain number of molecules with energies high enough to overcome it at a given temperature. The expression for the half-width of a spectral line for librational vibrations has the form

$$\Delta\omega = Ae^{-U/kT} + B, \quad (3)$$

where A is a constant factor, B is the natural line half-width (at $T = 0$), and U is the potential barrier to reorientation.

Thus, if the temperature behavior of the half-width of a line in the low-frequency Raman spectrum of a molecular crystal shows that the line corresponds to an orientational vibration, this expression can be used to estimate the potential barrier to reorientation of the molecules in this vibration. One can, therefore, attempt to separate the lines (vibrations) observed in a spectrum into those due to translations and to librations and assign the corresponding normal coordinates to them, i.e., specific displacements of the molecules involved in each vibration under study.

We start our analysis with vibrations of symmetry A_1. We observed and studied three strong lines in the spectrum, two of which correspond to fundamental vibrations with frequencies 38 (ν_2) and 70 cm^{-1} (ν_5), while the third line at 29 cm^{-1} (ω_1) is due to the second-order Raman process (all the frequencies are given for $T = 293$ K). The last line is possibly an overtone of the soft TO branch [of the $E(\nu_1)$ symmetry at the Brillouin zone center] at the M point at the zone edge. Group-theoretical analysis predicts that the first-order Raman spectrum should contain two lines of symmetry A_1, with one of them being due to translation and the other, to libration (Figs. 2a, 3). In the case of translation, this is a fully symmetric vibration mode (all three translationally inequivalent molecules shift in phase radially away from the center or toward it), which manifests itself strongly in Raman scattering. This translational vibration mode is associated with the line at 38 cm^{-1} (ν_2), which is also buttressed by the linear dependence of its half-width on T. Taking into account its large half-width and its exponential behavior, it appears natural to interpret the remaining line of symmetry A_1 at 70 cm^{-1} as the libration mode corresponding to in-phase rocking of all three molecules about their crystallographic or molecular C_2 axes (Fig. 2a).

The vibrations of the A_2 symmetry are acoustic (along the z axis) and IR-active optical vibrations (Figs. 2b, 2c), which were not studied in this work.

The twofold-degenerate vibrations of symmetry E, which are both Raman- and IR-active, are the most difficult to assign. As already mentioned, vibrations of the E symmetry consist of acoustic vibrations along the x and y axes (Figs. 2e, 2h) and five optical vibration modes, including two translation and three libration modes. The most interesting of them is the vibration mode at 16 cm^{-1} (ν_1); its frequency decreases to 8 cm^{-1} as the temperature is lowered and approaches the phase-transition point $T_c = 83.5$ K [5]. This vibration is the soft TO optical mode, whose softening is possibly induced by interaction with the soft TA acoustic mode of the same symmetry E at the Brillouin zone center. The small half-width and its linear temperature dependence up to the melting point suggest that this optical mode is of the translation type. A quantitative estimate of the frequency ratio of translations of symmetry E in the x–y plane and of translations along the optical z axis gives one grounds to conjecture that the soft TO mode ν_1 is a translational vibration in the basal plane (Figs. 2d, 2g), whereas the vibration mode at 58 cm^{-1} (ν_4) is a translation along the z axis (Figs. 2f, 2i), which follows from the linear dependence of the half-width of the corresponding line. It appears natural to assign the remaining vibration modes of symmetry E with frequencies of 38 (ν_2), 47 (ν_3), and 82 cm^{-1} (ν_6) to librations (which is supported by the exponential dependences of the half-widths of these lines); however, no sufficiently strong correlation between the observed vibrations and normal coordinates has thus far been demonstrated.

ACKNOWLEDGMENTS

The authors thank A.A. Kaplyanskiĭ for his support of the work and S.V. Karpov for valuable remarks.

This study was partially supported by the Russian Foundation for Basic Research, project no. 01-02-17599.

REFERENCES

1. K. Becker and H. Rose, Z. Phys. **14**, 369 (1923).
2. C. J. Brown and R. Sadanaga, Acta Crystallogr. **18**, 158 (1965).
3. M. More, G. Odou, and J. Lefebvre, Acta Crystallogr. B **43**, 398 (1987).
4. R. Vacher, M. Boissier, and J. Sapriel, Phys. Rev. B **23**, 215 (1981).
5. J. Sapriel, A. Boudou, and A. Perigaud, Phys. Rev. B **19**, 1484 (1979).
6. J. C. Toledano, Phys. Rev. B **20**, 1147 (1979).
7. S. Bhagavantam and T. Venkatarayudu, *Theory of Groups and Its Application to Physical Problems* (Andhara Univ., Waltair, 1951; Inostrannaya Literatura, Moscow, 1959).
8. J. A. Reissland, *The Physics of Phonons* (Wiley, New York, 1973; Mir, Moscow, 1975).
9. E. I. Ivanov and K. A. Valiev, Opt. Spektrosk. **19**, 897 (1965).

Translated by G. Skrebtsov

Physics of the Solid State, Vol. 44, No. 2, 2002, pp. 379–385. Translated from Fizika Tverdogo Tela, Vol. 44, No. 2, 2002, pp. 365–370.

LATTICE DYNAMICS AND PHASE TRANSITIONS

A Study of the Effect of Gradual Substitution $NH_4 \longrightarrow Cs$ on Phase Transitions in NH_4LiSO_4 Crystals

S. V. Mel'nikova, V. A. Grankina, and A. V. Kartashev

Kirensky Institute of Physics, Siberian Division, Russian Academy of Sciences, Akademgorodok, Krasnoyarsk, 660036 Russia

e-mail: flerov@iph.krasnoyarsk.su

Received June 18, 2001

Abstract—Solid solutions in the $Cs_x(NH_4)_{1-x}LiSO_4$ ($0 \le x \le 0.35$) system are grown and investigated. The birefringence ($n_a - n_b$) and the heat capacity are measured in the temperature range 100–530 K. The (x–T) phase diagram is constructed. It is demonstrated that the substitution of cesium for ammonium in the NH_4LiSO_4 crystal affects the transition temperatures in such a way that the region of the ferroelectric phase increases and the ferroelastic phase disappears at $x > 0.22$. The character of the high-temperature transition remains unchanged ($2\beta = 0.24 \pm 0.01$ for all compositions), but the birefringence anomaly and enthalpy decrease. As the concentration x increases, the low-temperature transition becomes more similar to a first-order transition: the birefringence jump δn and the temperature hysteresis ΔT increase. © *2002 MAIK "Nauka/Interperiodica".*

1. INTRODUCTION

Crystals of the $ALiSO_4$ (A = K, NH_4, Rb, and Cs) family contain LiO_4 and SO_4 tetrahedral groups that are linked into a framework structure of the tridymite type (cations A occupy large-sized holes). These crystals are characterized by various sequences of changes in the symmetry upon phase transitions due to step-by-step orientational ordering of the structural groups. Structural transformations in these compounds are primarily associated with changes in the orientation of sulfate groups [1]. In order to elucidate the subtle mechanisms responsible for the specific features of ordering in different compounds of this family, it is expedient to investigate mixed systems. A gradual replacement of cations in the A position by cations of another size induces local distortions that do not provide transformations of long-range environment but are sufficient to change the transition temperature. Eventually, this can lead to a change in the mechanism of phase transition.

There are many works concerned with the investigation of solid solutions belonging to the above family. The phase diagrams and the possibility of forming a vitreous phase have been studied in $Cs_xRb_{(1-x)}LiSO_4$ [2–6] and $K_xRb_{(1-x)}LiSO_4$ [7, 8] solid solutions. Kawamura *et al.* [9] performed an x-ray structural investigation of the NH_4LiSO_4–$RbLiSO_4$ system. For these compounds, the (x–T) regions of existence of structures with different symmetries were determined in the temperature range from the melting point to liquid-nitrogen temperatures. It was demonstrated that a change in the degree of substitution for the A^+ cation can result in the stabilization of particular phases, the disappearance of already existing phases, and the formation of new phases.

Ammonium lithium sulfate NH_4LiSO_4 has been extensively studied to date and remains a subject of investigation. It was established that this compound is characterized by the following sequence of changes in the symmetry: $Pmcn(c = c_0) \longleftrightarrow P2_1cn(c = c_0) \longleftrightarrow P2_1/c11(c = 2c_0) \longleftrightarrow C1c1(c = 2c_0)$ at T_{0i} = 460, 284, and 27 K, respectively [10–12]. The phase is ferroelectric with considerable spontaneous polarization at room temperature and ferroelastic below 284 K. On the other hand, there appear works in which new phase transitions in NH_4LiSO_4 are revealed or previously determined symmetry groups of the known phases are subjected to question [13].

Kruglik *et al.* [14] studied $CsLiSO_4$ crystals and observed only one ferroelastic phase transition from the initial phase with the symmetry $Pmcn(c = c_0)$ to the phase with the monoclinic symmetry $P112_1/n(c = c_0)$ at $T_0 \approx 201$ K.

The aim of the present work was to elucidate how the gradual replacement of ammonium cations by considerably larger-sized cations Cs^+ affects the temperature and the character of phase transitions in the NH_4LiSO_4 crystal. For this purpose, we measured the heat capacity and birefringence.

The NH_4LiSO_4 compound was investigated earlier by differential scanning calorimetry (DSC) [13, 15] and differential thermal analysis [16] at temperatures above room temperature, i.e., in the range of the high-temperature phase transition. The experimental data are contradictory. This is particularly true for the number of phase transitions and the corresponding changes in the enthalpy. In this respect, we studied not only the solid solutions but also the NH_4LiSO_4 compound over a wide

1063-7834/02/4402-0379$22.00

range of temperatures, including the low-temperature and high-temperature phase transitions. It should be noted that the temperature behavior of the birefringence of the NH_4LiSO_4 crystal in the ranges of the ferroelectric and ferroelastic phase transitions is sufficiently well understood [17, 18].

2. EXPERIMENTAL TECHNIQUE

The single crystals used in our measurements were obtained by two methods: (1) slow evaporation of the appropriate mixtures of NH_4LiSO_4 and $CsLiSO_4$ aqueous solutions at $T \approx 310$ K and (2) growth from a mixture of NH_4LiSO_4 and $CsLiSO_4$ solutions in caustic ammonia taken in required proportion. The initial compounds $CsLiSO_4$ and NH_4LiSO_4 were prepared according to the reactions

$$Cs_2SO_4 + Li_2SO_4 = 2CsLiSO_4,$$

$$(NH_4)_2SO_4 + Li_2SO_4 = 2(NH_4)LiSO_4.$$

The polycrystalline compounds synthesized were examined using x-ray powder diffraction analysis prior to dissolution in water [method (1)] or 25 wt % ammonia [method (2)].

The largest and most perfect single crystals in the form of hexagonal prisms were grown from mixtures of aqueous solutions. The quantitative composition of these crystals was determined by atomic absorption analysis. Analysis showed that, as a rule, the cesium content in the crystals is less than that in the as-batched composition. For example, single crystals with $x = 0.15$ were obtained at the as-batched composition with $x = 0.4$. The chemical composition of the crystals grown by the second method was closer to the as-batched composition, which made it possible to prepare the crystals with $x = 0.2$–0.35. For optical investigations, samples in the form of plates with different orientations and thicknesses were oriented on a URS x-ray instrument.

The plates prepared were used in polarization-optical investigations and measurements of the birefringence in the range from the liquid-nitrogen temperature to temperatures corresponding to the decomposition of the studied compounds (~530 K). The birefringence was measured on plates of the (001) section ($c \approx 8.7$ Å). The measurements were performed on a Berec compensator with an accuracy of $\cong 10^{-5}$ and a Senarmont compensator with a sensitivity of no less than 10^{-7}. The former compensator made it possible to investigate small-sized samples and to determine the birefringence magnitude.

The thermodynamic properties were studied on a DSM-2M differential scanning microcalorimeter modified for recording and processing of measured signals on a computer. This appreciably increased the amount of information obtained with the microcalorimeter. The measurements were carried out in the temperatures ranges 150–390 K with a low-temperature unit and in the range 340–510 K with a high-temperature unit. The upper limit of measurements was determined by the temperature of the onset of the NH_4LiSO_4 decomposition.

For the most part, calorimetric experiments were performed with powder samples. In a number of cases, when the solid solutions were studied in the form of crystals, close thermal contact between the sample and the cell was ensured by a KPT-8 organosilicon paste. The cesium concentrations (x) in the $Cs_x(NH_4)_{1-x}LiSO_4$ solid solutions were equal to 0, 0.045, 0.065, 0.09, 0.125, 0.15, and 0.22. The sample weight was approximately equal to 0.1 g.

In each experiment, the data on the DSM signals as functions of time were converted into the temperature dependence of the heat capacity for the studied compound with the use of the heat capacity of corundum as a reference. The enthalpy changes ΔH_i due to phase transitions were determined by integrating the function $\Delta C_p(T)$, where ΔC_p is the excess heat capacity. In order to increase the reliability of the results, we carried out four or six series of measurements with one or two solid-solution samples of each composition. In different series, the temperatures of phase transitions for the same sample and for different samples of the same solid solution differed by no more than 0.5–1.0 K. The enthalpy change was determined accurate to within 10–15%.

Finally, it should be noted that the polarization-optical observations revealed that the grown crystals contain extended regions of inhomogeneous stresses that disappear upon annealing. Moreover, the low-temperature transition at T_{02} in compounds with a sufficiently high cesium content (for example, at $x = 0.15$) was observed only after annealing. For this reason, prior to optical and thermal investigations, the samples were necessarily annealed at a temperature of approximately 470 K for 2 h.

3. RESULTS

Experimental calorimetric data in the form of temperature dependences of the excess heat capacities associated with high- and low-temperature phase transitions are shown in Fig. 1. An increase in the cesium concentration leads to a considerable decrease in the temperatures of both structural transformations and in the excess heat capacity at a maximum. This results in an increase in the error in determining the phase transition temperatures T_{0i} and the enthalpy changes ΔH_i. The data on T_{0i} and ΔH_i are listed in the table. It is seen that, as the cesium content in the solid solutions increases, the enthalpy of the high-temperature phase transition decreases substantially, whereas the enthalpy of the low-temperature phase transition remains constant to within the limits of the estimation error.

Figure 2 depicts the experimental temperature dependences of the birefringence $\Delta n_c = n_a - n_b$ for $Cs_x(NH_4)_{1-x}LiSO_4$ solid solutions with different

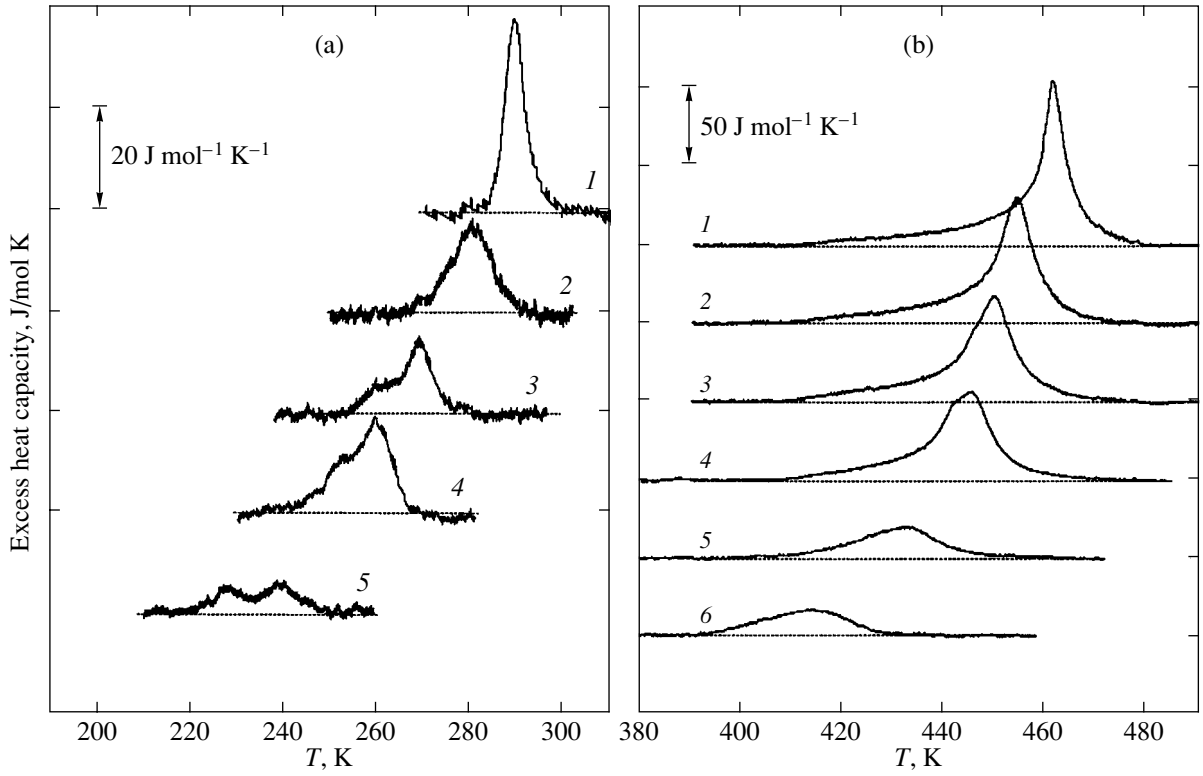

Fig. 1. Temperature dependences of the excess heat capacity for $Cs_x(NH_4)_{1-x}LiSO_4$ solid solutions in the vicinity of (a) low-temperature and (b) high-temperature phase transitions at different concentrations x: (*1*) 0, (*2*) 0.045, (*3*) 0.065, (*4*) 0.09, (*5*) 0.15, and (*6*) 0.22.

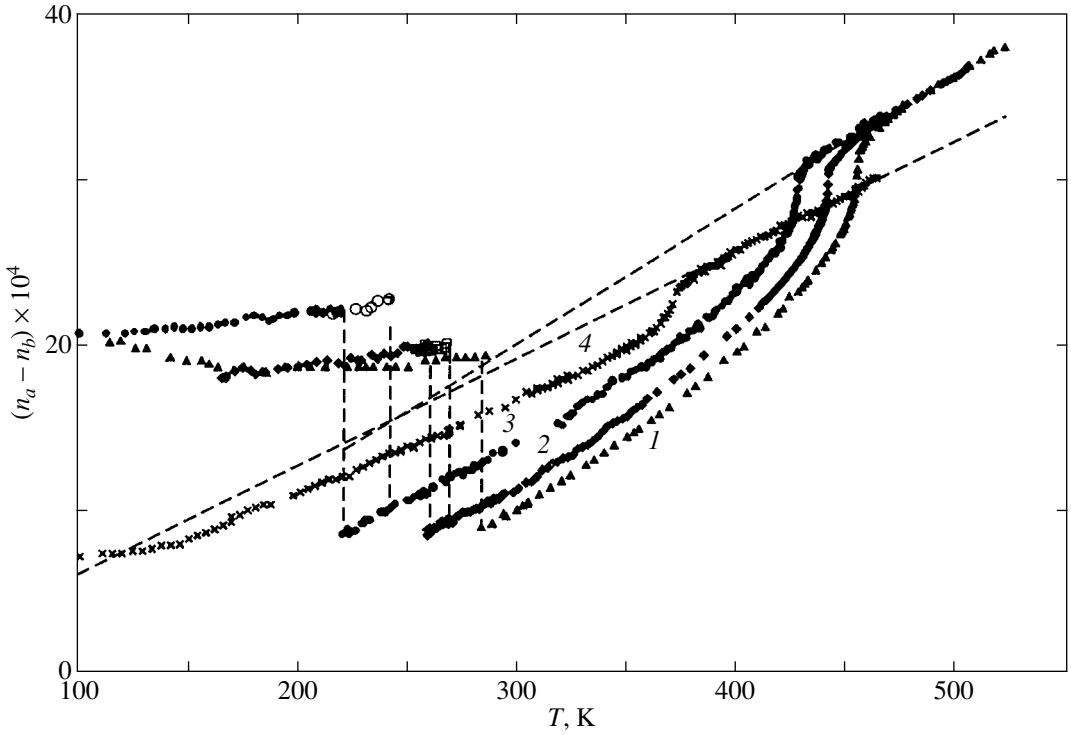

Fig. 2. Temperature dependences of the birefringence Δn_c upon heating (open circles and squares) and cooling (closed circles and squares) for samples at different cesium concentrations x: (*1*) 0, (*2*) 0.065, (*3*) 0.09, and (*4*) 0.35.

cesium concentrations x. It can be seen that the temperatures of the high-temperature (T_{01}) and low-temperature (T_{02}) transitions gradually decrease with an increase in the cesium content in the crystal. It is worth noting that the high-temperature phase transition does not change in character and only the anomalous component of the birefringence decreases progressively, which is in agreement with the above behavior of the enthalpy. The effect of the substitution on the phase transition temperature T_{02} is much more pronounced. An increase in the concentration x leads to an increase in the birefringence jump δn and in the temperature hysteresis ΔT_{02}: $\delta n \approx 10 \times 10^{-4}$ and $\Delta T_{02} = 2$ K at $x = 0$, $\delta n \approx 12 \times 10^{-4}$ and $\Delta T_{02} = 8.5$ K at $x = 0.065$, and $\delta n \approx 15 \times 10^{-4}$ and $\Delta T_{02} = 18$ K at $x = 0.15$. Only the high-temperature phase transition is observed in the solid solution with $x = 0.35$. Observations made under a microscope in polarized light indicate that, upon gradual substitution of cesium for ammonium, the sequence of changes in the symmetry of phases in the studied compounds remains identical to that in pure NH_4LiSO_4. Clear-cut and direct absences are observed in the range from 500 K to the temperature T_{02} of the transition to the monoclinic phase $P2_1/c11$. Below the T_{02} temperature, the twinning typical of this phase [18] is observed in the (100) section ($a \approx 5.2$ Å).

4. DISCUSSION

Figure 3 displays the phase diagram of the $Cs_x(NH_4)_{1-x}LiSO_4$ solid solutions with $x \le 0.35$, which was constructed using the results of optical and calorimetric measurements. The introduction of cesium ions into NH_4LiSO_4 decreases both the T_{01} temperature of the high-temperature structural phase transition from the orthorhombic phase *Pmcn* to the orthorhombic

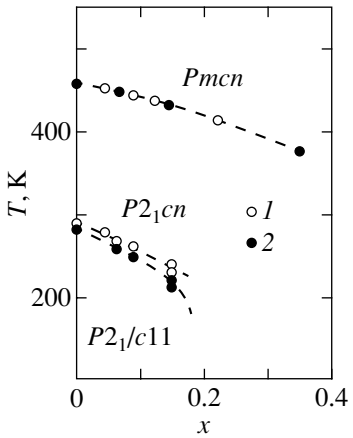

Fig. 3. Phase (x–T) diagram of the $Cs_x(NH_4)_{1-x}LiSO_4$ solid solutions in the concentration range x = 0–0.35: (*1*) DSC data obtained upon heating and (*2*) optical data obtained upon cooling.

polar phase $P2_1cn$ and the T_{02} temperature of the transition to the monoclinic phase $P2_1/c11$. Note that the T_{02} temperature changes considerably more strongly, so that the phase transition in the solution with the cesium concentration $x = 0.22$ is not observed above the liquid-nitrogen temperature and, hence, the region of existence of the ferroelectric phase becomes more extended. Chekmasova *et al.* [19] analyzed the influence of hydrostatic pressure on the phase transitions in pure NH_4LiSO_4 and revealed that the pressure appreciably affects the phase transition temperatures: the temperature of the high-temperature transition increases drastically ($dT_{01}/dp = 90$ K/GPa), whereas the temperature of the low-temperature transition decreases ($dT_{02}/dp = -26$ K/GPa). Our measurements demonstrate that, compared to hydrostatic pressure, the replacement of ammonium ions by larger-sized Cs ions in the structure has the opposite effect. This replacement favors the loosening of the structure and leads to a decrease in the T_{01} temperature of the $G_0 \longleftrightarrow G_1$ transition. At the same time, the compression and loosening of the structure identically affect the $G_1 \longleftrightarrow G_2$ transition and drastically decrease the region of existence of the G_2 phase. Therefore, it can be concluded that the G_2 phase is unstable.

The temperature dependences of the anomalous component of the birefringence in the range below the T_{01} temperature is plotted in Fig. 4. These dependences were obtained by subtracting the linear dependences of the birefringence (extrapolated from the initial phase) from the dependences displayed in Fig. 2. As can be seen, the pretransitional effects are observed in the range 5–10 K above the phase transition, which masks the weak first-order nature of this transition [17]. Moreover, it is seen that the birefringence anomaly accompanying the phase transition gradually decreases with an increase in x. Indeed, the maximum deviation of the birefringence from a linear dependence for pure NH_4LiSO_4 ($x = 0$) is determined as $\delta(n_a - n_b) = 10 \times 10^{-4}$, whereas the value of $\delta(n_a - n_b)$ for the sample with $x = 0.35$ is four times less ($\approx 2.5 \times 10^{-4}$).

The anomalous component of the birefringence $\delta(n_a - n_b)$ and the transition parameter η are related by the quadratic expression $\delta(n_a - n_b) \sim \eta^2 \sim (T - T_0)^{2\beta}$. With this relationship, it is possible to determine the critical exponent β and to fit the phase transition temperature T_{01} in such a way as to fulfill the above quadratic dependence. The determination of the phase transition temperature from birefringence curves is problematic, especially when the transition is smeared under the influence of any factor. In our case, the substitution leads to an increase in the fluctuation anomalies in the range of the T_{01} temperature. There are many techniques of determining the T_{01} temperature. In the present work, the phase transition temperature was fitted using linear dependences of the type shown in Fig. 4 according to the technique proposed by Kim

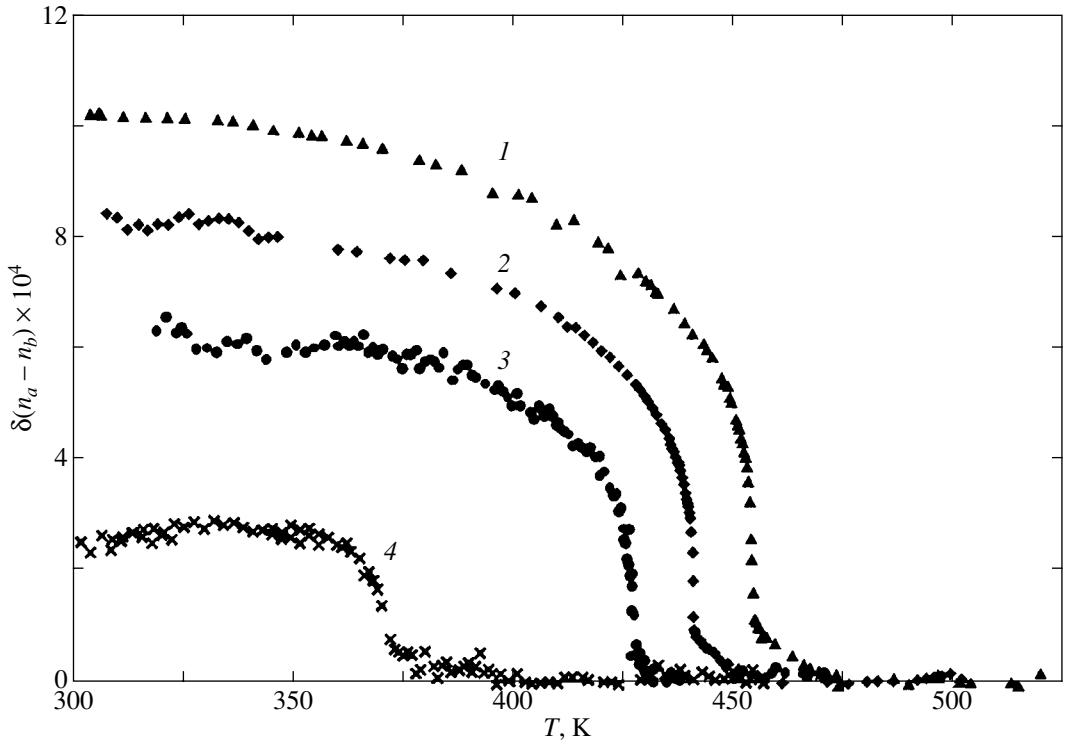

Fig. 4. Temperature dependences of the anomalous component $\delta(n_a - n_b)$ of the birefringence in the ferroelectric phase of the $Cs_x(NH_4)_{1-x}LiSO_4$ solid solutions at different concentrations x: (*1*) 0, (*2*) 0.065, (*3*) 0.09, and (*4*) 0.35.

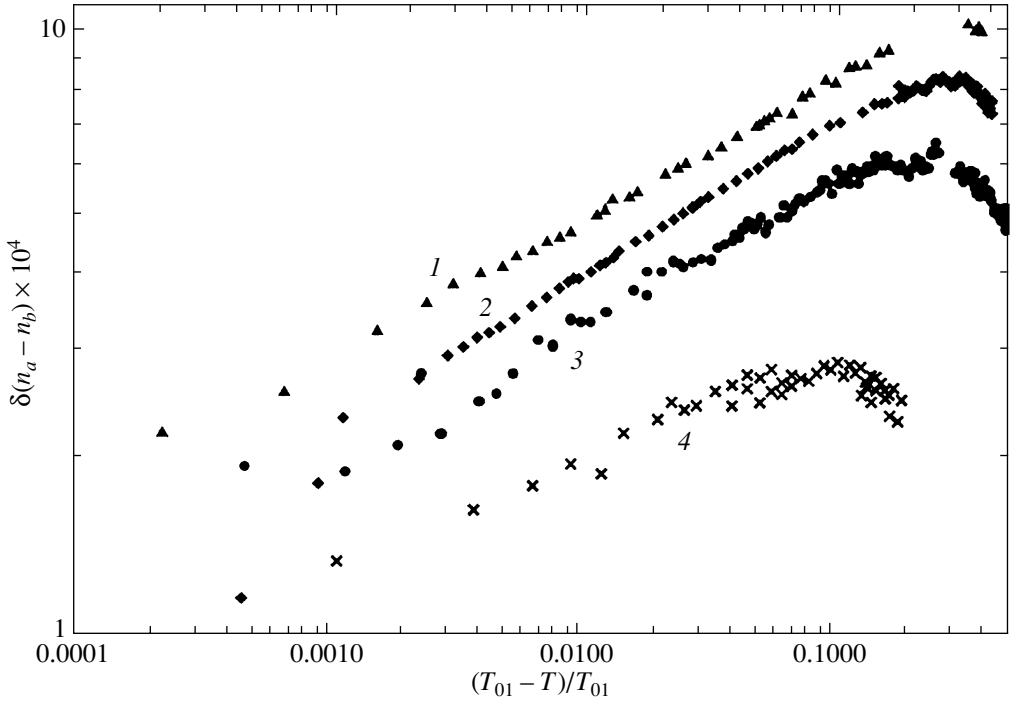

Fig. 5. Dependences $\delta(n_a - n_b)(T)$ below the T_{01} transition temperature on the logarithmic scale at different concentrations x: (*1*) 0, (*2*) 0.065, (*3*) 0.09, and (*4*) 0.35.

Thermodynamic parameters of phase transitions in $Cs_x(NH_4)_{1-x}LiSO_4$ solid solutions

x	T_{01}, K	ΔH_1, J/mol	T_{02}, K	ΔH_2, J/mol
0	460.5	1170	289	205
0.045	453	1045	280	190
0.065	449	990	268.5	200
0.09	445	930	260	230
0.15	431.5	530	229, 241	100
0.22	414.6	400	–	–

et al. [20]. The T_{01} temperatures obtained agree well with the results of thermal measurements.

Figure 5 shows the dependences of $\delta(n_a - n_b)$ on $(T_{01} - T)/T_{01}$ on the logarithmic scale for samples with different concentrations x. From the slopes of the straight lines, we obtain the "nonclassical" critical indices $2\beta = 0.24 \pm 0.01$ for all the studied samples. The dependence is linear in the temperature range $(T_{01} - T)$ from 0.5 to 90 K below the phase transition temperature. The small critical index can be associated with the closeness of the transition to a tricritical point and the effect of higher-order terms in the thermodynamic potential. It should be noted that a similar small critical index for the high-temperature phase transition in NH_4LiSO_4 was obtained earlier in [17]. The constant value of 2β for different compositions suggests that the transition remains unchanged in character with an increase in the degree of substitution of cesium for ammonium.

The enthalpy change ΔH_1 determined in our work for the high-temperature transformation in the NH_4LiSO_4 compound (see table) is nearly twice as large as that obtained by Solans *et al.* [13] (ΔH_1 = 610 J/mol) also with the use of the DSC technique. This considerable difference in the enthalpy change ΔH_1 can, most likely, be explained by the different approaches used to determine the anomalous heat capacity ranges. The function $\Delta C_p(T)$ was integrated in the temperature range 410–480 K in our work and only in a range of 6.2 K in the vicinity of the T_{01} temperature in [13]. However, the anomalous heat capacity over a wide temperature range below the T_{01} temperature is indicated by the data on the thermal expansion [21, 22] and the birefringence (Figs. 2, 4). It should be noted that our experimental data on the enthalpy change is in reasonable agreement with the change ΔH_1 = 1305 J/mol calculated by Tomaszewski and Pietraszko [22] from the Clausius–Clapeyron equation with the use of data on the volume change and dT_{01}/dp.

As far as we know, the calorimetric investigation of the low-temperature phase transition in NH_4LiSO_4 was performed for the first time in the present work. Since this transition is a pronounced first-order phase transformation, it can be assumed that the determined enthalpy change ΔH_2 predominantly corresponds to the latent heat. Using the data on the effect of hydrostatic pressure on the T_{02} temperature (dT_{02}/dp = –26 K/GPa [19]), the volume jump $\Delta V_2/V = 0.02\%$ at T_{02} was calculated from the Clausius–Clapeyron equation $(\Delta V_2/V)(T_{02}) = \Delta H_2(dT_{02}/dp)$.

Recently, it was found that there is one more heat capacity anomaly (at 335 [13] or 350 K [16]) which is unrelated to the known phase transitions in NH_4LiSO_4. Solans *et al.* [13] noted that this anomaly was revealed at the rate of change in the sample temperature dT/dt = 5 K/min and was not observed at dT/dt = 20 K/min. We performed measurements in the range between the T_{01} and T_{02} temperatures at a rate of 8 K/min. No anomalous changes in the heat capacity were observed at 335 K or at 350 K. It should be noted that the enthalpy change (120 J/mol) determined in [13] for the above anomaly is only half as large as the change ΔH_2 (see table). To put it differently, we can state with assurance that the additional anomaly in our experiments could be recorded quite reliably. Furthermore, the necessity of annealing the samples should be taken into account, especially as the samples used in [13] were grown by the short-cut method at a high temperature. For this reason, we are inclined to believe that, at least in our NH_4LiSO_4 sample, there occur only two phase transitions in the above temperature range.

The entropy changes ΔS_i due to phase transitions were determined from the obtained calorimetric data by integrating the function $(\Delta C_p/T)(T)$. These changes for both phase transitions in NH_4LiSO_4 turned out to be small (ΔS_1 = 2.5 J/mol K and ΔS_2 = 0.62 J/mol K) and comparable to the entropy change upon the phase transition in $CsLiSO_4$ (ΔS = 1.66 J/mol K) [23]. Therefore, reasoning from our experimental data, the phase transitions in NH_4LiSO_4 cannot be treated as pure order–disorder transformations.

In the immediate future, the heat capacity of the NH_4LiSO_4 compound will be measured on an adiabatic calorimeter with a higher sensitivity and accuracy compared to the DSM calorimeter. This will make it possible to determine more reliably the entropy changes and to solve the problem of the additional heat capacity anomaly in the temperature range from 330 to 350 K.

ACKNOWLEDGMENTS

This work was supported by the Russian Foundation for Basic Research, project no. 00-15-96790.

REFERENCES

1. K. S. Aleksandrov and B. V. Beznosikov, *Structural Phase Transitions in Crystals (The Potassium Sulfate Family)* (Nauka, Novosibirsk, 1993).

2. S. V. Mel'nikova, V. A. Grankina, and V. N. Voronov, Fiz. Tverd. Tela (St. Petersburg) **36** (4), 1126 (1994) [Phys. Solid State **36**, 612 (1994)].
3. S. V. Mel'nikova, A. D. Vasil'ev, V. N. Voronov, and A. F. Bovina, Fiz. Tverd. Tela (St. Petersburg) **37** (8), 2529 (1995) [Phys. Solid State **37**, 1387 (1995)].
4. S. V. Mel'nikova, V. A. Grankina, and V. N. Voronov, Fiz. Tverd. Tela (St. Petersburg) **36** (4), 1126 (1994) [Phys. Solid State **36**, 612 (1994)].
5. S. V. Melnikova, A. D. Vasiliev, V. A. Grankina, *et al.*, Ferroelectrics **170**, 139 (1995).
6. K. Hasebe and T. Asahi, Ferroelectrics **96**, 63 (1989).
7. S. V. Mel'nikova, M. V. Gorev, and V. A. Grankina, Fiz. Tverd. Tela (St. Petersburg) **40** (7), 1341 (1998) [Phys. Solid State **40**, 1219 (1998)].
8. R. L. Moreira, P. Bourson, U. A. Leitao, *et al.*, Phys. Rev. B **52** (17), 12591 (1995).
9. K. Kawamura, A. Karamashi, N. Nakamura, *et al.*, Ferroelectrics **105**, 279 (1990).
10. A. I. Kruglik, M. A. Simonov, and K. S. Aleksandrov, Kristallografiya **23**, 494 (1978) [Sov. Phys. Crystallogr. **23**, 274 (1978)].
11. K. Itoh, H. Ishikura, and E. Nakamura, Acta Crystallogr. B **37**, 664 (1981).
12. A. Dollase, Acta Crystallogr. B **25**, 2298 (1969).
13. X. Solans, J. Mata, M. T. Calvet, and M. Font-Bardia, J. Phys.: Condens. Matter **11**, 8995 (1999).
14. A. I. Kruglik, M. A. Simonov, and E. P. Zhelezin, Dokl. Akad. Nauk SSSR **247** (7), 1384 (1979) [Sov. Phys. Dokl. **24**, 596 (1979)].
15. G. M. Loiacono, M. Delfino, W. A. Smith, *et al.*, Ferroelectrics **23** (1), 89 (1980).
16. M. Polomska, B. Hilczer, and J. Baran, J. Mol. Struct. **325**, 105 (1994).
17. V. N. Anisimova and N. R. Ivanov, Kristallografiya **31** (5), 1018 (1986) [Sov. Phys. Crystallogr. **31**, 605 (1986)].
18. N. R. Ivanov and L. F. Kirpichnikova, Izv. Akad. Nauk SSSR, Ser. Fiz. **51** (12), 2216 (1987).
19. T. I. Chekmasova, I. S. Kabanov, and V. I. Yusvak, Phys. Status Solidi A **44**, K155 (1977).
20. D.-Y. Kim, J.-G. Yoon, and S.-I. Kwun, J. Phys. Soc. Jpn. **67** (3), 903 (1998).
21. I. M. Iskornev and I. N. Flerov, Fiz. Tverd. Tela (Leningrad) **19**, 1040 (1977) [Sov. Phys. Solid State **19**, 605 (1977)].
22. P. E. Tomaszewski and A. Pietraszko, Phys. Status Solidi **56**, 467 (1979).
23. K. S. Aleksandrov, L. I. Zherebtsova, I. M. Iskornev, *et al.*, Fiz. Tverd. Tela (Leningrad) **22**, 3673 (1980) [Sov. Phys. Solid State **22**, 2150 (1980)].

Translated by O. Borovik-Romanova

Physics of the Solid State, Vol. 44, No. 2, 2002, pp. 386–390. Translated from Fizika Tverdogo Tela, Vol. 44, No. 2, 2002, pp. 371–374.

LOW-DIMENSIONAL SYSTEMS AND SURFACE PHYSICS

Dispersionless Surface Polaritons in the Vicinity of Different Sections of Optically Uniaxial Crystals

V. I. Alshits and V. N. Lyubimov

Shubnikov Institute of Crystallography, Russian Academy of Sciences, Leninskiĭ pr. 59, Moscow, 117333 Russia

e-mail: alschits@ns.crys.ras.ru

Received June 8, 2001

Abstract—The sectors of propagation directions of dispersionless polaritons localized at the optically uniaxial crystal–optically isotropic medium interface are determined. The region of possible orientations of the crystal surface containing these sectors is revealed. The boundaries of the sector of possible propagation directions are analytically described as functions of the crystal surface orientation with respect to the optical axis of the crystal. Consideration is given to the optimum ratios of permittivities at which the width of the propagation sectors appears to be maximum. It is found that the boundaries of the sectors of polariton propagation along different surfaces change drastically in the limit of small dielectric anisotropy of the crystal. © *2002 MAIK "Nauka/Interperiodica".*

1. INTRODUCTION

Surface polaritons (surface electromagnetic waves) that exist near the boundaries of solids at negative permittivities are well understood [1–7]. The permittivities become negative in the vicinity of resonance frequencies under conditions of strong frequency dispersion. Apart from the dispersion polaritons, polaritons of another type can also exist in crystals at positive permittivities when the frequency dispersion is insignificant. The dispersionless surface polaritons that propagate in optically uniaxial crystals with the optical axis parallel to the crystal boundary were described earlier in [8, 9]. These polaritons can exist only in optically positive crystals bordering an isotropic medium and are characterized by a rather narrow sector of possible directions of polariton propagation: in actual systems, this sector is of the order of one angular degree (~1°).

The purpose of the present work was to investigate the conditions of existence for dispersionless surface polaritons in the vicinity of different sections of optically uniaxial crystals and to analyze the dependence of the sector of polariton propagation on the surface orientation. Moreover, we determined the optimum ratios between the permittivities of the crystal and the adjacent isotropic medium at which the sector of the existence of dispersionless surface polaritons is maximum. Finally, we considered a special case of weak dielectric anisotropy, when even insignificant changes in the permittivity substantially affect the existence region of the polaritons under investigation.

2. CHARACTERISTICS OF THE WAVE FIELD OF A POLARITON

The field of a polariton depends on two permittivities of the crystal (ε_e and ε_0) [10] and the permittivity ε of an isotropic medium bordering the crystal. Let us consider a coordinate system with the z axis perpendicular to the surface of the crystal (Fig. 1). It is assumed that the optical axis **c** lies in the xz plane and makes an angle ϑ with the z axis, whereas the propagation direction **m** lies in the xy boundary plane and forms an angle φ with the x axis; that is,

$$\mathbf{c} = (\sin\vartheta, 0, \cos\vartheta), \quad \mathbf{m} = (\cos\varphi, \sin\varphi, 0). \quad (1)$$

The electric component of the electromagnetic wave field of the polariton can be represented as

$$\mathbf{E}(\mathbf{r}, t) = \mathbf{E}(z)\exp\left[i\omega\left(\frac{\sqrt{\varepsilon_0}}{c}N\mathbf{m}\cdot\mathbf{r} - t\right)\right]. \quad (2)$$

Here, ω is the frequency, $\mathbf{r} = (x, y, z)$ is the radius vector of the current point, t is the time, c is the velocity of

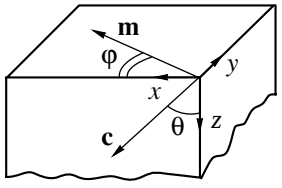

Fig. 1. Schematic representation of the studied crystal (**c** is the optical axis and **m** is the direction of polariton propagation).

1063-7834/02/4402-0386$22.00

light in free space, $N = c/v\sqrt{\varepsilon_0}$, $v = \omega/k$ is the phase velocity of the surface wave, and k is the wave number common to all partial waves.

In a crystal ($z \geq 0$), the wave field of the polariton under consideration is a two-partial surface wave, for which the vector amplitude in formula (2) has the following form:

$$\mathbf{E}(z) = a_0\mathbf{E}_0\exp\left(-\omega\frac{\sqrt{\varepsilon_0}}{c}p_0 z\right) + a_e\mathbf{E}_e\exp\left(-\omega\frac{\sqrt{\varepsilon_0}}{c}p_e z\right). \quad (3)$$

In an isotropic medium adjacent to the crystal ($z \leq 0$), the conjugate one-partial wave propagates and the vector amplitude in formula (2) takes the form

$$\mathbf{E}(z) = a\mathbf{E}\exp\left(\omega\frac{\sqrt{\varepsilon_0}}{c}pz\right). \quad (4)$$

The parameters of the wave field localization at the crystal boundary are defined by the relationships

$$p_0 \equiv p_0(\vartheta, \varphi) = \sqrt{N^2 - 1}, \quad p \equiv p(\vartheta, \varphi) = \sqrt{N^2 - \gamma}, \quad \gamma = \varepsilon/\varepsilon_0, \quad (5)$$

$$p_e \equiv p_e(\vartheta, \varphi) = \sqrt{N^2(d + \delta\cos^2\varphi) - (1 + \delta)d}/d\sin\vartheta + iN\delta\cot\vartheta\cos\varphi/d \equiv p_e^R + ip_e^I, \quad (6)$$

$$d \equiv d(\vartheta) = (1 + \delta\cos^2\vartheta)/\sin^2\vartheta, \quad \delta = \varepsilon_e/\varepsilon_0 - 1. \quad (7)$$

The amplitudes a_0, a_e, and a and the polarization vectors $\mathbf{E}_0$, $\mathbf{E}_e$, and $\mathbf{E}$ are determined from a system of Maxwell equations with standard boundary conditions at the interface. The criterion for the existence of nontrivial solutions to this system of homogeneous equations provides a means of determining the dispersion equation in the parameter $N \equiv N(\vartheta, \varphi)$ (or the wave velocity v); that is,

$$F(\vartheta, \varphi) \equiv (p + p_0)(p_0\cos\varphi + iN\cot\vartheta) \times [(\gamma p_0^2 + pp_e)\cos\varphi + i(p + \gamma p_e)N\cot\vartheta] - (p + p_e)(\gamma p_0 + p)\sin^2\varphi = 0. \quad (8)$$

Note that this equation in a different form is given in [2]. Moreover, a similar equation derived in [11] accounts for the magnetic anisotropy of the crystal. Algebraic (rather cumbersome) treatment proved that the real and imaginary parts of Eq. (8) are proportional to each other. On this basis, Eq. (8) can be rearranged to the real form

$$f(\vartheta, \varphi) \equiv [N^2\delta\cot^2\vartheta(\tilde{\delta} - \delta\cos^2\varphi/d)d - (p_e^R + p) \times (\gamma p_0 + p_e^R)](p_0 + p) - \tilde{\delta}(\tilde{\delta} - \delta/d)p_0 = 0, \quad (9)$$

in which we introduced the designation

$$\tilde{\delta} = \gamma - 1 = \varepsilon/\varepsilon_0 - 1. \quad (10)$$

Equation (9) allows us to determine the quantity N and, hence, the main characteristics of the polariton, namely, the dimensionless velocity $1/N$ and the wave field localization parameters [formulas (5), (6)].

3. THE EXISTENCE REGION OF DISPERSIONLESS SURFACE POLARITONS

The region of existence of surface polaritons is completely determined by relationships (5), (6), and (9), provided the wave number N and all the localization parameters p_0, p_e^R, and p are the real quantities.

Analysis demonstrates that this requirement can be satisfied only in the case when the permittivities of the media involved obey the following inequalities:

$$0 < \varepsilon_0 < \varepsilon < \varepsilon_e, \quad (11)$$

which are equivalent to the inequalities

$$0 < \tilde{\delta}/\delta < 1. \quad (12)$$

These conditions are satisfied only in optically positive crystals.

The boundaries of the region of possible angles ϑ and φ (i.e., the region of possible orientations of the crystal boundary and possible directions of polariton propagation) are specified by two conditions: (1) $p(\vartheta, \varphi) = 0$, when the wave in the isotropic medium is a bulk wave,

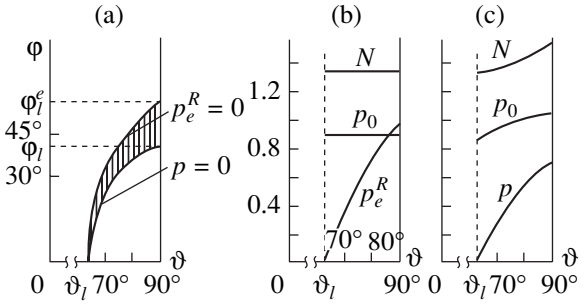

Fig. 2. Typical characteristics of polaritons: (a) the existence region (hatched) in the ϑ–φ coordinates, (b) the limiting parameters at the boundary of the existence region at $p(\vartheta, \varphi) = 0$, and (c) the limiting parameters at the boundary of the existence region at $p_e^R(\vartheta, \varphi) = 0$. The curves are plotted at $\delta = 4$ and $\tilde{\delta} = 0.8$ ($\vartheta_l \approx 63.4°$, $\varphi_l \approx 40.4°$, and $\varphi_l^e \approx 58.0°$).

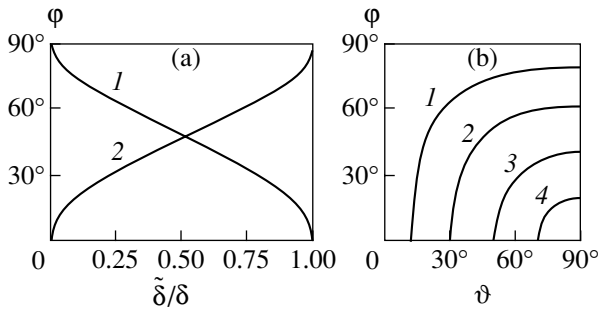

Fig. 3. Limiting characteristics of the existence region of polaritons as functions of the material parameters of the media: (a) (*1*) the angle ϑ_l determining the limiting orientation of the crystal boundary and (*2*) the angles $\varphi_l \approx \varphi_l^e$ in the limit $\delta \ll 1$ and (b) the $\varphi(\vartheta)$ curves for the existence region at $\delta \ll 1$ for the ratios $\tilde{\delta}/\delta$ = (*1*) 0.95, (*2*) 0.75, (*3*) 0.4, and (*4*) 0.10.

and (2) $p_e^R(\vartheta, \varphi) = 0$, when the extraordinary wave in the crystal is a bulk wave. The equation of the line $p(\vartheta, \varphi) = 0$ in the ϑ–φ coordinates can be represented in the explicit form (Fig. 2a)

$$g(\vartheta, \varphi) = (p_e^R + p_0)p_0 - \delta(\sin^2\varphi + \gamma\cot^2\vartheta)/d = 0. \quad (13)$$

Note that, for this line, the parameters $N = \sqrt{\gamma}$ and $p_0 = \sqrt{\tilde{\delta}}$ are independent of the angles ϑ and φ, whereas the p_e^R parameter described by formula (6) depends on these angles (Fig. 2b). For the benefit of clarity, the curves in Fig. 2 were plotted with the dielectric anisotropy parameter ($\delta = 4$) taken to be appreciably larger than the standard value.

The equation of the line $p_e^R(\vartheta, \varphi) = 0$ in the ϑ–φ coordinates can be written in the explicit form

$$g_0(\vartheta, \varphi) = [N^2\delta\cot^2\vartheta(\tilde{\delta} - \delta\cos^2\varphi/d)/d - \gamma p p_0] \times (p_0 + p) - \tilde{\delta}(\tilde{\delta} - \delta/d)p_0 = 0. \quad (14)$$

In this line, the parameter N is represented by the expression (Figs. 2a, 2c)

$$N(\vartheta, \varphi) = \sqrt{(1+\delta)d/(d + \cos^2\varphi)}. \quad (15)$$

As is seen from Fig. 2a, the region of the angles ϑ and φ, in which surface polaritons exist, can be characterized by three limiting angles:

$$\vartheta_l = \arccos\sqrt{\tilde{\delta}/\delta}, \quad \text{when} \quad \varphi = 0, \quad (16)$$

$$\varphi_l = \arcsin\sqrt{\frac{\tilde{\delta}}{\delta}(1+\kappa)}, \quad \kappa = \frac{1}{2}[-1 - \tilde{\delta} + \sqrt{(1-\tilde{\delta})^2 + 4\delta}], \quad \text{when} \quad \vartheta = 90°, \quad (17)$$

$$\varphi_l^e = \arcsin\sqrt{\frac{\tilde{\delta}}{\delta}(1+\kappa^e)}, \quad \kappa^e = (\delta - \tilde{\delta})\frac{(1+\delta)^2 + \delta - \tilde{\delta}}{(1+\delta)^2(1+\tilde{\delta}) - (\delta - \tilde{\delta})^2}, \quad (18)$$

when $\vartheta = 90°$.

By using these relationships (expressions for the angles φ_l and φ_l^e in other forms are given in [9]), we will analyze the possible maximum extension of the existence region of the polaritons under consideration.

4. ON THE POSSIBILITY OF CONTROLLING SECTORS OF POLARITON PROPAGATION

The region of the angles ϑ and φ, in which the studied polaritons exist, is determined by only two parameters, namely, the dielectric anisotropy of the crystal δ [formula (7)] and the parameter $\tilde{\delta}$ [formula (10)] that is dependent on the permittivity of the isotropic medium adjacent to the crystal. (It should be remembered that the parameters δ and $\tilde{\delta}$ satisfy inequalities (12).) The linear sizes and width of this region are completely specified by three limiting angles defined by relationships (16)–(18) (Fig. 2a).

The ϑ_l angle defined by expression (16) is a universal function of the $\tilde{\delta}/\delta$ ratio. Any ratio $\tilde{\delta}/\delta$ that satisfies inequalities (12) corresponds to the particular limiting orientation of the crystal surface, i.e., to the particular angle ϑ_l (Fig. 3a). Therefore, the ϑ_l angle can be controlled through changes in the permittivity of the isotropic medium adjacent to the crystal, i.e., by changing the $\tilde{\delta}$ parameter.

In the special case of weak dielectric anisotropy of the crystal, when the δ parameter is small and, according to inequalities (12), the $\tilde{\delta}$ parameter is also insignificant, the $\tilde{\delta}/\delta$ ratio in the limit takes an indefinite form of the 0/0 type. This ratio changes drastically even with insignificant variations in the material characteristics δ and $\tilde{\delta}$. In this case, the limiting angles also change abruptly and the existence region of the polaritons in the (ϑ, φ) plane becomes highly sensitive to the $\tilde{\delta}/\delta$ ratio but is found to be very narrow. At $\delta \ll 1$, we obtain the relationship

$$\varphi_l \approx \varphi_l^e \longrightarrow \arcsin\sqrt{\tilde{\delta}/\delta} = 90° - \vartheta_l, \quad (19)$$

because $\kappa - \kappa^e \sim \delta^2$ and $\Delta\varphi \sim \delta^2$ (Fig. 3a). As a result, the entire region of existence of polaritons virtually contracts into a line described by the expression

$$\varphi = \arccos\frac{\sqrt{1 - \tilde{\delta}/\delta}}{\sin\vartheta}. \quad (20)$$

The location of this line in the (ϑ, φ) plane substantially depends on the $\tilde{\delta}/\delta$ ratio (Fig. 3b). A comparison of Figs. 2a and 3b shows that the boundaries of the existence region change over a rather wide range with variations in the anisotropy parameters.

At specified permittivities of the crystal (i.e., at $\delta = \text{const}$), the width of the sector $\Delta\varphi$ of possible polariton-propagation directions depends on both the orientation of the crystal boundary and the permittivity of the isotropic medium: $\Delta\varphi = \Delta\varphi(\vartheta, \tilde{\delta})$. In particular, the sector width $\Delta\varphi$ has a maximum at $\vartheta = 90°$ (when the optical axis is aligned parallel to the crystal boundary). Furthermore, the maximum width $\tilde{\delta} = \tilde{\delta}_m(\delta)$ is observed at a certain permittivity of the isotropic medium, i.e., at $\Delta\varphi = (\Delta\varphi)_m$. Therefore, the maximum width $(\Delta\varphi)_m$ corresponds to a maximum in the dependence of the difference $(\varphi_l^e - \varphi_l)$ on the $\tilde{\delta}$ parameter at $\delta = \text{const}$ (Figs. 4a, 4b). The dependence $\tilde{\delta} = \tilde{\delta}_m(\delta)$ is plotted in Fig. 5a. This curve makes it possible to determine the permittivity of the isotropic medium $(\tilde{\delta})$ at which the sector of polariton propagation directions is maximum for the specified dielectric anisotropy δ of the crystal. The characteristics of these sectors are represented in Fig. 5b.

Thus, in the present work, we determined the sectors of existence of dispersionless surface polaritons localized at different sections of optically uniaxial crystals bordering an isotropic medium. In the vicinity of the boundaries of the sector of possible propagation directions, the dispersionless surface polaritons can be considered quasi-bulk polaritons, because the depth of their localization is large compared to the electromagnetic wavelength. In the case when we are dealing with wavelengths of the order of a micrometer (in the visible range and in the immediate vicinity), it becomes evident that, even with a localization depth of the order of hundreds or thousands of wavelengths, this quantity is always substantially less than the thickness of a real crystal. This implies that the waves under consideration remain surface waves.

The existence region of surface polaritons can be controlled using the dependences of the permittivities of the crystal and the adjacent isotropic medium on the frequency, temperature, pressure, and other external factors. By choosing isotropic media with the appropriate dielectric characteristics, it is possible to obtain the maximum sector of propagation directions of dispersionless surface polaritons. For example, according to the experimental data obtained in [12] for optically uniaxial crystals of the Hg_2Cl_2 calomel, the change in wavelength from 0.4 to 18 μm leads to a change in the dielectric anisotropy δ from ≈1.1 to ≈0.4 and, at $\delta \approx 1$, the maximum width $(\Delta\varphi)_m$ of the sector of possible propagation directions is approximately equal to 5°.

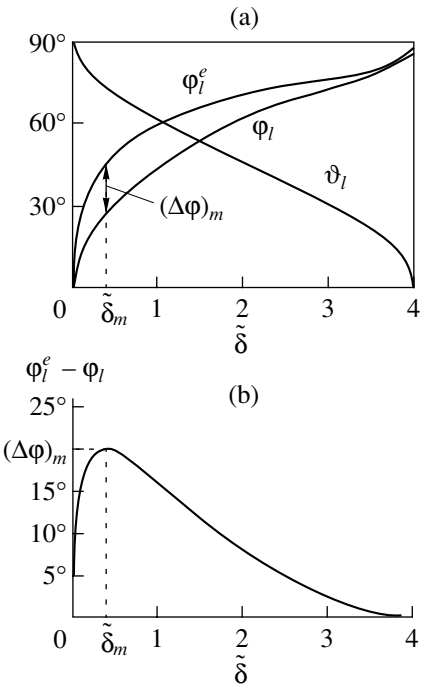

Fig. 4. Dependences of the limiting angles on the parameter $\tilde{\delta}$ at constant δ: (a) the angles ϑ_l, φ_l, and φ_l^e at $\delta = 4$ and (b) the difference $\varphi_l^e - \varphi_l$ at $\delta = 4$, $\tilde{\delta}_m \approx 0.31$, and $(\Delta\varphi)_m \approx 20°$.

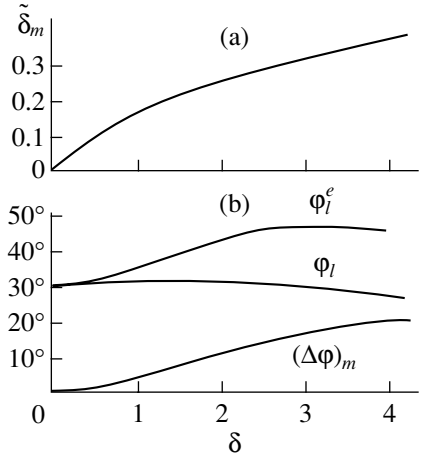

Fig. 5. Dependences of the optimum parameters on the dielectric anisotropy δ of the crystal: (a) the dielectric parameter $\tilde{\delta}_m$ of the isotropic medium and (b) the optimum parameters for the sector of propagation directions at $\tilde{\delta} = \tilde{\delta}_m(\delta)$.

The excitation of dispersionless surface polaritons can be achieved with frustrated total internal reflection [1, 7, 13]. The specific features of this method, as

applied to dispersion surface polaritons, were described in our recent work [7]. Qualitatively, these features remain the same in the case of dispersionless surface polaritons.

REFERENCES

1. *Surface Polaritons: Electromagnetic Waves at Surfaces and Interfaces*, Ed. by V. M. Agranovich and D. L. Mills (North-Holland, Amsterdam, 1982; Nauka, Moscow, 1985).
2. V. N. Lyubimov and D. G. Sannikov, Fiz. Tverd. Tela (Leningrad) **14**, 3 (1972) [Sov. Phys. Solid State **14**, 1 (1972)].
3. V. V. Bryksin, D. N. Mirlin, and Yu. A. Firsov, Usp. Fiz. Nauk **113** (1), 29 (1974) [Sov. Phys. Usp. **17**, 305 (1974)].
4. V. M. Agranovich, Usp. Fiz. Nauk **115** (2), 199 (1975) [Sov. Phys. Usp. **18**, 99 (1975)]; Usp. Fiz. Nauk **126** (4), 677 (1978) [Sov. Phys. Usp. **21**, 995 (1978)].
5. G. A. Puchkovskaya, V. L. Strizhevskii, Yu. A. Frolkov, *et al.*, Phys. Status Solidi B **89** (1), 27 (1978).
6. V. N. Lyubimov, Zh. Prikl. Spektrosk. **33** (5), 913 (1980).
7. V. I. Alshits, V. N. Lyubimov, and L. A. Shuvalov, Fiz. Tverd. Tela (St. Petersburg) **43** (7), 1322 (2001) [Phys. Solid State **43**, 1377 (2001)].
8. F. N. Marchevskiĭ, V. L. Strizhevskiĭ, and S. V. Strizhevskiĭ, Fiz. Tverd. Tela (Leningrad) **26** (5), 1501 (1984) [Sov. Phys. Solid State **26**, 911 (1984)].
9. M. I. D'yakonov, Zh. Éksp. Teor. Fiz. **94** (4), 119 (1988) [Sov. Phys. JETP **67**, 714 (1988)].
10. Yu. I. Sirotin and M. P. Shaskolskaya, *Fundamentals of Crystal Physics* (Nauka, Moscow, 1975; Mir, Moscow, 1982).
11. V. N. Lyubimov, Kristallografiya **17** (4), 816 (1972) [Sov. Phys. Crystallogr. **17**, 631 (1972)].
12. Z. B. Perekalina, C. Barta, J. Gregora, *et al.*, Opt. Spektrosk. **42** (6), 1134 (1977) [Opt. Spectrosc. **42**, 653 (1977)].
13. V. I. Alshits, A. S. Gorkunova, V. N. Lyubimov, *et al.*, in *Proceedings of the International Symposium on Trends in Continuum Physics* (World Scientific, Singapore, 1999), p. 28.

Translated by O. Borovik-Romanova

Physics of the Solid State, Vol. 44, No. 2, 2002, pp. 391–394. Translated from Fizika Tverdogo Tela, Vol. 44, No. 2, 2002, pp. 375–378.

LOW-DIMENSIONAL SYSTEMS AND SURFACE PHYSICS

Electron-Stimulated Desorption of Europium Atoms from the Surface of Oxidized Tungsten: Concentration Dependence of the Low-Energy Peak

S. Yu. Davydov

Ioffe Physicotechnical Institute, Russian Academy of Sciences, Politekhnicheskaya ul. 26, St. Petersburg, 194021 Russia
St. Petersburg State University of Electrical Engineering, St. Petersburg, 197376 Russia

Received June 22, 2001

Abstract—The nature of electron-stimulated desorption of europium atoms Eu^0 at low incident electron energies E_e (~30 eV) and the specific features of the dependence of the yield of europium atoms Eu^0 on their concentration on the surface of oxidized tungsten are discussed. The crucial stage is found to be the primary event of vacancy creation in the inner 5*p* shell of the europium adatom. As follows from estimates, only the first of the two possible ionization scenarios (intratomic electron transfer to the outer shell of the Eu adatom or ejection of the knocked-out electron into vacuum) results in Eu^0 desorption. The concentration threshold of the Eu^0 yield is determined. © *2002 MAIK "Nauka/Interperiodica".*

1. Electron-stimulated desorption (ESD) of europium atoms from a tungsten surface covered by an oxygen monolayer (O/W surface) was studied in [1, 2]. It was found that, in contrast to the ESD of alkali metals from the O/W surface studied in detail before in [3, 4], the dependence of the yield of Eu atoms q on the incident electron energy E_e has a clearly pronounced resonance character. To explain these features, an energy level diagram of the Eu–O/W adsorption system was constructed for low and high O/W surface coverages Θ by europium adatoms [5] and possible mechanisms of Eu^0 ESD were proposed [6]. In particular, the theory developed earlier in [7, 8] was successfully used to satisfactorily describe the concentration dependence $q(\Theta)$ of the yield of Eu atoms for the $q(E_e)$ peaks lying at E_e = 50 and 80 eV. It was assumed in [7, 8] that the $q(\Theta)$ dependence is determined primarily by the last stage in the ESD process, namely, by the ejection of particles, possibly accompanied by atom–ion charge exchange. From our preliminary estimates, however, it follows that this approach to describing the $q(\Theta)$ relation fails for the $q(E_e)$ peak at E_e = 33 eV (the 33-eV peak, for brevity); in this case, the experimentally observed concentration dependence of the Eu^0 yield differs strongly from E_e measured at E_e = 50 and 80 eV. The present work deals with interpretation of specific features of the 33-eV peak.

2. We will show that the specific features in the concentration dependence of the ESD yield of europium atoms for the 33-eV peak (see [2, Fig. 2]) are related to the primary event in the ESD process, namely, electron transfer from the inner 5*p* Eu shell to an outer Eu shell quasilevel, whose position depends on Θ. The involvement of the 5*p* vacancy in the process is indicated by the energy threshold for the escape of europium neutrals [1, 2].

We consider the following states in the europium adatom that are involved in the ESD process: (1) the 5*p* level with energy $\varepsilon(5p)$ that is filled by one electron before the excitation and is empty after the excitation, and (2) the two-electron quasilevel [with the centroid lying at the energy $\varepsilon(\Theta)$] that forms in the hybridization of the one-electron 6*s* and 6*p* states with the substrate and has an occupation number $n(\Theta) < 1$ before the excitation and $[1 + n(\Theta)]$ or $n(\Theta)$ after the excitation (see below). Here and subsequently, we assume that, in the ground state, only one sublevel of the 6*s* shell is involved in adsorption, i.e., that only one electron is capable of tunneling into the metal, which follows, for instance, from the decrease in the work function [5]. Note that the scenario of the first ESD stage proposed by us (scenario 1) was taken from [9].

The initial (ground-state) energy of the two-level system postulated by us can be written as

$$E_0(\Theta) = \varepsilon(\Theta)n(\Theta) + \varepsilon(5p). \quad (1)$$

We shall reckon the energy from the Fermi level of the system.

We consider two scenarios of formation of a 5*p* vacancy. In scenario 1, the 5*p* shell is ionized and the knocked-out electron is transferred to the two-electron quasilevel; i.e., an intra-adatom transition takes place. In this case, the potential energy of the excited system E_1 is

$$E_1(\Theta) = \varepsilon(\Theta)[1 + n(\Theta)] + Un(\Theta) - G[1 + n(\Theta)]. \quad (2)$$

1063-7834/02/4402-0391$22.00

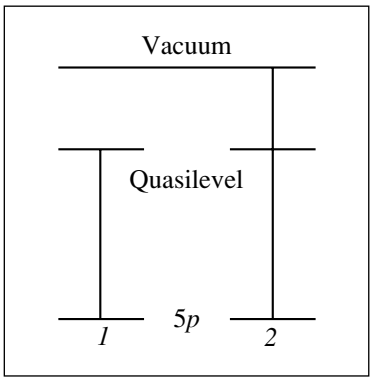

Fig. 1. Two scenarios, *1* and *2*, of 5*p*-level ionization of the europium adatom. Vertical lines show electron transfer from the 5*p* level of the europium adatom to its (*1*) quasilevel or (*2*) vacuum level.

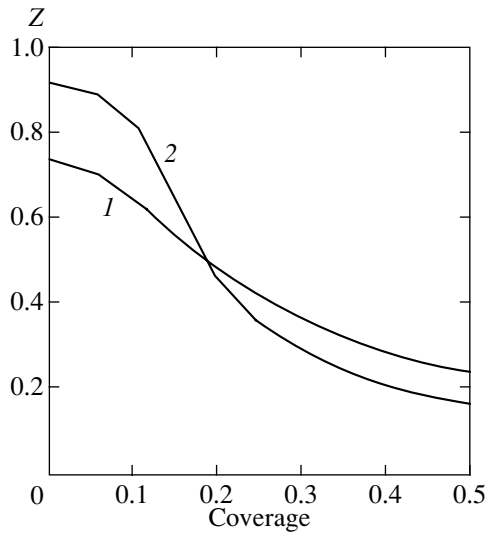

Fig. 2. Europium adatom charge *Z* plotted as a function of coverage Θ in the equilibrium state for Γ equal to (*1*) 1 and (*2*) 0.25 eV.

Here, U is the energy of electron repulsion at the quasilevel and G is the energy of attraction of the knocked-out electron to the 5*p* hole. This ionization process changes the potential energy of the system by W_1:

$$W_1 \equiv E_1 - E_0 = (U - G)n(\Theta) + \varepsilon(\Theta) - G - \varepsilon(5p). \quad (3)$$

In scenario 2, the electron is knocked out of the 5*p* shell into vacuum. The potential energy of this excited state E_2 and the change in potential energy W_2 are

$$\begin{aligned} E_2(\Theta) &= [\varepsilon(\Theta) - G]n(\Theta), \\ W_2 &= -Gn(\Theta) - \varepsilon(5p). \end{aligned} \quad (4)$$

Both scenarios are shown schematically (disregarding the quasilevel broadening) in Fig. 1. We consider some energy relations following from this scheme. According to [1, 2], the appearance threshold of europium atoms corresponds to an incident electron energy $E_e^{\text{th}} = 24$ eV, a figure close to the 5*p* electron binding energy in the europium atom, $\varepsilon_b \equiv E(O_3) = 26$ eV [6, 10]. Hence, for $E_e \geq E_e^{\text{th}}$, ionization is possible in scenario 2. In the case of ionization in scenario 1 for the same E_e, we have an energy excess $\delta E \approx \varphi + K$, where φ is the work function of oxidized tungsten (in Fig. 1, this approximately corresponds to the distance between the vacuum level and the quasilevel) and K is the kinetic energy of the knocked-out electron. Because the work function of oxidized tungsten is $\varphi \approx 5.5$ eV (see, e.g., [5]), δE is close in order of magnitude to surface plasmon energies in metals. Hence, for neutral europium ESD to occur for $E_e \geq E_e^{\text{th}}$, the excess energy has to be carried away by plasmons.

We consider the energy difference between excited states 1 and 2,

$$\begin{aligned} \Delta W \equiv W_1 - W_2 &= \Delta E \equiv E_1 - E_2 \\ &= Un(\Theta) + \varepsilon(\Theta) - G. \end{aligned} \quad (5)$$

If $\Delta W < 0$, scenario 1 is energetically preferable, and in the opposite case, scenario 2 will take place. Judging from the resonance character of the 33-eV peak and its threshold [1, 2], it appears reasonable to assume that it is scenario 1 that is responsible for Eu^0 ESD, because at high incident electron energies E_e, no Eu neutrals desorb, even though ionization in accordance with scenario 2 should take place.

3. To estimate ΔW, we have to calculate the ground-state population $n(\Theta)$ of the quasilevel. Such a calculation can be performed in a standard way (see, e.g., [11–13]):

$$\begin{aligned} n(\Theta) &= \pi^{-1}\operatorname{arccot}[\varepsilon(\Theta)/\Gamma], \\ \varepsilon(\Theta) &= \varepsilon_0 - \xi\Theta^{3/2}Z(\Theta), \\ \xi &= 2e^2\lambda^2 N_{\text{ML}}^{3/2}A, \quad Z(\Theta) = 1 - n(\Theta). \end{aligned} \quad (6)$$

Here, Γ is the quasilevel half-width, ξ is the adatom dipole–dipole coupling constant, Z is the adatom charge, $N_{\text{ML}} = 5 \times 10^{14}$ cm^{-2} is the europium adatom concentration in the monolayer, 2λ is the surface dipole arm, $A \approx 10$ is a coefficient depending weakly on the adsorbed-layer geometry [11], and ε_0 is the 6*s*-quasilevel energy at zero coverage. The $Z(\Theta)$ relation calculated using Eqs. (6) is plotted in Fig. 2. The quantity λ was taken to be equal to the sum of the europium and oxygen radii, which are 0.74 and 2.04 Å, respectively [14] (the mirror image plane was assumed to be coincident with the surface of the tungsten substrate); this yields $\varepsilon_0 = 1$ eV and $\xi = 24.89$ eV (for more details, see [5]). We also calculated the change in the work function

$\Delta\varphi$ of the Eu–O/W system caused by the coverage Θ using standard relations from [11–13]:

$$\Delta\varphi(\Theta) = -\Phi\Theta Z(\Theta), \quad \Phi = 4\pi e^2 \lambda N_{ML}. \qquad (7)$$

The results of the calculation are plotted in Fig. 3 for $\Phi = 25.15$ eV and are typical. Note that the case shown in Fig. 2 (curve *2*) corresponds to the minimum in the work function of the system. Unfortunately, we have no relevant experimental data at our disposal.

4. To estimate the Coulomb parameters U and G, we use the observation that the europium atoms stop desorbing for $\Theta^* = 0.35$. Based on the above assumption that it is the first (resonance) scenario of excitation that the ESD of Eu neutrals follows, we set

$$\Delta W \equiv Un(\Theta^*) + \varepsilon(\Theta^*) - G = 0. \qquad (8)$$

By using the calculated $Z(\Theta)$ and properly varying the parameter G, we can find the values of U that satisfy Eq. (8) (table). Taking the screening into account, both the values of the quantities U and G (see, for instance, [15]) and the relation between them ($G < U$) appear reasonable (because G describes the Coulomb interaction between an electron and a hole located in different atomic shells, while U characterizes the interaction between electrons in the same shell). The calculated change ΔW is plotted in Fig. 4 within the coverage interval from $\Theta = 0$ to $\Theta^* = 0.35$. We readily see that, first, an increase in the parameters U and G leads to a shift of $\Delta W(\Theta)$ toward negative values and, second, in the case illustrated by Fig. 4a, $\Delta W(\Theta)$ is a monotonic function, whereas in the case of Fig. 4b, the $\Delta W(\Theta)$ curve has a minimum. A comparison of Figs. 3 and 4 suggests the conclusion that the presence of a minimum in the dependence of the work function $\varphi(\Theta) = \varphi_0 + \Delta\varphi(\Theta)$ on coverage accounts for the minimum in $\Delta W(\Theta)$. Of particular interest is curve *1* in Fig. 4b, which demonstrates the existence of a threshold at coverages $\Theta_{th} < 0.05$, where ΔW becomes negative and ESD of Eu neutrals sets in. It is this concentration threshold ($\Theta_{th} \sim 0.03$) that was observed experimentally in [2]. Thus, we have obtained one more confirmation of europium atom desorption following scenario 1.

Thus, estimates show that the 33-eV peak itself and its concentration dependence are determined by the first stage in ESD, more specifically, by the transfer of a 5*p* electron of the europium adatom to its unfilled outer shell quasilevel, a process accompanied by plasmon excitation in the substrate. The same effect is observed in the case of an x-ray-produced hole [9].

The plasmon subsystem excitation, which is concomitant with the ESD of europium atoms, accounts for the anomalous width (~10 eV) of the resonant 33-eV peak. Even if the quasilevel hybridized with the oxygen band is sufficiently narrow (≤1–3 eV), the set of plasmon frequencies (which can exist in such a complex system) with far from small dispersion (see, e.g., [16])

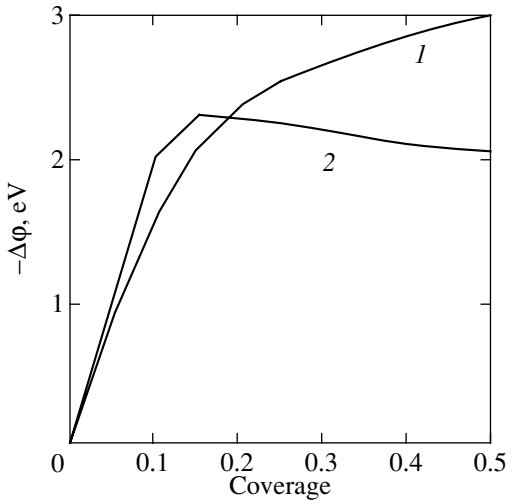

Fig. 3. Change in the work function ($-\Delta\varphi$) plotted as a function of coverage Θ in the equilibrium state for Γ equal to (*1*) 1 and (*2*) 0.25 eV.

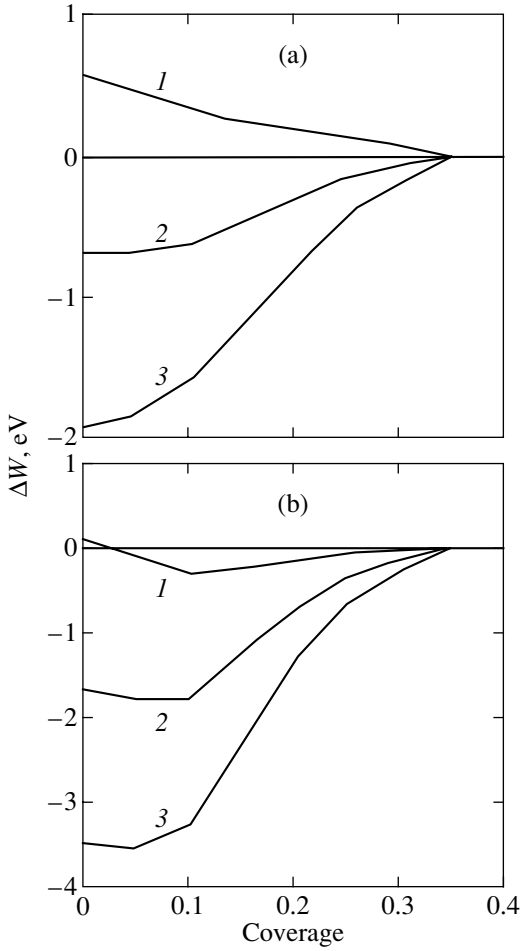

Fig. 4. Difference between the excited-state energies ΔW plotted as a function of coverage Θ for Γ equal to (a) 1 and (b) 0.25 eV; $G = 1$ (curve *1*), 2 (*2*), and 3 eV (*3*).

Calculated values of the electron repulsion energy U

G, eV	U, eV	
	$\Gamma = 1$ eV	$\Gamma = 0.25$ eV
1	2.41	1.53
2	3.87	2.86
3	5.34	4.18
4	6.81	5.50
5	8.27	6.82

is large enough to account for the energy width of the 33-eV peak.

ACKNOWLEDGMENTS

The author is indebted to V.N. Ageev, Yu.A. Kuznetsov, and N.D. Potekhina for stimulating discussions.

This study was supported by the Russian Foundation for Basic Research (project no. 99-02-17972) within the Russian Federal program "Atomic Surface Structures" (project no. 4.5.99).

REFERENCES

1. V. N. Ageev and Yu. A. Kuznetsov, Pis'ma Zh. Tekh. Fiz. **26** (13), 86 (2000) [Tech. Phys. Lett. **26**, 579 (2000)].
2. V. N. Ageev, Yu. A. Kuznetsov, and N. D. Potekhina, Fiz. Tverd. Tela (St. Petersburg) **43** (10), 1894 (2001) [Phys. Solid State **43**, 1972 (2001)].
3. V. N. Ageev, O. P. Burmistrova, and Yu. A. Kuznetsov, Usp. Fiz. Nauk **158** (3), 389 (1989) [Sov. Phys. Usp. **32**, 588 (1989)].
4. V. N. Ageev, Prog. Surf. Sci. **47** (1/2), 55 (1994).
5. S. Yu. Davydov, Pis'ma Zh. Tekh. Fiz. **27** (7), 68 (2001) [Tech. Phys. Lett. **27**, 295 (2001)].
6. S. Yu. Davydov, Fiz. Tverd. Tela (St. Petersburg) **43** (9), 1710 (2001) [Phys. Solid State **43**, 1783 (2001)].
7. S. Y. Davydov, Surf. Sci. **407** (1–3), L652 (1998).
8. S. Y. Davydov, Surf. Sci. **411** (1–3), L878 (1998).
9. J. W. Gadzuk and S. Doniach, Surf. Sci. **77** (3), 427 (1978).
10. A. A. Radtsig and B. M. Smirnov, *Reference Data on Atoms, Molecules, and Ions* (Énergoatomizdat, Moscow, 1986; Springer, Berlin, 1985).
11. J. P. Muscat and D. M. Newns, J. Phys. C **7** (15), 2630 (1974).
12. S. Y. Davydov, Appl. Surf. Sci. **140** (1), 52 (1999).
13. S. Yu. Davydov, Fiz. Tverd. Tela (St. Petersburg) **41** (9), 1543 (1999) [Phys. Solid State **41**, 1413 (1999)].
14. *Handbook of Physical Quantities*, Ed. by I. S. Grigoriev and E. Z. Meilikhov (Énergoatomizdat, Moscow, 1991; CRC Press, Boca Raton, 1997).
15. W. A. Harrison, Phys. Rev. B **31** (4), 2121 (1985).
16. N. H. March and M. Parrinello, *Collective Effects in Solids and Liquids* (Hilger, Bristol, 1982; Mir, Moscow, 1986).

Translated by G. Skrebtsov

Physics of the Solid State, Vol. 44, No. 2, 2002, pp. 395–398. Translated from Fizika Tverdogo Tela, Vol. 44, No. 2, 2002, pp. 379–382.

POLYMERS AND LIQUID CRYSTALS

Third Harmonic Generation in Copolymer Films with Optically Nonlinear N-Substituted 4-Nitroazobenzene in the Side and Main Polymer Chains

G. K. Lebedeva*, N. L. Loretsyan*, V. N. Ivanova*, K. A. Romashkova*, V. A. Lukoshkin, and V. V. Kudryavtsev***

**Institute of High-Molecular Compounds, Russian Academy of Sciences, St. Petersburg, 199004 Russia*
e-mail: kudryav@hq.macro.ru
***Ioffe Physicotechnical Institute, Russian Academy of Sciences, Politekhnicheskaya ul. 26, St. Petersburg, 194021 Russia*
e-mail: V.Lukosh@pop.ioffe.rssi.ru
Received May 22, 2001; in final form, June 25, 2001

Abstract—The third-order nonlinear optical susceptibility $\chi^{(3)}(3\omega; \omega, \omega, \omega)$ of two types of copolymer films containing optically nonlinear N-substituted nitroazobenzene in the side (methacrylic series copolymers) and main (copolyimidoamido esters) polymer chains is investigated using the third harmonic generation method at a wavelength of 1.064 μm. © *2002 MAIK "Nauka/Interperiodica".*

1. Nonlinear optical (NLO) materials have attracted the growing interest of researchers owing to their great potential applications in various fields (e.g., telecommunication, optical systems of information storage and processing, and purely optical system controlling luminous fluxes). Organic compounds, for example, dyes with a developed system of delocalized π electrons, which contain polar substituents of the donor–acceptor type, occupy a significant place among such materials. These compounds are distinguished by high values of nonresonant NLO susceptibility, a quick electron response, a high radiation resistance, and a low loss level. In addition, the unlimited potential of organic synthesis makes it possible to synthesize purposefully high-quality optical materials with preset properties. Film-forming polymers are materials used as matrices for this type of NLO compound (NLO chromophores). The form of organization of chromophore molecules in a film determines, to a considerable extent, the effectiveness of the nonlinear properties of the medium [1–3].

Polymer materials with covalently attached chromophore groups making the main contribution to the hyperpolarizability of the system are extremely promising because they can be used to obtain multifunctional optically homogeneous and structurally ordered films with a high chromophore concentration [4].

It is well known that the N-substituted 4-nitroazobenzene dye possesses high hyperpolarizabilities of the lowest order β and the high chemical and thermal stability required for the operation of optoelectronic devices [5]. The publications relevant to analysis of the NLO properties of polymer materials containing this chromophore are mainly devoted to the study of second-order NLO properties. The third-order NLO response, determining the light-induced variation of the refractive index $\Delta n(I)$ (I is the intensity of exciting radiation) and ensuring the optical control of luminous fluxes in the medium [6], has been studied insufficiently. It is known that the contribution to the nonlinear change Δn comes from various processes (thermal, orientations, etc). Electronic processes, which are sensitive to variations in the controlling optical radiation in real time, appear to be the most attractive from the viewpoint of optoelectronic applications. The third-harmonic generation (THG) technique is perfectly suitable for measuring third-order electronic optical nonlinearity. The process of harmonic generation involves only optical frequencies and is too fast to be followed by orientational, vibrational, or rotational processes.

In the present work, the THG method is used to study the NLO properties of two types of new film-forming multifunctional copolymers of methyl methacrylates and copolyimidoamido ethers with N-substituted 4-nitroazobenzene in the side and main chains (Figs. 1–3).

Copolymer I contains side links in the form of fluoroalkyl radicals and of chromophores that are derivatives of cinnamic acid. Fluoroalkyl radicals make it possible to obtain structurally ordered films using the Langmuir–Blodgett technique. Fragments of cinnamic acid are capable of creating coarse-mesh structures upon UV irradiation and of stabilizing the orientation of NLO chromophores.

The main chains of copolymers II–IV contain structural elements of different electron origin: electron-acceptor imide fragments and electron-donor fragments (derivatives of 2-phenyl benzimidazole) capable of participating in intra- and interchain interaction and

1063-7834/02/4402-0395$22.00 © 2002 MAIK "Nauka/Interperiodica"

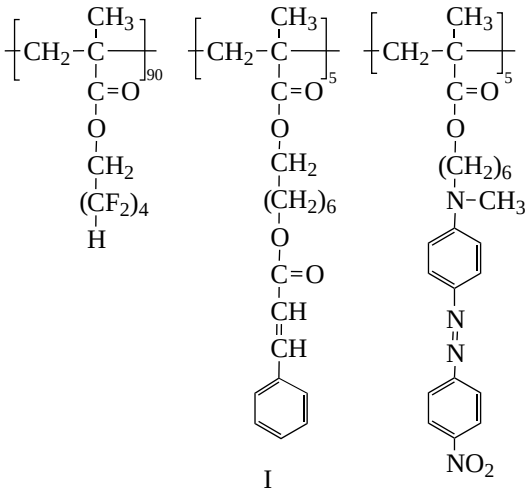

I

Fig. 1. Structural formula of copolymer I based on methyl methacrylates.

of inducing the photoconductivity property in the copolymers. The combination of this property with the NLO activity of the copolymer is a necessary condition for the holographic recording of information.

2. The ^{1}H NMR spectra were recorded on a Bruker AC-200 device (200.1 MHz) in relation to solvent signals. The electronic absorption spectra were obtained on a Specord M-40 spectrophotometer. Copolymer films were subjected to mechanical testing on a UTS-10 universal machine (manufactured at the German UTS Test System Company). The films were prepared by pouring the corresponding polymer solutions onto glass substrates, followed by stepwise drying at temperatures of 50, 80, 100, 120, and 150°C for 6 h at 50°C and for 1 h at the other temperatures. During testing, the stress–strain diagram of a sample was recorded. The softening temperature T_s was determined using differential scanning calorimetry (DSC) on a DSM-2M calorimeter at a scanning rate of 16°C/min [the weighed portion was 0.02 g; the threshold sensitivity was 10^{-4} W (for copolymers of methacrylates)], as well as using the thermomechanical method on a UMIV-3 device at a heating rate of 5°C/min and under a tensile stress of 0.25 MPa (copolyimidoamido ethers).

Copolymer I was synthesized through radical polymerization of octafluoroamylmethacrylate, methacryloyl oxyhexyl cinnamate, and N-substituted 4-nitroazobenzene methacrylate in a ratio of 90 : 5 : 5 mol % in a 15% solution of dimethyl acetamide (DMMA) in the presence of 0.4 wt % benzoyl peroxide at 60°C for 20 h in ampules in the atmosphere of an inert gas. A copolymer separated in the form of a thin film on the water surface and was purified through reprecipitation of the solution in acetone by water. The samples were dried in vacuum at 60°C to constant weight. The copolymer yield after double reprecipitation was 80%; i.e., a relatively high-molecular fraction was separated. The characteristic viscosity in cyclohexanone was 0.144×10^2 g cm^{-3} and T_g = 280°C according to the DSC data.

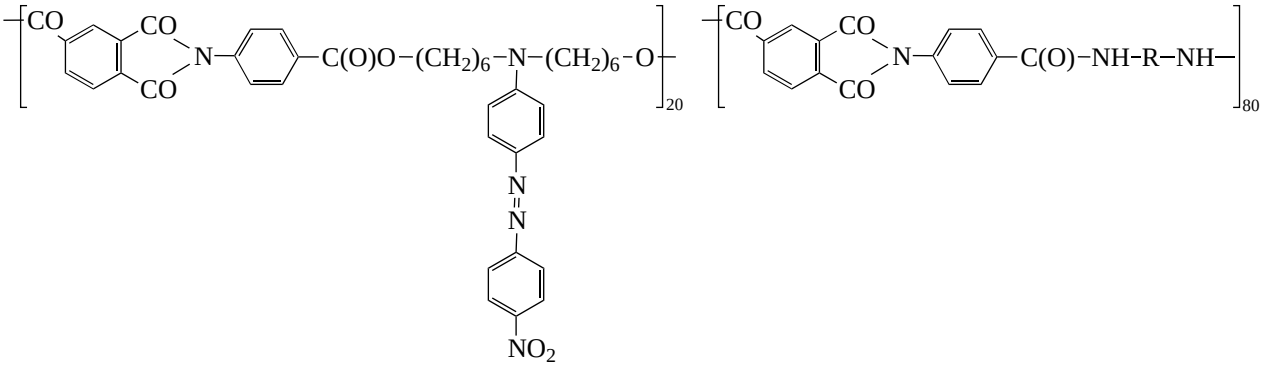

II, III

II: R =

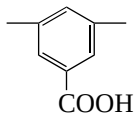

III: R =

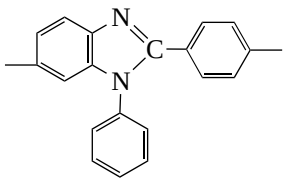

Fig. 2. Structural formulas of copolyimidoamido esters II and III.

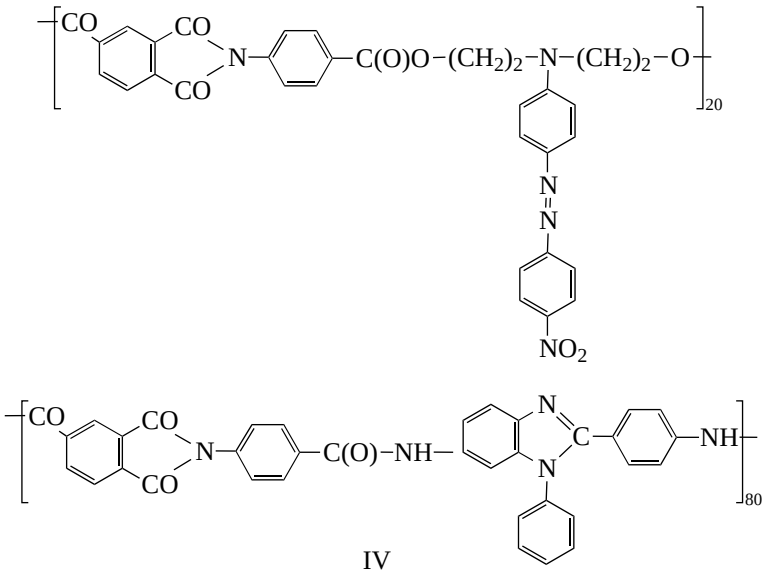

IV

Fig. 3. Structural formula of copolyimidoamido ester IV.

The ^{1}H NMR spectrum of a chromophore in a copolymer (deuterized acetone $(CD_3)_2CO$ was used as a standard) corresponds to the following contents δ, ppm: 1.45–1.72 (CH_2), 3.16 (NCH_3), 3.56 (NCH_2), 4.05 (CH_2O), 7.39–8.00 (Aryl, where Aryl stands for aromatic cycle), and 8.40 (Aryl-NO_2).

The ratio of fragments in the copolymer is estimated from the ratio of the signals from individual groups in the ^{1}H NMR spectrum.

The UV spectrum of a copolymer-I film has a long-wavelength absorption peak at λ = 473 nm.

Copolyimidoamido esters II–IV were synthesized through low-temperature copolycondensation in a DMAA solution according to the techniques described in [7, 8] and were purified through reprecipitation from the solution in DMAA into water and extraction of the unreacted amount of dye by chloroform during boiling in a Soxhlet apparatus. The yield was 50–70%.

The ^{1}H NMR spectra of solutions of copolymers II–IV in deuterated dimethyl sulfoxide (DMSO-d_6) contain signals typical of a chromophore fragment and correspond to the following contents δ, ppm: 1.30–1.80 (CH_2), 3.46 (NCH_2), 4.35 (CH_2O), and 6.80 (Aryl).

The fraction of fragments with a chromophore in the copolymer (15%) was estimated from the ratio of the signals from individual groups in the ^{1}H NMR spectrum.

The UV spectra of copolymer-II–IV films have a long-wavelength absorption peak at λ = 525 (II), 515 (III), and 490 nm (IV).

Copolymer films possess good stress–strain properties: the breaking strength lies between 100 and 120 MPa, and the elongation per unit length amounts to 25%. The thermal characteristics are high; the mass loss temperature is τ_0 = 330–430°C.

The NLO properties of the synthesized copolymers were estimated using the THG method. Pumping of the samples in the form of films 1 μm thick on a cover glass was carried out by a pulsed YAG : Nd^{3+} laser operating at a wavelength of 1.064 μm. The laser operated in the Q-switching mode with a pulse duration of 15 ns. The radiant energy in a pulse was varied to up to 30 mJ. The Gaussian spatial profile of the laser beam was set by selecting the higher transverse modes with the help of an intracavity diaphragm. The *P*-polarized beam was focused on the sample through a convex spherical lens with f = 100 mm. A part of the beam was split by a splitter and directed to a calibrated photodiode FD-24K for monitoring of the pumping pulse energy. The third harmonic radiation was directed by a system of lenses to the inlet slit of a grating monochromator (MDR-2) and then to a photomultiplier (FEU-106). Electric signals from both photodetectors were fed to integrating analog-to-digital converters and then, through the apparatus interface CAMAC, to a personal computer for subsequent processing.

The NLO susceptibility of polymer films was estimated through comparison with a standard sample under identical conditions (a 1-mm thick fused quartz plate oriented using the first intensity peak of the Maker fringes for the third harmonic) [9]. The values of $\chi^{(3)}(3\omega; \omega, \omega, \omega)$ for the copolymers were 3.7×10^{-13} esu (I) and $(1.5–2.6) \times 10^{-13}$ esu (II–IV).

3. Thus, new optically transparent film-forming multifunctional copolymers with an NLO-active chromophore [N-substituted 4-nitroazobenzene in the side (copolymethacrylates) and main (copolyimidoamido esters) chains] were synthesized.

It is shown that the films of the synthesized copolymers possess NLO activity (third harmonic); the value of $\chi^{(3)}$ amounts to 3.7×10^{-13} esu for copolymethacrylates and $(1.5–2.6) \times 10^{-13}$ esu for copolyimidoamido esters; i.e., the polymer matrix exhibiting strong intra- and interchain interactions weakly affects the NLO properties of a chromophore.

The films of the synthesized polymers are of interest for further investigations into NLO properties.

ACKNOWLEDGMENTS

The authors are grateful to the staff members of the Department of Chemical Technology of Organic Dyes and Phototropic Compounds of the St. Petersburg State Technological Institute L.I. Rudaya and N.V. Klimova for providing the samples of 2-phenylbenzimidazole derivatives and for scientific consultations.

REFERENCES

1. Naoto Tsutsumi, Osamu Matsumoto, and Wataru Sakai, ACS Symp. **672** (11), 151 (1997).
2. R. D. Miller, D. M. Burlanot, M. Yurich, *et al.*, ACS Symp. Ser. **672** (8), 100 (1997).
3. R. Centore, S. Concilio, B. Panunzi, *et al.*, J. Polym. Sci., Part A: Polym. Chem. **37**, 603 (1999).
4. M. Dobler, Ch. Weder, P. Neuenschwander, and Ulrich W. Suter, Macromolecules **31**, 6184 (1998).
5. O. A. Antsipetrov, N. N. Akhmediev, I. M. Baranova, *et al.*, Zh. Éksp. Teor. Fiz. **89**, 911 (1985) [Sov. Phys. JETP **62**, 524 (1985)].
6. V. V. Shelkovnikov, V. P. Safonov, A. I. Plekhanov, and F. A. Zhuravlev, Zh. Strukt. Khim. **34** (6), 90 (1993).
7. V. A. Gusinskaya, M. M. Koton, T. V. Batrakova, and K. A. Romashkova, Vysokomol. Soedin., Ser. A **18** (12), 26 (1976).
8. V. V. Korshak, S. V. Vinogradova, V. A. Vasnev, *et al.*, Vysokomol. Soedin., Ser. A **16** (11), 2456 (1974).
9. K. Kubodera and H. Kobayashi, Mol. Cryst. Liq. Cryst. Sci. Technol., Sect. A **182**, 103 (1990).

Translated by N. Wadhwa